nuclear fusion
IAEA

REVIEW • OPEN ACCESS

Diagnostics: Chapter 8 of the special issue: on the path to tokamak burning plasma operation

To cite this article: D. Mazon *et al* 2025 *Nucl. Fusion* **65** 113001

OPEN ACCESS
IOP Publishing | International Atomic Energy Agency
Nuclear Fusion
Nucl. Fusion **65** (2025) 113001 (195pp)
https://doi.org/10.1088/1741-4326/adfc7c

Diagnostics

Chapter 8 of the special issue: on the path to tokamak burning plasma operation

D. Mazon[1,*], G. Vayakis[2], M. Walsh[2], G. Yun[3], S.-H. Hong[4], B. Peterson[5], M.H. Aumeunier[1], A. Bultel[6], C. Klepper[7], D. Rasmussen[7], H. Choi[8], C. Grisolia[1], K. Kim[8], S. Oh[8], C. Sun[8], M. Scholz[9], B. Esposito[2], D. Marocco[10], F. Belli[10], L. Bertalot[2], B. Coriton[2], V. Ginv[2], D. Gin[2], J. Dankowski[2], A. Hjalmarsson[11], V. Krasilnikov[2], G. Ericsson[11], M. Tardochi[12], D. Rigamonti[12], M. Nocente[12], M. Garcia-Munoz[13], M. Ishikawa[14], M. Cheon[8], J. Jo[15], S. Zoletnik[16], O. Asztalos[16,17], M. Bandyopadhay[18], P. Bharathi[18], M. de Bock[2], O. Ford[19], M.G. von Hellermann[20], D.W. Johnson[21], J. Ko[8], S. Menmuir[22], Ph. Mertens[20], A.H. Nielsen[23], G.I. Pokol[16,17], S.V. Serov[2], M.J. Singh[18], S.N. Tugarinov[24], G.L. Vyas[18], M.G. O'Mullane[25], Ling Zhang[26], R. Barnsley[2], R. Tieulent[2], D. Colette[2], V.S. Neverov[27], R. Scannell[28], H. Liu[26], E. Mukhin[29], E. Yatsuka[14], A. Gorbunov[27], L. Giudicotti[30], G. Kurskiev[29], J. Chen[10], M.A. Van Zeeland[4], D. Finkenthal[31], R. Imazawa[32], D. Brower[33], A. Sirinelli[2], T. Akiyama[4], T. Carlstrom[4], M. Lesher[4], C. Watts[2], M. Bassan[2], M. Austin[34,4], S.B. Korsholm[35], Y. Liu[2,26], S. Danani[18], C. Muscatello[2], W.L. Rowan[34], V. Vershkov[24], G. Wang[33], J.L. Xie[36], M. Zerbini[10], Y.L. Zhu[37], I. Ďuran[38], A. Gusarov[39], K. Vukolov[27], A. Litnovsky[40], L. Moser[2,41], N. Babinov[29], A. Dmitriev[41,29], B. Kim[5], L. Marot[41], A. Razdobarin[29], A. Rogov[42], D. Samsonov[29], C. Seon[43], K. Soni[41], R. Yan[26], M.R. de Baar[44,45], L. Zabeo[2], M. Schneider[2], Th. Blanken[44,45], Th. Bosman[44], T. Ravensbergen[2], B. van de Boorn[44], C. Orrico[45], R. Fischer[46], A. Bock[46], S.S. Denk[4], A. Medvedeva[47], M. Salewski[48], D. Stieglitz[46], the ASDEX Upgrade Team[a] and the WEST Team[b]

[1] CEA, IRFM F-13108, Saint Paul Lez Durance, France
[2] ITER Organization, Route de Vinon sur Verdon, CS 90 046–13067 Saint Paul Lez Durance Cedex, France
[3] Department of Physics and Division of Advanced Nuclear Engineering, Pohang University of Science and Technology, Pohang, Gyeongbuk 37673, Korea, Republic Of
[4] General Atomics, San Diego, CA, United States of America
[5] National Institute of Fusion Science, Toki, Japan
[6] CORIA, Saint-Etienne du Rouvray Cedex, France
[7] Oak Ridge National Laboratory, Oak Ridge, United States of America
[8] Korea Institute of Fusion Energy, Daejeon, Korea, Republic Of
[9] Institute of Nuclear Physics Polish Academy of Sciences, Krakow, Poland
[10] Associazione Euratom-ENEA sulla Fusione, Frascati, Roma, Italy
[11] Department of Physics and Astronomy, Uppsala University, Uppsala, Sweden
[12] Institute for Plasma Science and Technology, National Research Council, Milan 20125, Italy

[a] See Zohm *et al* 2024 (https://doi.org/10.1088/1741-4326/ad249d) for the ASDEX Upgrade Team.
[b] http://west.cea.fr/WESTteam.
[*] Author to whom any correspondence should be addressed.

[13] Department of Atomic, Molecular and Nuclear Physics, University of Seville, 41012 Seville, Spain
[14] Fusion Research and Development Directorate, Japan Atomic Energy Agency, Naka, Ibaraki 311-0193, Japan
[15] Department of Energy Systems Engineering, Seoul National University, Seoul, Korea, Republic Of
[16] Centre for Energy Research, Budapest, Hungary
[17] Budapest University of Technology and Economics, Budapest, Hungary
[18] ITER-India, Institute for Plasma Research, Gandhinagar, India
[19] Max-Planck Institut für Plasmaphysik, Greifswald, Germany
[20] Forschungszentrum Jülich, Jülich, Germany
[21] Princeton Plasma Physics Laboratory, Princeton, NJ, United States of America
[22] KTH Royal Institute of Technology, Stockholm, Sweden
[23] Technical University of Denmark, Kgs. Lyngby, Denmark
[24] Institution 'Project Center ITER', Moscow, Russian Federation
[25] Department of Physics, University of Strathclyde, Glasgow G4 0NG, United Kingdom of Great Britain and Northern Ireland
[26] Institute of Plasma Physics, Chinese Academy of Sciences, Hefei 230031, China
[27] National Research Centre 'Kurchatov Institute', Moscow 123182, Russian Federation
[28] UKAEA, Culham Science Centre, Abingdon OX14 3DB, United Kingdom of Great Britain and Northern Ireland
[29] Ioffe Physical Technical Institute, 26 Polytechniheskaya, 194021 St Petersburg, Russian Federation
[30] Department of Physics and Astronomy, Padova University, Via Marzolo 8, 35131 Padova, Italy
[31] Palomar Scientific Instruments, San Marcos, CA 92069, United States of America
[32] National Institutes for Quantum and Radiological Science and Technology, Naka, Japan
[33] Department of Physics and Astronomy, University of California Los Angeles, Los Angeles, CA 90095, United States of America
[34] Institute for Fusion Studies, University of Texas at Austin, Austin, TX 78712, United States of America
[35] Department of Physics, Technical University of Denmark, 2800 Kgs. Lyngby, Denmark
[36] University of Science and Technology of China, Hefei, China
[37] Department of Electrical and Computer Engineering, University of California, Davis, CA 95616, United States of America
[38] Institute of Plasma Physics of the Czech Academy of Sciences, Prague, Czech Republic
[39] SCK CEN, B-2400 Mol, Belgium
[40] Forschungszentrum Jülich GmbH, Institut für Energie und Klimaforschung, 52425 Jülich, Germany
[41] University of Basel, Klingelbergstrasse 82, CH-4056 Basel, Switzerland
[42] Fusion Centre, 123182 Moscow, Russian Federation
[43] National Institutes for Quantum Science and Technology, Naka, Ibaraki 801-1, Japan
[44] NWO Institute DIFFER, De Zaale 20, Eindhoven, Eindhoven, Netherlands
[45] Technische Universiteit Eindhoven, Eindhoven, Netherlands
[46] Max-Planck-Institut für Plasmaphysik, Garching, Germany
[47] Aix Marseille University, CNRS, Centrale Marseille, M2P2, Marseille, France
[48] Department of Physics, Technical University of Denmark, Kgs. Lyngby, Denmark

E-mail: didier.mazon@cea.fr

Received 6 January 2025, revised 29 July 2025
Accepted for publication 18 August 2025
Published 10 October 2025

Abstract

This chapter presents the activity conducted by the ITPA topical group (TG) on Diagnostics over about the last 15 years. Following a general introduction of the ITER Diagnostics led by their measurement roles, the document is organized in several subchapters detailing the design support, research and development activity conducted by each of the specialist working groups (WGs) of the TG. Please note that the magnetic diagnostics were supported at the TG without a specific WG. Their status is included in the general introduction. In the following some highlights of the subchapter's contents are provided. Recent advances in ITER first wall (FW) diagnostics for the measurements of plasma-metallic wall interaction in support of the ITER research plan are reported. An InfraRed imaging Video Bolometer for ITER has been developed and tested on several tokamaks to measure the radiated power loss. A laser-induced breakdown spectroscopy (LIBS) technique which utilizes a pulsed laser beam to ablate locally by

forming a crater, will measure local tritium inventory in the FW material. Real-time Residual Gas Analyzers will measure the neutral gas composition in a divertor port and an equatorial port during plasma operation. Due to the full metallic FW environment, the plasma-wall interaction in ITER will face several challenges such as the compromised radiated power and divertor heat flux measurements by reflection. Ray tracing and analysis codes have been developed to eliminate and correct the effects of reflection in the measurements. The characteristics of the reflecting surfaces depending on the roughness and angle of the incidence have been measured by dedicated experiments, and the results were applied to the reflection elimination. For the measurement of the metallic impurity radiation induced by eroded metallic atoms, a vacuum ultraviolet spectrometer has been developed and tested. An extensive thermonuclear diagnostic suite will be required to support the operation of ITER and the planned experimental program for future burning plasma experiments. Due to the harsh environmental conditions, the implementation of diagnostic systems in ITER is a major challenge. These conditions include high levels of neutron and gamma fluxes, neutron heating, particle bombardment. Therefore, the selection and design of diagnostic systems must take into account a number of phenomena previously unseen in diagnostic design. For this reason, the measurement of neutrons and confined or lost fast ions, with particular emphasis on alpha particles, is critical to ITER. The diagnostics associated with these measurements will be important for future plasma-burning experiments at ITER. The high neutron emission and very large plasma size in ITER make neutron diagnostics the main diagnostic method used to measure plasma parameters such as fusion power, fusion power density, ion temperature, energy of fast ions and their spatial distributions in the plasma core. Active spectroscopy techniques are methods where a neutral particle beam is injected into the plasma and information on plasma parameters is extracted from the measurement of line emission resulting from the beam-plasma interaction, either by plasma ions or by beam atoms. Spatial localization is achieved by crossing the beamline and multiple observation lines. The ITER plasma will be a high temperature, moderately dense, fully ionized collisional plasma. The plasma facing surfaces are principally metallic being fashioned from beryllium or tungsten but many other elements, arising from either structural or from operational needs, may enter this plasma. The energy range of the emitted photons range from meV (infra-red) to multi keV (x-rays) and originate from all areas of the plasma volume. The primary role of passive emission diagnostics is to identify what is in the plasma from spectral signatures. Extracting quantitative information from these measurements such as impurity content, ion temperature, rotation, degree of detachment and radiated power depends on calibrated instruments, a physics model of the atomic and molecular processes and plasma transport and an analysis workflow that takes into account environmental effects such as reflections. The particular needs for ITER have prompted a multi-machine, many-year effort to address all these aspects and this chapter reviews the work on diagnostic design, experiments and new analysis techniques. An overview of the laser diagnostics to be implemented on ITER is also provided in this paper. This includes descriptions of the Thomson scattering in the core, edge and divertor regions, polarimetry and interferometry diagnostics used for measuring plasma density and also measurements of helium density in the divertor using Laser Induced Flourescence. Techniques which can allow improvements on current measurements are also addressed in particular expanding poloidal polarimetry measurements to measure field fluctuations and proposed use of dispersion interferometery which has a number of advantages over existing methods. This paper identifies particular areas where further research and testing on existing tokamaks is useful even at this advanced stage to inform the design of diagnostics for ITER. Outstanding areas of concern for the implementation of laser diagnostics, in particular with a view to reliable operation are identified. An overview of the latest developments of microwave diagnostic systems and techniques is given. The primary focus is the contributions for ITER—the next step burning plasma experiment—which is supplemented by describing recent progress of techniques applicable for fusion experiments beyond ITER. The contributions are intentionally kept concise, and are being supplemented by a rich list of references for further studies. Radiation induced effects are receiving continuous and well-deserved attention of the ITER diagnostic community and they are in many cases one of the primary design drivers of the ITER diagnostic systems. The paper summarizes recent progress in this area focusing primarily on the ITER diagnostics but in some cases provides also outlook for the possible solutions for even more demanding radiation environment of fusion reactors beyond ITER. Despite advancements in the area of modeling and simulation of various radiation induced effects,

experimental testing in a nuclear environment as close as possible to the target one is still seen as unavoidable for proper qualification of particular diagnostic functional elements. Recent advancement within three diagnostic areas: optical diagnostics, magnetics and bolometers is covered. Encouraging results on qualification of silica glass vacuum window assemblies are presented. In the area of magnetic sensors, progress of irradiation tests performed on ITER in-vessel LTCC inductive sensors is presented with outlook for novel technological approaches to inductive sensors utilizing thick printing and photolithography technologies being highlighted. Summary of advancements in the area of steady state magnetic field sensors based on Hall effect is given. New results of neutron irradiation test of the ITER borosilicate glass inserts for vacuum electrical feedthroughs are summarized finding negligible swelling at target level of neutron fluence. Off-line irradiation tests of fiber optic current sensors for plasma current measurement demonstrated that both for gamma doses up to 5 MGy and a total neutron fluence up to 10^{15} cm^{-2}, radiation induced changes are still compatible with required measurement accuracy on ITER. The ITER bolometers are given as an example how considering radiation effects may influence the diagnostic design. Finally, outlook for future main R&D directions is outlined. All optical and laser-based diagnostics in ITER will be using mirrors to guide plasma radiation toward detectors, cameras and sensors. In the hostile plasma, radiation and particle environment the optical characteristics of diagnostic mirrors will degrade directly affecting the entire performance of involved diagnostic systems. An assessment of factors affecting mirror performance is provided. Among the prime adverse factors are deposition of plasma impurities, sputtering of mirror surface and steam ingress in the vicinity of mirrors. Within the International Tokamak Physics Activity with active support by ITER central team and domestic agencies, the structured research and development (R&D) program on mitigation of risks for diagnostic mirrors is underway. Within this program the mirror material development, the passive mitigation of mirror degradation by using diagnostic ducts and shutters along with an active mirror recovery program comprising the *in-situ* mirror cleaning and calibration is underway. Recent developments in diagnostic mirror R&D are described in this Chapter along with an example of their implementation of R&D solutions in ITER Infrared Thermography diagnostic. An assessment of still open engineering and physics questions, considerations on mirror risks during an early phase of ITER operation are given along with an overview of diagnostic mirror evolution in the late ITER operation stage toward the demonstration fusion power plant. Several crucial areas of diagnostic R&D outlined in ITER Research Plan are addressed. The basic control groups in a fusion reactor can be broken-down in five categories: (1) plasma position, magnetic configuration, and plasma current control, (2) profile control and confinement optimization, (3) MHD control and suppression, (4) edge dissipation control, radiation and plasma exhaust control and (5) break-down optimization. These categories are coupled via the physics (a control action in one domain will affect the other domains) and via shared actuators (e.g. ECRH for impurity accumulation avoidance, current density distribution control and MHD suppression). Consequently, a supervisory control system should determine the priority of the various control tasks, their couplings, and the interfaces with the safety and interlock system. For the systematic development of the various controllers taking the complexity of the plasma and the control system into account, a model-based approach is required. A short historical overview is given of the developments in systems and control theory and control engineering with special emphasis on those developments that are most relevant for Nuclear Fusion research and operation. An overview is given of the state of the field of fusion plasma control for the control categories. It will be shown how synthetic diagnostics are being developed in ITER and how they are used in diagnostic design and design validation and how they can be in model-based controller synthesis using relatively simple models. In modern control methods, multiple diagnostics are used to constrain relatively simple models. The constrained models provide an estimate for the state. This opens the route to state controllers, such as model predictive control. A major challenge in nuclear fusion research is the coherent combination of data from heterogeneous diagnostics and modeling codes for machine control and safety as well as physics studies. Measured data from different diagnostics often provide information about the same subset of physical parameters. Additionally, information provided by some diagnostics might be needed for the analysis of other diagnostics. A joint analysis of complementary and redundant data allows, e.g. to improve the reliability of parameter estimation, to increase the spatial and temporal resolution of profiles, to obtain synergistic effects, to consider diagnostics interdependencies and to find and resolve data

inconsistencies. Physics-based modeling and parameter relationships provide additional information improving the treatment of ill-posed inversion problems. A coherent combination of all kind of available information within a probabilistic framework allows for improved data analysis results. The concept of integrated data analysis (IDA) in the framework of Bayesian probability theory is outlined and contrasted with conventional data analysis. Components of the probabilistic approach are summarized and specific ingredients beneficial for data analysis at fusion devices are discussed.

This paper is part of the Special Issue: *On the Path to Tokamak Burning Plasma Operation: A collection of papers prepared by the ITPA Topical Physics Groups reviewing progress in the development of the physics basis for burning plasma operation*.

Keywords: diagnostics, ITER, radiated power loss, neutron irradiation, diagnostic mirrors, real-time, plasma control, integrated data analysis

(Some figures may appear in colour only in the online journal)

Contents

1. Introduction to diagnostic measurement in ITER 6
2. Preparation for the measurements of plasma-metallic wall interaction in support of the ITER research plan: divertor power flux, impurity, and tritium retention 29
3. Status of the diagnostics of fusion products at ITER 39
4. Progress in ITER diagnostics, active spectroscopy 63
5. Passive emission diagnostics for high performance metal tokamaks 78
6. Laser aided diagnostics 93
7. Microwave diagnostics 110
8. Influence of radiation effects on the refinement of the ITER design 124
9. Diagnostic mirrors for ITER: status and perspectives 134
10. Synthetic diagnostics for real time plasma control studies and diagnostic design 150
11. Integrated data analysis and validation 161

References 178

1. Introduction to diagnostic measurement in ITER

Didier Mazon[1], George Vayakis[2], Michael Walsh[2] and Gunsu Yun[3]

1.1. Introduction

This summary of the state of burning plasma diagnostics by the International Tokamak Physics Activity (ITPA) Diagnostics topic group (TG) finds ITER and its diagnostics mid-construction. This is a marked change from previous records of the state of ITER and burning plasma measurements and diagnostics. The 1995 Varenna conference saw the first airing of the ITER diagnostic set and its requirements in an integrated form [1]. By the end of the first ITER Engineering Design Activity phase [2, 3] these were consolidated and are visibly correlated with the present designs and requirements. The 'Progress in the ITER Physics Basis', in 2007, summarized the ITER diagnostic design as adopted for construction [4]. Since then, diagnostic design and R&D has continued within the ITER design teams with the support of the ITPA, to the point where the details of the design solution and the expected performance are mostly clear. The ITPA diagnostic TG initiated, coordinated and reviewed extensive R&D efforts to support this, through high priority items (HP), Joint Experiments (JEX) and Actions that are summarized in this introductory subchapter and with results elaborated in the subchapters that follow. The adoption of the phased approach to ITER operation [5] resulted in the phasing of diagnostic installation, nevertheless work is ongoing across all systems. In parallel, R&D is still ongoing, as part of the diagnostic supply and as a voluntary effort to support the identified needs in diagnostics.

This subchapter introduces updated roles and requirements for ITER measurements and a summary of the design and R&D basis for these with reference to the subchapters that follow. For magnetics-related measurements, it contains an extensive section on the related diagnostic progress as this topic is not covered elsewhere. Overall, this subchapter summarizes the progress of the key issues identified from the perspective of the ITPA Diagnostics TG, but including progress achieved as part of the ITER construction programme where appropriate.

1.2. Requirements for plasma measurements

Plasma measurement in ITER is organized in measurement groups, evolved from the original groupings of [1] to reflect partly a functional (e.g. divertor operation), partly a technique (e.g. passive spectroscopy) and partly a physical process (e.g. halo current) taxonomy. In tracking progress and coverage of the measurement needs, the specific measurement parameters (MPs) of table 10 have proven more useful than the groups. This table lays out for each parameter the key conditions and performance expected. It is not exhaustive: measurement group 2, plasma position and shape, for example, could list many more parameters and more sophisticated versions of the ones shown. The spirit of this specification is that a state-of-the-art diagnostic set designed to meet it should ensure adequate performance for machine operation parameters related to the one shown.

This table has evolved over time. A full comparison of table 10 to the version used in [4] would show numerous detailed changes in parameter specifications. No 'To be determined' (TBD) values remain in the table. Resolutions are now mostly adapted to the final ITER plasma size. In addition, there are some new groups and requirements on dust, tritium and stray electron cyclotron heating (ECH) monitoring as well as the first safety related plasma measurement requirements, on fusion power and total toroidal current.

1.2.1. MP roles in ITER.

Table 10 defines the specification for the ITER diagnostics. ITER diagnostics designs aim to meet it, sometimes individually, sometimes in combination. In parallel, they target many other requirements including safety, maintainability, reliability and availability. The ITER environment strongly influences the last two, both close to the plasma (particle and radiation emission) and further away (nuclear effects due to neutrons and gammas, access limitations, etc) [6]. The work of the ITPA for radiation effects (section 3.7) and first mirror selection (section 3.8) directly supports the resolution of these reliability and availability issues.

Engineering constraints aside, the measurement role drives the specifications and design of the diagnostic equipment. ITER classifies the *measurement roles* with respect to the importance of each parameter to plasma control in four groups: machine protection (MP), basic control (BC), advanced control (AC) and physics operation (PHY). At the same time, working to meet the measurement specification for each parameter, *diagnostic contributions* can be:

- *Primary:* the contribution (range, resolution accuracy etc) of the diagnostic meets the parameter specification.
- *Backup:* the contribution of the diagnostic is a good match to the parameter but there is a limitation (for example, the diagnostic has to be reconfigured to be a good match compromising some other function, or the range of the parameter is not fully covered) which means it is not intended to be routinely used this way.
- *Supplementary:* the contribution of the diagnostic appears a poor match to the parameter but none the less essential. Examples include calibration of a diagnostic that is primary contributor or having excellent accuracy over a small part of the range.

ITER diagnostic design has, in this context, tried to achieve at least one primary contributor to each parameter, ideally two (to ease availability needs). The tables of section 3, below, summarize the primary contributors for each parameter and for each of the measurement areas.

1.3. Progress in the basis for plasma measurements

Work in the ITPA diagnostics topic group has been organized around specialist working groups (WGs) that have looked after, in the first instance, functional groups of diagnostics with

similar techniques and/or plasma parameters. Progress relevant to ITER research and constructions is summarized for each group in sections 3.1–3.6 below with more details in corresponding subchapters.

In addition to these groups experts are working on issues across multiple systems: radiation effects, first mirrors, real-time diagnostics, and integrated data analysis (IDA). Sections 3.7–3.10 summarize their progress.

Together these groups, comprising several hundred participants, have worked directly on most of the ITER systems and MPs. An exception is the set of magnetic diagnostics that, because of its tight integration both with the core of ITER and plasma control, has been directly managed by the ITER Organization and the EU Domestic Agency, nonetheless strongly benefitting from ITPA support from the works of the cross-functional groups, in particular the radiation effects group. Section 3.11 summarizes recent progress in this area.

1.3.1. First wall (FW) measurements. The ITER FW is metallic and subject to intense fluxes of all kinds. Its surface will evolve during operation, eroding, accruing deposits, absorbing particles and consequently changing its optical, mechanical and thermal properties. The erosion products in turn become a source of deposits to the wall, but also to first mirrors and to dust accumulating on the floor of the machine together with co-deposited tritium. The ITER design includes a number of diagnostics aimed at the related parameters, either of the FW itself or the plasma areas and fluxes directly affecting it (table 1).

The dedicated subchapter 2 reports on recent advances in ITER FW diagnostics for the measurements of plasma-metallic wall interaction in support of the ITER research plan. An InfraRed imaging Video Bolometer (IRVB) for ITER has been developed and tested on several tokamaks to measure the radiated power loss. A laser-induced breakdown spectroscopy (LIBS) technique that utilizes a pulsed laser beam to ablate locally forming a crater, will measure local tritium inventory in the FW material. Real-time residual gas Analyzers (DRGAs) will measure the neutral gas composition in a divertor port and an equatorial port during plasma operation. For the measurement of the metallic impurity radiation induced by eroded metallic atoms, a vacuum ultraviolet (VUV) spectrometer has been developed and tested.

Due to the full metallic FW environment, the plasma-wall interaction in ITER will face several challenges disentangling reflections from radiated power and divertor heat flux measurements. Ray tracing and analysis codes have been developed to eliminate and correct the effects of reflection in the measurements. The characteristics of the reflecting surfaces depending on the roughness and angle of the incidence have been measured by dedicated experiments, and the results were applied to the reflection elimination.

1.3.2. Fusion product (FP) measurements. For ITER, FP diagnostics contribute to a large number of parameters in a primary role, with the fusion power and fluence being key indicators of performance. Table 2 shows the primary contributions. Key backup and supplementary (supporting) contributions are detailed in the dedicated subchapter 3.

In the 2007 summary [4], the performance against parameter 014 (n- and α-source profile) was listed as not yet known and the progenitor of parameters 071 & 072 (alpha particle loss) was listed as expected not to be met. In the intervening years, much progress has been made on neutron calibration with dedicated workshops. Better design definition of the calibration and neutron activation systems (NASs) means the measurement performance for the neutron source profile is now known. Gamma ray spectroscopy is also being developed to track the spatial profile of the fast ions directly. As regards alpha particle loss, a dedicated fast ion loss detector is now under detailed design, supported by studies reported in the subchapter 3, but additional work is needed to assess the radiation effects on its scintillator and develop alternatives if it turns out that the lifetime is insufficient.

Additional progress reported in the subchapter includes an integrated design for a high-resolution neutron spectrometer (HRNS) addressing parameter 020 (n_T/n_D in the core) with simultaneous capability for T_i measurements.

1.3.3. Active spectroscopy. ITER uses several diagnostics that rely on beams injected into the plasma interacting with it and emitting light (by plasma ions or beam atoms), from which plasma parameters are extracted from the line emission. Using the charge exchange (CX), beam-emission (BES) and motional Stark effect (MSE) spectroscopic techniques they can extract Z_{eff} for BC, plasma flow and impurity profiles, including *He* ash for AC as well as information on Z_{eff}, q and T_i profiles for physics. For ITER, active spectroscopy diagnostics use both the heating beams and a dedicated diagnostic neutral beam (DNB), but have to operate in a different environment to present machines due to the large size and high density of the ITER plasma. The dedicated subchapter 4 presents the details of their planned implementation and performance. In addition to the primary contributions of these systems (table 3), the subchapter presents opportunities for additional measurements of fast-ion CX for confined and escaping alphas as well as ^{3}He-minority heating and slowing down beam ions. It also includes a detailed assessment, including synthetic diagnostic simulation of BES, of the measurement possibilities for edge fluctuation measurement. Finally, it summarizes the state of development of the dedicated 100 keV DNB.

1.3.4. Passive spectroscopy. The primary role of passive emission diagnostics is to identify what is in the plasma from spectral signatures. Extracting quantitative information from these measurements such as impurity content, ion temperature, rotation, degree of detachment and radiated power depends on calibrated instruments, a physics model of the atomic and molecular processes and plasma transport and an analysis workflow that takes into account environmental effects such as reflections. The list of instruments and their primary contributions to the ITER parameter set are listed in table 4.

Table 1. Primary contributions of the first wall related diagnostics by operational role and parameter.

System	Role	Parameter
D1: Bolometers	MP	009a: P_{rad} total
	BC	007a: P_{rad} total, divertor
		008a: P_{rad} total, main plasma
		083a: P_{rad} profile, main plasma + upper X-point
	AC	008b. P_{rad}, top region (upper X-point)
		082a. Divertor Prad Profile
	PHY	007b: P_{rad} total (transient), divertor
		008c: P_{rad} total (transient), main plasma + upper X-point
		009b: P_{rad} (transient) total
		082b: Divertor P_{rad} (transient) Profile
		083b: P_{rad} profile (transient), main plasma + upper X-point
		083c: P_{rad} vertical line integrals (transient) main plasma + upper X-point
G1: IR cameras, vis/IR TV (Midplane)	MP	039: Max. surface temperature, divertor
		042: Surface luminance, FW
	BC	043: Surface temperature, FW
		079: Γ_d, Γ_t
	AC	085: Power load
		086: Surface temperature
	PHY	034: E_{max} runaway
		035: I runaway
		044: Surface temperature during ELMs, FW
G3: Pressure gauges	BC	038: Gas pressure, divertor (P_{div})
		046: Gas pressure, main (P_{main})
		048: Gas pressure, duct (P_{duct})
G4: Residual gas analyzers	BC	037: Gas composition (Fuel, He, impurities) (P_{div})
		045: Gas composition (Fuel, He, impurities), main (P_{main})
		047: Gas composition (Fuel, He, impurities), duct (P_{duct})
	PHY	099a. Divertor Surface H, D, T Concentration (Inner baffle)
G6: IR thermography (divertor)	AC	085: Power load
		086: Surface temperature
G7: Langmuir probes	AC	080b: Divertor Target Parallel Ion Flux
	PHY	080a: n_e, divertor target
		081: T_e, divertor target
G8: Erosion monitor	PHY	040a. Fine surface metrology—Divertor
G9: Dust monitor	PHY	097a: Surface concentration of mobilizable dust (divertor cassette body under the dome and VV floor)
		097b: Dust size distribution
		097 c: Viewing of dust area on and under the divertor
GA: IR cameras: vis/IR TV (Upper)	MP	039: Max. surface temperature, divertor
		042: Surface luminance, FW
	BC	043: Surface temperature, FW
		079: Γ_d, Γ_t
	AC	085: Power load
		086: Surface temperature
	PHY	044: Surface temperature during ELMs, FW
GC: Tritium monitor	PHY	099a. Divertor surface H, D, T Concentration (Inner baffle)
GD: FW samples	PHY	040b. Fine net erosion and re-deposition—first wall
		099b. First wall surface H, D, T Concentration

Table 2. Primary contributions of the fusion product diagnostics by operational role and parameter.

System	Role	Parameter
B1: Radial neutron camera	AC PHY	014: Neutron- and α-source profile 013: Fusion power density
B2: Vertical neutron camera	AC PHY	014: Neutron- and α-source profile 013: Fusion power density
B4.A0: Neutron flux monitor (NFM) DT Eq#08	BC	012: Fusion power
B4.B0: NFM DT Eq#17	BC	012: Fusion power
B4.C0: NFM DD Eq#01	BC	012: Fusion power
B7: Radial gamma ray spectrometers	PHY	034: $E_{\max}$ runaway 035: I runaway 068: Alpha density profile
B8: neutron activation system	BC	077: First wall neutron fluence
B9: Lost alpha monitor	AC PHY	072: Fast particle loss flux 071 Fast particle loss distribution
BB: High resolution neutron spectrometer	BC	020. n_T/n_D core (Integral)
BC: Divertor neutron flux monitors	MP BC	015: Total neutron flux 012: Fusion power
BD: Vertical gamma ray spectrometers	PHY	034: $E_{\max}$ runaway 035: I runaway 068: Alpha density profile
E8: Neutral particle analyzer	BC PHY	020. n_T/n_D Core (Integral) 076: n_T/n_D, edge 075: n_H/n_D, edge 094: n_H/n_D, core

Table 3. Primary contributions of the active spectroscopy diagnostics by operational role and parameter.

System	Role	Parameter
E1: CXRS based on DNB (Core)	BC AC PHY	029: $<Z_{\text{eff}}>$ 019: v_{TOR} 064: Core T_i profile 066: n_{He}/n_e profile, core 067: ^{3}He concentration profile 074: Fractional content profile, $Z \leqslant 10$ 059: Z_{eff} profile
EB: MSE based on heating beam	AC PHY	057: r ($q = 1.5,2$)/a 058: r (qmin)/a 056: q profile
EC: CXRS based on DNB (Edge)	BC AC PHY 	029: $<Z_{\text{eff}}>$ 018: v_{POL} 019: v_{TOR} 067: ^{3}He concentration profile 074: Fractional content profile, $Z \leqslant 10$ 059: Z_{eff} profile 065: Edge T_i profile
EF: Beam emission spectroscopy	PHY	065: Edge T_i profile

Table 4. Primary contributions of the passive spectroscopy diagnostics by operational role and parameter.

System	Role	Parameter
E3: VUV survey	BC	022: Be, C, O rel. conc. 024: Cu rel. conc. 026: Extrinsic (Ne, Ar, Kr) rel. conc. 028: W rel. conc.
E4: Impurity influx monitor (Div. Vis/UV)	MP BC PHY	078: Γ_{Be}, Γ_c, Γ_w 041: Position of the ionization front, divertor 079: Γ_d, Γ_t 092: T_i profile, divertor
E5: Core imaging x-ray spectrometer (CIXS)	AC	018: v_{POL} 019: v_{TOR} 064: Core T_i profile 073: Fractional content profile, $Z > 10$
E7: Radial x-ray camera	MP PHY	017: B_{theta}(complex, at wall)/$<B_p>$ 032: ELM temperature transient 034: E_{max} runaway 035: I runaway 083b: P_{rad} profile (transient), main plasma + upper X-point
ED: X-ray crystal spec survey	MP BC	021a: C,O influx 021b: Be influx 023: Cu Influx 027: W influx 022: Be, C, O rel. conc. 024: Cu rel. conc. 025: Extrinsic (Ne, Ar, Kr) influx 026: Extrinsic (Ne, Ar, Kr) rel. conc. 028: W rel. conc.
EE: Hard x-ray monitor (H-phase)	PHY	034: E_{max} runaway 035: I runaway
EG: Divertor VUV spectroscopy	MP	078: Γ_{Be}, Γ_c, Γ_w
EH: VUV edge imaging	AC	073: Fractional content profile, $Z > 10$ 074: Fractional content profile, $Z \leqslant 10$
EI: X-ray crystal spectroscopy edge imaging	AC PHY	018: v_{POL} 065: Edge T_i profile

The ITER plasma will be a high temperature, moderately dense, fully ionized collisional plasma. The plasma facing surfaces are principally metallic being fashioned from beryllium or tungsten but many other elements, arising from either structural or from operational needs, may enter this plasma. The energy range of the emitted photons range from meV (infrared) to multi keV (x-rays) and originate from all areas of the plasma volume. The particular needs for ITER have prompted a multi-machine, many-year effort to address all these aspects and the dedicated subchapter 5 reviews the work on diagnostic design, experiments and new analysis techniques.

1.3.5. Laser-aided measurements. This group of measurements has a wide number of primary roles, in BC of the main plasma density and divertor He concentration, AC of temperature, density and q profile parameters in the core and edge as well as physics information on divertor density and temperature (table 5).

The specific subchapter 6 provides an overview of these laser-aided diagnostics. The subchapter notes significant progress across these systems, from new components (such as lasers, spectrometers) to new techniques (e.g. LIQ) and methods to work at high temperature (polarimetry corrections, polarization TS). It also addresses techniques that can allow improvements on current measurements, in particular expanding poloidal polarimetry measurements to measure field fluctuations and the proposed use of DI, which has a number of advantages over existing methods. This paper identifies particular areas where further research and testing on existing tokamaks is useful, even at this advanced stage, to inform the design of diagnostics for ITER. It also identifies outstanding

Table 5. Primary contributions of the laser-aided diagnostics by operational role and parameter.

System	Role	Parameter
C1: Core plasma Thomson scattering	AC	052: Core T_e profile
	AC	054: Core n_e profile
C2: Thomson scattering—edge	AC	055: Edge n_e profile
	PHY	053: Edge T_e profile
C4: Thomson scattering (Divertor, Outer)	PHY	090. n_e Divertor
	PHY	091: T_e, divertor
C5: Toroidal interferometer/ Polarimeter	BC	011: $\int n_e \, dl / \int dl$
	PHY	063: TAE $\delta N/n$, $\delta T/T$
C6:Polarimeter poloidal	AC	057: r ($q = 1.5,2$)/a
	AC	058: r (q_{min})/a
	PHY	056: q profile
EA: Laser-induced fluorescence	BC	087: n_{He}, divertor
FA: Density interferometer polarimeter (DIP)	BC	011: $\int n_e \, dl / \int dl$
	PHY	090: n_e profile, divertor

areas of concern for the implementation of laser diagnostics, in particular with a view to reliable operation.

1.3.6. Microwave measurements. Microwave diagnostics are routinely used for core and edge density and temperature profile measurements and on ITER they certainly aim to fulfill that role. In comparing table 6 with the state of this part of the ITER measurement suite in 2007 [4] some key differences are apparent. The plasma position reflectometer (PPR) is absent. It proved impossible to integrate the number of sightlines sufficient to correct the full separatrix (around nine are needed) and, at the same time, progress in magnetics R&D described in section 1.3.11 was sufficient to enable hour-long pulses. A new system, the in-vessel ECH detectors, essentially bolometers for the mm-wave range, measures stray ECH using hundreds of distributed sensors. The dedicated subchapter 7 lays out the design progress with this and all key microwave systems: There have been advances in microwave systems which all lead to more accurate and reliable measurements of key plasma parameters. Refinements in theory, techniques, and hardware bring the diagnostics to full readiness for burning plasma conditions. The systems have been hardened against damage due to intense stray ECH and all the long transmission lines have been optimized for transmission, including the effects of atmospheric humidity. Bursting emission from low-collisionality plasmas remains an operational risk, however.

1.3.7. Radiation effects. The specialized WG on radiation effects has been working on radiation related issues affecting multiple groups of diagnostics, steadily since the inception of the ITPA. In the ITER case, radiation affects primarily ceramics and glasses to the boundary of the vacuum vessel (VV) and all manner of composite materials outside it. Since the previous update, the work of the group has shifted from reporting on basic single material studies and mineral insulated cable assemblies [4] to composite devices functionally similar to those used in ITER and exposed to radiation. These include windows (diffusion-bonded silica metal assemblies), bolometers, coils and hall probes (multi-metal and glass/ceramic layers), optical fibers (concentric glasses and metal or polymer sheath construction) and feedthroughs (metal and glass composite assemblies). The dedicated subchapter 8 summarizes the progress in this area.

1.3.8. First mirror selection. This topic has generated its own specialized WG, as the material aspects affecting the first mirrors exposed to plasma and radiation are similar across multiple systems. The group strived to produce a guide to the diagnostics designer in the optical domain to allow mirror selection taking into account plasma impurities, sputtering of the mirror surface and, more recently, steam ingress from coolant leaks inside the device. The recipe to maintain good reflectivity includes good placement and surround design, material selection for endurance of the conditions and active recovery features including *in situ* cleaning. This last topic is particularly active.

The dedicated subchapter 9 gives a concise overview of the main results of the structured and coordinated international R&D in the field of diagnostic mirrors and outlines remaining work to resolve open issues for ITER and to prepare the work for DEMO.

1.3.9. Real time operation of diagnostics. ITER has long prioritized diagnostic measurements with respect to control, and table 10: Specification for plasma measurements on ITER, reflects this philosophy. The implementation of the relevant controllers is within the plasma control system (PCS) and indeed plasma control has its own dedicated topic group and Subchapter 10. However, the preparation of models relies on good models of the diagnostics and the preparation of

Table 6. Primary contributions of the microwave diagnostics by operational role and parameter.

System	Role	Parameter
C7: Collective Thomson scattering	PHY	068: Alpha density profile 069: Alpha energy spectrum 070: p, D, T, ^{3}He energy spectrum
F1 ECE	AC	052: Core T_e profile 061: NTM δT/Te. (complex; 100 ms integration time)
F2: Reflectometer (Main Plasma, LFS)	AC PHY	055: Edge *n*e profile 031: ELM density transient 063: TAE $\delta n/n$, $\delta T/T$
F9: Reflectometer (Main Plasma, HFS)	AC PHY	054: Core *n*e profile 031: ELM density transient 063: TAE $\delta n/n$, $\delta T/T$
GB: In-vessel ECH detectors	BC	103: In-vessel ECH stray radiation intensity

such models relies on, amongst other things a good idea of the use case and combination to which the data will be put. Furthermore, the controllers need real-time data of sufficient quality and the definition of sufficient and the optimal way to derive it from the diagnostics again relies on the use case and the overall control implementation.

A dedicated WG is now working towards the systematic development of the controllers and underlying synthetic systems and the corresponding subchapter 10 lays out the progress in this area.

1.3.10. IDA. ITER measurements for control and physics understanding have formal availability targets to ensure high efficiency operation of the physics program in the ITER research plan (IRP [5]). To meet the availability, redundancy is inbuilt to the design of individual systems and, for many measurements, more than one diagnostic has a primary contribution, e.g. TS and ECE to core electron temperature. In turn, both depend on the equilibrium reconstruction. In this situation, analysis of the errors and biases of a particular diagnostic can be difficult. For a particular output, such as T_e, IDA based on a Bayesian probabilistic approach can be used to combine the information in a rigorous way, improve the reliability of parameter estimation and find inconsistencies. The corresponding work of the recently formed IDA WG, see subchapter 11, shows ITER and other examples of synergy between two diagnostics, three-way profile information combination, improved magnetic equilibrium reconstruction and velocity-space tomography. This work and its benchmarking on running devices will enable to get the most out of ITER operation.

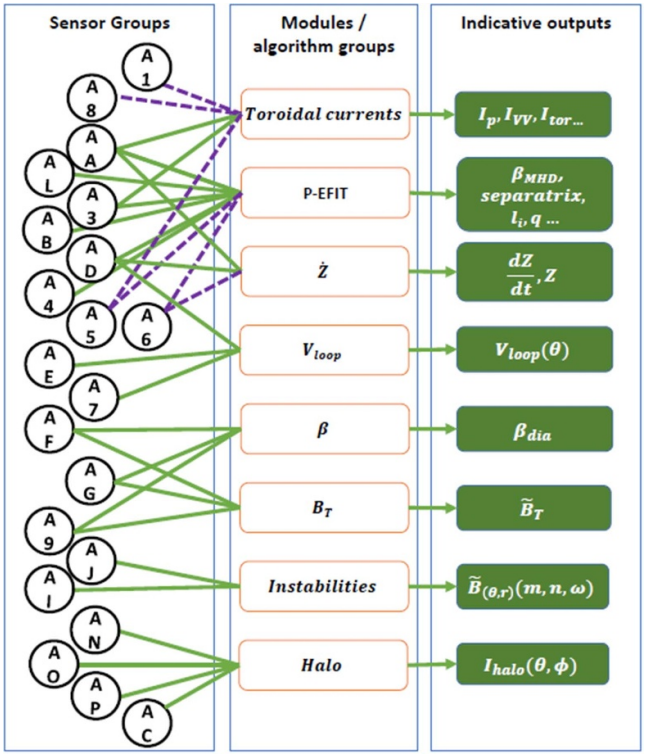

Figure 1. Main contributions of the magnetics sensor groups (A1 … A9 and AA … AO, explained in table 7 with the exception of A5/A6, the steady state sensors, A8, the fiber optic current sensor, AN, the divertor Rogowskis and AO and AC, the toroidal coil sets) to the software modules in preparation. Each module is configurable to accept inputs from most sensors, including backup groups (not shown). Dashed lines indicate expected information flow for long pulse correction.

1.3.11. Magnetic measurements. Magnetic diagnostics in ITER interact strongly with the details of internal component engineering for the ITER load assembly. Their design is now almost complete and although it has evolved since the physics basis was last revised [4], the system is recognizably similar [7]. Sensors contribute to multiple measurements, sometimes via multiple software modules, in a manner similar to that described in [8, 9]. Specific modules include real-time equilibrium reconstruction, plasma current, vertical speed, loop voltage, energy, instability measurements, toroidal field variation and halo reconstruction (figure 1). The modules are configurable and this makes mapping all the potential uses of the

Table 7. Primary contributions of the magnetics by operational role and parameter.

Sub-System	Role	Parameter
A1: Continuous external Rogowskis	MP	001b:Itor
A9: Diamagnetic compensation coils (Outer)	BC	051. Toroidal Magnetic Field BT
AA: Tangential coils (Inner)	MP BC	001a: Ip 003: DZ/dt of current centroid 004: Main plasma gaps, Dsep
AB: Normal coils (Inner)	BC	004: Main plasma gaps, Dsep
AD: Partial flux loops	MP BC	003: DZ/dt of current centroid 004: Main plasma gaps, Dsep
AE: Continuous flux loops (Inner)	BC	005: V loop
AF: Diamagnetic main loop	MP	006: βp
AG: Diamagnetic compensation coils (Inner)	MP	006: βp
AI: Magneto hydro dynamic saddles	MP	016a: Br/<Bp> RWM 016b: Br/<Bp> Error Field
AJ: High frequency sensors	MP PHY	017: B_{theta}(complex, at wall)/<Bp> 060: Fishbone B_{theta}(mode)/<Bp> 062: TAE B_{theta}(complex)/<Bp>
AL: Divertor equilibrium coils	BC	002: Channel location, divertor (r dir.)
AP: Rogowskis (Blanket)	MP	050a Poloidal current in one sector

groups of sensors very complex, but the primary contributions are listed in table 7, after [7] and are discussed below grouped by software module.

The modules reside in a plant system controller originally conceived to run in the diagnostic hall but recently relocated to the main server room, with the exception of the interlock systems running directly in the acquisition aggregator boards [10]. Multiple instances of the modules can be running. The system feeds multiple clients; the data flows are summarized in figure 2. Specially developed integrators are used to accommodate all inductive signals, based on the concept developed for W7X [11], but redesigned *ab initio* to accommodate voltages up to 1 kV and parallel streaming of up to 30 modules into a single high bandwidth aggregator board [12]. Presently, an end-to-end prototype system is under test on WEST.

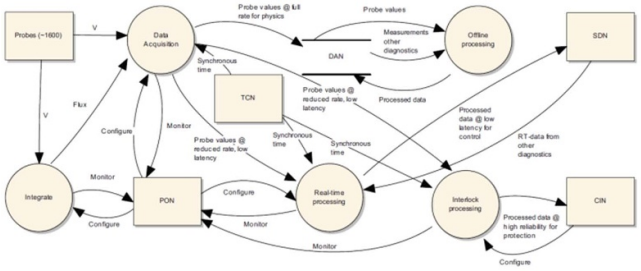

Figure 2. Context data flow diagram of the magnetics diagnostic. The system interfaces to all the central I&C networks, feeding the acquired data to algorithms. Reprinted from [10], Copyright (2015), with permission from Elsevier.

1.3.11.1. Plasma current and related parameters. Plasma current (I_{p}) measurements for plasma control and investment protection are derived by the in-vessel pickup coils (IVCs). Six sets of equilibrium IVCs (Tangential coils AA) provide independent estimates from as many sectors with a basic bandwidth in the kHz range and an overall error below 1%. An FPGA-based high reliability system [12] provides a real-time 'Best-Ip' estimate to the investment protection ('interlock', CIS) system; simultaneously real-time feedback within the PCS ensures the plasma stays within Central Interlock System (CIS) limits. Fiber-optic current sensors (FOCS, A8) can restrict, on a slower timescale, the total toroidal current (I_{tor}). Together with the Continuous External Rogowskis (CER, A1) embedded in the Toroidal Field Coils (TFCs), they can be absolutely calibrated on demand using the ITER in-vessel radial field coils and can correct other sensors for integration drift.

IVCs (AA, but also normal coils, AB, and toroidal coils, AC, of similar construction) are in manufacture, following a development path to mitigate radiation effects, in particular radiation-induced currents [13]. After numerous engineering studies [14–17], optimized platforms are in production, using extensively optimized low temperature co-fired ceramic (LTCC) coils with a silver winding in a glass-ceramic matrix (figures 3 and 4). Two variants are included in the

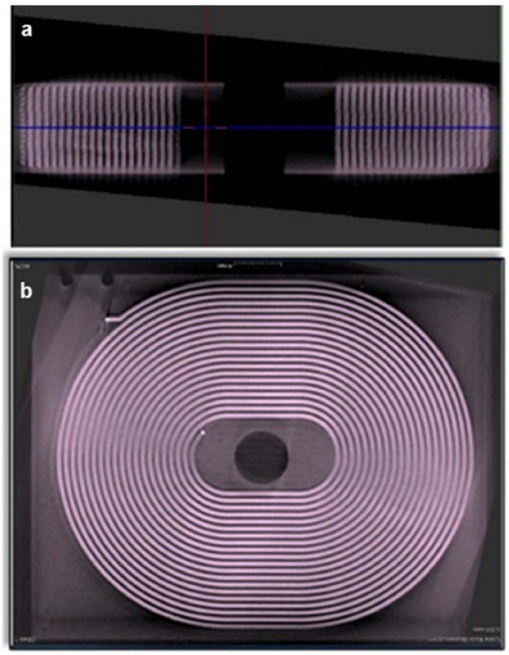

Figure 3. X-ray of an ITER LTCC sensor showing layers from the side (*a*) and from the top (*b*). The size is approx. 40 × 30 × 8 mm. Reprinted from [18], Copyright (2022), with permission from Elsevier.

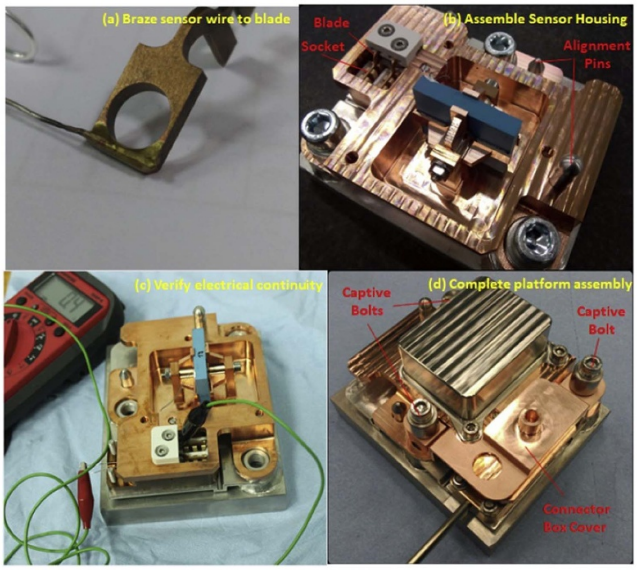

Figure 4. Construction of a remote handling-compatible ITER in-vessel pick-up coil incorporating an LTCC coil (blue), placed on a CuCrZr base plate with an Inconel shield designed to allow a DC-15 kHz pass band. In the production run, the shield is copper-coated to reflect electron cyclotron frequencies. Reprinted from [16], Copyright (2019), with permission from Elsevier.

manufacturing run designed to null radiation induced currents in different ways. A specially designed calibration rig and process records the effective axis (orientation) of each sensor to ∼0.1 mrad. Calibration of the effective area with frequency is in the preparation stage.

Production of CERs is nearing completion. They are based on a composite design using a two-layer helically wound cable with fiberglass and polyimide insulation. The main TFC impregnation process also impregnates the CER and sets it in its channels within the structure. The performance of these coils has been analyzed [19, 20] and verified experimentally [19, 21]. All coils (three for use and one in the spare TFC) are already installed in their respective TFCs [22]; only on-site connection activities remain.

The FOCS is conceptually like the CER with the strong advantage of immunity from drift and electromagnetic interference [22–24]. Materials selection and interface design is complete and manufacturing of components trapped within the cryostat and building is proceeding [25, 26].

1.3.11.2. Plasma shape and speed. By the definition of ITER, plasma vertical speed, $\dot{z}$, a diagnostic performance parameter (table 10, parameter 003) is linked both to the plasma current and the absolute position of the current centroid, as the in vessel coils measure directly the rate of change of the zI_p product and I_p so that $\dot{z}I_p = \left(z\dot{I}_p\right) - z\dot{I}_p$. The estimate of z, the plasma centroid height, in turn requires time-integrated measurements, not just of field tangential to the vessel but also of the normal components. For this reason, the sensors that enter the of plasma shape and speed algorithms include both poloidal field axes. The speed measurement employs optimized summation of the signals for the coils and saddle loops and is available in real-time for plasma control.

The tangential (AA), normal (AB) and divertor (AL) coils, together with the saddle loops (AD) provide data to derive equilibria [7] using the P-EFIT code [27, 28]. The P-EFIT code is also used to derive estimates of other quantities (e.g. β_{eq}, q) as well as to broadcast an equilibrium grid for other users and estimates of the plasma wall gaps.

Shunts (AM, not shown in figure 1) are also included in the divertor measurements. They use the cassette body (CB) as the shunt element, to resolve cassette currents similarly to the Halo Rogowskis described in a later section. If sufficiently large, these currents can influence the shape reconstruction. They can also be used for detachment identification [29].

The construction of the in-vessel coils has been discussed in the preceding section, with the exception of the divertor coils (AL) that operate in a special high temperature and high neutron flux environment but with lower frequency requirements. A special CuCrZr monoblock heatsink houses pairs of these coils set at 90° to measure both poloidal field components in the poloidal plane (figure 5).

In ITER, flux loops are being installed both inside and outside the VV, with different design constraints and measurement requirements. They are mounted on the inner and outer walls of the vessel, in all nine sectors. In total, there are 237 flux loops of varying sizes, which represents ∼1/5th of all magnetic diagnostic sensors.

The flux loops on the inner skin include partial flux loops (AD) that are of relatively modest size. In addition, there are the rather larger magneto-hydrodynamic (MHD, AI) flux loops. Finally, there are the full poloidal diamagnetic loops

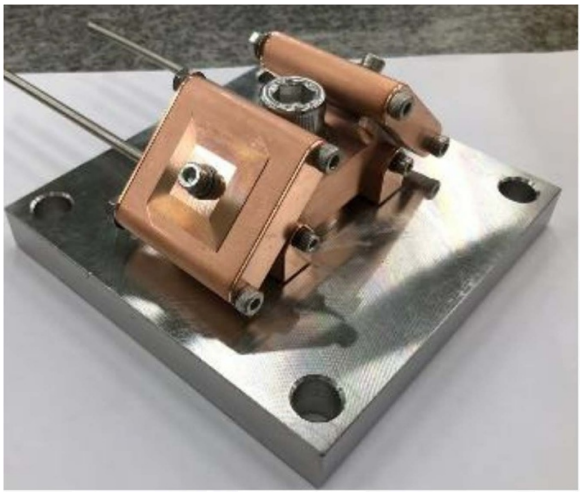

Figure 5. A two-axis coil prototype (55.AL) about to undergo thermal and vibration tests. Bolts through the LTCC sensors, in combination with copper foam ensure the *in-vacuo* heat transfer to the main block representing the ITER divertor. Frequency response is a few tens of Hz.

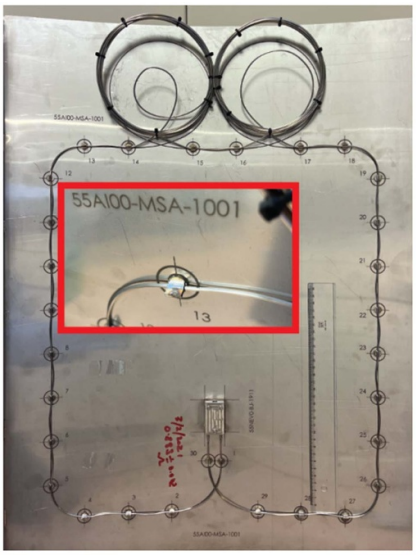

Figure 6. Trial assembly of a saddle loop showing the main features: Clips (numbered 1–30); junction box (lower center); cable relief (top; actual installed loops use smaller relief areas). Inset: Clip #13 (top left of main picture) welded shut.

(AF) and the full toroidal voltage loops (AE). On the outer skin there exist only the full toroidal voltage loops (A7). Due to the high radiation dose rates and temperatures inside the VV, the flux loops are made from Mineral Insulated (MI) cables. These cables comprise a stainless-steel outer sheath, of order 0.3 mm thick, encasing aluminum oxide (alumina, Al_2O_3) insulation which surrounds a single, central oxygen free copper (OFC) or copper alloy (CuNi2Si, UNS C70260) conductor. The diameter is adjusted to the expected voltage and the terminations are tested for the expected pressure conditions (UHV to 100 Pa up to 1 kV) [30].

Special clips and terminations are developed. The clips are designed for short cycle stud welding onto any metal surface; the loops are then formed (including intentional undulations to relieve relative thermal strain and resultant fatigue) and the clips resistance-welded shut (figure 6). The process is suitable for the industrial assembly process of the several tens of thousands of clips necessary.

For long pulses, drift arising in the shape measurements can be compensated in principle by measurements of the field components on the external VV skin, either inductively (Outer vessel tangential and normal coils, A3 and A4) or using steady state sensors (tangential, A5 and normal A6, respectively. This correction can be applied in real time if needed [31, 32].

The outer vessel coil design takes advantage of the substantially lower dB/dt outside the ITER VV to implement a large effective area coil of $O(2m^2)$ with modest output voltage and high immunity to parasitic pickup areas and, to some extent, radiation-induced currents [33]. It uses polyimide insulated winding packs (figure 7) and is attached to the ITER VV in a permanent fashion, using a high-strength sprung support system and internal strain relief, designed to cope with rapid cooling to 70 K (from potential He cooling leaks) and baking to 200 °C (figure 8).

The steady state sensors are much smaller but present unique challenges. Early work [34, 35] focused on strongly-doped InSb sensors, the idea being that the relatively large number of carriers would confer higher radiation immunity. Later, the work focused on Bismuth (Bi) sensors that exhibit much higher radiation immunity but have certain other difficulties, in particular non-linear behavior, relatively large temperature sensitivity requiring temperature monitoring to 0.3 K and a tendency to oxidize rapidly on exposure to air.

The sensors' construction, mounting and on-board temperature monitoring are all critical in the ITER environment [36]. The sensing elements (figure 9) are thin cross-shaped Bi layers deposited on a ceramic/copper circuit board with specially tapered contact regions and passivated by additional ceramic coating. Two such elements set in one housing to measure both poloidal field components. The entire unit is calibrated against temperature and field and, to ensure the temperature calibration is usable to $<$0.3 K, an on-board indium (In) cavity provides a fixed reference to the triple point of In at every ITER baking cycle [37].

These Bi-based sensors were qualified for ITER and will be installed on one out of the three sectors reserved for this use. The high attrition rate of the Bi layers in manufacture is a risk in service so, for the remaining sectors, antimony (Sb) sensors are undergoing trials. These offer better linearity, slightly lower temperature sensitivity and improved resistance to oxidation with lower but acceptable sensitivity. The ultimate radiation hardness of similar sensors should approach that of ceramic/metal induction loops based on mineral insulate cable (several dpa) so that, in hybrid operation as suggested in [31], should last as long as a reactor-grade breeding blanket exchange time. This offers the prospect of steady-state magnetic control of a reactor grade tokamak.

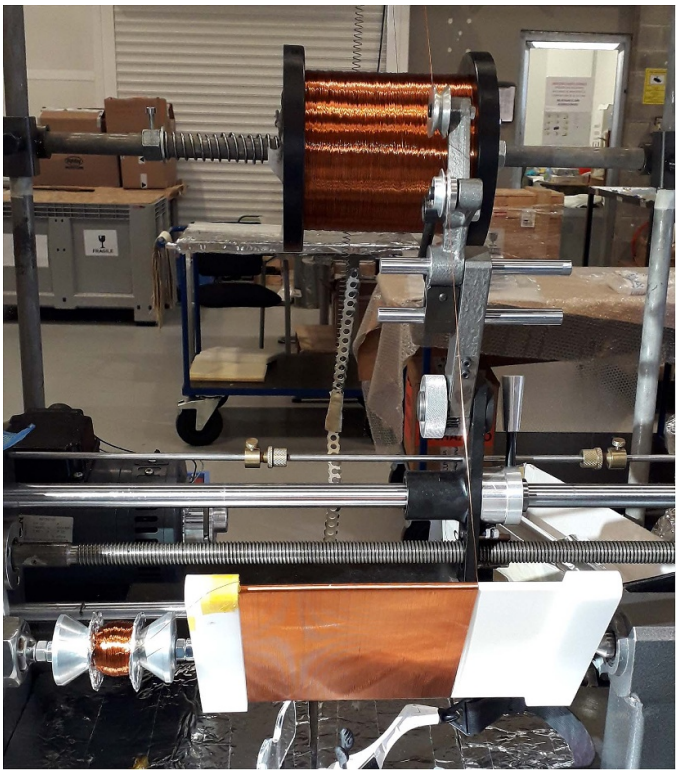

Figure 7. Winding process of an ITER outer vessel coil. Similar to the prototypes [33], the former is alumina ceramic and the winding is made of polyimide-coated wire.

1.3.11.3. Loop voltage, plasma energy and toroidal field. Loop voltage is a BC measurement for monitoring current drive that requires relatively little processing. In ITER, in-vessel continuous (AE) and outer vessel (A7) flux loops, constructed similarly to the partial flux loops (AD) but running toroidally at multiple locations and with thicker cable rated for higher voltage, supply eight such values in-vessel and four for the outer vessel. Values at other locations can be computed using the partial flux loops and/or the similar but larger MHD loops (AI, functional description in next section) by poloidal fitting. In this way, approximately 20 locations can be monitored in-vessel without heavy computational requirements and there is sufficient redundancy to ensure availability for the ITER lifetime.

Plasma energy is a BC and stability check tool and in ITER is computed two ways: as a product of the P-EFIT equilibrium calculation (β_{eq} *or* β_{MHD}) and directly by a compensated full poloidal flux loop system at three toroidal locations. The loops are implemented with the same technology as the saddle loops (AD, described in the shape and speed section), but use a two-turn configuration to allow symmetric deviations around obstacles. Basic vacuum field compensation is by means of toroidal coils (AG) with large effective area (2 m^2) optimized for low thermoelectric voltage generation at the expense of speed. These coils are supplemented with measurements outside the VV that are slower still but offer improved immunity from radiation (A9).

The AG coils are under pre-series manufacture. They are wound on a CuCrZr bobbin with thin mineral insulated wire, then fully vacuum brazed to the heatsink to ensure thermal gradients in service below 2 K. Prototypes are undergoing calibration trial (figure 11).

For energy measurements, the basic accuracy is limited by the accuracy of the compensation coils, and by any large non-axisymmetric eddy currents, as in disruptions [38]. In most conditions, the requirements (Parameter 04 of table 10) can be met.

The AG and A9 coils also measure toroidal field variation that requires a basic accuracy below 1 mT (Parameter 51 of table 10), like that needed for plasma energy.

1.3.11.4. Measurement of instabilities. Many of the coils and loops mentioned so far contribute to instability measurement. In most cases they have a backup or supplementary role to the dedicated instability detectors, that is, the MHD saddle loops, AI, visible in figure 10 and replicated in all manufacturing sectors and the high frequency (HF) coils, AJ, that are organized in a non-uniform but approximately symmetric set as described in [7].

MHD loops are set to detect mainly low (m,n) MHD modes, Parameter 08 of table 10. They are constructed similarly to the saddle loops (AD) but are much larger. As defined the plane of the VV, they can achieve detection to (m, n) $\sim$(4, 4), sufficient to capture the field structure emerging from a mode locking before disruptions, a resistive wall mode (RWM) or a large error field. Their sensitivity is limited only by integrator drift ($\sim$0.1 mT equivalent for a 1 h pulse). Finer poloidal

Figure 8. Top: ITER VV Sector 6, the inboard outer vessel pickup coils tangential (top row) and normal (bottom row) clearly visible. Bottom: Close-up of a tangential coil. Inconel plates and fiberglass preload the winding pack into the Inconel case; Four welds to vacuum vessel bosses hold the sprung legs in place to allow an operating range 70–573 K without rotation.

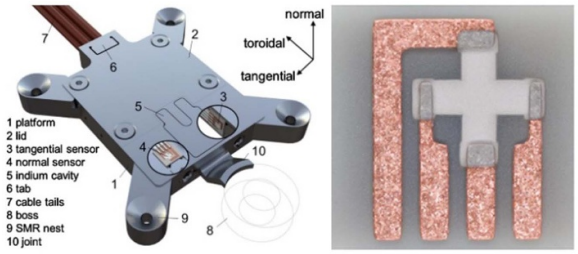

Figure 9. Construction of the steady state sensors in ITER (left, $\sim 8 \times 8$ cm)) and the final version of the Bi-based sensor chip for ITER (right, $\sim 4 \times 4$ mm).

(and toroidal) peaking can be sensed by a combination of their measurements with the saddle loops but with higher noise floor (due to their smaller average area).

For high frequency modes (over a few tens of Hz, Parameters 09 and 27 of table 10) covering everything up to the highest toroidal Alfvén eigenmodes (TAEs) expected in ITER, the VV eddy penetration time reduces the sensitivity of the loops and the main signals come from the 207 high frequency coils (figure 12). Their distribution captures, in quasi-regular sampling, nominal n-numbers up to

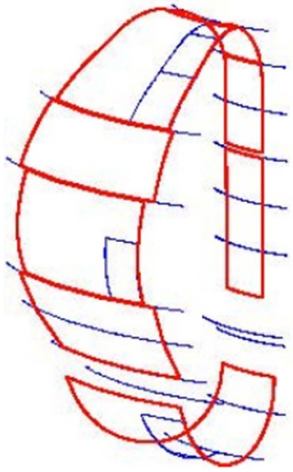

Figure 10. A sector where MHD loops (AI, red) coexist with partial flux (saddle) loops (rectangles, blue) and full toroidal flux loops (lines, blue).

$n \sim 9$ and m-numbers (again defined on the VV plane) up to $m \sim 10$. Port arrays can locally sample even higher n-numbers, but given the structure of the eddy current signature

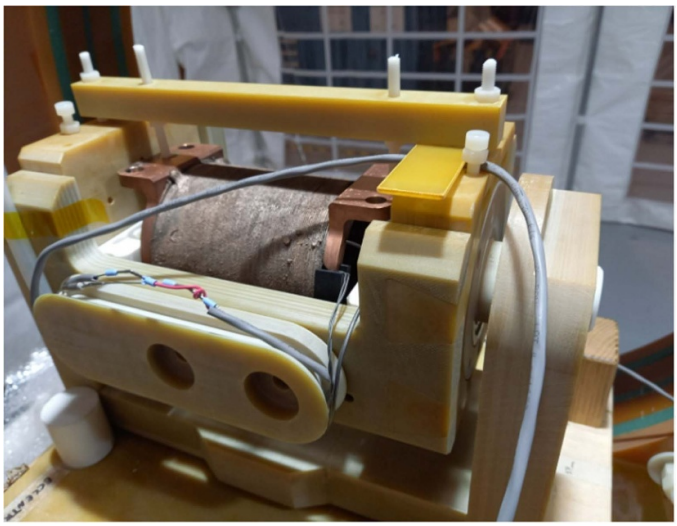

Figure 11. Pre-series toroidal compensation coil (AG) undergoing calibration trials in a Helmholtz rig (outside the field of view). The coil is in a special support cradle, designed to determine the coil axis to better than 0.1 mrad. The overall accuracy is 0.1%.

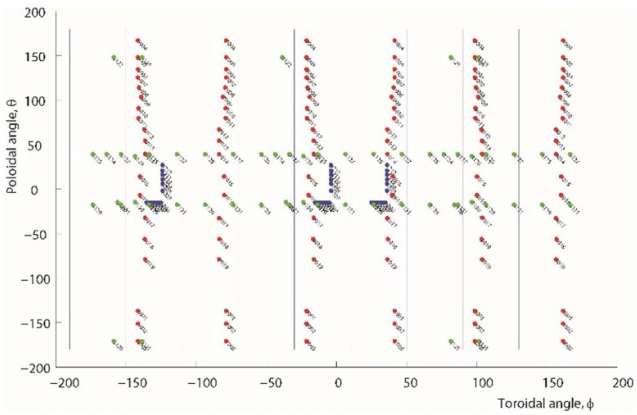

Figure 12. Distribution of the HF coils (55.AJ) in ITER. There are two higher density belts (arrays, green dots) running toroidally on the low field side ($\boldsymbol{\theta} = 0^\circ$) and two others on the high field side ($\boldsymbol{\theta} = -180^\circ$), as well as six arrays in the poloidal plane (red) and three sets of high-density measurements near the edges of ports (blue). All coils measure poloidal field except for the high-density sensors below the equatorial ports (toroidal field).

from the blanket modules, cannot resolve the true local mode structure.

These coils fit into the same platform used for the plasma shape and current measurement coils, with the key difference being the substitution of a tungsten-coated aluminum nitride (AlN) protection shield for the copper-coated Inconel 718 shield of the former. This shifts the −3 dB point of the case from ∼30 kHz to ∼500 kHz while allowing for extremely high ECH local heat load. Special supports are used for the arrays near the ports (figure 13). Further construction and performance details can be found in [39].

1.3.11.5. Measurement of halo currents. Halo current measurements are needed to understand the disruption process and as an input to calculations of VV forces and strains. The related parameter (50 in table 10) requires resolving the halo in each of the nine ITER sectors. In practice, the key measurement of the halo in ITER is the current injected in the FW panels, measured by Rogowskis (AP) surrounding the earth straps of the modules. Around 30% of all the panels are sampled (figure 14). These measurements are complimented by Rogowskis around divertor cassette components (AN) that can resolve the current entering and leaving the cassette at six toroidal locations, as well as toroidal coils to measure the flux compression during the vertical displacement events (VDEs, AC at the top of the VV and AO on six cassettes) (figure 15). The halo current injection map is incomplete, so considerable effort went into the method of reconstruction of the full pattern [40–43] and to demonstrate that the measurement requirements can be met.

Construction of the Rogowskis has evolved but from the beginning (figure 16) [14] the designs employed mineral insulated cable construction. Prototyping of integrated (brazed) versions of the sensors in underway.

1.4. Summary of progress with open issues and outlook for diagnostic operation in ITER

The ITPA Diagnostic TG has operated across a broad range of topics organized in high priority areas (HP, table 8) and (usually linked) joint experiments (JEX). JEX are indexed in table 9. The work centered on the new challenges offered by ITER. For example, long pulses with superconducting radial field coils require close control of the noise in the related feedback system to keep eddy current losses low (DIAG-1). After an assessment within this and the MHD topic group, the related specification was captured in the specification of parameter 3 of table 10.

Other closed topics since the last IPB update include DIAG-3, the discrepancy between TS and ECE measurements. The trigger for this activity was a report of an apparent discrepancy at JET [49]. Following work at C-MOD [50], correction stop

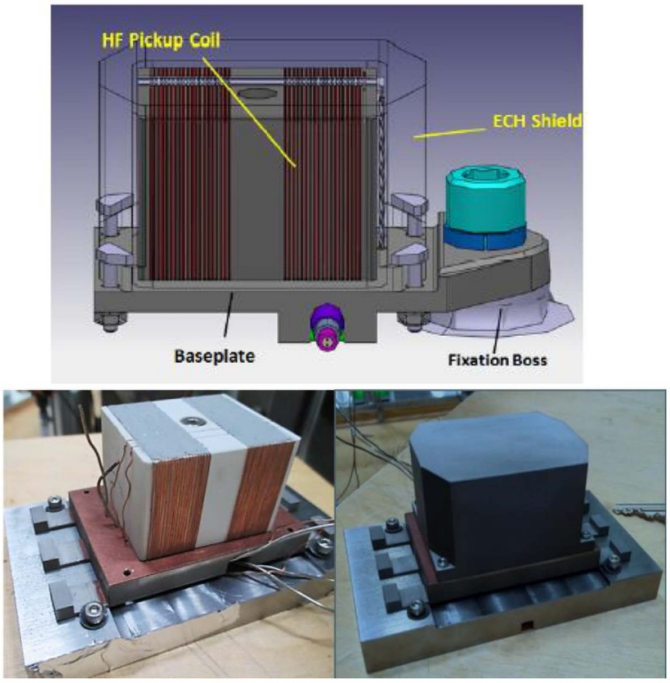

Figure 13. High frequency sensor design for the port arrays (top) and early prototype without (lower left) and with (lower right) the W-on-AlN ECH shield.

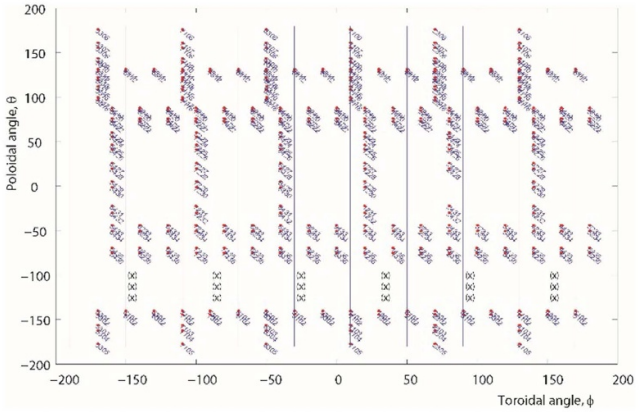

Figure 14. Distribution of the halo measurement Rogowskis on the ITER first wall panels (twin red dots per panel). The empty belt at around −120° poloidal angle corresponds to the divertor region, where six cassettes are sampled, indicated by (x).

the JET calibrations [51] and review at ITPA of JET campaigns available in 2016, the JEX was closed. More recent work on JET data shows a non-random discrepancy at high T with systematic behavior [52] and the topic (though not the JEX) is followed again closely.

Active topics include the first mirror tests and strategy, now very mature and discussed in section 3.8 and in subchapter 9 and wall reflections with the latest developments in section 3.1 and in subchapter 2 and a record of incremental progress is in the additional references of table 9.

More recently and as the ITER diagnostic set matures, the Topic Group has increased emphasis on preparation for operation and exploitation of ITER. Additional WGs for real-time operation, see subchapter 10, and IDA, see subchapter 11, grapple with the optimization of the data flows and data treatment needed to operate ITER with high efficiency and to ensure high quality data. These two WGs manage DIAG-12, whose objective is to develop, customize and validate synthetic diagnostic models, along with associated test cases within the IMAS framework [53]. These models should be made available prior each phase of the ITER Research Plan.

Other recent JEX support techniques whose implementation on ITER came relatively late, such as LIBS for FW survey of T (LIBS, section 3.1 and subchapter 2), now possible to install on the planned Agile Robot Transporter (similar to [54]) and the Fast Ion Loss Detector [55] now being integrated in ITER. In more detail:

- *DIAG-13: LIBS for in-situ T retention measurement.* This is in support of the IRP activity A.9 [56]. The main objective is to measure D/T concentration in the ITER FW and to constraint H trapping modeling codes.
- *DIAG-14: laser induced desorption spectroscopy (LIDS) for tritium quantification.* This proposal is in support of IRP A.7 [56] and the JEX activities include two different methods: LID-QMS (ms pulse) and LIDS (ms pulse; in the presence *f* background plasma) vs. LIA-QMS and LIBS.
- *DIAG-15: Density control with pellets.* This proposal is in support of HP#3 (table 8). The proposed activities include systematic controller design through system identification using frequency domain analysis (e.g. of N II front control with N2 seeding) and multi-input multi-output (MIMO) control of radiative loss processes.

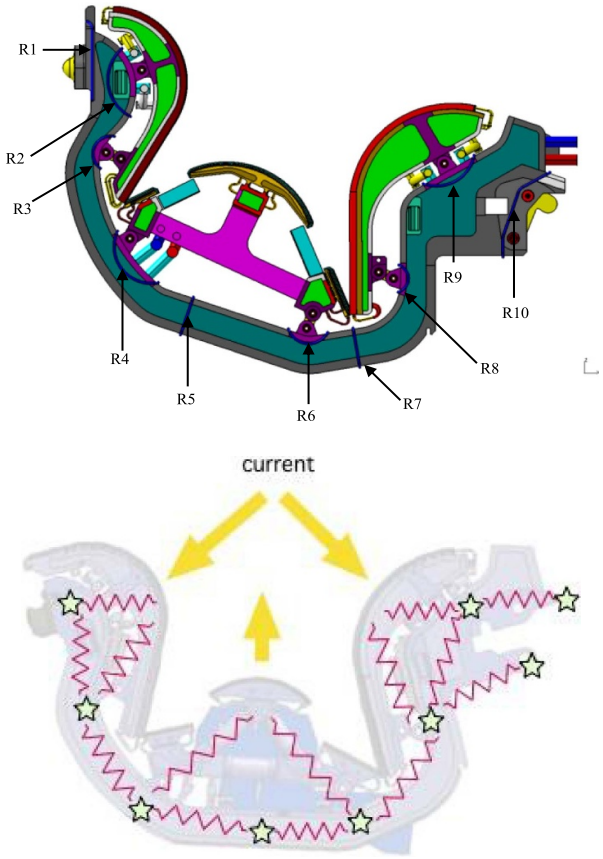

Figure 15. Distribution of Rogowskis on the sampled cassettes (top, blue belts) and simplified electrical network showing the plasma currents to be resolved (bottom, yellow).

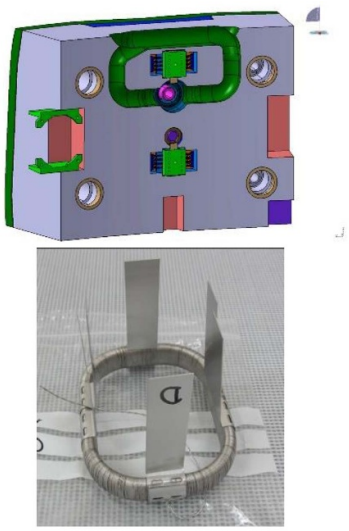

Figure 16. View of the back side of the blanket module showing the location of the two Rogowski coils surrounding the grounding straps (left); picture of a brazed Rogowski prototype (left) employing 0.5 mm MI cable and four welding tabs (D).

Diagnostic measurements for ITER benefitted enormously from the work of the ITPA topic group. ITER is now progressing towards operation. In this phase, diagnostics are being installed and tested and in parallel, plans for the research plan are being refined. This process will continue to throw up questions of diagnostic performance, efficacy and interoperability as the measurements will have to come together to support ITER's evolving plans. The commitment of this group to support ITER in this phase remains essential to prepare ITER to carry out its mission effectively.

Table 8. List of currently active high priority items for the ITPA TG.

Item	Description	Covered by
HP#1	Optimize lifetime of plasma facing mirrors used in optical systems	DIAG-2
HP#2	Assess impact of microwaves on diagnostic systems	All SWG
HP#3	Assess plasma control system measurement requirements	DIAG-11
HP#4	Develop diagnostic, calibration techniques and strategies compatible with the burning plasma environment	All SWG
HP#5	Develop inversion reconstruction techniques (tomography, equilibrium…)	All SWG

Table 9. List of diagnostic joint experiments (involving at least two organizations excluding ITER IO) and status.

JEX	Start	Status	Activity	References
DIAG-1	2000	Closed	Assessment of the effect of noise on vertical velocity measurement	See text
DIAG-2	2000	Active	Environmental tests on first mirrors	Section 3.8, subchapter 9
DIAG-3	2007	Closed	Resolving the discrepancy between ECE and TS at high Te	See text
DIAG-4	2009	Closed	Test of capacitance micro-balances in tokamak	[44]
DIAG-5	2010	Closed	Field test of an activation probe	[45, 46]
DIAG-6	2010	Closed	Comparisons of charge exchange recombination (CXRS) spectroscopy and x-ray imaging crystal spectroscopy (XICS)	[45]
DIAG-7	2010	Closed	Distributed monitoring of microwave power density	[45–47]
DIAG-8	2010	Active	Benchmark of wall reflections	Section 3.1, subchapter 2, [45, 46, 48]
DIAG-9		Closed	Spectral MSE (MSE-LS) experiments as design driver for ITER MSE	
DIAG-10		Closed	Minimizing microwave absorption in vacuum windows	
DIAG-11	2017	Active	Determination of the runaway electron distribution function by spectral gamma ray Bremsstrahlung measurements during disruptions	
DIAG-12	2020	Active	Development of synthetic diagnostics for ITER	See text
DIAG-13	2021	Active	Development of the LIBS technique in view of its implementation in ITER	See text
DIAG 14	2023	Active	LIDT studies for T quantification in ITER	See text
DIAG 15	2023	Active	Observation and control of the electron density and impurity distribution using small pellets	See text

Table 10. Specification for plasma measurements on ITER, derived from [57].

Measurement group	Parameter	Range	Condition	Resolution		Accuracy
				Time or Freq.	Spatial or Wave No.	
01. Plasma current	001a: Ip	0–1 MA	Default	1 ms	Integral	10 kA
		1–17.5 MA	Default	1 ms	Integral	1%
		20–0 MA	Ip quench	0.1 ms	Integral	30% + 10 kA
	001b:Itor	1–20 MA	Default	10 ms	Integral	1% + 10 KA
	100: Plasma current for CSS [Central Safety System]	5–20 MA	Normal operation	1 s	Integrated	1% (2 σ)
02. Plasma position and shape	002: Channel location, divertor (r dir.)		Ip >3 MA	10 ms	—	10 mm
			Ip quench	10 ms	—	20 mm
	003: DZ/dt of current centroid	0–5 m s^{-1}	Default	1 ms	Sum of 3 or more toroidally symmetric positions	10 mm s^{-1} (system noise) + 50% (depending on plasma scenario) + plasma noise
	004: Main plasma gaps, Dsep		Ip >2 MA, full bore	10 ms	—	10 mm except gap 5 (25 mm)
			Ip quench	10 ms	—	20 mm
03. Loop voltage	005: V loop	0–1000 V	Ip quench	1 ms	20 points	10% + 5 mV
		0–30 V	Default	1 ms	20 points	5 mV
04. Plasma energy	006: βp	0.01–5	Ip >3 MA	10 ms	Integral	0.05 + 5%
			Ip quench	0.1 ms	Integral	30%
05. Radiated power	007a: Prad total, divertor	1–300 MW	Stationary	10 ms	Integral	10%
	007b: Prad total (transient), divertor	25 MW—100 GW	Transients	1 ms	Integral	20%
	008a: Prad total, main plasma	1–300 MW	Stationary	10 ms	Integral	10%
	008b. Prad, top region (upper X-point)	0.1–20 MW	Stationary	10 ms	Integral	10%
	008 c: Prad total (transient), main plasma + upper X-point	50 MW—200 GW	Transients	1 ms	Integrated, 4 toroidal locations	20%
	009a: Prad total	1–300 MW	Stationary	10 ms	Integral	10%
	009b: Prad (transient) total	50 MW—200 GW	Transients	1 ms	integrated, 4 toroidal locations	20%
06. Line-averaged electron density	011: Line-averaged electron density	1×10^{18}–4×10^{20} m^{-3}	Default	1 ms	Integrated	1%
		8×10^{20}–2×10^{22} m^{-3}	DMS	1 ms	Integrated	100%

(Continued.)

Table 10. (Continued.)

Measurement group	Parameter	Range	Condition	Resolution		Accuracy
				Time or Freq.	Spatial or Wave No.	
07. Neutron flux and emissivity	012: Fusion power	100 kW—0.9 GW		1 ms	Integrated	10%
	013: Fusion power density	1 kW.m^{-3}–4 MW.m^{-3}		1 ms	a/10	10%
	014: Neutron- and α-source profile	1×10^{14} -1.4×10^{18} n.m^{-3}.s^{-1}		1 ms	a/10	10%
	015: Total neutron flux	1×10^{14}–3.2×10^{20} n.s^{-1}		1 ms	integrated	10%
	102.Total fusion power for safety relevant measurements determination	70 MW—0.9 GW		1 s	None	10% + 10 MW
08. Error field, locked mode and RWM identification	016a: Br/<Bp> RWM	1×10^{-4}–2×10^{-2}		1 ms	{0,1} < {*m,n*} < {3,2}	30%
	016b: Br/<Bp> Error Field	1×10^{-4}–2×10^{-2}		1 ms	{0,1} < {*m,n*} < {3,1}	30%
	016 c: Br/<Bp> Locked Mode	1×10^{-4}–2×10^{-2}		1 ms	{0,1} < {*m,n*} < {10,3}	30%
09. Low (*m,n*) MHD modes, sawteeth, locked modes, and disruption precursors	017: Btheta/<Bp>	1×10^{-4}–2×10^{-2}		10 Hz—35 KHz	{0,1} < {*m,n*} < {10,7}	10%
10. Plasma rotation	018: vPOL	1–50 km s^{-1}		10 ms	*a*/30*	30%
	019: vTOR	1–200 km s^{-1}		10 ms	*a*/30	30%
11. Fuel ratio in plasma core	020. nT/nD Core	0.01–10	*r/a* <0.85	100 ms	Integral	20%
12. Impurity species monitoring	021a: C, O influx	1×10^{16}–5×10^{19} m^{-2} s^{-1}		10 ms	Integral	10% (rel)
	021b: Be influx	1×10^{16}–5×10^{19} m^{-2} s^{-1}		10 ms	Integral	10% (rel)
	021 c: Be influx distribution	1×10^{16}–5×10^{19} m^{-2} s^{-1}	Be influx distribution	10 ms	Local, 15–40 mm	10% (rel)
	022: Be, C, O Relative Concentration	1×10^{-4}–5×10^{-2}		10 ms	Integral	10% (rel)
	023: Cu Influx	1×10^{15}–5×10^{18} m^{-2} s^{-1}		10 ms	Integral	10% (rel)
	024: Cu rel. conc.	1×10^{-5}–5×10^{-3}		10 ms	Integral	10% (rel)
	025: Extrinsic (Ne, Ar, Kr) influx	1×10^{16}–2×10^{19} m^{-1} s^{-1}		10 ms	Integral	10% (rel)
	026: Extrinsic (Ne, Ar, Kr) Relative Concentration	1×10^{-4}–2×10^{-2}		10 ms	Integral	10% (rel)

(Continued.)

Table 10. (Continued.)

	027: W influx	1×10^{14}–5×10^{17} $^{-2}$ s^{-1}		10 ms	Integral	10% (rel)
	028: W Relative Concentration	1×10^{-6}–5×10^{-4}		10 ms	Integral	10% (rel)
13. Zeff (line-averaged)	029. Line-averaged Zeff	1–5		10 ms	Integral	20%
14. H-mode, ELMs and L-H mode transition indicator	030: ELM visible radiation bursts			0.02 ms	Main plasma integral, Divertor one site	—
	031: ELM density transient	5×10^{18}–3×10^{20} m^{-3}	r/a >0.85	10 ms	5 mm	5%
	032: ELM temperature transient	0.05–10 keV	r/a >0.85	0.1 ms	5 mm	10%
	033: L-H Dα step			0.02 ms	Main plasma integral, Divertor one site	—
15. Runaway electrons	034: Emax runaway	1–100 MeV		10 ms	—	20%
	035: I runaway	(0.05–0.7) × Ip	After thermal quench	10 ms	—	30% (rel)
		0–5 MA	Failed breakdown	10 ms		50 kA
16. Divertor operational parameters	037: Gas composition (Fuel, He, impurities) (P div)	$(1 \times 10^{-4}$–1) × Pdiv		1 s	Several points	20%
	038: Gas pressure, divertor (Pdiv)	1×10^{-4}–20 Pa		50 ms	Several points	20%
	039: Max. surface temperature, divertor	200 °C–3600 °C		2 ms	—	10%
	040a. Fine surface metrology—Divertor	0–1 mm	Default	<1 per discharge	1 mm	10 μm
	040b. Fine net erosion and redeposition—first wall	0–100 μm	LTM [Long Term Maintenance]	Sample retrieval possible only during LTM	50 locations on 700 m2 [of first wall]	1 μm
	041: Position of the ionization front, divertor	0–1 m		1 ms	100 mm	—
17. First wall (FW) visible image & wall temperature	042: Surface luminance, FW	40 -1×10^{5} cd m^{-2}	All heating ports, upper strike region, dome, baffle. >50% of rest, evenly distributed.	10 ms	3 mm	30% absolute, 1% relative

(Continued.)

Table 10. (Continued.)

Measurement group	Parameter	Range	Condition	Resolution		Accuracy
				Time or Freq.	Spatial or Wave No.	
	043: Surface temperature, FW	200 °C–3600 °C	All heating ports, upper strike region, dome, baffle. >50% of rest, evenly distributed.	10 ms	5 mm	20 °C
	044: Surface temperature during ELMs, FW	400 °C–3600 °C		20 us	5 mm	20 °C
18. Gas pressure and composition in main chamber	045: Gas composition (Fuel, He, impurities), main (Pmain)	$(1 \times 10^{-4}$–1) Pmain		10 ms	Several points	50%
	046: Gas pressure, main (Pmain)	1×10^{-4}–1 Pa		1 s	Several points	20%
19. Gas pressure and composition in vacuum ducts	047: Gas composition (Fuel, He, impurities), duct (Pduct)	$(1 \times 10^{-4}$–1) ·Pduct		1 s	Several points	20%
	048: Gas pressure, duct (Pduct)	1×10^{-4}–20 Pa		100 ms	Several points	20%
20. In- vessel inspection	049: Wall image	100% coverage of FW and divertor			1 mm	
21. Halo currents	050a: Poloidal current in one sector	0.01–0.1 Ip	In disruption	1 ms	9 sectors, between injection points to VV	20%
	050b: Current distribution in divertor cassette	0–190 kA	In disruption	1 ms	6 cassette targets, dome, VV connections	20%
22. Toroidal magnetic field	051: Toroidal Magnetic Field BT	−5.5–+5.5 T	Variation in pulse	1 s	2 locations	1 mT + 0.1%
23. Electron temperature profile	052: Core Te profile	0.5–40 keV	r/a <0.85	10 ms	a/30	10%
	053: Edge Te profile	0.05–10 keV	r/a >0.85	10 ms	5 mm	10%
24. Electron density profile	054: Core ne profile	3×10^{19}–3×10^{20} m^{-3}	r/a <0.85	10 ms	a/30	5%
	055: Edge ne profile	5×10^{18}–3×10^{20} m^{-3}	r/a >0.85	10 ms	5 mm	5%
25. Current profile	056: q profile	0.5–5	Physics study	10 ms	a/20	10%
		5–9	Physics study	10 ms	a/20	50%
	057: Normalized Position of q = 1.5,2 surfaces	0.3–0.9	NTM Feedback	10 ms	—	50 mm/a

(Continued.)

Table 10. (Continued.)

	058: Normalized Position of qmin	0.3–0.7	NTM Feedback	1 s	—	50 mm/a
26. Zeff profile	059: Zeff profile	1.0–5.0	Default Transients	100 ms 10 ms	*a*/10 *a*/10	10% 20%
27. High frequency instabilities (MHD, NTMs, AEs, turbulence)	060: Fishbone Btheta(mode)/ <Bp>	1×10^{-4}– 5×10^{-2}		0.1–10 kHz	(m,n) = (1,1)	30%
	061: NTM δT/Te	(0.1–5) $\times$ 1 $\times$ 10^{-2}	Te >1 keV,	0.1–10 kHz	Island width >20 mm	1 × 10-3
	062: TAE Btheta/<Bp>	1×10^{-6}– 4×10^{-4}		30 kHz— 0.5 MHz	N = 2–50	30%
	063: TAE $\delta N/n$, $\delta T/T$	5×10^{-6}– 5×10^{-4}		30 kHz— 0.5 MHz	n = 2–50	30% (rel)
28. Ion temperature profile	064: Core Ti	0.5–40 keV	*r/a* <0.85	100 ms	*a*/30	10%
	065: Edge Ti	0.05–10 keV	*r/a* >0.85	100 ms	10–20 mm	10%
29. Core He density	066: Core nHe/ne	1%–20%	*r/a* <0.85	100 ms	*a*/10	10%
	067: 3He concentration profile	1%–10%	*r/a* <0.85	100 ms	*a*/10	10%
30. Confined alphas and fast ions	068: Alpha Density profile	(0.1–2) E18 m^{-3}		100 ms	*a*/10	20%
	069: Alpha energy spectrum	0.1–3.5 MeV		100 ms	*a*/10	20%
	070: p, D, T He3 energy spectrum	0.1–1 MeV		100 ms	*a*/20	20%
31. Escaping alphas and fast ions	071: Fast particle loss distribution	±1 v‖/v	Steady-state and transient	5 μs	Discrete measurement regions	20%
		0.1–5 MeV	Steady-state and transient	5 μs	Discrete measurement regions	20%
	072: Fast particle loss flux	0.2–20 MW m^2	Steady-state and transient	5 μs	Discrete measurement region	10%
32. Impurity density profile	073: Fractional content, Z >10	0.01–0.3%	*r/a* <0.85 *r/a* >0.85	100 ms 100 ms	*a*/10 50 mm	20% *c*
	074: Fractional content, $Z \leqslant 10$	0.5%–20%	*r/a* <0.85 *r/a* >0.85	100 ms 100 ms	*a*/10 50 mm	20% 20%
33. Fuel ratio in edge	075: n_H/n_D, edge	0.01–0.1	*r/a* >0.85	100 ms	Radial integral	20%
	076: n_T/n_D, edge	0.01–10	*r/a* >0.85	100 ms	Radial integral	20%

(Continued.)

Table 10. (Continued.)

Measurement group	Parameter	Range	Condition	Resolution		Accuracy
				Time or Freq.	Spatial or Wave No.	
34. Neutron fluence	077: First wall neutron fluence	0.1–1 MWa m^{-2}			Several poloidal points	10%
	101: Neutron fluence for lifetime	0–0.4 MWa m^{-2}	Normal operation	1 d	Equatorial midplane DFW	0.03 Mwa m^{-2} (2σ)
35. Impurity and D, T influx in divertor	078: Be, C, W influx in divertor	1×10^{17}–1×10^{22} at s^{-1}		1 ms	50 mm	30%
	079: D2, T2 influx in divertor	1×10^{19}–1×10^{25} at s^{-1}		1 ms	50 mm	30%
36. Plasma parameters at the divertor targets	080a: ne, divertor target	1×10^{18}–1×10^{22} m^{-3}		1 ms	3 mm resolvability, 24 mm interval	30%
	080b: Divertor Target Parallel Ion Flux	1×10^{4}–1×10^{7} Am^{-2}		0.01 ms	3 mm resolvability, 24 mm interval	30%
	081: Te, divertor target	1 eV—150 keV		1 ms	3 mm resolvability, 24 mm interval	30%
37. Radiation profile	082a. Divertor Prad Profile	0.1–300 MWm^{-3}	Stationary	10 ms	50 mm	10%
	082b: Divertor Prad (transient) Profile	0.03–20 GWm^{-3}	Transient	1 ms	50 mm	20%
	083a: Prad profile, main plasma + upper X-point	0.001–100 MWm^{-3}	Stationary	10 ms	100 mm	20%
	083b: Prad profile (transient), main plasma + upper X-point	10 MWm^{-3}–1 GWm^{-3}	Transient	1 ms	100 mm	20%
	083 c: Prad vertical line integrals (transient) main plasma + upper X-point	30 MW m^{-2}–8 GW m^{-2}	Transient	1 ms	3-5 vertical line integrals at 4 toroidal locations	20%
38. Heat loading profile in divertor	085: Power load	0.02–5 GW m^{-2}	Disruption	0.02 ms	3 mm	20%
		0.1–25 MW m^{-2}	Default	2 ms	3 mm	10%
	086: Surface temperature	1000 °C–3600 °C		0.02 ms	3 mm	10%
		200 °C–1000 °C		2 ms	3 mm	10%
39. Divertor Helium density	087: nHe, divertor	1×10^{17}–1×10^{19} m^{-3}		1 ms		20%
40. Fuel ratio in divertor	088: nH/nD, divertor	0.01–0.1		100 ms	Integral	20%
	089: nT/nD, divertor	0.01–10		100 ms	Integral	20%
41. Divertor electron parameters	090. ne Divertor	1×10^{19}–1×10^{22} m^{-3}		1 ms	50 mm × 3 mm	30%
	091: Te, divertor	0.3–200 eV		1 ms	50 mm × 3 mm	20%

(Continued.)

Table 10. (Continued.)

42. Ion temperature in the divertor	092: Ti profile, divertor	0.3–200 eV		1 ms	50 mm × 3 mm	20%
43. Divertor flow	093: Vp Divertor	1×10^3–1×10^5 ms^{-1}		1 ms	50 mm × 3 mm	20%
44. nH/nD ratio in plasma core	094: nH/nD, core	0.01–0.1	r/a <0.85	100 ms	Integral	20%
45. Neutral density between plasma and first wall	095. D/T Influx in Chamber	1×10^{18}–1×10^{20} at m^{-2} s^{-1}		100 ms	Several positions	30%
46. Dust monitoring	097a: Surface Concentration of mobilizable dust (divertor cassette body under the dome and VV floor)	0.01 ∼ 40 kg m^{-2}		Once every LTM or on demand	Integral	± factor 5
	097b: Dust size distribution	1–200 μm	6 bins per decade (E6)	Once every LTM or on demand	Integral	±20% (relative)
	097 c: Viewing of dust area on and under the divertor	4 mm × 2 m		Once every LTM or on demand	100 μm	±50%
47. Tritium Monitoring	099a. Divertor Surface H, D, T Concentration (Inner baffle)	1×10^{21}–2×10^{24} m^{-2}	Outside plasma pulses under vacuum condition	On demand	Individual points 5 mm lateral resolution	50% abs, 20% relative
	099b. First Wall Surface H, D, T Concentration	1×10^{18}–2×10^{23} m^{-2}	LTM	On request during LTM	50 locations on 700 m2	20%
48. In-vessel ECH stray radiation	103: In-vessel ECH stray radiation intensity	Breakdown: Up to 3 MW m^{-2} during 5.5 sec		10 ms	5–9 sectors. Up to 20 sensors/sector	100 kW m^{-2}
		Normal operation: Up to 1.25 MW m^{-2} during pulse		10 ms	5–9 sectors. Up to 20 sensors/sector	100 kW m^{-2}

(*) a/X is generally taken as the nominal minor radius, 2 m X^{-1}. $a/10 = 200$ mm etc.

2. Preparation for the measurements of plasma-metallic wall interaction in support of the ITER research plan: divertor power flux, impurity, and tritium retention

S.-H. Hong[4], B. Peterson[5], M.H. Aumeunier[1], A. Bultel[6], C. Klepper[7], D. Rasmussen[7], H. Choi[8], C. Grisolia[1], K. Kim[8], S. Oh[8] and C. Sun[8]

2.1. Introduction

To achieve the research goals of ITER, governing challenges of plasma-wall interaction are inevitable, especially achieving $Q = 10$ scenarios with a minimal amount of metallic impurities inside the core [58]. Furthermore, very high heat flux to the tungsten divertor is expected as well as neutron wall loading originating from the D–T reaction [59]. Detached plasma operation scenarios with high-precision measurements of the divertor power flux and impurity contents in the core and SOL are required, which will provide sophisticated and accurate input for plasma control [60]. Furthermore, ITER is licensed as a nuclear facility which needs to follow very strict license control on the amount of tritium inside the machine as well as on-site [61].

The heat flux on the divertor will be measured by an in-vessel infrared (IR) camera system looking down from the top slanted ports. The IR camera system needs to be calibrated for the measurements of the temperature of the tungsten divertor surface (monoblocks). The global power balance including plasma heating and current drive can be evaluated by the measurements of the plasma stored energy and total radiated power from the plasma.

Note that, the heat flux measurements by an IR camera strongly depend on the condition of the surface [62]. Change of the surface emissivity will result in wrong measurements of the monoblock temperature leading to wrong heat flux estimates. If the emissivity changes as a function of time, the changes must be followed: erosion of the tungsten surface by ion bombardment and corresponding prompt redeposition of tungsten atoms change the emissivity of the surface as well as the sputtering threshold. Furthermore, the redeposition of eroded FW materials (beryllium and tungsten) onto the FW mirror has to be mitigated [63].

As the FW of ITER will be a full metal wall consisting of beryllium and tungsten, there will be a large portion of stray radiation caused by reflection from the FW [64]. Such reflection caused by the wall gives wrong information to the local temperature measurements, the location of hot spots, and finally to the global power balance. Therefore, a dedicated technique to identify and remove the reflected patterns from the measurements based on various cameras installed at ITER is essential.

Due to the use of tritium in the fusion plasma operation phase, active monitoring of tritium inside the VV is mandatory [65]. A LIBS and a LIDS are under development.

In this subchapter, we will discuss the progress of plasma-surface interaction diagnostics, including specific design issues, and their limitations. In section 2, the development of an image bolometer system for ITER will be described in detail. In section 3, the development of the ITER prototype VUV spectrometer will be discussed. The status of the development of LIBS and LIDS for ITER will be followed in section 4. In section 5, technical challenges in the measurements of the plasma-wall interaction at ITER, i.e. the development of reflection elimination techniques and the systematic measurements of emissivity and the bi-directional refraction distribution function (BRDF) of tungsten, and the angular dependence of IR measurements will be described. The subchapter will be summarized in section 6.

2.2. Measurements of radiated power loss by imaging bolometers

For the purpose of the measurement of radiated power from ITER, the resistive bolometer (RB), which has a long history in fusion studies [66–69], is the primary detector being considered and prepared for installation. The RB is relatively compact, which permits it to be installed in the FW and divertor surrounding the plasma at one poloidal cross-section. This enables tomographic inversion of the line-averaged data to produce a local measurement of the radiated power density [69, 70]. One of the main drawbacks of the RB is the lamellar construction of the detector head, consisting of a radiation-absorbing metal foil, an insulating membrane, and a metallic meander that forms the resistor. Intrinsic stresses from the manufacturing process paired with different thermal expansion coefficients for absorber and membrane led to high localized stresses and breaking during the fatigue cycle under thermal cycling [71] for the prototypes based on Pt absorbers on a SiN membrane. However, this problem has been solved using an Au absorber layer instead of Pt [72]. Prototypes with different configurations and 20 μm thick Au absorbers, as necessary for ITER, have been shown to withstand thermal cycling up to 400 °C. Much research has been performed in the development of these detectors in the 14 years since the publication of the Progress in the ITER Physics Basis [4] and a diagnostic review [69]. The work on the RB has been recently reviewed [72] and therefore, the associated design and procurement activities for ITER will not be covered in this article.

Another type of detector that has seen much development in the last 14 years is the IRVB [73, 74]. The IRVB consists of one large metal foil held in a metal frame that absorbs the radiation incident through an aperture. The resulting temperature increase of the foil is measured by an IR camera located outside of the bioshield. IR optics bring the IR signal out of the bioshield and through the vacuum interface, avoiding the use of signal wires. The IRVB is being considered for application to ITER and future fusion reactors due to its use of inherently reactor relevant materials and its lack of wired feedthroughs, avoiding the risks of leaks. In contrast, the resistive bolometers require four wires for each channel to be brought through the vacuum interface. In comparison to the RB, the relative disadvantages of the IRVB are the large size and lower sensitivity. However, the sensitivity advantage of the RB is lost to some extent in the presence of radio-frequency-wave-induced noise if the detectors are not adequately shielded, which does

not plague an IRVB since all electrical wiring is located in the IR camera which can be properly shielded [75]. The RBs also have a well-developed *in-situ* calibration system using ohmic heating of the foil which allows calibration of the foils between discharges [76]. The large size of the IRVB and the necessity that all of the channels for one IRVB would view the plasma through the same aperture, require that it be installed in a port plug with a tangential view, relying on the assumption of toroidal symmetry in order to perform the tomographic inversion. Considering the differences between the two concepts in foil temperature measurement, lines of sight (LOS), and possible failure modes, they represent complementary approaches to the measurement of radiated power, which would provide some redundancy and assure the uninterrupted measurement of radiated power in ITER in case either would fail. Also, the differing LOS of the two concepts could be combined to enhance the tomography and the study of toroidal asymmetries in radiation.

In this section, we will summarize the development of the IRVB and discuss the possibility of applying it to ITER. The primary developments that will be reviewed are of a uniform and reproducible blackening of the absorbing foil, of an *in-situ* calibration system [77, 78] and the successful application of IRVBs to LHD [79], JT-60U [80], KSTAR [81], C-Mod [75], and MAST-U [82]. Finally, we will evaluate the viability of the application to ITER in terms of the estimated SNR.

2.2.1. Development of the IRVB. Significant progress has been made in the development of the IRVB detector foil through the procurement of a vacuum vapor deposition facility for blackening the metal absorber foil with graphite. Blackening of the foil is necessary on the plasma side to increase absorption in the visible spectrum and on the IR camera side to improve the IR emissivity of the foil. Previously an aerosol graphite colloid called Aerogdag was used to hand spray a graphite coating on the foil. This resulted in a thick coating on the order of 5–8 μms [83] which turned out to be quite non-uniform and also not reproducible on both sides of the foil. The nonuniformity and irreproducibility could be compensated for in the calibration but may cause problems in the analysis and is better to be avoided. Therefore, a vacuum vapor evaporation facility was purchased and adapted to the coating of graphite on the metal foils [78]. This resulted in the ability to reproducibly control the thickness of the coating to within about 20 nm and allowed the determination of the optimal thickness of the coating to be 160 nm. Observation with a scanning electron microscope (SEM) also showed the coated surface to be much more uniform than in the hand-sprayed case.

Other progress in the development of the IRVB involved the improvement in calibration techniques and the development of an *in-situ* calibration system. Calibration of the IRVB foil involves the determination of the local values of the thermal and optical properties of the foil by using a HeNe laser or UV diodes. These properties include the thermal diffusivity and conductivity of the foil and the blackbody emissivity of the graphite coating. These parameters are then used in the two-dimensional heat diffusion equation to solve for the incident radiated power from the temperature distribution on the foil measured by the IR camera. In order to take into account nonuniformities in the parameters and in the foil thickness, each point of the foil must be calibrated with a spatial resolution equivalent to that of the IRVB. In other words, each IRVB pixel must be individually calibrated. With the IRVB, calibration of the foil is done by heating the foil with a HeNe laser [73] or UV diodes [84] and measuring the change in the resulting temperature profile on the foil. In the laboratory, we move the foil keeping the IR camera and laser fixed in order to sample each part of the foil [84]. For *in-situ* calibration however, the laser must be moved from spot to spot on the foil. This type of system was realized on JT-60U [85, 86] and LHD [77, 78].

2.2.2. Application of the IRVB to various devices. IRVBs have been applied to numerous devices. The first IRVB was installed on LHD [87] and up to four IRVBs have been simultaneously operated on LHD providing radiation images for comparison of synthetic images from EMC3-Eirene [88] and in an attempt at three-dimensional tomography [89]. Two different versions of the IRVB were tested on JT-60U. The first used a relatively low-cost, low-performance IR camera with a 2.5 μm thick $\times$ 9 cm $\times$ 7 cm gold foil with a semi-tangential view of the plasma from a 5 mm $\times$ 5 mm aperture [90]. This IRVB was the first to demonstrate two-dimensional radiation profiles in a tokamak through tomographic inversion and clearly showed the increase in core radiation during the introduction of iron impurities into the plasma [91, 92]. Just prior to the shutdown of JT60-U this IRVB was upgraded with a 5 μm Ta foil and an advanced IR camera with periscope optics. This resulted in a 30-fold improvement in sensitivity compared to the previous version [80]. This IRVB was later transferred to the KSTAR experiment and after upgrading the IR camera [81], it routinely provided total radiated power measurements and 2D profiles through tomographic inversion [92] as the only bolometer diagnostic on KSTAR. The third application of the IRVB to a tokamak took place on the C-mod experiment. This experiment showed good agreement between the RBs and IRVB and demonstrated the noise-free advantage of the IRVB compared to the RBs during radio-wave heating [75]. Recently the IRVB has been installed in the MAST-U experiment, demonstrating the advantages of the two dimensional view of the plasma in filling in gaps in the RB fields of view of the super-x divertor [82].

2.2.3. Investigating the viability of an IRVB for ITER. During the last six years, investigations have been made into the viability of an IRVB for ITER. An example of a tangential field of view of an IRVB for ITER is shown in figure 17. The 7 cm $\times$ 9 cm Pt foil center is located at a major radius of 8.56 m and a height of 0.44 m above the midplane in an arbitrary location in an equatorial port. The aperture is 6 mm $\times$ 6 mm and is located 7.8 cm in front of the foil. The aperture and foil have a downward tilt of 4 degrees with respect to the horizontal. An IR camera and IR optical system with 1024 $\times$ 1280 pixels,

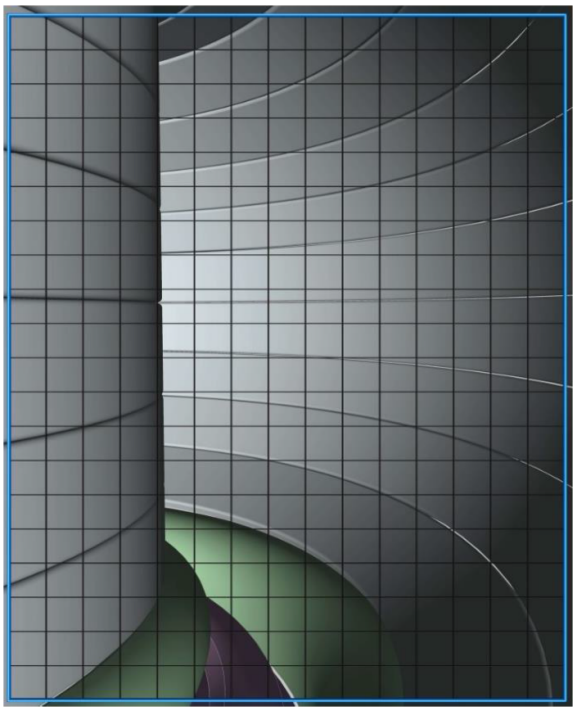

Figure 17. Field of view for an IRVB in ITER.

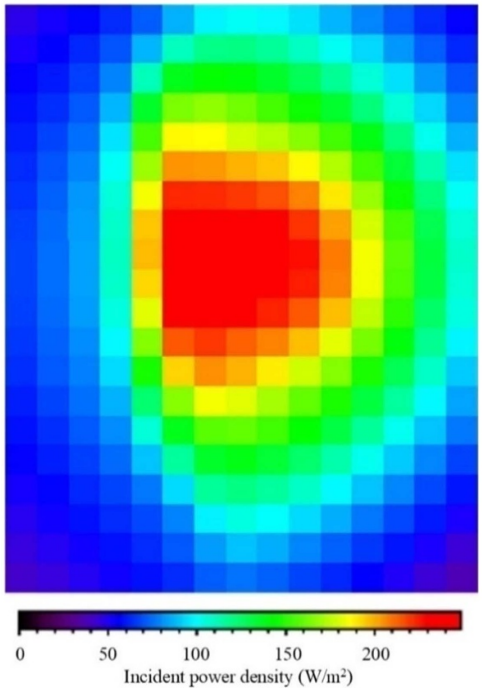

Figure 18. Synthetic image of radiation form SOLPS and SANCO models from the IRVB with the field of view shown in figure 17.

105 f s^{-1} and a sensitivity of the foil temperature of 15 mK is assumed. Using location and photon energy spectrum dependent models of the radiation from SOLPS (edge) and SANCO (core) we determine that the Pt foil thickness necessary to stop 90% of the incident power from the highest energy channel to be 36 μm. Using this thickness, we achieve an IRVB with 15 $\times$ 20 channels, a sensitivity of 3.8 W m^{-2} and a SNR of 65 for the maximum signal of 250 W m^{-2} from synthetic images shown in figure 18 calculated from the SOLPS and SANCO models [93]. In addition a feasibility study involving two tangentially viewing IRVBs (one viewing the entire crossection and one viewing the divertor) located in existing VIS/IR diagnostic locations in ITER was carried out including analysis of SNRs and nuclear heating [94]. The IRVBs each had 15 $\times$ 20 pixels and thicknesses of 30 and 10 μms, respectively, which should stop 95% of the radiated power incident on the foil. This resulted in SNRs of 77 and 59, respectively. Monte Carlo Nuclear Particle code analysis showed the neutron heating of the foil to be below the estimated signal noise level. However, heating by secondary gammas was on the order of half of the expected signal level, indicating the need for some sort of countermeasures.

2.2.4. Summary. In conclusion, recent progress has shown that the IRVB should be applicable to ITER and future fusion reactors as a primary radiation diagnostic or one that is complementary to the conventional RBs and provides necessary redundancy. Future work will include tomographic modeling to determine the necessary foil thickness and spatial resolution. Future diagnostic design should include consideration of the necessary cooling of the foil frame and the IR optics (needed to bring the IR signal from the foil to the IR camera located behind the bioshield, similar to VIS/IR diagnostics) to insure adequate sensitivity of the diagnostic and effects of thermal radiation from hot components on the measurement signal in addition to ITER relevant prototype testing.

2.3. Impurity measurements by ITER VUV spectrometer

Most of the line emissions from plasmas in ITER are expected to be in the VUV or soft x-ray (SXR) wavelength ranges of 0.05–200 nm. These line emissions mainly originate from intrinsic impurities such as Be (the FW), O (oxidized layer on the FW), He (the residual gas after glow discharge or He ash), Cu (the hidden layer of the FW or divertor), Fe (diagnostic FW (DFW)), Ni (DFW) and W (divertor). Furthermore, line emission from extrinsically injected atoms for operations of a radiative divertor (Ar, Ne, and Kr) are also expected. Monitoring of these impurity species is required to diagnose the overall machine conditions and impending fault conditions during long-pulse operation.

In ITER, three sets of distinct VUV spectrometers in different places are employed to facilitate impurity monitoring with full coverage of different regions of plasmas in core, edge, and divertor as seen in figure 19 [95–97].

The design of the VUV core survey spectrometer is optimized for the monitoring of impurity species of all relevant impurity ions over a broad spectral range of 2.4–160 nm [95, 98]. The required sensitivity of the spectrometer is derived from the calculated photon emissivities of impurity species from plasma emission modeling of ITER using the SANCO impurity transport code [99] or SOLPS-ITER code [100]. High spectral resolution at 10 ms time resolution is accomplished

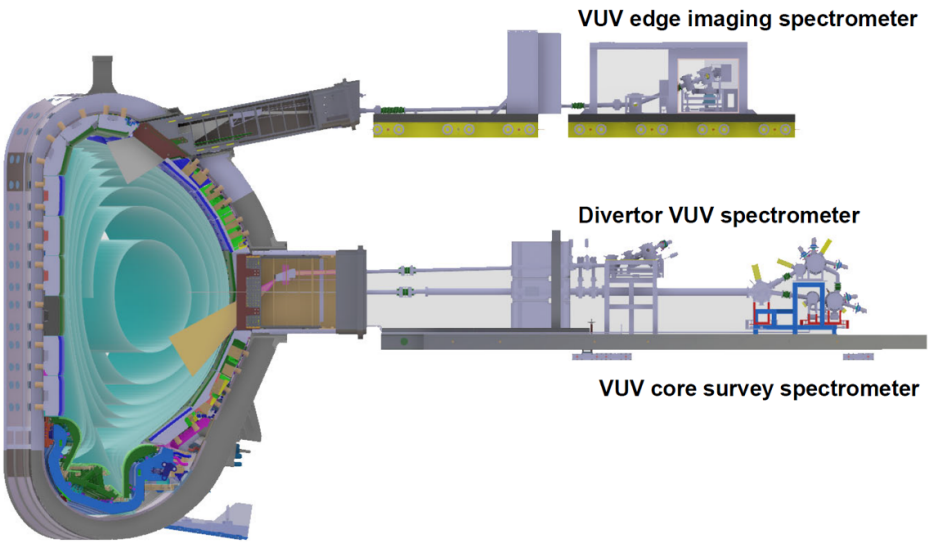

Figure 19. Overview of three ITER VUV spectrometers, VUV core survey spectrometer, divertor VUV spectrometer located in equatorial port, and VUV edge imaging spectrometer located in upper port.

by implementing a five-channel spectrometer for the broad wavelength range of 2.4–160 nm. A spectral resolution, $\lambda/\Delta\lambda$, of several hundred ($\sim$500) with a high throughput and etendue of $\sim 1 \times 10^{-4}$ mm^{2}sr resulted as the output of the design optimization for geometry parameters of a spectrometer using a toroidal shaped grating [101]. To verify the design of the ITER VUV spectrometer with regard to alignment and efficiency, a prototype VUV spectrometer has been developed [95, 96]. The prototype VUV core survey spectrometer with a wavelength ranging from 14.6 nm to 32 nm was installed at KSTAR after a calibration test in the laboratory [95, 96]. This custom-designed prototype spectrometer with toroidal grating and back-illuminated CCD detector was tested successfully, especially, in the tungsten injection experiment during the KSTAR experimental campaign of 2016.

The primary role of the ITER divertor VUV spectrometer is to measure radiation from impurity ions, especially tungsten ions, in the divertor region. In the previous design for ITER-98 in 1998, the divertor cassette in the ITER lower port was supposed to accommodate the ITER divertor VUV spectrometer [102]. However, it was found that the expected deposition on the field mirror would be severe in the lower port near the divertor plasma compared to the equatorial or the upper ports. The available space in the lower port is also very limited. For this reason, the equatorial port #11 of ITER accommodates the present ITER divertor VUV spectrometer, with one cylindrical field mirror in the port plug and one ellipsoidal collimation mirror after the bio-shield, as seen in figure 19 [96]. The wavelength range was chosen to be from 14.6 nm to 32 nm, targeting the emission from tungsten ions, which would be the main impurity species in divertor plasmas.

The VUV edge imaging spectrometer system located in the upper port is optimized for monitoring of the one-dimensional impurity distribution profile in the plasma edge region of $0.85 < r/R < 1.03$ [97]. The wavelength range of 17—32 nm was chosen for the VUV edge imaging spectrometer to contain important spectral lines. About ten spatial-resolving (imaging) points are to be monitored along a $\sim$1000 mm long line across the flux surfaces in the plasma edge region, as seen in figure 19. The required time resolution for the VUV edge imaging spectrometer is 100 ms.

To minimize risks related to the degradation of the field mirror (the first mirror) due to deposition, erosion, and heating, the field mirror is set back from the plasma as far as possible while maintaining the required poloidal view. Ray-tracing analysis for the collection optics was conducted to allow the mirror solid angle to the plasma to be minimized, with a small entrance pupil at the shutter location. The wavelength range has been chosen so as to minimize reflectivity changes due to deposits of plasma impurities.

Since a full tungsten divertor was included in the baseline design of the ITER divertor in 2013, a wide range of research has been performed for the tungsten divertor, not only for engineering purposes but also to investigate the effect of tungsten ions on plasma performance. To study the effect of the tungsten ions on plasma performance, VUV spectrometers have been used to measure tungsten emission lines in various magnetic fusion devices such as JET (ITER-like wall (ILW)), ASDEX-U, WEST, LHD, EAST, HL-2A, and KSTAR. Recently dedicated experiments using tungsten pellets or injected tungsten dust have been performed to investigate tungsten emission lines in LHD, EAST, and KSTAR [96, 103, 104]. Through these experiments, emission lines from tungsten ions (around from W +24 to W +45) could be identified in the wavelength range of 2–7 nm. In the wavelength range of 15–30 nm, overall unidentified line arrays (quasi-continuum) are typically observed from low charge state ions of tungsten (e.g. W +6), and only a limited number of lines could be identified. Based on these results, the wavelength channel 2–7 nm of ITER VUV core survey spectrometer is expected to be the main channel to measure tungsten ions emission from main plasmas. Due to the limitation of the grazing angle of the first mirror $\sim$16 degree for ITER divertor VUV spectrometer from the space constraints, this

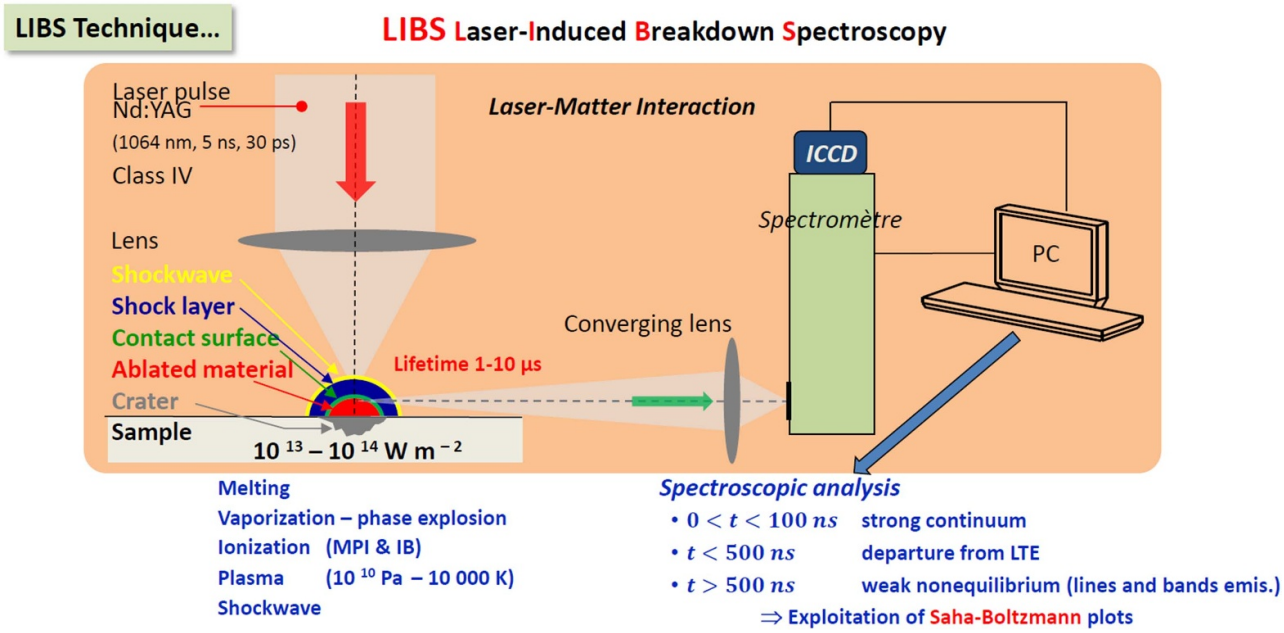

Figure 20. Global view of the LIBS technique implementation.

spectrometer was designed to monitor the low charge state lines of tungsten in the wavelength range of 15–30 nm.

2.4. Tritium monitoring

2.4.1. Laser induced breakdown spectrometer (LIBS). LIBS is a technique for non-contact measurement of the multi-elemental atomic composition of a sample based on the production of a laser-induced plasma [105]. For applications dedicated to nuclear fusion, only the analysis of solid surfaces is developed [106, 107]. Heated by the absorption of photons on the diameter of a pulsed laser beam (typically picosecond or nanosecond), the material is ablated locally by forming a crater and is found in the state of plasma while emitting radiation during its relaxation (cf figure 20). This radiation first appears as a purely thermal continuum, then as first ionic and then atomic lines before taking the form of molecular bands depending on the surrounding conditions (nature of the gas and level of pressure) [108].

The measurement consists in triggering the acquisition at a time sufficiently long from the deposition of the laser energy to allow the observation of plasma spectral lines. The acquisition lasts long enough in relation to the typical time scales of the plasma life time in order to observe spectral lines of low intensity. The intensity of the observed spectral lines depends on the presence of the corresponding elements in the matrix. It also depends on how the sample is ablated. The relative size of the laser spot compared to that of the material grains, their composition, the internal composition gradients as well as the surface condition of the sample play an important role in the observation of the spectral lines. These dependencies are grouped under the term of 'matrix' effects [109].

The observed lines then allow the determination of the atomic composition of the sample in two ways. We can first use calibrated samples of known composition and that are validated by alternative analysis techniques providing 'calibration curves'. By simple comparison, the composition of the material can then be deduced [110]. This approach cannot work for samples of unknown composition or for samples that cannot be subject to *a priori* compositional control. It is therefore very limited.

The second approach, therefore more universal, consists in ensuring that the plasma is in local thermodynamic equilibrium (LTE). This is the 'calibration free' method [111]. This can be achieved if the plasma has had time to relax, that takes few hundred of ns. In addition, this state of equilibrium is better obtained if the plasma relaxes under a confinement obtained with a dedicated gas. The pressure of this gas can be lower or equal to 10^5 Pa. This keeps its internal collision frequencies at sufficiently high levels. Working in argon is very often effective in this respect. Under these conditions, it is possible to reconstruct the spectra using spectral databases and compare them to the experimental one to derive the sample composition.

The LIBS lateral spatial resolution depends on the size of the laser spot on the sample and is improved by the use of a top-hat laser beam. The depth resolution that can be achieved with the LIBS technique is limited by the thermal diffusion in the sample after irradiation which depends on the duration of the pulse. Using an ns laser pulse, the ablated depth is often on the order of a few μm. If ps laser pulses are used, this depth can be reduced to a few hundred nm, but with a significant reduction in the intensity of the lines of interest. This is then very limiting because a shot-to-shot analysis must be carried out in order to measure the depth concentration gradient.

The activities developed around the LIBS technique applied to fusion materials analysis are developed in the frame of the ITPA coordinated activity along two major themes: laboratory

studies concerning the development of LIBS on beryllium relevant ITER samples including modeling activities and the integration of LIBS probes on remote handling arms for tokamak tests [112]. These developments bring together institutes, laboratories and universities as CORIA-CEA, ENEA, VTT, Comenius University, University of Tartu, IPPLM, INFLPR. In what follows, we will concentrate on beryllium-related activities. However, it should be pointed out that LIBS was already used in the mid 2000s to study the composition of codeposited carbon layers [113, 114]. It can also be used to assess the composition of boron codeposited layers as such obtain after boronization of a metal tokamak operating with W, for example [115].

2.4.1.1. Laboratory activities. Beryllium is constituting the FW of the ITER tokamak, and is tested as a priority. It is of major importance to get a reliable technique able to measure with a good accuracy the concentration of hydrogen in the ITER vessel walls. An embedded LIBS operating at atmospheric pressure is considered as one of the possible diagnostic solutions. During LIBS experiments on Be bulk materials, micro-nanoparticles of Be are released due to the ablation process. LIBS experiments must therefore be carried out in a very strict framework given the toxicity of these dusts. Tests are also carried out on other materials considered to be substitutes for beryllium and easier to handle. The samples studied can be loaded with hydrogen (D, H, and T), N, He and the experiments are carried out in rare gases. The objectives focus on the experimental conditions allowing the spectral resolution of the α lines of the Balmer series of hydrogen isotopes (the most intense) [116], in particular between Dα and Tα separated by 0.054 nm. These measurements are carried out in ns and ps mode [117], in accumulated or shot-to-shot mode in order to test the profilometric measurement capacities. The measurement must be coupled with ex situ determinations of the depth ablated by pulse. The results are compared with those obtained by other surface analysis methods as RBS, NRA, TOF-ERDA, SIMS, etc [118]. The agreement is very satisfactory. It should be noted that the first LIBS measurement of the tritium content of a sample was carried out in 2022 by CORIA-CEA. Tests were also carried out on deuterated tiles that had stayed in JET and made available to other partners. Deuterium and hydrogen are measured, as well as metallic pollution [119]. The measurement of helium in the sample is also tested [120]. Helium can be implanted in tokamak at the surface of the material due to plasma implantation. It can also be produced in the bulk material due for instance to tritium decay. However, helium measurement turns out to be very difficult due to the high volatility of this element and the difficulty in exciting it electronically. Double-pulse experiments are currently being carried out to test the heating of the plasma produced by a first pulse in order to increase the population density of the upper level of the transition, and therefore the intensity of the emission line [121]. This is done in picosecond regime in order to keep the capacity of profilometric studies [113].

These experiments are carried out in parallel with modeling studies aimed at reproducing the results and allowing their optimization. Two axes are developed. The first one consists of calculating the expected spectrum under LTE conditions and verifying that the necessary databases are sufficiently accurate. This reconstruction of the spectra is based on the resolution of the radiative transfer equation [122]. The second axis exploits the capabilities of artificial intelligence AI [123]. An extensive database is acquired under controlled conditions over wide ranges of parameters of interest such as hydrogen content, plasma temperature and electron density, etc. Then the AI learns to recognize from this base the characteristics of the plasma emitting the new spectrum that it can observe during an additional experiment. The measurement is thus optimized and made significantly faster.

2.4.1.2. LIBS integration in tokamak. LIBS tests were carried out manually in the EAST tokamak in particular to detect metallic impurities on the limiter. W, Mo and Fe were observed [124, 125]. A compact LIBS probe has been specifically developed to perform these experiments.

Other tests have been carried out by exploiting the capacity of remote handling using robot arms. A solution was tested by ENEA in the FTU tokamak [126]. A compact ns laser source is positioned at the end of a remote arm. The analysis is being carried out by a spectrometer which is also external. A suitable metal cone is positioned on the optical axis in the immediate vicinity of the surface to be analyzed in order to sweep the area with an argon flow allowing the production of laser-induced plasmas in LTE. Metallic pollution has been analyzed as well as the presence of hydrogen and deuterium.

Another solution was tested in the WEST tokamak. A LIBS probe was designed and implemented by CEA-CORIA to equip the end of the WEST articulated inspection arm; the AIA [127]. The probe works at atmospheric pressure. The laser source is ns type. It is positioned outside the tokamak. Two optical fibers are used. The first fiber carries the laser pulse to the head of the probe equipped with adapted optics allowing it to be focused without loss on the wall to be analyzed. The second fiber collects part of the light emitted by the LIBS plasma which leads it to the spectrometer also placed outside the tokamak for analysis. Measurements were made on the tokamak divertor. The metallic impurities have been also measured.

As part of the ITPA activities, the teams intend to carry out the validation of the measurement by LIBS of the quantity of tritium contained in ITER-relevant beryllium samples in the form of deposits but also massive materials.

2.4.2. Real-time residual gas analysis. Residual gas analysis in real-time, i.e. including during plasma operations, will be provided on ITER by DRGAs. DRGAs will measure the neutral gas composition in a divertor port and an equatorial port during plasma operation. Plasma-relevant response time is enabled by assuring most practical and safe proximity to the regions to be sampled (i.e. divertor pumping ducts and main chamber, respectively) and plasma operations-compatibility is assured by selection of radiation resilient sensor heads and the removal of electronics to the diagnostics building.

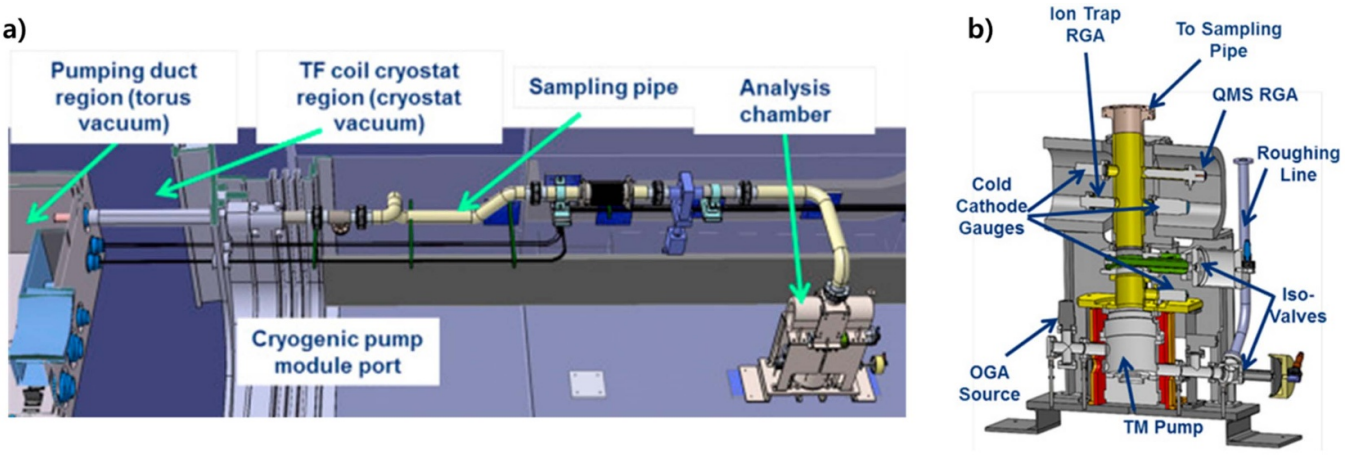

Figure 21. (*a*) RGA integrated into the equatorial 11 port cell support structure [115] and (*b*) analysis chamber.

US-DA has procured two DRGA subsystems, which comprise a connection from the vacuum chamber to an analysis chamber in the port cell (figure 21(*a*)). The analysis station includes not only quadrupole mass spectrometers (commonly called RGAs) but also optical gas analyzers, OGAs, which use a low temperature plasma to provide the excitation of the neutrals (figure 21(*b*)). A combination of the two technologies is critical for resolving fusion fuel cycle-relevant gases. Unlike other Type-2 diagnostics (e.g. the Survey VUV system) the pumping system that is integrated with the DRGA is also a critical part of the measurement. A detailed description of DRGAs, as well as the physics basis for the design and challenges in its completion, is provided in Klepper *et al* [128].

DRGAs at the divertor will play the largest role in the ITER Research Plan and, for this reason, a scope expansion is under consideration to provide two additional systems for the divertor for redundancy. By accessing the sub-divertor region, these systems will be most important for providing real-time information on the hydrogen isotopic content (i.e. H/D/T) in the main plasma, and on the D–T burn via detection of ^{4}He produced as fusion ash and then being channeled by the divertor into the pumping ducts. As such, they provide a global measurement that correlates well with the main plasma content, in plasma-wall equilibration timescales (a few seconds) [129].

DRGAs will also play an important role in analyzing impurities detached from the inner wall, especially important for various wall conditioning techniques: baking, glow discharge cleaning (GDC), ion cyclotron wall conditioning (ICWC)/electron cyclotron wall conditioning (ECWC). Baking of the VV and blanket/FW at 200 °C and 240 °C will remove water and part of hydrogen isotopes, while H or He ions bombard the inner wall to desorb/desaturate surfaces and remove medium Z impurities. Because the toroidal magnetic field will be on during the plasma campaign, the use of GDC as the intershot wall conditioning technique will be limited. ICWC and ECWC need to be developed for the conditioning of the FW surfaces between pulses. In order to optimize the efficiency of those wall conditioning techniques, qualitative and quantitative assessment of the exhaust gas must be performed. Sampling the sub-divertor through a $<\sim$1 mm diameter pressure reducing orifice, the divertor DRGA is optimized for high neutral gas pressure measurements ($\sim$0.1–10 Pa). Therefore, for new applications, such as LID-QMS for T monitoring between shots (Sub-section 4.2) the Equatorial Port DRGA (EP-DRGA, integrated into EP-11) will likely be used, as its sampling pipe is less constricted, designed to dynamically sample main chamber neutral pressures in the 0.001–0.1 Pa range, albeit with $\sim$10 s response time. The EP-DRGA design is less advanced than the divertor DRGA, but the interface between DRGA and T-monitor (i.e. LID-QMS) is currently in work between the two diagnostic teams.

2.5. Technical challenges in the measurements of the plasma-wall interaction at ITER

2.5.1. Elimination of reflection caused by metallic wall. The performances of plasmas strongly depend on the ability to simultaneously monitor and control the plasma-wall interaction for protecting the walls from excessive heat loads. Infra-red (IR) measurement is a key diagnostic to provide thermal images of the plasma facing components (PFC) under plasma exposure. Nevertheless, with the introduction of all-metal walls in today's fusion devices, additional difficulties result in the interpretation of IR measurements through disturbance phenomena such as reflections and/or emissivity variation with surface temperature and plasma exposition (surface erosion/deposition on monitored PFCs). This can lead to inaccurate PFC surface temperature estimation and interpretation of 'false hot spots'. Currently there are no experimental techniques mature enough to overcome these phenomena. A numerical approach is being developed to predict and solve unknown emissivity and reflections features. Such approach is based on an end-to-end simulation (or so-called synthetic diagnostic) able to model all physical phenomena involved in the IR measurement chain (plasma-wall interaction, thermic, photonic and optic).

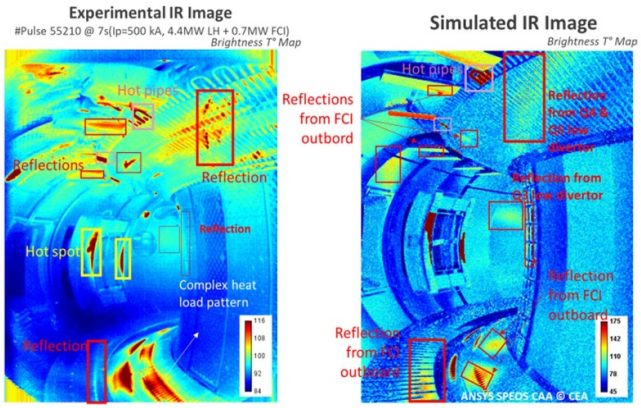

Figure 22. Infrared experimental image (left) and simulated image (right) of ITER-like wide angle tangential view of WEST tokamak. The IR ray tracer is able to separate the thermal events from false hot spots caused by multiple reflections and provide the origin of reflections. Reproduced from [133]. CC BY 4.0.

Ray tracing simulation is also a remarkable tool to intuitively anticipate photon behavior in complex geometries with changing optical materials properties. The ray tracing code developed by the company ANSYS-OPTIS has already been applied on several devices (Tore Supra, WEST, JET, AUG, W7X, ITER) for improving the understanding of IR images in a fully reflective and radiative environment [130–132]. Applied to WEST and AUG, this allowed discriminating both the real heat load deposition from false hot spots (figure 22), while demonstrating the potential impact of a variable emission model on plasma-facing units (PFUs) [133, 134]. Another open-source ray tracing code, Raysect, has been used for modeling volume sources and tested on the AUG bolometry system [135, 136]. W_{ray} and W_{ana} are package simulators being newly developed for the ray tracing and reflection analysis for KSTAR [137]. The technique is being built on the simple idea that the reflections can be discriminated from the true signal when all ray information is given since an optical system (reflection and refraction) is an intrinsically linear system. W_{ray} is a ray tracing code finding all input ray paths, while W_{ana} is a reconstruction code finding the true signal without the contributions of reflections. W_{ray} utilizes bound volume hierarchy (BVH) and multi-thread processing for high speed. The code is based on 'Unity' to reduce the coding load outside ray-tracing, and the photo image generated by W_{ray} is shown in figure 23.

Once all ray tracing roots are given, the reflection elimination in a real geometry can be examined. The algorithm is applied to the temperature profiling of the KSTAR PFCs with assumptions of uniform temperature over a single PFC and toroidal symmetry. Figure 24 shows that the reflection is gradually eliminated through error-back-propagations.

In parallel, several laboratory experiments have been conducted to establish a comprehensive model of the material emission and reflectance as a function of roughness, temperature, wavelength, and machining. Before being exposed, it is found that the tungsten emissivity ranges around 0.1–0.2 at 4 μm with a low temperature dependence [138, 139]. These laboratory experiments have proven the angular dependency and a highly specular response of reflectance, which has been confirmed by comparing simulated and experimental images in WEST and AUG. Moreover, these measurements also reveal that the behavior of emission and reflectance varies significantly with sample roughness and machining process. This has been confirmed by experiments in WEST and AUG, showing that thermal optical properties of materials change as the plasma operation progresses [140]. The challenge is now how to monitor these modifications without direct access to in-vessel components. Simulations coupled with dedicated experiments are essential. In WEST, a method based on the double heating process was developed to estimate *in-situ* the emissivity of the W-coated graphite divertor tiles in the WEST tokamak [140]. This method takes advantage of the divertor temperature increase during the plasma operation and uses photonic calculation to disentangle the emitted and reflected parts in the measured radiance. The results show a strong variation of the emissivity along the divertor W surfaces with a factor 4 variation after the experimental campaigns. An alternative method is also currently explored in to identify the emissivity or temperature profile on the divertor PFCs by solving an inverse problem. The method consists in solving a least squares problem that minimizes iteratively the difference between the measured IR image and a modelized image built with a forward radiative model in which all reflections are taken into account [141]. From a numerical prototype, it is shown that target emissivity value can be recovered from a controlled vessel baking scene (with uniform and known temperature) using an inverse thermography method for filtering reflections with an error of 6%. When the emissivity profile is identified, the same method is used to recover the temperature with an accuracy better than 3% after removing the reflections [142]. Recent new methods based on machine learning techniques have also achieved encouraging results in filtering reflections and retrieving the surface temperatures with high accuracy (better than 10%) without knowing emissivity [143]. The next step is to validate all these new numerical approaches on controlled experiments in laboratory before they are automatically used on tokamaks. For the KSTAR tokamak, an experimental setup, W_{emi}, for the measurement of PFC surface properties is constructed and measured the BRDF as shown in figure 25. W_{emi} is equipped with two surfaces mimicking the reflection by W surface near the light source (e.g. target strike point region), where two surfaces are located very closely. For instance, the V-shaped neutral reflector plates at the bottom of the ITER divertor would be examples. In W_{emi}, the second surface can make an angle between 45° to 90° and W surfaces with various roughness are ready to measure.

Figure 26 shows examples of the emissivity and reflectance measurements by W_{emi}. The temperature of the primary tungsten tile (at 90°) is varied from room temperature up to 700 °C. The emissivity at the temperature of 250 °C was 0.15 and it increases to 0.35 at 500 °C. After that, the emissivity seems to be saturated, but this needs to be confirmed. The reflectance from room temperature up to about 500 °C was about 1 %, and then it increased exponentially to 5.3% at a temperature

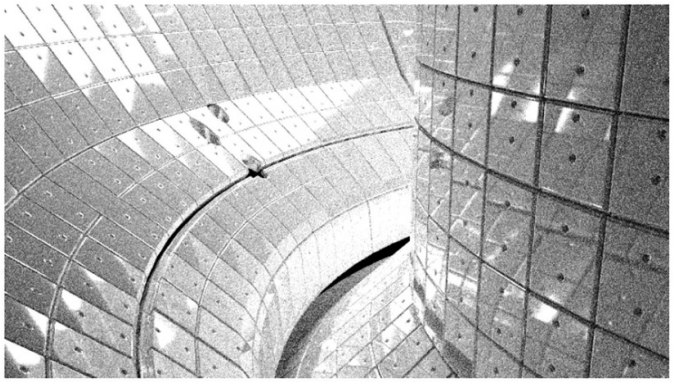

Figure 23. A typical photo image generated with 'W_{ray}'.

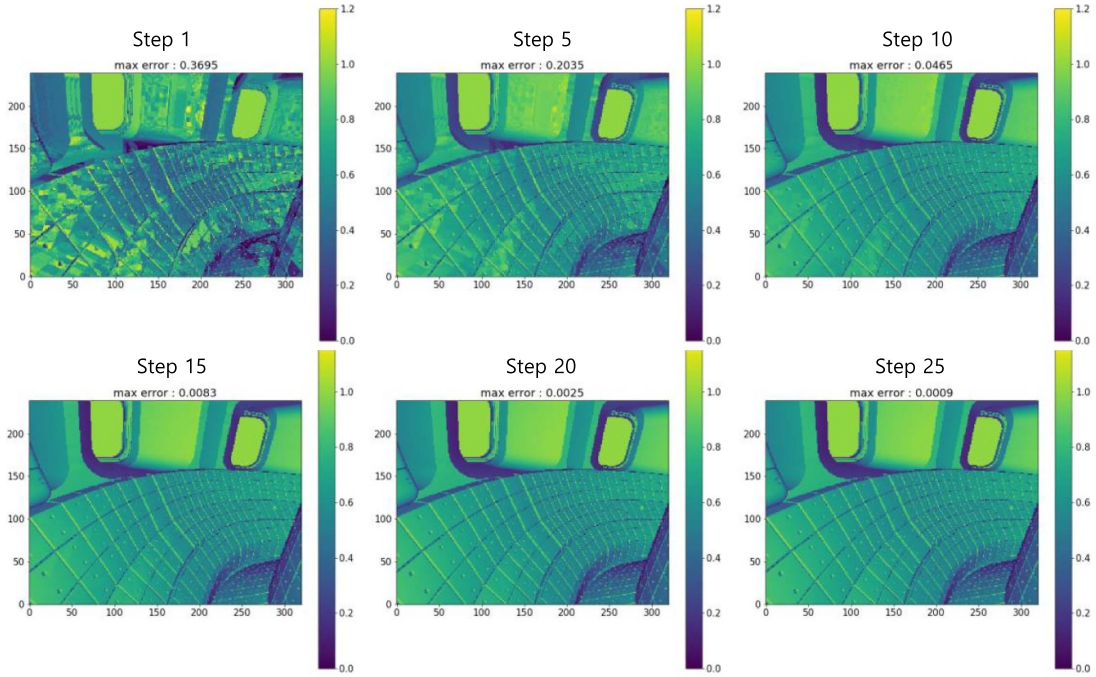

Figure 24. The algorithm test for the elimination of the reflections with error back propagations.

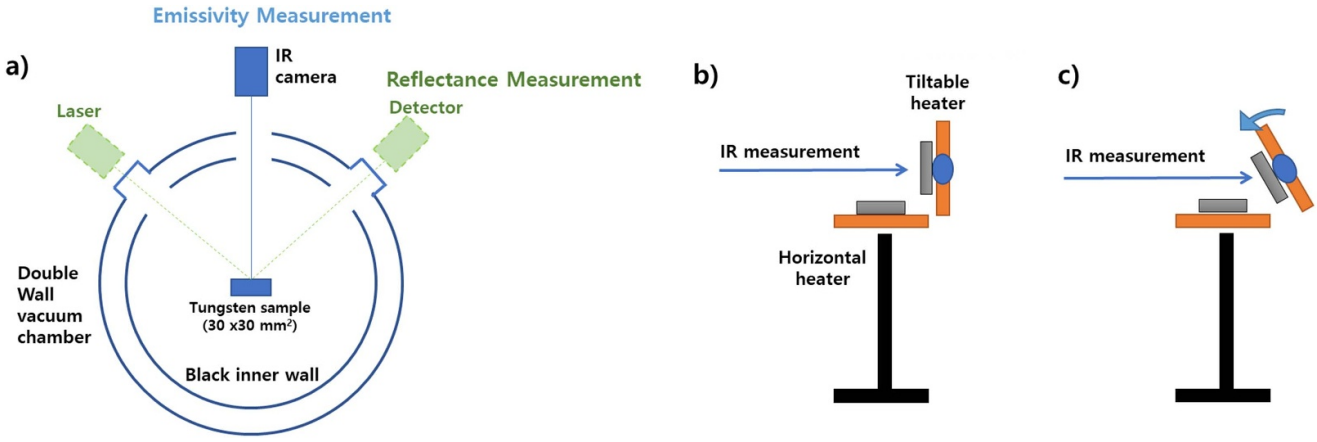

Figure 25. The setup for the emissivity and reflectance measurement of PFCs.

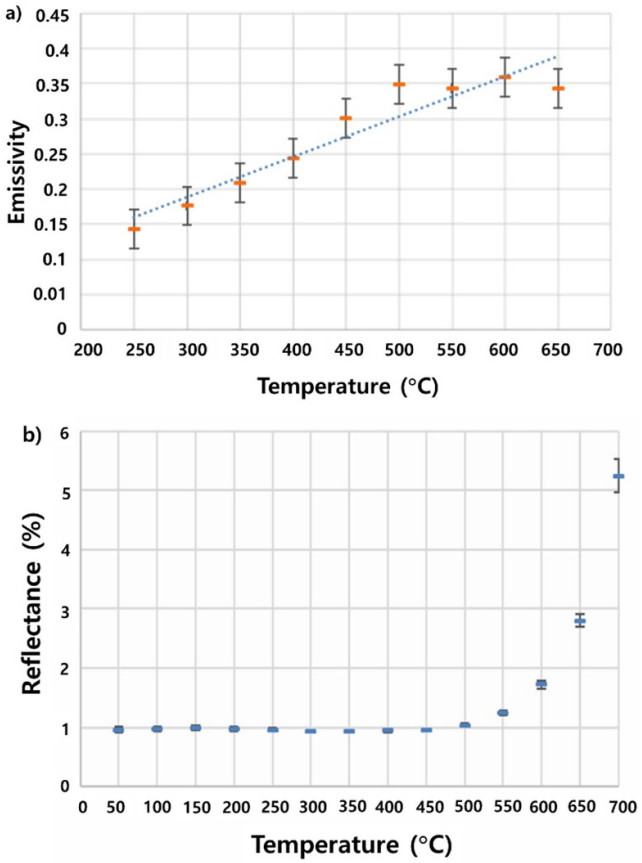

Figure 26. (*a*) The emissivity and (*b*) reflectance measurement of W PFC.

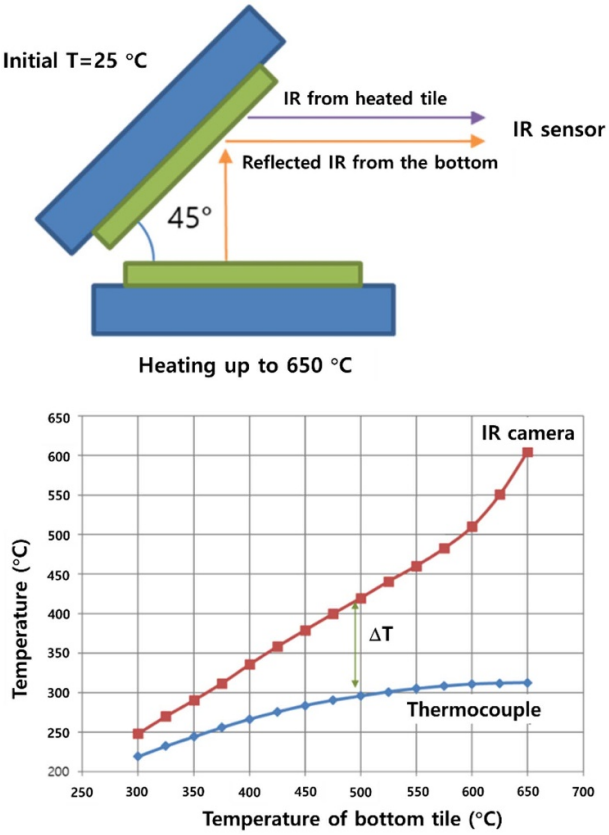

Figure 27. The temperature measurements affected by adjacent tiles.

of 700 °C. Both measurements show that the emissivity and reflectance have been changed as a function of the tungsten temperature.

Figure 27 shows the temperature measurements of two tiles which make an angle of 45° with respect to each other. The temperatures of both tiles were measured by both thermocouples and an IR camera looking at the tilted tile. The bottom tile was heated from room temperature up to 650 °C, while the tilted tile was not heated directly. Nevertheless, the temperature of the tilted tile was increased by radiated heat from the bottom tile. The temperature measured by the thermocouple inserted in the bottom tile was used as *X*-axis. As the temperature of the bottom tile increases, both temperatures measured by the thermocouple and IR show different behavior. The temperature measured by the thermocouple increases slowly and is saturated at a temperature around 300 °C, while the temperature measured by the IR camera increases further up to 600 °C. It is evident that the IR camera did not measure the temperature of the tilted tile, but it measured the temperature of the bottom tile by reflection. Further measurements and modeling of the IR signature will be performed.

2.5.2. Deposition of impurities on first mirrors. The ITER VUV spectrometers use mirrors to extract the impurities' emission light from divertor and edge plasma regions to the detector. The first mirror (field mirror) is the front-end element of the plasma-viewing optical system and directly exposed to deposition by neutral particles from the wall (subchapter 8.2). The deposition on this mirror is the main cause of the degradation that is detrimental to accurate measurement of the optical signal. Therefore, passive mitigation of impurity deposition was adopted as the mitigation strategy for the first mirror of the ITER VUV spectrometer, due to difficulty to apply a mirror cleaning technique considering the required roughness value of VUV wavelength range (sub-nanometer).

As will be described in subchapter 8.2, applying a baffled duct is one of the representative deposition mitigation techniques. Simulations as well as various experiments with different geometries of the baffled ducts have been performed in LHD, and TEXTOR. Especially, systematic mitigation efficiency tests by baffled duct geometries are performed with three differently shaped baffled ducts (short, long, short + expanded volume) in KSTAR.

The results are summarized in table 11. Here, the degradation of the mirror was measured ex-situ by measuring the reflectivity using the Dα line (654.9 nm) reflectance on a visible mirror.

The investigation of the *in-situ* deposition or erosion effect on the mirror surface with the baffled duct was conducted by using quartz crystal microbalances (QCMs) installed in KSTAR. The detailed result of *in-situ* deposition measurements is shown in chapter 2.

Table 11. Measured reflectivity of gold coated mirror after deposition of the mirrors at KSTAR corresponding to each geometry of baffle duct in front of the mirror.

Baffle geometry	Absolute reflectance (Relative Reflectance %)
Short baffled duct	44.3 (46.8)
Long baffled duct	59.6 (63.0), 56.9 (60.1)
Short baffled duct + expanded volume	90.7 (95.8)
Reference mirror	94.6 (100)

2.6. Summary

In this subchapter, we have briefly reported the recent advances in diagnostics for the measurements of plasma-wall interaction in support of the ITER research plan. Other than describing the progress of the preparation of basic and conventional diagnostics for the plasma-wall interaction such as Langmuir probe arrays or visible spectroscopy, the research was focused on the new developments in diagnostics and measurement techniques required to achieve the ITER research goals.

Radiated power can be accurately measured by the IRVB, which has been developed and tested on several tokamaks. With sophisticated techniques of ray tracing and reflection correction algorithms, the critical issue for the estimation of divertor heat flux caused by the reflection of plasma radiation under the metallic FW device will be solved. The characteristics of the reflecting surfaces depending on the roughness and angle of incident have been studied by a dedicated experiments and the results were applied to the developed codes for the reflection elimination.

For the measurement of the metallic impurity radiation induced by eroded metallic atoms, a VUV spectrometer has been developed.

Tritium inventory on the FW will be monitored by the LIBS technique, and DRGAs will measure the neutral gas composition in a divertor port and an equatorial port.

Those FW diagnostics will play a key role in the ITER operation and are essential for the successful execution of the ITER research plan.

3. Status of the diagnostics of fusion products at ITER

M. Scholz[9], B. Esposito[2], D. Marocco[10], F. Belli[10], L. Bertalot[2], B. Coriton[2], V. Ginv[2], D. Gin[2], J. Dankowski[2], A. Hjalmarsson[11], V. Krasilnikov[2], G. Ericsson[11], M. Tardochi[12], D. Rigamonti[12], M. Nocente[12], M. Garcia-Munoz[13], M. Ishikawa[14], M. Cheon[8] and J. Jo[15]

3.1. Introduction

ITER will be the first tokamak in which the ratio of fusion power to plasma heating power will be greater than Q = 1 and finally should reach $Q = 10$. ITER will be the first fusion device with burning plasma, in which the collective behavior of alpha particles and of other fast and thermal ions will occur. For this reason, measurements of neutrons and confined or lost fast ions, with an emphasis on alpha particles, are crucial for ITER. Diagnostics related to these measurements will be important for future experiments in burning plasma at ITER. High neutron emission and the very large plasma size in ITER make the neutron diagnostics the main diagnostics used to measure plasma parameters such as the fusion power, the fusion power density, the ion temperature, the fast ion energy and their spatial distributions in the plasma core.

The set of neutron diagnostics for ITER should meet the specific requirements of long life under the influence of large neutron fluxes and fluences, estimated to between 30 and 10^4 times greater than those occurring during the maximum DT discharge at JET. This means that the neutron diagnostic systems will work under a strong radiation load, which will require the use of massive radiation shielding. Thus, neutron diagnostics in ITER such as the neutron cameras and spectrometers will have limited angular fields of view, which challenges their absolute calibration.

The neutron diagnostics under development for ITER are in various stages of readiness and include: the radial (RNC) [144] and vertical (VNC) [145] neutron cameras, the internal [146], external [147] and divertor neutron flux monitors (NFM), the NAS [148] and the HRNS [149].

As in the case of neutron emission measurements, a very important issue in large tokamaks such as ITER is the measurement of confined and lost alpha particles. The problem will be significant for ITER. For confined alpha particles, various diagnostic proposals are considered based on CX recombination spectroscopy (CXRS) or on the measurement of the neutron high-energy tail produced by alpha knock-on energetic ions [150] using HRNS. A passive method that can be used is the measurement of alpha particles by gamma radiation spectroscopy using the reactions ^{9}Be $(\alpha, n\gamma)$ ^{12}C and ^{10}B $(\alpha, p\gamma)$ ^{13}C [151].

This subchapter on diagnostics of FPs for the ITER experiment covers in the next section the measurement specifications and the operational role of each diagnostic for FPs. Diagnostics of alpha particles and neutrons are covered in the following sections (from 3 to 8). Section 9 describes the *in-situ* calibration strategy for neutron diagnostics. In section 10 we give a short description of alternative diagnostic techniques to measure fast particles excluding gamma spectroscopy and FILD detectors, which are described in this subchapter (see section 3). The last section of this subchapter is a summary.

3.2. Operational role and measurement specifications of FP diagnostic subsystems

The burning plasma parameters that will be measured in ITER with the required accuracy, measurement ranges and resolutions are presented in table 12. All these parameters are divided in three categories (see column 2 in the table) according to their following role:

- (1a) measurements for MP and BC,
- (1b) for AC;
- (2) for performance evaluation and physics.

Table 12. Parameters measured by ITER fusion product diagnostics, their role and requirements.

Parameters	Role	Range	Time resolution	Accuracy
Fusion power	1a	0.1–900 MW	1 ms	10%
Fusion power density	2	1–4 10^3 kWm^{-3}	1 ms	10%
Total neutron flux	1a	10^{14}–3.2 $\cdot 10^{20}$ ns^{-1}m^{-3}	1 ms	10%
Neutron-and-alpha source profile	1b	10^{14}–1.4 $\cdot 10^{18}$ ns^{-1}m^{-3}	1 ms	10%
Core ion temperature	1b	0.5–40 keV	100 ms	10%
n_T/n_D fuel ratio in plasma core	1a	0.01–10	100 ms	20%
Neutron fluence on the first wall	1b	0.1–1 MWym^{-2}	10 s	10%
Confined α particle energy and spatial distribution	2	0.1–1 MWym^{-2} (0.1–2)$\cdot 10^{18}$ m^{-3}	100 ms	20%
Fast ion energy and spatial distribution	2	0.1–1 MeV	100 ms	20%

Table 13. Fusion product diagnostic systems.

Sub-system	Types	Meas. parameter no. (primary role in bold)
Micro-fission chamber (In Vessel) External neutron flux monitor (In Port) Divertor neutron flux monitor	A–Neutron flux monitor (NFM)	**1**,2 (and 5 for external NFM only) (MFC has no primary role)
Neutron activation system	B–NAS	**1**,2,**5**,8,9
Radial neutron camera Vertical neutron camera	C–Neutron profile monitors (NPM)	1,**2**,3,4,5,6,7,8,**9**
High resolution neutron spectrometer	D–Neutron spectrometer (HRNS)	1,**4**,6,7
Gamma ray spectrometer	E–Radial gamma ray spectrometer (RGRS)	2,4,6,7
Lost ions probes	F–Fast-ion loss detectors (FILD)	6,7

The category 1a and 1b means that the machine cannot be operated without working diagnostics providing every 1a parameters and 1b parameters, respectively.

The FP diagnostics of ITER are presented in table 13. They are grouped into six types A—F as shown in table 13.

The neutron diagnostics play an important role in measuring plasma parameters in burning plasma experiments. The main parameters measured by this system are the reaction rate, i.e. fusion power, the neutron source/alpha profiles and the fuel ratio (n_T/n_D).). Each of these parameters is measured by one or two primary systems and should be supported by a different secondary subsystem to ensure high reliability of the measurements. Primary diagnostic means that this system is well-suited to performing a given measurement. The relation between the above mentioned parameters and the subsystem is shown in table 14.

For example, from table 14, it can be seen that the fusion output can be determined by a combination of a NFM with the required time resolution (A—primary), but also its measurement can be assisted by the NAS (B), the neutron profile monitors (C) and the neutron spectrometer (D). NFMs can be calibrated *in situ* because their sensitivity can change during ITER lifetime. The activation system is highly reliable and free from electromagnetic contamination, although it is not time resolved. Correction for plasma position and neutron source profile changes will be provided by the profile monitors (C—supporting).

Additionally, the High Resolution Neutron Spectrometer (HRNS, B—supporting) can independently provide the absolute fusion output by sampling a line—integrated volume near the center [152]. This example shows that such an organization of the whole neutron system for ITER (see tables presented) should allow for the cross-checking of the mentioned subsystems and their complementarity. This will allow to obtain reliable results of neutron measurements with a given accuracy in the case of burning plasma experiments in ITER.

Table 14. The relation between parameters to be measured and neutron subsystem to be used.

	The neutron subsystem to be used.			
Parameters to be measured	A–Neutron flux monitor (NFM)	B–Neutron activation system (NAS)	C–Neutron profile monitors (NPM)	D–High-resolution neutron spectrometer (HRNS)
Fusion power	Primary	Supporting	Supporting	N/A
Neutron source profiles	Supporting	Supporting	Primary	Supporting
The fuel ratio (n_T/n_D).			Supporting	Primary

More detailed discussions about the status and development issues of individual neutron diagnostic systems are included in the following sections.

3.3. Alpha particle measurements

3.3.1. Gamma ray spectroscopy. Gamma-ray spectroscopy is a recent technique based on the detection of gamma-rays in the energy range of MeV. In a fusion plasma, gamma-rays are mainly emitted from the de-excitation of a nucleus as the result of nuclear reactions occurring between impurities and fast ions. In order to have a significant gamma emission, the ions need to be energetic, typically with energies higher than 0.5 MeV. The spectroscopic measurement of the emitted gamma-rays allows to study the energy distribution of the fast ions and their slowing down in the plasma. When the gamma-rays are measured along many LOS, the spatial profile of the fast ions can be inferred. ITER will explore for the first time the physics of a burning plasma in which the heating fraction released by the slowing down of the fusion α particles exceed that of the external heating system. For this reason, the study of the α particles will be crucial. This can be done by observing the 4.44 MeV gamma-ray line emitted by the $^{12}C(n,\alpha)^{9}Be$ reactions that occur in the plasma between the fusion α particles and the ^{9}Be impurities that are present due to the erosion of the ITER FW. The measurement of the intensity and the shape of the 4.44 MeV peak requires the use of dedicated instrumentation with energy resolution better than 1.5% and with counting rate capability higher than 1 MHz. The conceptual design of the Radial Gamma-Ray Spectrometer (RGRS) system for ITER has been studied and will be finalized by the end of the 2026. The system consists of a set of gamma-ray spectrometers placed along the radial line of sights (LOSs) and are integrated in the radial neutron camera (RNC) (figure 37, section 3.4) which is described in section 4. The design of the system took advantage on the experience gained at the Joint European Torus (JET) which is the fusion experiment equipped with the most advanced set of gamma-ray diagnostics. The selected scintillator crystals are large $LaBr_3$ ($3'' \times 6''$, diameter, height) coupled to photomultiplier (PMT) tubes provided with active voltage dividers. To reduce the direct 14 MeV neutron background, the RGRS will be provided with 120 cm long lithium hydride (LiH) attenuators [153] placed in front of each detector. To partially reduce the load of the gamma-ray background induced by neutrons interacting with the tokamak structure and the surrounding materials, a shielding based on iron and concrete has been designed to attenuate the radiation load coming from the side of the detectors. The RGRS system consists of three dedicated LOS of 40 mm diameter and a shared one with the RNC whose diameter is 25 mm (see figure 37).

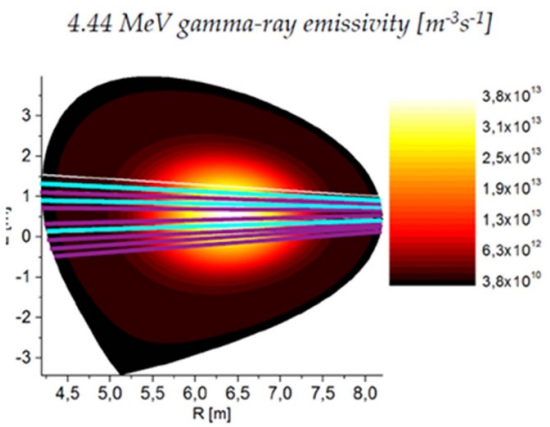

Figure 28. 4.44 MeV γ-ray (right) emissivities (particles m^{-3} s^{-1}) in the poloidal plane for the ITER 500 MW DT scenario Reproduced from [156]. © 2017 IAEA, Vienna. All rights reserved.

The expected 4.44 MeV emissivity for the full power 500 MW ITER scenario has been calculated with the GENESIS code [154] (see figure 28) while the expected pulse height spectrum measured by the LaBr3 scintillators has been simulated with an MCNP code (see figure 29) [155]. Calculations revealed a count rate of 12 kHz of the 4.44 MeV signal when a LoS of 40 mm is used, while a count rate of 1.8 kHz is calculated for the 25 mm diameter collimator.

3.3.2. FILD detectors. Energetic particle losses are routinely measured in present tokamaks using charged particle collectors located at the edge of the plasma. Most Fast-Ion Loss Detectors (FILD) [157] use, as active component, Faraday Cups (FCs), scintillators or a combination of both [55, 157–169]. Charged particle collectors are often complemented with IR measurements of the heat load caused by the escaping ions on the PFCs. While charged particle collectors give velocity-space resolved measurements of escaping ions with Alfvenic temporal resolution at a certain position, IR-measurements can cover the entire 3D wall. Just IR-measurements would not be sufficient to diagnose fast-ion losses as they cannot discriminate between thermal and

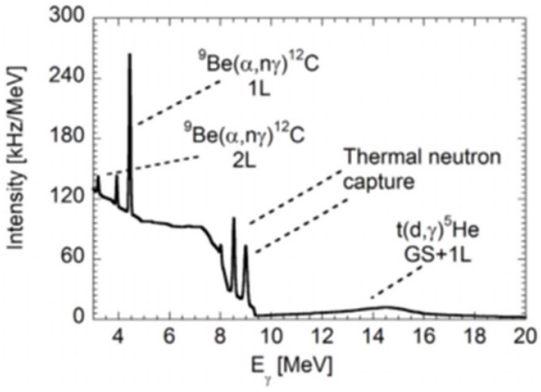

Figure 29. Expected pulse height spectrum on LaBr3 (40 mm diameter collimator) for the 500 MW DT scenario at ITER. Reproduced from [156]. © 2017 IAEA, Vienna. All rights reserved.

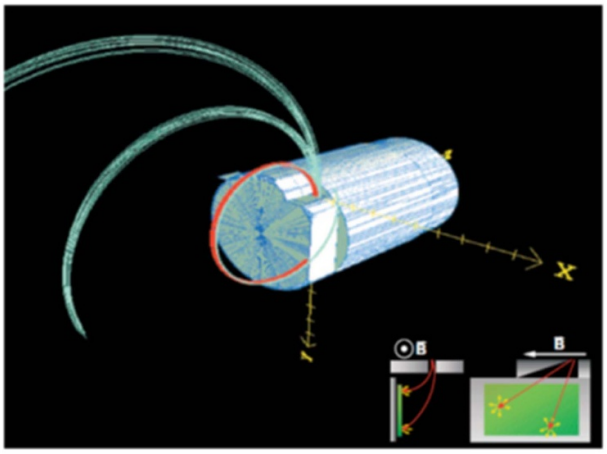

Figure 30. CAD view of FILD head with some escaping ion trajectories hitting the detector. In blue particle trajectories which enter into the scintillator chamber and in red particle trajectories blocked by the graphite protection. The inset on the right-bottom part of the figure shows the collimating process. Reprinted from [157], with the permission of AIP Publishing.

fast-ion losses, give no information on the velocity-space of the losses or typically have limited temporal resolution well below the Alfvenic time-scale.

3.3.2.1. FILD operational principle in-port RNC detectors. FILD systems work as magnetic spectrometers dispersing the escaping ions by means of a collimator on a scintillator plate. The hit points of the impinging ions on the scintillator plate are given by the particle energy (gyroradius) and pitch-angle (v_{par}/v_{tot}). Figure 30 shows the head of a FILD system mounted on the midplane manipulator of the ASDEX Upgrade tokamaks. The inset illustrates the FILD operational principle with particles with different trajectories hitting the scintillator plate at different positions. Scintillator-based FILD systems often use FCs embedded in scintillator plates to obtain absolute measurements of escaping ions. Figure 31 shows an AUG

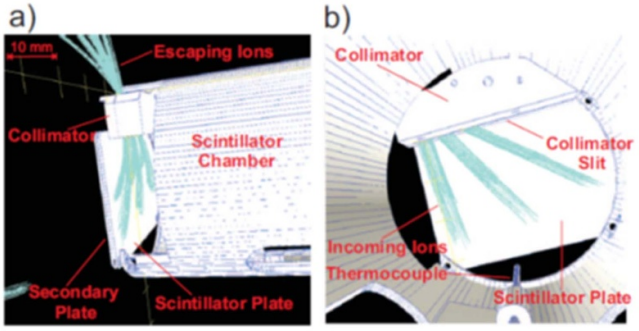

Figure 31. (*a*) Lateral view of detector head without graphite protection. Trajectories of particles with three different pitch angles, 87°, 70°, and 50°, and two different gyroradii, 3 and 6 cm, entering through the collimator and hitting the scintillator plate are also shown. (*b*) Inside view of the detector head with the simulated trajectories of particles with pitch angles 87°, 70°, and 50°. On the bottom the thermoelement is indicated. The particle trajectories were calculated forward and backward from the first aperture slit with the starting point randomly distributed over the whole slit. Reprinted from [157], with the permission of AIP Publishing.

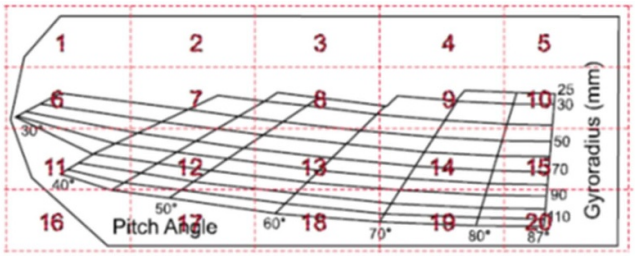

Figure 32. Pitch-angle—gyroradius strike map with PMT array layout overlaid. Reprinted from [157], with the permission of AIP Publishing.

FILD detector head without graphite protection with the main components of the detector head indicated in red.

Most present FILD devices measure simultaneously the escaping ions hitting the scintillator plate with three systems; a FC embedded in a scintillator plate, a CCD camera to look at the escaping ion velocity-space and a PMT tube array with Alfvenic temporal resolution to obtain MHz measurements of escaping ions fluxes. The layout of the PMT array covering the entire scintillator plate of an AUG FILD is shown in figure 32.

3.3.2.2. Measurement requirements for ITER. Following this operational principle, the ideal ITER FILD system should fulfill the following measurement requirements;

A. temporal resolution;
   FILD with Alfvénic temporal resolution is highly recommended in order to identify the MHD fluctuations responsible for the measured fast-ion losses in a sea of MHD fluctuations. A MHz temporal resolution is set by the Alfvénic time, $\tau_A = R_0/v_A \sim 1\ \mu$s. This is obtained for a standard ITER DT case with an Alfvén speed $v_A = 8 \times 10^6$ m s^{-1}

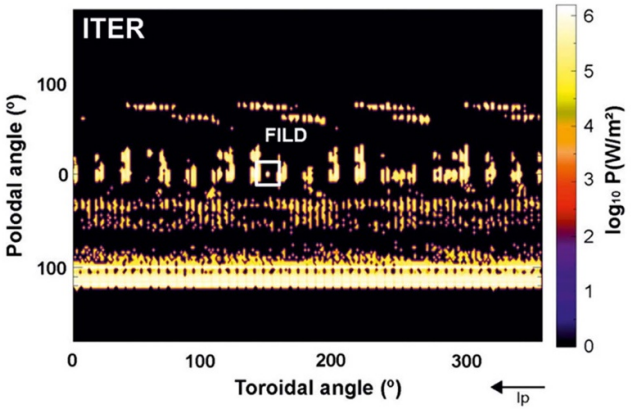

Figure 33. ASCOT simulations of alpha particle heat load in ITER on a 3D first wall due to an externally applied n = 4 RMP. The location of the FILD head is indicated with a white box. Reprinted from [55], with the permission of AIP Publishing.

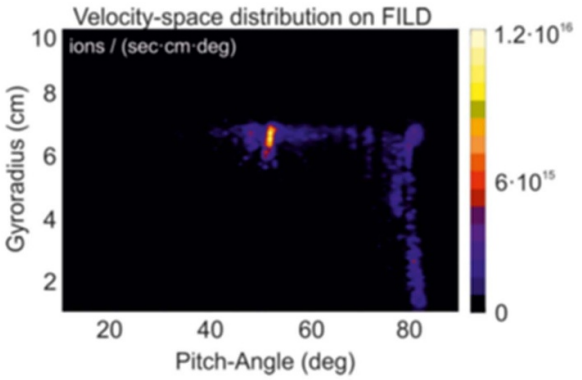

Figure 34. ASCOT simulations. Velocity-space of alpha particle losses hitting the FILD detector head in the presence of an externally applied n = 4 RMP. Reprinted from [157], with the permission of AIP Publishing.

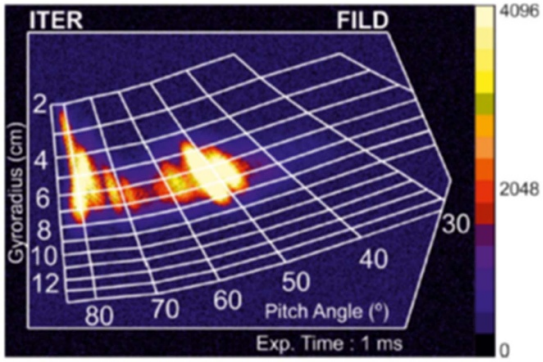

Figure 35. A synthetic FILD measurement of alpha particle losses induced by the applied n = 4 RMP. Reprinted from [157], with the permission of AIP Publishing.

calculated with $B_T = 5.2$ T, a 50%–50% D–T mixture and an electron density, $ne = 8 \times 10^{19}$ m^{-3}

B. spatial resolution;
The heat load spatial pattern shown in figure 33 gives an estimate of the spatial resolution the FILD should have in ITER. A spatial resolution similar to the gyroradius of the fusion born alpha-particles, $r_L \sim 7$ cm, seems to be required to be able to resolve the expected heat load wall structures.

C. Velocity-space range and resolution;
Wave-particle resonances can occur over almost the entire fast-ion phase-space. In order to identify the wave-particle resonances responsible for the actual fast-ion transport/loss, a wide velocity-space coverage and reasonably good energy and pitch- angle resolution are thus necessary.

Figure 34 shows the velocity-space of the escaping ions collected at the head of the FILD system with its aperture located 11 cm outside of the DFW in the ASCOT simulations presented here. The losses appear over the entire energy range, from ∼6.5 cm (corresponding to the alpha-particle birth energy) down to the thermal energy at large pitch-angles, ∼80°. Similarly, a broad escaping ion pitch-angle range, from 40° to 85°, with an energy similar to the birth energy, appears in the simulated losses at the FILD system. As in recent experimental observations, clear structures at certain pitch-angles are observed.

3.3.2.3. ITER FILD synthetic measurement. The ITER FILD system will likely be a charged particle collector composed of both a scintillator and a FCs´ matrix, located in the 55.B9 port plug. Recently, a conceptual design of a reciprocating FILD system with outstanding velocity-space resolution has been developed [157]. Full orbit ASCOT simulations have been used to estimate the flux of fusion-born alpha particles on a realistic 3D wall. Externally applied resonant magnetic perturbations (RMPs) were used to mimic the effect of symmetry breaking 3D magnetic perturbation on the ITER alpha particle population.

A synthetic FILD measurement of alpha particle losses induced by the applied $n = 4$ RMP, including scintillator background emission produced by neutron-driven nuclear reactions in the scintillator coating itself, is shown in figure 35.

The synthetic CCD camera shows several populations of alpha particle losses with well-defined pitch-angles and different energies illustrating the potential of such a diagnostic to contribute to the ITER success.

3.4. RNC

3.4.1. Motivation. The primary role of the RNC is to provide—through reconstruction techniques applied to the line-integrated neutron fluxes—time-resolved measurements of the neutron and α-source profile (i.e. Neutron Emissivity, neutrons emitted per unit time and volume (s^{-1} m^{-3})) and the fusion power density. Additional measurements provided by the RNC are the core ion temperature and the fuel ratio profiles.

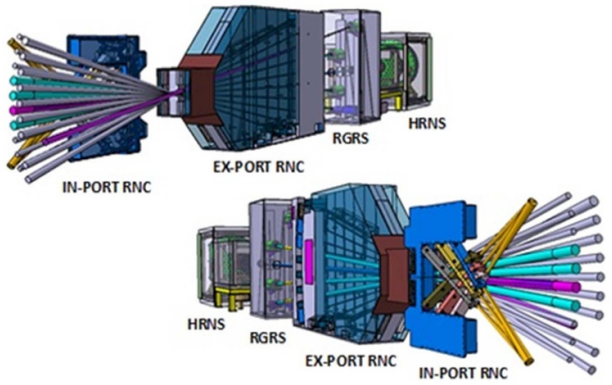

Figure 36. Layout of Radial Neutron Camera. The two interfacing diagnostics (Radial Gamma Ray Spectrometer (RGRS) and High Resolution Neutron Spectrometer (HRNS)) are also indicated. In-port RNC LOS are depicted in yellow, ex-port RNC LOS in grey, RGRS LOS in blue and HRNS LOS in pink.

3.4.2. Design. The RNC is located in ITER Equatorial Port #01 (EP#01) and is composed of two collimating structures, namely the In-port RNC system and the Ex-port RNC system viewing the plasma radially through apertures in the diagnostic shielding module (DSM) of the port plug (figure 36).

RNC measures the uncollided 14 MeV and 2.5 MeV neutrons from deuterium–tritium (DT) and deuterium–deuterium (DD) fusion reactions through an array of neutron flux detectors located in collimated LOS, 6 for the In-Port and 16 for the Ex-Port. Figure 37 shows the LOS through the plasma and their geometrical details.

A design process model based on system engineering has been adopted, leading to a qualitative and quantitative methodology for the identification of the RNC baseline architecture [170].

3.4.3. Current status. The preliminary and final design reviews (PDR, FDR) for the In-port RNC and the PDR for the ex-Port RNC have been successfully completed. On-going work is related to the preparation of the FDR for the ex-port RNC which is planned for mid-2025.

All main interfaces have been identified [171]. An extensive campaign of R&D and testing of prototyped RNC components is also on-going, focusing on neutron detectors (radiation hardness [172–174], technical specifications [175, 176]), electrical feedthroughs, front-end-electronics (electro-magnetic compatibility (EMC)) and assessment of real-time emissivity reconstruction capability.

MCNP Monte Carlo code analysis is extensively used [177] in order to enhance the diagnostic measurement performance and to evaluate the nuclear loads on the structural elements, detectors and associated components.

A calibration procedure has been defined that relies on embedded sources, reference ITER pulses and cross-calibration with ITER fission chambers (FCs) and NASs coupled to Monte Carlo simulations of radiation transport [178].

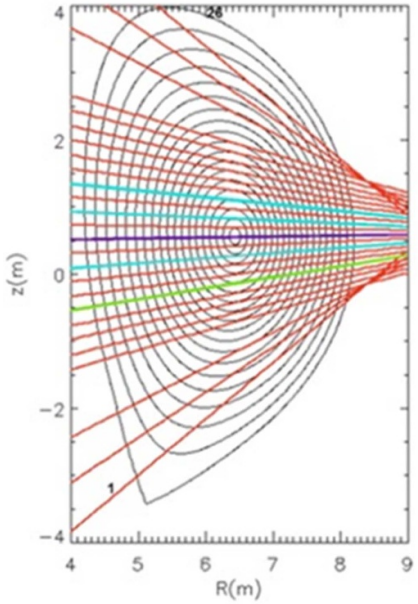

LOS #	Location	LOS angle* (°)	Collimator diameter (mm)	Collimator length (m)	r/a **
1	In-port	50.0	32	944	0.85
2	In-port	56.0	32	1294	0.76
3	In-port	62.5	32	1463	0.67
4	Ex-port	73.9	11	2600	0.5
5	Ex-port	75.5	11	3000	0.45
6	Ex-port	77.3	11	3000	0.39
7	Ex-port	78.9	11	3000	0.34
8	*shared RNC and RGRS*	80.7	11	3000	0.28
9	Ex-port	82.3	11	3000	0.23
10	Ex-port	84.1	11	3000	0.17
11	*exclusive use RGRS*	85.7	--	--	0.12
12	Ex-port	87.5	11	3000	0.07
13	*exclusive use HRNS*	89.1	--	--	0.02
14	Ex-port	90.9	11	3000	0.05
15	*exclusive use RGRS*	92.5	--	--	0.1
16	Ex-port	94.3	11	3000	0.16
17	*exclusive use RGRS*	95.9	--	--	0.21
18	Ex-port	97.7	11	3000	0.26
19	Ex-port	99.3	11	3000	0.31
20	Ex-port	101.1	11	3000	0.37
21	Ex-port	102.7	11	2300	0.42
22	Ex-port	104.5	11	1800	0.48
23	Ex-port	106.1	8	1400	0.54
24	In-port	117.5	32	1463	0.7
25	In-port	124.0	32	1294	0.8
26	In-port	130.0	32	944	0.88

*Clockwise from a vertical line.
** Calculated for Q=5 scenario

	FOCUS COORDINATES (mm)			Focus - front collimating unit distance (mm)
	x	y	z	
Ex-port	11048	-119	620	1500
In-port Upper	8410	446	-132	1041
In-port Lower	8410	406	1372	1041

Figure 37. RNC LOS (top) and geometrical details (bottom).

3.4.4. Measurement requirements. ITER FP MPs are detailed in table 12 (section 3.2). RNC is designed to measure the fusion power density in the range 1 kW m^{-3}–4 MW m^{-3} with 10% accuracy. The neutron and alpha source profile shall be measured in the range $10^{14} - 1.4 \cdot 10^{18}\,s^{-1}m^{-3}$ with 10% accuracy. Both measurements should be performed with time resolutions of 1 ms (off-line) and 10 ms (real-time) and a spatial resolution of $a/10$ (a = tokamak minor radius).

3.4.5. Subsystem designs.

3.4.5.1. In-port RNC. The In-port RNC is located in Drawer #3 of the Port Plug of EP#01 and is devoted to probe the edge of the plasma. The detectors are located in a Cassette

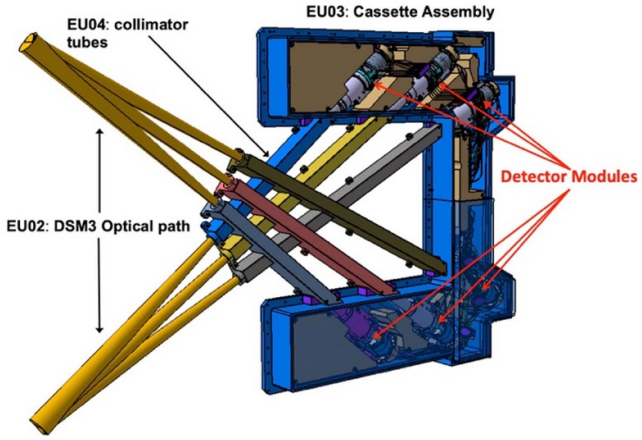

Figure 38. In-port RNC cassette assembly.

Table 15. Characteristics of in-port RNC 238 U fission chamber.

^{238}U fission chamber	
Diameter sensitive area (mm)	32
^{238}U total mass (mg)	145
^{238}U coating thickness (mm)	0.45 mm
^{238}U coating purity (%)	Better than 9.99 $\pm$ 0.01
Efficiency (14 MeV) (counts/neutron)	5.4×10^{-5}

Assembly (3 detector modules in the Upper part of the Cassette and 3 detector modules in the Lower part of the cassette, figure 38).

The LOS traverse the DSM and reach the FW. The In-port RNC Embarked Units are:

- EU02 (DSM 3 optical path): shaped conical voids within the DSM and the DFW corresponding to each LOS.
- EU03 (cassette assembly): sealed container connected to the secondary vacuum (service vacuum system) enclosing the detector modules, the beam dumps & shielding material.
- EU04 (collimator tubes): there is one tube for each LOS and the whole system is connected to the DSM and to the cassette assembly.

The in-port RNC has two sets of dedicated vacuum and electrical feedthroughs, respectively on the cassette assembly and on the closure plate. The detector module associated to each LOS contains a FC and a single crystal diamond (sCD) matrix. The main features of these neutron detectors are summarized in tables 15 and 16.

The two detectors are mounted as shown in figure 38.

3.4.5.2. Ex-port RNC. The ex-port RNC is devoted to probe the core of the plasma. Detectors and collimators are distributed on two planes hosted in a massive shielded structure (Shielding Block) located in the port interspace (10 LOS on the left hand side looking at the plasma and 6 LOS on the right hand side). Penetrations in the DSM allow the LOS to reach

Table 16. Characteristics of In-Port RNC sCD matrix.

sCD matrix	
Diameter sensitive area (mm)	32
Form	$\approx$30 pixels, 4.5 $\times$ 4.5 mm arranged in two groups
Thickness (μm)	50
Efficiency (14 MeV) (counts/neutron)	5.4×10^{-5}
Embedded alpha calibration source (one per matrix)	Mixed ^{244}Cm/^{239}Pu/^{241}Am $\sim$6 kBq

the DFW. The thickness of the closure plate at the level of the ex-port RNC LOS is reduced (22 mm) in order to minimize the interactions with neutrons; the region of the closure plate with reduced thickness is defined as 'closure plate customization'.

The ex-port RNC has strong physical interfaces with two diagnostics: the HRNS and the RGRS. The ex-port RNC embarked units are:

- *EU01 (DSM 2 Optical Path):* shaped conical voids within DSM Drawer#2 and DFW corresponding to Export LOS.
- *EU11 (IS Equipment*): massive Shielding Block structure located on EP01 Interspace Supporting Structure (ISS) and hosting the ex-port RNC flight tubes,

Collimation units, detector modules, and beam dumps. The detector module associated to each LOS contains:

- a ^{4}He scintillator (internal pressure = 100 bar, length = 30 mm, diameter 44 mm) as main detector for full power DT measurements;
- a sCD matrix (same as for the in-port: 4 pixels, 4 $\times$ 4 $\times$ 0.1 mm) as backup detector for full power DT measurements;
- a EJ-276 G plastic scintillator (15 mm thick $\times$ 15 mm diameter) for low power DT measurements.

PMTs resistant to intense magnetic fields (fine mesh type) are selected for the two scintillators and are located outside the collimating neutron channel in order to avoid direct neutron flux. In this position, PMTs with silica windows withstand the environmental conditions (>200 kGy and >10^{14} n cm^{-2}).

The sCD is the first detector along the LOS, followed by the ^{4}He scintillator and by the plastic scintillator that is the last one, in order to minimize effects of scattering on the other detectors due to its constituent hydrogenous materials.

The Shielding Block (figure 39) is a sandwich structure containing and protecting the ex-port neutron diagnostics frame and is designed to minimize the background due to scattered neutrons at the position of RNC detectors. It is based on a self-supporting stainless steel structure for the collimators and panels of a castable reactor shielding material made of a borated hydrogenated mix (low density: 1.68 g cm^{-3}, boron content: 5%).

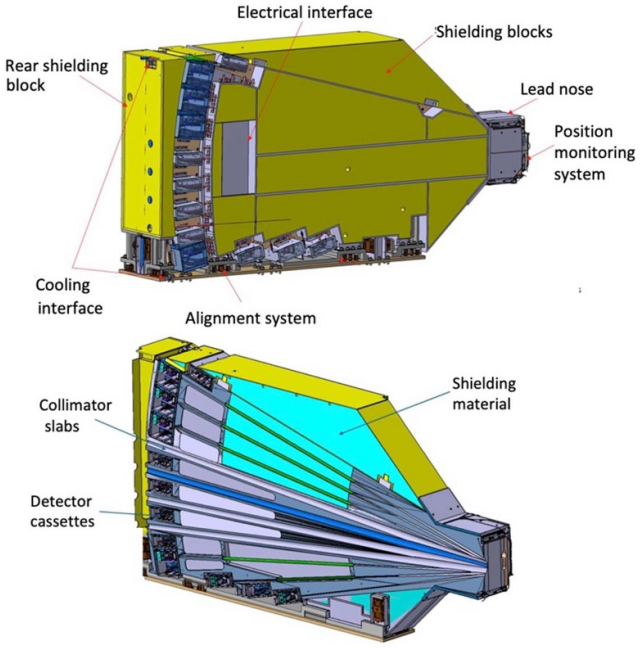

Figure 39. Sketch of the ex-port shielding block. Reproduced from [179]. CC BY 4.0.

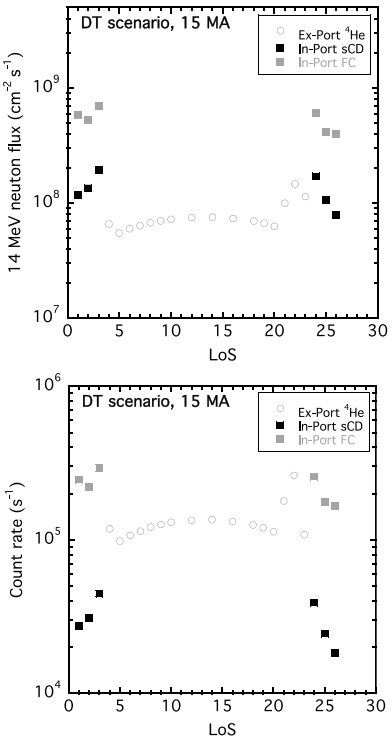

Figure 40. Neutron fluxes at detector position and count rates. Material attenuation along LoS is taken into account.

3.4.5.3. System performance analysis. The performance of the diagnostic system has been assessed through 1D and 2D neutron emissivity reconstruction analysis through: (a) a 1D reconstruction code (Measurement Simulation Software Tool (MSST) using constant emissivity on magnetic flux surfaces as from IO input emissivity profiles) based on Tikhonov regularization with first derivative objective functional [180, 181] and (b) a tomography code based on the Minimum Fisher Regularization (MFR) method that can include the total neutron yield value provided by an independent diagnostic as additional constraint in the tomography procedure [182].

The neutron fluxes at the detector positions as well as the expected uncollided neutron count rates (above selected detectors energy thresholds) used as input for the analysis are shown in figure 40. The two codes were used to reconstruct the DT $Q = 10$ scenario (yield $= 1.8 \times 10^{20}$ n s^{-1}) with 10 ms time resolution: 100 synthetic datasets were used in the MFR case and 1000 in the MSST case. The analysis was carried out considering only background and statistical errors and assuming a random Gaussian noise with 10% amplitude as error for total neutron yield.

Figure 41 shows the results of the performance analysis, in terms of emissivity reconstruction and relative accuracy, obtained using the MFR method. The improvement in the RNC 2D reconstruction of the neutron emissivity obtained by using the total neutron yield [183] is also evident: the extension of the spatial region in which the accuracy of the reconstruction is better than 10 %, the better reconstruction of peaked emissivity profiles and the robustness against measurements noise and LOS data loss, picture from [179].

The consistency of the two different analysis methods is shown by figure 42 that compares the accuracy provided by MFR and MSST.

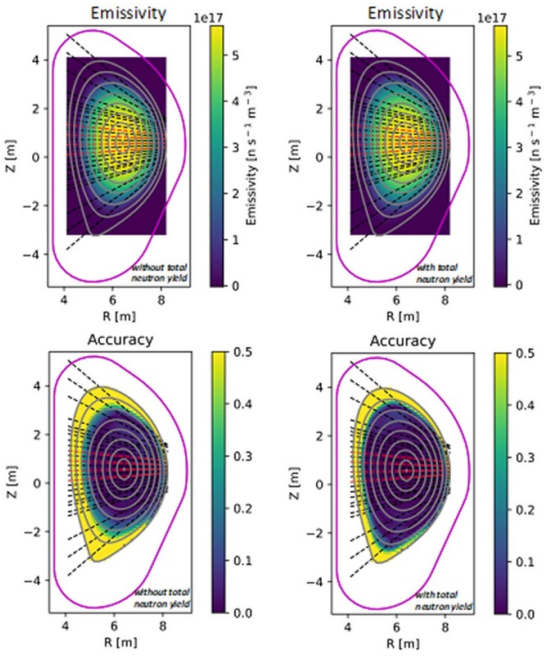

Figure 41. MFR reconstruction results with and without inclusion of total neutron yield constraint. Top: 2D maps of reconstructed neutron emissivity (average value). Center: 2D maps of reconstruction accuracy. Reproduced from [179]. CC BY 4.0.

Table 17 summarizes the ITER scenarios used in the RNC performance analysis simulations.

The associated achievable performances are provided in table 18: the profile regions (in terms of r/a range and

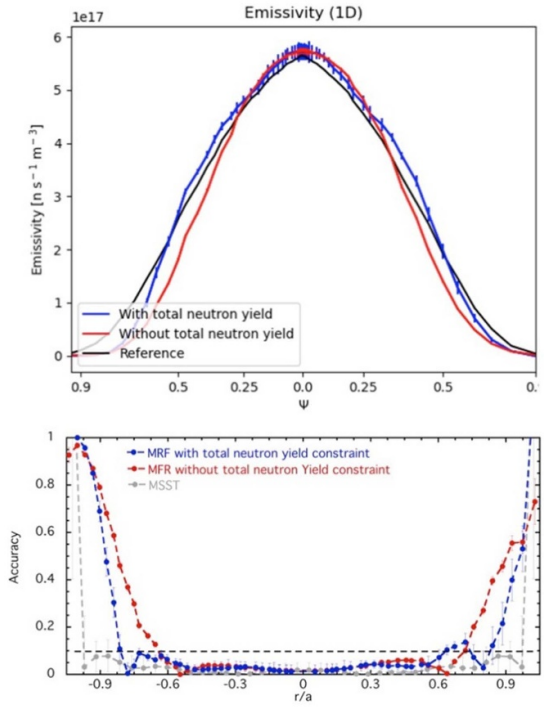

Figure 42. 1D profiles of average reconstructed emissivity (top) and of reconstruction accuracy with 1? error (bottom); the accuracy from the MSST reconstruction is also shown for comparison.

associated emissivity) in which such performances are achievable in real-time simultaneously are also indicated.

The table is based on MSST 1D simulations that include direct errors (Poisson statistical error, background due to scattered neutrons, random noise on acquired detector pulses, attenuation, detector efficiency, etendue) and indirect errors (equilibrium reconstruction). An implementation in real-time of the MSST reconstruction code demonstrates that the acquisition and processing phases leading to neutron emissivity reconstruction can be carried out respectively in 0.2 ms and 1.5 ms (total time $\ll$10 ms) [184–187].

Note that the time resolution requirement for measurements provided not in real-time (1 ms) is anyway achievable thanks to the use of digital acquisition systems (see e.g. [188]).

3.5. Vertical neutron camera (VNC)

3.5.1. Introduction. The VNC (55.B2) diagnostic is a system of fan-shape multichannel collimators and neutron detectors. VNC together with 55B1 RNC provides time-resolved measurements of Fusion power density profile and neutron & α source profile. So, the system is primary of measurement of parameters (MPs) 13 and 14 of ITER measurement 07 [189], also it has supplementary or backup role for another 5 ITER MPs.

The system will be functional only for the last phase (DT), but deliveries for earlier stages are needed for integration components into port integrator(s) structures.

The recent publications on the system include [190–192].

The VNC is composed of two fan-shaped collimating structures: upper (UVNC, 55.B2.B0)—in upper port 18 (UP18)—predominantly observing plasma area near inductor, and lower (LVNC, 55.B2.A0)—in lower port 14 (LP14)—mainly collecting signal from $R > R0$ region. Totally plasma is observed vertically by 11 LOS (figure 43).

In scenarios/approach of the symmetry of the neutron emission on the magnetic surfaces having two chambers increases reliability and availability of the measurements. However also two working in parallel subsystems allows getting data on the symmetry breaking, which can, for example, be crucial for following dynamics of the trapped vs confined fractions of the fast ions. Finally, application of two systems 55.B1 and 55.B2 can further be considered for both improve of robustness and for getting advanced details on the emission symmetry breaking. Minimizing assumptions on symmetry and providing so more general tomographic reconstruction data to NFMs allows to ensure having more precise data on primary measurements on total fusion power and neutron production.

3.5.2. Design. Multiple solutions are shared between LVNC and UVNC. First of all, it includes I&C, so that one dedicated FDR will cover relevant aspect of both subsystems. Further, for cooling and efficient backing of the in-vessel components IBED water circuits are implemented. As soon as FCs have internal volume with 3 Bar pressure, following ITER vacuum requirements it has to be enveloped with guiding volume connected to SVS (service vacuum system). Then detector units share similar configuration with 2 FCs, 2 SCD and also ^{137}Cs + ^{241}Am sources.

However, LVNC and UVNC features multiple crucial differences and sub sections below will more concentrate on respected individual aspects of designs.

3.5.2.1. Lower VNC. On the figure 44 it is presented cross section for the key relevant to LVNC operation elements inside VV.

Conical LoS employed for LVNC. They starts in detector module in the diagnostic rack (bottom), coming through divertor cassette (DC; blue areas in the middle), have focal point in the cut outs of the FW/blankets modules. This required particular design of the DC #40 and mentioned of blanket shield block and FW (SB&FW #18C14). Aside of collimating holes in DC #40, also it features absence of the pump slot—in order to reduce neutron background for the detectors.

In order to ensure required accuracy of measurements non-obstructed direct view on plasma is needed with well defined geometry of all elements forming LoS. So dedicated tolerances studies were initiated. First part included analysis of the tolerances values itself. Exact position of the blankets as well as divertor cassettes relative to VV will be optimized based on the actual magnetic configuration of the ITER with corresponding shift of up to 20 mm in each of vertical and radial directions. However all the elements on the chain (also including diagnostic rack) is conceived to have the same move keeping thus geometry of the LoS.

Table 17. ITER scenarios used in the RNC performance analysis.

Code	I_p (MA)	B (T)	Fuel	Fusion power (MW)	Peak neutron emissivity (s^{-1} m^{-3})	Neutron yield (s^{-1})
DT $Q = 10$	15	5.3	DT	500	5.7×10^{17}	1.8×10^{20}
DT $Q = 5$	15	5.3	DT	255	3.7×10^{17}	9.8×10^{19}
DT low	7.5	2.65	DT	23	4.9×10^{16}	8.4×10^{18}
DD high	7.5	5.3	DD	1	3.1×10^{15}	1×10^{18}

Table 18. Summary of RNC performance for neutron emissivity profile measurements (real-time).

Scenario #	Neutron emissivity range ($s^{-1}m^{-3}$)	Time resolution (ms)	Accuracy	Spatial resolution	r/a
DT $Q = 10$	1.4×10^{17}–5.7×10^{17}	10	10%	$a/10$	<0.8
DT $Q = 5$	1.6×10^{17}–3.3×10^{17}	10	10%	$a/10$	0.25–0.6
DT low	3.7×10^{15}–4×10^{16}	100	10%	$a/10$	0.2–0.8
DD high	1.5×10^{15}–3.8×10^{15}	10	20%	$a/10$	<0.6

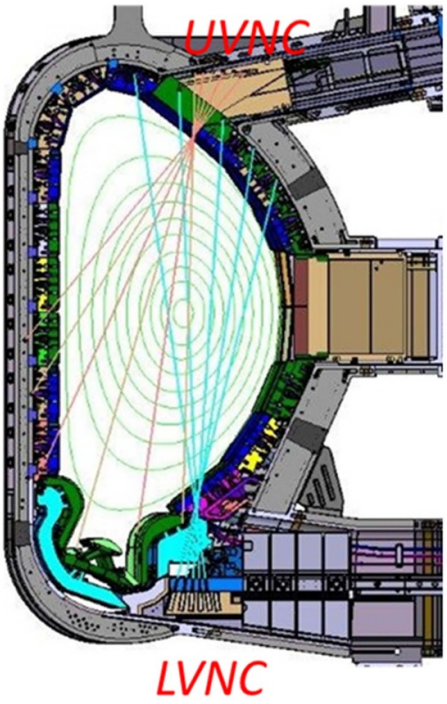

Figure 43. Schematic view show VNC LoS, magnetic field contours. LVNC and UVNC subsystems are rotated to the one *Z-X* plane for representation purpose.

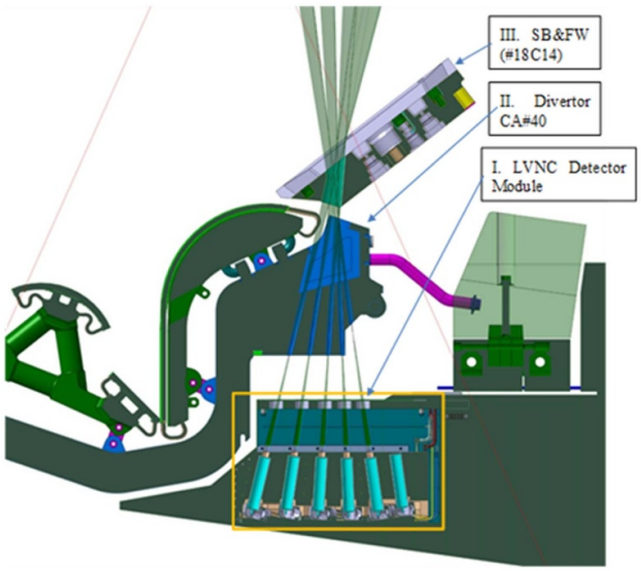

Figure 44. LoS arrangement for LVNC. LVNC module roughly outlined with yellow rectangle to separate from Rack area.

After dedicated investigation the misalignments of targets expected based on as-build preliminary analysis was found 0–4 mm in toroidal direction and 0–5 mm in poloidal and radial directions. Second part of the study based on MCNP simulations confirmed that measurements inaccuracy due to geometry uncertainties (also considering other contributors) can be kept within necessary 10% level.

Finally, one more key effect considered is pre compression of the divertor cassettes installation. Indeed, in configuration management models (CMMs), the LoS of the LVNC diagnostic system and the collimating holes in the LVNC CB are aligned in context (while DC can be seen as clashing with its fixation elements—to describe pre compression). Reverse engineering action was undertaken to consider deformation of the LVNC CB in the area under the proper set of loads, basing on structural analysis to include dead weight, pre-compression, thermal expansion in operation condition, effect of coolant pressure and irradiation effect. At the same time following latest studies collimating holes diameter was increase from 30 to 40 mm in this area—which further improved robustness of solution, accords to recommendations of the manufacturability investigations and was found to further improve signal/noise ratio.

In the figure 45 is given detector module. Its upper part serves as an alignment frame (which ensures mechanical fixation in the rack).

It allows to shift the whole assembly for ±5 mm each direction and rotate for 5± mrad relatively to each coordinate

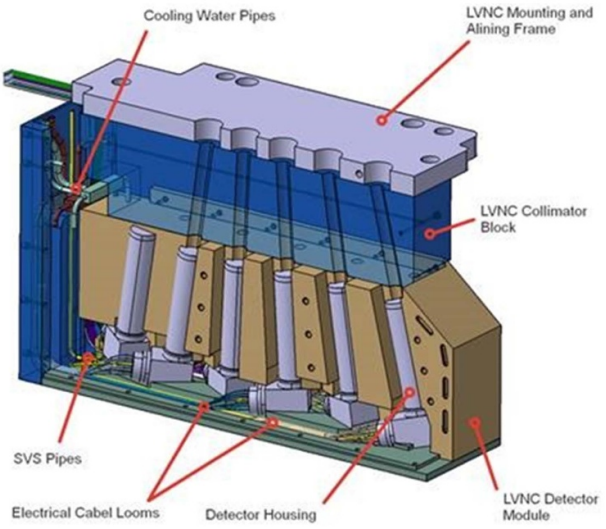

Figure 45. LVNC detectors module.

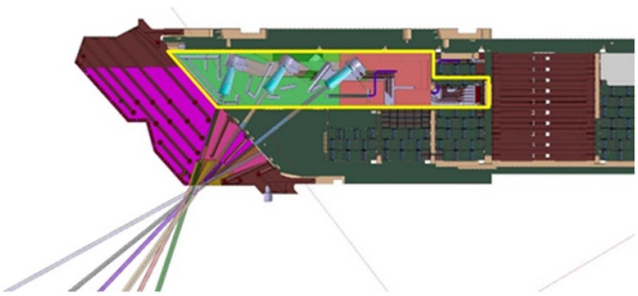

Figure 46. Section of UVNC in UP Port Plug. 55.B2 detector module is outlined with yellow. Section is done via one half of 55.B2.B0, still LoS for both are visible. Pink area in front of module—DFW with dedicated water cooling lines.

axis. Adjustment is done with the bolts on the fixation points to diagnostic rack. Five detector units of the module observe plasma, while the last one do not have associated collimating holes thus providing data on neutron and/or EM background for measurements.

3.5.2.2. Upper VNC. In the figure 46 it is depicted UVNC design in UP18 port plug. Detectors module consists of two boxes independently attached to DSM body. Between two UVNC halves there is a 25 mm slot made for VUV (55.EH) diagnostic system. Each half implements three lines of view, no 'blind' channels foreseen for UVNC.

No divertor or blanket elements participating UVNC, but instead DSM and DFW elements. The latter elements are directly bolted together and also closer to detectors than relevant elements of LVNC thus giving no need for complex tolerances analysis here. However other challenges were faced during development of the Upper Camera. So, in the analysis of 2017 it was found for UVNC signal to background (S/B) being <1 for all the channels. Hence optimization was proposed.

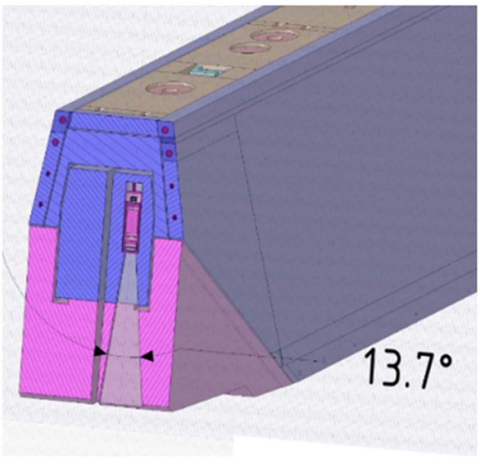

Figure 47. Collimation for UVNC detectors. First iteration extending LoS—upto 13.7° of larger side of rectangle.

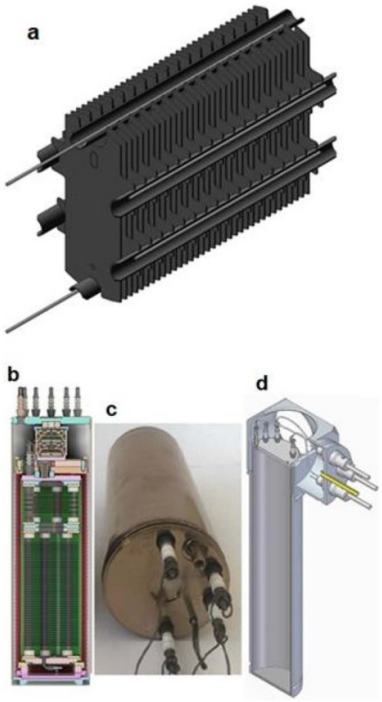

Figure 48. Detector units of UVNC. (*a*)—electrodes, (*b*)—detector unit model (section), (*c*)—detector unit mock-up, (*d*)—detector unit inside housing structure (implementing SVS enveloping).

First step was changing collimator shape from cylindrical (as it is still in LVNC) to rectangular—extended in the direction of the magnetic surface (see figure 47).

Then the electrodes of the FCs were adjusted accordingly (see figure 48(*a*)), model of detector unit updated (figure 48(*b*)), simulation performed and mock up (figure 48(*c*)) manufactured and tested.

One of the most complicated component of these collimators implementation became development of the DFW cutouts. Indeed, this first PFC needs dense system of cooling channels,

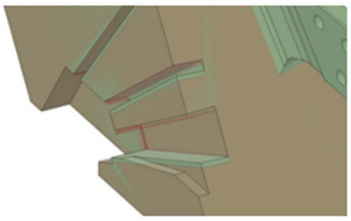

Figure 49. Collimation for UVNC detectors. Dedicated DFW cutouts geometry.

which can be manufactured only if set of strict restrictions applied, for example, minimum distance between cutouts, their profile. This led to a slight worsening of collimation efficiency: particularly because some cutouts for LoS had to be united, others left only at one half (box)—see figure 49. Still S/B became much better (typically ∼3–4) than before making LoS rectangular.

As the next step, detector Unit housing was redone to implement electrodes coming out at the side (figure (48*d*)) instead of the cylinder basement (as it was considered before). That made Housing shorter gaining addition space for the shielding material with collimators in front of the detectors. More information on the optimizations can be found in [190].

3.5.3. Measurements requirements and system performance analysis. Requirements for the primary measurements are given in tables 19 and 20. It is taken from latest approved 55.B2 sSRD (sub system requirement document).

In order to justify suggested design, ability of diagnostic performance to fulfill sSRD measurements requirement checked with modeling, based on multiple MCNP simulations, described in [191]. Green function formalism was applied, as shown in figure 50 cited from given reference.

This approach allows quick calculation of the detector response for different plasma configuration (without need of full scale MCNP modeling for each case), and was applied to demonstrate required diagnostic performance. Statistical errors, inaccuracies of magnetic surface shape, inaccuracies of contribution matrix calculations were analyzed to prove that reconstructed profiles are tolerant to input data errors for the reverse problem under consideration.

Indeed, even in case of large errors (e.g. statistical) median of reconstructed quantity remains close to the true value. For one of the MPs restoration quality demonstrated in the figure 51.

3.5.4. Shielded cabinets. Neutron detectors (including FCs and sCDs) produce weak signals in mkA range, which requires usage of preamplifier located not father than dozens meters from detectors. This forces various neutron diagnostics to have corresponding electronics in ITER port cells. Operation conditions there are hostile for electronics, including high radiation and electromagnetic fields [193]. In order to protect preamplifiers dedicated shielding is foreseen.

Despite just recently having last PDR, VNC have one of the most advanced (among ITER systems) designs of the shielded cabinets. Current CAD model for LP14 is given on the figure 52.

In lower port 14 common shielding approach applied with LVNC cabinet hosting both preamplifiers of 55.B2 (red color on left image of figure 52) also of DNFM (red units). Most of the cabinet volume constitutes protection against neutrons.

And using of common shielding approach allows to limit with couple dozen percent's increase of the weight, space and cost for extending solution on two system, while independent cubicles would require doubling these values. Depending on the neighbors in other ports common shielding is planned to be used there as well.

Shielded cabinets of VNC are located in the port cell support structure (PCSS) and consists of neutron shielding made of B4C blocks, gamma shielding made of tungsten block and pure iron plates for magnetic screening. Tungsten block and iron plates are fixed at the stainless steel supporting frame. This frame has doors from the front and back sides to provide access to electronic components.

One of the key analyses justifying shielding solution is MCNP calculations, which for LVNC shielded cabinet confirmed necessary level of neutron attenuations from $\sim 10^6$ to allowed for non—radiation hard electronics 10^2 n (s^{-1} cm^{-2}). Attenuation of the neutron flux dependence from the point position inside the shielded cabinet for one of its cross sections is given in the figure 53.

3.6. NFM

3.6.1. Introduction. NFMs are among the most important systems in nuclear fusion devices as they are used to measure total neutron emission rate and then to evaluate fusion power. In ITER, the total neutron emission rate will be measured by three types of the NFMs: the NFM [194], the Divertor NFM (DNFM) [195] and the microfission chamber (MFC) [196].

Requirements for the NFMs are given in table 21. Table 22 shows the role of measurement of the required parameters for the NFMs. They are taken from latest approved SRD-55 (system requirement document) [197]. The NFMs shall measure the total neutron flux and then evaluate the fusion power with time resolution of 1 ms and accuracy of 10% in certain plasma parameter range.

3.6.2. Microfission chamber.

3.6.2.1. General description. The MFC is operated as the in-vessel NFM in ITER. An MFC detector is a pencil-sized gas counter (14 mm in diameter and 200 mm in length) containing fissionable material (235U) that can be installed in the VV. Figure 54(*a*) shows a cross sectional view of the MFC detector used in ITER.

A coating of UO_2 covers the outer cylindrical electrode of the MFC. The active length of the device is 76 mm, with a total of 10 mg of 235 U used. The MFC detector is filled with argon gas at 14 atm, which serves as the ionization gas. The

Table 19. Fusion power density profile measurement parameter requirements.

Parameter	Range	Time Res.	Spatial Res.	Accuracy	Role
013a. Fusion power density	1–20 kW·m^{-3}	1 ms	a/10	20%	1a.2 BC
013b. Fusion power density	20–4000 kW·m^{-3}	1 ms	a/10	10%	1a2. BC

Table 20. Neutron-and-Alpha-source profile measurement parameter requirements.

Parameter	Range	Time Res.	Spatial Res.	Accuracy	Role
014. Neutron-and-alpha-source profile	10^{14}–$1.4{\cdot}10^{18}$ nm^{-3}s^{-1}	1 ms	a/10	10%	1b.AC

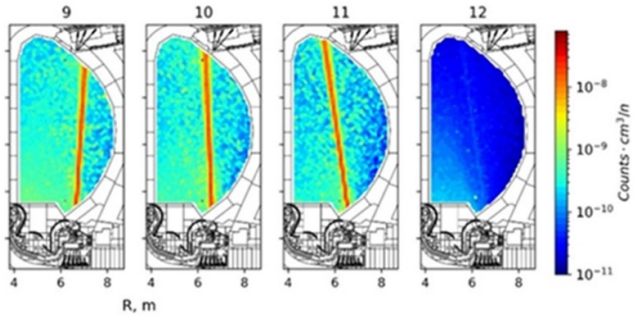

Figure 50. DT neutron contribution matrix for fission chambers (sensitivity of particular detectors of LVNC to different point of the plasma cross section).

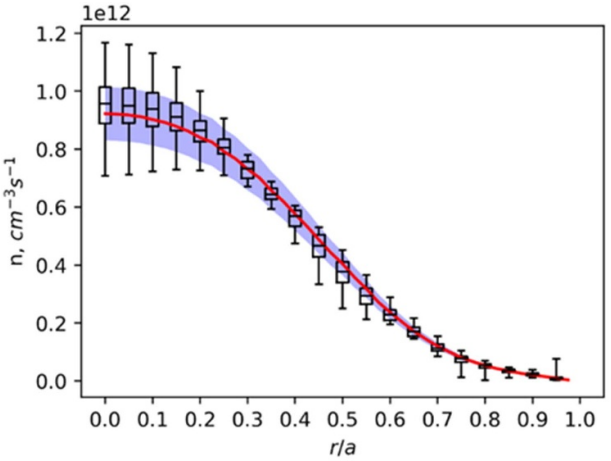

Figure 51. Neutron source profile reconstruction for reference source DT, $I = 15$ MA, $P = 500$ MW.

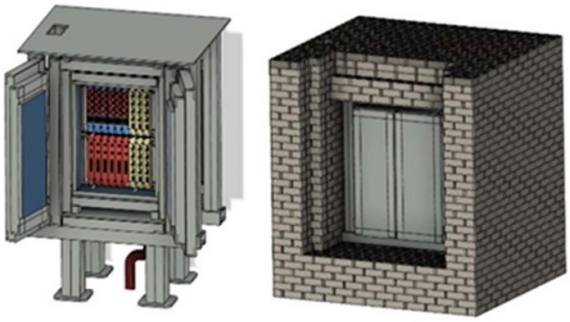

Figure 52. LVNC shielding cabinet on PCSS of LP14. Left—internal structure ensuring protection against EM and γ fields, right—external protection from B4C bricks for efficient neutrons attenuation.

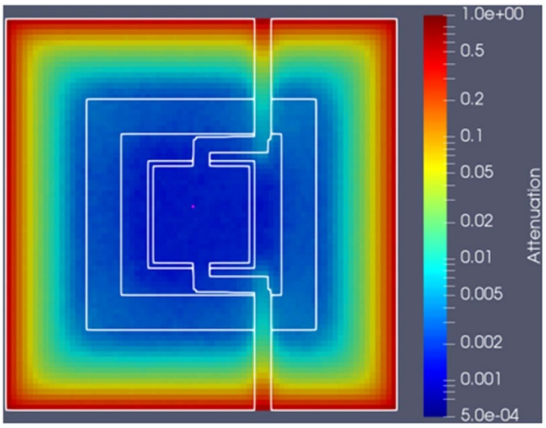

Figure 53. Spherical source. Neutron attenuation.

housing material is fabricated from stainless steel 304 l and the electric insulator is composed of alumina (Al_2O_3). The structure of the tri-axial MI cable is shown in figure 54(*b*). The core is formed of Cu, while SiO_2 is used as an electric insulator between core and inner sheaths and between inner and outer sheaths. Argon gas fills the inner sheath to prevent any discharge between the core and the inner sheath. The MI cable has been designed based on proven MI cables used in several fission reactors. Based on its use in fission reactors and on the results of Monte Carlo N-particle (MCNP [198] neutronic calculations for the ITER conditions, it has been confirmed that the MI cable can operate without any problems under ITER radiation conditions during the ITER lifetime.

The MFC detectors will be installed between the VV and blanket modules at both the upper and lower outboard positions, as shown in figure 55.

The reason for installing the MFC detectors in such locations is to compensate for the change in sensitivity of each detector when the plasma shape changes [199]. At each proposed location, two MFC detectors will be installed. The deployment of dual MFC detectors at each location improves redundancy. The MI cables are routed from the upper and lower detector positions to the upper port and connected to the

Table 21. Fusion power density profile measurement parameter requirements.

Parameter	Range	Time Res.	Spatial Res.	Accuracy	Role
012 Fusion power	100 kW—0.9 GW	1 ms	Integrated	10%	1a.2 BC
015. Total neutron flux	10^{14}–$3.2{\cdot}10^{20}$ ns^{-1}	1 ms	Integrated	10%	1a.1 MP

Table 22. Fusion power density profile measurement parameter requirements.

Parameter	Primary	Supplementary
012 Fusion power	55.B4 Neutron flux monitors 55.BC Divertor neutron flux Monitors	55.B3 Microfission Chambers
015. Total neutron flux	55.B4 Neutron flux monitors 55.BC Divertor neutron flux Monitors	55.B3 Microfission Chambers

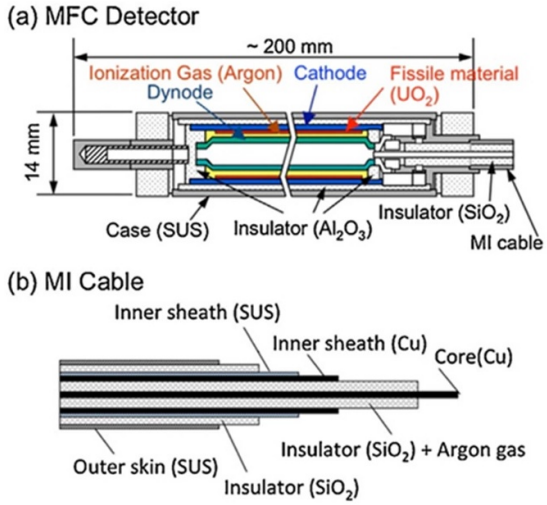

Figure 54. MFC detection system: (*a*) Schematic of the MFC for ITER; (*b*) the structure of the MI cable.

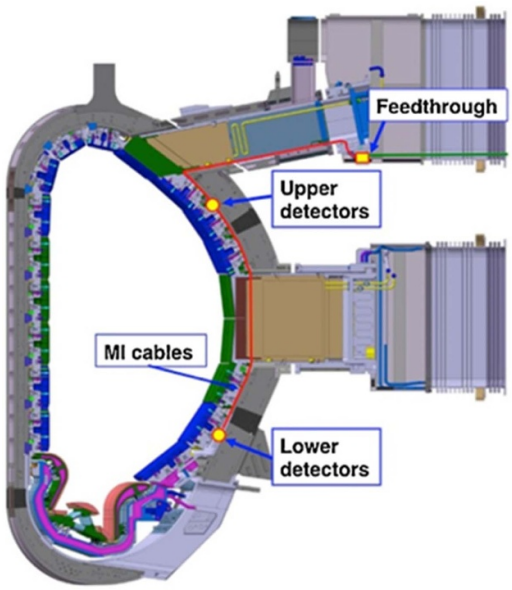

Figure 55. Arrangement of the poloidal cross section of the in-vessel components of the MFC system on ITER tokamak.

soft cable at the feed through in the upper port. The lengths of the MI cable for the upper and the lower MFCs are about 4 and 11 m, respectively.

The current plans for installing the in-vessel components of the MFC system into the VV require the MFC detectors and MI cables to be installed at different times. As the MFC contains fission material (^{235}U), it should be installed in the VV after first plasma operations in order to ensure safety. On the other hand, the MI cables are scheduled to be installed in the early phases of the process of assembling the tokamak to allow for their routing under the water manifold and to avoid interface conflicts with other in-vessel components. Therefore, it is necessary to connect the MFC detectors (with short MI cables) to the MI cables inside the VV. Although MFC detectors and MI cables are manufactured as a unit in fission reactors, in ITER the MFCs and the MI cables use a connector which was designed in a previous study. Figure 56 shows the structure of the connector. The core is connected by resistance spot welding using Ni-foil, which has a good track record in neutron detectors for fission reactors. Ceramic shields are inserted as insulators to avoid any contact of the Ni-foil with the inner sheath as well as to avoid any contact between the inner sheath and the outer sheath. The workability of the connection between the MFC detector and the MI cable in the limited space within the VV has been demonstrated in several tests.

3.6.2.2. System performance analysis. As described above, the MFC detectors will be installed upper and lower outboard positions to compensate for the change in sensitivity of each detector when the plasma shape changes. It has been confirmed by Neutronic calculations using MCNP [198].

Dependence of the detection efficiencies on the horizontal plasma shift is shown in figure 57(*a*). The detection efficiencies are very weak functions against the horizontal plasma position. Dependence of the detection efficiencies on the vertical plasma shift is shown also in figure 57(*b*). The detection

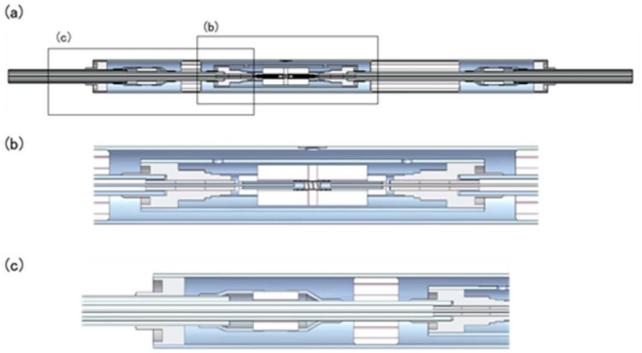

Figure 56. Schematic view of the vacuum tight tri-axial connector of the MI cable; (*a*) the external appearance, (*b*) the inner structure of the core region and (*c*) the inner structure of the side region.

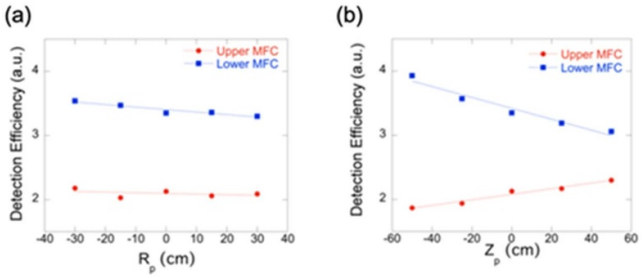

Figure 57. Dependence of the detection efficiencies on the horizontal plasma shift (*a*) and the vertical shift (*b*).

efficiencies of the upper MFC increases monotonically with the vertical plasma shift. On the other hand, that of the lower MFC decreases.

The total neutron emission rate can be represented by the linear combination of the MFC counts as follows,

$$S_n = \frac{w_{\mathrm{Up}} C_{\mathrm{up}}}{\varepsilon_{\mathrm{up}}} + \frac{w_{\mathrm{low}} C_{\mathrm{low}}}{\varepsilon_{\mathrm{low}}}, \quad w_{\mathrm{up}} + w_{\mathrm{low}} = 1$$

where S_{n} is the total emission rate, w_{i} is a weight for the linear combination. C_{i} is a count rate, and ε_i is detection efficiency for the reference plasma parameters. The weight w_{i} are determined to minimize the deviation of the total neutron emission rate from the neutronic analysis. The errors of the total neutron emission rate due to change in the plasma parameters are shown in figure 58. It was found that the error due to change in the plasma parameters are less than $\pm 3\%$.

The MFC detectors are installed in a VV and cannot be replaced. Therefore, it is necessary to demonstrate the MFC can properly measure the total neutron emission rate over the operational period of ITER.

A lifetime of the MFC is determined by the change of the sensitivity of the chamber due to the burn-up of the fissile material. ^{235}U is burned up through mainly fission and neutron capture reactions. So, the number of ^{235}U atoms, $N_{235\mathrm{U}}$, is represented by following equation;

$$\frac{\mathrm{d}}{\mathrm{d}t} N_{235\mathrm{U}}(t) = -N_{235\mathrm{U}}(t)\,\phi\,(\sigma_{f\,235\mathrm{U}} + \sigma_{C235\mathrm{U}}) \tag{3.1}$$

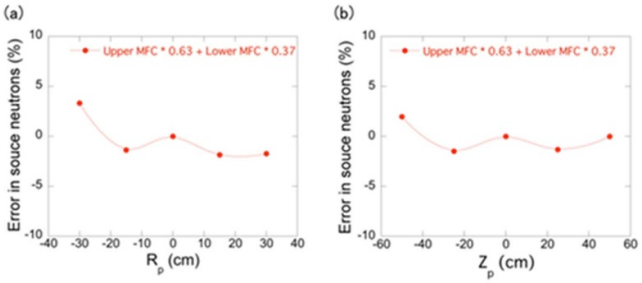

Figure 58. Error of the detection efficiencies for (*a*) the horizontal plasma shift and (*b*) vertical shift.

where σ_{f235U} and σ_{C235U} are averaged fission and neutron capture cross-sections defined by

$$\sigma = \frac{\int \sigma(E)\,\phi(E)\,\mathrm{d}E}{\int \phi(E)\,\mathrm{d}E} \tag{3.2}$$

where $\phi(E)$ is the neutron energy spectrum at the micro FC. From equation (3.1),

$$\begin{aligned} N_{235\mathrm{U}}(t) &= N_{235\mathrm{U}}(0)\,\mathrm{Exp}\{-\phi\,(\sigma_{f235\mathrm{U}} + \sigma_{C235\mathrm{U}})\,t\} \\ &\approx N_{235\mathrm{U}}(0)\,\{1 - \phi\,(\sigma_{f235\mathrm{U}} + \sigma_{C235\mathrm{U}})\,t\} \\ &\approx N_{235U}(0)\,(1 - \phi\sigma_{f235\mathrm{U}}t) \end{aligned}$$

is obtained. For the detector position behind a blanket (typically #12), the burn-up of ^{235}U atoms is dominated by the fission reaction, because the fission cross-section is about 10^2 larger than the capture one. The burn-up rate of $\varphi(\sigma_{\mathrm{f235U}})$ is estimated 2.7×10^{-11} s^{-1}. The change of the sensitivity is estimated to be only 0.1% behind blankets for the ITER life time which is equivalent to 0.5 GW year. So ^{235}U chambers can be used without replacement in the ITER lifetime.

The effect of the strong magnetic field on the FC is another problem. In the FC, the electron induced current from ionization by fission fragments is measured. So, the electron drift orbit in the magnetic field was calculated. The electron drift velocity $\boldsymbol{u}$ is represented by

$$\boldsymbol{u} = \frac{\mu_{\mathrm{e}}}{1 + \omega_{\mathrm{c}}^2/\nu^2}\left[E + \frac{\boldsymbol{E}\times\boldsymbol{B}}{B}\frac{\omega_{\mathrm{c}}}{\nu} + \frac{(\boldsymbol{E}\cdot\boldsymbol{B})}{B^2}\frac{\omega_{\mathrm{c}}^2}{\nu^2}\right] \tag{3.3}$$

where μ_{e} is the electron mobility, ν is the collision frequency of the electron to neutral atoms, and ω_{c} is the electron cyclotron (EC) frequency in the magnetic field **B**. Assuming $E = (E_x, 0, 0)$ and $B = (0, 0, B_z)$,

$$\boldsymbol{u} = \left(\frac{\mu_{\mathrm{e}} E_{\mathrm{X}}}{1 + \omega_{\mathrm{c}}^2/\nu^2}, \frac{\mu_{\mathrm{e}} E_{\mathrm{X}}}{1 + \omega_{\mathrm{c}}^2/\nu^2}\frac{\omega_{\mathrm{c}}}{\nu}, 0\right). \tag{3.4}$$

An angle between **u** and **E**, Lorentz angle α, is represented by $\tan\alpha = \omega_{\mathrm{c}}/\nu$. In the case of the MFC with 14.6 atm Argon gas, applied voltage of 200 V to 0.5 mm electrode gap, in the magnetic field of 5.7 T, the drift velocity without magnetic field is $u_0 \approx 3 \times 10^3$ m s^{-1}. The Lorentz angle is evaluated as $\tan\alpha \approx 0.04 \ll 1$. Thus, the magnetic effect on the electron drift velocity is to be negligible.

3.6.2.3. Summary. The MFC system is being developed for installation and plasma operation in ITER. The MFC must withstand the extremely harsh environment inside the VV, such as high heat load and high electromagnetic forces. In addition, the MFC system must be able to accurately measure total neutron emission rate in various noisy environments outside the VV. In order to achieve the ITER requirements, Japan Domestic Agency is intensively advancing the detailed design of the MFC from various perspectives, including structural integrity and noise suppression.

3.7. NAS

3.7.1. Introduction. The NAS is a diagnostic measuring the absolute neutron flux and fluence on the FW [200]. It utilizes pneumatic post method to send a sample of material close to the plasma, where it gets activated by neutrons. The sample is then retrieved back with the same pneumatic post technique and the activation of the sample is measured with gamma-ray spectrometers [201]. The main goal of the ITER NAS is to evaluate the total neutron production rate from all over the plasma. The measurement accuracy depends on the position and profile of the plasma and the variation of material in front of the irradiation end (IE). It is required to minimize the amount of material and its density variation across the volume between the plasma and the IE. The influence from in-vessel materials such as the DFW, blanket modules, and divertor cassettes, that are located near the IEs is unavoidable. A number of irradiation positions located above and below the plasma as well as on high-field side and low-field side has been selected for the ITER NAS to compensate the strong influence from these components, as well as the plasma shape and position variations.

3.7.2. Generic description. The ITER NAS measures gamma radiation from samples activated by fusion neutron flux. Encapsulated samples are transferred between IEs and counting station by the nitrogen driving gas. Tubes of diameter 12.7 mm will be used for the transfer lines of the capsule.

NAS consists of IEs, pneumatic transfer system and the counting station (figure 59) [201]. The counting station includes gas supply, distribution station (carousel), interstations transfer lines, cooling docks, counting docks with gamma detectors and the ultimate disposal dock. The control system will assure fully automated operations including capsule loading, transmission to and from IE, storage for cooling, gamma activation measurements and transition to disposal dock [202].

Due to the large size and the elongated shape of ITER plasma, multiple positions for the IEs in toroidal section are required for highly reliable measurements. Four IE locations per toroidal section (A, B, C and D in figure 60) are planned for ITER NAS considering the reliability of the measurement and redundancy of the system.

Transfer tubes of the NAS should be bent many times to reach the IEs from the transfer station. To avoid the capsule to get stuck around tube bends, there should be a minimum

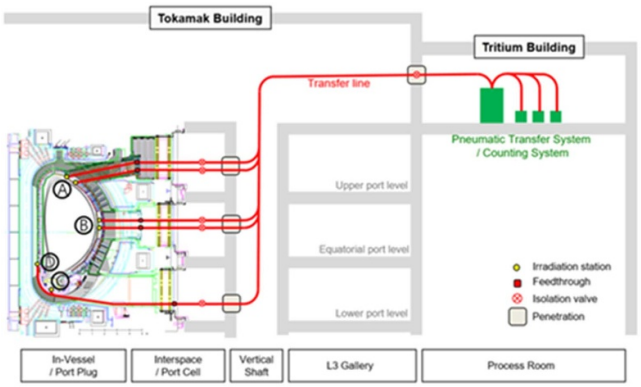

Figure 59. The scheme of neutron activation system for ITER.

bending radius of the tube in designing tube route. All bends of the tube should have a larger radius than this minimum bending radius. Assuming the capsule of outer diameter 8 mm and length 30 mm, and the tube of inner diameter (ID) 9 mm, the minimum bending radius of the tube is about 100 mm. The current design value of the minimum bending radius is 150 mm, with a safety factor of 50% applied.

The port allocation for the NAS is #11 and #18 for the upper port, #11 and #17 for the equatorial port, and #12 and #18 for the lower ports. For points A and B, the IEs will be located inside the port plugs. Other IEs will be installed on the VV wall with the pipelines routed through the lower level ports [203]. In total 12 IEs will be installed.

The transfer system distributes capsules to the appropriate locations such as IE, counting station, or disposal dock. It consists of capsule loader and distribution machine—carousel. When a capsule is loaded on the carousel from the loader, the platter inside the carousel rotates to place capsule to the point connected to the designated place.

The counting station is located outside the tokamak building, where the neutron flux effect on the detectors is negligible. Detectors such as HPGe or NaI will be used to count gamma-rays from the activated samples. The required parameters for the NAS such as neutron fluence will be evaluated from the gamma spectrum considering the location of the IE, sample material and its mass, and irradiation and cooling time.

3.7.3. Evaluation of measurement accuracy. The measurement accuracy of the NAS with 12 IEs is estimated using MCNP calculations. The response of each irradiation location is evaluated by changing the location and the profile of the neutron source (see figure 60).

The evaluated result of the neutron source displacement effect (top part of figure 60) shows that the upper port is the best position for the irradiation due to its lowest sensitivity to the plasma position. The induced error due to the vertical displacement can be even lower when it is compensated with the measurement at the divertor position, as long as the IE at the divertor is well characterized during the plasma operation. It is estimated that the induced error from the neutron source displacement can be $\sim\pm1\%$ even without compensation from other diagnostics, from the simultaneous measurement from

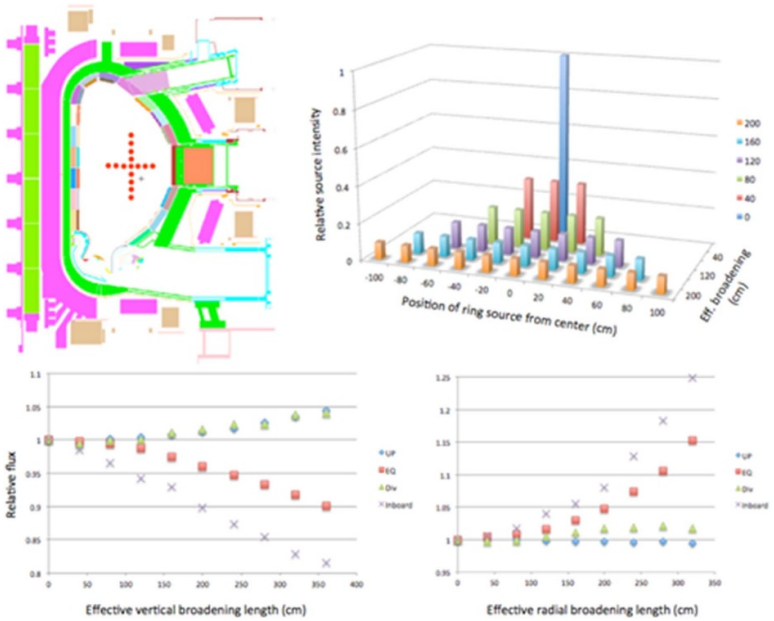

Figure 60. Evaluation of the effect of neutron source position and broadening.

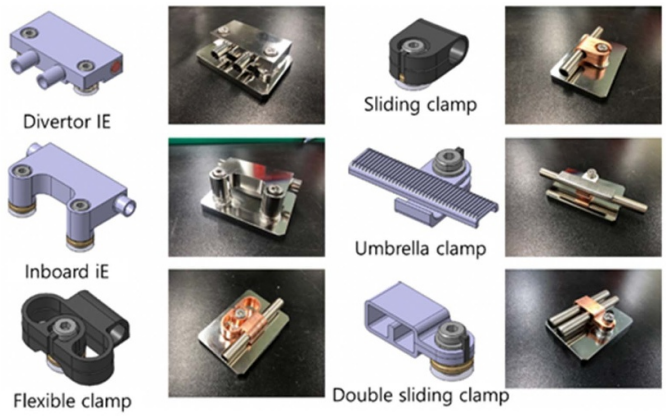

Figure 61. Examples of NAS in-vessel clamps CADs and their prototypes.

the upper and divertor position, when the displacement range is within ± 20 cm vertically and radially. The equatorial port position can be used for backup when the data are compensated from other diagnostics.

The effect of neutron source broadening (bottom part of figure 61) on the measurement, which cannot be estimated during the in-vessel calibration, was evaluated. The result also indicates that the upper port is the best position, because it has the lowest effect from the neutron source broadening, and shows good characteristic of depending only on the vertical broadening. It is interesting to note that the equatorial port position shows symmetric measurement with the upper port position. Therefore, the simultaneous measurements from the upper and equatorial port position are expected to provide the total neutron production with the broadening error of $\sim 1\%$ without compensation from other diagnostics, when the profile peaking factor is in the range of $3 < \alpha < 7$.

The calculations show that the combination of measurements from the upper port, equatorial port, and divertor region can provide a relatively good evaluation of the total neutron production in the plasma. In spite of the low reliability of the measurement from the inboard midplane position, it is reasonable to keep these IEs, as they are the only ones capable of providing the absolute value of the neutron flux coming to the inboard side.

3.7.4. Design of the NAS components for ITER. Thermal analysis has made significant impact on the design of the NAS front-end components, as all NAS components installed inside the VV shall follow the design guideline SDC-IC (Structural Design Criteria for ITER In-vessel Components), which requires the maximum temperature of the components to be less than about 400 °C. In order to guarantee stable

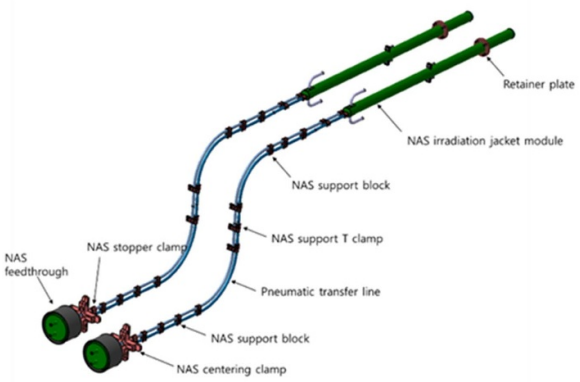

Figure 62. Components of NAS IEs in equatoril port plug 11.

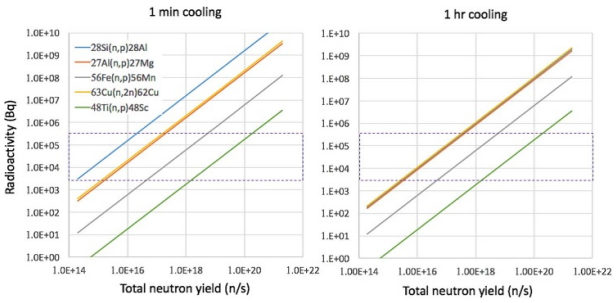

Figure 63. Radioactivity of samples (a) at the equatorial port irradiation end by 1 s irradiation, (b) at the divertor irradiation end by 100 s irradiation.

temperature of the in-vessel components, these tubes and IEs are clamped to the VV with a maximum pitch of 20 cm. The clamps (figure 61) are particularly designed to maximize heat sink and provide cover from stray plasma radiation where necessary. The material of clamps and IEs is CuCrZn, while the tubes and the boxes, used for attachment to the VV, are stainless steel SS316.

Port plug IEs represent coaxial structures aimed at minimizing dimensions and maximizing cooling features. (figure 62). Most components will be fabricated from SS316L. The front part of the IE is enclosed with the coolant housing, which is connected with the coolant tubing. Two guiding rings are attached on the outside of the coolant housing for a smooth insertion of the IE into the DSM. The feedthroughs will be welded on the closure plate of the port plugs.

Transfer station consists of many moving components such as a servo-motor, linear actuators and many solenoid or gas-driven valves. Pneumatic properties of the transfer system for transferring the capsule are as in table 23:

Table 23. Pneumatic properties of the transfer system for transferring the capsule.

Pressure of gas in reservoir:	∼8 bars max
Pressure of driving gas	1 −8 bar
OD of sample transfer tube	12.7 mm
Thickness of sample transfer tube	1.25 mm
OD of retrieving gas tube	12.7 mm
Thickness of retrieving gas tube	1.25 mm
Diameter of capsule	∼8 mm
Length of capsule	∼20 mm

Samples will be transferred to the designated position by the action of a distribution machine—carousel. A rotating platter inside the carousel will transfer the sample to the loading position that is connected to the designated IE. When the samples are ready, the valves behind are opened to shoot them to the designated positions. A programmable logic controller will control the operation of the transfer system.

Counting station measures gamma-rays from the activated samples. It consists of gamma-ray detector, signal processing electronics such as high voltage supply, preamplifier, amplifier, and multi-channel analyzer, and data analyzing software. Many gamma-ray detectors such as gas chambers, scintillators, and semiconductor detectors are commercially available. Amongst these detectors NaI detectors and HPGe detectors are the most commonly used ones for neutron activation analysis, but other types of detector are also considered. Appropriate detectors will be chosen for the proper operation of ITER NAS considering state of the art.

3.7.5. Performance assessment. The primary role of the NAS is to provide the FW fluence. Considering the plasma shot based operational method of NAS, it is also important to have a shot-integrated measurement ability regardless of the performance of the plasma such as the discharge time and the total neutron yield. NAS is expected to provide the measurement data in the discharge time of 1 s (neutron flux with higher temporal resolution can be measured by time-resolved neutron diagnostics such as NFM)—a few hundred sec, and in the neutron yield of 10^{14}–3.2×10^{20} s^{-1}. Neutron transport and activation calculations using MCNP and FISPACT code showed that NAS can measure the whole neutron yield range thanks to the freedom of selecting the irradiation locations, kinds and mass of samples, cooling time, etc.

In order to provide necessary statistics and avoid saturation, the radioactivity of the irradiated samples should be in the region of 2×10^3–2×10^5 Bq. Preliminary performance assessment has demonstrated (figure 63) that it is possible to select necessary activation foil material and size for all required values of neutron yields [204].

3.7.6. Summary. The ITER NAS that has been briefly presented hereabove is under development by the Korean Domestic Agency of ITER. Despite the challenges driven by ITER's unprecedented thermal, electromagnetic and nuclear loads, high radiation and activation in full-power operation leading to very limited personnel access and highest safety and reliability requirements [6], despite all these aspects the presented NAS design proves to be suitable to satisfy ITER's measurement requirements.

Table 24. Measurements and their requirements for a HRNS system at ITER, taken from [149].

Measurement	Parameter	Parameter range	Condition	Time resolution (ms)	Accuracy (%)
Fuel ion ratio in the core	n_t/n_d	0.01–10	DT plasma if P_{fus} >0.5 MW NBI Present if n_t/n_d <0.1 NBI absent T_i known	100	20
Ion temperature in the core	Core T_i	5–40 keV	P_{fus} >0.5 MW	100	20

3.8. Neutron spectrometers

Neutron spectroscopy is one of the few methods with an established capability to determine ion density ratios, n_t/n_d, in the plasma core. The ITER requirement for the determination of n_t/n_d is an accuracy of 20% within a time window of 100 ms (see table 24). Moreover, this should be accomplished for a fusion power range of approximately three orders of magnitude, from pure deuterium to 50/50 DT plasmas. To achieve these requirements, recent developments in neutron spectroscopy techniques, DAQ and data analysis methods have been included in a conceptual design [149] and should to be further developed in a final design.

The main role of a HRNS system at ITER is to measure the fuel ion ratio, n_t/n_d, in the ITER core in DT operations. A secondary role is to contribute to measurements of the fuel ion temperature in the core. In addition, a HRNS could also contribute to measurements of other operational and physics parameters, such as the fusion power, fast ions distribution functions and heating effects and efficiency.

The ability of neutron spectrometry to provide measurements of n_t/n_d has been reported in a number of publications. For the thin-foil techniques, data from JET DTE1 have been analyzed using measurements from the Magnetic Proton Recoil spectrometer, MPR [205, 206]. Moreover, rather recently JET DTE1 data from the TANDEM neutron spectrometer [207–209] were used to make n_t/n_d estimates using analysis methods similar to those used for the MPR. This is of ITER relevance since TANDEM uses a neutron detection technique closely resembling the thin-foil proton recoil (TPR) technique suggested for the HRNS system. For the time of flight (TOF) techniques, in recent JET DT operations it has been shown that n_t/n_d can be estimated in minority T plasmas, D(T) and majority T plasmas, (D)T.

First we give a brief review of the main points of the proposed ITER HRNS system, then we will report on some pertinent recent and ongoing instrumental and method developments.

The case for and a preliminary design of a HRNS at ITER has been made in the article 'Conceptual design of the high resolution neutron spectrometer for ITER' [149]. Due to the required performance over a wide range of fusion power, no single instrument has been found to fulfill the requirements. Therefore, the proposed HRNS system is composed of a system of four spectrometers, employing different detection techniques. From previous experience with other projects and implementations of neutron spectrometers in fusion, the paper concluded that there are several spectroscopic techniques that have a good, proven record for fusion applications and thus should be considered for ITER. The proposed ITER HRNS therefore consists of (i) a set of TPR spectrometers, (ii) a matrix of neutron diamond detectors (NDDs), (iii) a back-scatter TOF (bTOF) spectrometer and (iv) a forward scattering TOF (fTOF) spectrometer; the latter is intended for D and D(T) plasma operations. These four neutron spectrometers can fulfill the measurement requirements for an ITER power range of 0.5–500 MW. The conceptual design of the system is described in some detail in the article, and will only be briefly mentioned here.

The planned location of the HRNS system is in ITER's equatorial port cell #1, and figure 5 in [149] shows the layout of the complete system. This allows for the use of a single radial LOS into the plasma core. The HRNS shares this Port Cell with some other neutron/gamma systems, namely the RNC and the gamma ray camera.

3.8.1. TPR technique. The TPR spectrometer system is intended for the highest performance plasmas, in the fusion power range, P_{fus}, 100–500 MW. It is based on the measurement of forward scattered protons from elastic (*n,p*) scattering on hydrogen in a passive, thin CH_2 foil. A set of two (radially) segmented Si detectors measure the recoil protons in coincidence in a restricted angular range. The two Si detectors are arranged as a d*E*-*E* pair (thin d*E*, thick *E* detector) in order to improve proton identification and reduce background. TPR spectrometers are inherently low-efficiency devices, and therefore, in order to boost count rates, the proposed TPR system consists of three identical sets of CH_2 converter foil and double detector arrangements placed one after another in a vacuum tight cylinder. Figure 6 in [149] shows a more detailed picture of the TPR system in the HRNS design. The vacuum chamber should maintain a pressure level of about 10^{-4} mbar or better, as this is sufficient to avoid detrimental energy loss of the recoil protons in transit from the scattering foil to the detectors.

Silicon detectors are a well-proven detection technique, used extensively in high-energy physics experiments, and also in fusion research. An energy resolution FWHM <2% is achievable, providing a performance that is sufficient for neutron spectroscopy applications. The estimated count rate of the Si detectors at the highest fusion power is about 250 kHz, which when spread out over several segments can be reduced to comfortable levels of a few 10 s kHz per segment. With

suitably fast preamplifiers and similarly fast backend DAQ electronics, processing of signals due to the direct neutron induced events should not pose any serious challenge. However, a more thorough investigation of background events due to scattered neutrons and gammas will be necessary for the final design. An extension of the present, rather thin, radiation shielding around the TPR system is probably necessary.

3.8.2. NDD. Diamond detectors for fusion neutrons in the 14 MeV region (DT plasmas) rely primarily on the $^{12}C(n,\alpha)^{9}Be$ reaction, which produces two charged particles in the final state. The Q value of the reaction is 5.702 MeV and it is thus only suited for neutrons from T and DT plasmas. A matrix of NDDs is proposed as part of the ITER HRNS system, and a picture can be found in [149], in order to provide redundancy in measurements in the higher end of fusion power, thereby providing complementary measurements to the TPR and TOF instruments. It also provides data from an alternative technique, which could be important to understand specific issues associated with the other techniques.

The NDD is to be placed inside the TPR vacuum chamber, behind that system. The resolution of NDDs is about 1% at 14 MeV and allows high resolution 14 MeV neutron spectroscopy measurements. For a single NDD element (radius 2 mm, thickness 0.5 mm) a total count rate of around 100 kHz is estimated for a $P_{fus} \sim 50$ MW. To handle higher P_{fus} a reduction of the NDD element size is required to maintain a total count rate of approximately 100 kHz in a single detector. To collect sufficient counting statistics a suitable number of NDD elements in a matrix are therefore needed. Similarly to the Si detectors of the TPR, this can be handled with modern, standard pre-amplifiers and fast, digital DAQ systems.

As they are installed in essentially the same location as the TPR, also the NDD system would benefit from a more extensive radiation shield around the TPR/NDD vacuum chamber.

NDD have been installed in many fusion devices but quite few relevant physics results have so far been published from their use in high-performance DT operations. Therefore, the high-performance DT operations at JET in 2021 should provide much valuable experience in doing spectroscopy on the intended (n,α) peak in the NDD pulse height spectrum. It should be noted that the performance of the NDD devices as spectrometers of DT fusion neutrons has been convincingly shown in for example characterization of DT neutron generators (NGs). For ITER applications, the challenge rather lies in the expected high count rates, operations over extended periods of time, high levels of background etc. It is also important to investigate the effect of the ^{13}C content in NDD elements for estimating n_T/n_D.

Further developments of the NDD technique for an ITER HRNS system should include, e.g. careful assessment of their performance in high-performance DT operations (JET 2021), tests of detectors, signal electronics and acquisition at the highest rates envisaged at ITER and neutron transport calculations to design an optimal radiation shield for the HRNS TPR/NDD systems.

3.8.3. TOF technique. TOF systems for fusion rely on elastic scattering of a fusion neutron on hydrogen in two sets of detectors (proton/proton or deuteron/proton), one giving a start and the other a stop signal for the flight-time measurement. With a known distance between the detectors of the two sets, and relying on two-body kinematics, the neutron velocity (energy) can be determined. Since it is the neutron that is traversing the system and being responsible for both start and stop signals, the in-beam material of the TOF system's start detectors can be substantially thicker than in the TPR case, thereby offering much higher efficiency. TOF systems can therefore offer good performance in plasmas of relatively modest neutron emission rates. A resolution of FWHM = 5.8% is obtained for the TOFOR system at JET for 2.5 MeV neutrons [210]. In recent D(T) experiments at JET, together with simulations, it has been possible to evaluate the performance of the TOFOR spectrometer in a range of minority T operations. It has then been estimated that DD neutron spectroscopy can be performed with TOFOR for a tritium concentration of up to approximately 20%, provided that the count rate capability for TOFOR is not exceeded, corresponding roughly to a signal to background ratio (SBR) for the DD peak on the order of 1. Such performance is possibly sufficient for the intended use of TOF systems at ITER, but further investigations should be made.

Two TOF systems are envisaged for the ITER HRNS: a conventional forward scattering system mainly intended for D and D(T) operations, and a back-scatter TOF system for the lower power ranges in DT operations. To reduce the volume of the full HRNS system, the two TOF systems are intertwined with each other, as shown in figure 8 in [149]. In order to extend the operational range of the back TOF (bTOF) it is proposed to install a flexible collimator in front of the system, in order to reduce the neutron flux on the in-beam detectors in high-power operations.

Extensive experience with the conventional forward TOF (fTOF) technique has been obtained at JET in the last decade through the TOFOR system. The design and operational experience from TOFOR has shown that TOF systems for fusion can be reliably modeled using state-of-the-art nuclear simulation codes like GEANT4 [211] and MCNP [212]. Experiments show that important operational parameters, like the influence of scattered neutrons and gamma background, the level of random events in the data (in high power operations mainly due to detection of non-correlated neutrons in the detectors of the system) and the details of individual detector response are well understood using modern simulation tools. This builds confidence in designing both the fTOF and bTOF systems for ITER. With the implementation of modern digital DAQ electronics, it is possible to somewhat reduce the influence of random coincidences through kinematic cuts [213, 214].

The backscatter TOF (bTOF) builds on the successful implementation of fTOF in fusion, notably the TOFOR spectrometer at JET.

The bTOF technique relies on single elastic scattering of a neutron on a deuterium nucleus in the start detector and subsequently detecting the same neutron in the stop detector,

placed at a well-known distance in the backwards direction. This arrangement has a two-fold advantage for detection of neutrons in the 14 MeV region: first, it gives a fairly low energy to the backscattered neutron, reducing its velocity, and thereby increasing the flight time of the neutron before it reaches the stop detector; second, it gives a large energy to the recoil deuteron, thereby improving the possibility to accurately measure the timing and energy of that particle. Deuterated scintillators, in either liquid or solid form, are envisaged as start detectors. Thus, a bTOF system can be expected to exhibit many performance parameters similar or better compared to a conventional fTOF: the size and flight times would be similar, and thereby also the achievable time resolution. The high energy of the recoil deuteron would improve the possibilities to perform accurate timing and kinematical cuts. Performance studies using Monte-Carlo (MC) methods of bTOF systems are presented in [215].

Further development of the fTOF system should include assessment of the operational limits in D(T) for performing n_t/n_d measurements. Another line of investigation could focus on improving the performance of the start detectors. The solid case for a bTOF system notwithstanding, development of a pilot bTOF system and tests in a 14 MeV facility would be important to gain experimental experience with the technique [216]. In addition, the space-saving arrangement of intertwined TOF systems should be simulated in more detail to assess the possible interference the systems might cause to each other. Finally, a detailed, overall assessment of the background radiation environment for the TOF systems should be made, including both the background from the system's own beam dump and background entering the system area from outside.

3.8.4. Recent developments. In the following we will report on some recent relevant developments with significance to the HRNS ITER mission. This includes: (i) method development of density measurements using the TOF technique at JET; (ii) recent work on the TPR technique; (iii) T_i measurements with fTOF in thermal (ohmic heating only) plasmas at JET.

3.8.4.1. Density measurements using the TOF technique in D(T) and (D)T at JET. The operations at JET with significant amounts of tritium in 2020–2021, ending with a high-performance campaign in full 50:50 DT, offers ample opportunities to develop the n_t/n_d method with the available neutron spectrometers at JET. Some results have so far been presented for the fTOF technique, at JET represented by the TOFOR spectrometer [217]. The fTOF method has so far been applied to D(T) and (D)T plasmas with trace amounts of up to a few percent of either tritium in a D dominated plasma, D(T), or deuterium in a T dominated plasma, (D)T. The results confirm previous assessments and are consistent, within uncertainties and other experimental circumstances, with other JET diagnostic systems [217]. An example of TOFOR time resolved results of $n_t/(n_t + n_d)$ in a (D)T plasma, JET discharge #99093, is shown in figure 64.

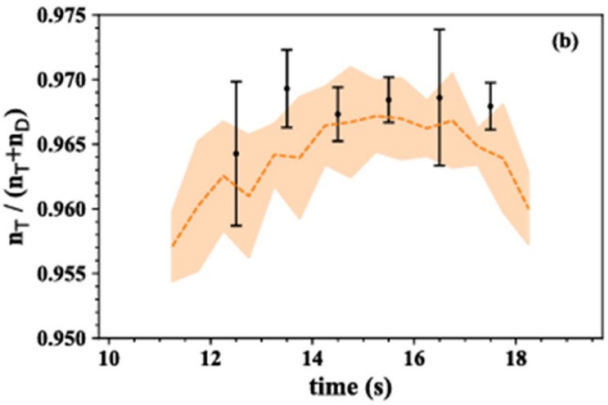

Figure 64. Time evolution of $n_t/(n_t + n_d)$ for JET discharge #99 093 as derived from TOFOR (points with error bars) and gas analyzer KT5P (dashed line with shadowed uncertainty band). Reproduced from [217]. CC BY 4.0.

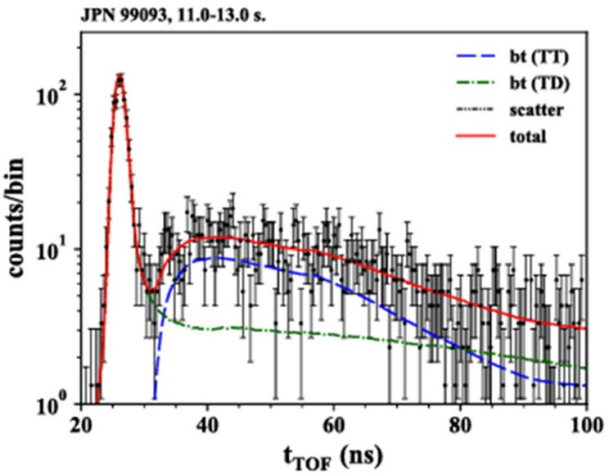

Figure 65. TOFOR time-of-flight spectrum integrated in a time interval of 2 s (JET time 11–13 s), used to estimate $n_t/(n_t + n_d)$. Model components of NBI (DT) and NBI (TT) and scattered neutron are used for the fit to measurement data. Reproduced from [217]. CC BY 4.0.

The result is for a neutron production dominated by tritium neutral beam ions reacting with the bulk plasma, mainly consisting of T ions. A roughly constant beam T ion power of 20 MW was injected into the plasma between 10 and 18 s resulting in a fairly constant $n_t/(n_t + n_d)$ result for TOFOR. Comparing the TOFOR result with the gas analyzer KT5P [218, 219], an optical diagnostic used in combination with a Penning gauge located below the divertor, gives a consistent picture, although small systematic differences have been observed for other pulses. Some differences are to be expected, considering the different locations of the active measurements of the two diagnostics.

Figure 65 shows the TOF spectrum for the same plasma discharge after subtraction of the random background. Features in the spectrum can be associated with neutron emission from DT and TT reactions, allowing for the detailed time resolved analysis presented here. The data from JET should make it possible to assess the limit of the n_t/n_d method using fTOF

which in previous simulation studies has been estimated at $n_t/n_d < 0.2$ [220].

3.8.4.2. Recent work on the TPR technique. Proton range telescopes based on silicon detectors is a well-established technique in nuclear physics and applications. However, apart from the now mothballed TANDEM instrument at JET, the technique has not been used at fusion devices, presumably due to the rather scarce opportunity of DT experiments. Here we can report on two lines of recent progress in the use of the TPR technique in fusion: first, we have tested the n_t/n_d method on data from the JET TANDEM spectrometer with good results; second, we have investigated a pilot set-up similar to that proposed for the ITER HRNS TPR implementation [221].

Analysis of TPR (TANDEM) data from the JET DTE1 campaign in 1997 [221] has corroborated the previously published results from the MPR spectrometer [215]. These A d*E*-*E* setup of two segmented silicon detectors has been tested at a 14 MeV neutron source at Lund University, Sweden [221]. The detectors were of somewhat poor quality, and only a few of the detectors radial segments could be equipped with signal processing and DAQ electronics. Also, further improvements in pre-amplifier electronics are certainly required. Still, the results corroborate the main conclusions from earlier simulation studies that coincidence d*E*-*E* measurements will be able to obtain the spectroscopic energy resolution needed together with background elimination to estimate n_t/n_d for ITER scenarios investigated in [149].

3.8.4.3. Ti measurements with fTOF in thermal (ohmic heating only) plasmas at JET. Measurement of the ion temperature is a supplementary function of the HRNS system. The measurement relies on the identification and analysis of the pure thermal neutron emission from a D, T or DT plasma. However, in most present (pre ITER) fusion experiments, the thermal neutron emission is only a small fraction of the total emission, which is normally dominated by emission from fusion reactions between fuel ions from the heating populations and the thermal bulk. In a few cases when only ohmic heating was applied has the Ti been possible to determine. This was for example reported in [222] using the MPR in the DTE1 experiment at JET, where an ion temperature of about 3 keV was reported for ohmic plasmas. More recently, using the fTOF technique, thermal temperatures of ohmic plasmas at JET in D operations were reported [223]. The reported values were in the range $T_i = 2.5$–3.2 keV and quite consistent with the JET crystal x-ray spectrometer and with the dependence of reactivity on T_i.

3.8.5. Conclusion. The proposed (enabled) HRNS system for ITER is based on well-established neutron spectrometry techniques. The required performance of the included subsystems, in terms of energy resolution, count rate etc, has for the most part already been achieved in systems installed at JET. The ability of neutron spectroscopy to perform its main (n_t/n_d) and secondary (Ti) functions has been established in a number of published studies using data from D, T and DT operations at JET. Some recent developments in JET DTE2 and in instrumental techniques corroborate these earlier studies and thus strengthens the case for installing the proposed HRNS system on ITER.

Figure 66. Compact neutron generator VNIIA NG-24.

3.9. In-situ *neutron diagnostic calibration*

ITER neutron detectors need to be absolutely calibrated in their ultimate positions in order to eliminate systematic errors associated with scattering features of the machine. *In-Situ* calibrations are routinely performed at nuclear installations where high precision of neutron yield measurements are required. ITER project requirements (PRs) state the value of 10% as the maximum allowable neutron yield (and thus fusion power) measurement uncertainty [224].

To perform *in-situ* calibration, a neutron source (permanent radioactive source or a NG) is introduced at different positions inside the vessel or moved around the torus to form a quasi-ring-source. The aim is to simulate plasma neutron emission as realistically as possible. In ITER, only the most sensitive detectors can be calibrated with compact neutron sources in a reasonable time. These diagnostics are:

- NFMs (in equatorial ports #1 and #7),
- divertor NFMs,
- micro-FCs and NAS.

The less sensitive detectors will be cross-calibrated during plasma operation. Compact NG with yields of up to 10^{11} and 10^9 n s^{-1} od DT and DD neutrons, respectively, will be employed at ITER. This decision is driven by performance (high neutron yield) and safety with respect to a ^{252}Cf source.

In order to minimize the calibration time, the most powerful commercially available compact NG VNIIA NG-24 (figure 66) has been chosen.

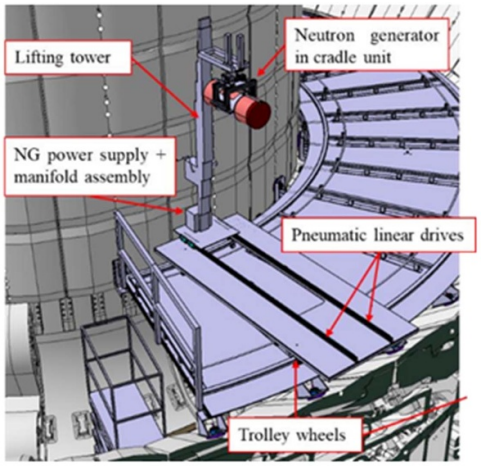

Figure 67. Conceptual design of the IVNC-1 NG manipulator.

Three calibration campaigns are foreseen for ITER:

1. In-vessel neutron calibration campaign 1 (IVNC1) with DD NG with strength of 10^9 n s^{-1}, just before the pre-fusion power operation 1 (PFPO-1) where neutron yield measurements are required by the Project. The DD NG will be deployed in limited areas in front of ports 18, 1 and 2.
2. IVNC-2 campaign is required before the start of PFPO-2 due ITER configuration change. This recalibration will be done with DD NG aiming to minimize machine activation in the process. Unlike IVNC-1, a full toroidal scan is planned for the IVNC-2 campaign.
3. The IVNC-3 campaign will be performed with 14 MeV DT NG just before the full power operation (FPO) Phase.

Each of the three campaigns is scheduled to last for 2 weeks of net NG in-vessel operation time, preceded and followed by preparation, assembly and disassembly periods. The IVNC-1 will be performed right after the partial installation of the blanket modules; therefore human access will be possible for the preparation, assembly and disassembly procedures. Conceptual design of the IVNC-1 NG manipulator is shown in figure 67.

The IVNC-2 and 3 will be performed after the FW modules have been exposed to plasma. Human access will be prohibited in the VV due to radiation and beryllium hazards. These campaigns will be performed with the use of a remote handling tool called the agile remote transporter (ART). The same tool that will be used for blanket modules replacement and optical diagnostic calibrations. At the current stage of the project, the ART is in the conceptual design phase (figure 68).

Studies have been launched with the following purposes:

- development of the high-accuracy NG yield monitoring system for DT and particularly for DD NGs;
- minimization of the NG yield anisotropy;
- development of the remote-handling capabilities of the NG unit with the attached yield monitoring system.
- Optimization of the calibration campaigns.

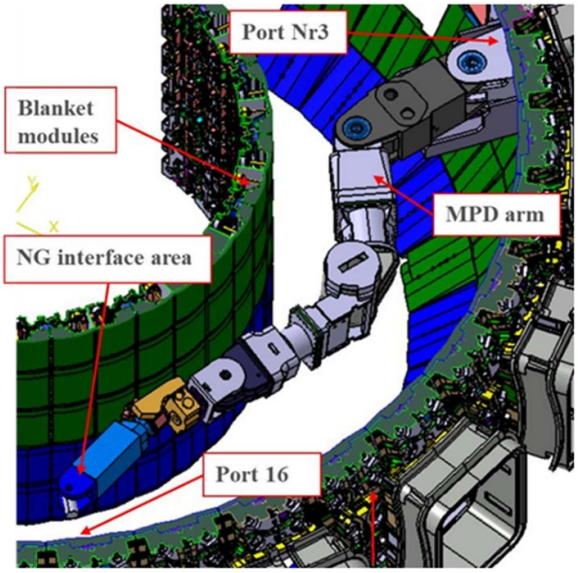

Figure 68. Conceptual design of the agile remote transporter (ART).

3.10. Alternative diagnostic techniques to fuel products measurements

In addition to neutron diagnostic systems, several other diagnostic systems considered for ITER can provide information on some of the plasma physical parameters listed in table 12. Systems discussed in this section include neutral particle analyzers (NPA), recombination CX spectroscopy (CXRS), and collective TS (CTS). This section is not intended to provide a complete assessment of the capabilities of these systems. Here we will only give a brief summary of the techniques and some of their problems and limitations. The full description of these diagnostic techniques is presented in other parts of the chapter dedicated to ITER-specific diagnostics.

3.10.1. CXRS. It is anticipated that CXRS diagnostics will provide information on plasma parameters such as plasma rotation, ion temperature profile, impurity density profile and alpha particle density profile. Active CXRS spectroscopy requires neutral beams. In the case of ITER, two types of such beams are envisaged, the first being a DNB providing deuterons with an energy of 100 keV and a second neutral heating beam (HNB) providing deuterons with an energy of 1 MeV.

Probing the plasma with the DNB beam is believed to be insufficient for high-quality measurements of plasma parameters in the core. On the other hand, measurements with high-energy HNB, due to better penetration of the beam, can sample the distribution functions of the confined α particles up to significant energies.

For α particle measurements, it seems that CXRS for DNB will be able to provide information on the distribution of alpha particles slowed down to an energy of 0.4 MeV, and when using HNB to an energy of 0.6 MeV. The limitation of this diagnostics may be the required small measurement angle.

Moreover, the presence of the high-energy ^{3}He population due to RF heating may further complicate these measurements.

Results for plasma rotation and ion temperature profile will depend on plasma impurities measurements. Differences between measurements for plasma fuel ions by neutron diagnostics and CXRS may occur for fast transients, have been observed for fast transients, for example at the onset of beam heating.

3.10.2. CTS. CTS diagnostics probes the ion VDF at the intersection of the probing and receiving 'beams' and in the direction of the difference between received and the emitted radiation (the detailed description could be found in subchapter 7, section 7.6). The CTS consists of one or more combinations of probe beams and receiving antennas in the microwave frequency range of 100 GHz, e.g. for the ASDEX tokamak, while the proposed system for ITER will be based on 60 GHz.

An important feature of the CTS technique is that the signal strength is proportional to the ion charge in the square (Z_i^2), which makes CTS a good candidate for alpha particle measurements ($Z_i^2 = 4$), even when such ions have a low concentrations. However, the disadvantage of this system will be the low relative efficiency of fuel ion measurements. ($Z_i^2 = 1$).

CTS is therefore a good candidate for diagnostics that gives information on the distribution function of fast ion, in particular for the fast alpha particle population.

3.10.3. NPA. NPA systems have been installed in many major fusion devices around the world and have a long history of providing experimental data. The rate of neutralized ions reaching the NPA system is a function of essentially the following factors (integrated at all points within the NPA line of side (LoS)):

- the local energy distribution of ions with velocities in the direction of NPA (it is usually considered that the capture of electrons does not significantly change the speed of the ion),
- the probability of local neutralization,
- plasma transparency for the outgoing atom.

Using measurements and modeling of plasma ion density (and impurities), temperature profiles, as well as data from atomic physics, it is possible to compare the measured streams of neutralized ions with the calculated ones and thus draw conclusions about the state of fuel ions in the plasma. To some extent, the interpretation process is similar to that of plasma neutron emission analysis, with the significant difference that for neutrons plasma transparency is equal to one.

Due to the fairly complex plasma modeling required for the interpretation of NPA data, this diagnostic seems to provide mainly qualitative data, where differences in the neutral particle flux for different plasma conditions are taken as an indication of presence or absence of tails of high energy particle in the plasma. This extensive and complex modeling so far seems to preclude the NPA from delivering more quantified results on a routine basis on every discharge, although quite detailed results are certainly obtained when special analytical efforts are made.

Typically, two NPA systems gathering integrated data from the same LoS are considered. One Low Energy NPA (LENPA) system covering an energy range of 10–200 keV with the ability to simultaneously measure neutralized hydrogen (H), deuterium (D) and tritium (T) ions. While the second high energy NPA (HENPA) should measure α particles with energies of 0.1–4 MeV, i.e. over their entire slowing-down energy range. The LENPA low energy system should provide information on the energy distribution functions of the neutralized fuel ions (deuterium and tritium) as well as protons and the fuel density ratio n_d/n_t in the plasma core. In contrast, the main purpose of the HENPA system is to provide information on the number density and energy distribution function of the confined α particles. Such a tandem system was planned for ITER. However, both systems have their drawbacks. In the case of the LENPA low energy system, there is a problem of data analysis when we are dealing with very flat ionic plasma temperature profiles and when a clear presence of hydrogen isotope composition in the plasma core cannot be expected. In addition, this system is limited by poor penetration of neutral particles from the core into the analyzer.

In turn, for the high-energy system (HENPA), a specific problem is that energetic α particles with energy E_α are indistinguishable from energetic deuterons with energy $E_d = E_\alpha/2$; it means that deuterons of the NB beam with an energy of 1 MeV limit the usefulness of HENPA for $E_\alpha < 2$ MeV. It may also be a problem using this system to measure high energy deuteron populations due to the heating of the ion cyclotron resonance heating (ICRH). In addition, the neutralization of α particles depends on the impurity ions (such as Be^{2+} and C^{4+}) that act as electron donors, and the density profiles of these impurities must be known (or modeled) with high accuracy in order to correctly interpret NPA measurements.

The limitation of this system seems to be the poor ability to distinguish between ions of different kinds, so that in practice only the population of fast alpha particles can be measured. Preliminary evaluations show that the measurement requirements for ITER can be met precisely for alpha particles.

3.11. Summary and conclusions

The ITER FP diagnostics provide key information on the ion populations in burning plasmas. Several measurement techniques have been considered aiming to measure among:

(a) the total neutron emission rate, i.e. fusion power; (FP is the only diagnostic system able to measure directly the fusion power/ total neutron emission)
(b) neutron emission profile from different plasma/magnetic configuration/scenarios, as well the spatial distribution of ions populations, confined alpha and lost alphas;
(c) the energy features: thermal and fast energies distributions of the neutrons and ions populations, confined alpha and lost alphas;
(d) accuracy 10%: particular attention is given also to the development of the neutron calibration strategy whose

main scope is to achieve the required accuracy of 10% for the measurement of fusion power.

ITER is now advancing through the construction phase. Most of the FP systems are under FDRs and some FP are already in the manufacturing phase.

This paper provides an overview of the FPs diagnostic systems and the associated engineering issues.

4. Progress in ITER diagnostics, active spectroscopy

S. Zoletnik[16], O. Asztalos[16,17], M. Bandyopadhay[18], P.Bharathi[18], M. de Bock[2], O. Ford[19], M. G. von Hellermann[20], D. W. Johnson[21], J. Ko[8], S. Menmuir[22], Ph. Mertens[20], A.H. Nielsen[23], G.I. Pokol[16,17], S.V. Serov[2], M.J. Singh[3], S.N. Tugarinov[24] and G. L. Vyas[18]

4.1. Active spectroscopy diagnostics

Charge exchange (CX) between the beam atoms and the plasma ions results in excited plasma ions and the spectral broadening and shift of their radiation represents the ion temperature and velocity. If the CX occurs on impurity ions the emission intensity can be used to calculate the impurity ion density. These measurements are called CXRS. Line radiation by the beam atoms contains information on the exciting plasma electron density (beam emission spectroscopy, BES), and the Stark split of the spectra by the $v \times B$ electric field can be used for calculating the magnetic field value and/or direction (MSE). On present-day fusion experiments CXRS is one of the standard methods for the measurement of ion temperature, flow velocity and impurity concentrations, while the plasma current distribution is measured by MSE. Density profiles and fluctuations are measured by BES [225]. The beams can be either Heating Neutral Beams (HNBs) or specialized DNB of the plasma species, or alkali atoms for the plasma edge measurement.

In all cases the key elements of the setup are the atomic beam with sufficient penetration depth and particle flux, and a high etendue optical observation system together with a suitable detection system. The location of the observation system is also of high importance due to two factors: first the extent of the intersection area between the beam and observation channels should be limited, to keep the spatial resolution at a reasonable value. This would call for near-perpendicular beam-observation angle and view along the magnetic field lines. The second factor is spectral discrimination between the passive plasma radiation and active emission either from the beam or the plasma. This separation is possible for the beam emission measurement by utilizing the Doppler shift resulting from beam atom velocity and requires sufficiently non-perpendicular observation.

On ITER active spectroscopy diagnostics are being developed on both the heating beams and a DNB. However, the situation will be quite different from present-day devices. The first problem is the large size and high density of the plasma which renders alkali metal (Li, Na) beams unsuitable for edge measurement due to their shallow penetration. Also, heating beams must operate around MeV energy to deposit power deep enough in the plasma. The CX cross-sections typically have a maximum around 30–100 keV beam energy therefore these high energy beams have too low CX cross-section and cannot be used for CXRS. The high beam velocity is a problem for BES as well, due to the long lifetime of the excited states, causing spatial smearing. Due to these problems a decision has been taken to install a DNB with ∼100 keV energy for CXRS on the He ash and other impurities. For MSE both the HNB and DNB are considered.

ITER also provides limited choice on the observation directions as all observation systems must be located in a limited number of ports. Even more problematic is the strong radiation background and expected damage to optical components by plasma sputtering and deposition. These problems are not specific to active spectroscopy diagnostics therefore discussed in subchapter 4 of this paper.

The planned active spectroscopy diagnostics have been outlined and their difficulties listed in Donné *et al* [4]: MSE is planned on the heating beams for the plasma current profile (safety factor) measurement, while multiple CXRS observation setups are planned for a dedicated diagnostic hydrogen beam. These latter have multiple measurement aims: He and other impurity concentrations, ion temperature, flow velocities. Additionally, to these primary roles the CXRS setups might also contribute to other measurements as well. The plans since the publication of [4] remain basically unchanged, but problems and possibilities have been understood and the designs have made considerable progress. The following sections describe the progress made in key areas of the ITER active spectroscopy diagnostics since the publication of [4].

4.1.1. MSE.

It was recognized early that the traditional MSE line polarization (MSE-LP) technique [226] would be difficult to adapt to ITER, due to the sensitivity of these measurements to spurious effects on polarization from even very thin mirror coatings. Due to the time required for effective mirror cleaning (see subchapter 9) of this paper and the nonuniformity of the cleaning, such coatings will accumulate in nonuniform spatial distributions between cleaning campaigns. Calibration schemes to compensate for the impact of such coatings do not exist.

An alternative approach uses high-resolution fitting of the line splitting and intensity ratios (MSE-LS) in the Stark spectrum of D_α to make a precision measurement of the local value of the motional electric field magnitude at many positions along the beam trajectory through the ITER plasma [227]. The initial design concept for MSE on ITER featured both LP and LS techniques. There have been demonstrations of MSE-LS and comparisons of both techniques on several devices (JET [228], ASDEX-Upgrade [229], DIII-D [230, 231], C-Mod [232], MST [233, 234] and most recently KSTAR [235, 236]) that measured that line splitting data are consistent with expectations based on equilibria constrained by conventional MSE-LP data. These studies feature only a few spatial positions, and spectra in which the line widths are comparable

to the line splitting. (On ITER there is better separation, with width $\sim 0.5 \times$ splitting).

The ITER MSE diagnostic design strategy called for a decision point on the viability of both techniques. Leading up to the decision, there was effort to identify a means to calibrate MSE-LP measurements, to assess the use of MSE-LS data to constrain equilibrium reconstructions, and to evaluate sources of systematic error in the MSE-LS approach.

MSE-LP calibration typically relies on acquiring data with 'beam into gas', with varying magnetic field configurations. This procedure is not permitted on ITER, hence 'built-in' calibration schemes were considered. At the position of the shutter near the FW, a rotating polarizer or a localized plasma source would be needed. In the latter case, the polarization direction of the Zeeman π-line would be analyzed with Fabry–Perot filters. Both concepts involved front-end components with high reliability risk in the harsh FW environment and were hence rejected.

There were two studies assessing the use of MSE-LS data to constrain equilibrium reconstructions. The first used the ESC code in the context of ITER parameters to simulate the equilibrium reconstruction variance when using combinations of MSE-LP and LS data in the determination of $q(r)$ and $p(r)$ [237]. A second study investigated the EFIT reconstruction code modified to implement either simulated or experimental MSE-LS data on DIII-D [238]. The studies indicate that at least 20 spatial positions are needed with $\delta E/E < 1\%$ in order to achieve 5% error on $q(r)$ with MSE-LS alone, and that MSE-LS alone is a better constraint on $p(r)$ than MSE-LP alone.

An ITER MSE simulation code was used to address systematic errors in the interpretation of ITER MSE-LS data. Included were errors in the beam energies, aperture locations, and beam and sightline shifts and tilts. The plan was to look at HNB1 and HNB2, as well as the DNB. Modeling was done for all of these. This study estimated the accuracies required in the above parameters to achieve $\delta E/E < 1\%$. Beam energies need to be known to $<1\%$, aperture and object locations to <10 mm, and sightline and beam angles to <2 mrad. Concepts for obtaining and cross-checking this data exist, but design details have yet to be developed.

MSE-LP systems are considered essential diagnostics on magnetic fusion devices. An MSE-LS system with enough spatial coverage to be able to constrain an equilibrium reconstruction does not yet exist. However, experimental data from many devices and detailed simulations indicate that such a system can meet ITER's measurement requirements, provided the geometry and beam energy can be accurately known. Hence, it was decided to proceed with MSE-LS alone, with a design featuring adequate spatial resolution [239].

Design of the ITER MSE-LS system is progressing, with present effort focused on integration of port plug components. The above decision eases constraints on the design. For example, the viewing apertures can be smaller, simplifying integration of viewing optics and shutters. The back-end design is also simpler, since fewer fiber bundles are needed and polychromators and polarimeters are eliminated. The beams are viewed with independent optical systems located in two equatorial port plugs (EPPs). Both are equipped with mirror cleaning systems. The total number of spatial positions is expected to be about 30.

Meanwhile, researchers continue to develop the MSE-LS technique. One example is recent data from KSTAR, described in the next section.

4.1.2. Example of MSE-LS data on KSTAR. The KSTAR tokamak has been operating the conventional PEM MSE polarimeter, MSE-LP, system since 2015 [240, 241]. Along with this, the feasibility of the MSE-LS approach has been also investigated based on the spectroscopic measurements. These activities have been motivated by the need for a test-bed for ITER MSE research and development [235, 236]. It is noted that the MSE spectrum measurements at the KSTAR tokamak have favorable conditions in that the viewing angles and the beam energies are such that the full energy component is well separated from the rest of the beam emission components, which means not only the adjacent components like the half energy MSE multiplets, but also the background-like components such as thermal and fast-ion deuterium Balmer-α (FIDA) emissions have little effect on the spectral fitting.

Figure 69 shows an example of the MSE spectra with the fitting on them to calculate the magnitude of the total magnetic field at two time slices of a plasma discharge—one with a low plasma density (1.8×10^{19} m^{-3}) and the other with a medium density (3.5×10^{19} m^{-3}). The spectrum measurements are made through three channels—core, mid-minor radius, and edge—out of 25 full MSE channels, the rest being connected to the MSE-LP polarimeter, so that both LS and LP measurements are simultaneously possible. A multi-Gaussian fit model on the full energy component takes into account the channel-dependent asymmetry around the $\sigma 0$ component, clearly observed in the measured spectra in figure 69. The background that includes the FIDA component is assumed to be linear in wavelength. The Stark splitting and the relative intensities among the MSE components are treated as free parameters. The fitting works reasonably well with both low and medium plasma densities.

The vertical magnetic field can be inferred from the Stark splitting with a fixed toroidal field, and this is compared with that from the LP method. This comparison is given in figure 70 where the radial profiles of the vertical field measured from the MSE-LP polarimetry are plotted along with those from the spectral fit method illustrated in figure 69 for three MSE channels (Chs 2, 15, and 23). The profiles from two different time points correspond to the two time slices given in figure 69 (low and medium densities). It is shown that the vertical fields inferred from the LS approach are reasonably aligned with these LP-base profiles. The comparison using two profiles also implies that with slight offsets, the vertical fields obtained from the MSE-LS exhibit similar sensitivities as those from the MSE-LP over two different densities.

Several issues still remain regarding the spectral MSE research in KSTAR. The spectral fit procedure would be considerably complicated in the cases with multiple ion-source

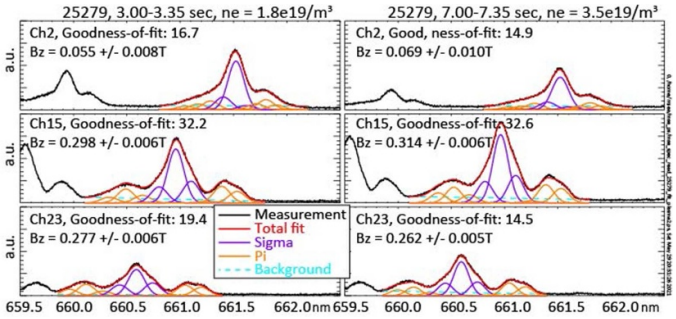

Figure 69. Example of the MSE-LS approach in KSTAR—the multi-Gaussian fits for the full energy components of the beam emission at two different time points (integrated over 0.5 sec)—low (left column) and medium (right column) densities—through three MSE lines of sight (from top to bottom plots). Chs 2, 15 and 23 are the core, mid-minor radius, and edge channels, respectively.

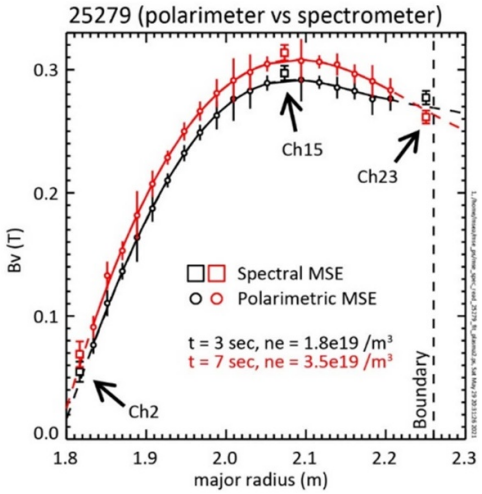

Figure 70. Comparison of the MSE-LP (polarimeter) and MSE-LS (spectrometer) approaches in the measurement of the vertical field at two different densities. The vertical fields from channels 2, 15, and 23 are from the spectral fits given in figure.

injections due to the spectral overlaps. The sensitivity of the spectral approach also needs to be tested further for discharges where non-monotonic pitch angle, thereby $q(r)$, profiles are expected such as the cases with internal transport barriers or off-axis current drive. Such topics are being investigated at KSTAR associated with the conventional and routine MSE-LP measurements.

4.1.3. CXRS on ITER. CXRS has been considered already in the first ITER design [3] as a possible diagnostic for impurity concentrations, thermalized Helium ash, poloidal rotation measurement using a dedicated diagnostic beam. First feasibility studies for ITER in [3] showed that local measurements of light impurity densities, ion temperatures, and rotation profiles will be possible only outside of $r/a = 0.5$ with a 0.1 s time resolution for the highest density plasmas considered. In Tugarinov *et al* [242] it was shown that optimized viewing geometry and spectroscopic equipment will allow increasing the SNR significantly. The feasibility of CXRS measurements was demonstrated from the edge to $r/a = 0.3$ for the highest plasma density $n_e = 1.4 \times 10^{20}$ m^{-3}. Further development for the CXRS diagnostic for ITER, including design optimization and modeling, is described in [243–247].

According to the ITER requirements [4] the CXRS diagnostic should measure ion temperature radial profiles, impurity density profiles, and rotation velocity profiles with a 100 ms time resolution and a 10%–30% accuracy. The spatial resolution should be 20 mm for the plasma boundary ($r/a > 0.85$) and 66 mm for the central part of the plasma column ($0 \leqslant r/a \leqslant 0.85$). Because of the modulation of the DNB, the time resolution for the ITER CXRS diagnostic is relaxed to 200 ms when the DNB is operated in 'burst' mode (3s at 5 Hz with a 20 s cooling down period) and to 1.5 s when the DNB is operated in 'control mode' (100 ms DNB pulse every 1.5 s).

Three CXRS optical views are foreseen [4]; one for the core and two for the edge/pedestal region. This basic layout has been kept and the progress on them is described below.

4.1.4. Progress in ITER core CXRS measurement setup. The optical layout of the core CXRS diagnostic is now mature, at the technical level of a PDR. It comprises the following features (see figure 71 for the optical layout):

In the port plug:

- a front mirror unit (FMU) which protects and contains the entrance aperture, the first mirror M1 and its cleaning system;
- a set of two pairs of mirrors to transport the light to the vacuum windows assembly (VWA). They are arranged in the form of two doglegs to allow for appropriate neutron shielding;
- a separate embedded unit which contains the fast actively cooled frictionless shutter and its actuator;
- a calibration system to monitor the degradation of M1 by illuminating the back of the shutter blade which, in normally closed position, is located at the entrance aperture (cf section on Calibration).

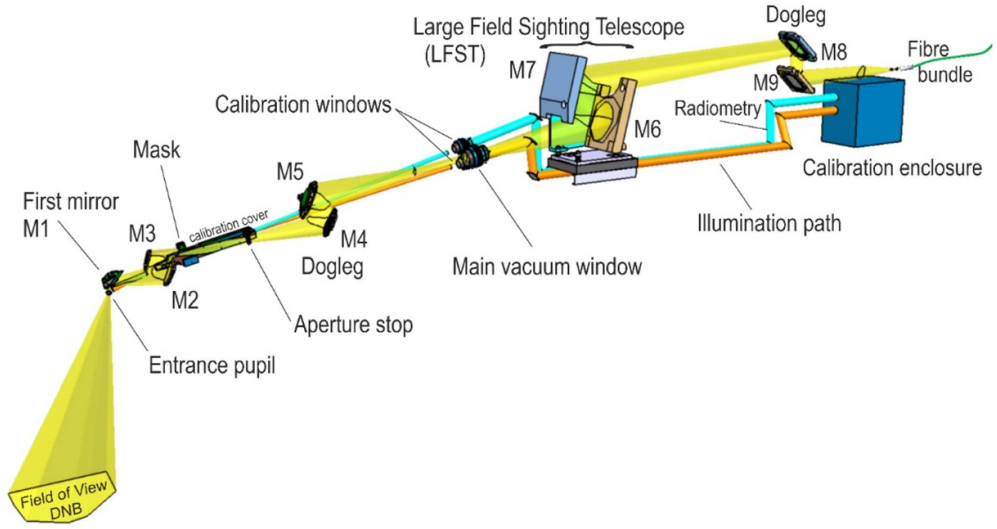

Figure 71. Core CXRS optical layout and general setup in UPP03, interspace and port cell.

Ex-vessel components:

- a telescope in the interspace, a 'dogleg' in the bioshield and a couple of lenses in the port cell to feed the long glass fiber bundle to the spectrometers in the tritium building;
- ancillaries to the port plug systems, like a beam finder to check the line-of-sight in absence of light from the torus (no plasma operation, closed shutter) and the pneumatic helium drive for the shutter.

A full account of the current status is given in [248, 249]. Both references present an overview of the system.

4.1.5. Optical performance. More than in the case of CXRS in the edge plasma, the biggest challenge of CXRS applied to the core plasma is the detection of signals which become radially weaker to the plasma center with attenuation of the observed DNB. Accordingly, the expected photon yield of the whole diagnostic requires a maximized etendue and transmission **T**. The latter reaches about 40% for the plug components including the vacuum window assembly, 70% from the window to the fiber, 82% for the fiber and 35% for a typical spectrometer. For the complete system, the estimated **T** is thus slightly in excess of 8%.

Similarly, the image is sharp enough for the requirements on spatial resolution to be fulfilled: 67 mm wide channels in the radial direction for the range $r/a \in [0,0.6]$ with a possible extension to $r/a = 0.7$, 250 mm in focal depth, within which the specified $a/30$ resolution can be realized. A radial overlap with the edge CXRS system is achieved. A minimal modulation transfer function (MTF > 0.6) and a maximum spot size at the coupling to the transfer fiber were specified. The risk of vignetting through deformations of the port plug and displacement of the optical beam at the plug output window is minimized by adding a margin >10 mm to the free window aperture. In connection to this, the optical design was selected to be as robust as can be against distortions of the plug optics under loads of all types. It covers the spectral ranges:

- λ460 nm band (He, Be)—around 468 nm which enables observation of He II, Be IV;
- λ520 nm band (C, Ne, Ar, Kr)—around 527 nm, for Ne IV, Be II, Ne X and Ar XVII/XVI; and
- λ656 nm band (Balmer α) with H_α, D_α,T_α at 656 nm.

The system is thus designed for the visible spectral range with the blue region, down to about 450 nm, the most difficult to achieve but also the most important one.

4.2. Other main drivers

A safety requirement and an important design driver of the diagnostic is the shielding efficiency of the in-vessel optical layout against neutrons. It is optimized by the second mirror 'dogleg' at the back, close to the windows assembly at the plug closure plate. This allows to protect the magnetic coils and stay in the interspace below the maximum tolerable shutdown dose rate.

For investment protection and a long measurement phase without intervention, the FMU ducts are designed to keep the front mirror as far as possible from the entrance aperture, which was reduced to ø35 mm. The FMU is designed to accommodate the insertion of a shutter blade which is fast enough (0.7 s opening or closing time) to follow the main modulation of the DNB (duty cycle: 3 s on/20 s off). Furthermore, a cleaning device is installed for the first mirror to remove deposits by impurities which would have reached the reflecting surface (see section on mirrors).

The remote handling criteria for maintainability are attained by designing different embedded units as recommended by the Port Integrator. Each of them can be extracted and exchanged upon need. Note that no scheduled maintenance is foreseen, only inspection of the windows and of ex-vessel

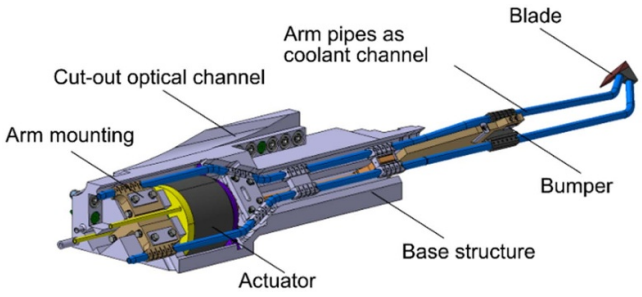

Figure 72. Shutter embedded unit of the core CXRS system.

components, regularly, plus monitoring of the optics transmission in the plug by means of the calibration system.

4.2.1. Hardware selection and overall performance. The first mirror, made of rhodium [250], has a reflectance $\mathcal{R} \geqslant 73\%$. It resists corrosion and sputtering by impinging particles from the main plasma (up to 10^{18} $m^{-2}s^{-1}$) or ions in the RF cleaning discharge ($\leqslant$0.2 mA cm^{-2}). A thin monocrystalline Rh plate seems preferable for a more uniform physical sputtering. See subchapter 9 on mirrors for more details.

The shutter is frictionless to avoid seizing and driven by a pneumatic actuator which requires only two pipes for the feedthrough at the plug closure plate. It is a compact embedded unit in one piece [251], see figure 72. The very first version, which had two arms and was less compact, was successfully tested to 10^6 cycles. It gives confidence about the ruggedness of this piece of equipment since the lifetime expected for ITER amounts to about 6.6×10^5 cycles.

The fibers in the bundle are defined with a numerical aperture NA = 0.22 and a core of ø 600 μm. Unlike the edge CXRS system they start in the port cell, are therefore less vulnerable to radiation effects so they are considered a lifetime component. The selection of adequate spectrometers is under investigation, with candidates as described in the Section below on high etendue spectrometers (HESs).

4.2.2. Progress in ITER edge and pedestal CXRS measurement setup. With the aim of providing optimum radial resolution as well as the means for complementary toroidal and poloidal velocity measurements, two observation periscopes have been designed for the CXRS Edge system in Eq-port #3: lower periscope for observation in radial range $0.5 \leqslant r/a \leqslant 1$ (Edge observation), and upper periscope for CXRS observation in radial range $0.85 \leqslant r/a \leqslant 1$ (Pedestal observation). Figure 73 shows the present layout for the ITER CXRS diagnostic LOS: CXRS Edge and Pedestal are mostly toroidal systems with a $\pm 10^\circ$ angle to the horizontal plane. Similarly to the core CXRS diagnostic the layout of the edge and pedestal CXRS diagnostic is now mature, at the technical level of a PDR.

Components of the ITER CXRS Edge diagnostic are distributed throughout the ITER tokamak complex. The front-end optics are installed in Equatorial Port 3 (EP3), viewing the DNB. The collected light reaches the EP3 Interspace through vacuum windows. Then it is transmitted along fiber bundles to the diagnostic room in the adjacent Tritium building, accommodating the back end of the CXRS Edge system. That includes HESs, detectors and Instrumentation & Control (I&C) cubicles.

The light collection system produces an image of the DNB in the image plane, located in the EP3 interspace. The plasma facing element of the light collection system is the flat First Mirror. Hot plasma particles can significantly modify the optical properties on mirrors due to erosion and deposition. That is why a sandwich design is used: single crystal molybdenum segments are fixed on poly-crystal molybdenum substrate by hot isostatic pressing (HIP). Molybdenum has a better sputtering resistance than the rhodium proposed for the CXRS core, but a lower reflectivity. The latter is acceptable due to the higher signal levels available at the plasma edge. To extend mirror lifetime during DNB off time a protective shutter is used, and a mirror cleaning system is proposed for occasionally removing plasma deposits.

The light collected by the first mirrors is transmitted through the port plug by mirrors and crosses the vacuum barrier through optical windows with the biggest available clear aperture diameter of 160 mm. Each window consists of two Fused Silica wedged disks, which are also tilted 2° with respect to the optical axis. This avoids any parallel surfaces to mitigate parasitic reflections. Fused silica material was chosen because of its high radiation resistance, high optical transmission, considerable experience in manufacturing and relatively low cost.

The ex-vessel lens assemblies produce an image of the observed area of the DNB. The fiber bundle heads are placed into the image plane of the light collection system. Special fiber head alignment systems ensure proper alignment onto the image. The light signal is transmitted from the port cell via the interspace fiber bundles to the optical connector on the outside of the bioshield. Then light is transmitted to spectrometers in the diagnostic area of the tritium building via the main fiber bundles.

To meet the radial resolution requirements the CXRS Edge diagnostic system has 26 spatial channels: 10 core channels ($0.5 < r/a < 0.85$) and 16 edge channels ($r/a > 0.85$), while the pedestal optics has 16 channels. Because core channels have smaller active signal intensity, they cover a larger area of the DNB than edge channels. Distances between these strips were chosen to provide a spatial resolution of 20 mm at the plasma edge and 67 mm closer to the center. As an example, the Pedestal system layout is shown in figure 74. The integrated fiber bundle assembly includes: the fiber bundle channels as per radial locations (for CXRS pedestal, 16 active channels and 4 passive channels), the bundle to bundle coupling connections (ISS fiber to main fiber coupling after the bio shield), the required terminations (for image coupling, for spectrometer entrance slit coupling), and arrangement of the calibration fibers (to inject calibration light signal into the light collection and transmission path as shown in figure 76). The optical fibers are organized into bundles containing four optical channels. For ITER-measurements, five bundles to cover the 20 radial locations are needed. The fiber head of each bundle has a

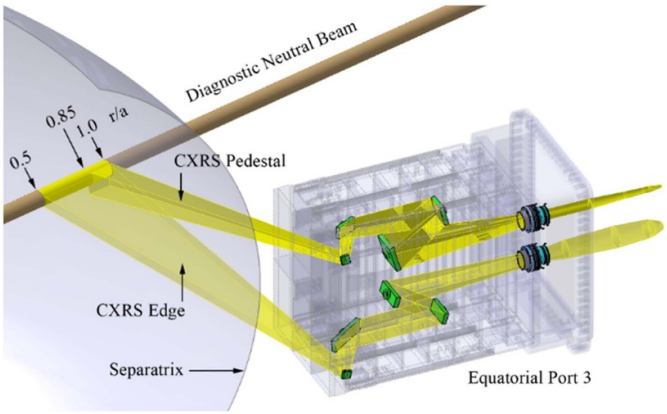

Figure 73. ITER CXRS edge and pedestal diagnostic periscopes layout looking at the DNB.

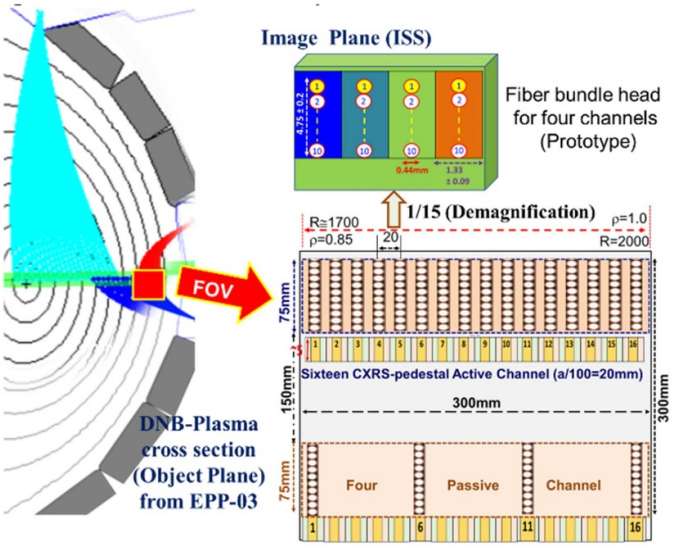

Figure 74. CXRS-pedestal light collection fiber image on the DNB and arrangement in the image plane.

10×4 matrix of fibers. Each column has ten fibers and denoted as one channel in ITER-CXRS-pedestal diagnostics. In each channel, nine fibers are for light collection, and one is reserved for calibration.

In the interspace, fiber bundles are subjected to neutron and gamma radiation influence. These bundles contain radiation hard fibers (low OH content, H diffused fused silica [252]), but nevertheless may acquire damages and lose transmission. Partly, light transmission can be restored by annealing the optical fibers. For this, the design provides an integrated heating tape (at temperatures up to 200 °C–300 °C) to allow annealing of the radiation damage.

The measurement performance assessment of the Edge CXRS diagnostic can be found in Serov *et al* [253]. Several scenarios, covering all expected baseline operation regimes for ITER, were used. The modeling was done for various low-Z impurity (He, Be, C, and Ne) concentrations for the whole spatial range. Statistical errors for ion temperature, density, and rotation velocity were calculated. Minimum concentrations, allowing measurements with the required accuracy, were obtained. Effort was made to review other non-statistical error sources for the CXRS measurements, including wall reflections, multiple tungsten lines in CX spectra, effects on the active CX line shape, calibration, and positioning uncertainties. Consideration of the major error sources showed that the CXRS Edge system will be able to meet all ITER measurement requirements, apart from the requirements for the poloidal rotation velocity measurements.

4.3. Ion temperature measurement in a carbon-free machine

The transition in ITER wall material away from carbon to a beryllium–tungsten combination has had implications for the CXRS measurement of ion temperature (T_i) and rotation. Previously the CVI $n = 8$–7 CX line at 529.0 nm was routinely used and benefitted from being the dominant line in a comparatively clear spectral region. With a metallic FW the CXRS situation is less ideal; the CX lines of Beryllium may not be the dominant feature and the presence of many additional spectral lines give a more complex background spectrum. The analysis

of the CX to determine T_i must be adapted and developed to cope with the new circumstances for which the JET experiment offered the best possibilities.

The beryllium and tungsten material combination of the JET ILW saw the introduction of additional impurities into the plasma and many spectral lines are observed throughout the CX spectral regions of interest. These are mainly from tungsten and include narrow emission lines of neutral WI [254] as well as magnetic dipole transitions of various W charge states [255] and W CX emissions. The lines observed depend on the conditions in the plasma and the location viewed. Spectral lines from other impurities are also seen for example due to transient events. When the CX line is dominant in the spectrum then a good determination of T_i and its uncertainty can be obtained. However, when the CX intensity is less favorable compared to the background nuisance lines then the T_i and the quality of T_i obtained from the multi-Gaussian fitting of the spectral region can be affected. There can also be an interplay in the fit between the intensity and width of the CX and nuisance lines. To reduce the influence of the nuisance lines it is valuable to have a good understanding of what these lines are; additional constraints can also improve the fit and assessment of uncertainty. Having both red and blue Doppler-shifted views through the plasma at JET has been greatly beneficial in identifying and constraining the background spectral lines we observe. This knowledge can also then feed forward into the CX analysis on other devices such as on ITER where the different viewing geometry will not offer this opportunity.

The influence of the nuisance lines in the core-CX analysis can also be reduced by using beam modulation or notching, where short off notches are introduced in one or more of the neutral beam injections (NBIs) seen by the CX lines-of-sight. For the CX analysis we subtract the spectrum measured in the beam notch from that measured with the beam on, with the aim to reduce the background and leave a simplified spectrum to fit. This can bring us back to the situation where the CX is again dominant in the spectra. It is most effective where the background lines have not changed, such as in stationary conditions, close to the notch, or using selective matching of the active and notch camera frames. Including notches in the NBI at JET requires additional effort by the scientific teams and it can be a compromise on what is acceptable to the scenario in terms of disturbing the injected power. Any CX contributions of non-notched beams are also subtracted, which at JET is a factor to consider in the use of this technique with the impurity-CX where the basic intensity may already be low. The extent and quality of the T_i measurement ultimately depends on having enough CX intensity available. Use of a single dedicated diagnostic beam in ITER will simplify the situation as it does not require notches in the main injected beam power as well as removing the complication of multiple beams contributing to the CX, it is planned that the ITER diagnostic beam will be modulated.

The switch to the ILW at JET reduced the intrinsic C levels by at least an order of magnitude compared to the C-Wall era. Whilst the CVI-CX line is still observed it is difficult to obtain good T_i measurements from the CVI-CX alone in most plasma conditions, in particular, in the core region. The intrinsic beryllium offers the possibility of using the BeIV-CX lines at 465.8 nm $n = 6$–5 and 468.5 nm $n = 8$–6 to derive T_i. These are routinely measured; however, it is challenging to get an independent T_i from the BeIV-CX and so this is mainly used for ion density. The Be intrinsic concentration is fairly low and the spectral region of these CX lines again has multiple W nuisance lines which need to be taken into account. The BeIV-CX analysis can also be further complicated by the HeII $n = 4$–3 CX transition at 468.5 nm when there is Helium present. The HeII-CX itself also has the potential for deriving T_i if the line is strong enough and the spectral region can be fitted well.

Injecting a small amount of another impurity into the plasma gives us back more control of the CX intensity than having to rely on the intrinsic emissions. By adding Neon, the NeX-CX $n = 11$–10 line at 524.9 nm can be exploited for T_i. The amount of Neon required for good measurement to the core depends on the plasma conditions, and the inclusion of this extra radiating species must be acceptable to the experimental scenario. However, even with low concentration, an improved T_i can be obtained to the core. Tungsten nuisance lines are also present in the NeX-CX spectral region of interest and can influence the CX analysis unless successfully included in the fitting or reduced through beam notches. The proximity of the NeX-CX to the CVI-CX in the spectra means that any residual CIV-CX present can be used to add constraint to the analysis. The use of neon for CX has become routine in many JET experiments [255]. Adding an impurity species such as neon will be even more important for ITER where there will be even less or no carbon CX available.

The main ion (H,D,T) $n = 3$–2 CX emission at 656 nm is now also routinely measured at JET [256]. The relative position of the CX line and beam emission spectra influence where good T_i can be obtained. Where there is a mix of fuel isotopes the contributions from all isotopes must also be included. The beam notch analysis technique to simplify the spectra, typically by selectively matching active and notch frames, is required for analysis of this CX. At JET beam notches may not be suitable or wanted in the experimental scenario which can limit the availability of this T_i measurement; with its dedicated modulated diagnostic beam ITER will not have this constraint.

Without carbon we can no longer rely on the old standard CVI-CX for core ion temperature measurement. The flexibility of having multiple systems and techniques available at JET has proven beneficial to maximize the potential for and reliability of obtaining good T_i. Injecting a small amount of neon as an additional impurity gives more control of the CX intensity than relying on the intrinsic impurities present and can enable good T_i measurement into the core. Having a sufficient intensity of the CX line is crucial. The use of notches in the NBI to help separate the CX from the background spectra and exploiting the main-ion CX for T_i have also proven valuable. It has been essential to develop the CX analysis to take into account the increased complexity of the spectral regions of the CX lines, to reduce the influence of the nuisance spectral lines which could otherwise affect the T_i obtained.

4.3.1. Advanced spectral evaluation methods. ITER CXRS measurements become complicated because of the low SNR due to strong attenuation of the DNB, caused by the large size and high density of the plasma. Other complicating factors are the presence of other spectral lines due to CX reactions with the edge neutrals [257] (passive CX line) and due to the electron impact excitation [258] (edge lines) and multiple tungsten lines [254].

Therefore, modeling is important for the development of the CXRS diagnostic. For this purpose, the simulation of spectra (SOS) code [259] could be utilized. It was developed for predicting beam-induced spectroscopy diagnostic performance on fusion devices. In particular, it has models for all main CXRS spectrum components and could also be used for spectra fitting and error estimation. The spectrum is constructed from the following components, modeled separately: active CX line, passive CX line, edge electron impact excitation lines, bremsstrahlung continuum, and statistical noise. The obtained spectrum is fitted using least-squares minimization procedure. Intensity, temperature, and rotation velocity errors are calculated from the active CX line fitting 95% confidence intervals (corresponding to $\pm 2\sigma$). The main source of atomic data is the ADAS database [260, 261].

The SOS models were validated using experimental data from several tokamaks, e.g. JET [261], TEXTOR [262] and EAST [263]. The benchmarking process will not be discussed in this paper. Results of the benchmarking against JET experimental data [264] demonstrate that the SOS code allows reasonable CXRS spectra predictions and could be used for active spectroscopy diagnostic development for ITER.

4.3.2. High-etendue spectrometers. Due to the low active light intensity and high background the spectrometers for the CXRS diagnostics should have high etendue and high transmission combined with the necessary spectral resolution in a few limited spectral ranges. These requirements cannot be fulfilled with commercial spectrometers; therefore, special devices need to be developed.

To provide plasma parameter measurements according to ITER requirements the CXRS edge diagnostic system spectrometer should be able to collect spectra in wavelength regions indicated above. To fulfill the above requirements the high etendue, high resolution spectrometer (HES) of the CXRS Edge system will have three channels, covering all the lines listed: blue (468 $\pm$ 5 nm), green (529 $\pm$ 5 nm) and red (656 $\pm$ 6 nm).

A multi-channel HES spectrometer prototype, based on transmission gratings, was designed and built for the CXRS Edge system. The principle scheme of the HES spectrometer is shown in figure 75, while table 25 lists the technical specifications obtained during the laboratory tests. These laboratory tests were done without the light traps/viewing dump, which are shown in figure 74. Light traps and shields will be installed for further spectrometer properties improvements. In addition, interference filters will be installed in front of the image plane in each spectral channel in order to reduce the stray light level. One more future step is the improvement of the diffraction and transmission efficiency of the holographic gratings. It is expected that the diffraction efficiency could be increased up to 50% and the transmission efficiency up to 85–95%. More details about the CXRS edge spectrometer can be found in Tugarinov *et al* [265].

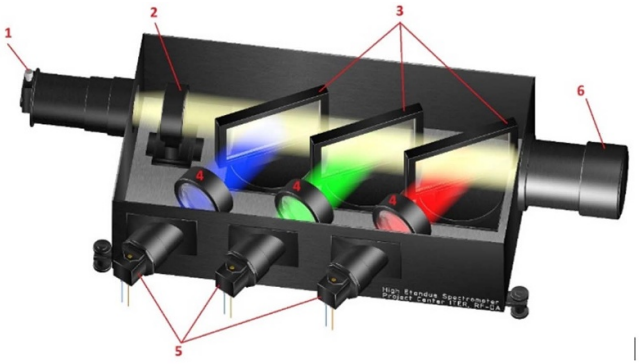

Figure 75. Principle scheme of the optimized multi-channel HES spectrometer: entrance slit (1), collimator objective lens (2), holographic transmission gratings for 468 $\pm$ 5 nm, 529 $\pm$ 5 nm and 656 $\pm$ 6 nm spectral ranges respectively (3), camera objective lenses (4), sCMOS XIMEA cameras (5), light traps/viewing dump (6).

Table 25. Technical specifications of the prototype HES spectrometer.

Dispersion (blue/green/red),	3.4/3.6/5.0 Å mm−
Transmission (blue/green/red)	35/34/25%
Max. spectral resolution	∼0.1 Å
F-number	3
Magnification	1
Entrance slit width	0.4–1 mm
Entrance slit height	20 mm
Image plane size	20 × 25 mm
Contrast	>750 000

For the spectrometer design of the core CXRS diagnostic a different approach was adapted. A prototype spectrometer was designed by TNO company, Forschungzentrum Jülich and the Eindhoven University of Technology [266]. As designed, it meets the ITER design requirements of 1 mm^2 SR etendue for a single optical channel of the core CXRS optics, accepting light from NA = 0.22 fibers at the input. A single large lens is used for both collimation and focusing and a single grating used for all three spectral channels, providing measurements of hydrogen and its isotopes, carbon, neon, helium and beryllium simultaneously. The spectrometer was tested initially at TEXTOR and then moved to ASDEX Upgrade where it was used predominantly for helium measurements [267] including a feasibility assessment of measuring fast-helium from fusion reactions on ITER [268]. More recently, the spectrometer was moved to Wendelstein 7-X where it is now the primary CXRS spectrometer [269]. The spectrometer was notably easy to reassemble and to align due to the excellent mechanical design and clean separation of the input stage, slits and of each spectral channel. This results from the particular optical design which also separates the focusing, making it easy to achieve good wavelength resolution across the

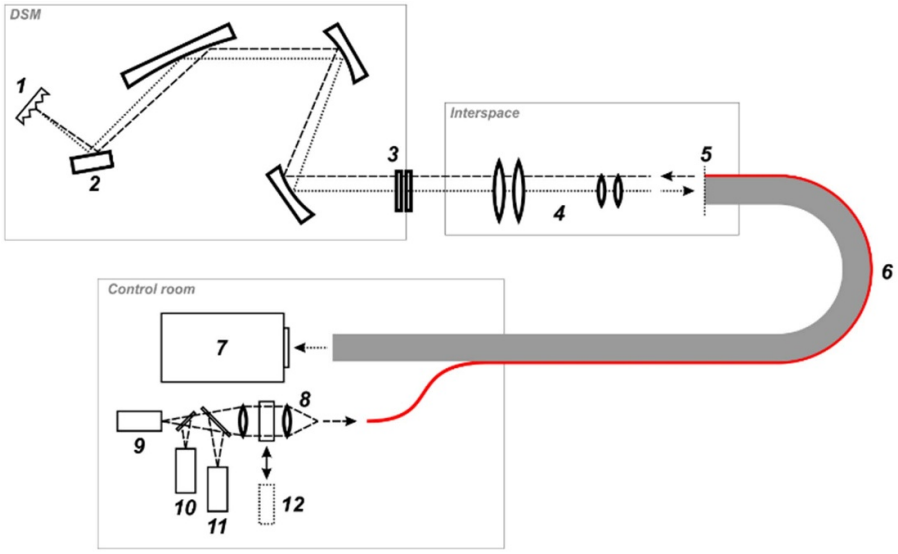

Figure 76. The scheme of the developed technique for transmission and wavelength calibration of an optical circuit. Indicated: shutter with retroreflector (1), first mirror (2), vacuum window (3), out of vacuum optics (4), image plane (5), main fiber bundle with an additional fiber (6), spectrometer (7), illumination system optics (8), calibration light source (9), neon lamp (10), detector for light source control (11), movable Fabry–Pérot interferometer (12).

entirety of all three wavelength bands and across all spatial channels. The separation allows the slit width to be independently changed for each spectral channel with ease. A small amount of cross-talk between spatial channels is observed at W7-X due to their dense packing but this would likely not be significant in the ITER case. Experience has shown the spectrometer to be very stable, with a drift of only 10 pm over a day due to temperature changes, making pre- and post-shot calibrations sufficient even for long pulse operation.

Both spectrometer designs for the ITER CXRS diagnostics basically fulfill ITER requirements on etendue, spectral resolution and throughput, which demonstrates that construction of suitable spectrometers is possible. However, the necessary total etendue of all observation channels can be fulfilled only by multiple devices, therefore the decision on the final spectrometers will surely be affected by cost limits.

4.4. Calibration methods

Three calibrations can be considered for the spectroscopy diagnostics: spatial, wavelength and intensity. The spatial calibration of the diagnostics is assumed to rely on optical tests before installation and device metrology during installation, no special spatial calibration procedures are assumed to be built into the diagnostics.

For intensity calibration one should consider that the CX signal intensity I_{CXRS} of an impurity line depends on the product of local beam and impurity density. Calculating beam attenuation from plasma parameter profiles the impurity density can be obtained from the measured line intensity, therefore a method for transmission calibration is necessary to compensate for the change in the reflectivity of the first mirror, transmission of lenses and most importantly the optical fibers. The calibration procedure should test the whole optical chain from the first mirror to the spectrometer and should be repeatable during the ITER lifetime without the need for access to the diagnostic. The calibration requirements are somewhat relaxed by the fact that the beam light emission signal (I_{BES}, H_α for the DNB) depends on the product of the beam intensity and the electron density. If the BES light is collected from exactly the same volume as the impurity radiation the relative density of the impurity becomes [246]:

$$\frac{n_Z}{n_\mathrm{e}} = \frac{I_{\mathrm{CXRS}}}{I_{\mathrm{BES}}}\frac{Q_{\mathrm{BES}}}{Q_{\mathrm{CXRS}}}$$

where Q_{BES} and Q_{CXRS} are atomic emission rates dependent on plasma parameters. Therefore, the calibration process need not be absolute, but only relative between the BES and CXRS wavelengths.

It is unlikely that there will be any means of positioning a calibrated uniform source, typically an integrating sphere, within the VV after operations have commenced – possibly not even during installation and adjustment where it is highly desirable. Other schemes like bremsstrahlung-based calibration, branching ratio calibration (between different Balmer lines) were considered but were not found to be suitable as the main calibration tool. In the two CXRS systems a somewhat different setup is considered although both are based on collection of a calibration light transmitted through the collection system.

4.4.1. Calibration in the edge CXRS system. For the edge CXRS systems the calibration principle is based on the use of a light reflecting element (retroreflector or mirror), which is placed on the back side of the first mirror's shutter plate. The scheme of the developed technique for transmission and wavelength calibration of the optical circuit is presented in figure 76. An additional optical fiber is added to the main fiber

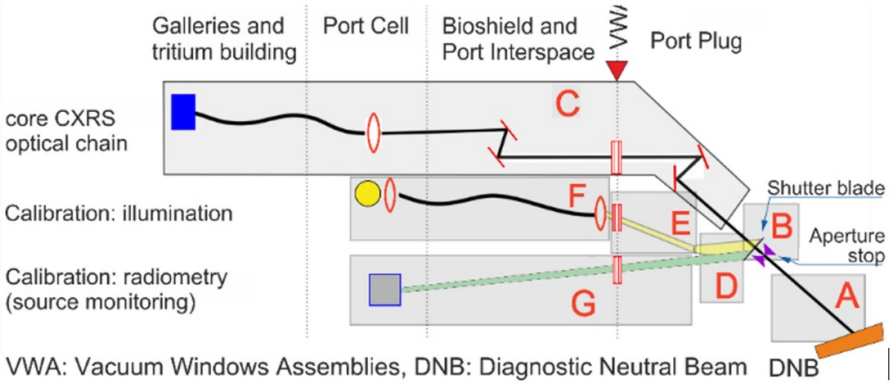

Figure 77. Schematic view of the calibration system of the core-plasma CXRS. A-object region with diagnostic neutral beam; B-aperture stop (entrance pupil) and shutter blade with diffuser coating on the backside; C: main optics for observation; D-overlap of illumination and radiometer systems in the front mirror unit; E-illumination path in vessel; F-idem ex-vessel; G-radiometric optical path.

bundle (6). The main fiber bundle is connected directly to the entrance slit of the spectrometer (7), which is placed in a diagnostic area in tritium building. The additional optical fiber is illuminated by a light source (9) in spatial angle according to the spectrometer's light transmission ability. Light from the additional fiber passes through the entire aperture of the light collection system (5–4–3–2) and reflects from the retroreflector (1). Then reflected light goes back through the entire optical circuit and illuminates main fiber bundle in the image plane (5).

The idea is that by illuminating one fiber from the diagnostic area we could illuminate all the other fibers using reflected light, which will be transported to a spectrometer where it can be detected and analyzed. This scheme will allow periodical transmission calibrations for the system and could also be used to perform a wavelength calibration of the spectrometer. For this purpose, a special calibration technique, described in Shabashov *et al* [270], could be applied. It uses a combination of the fringe pattern created with a Fabry–Pérot interferometer (12) and a neon lamp (10) spectrum for accurate wavelength calibration.

The possibility of this calibration scheme was demonstrated using both modeling and laboratory tests.

4.4.2. Calibration in the core CXRS system. The calibration scheme for the core CXRS system aims at measuring the transmission of the optical system, it provides the conversion factor between detector signal levels and spectral radiance (a photon intensity in units similar to $photon/m^2 s Sr nm$). As a minimum, the calibration must provide the relative sensitivity as a function of wavelength but an absolute calibration is fully advisable.

The original proposed concept uses a white light source located at a distance of ∼5.2 m from a diffuser located on the back of the diagnostic shutter, as shown in figure 77. Some of the scattered light is collected by a radiometer which thereby measures the absolute spectral radiance of the diffuser. The calibration scheme uses a bent light path, in fact a single mirror in a tightly baffled light path, to introduce light onto the shutter/diffuser equally in both its open and closed positions. When open, the diffuser radiance is measured by the directly viewing radiometer and we rely on this radiance being the same when the shutter is in the closed (calibration) position to collect the light through the full observation path of the diagnostic. A slight tilt of the diffuser plate in the order of 20° with respect to the plane of the shutter blade, in the direction of the illumination and radiometer channels, increases the spectral radiance of the diffuser by almost a factor of 3.

The initially planned location for the source and the radiometer was the interspace (IS), close to the two windows through the closure plate of the port plug. However, concerns were raised regarding access to the IS for maintaining the system. As a result, a scheme for relocation of the light source and radiometer in the port cell was developed on the basis of either optical fiber or mirror relay optics. Both options are conceivable. Furthermore, a bare tungsten-halogen lamp without intervening optics between it and the shutter could be used but it is anticipated that alternative light sources will provide considerably higher irradiance levels at the shutter. Such sources, for instance high-brightness laser-driven light sources, are worth considering and ought to be tested. A 1:2 prototype of the whole system is proposed for assessment.

With the proposed calibration system, which intrinsically represents an absolute calibration, we gain – over the pure ratio between the beam-emission and charge-exchange (CX) wavelengths – the potential to measure the bremsstrahlung or Z_{eff} profile, impurity influxes, measure the DNB attenuation, monitor the rate of deterioration of the first mirror, with the possibility of limiting the use of the diagnostic, if this is severe, and evaluate the efficacy of *in-situ* mirror cleaning. This calibration method is, however, more challenging to technically integrate and its implementation is under review.

4.5. Additional measurement possibilities with active beam techniques

The active spectroscopy diagnostics on ITER aim at a few main purposes, but the optics and beams would provide the possibility for some additional measurements which are being used on present-day devices. Although they are not part of the

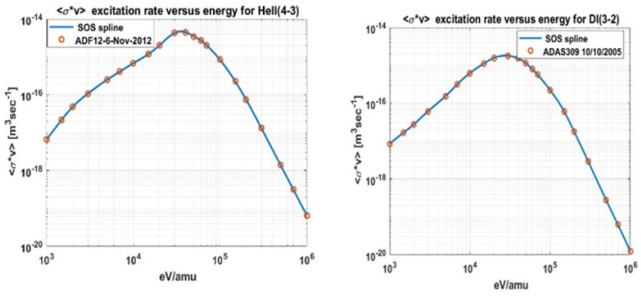

Figure 78. Atomic emission rate for fast ion CXRS on He2+ and D +.

approved ITER diagnostic set, but they are already included or proposed as a supplementary use of the diagnostics.

4.5.1. Fast ion CXRS (FICXS) for confined and escaping alpha particles. Four separate FICXS cases are usually addressed by spectral modeling codes: Confined fusion α particles, escaping α particles, $^3He^{+2}$ minority heating and finally, slowing- down beam ions (also known as Fast-Ion D-Alpha or FIDA).

The common feature is the procedure of calculating the observed CX spectrum from the convolution of a three-dim VDF with a collision velocity dependent CX emission rate function. Recently revised ADAS [260] emission rates are shown in figure 78. The VDFs can be isotropic as for the case of slowing-down fusion alpha particles or anisotropic for slowing-down beam ions [271]. The main-goal of FICXS modeling is the deduction of fast ion densities, verification of slowing-down velocity distribution features, assessment of fast ion losses and associated anisotropic issues.

Absolute fast ion density modeling is linked to the calculation of a fast ion source rate which in the case of confined fusion alpha particles is based on toroidally symmetric profiles for n_d, n_t and T_i. By contrast, an anisotropic Fokker–Planck beam injection model (see [271]) applies for slowing-down beam ions. Numerical treatment of Source rate calculations may differ significantly in different simulation codes such as TRANSP [272] or SOS [259]. A particularity for the Beam Fast Ion CXRS modeling of a broad-band Balmer Alpha spectrum (or FIDA, Fast Ion Dalpha spectrum) is the dual role of the beam as a source of fast ions and at the same time as a probe beam for the diagnosing CXRS process. Figure 79 through figure 82 illustrate characteristic features for the four types of FICXS spectra: confined and escaping alpha particles, He3 minority heating and NBI slowing down ions.

4.5.2. Measurement possibilities for turbulence and MHD waves. Currently, millimeter-wave reflectometry is envisioned as the primary diagnostic for the measurement of plasma density fluctuations [273]. In the SOL high amplitude fluctuation (blobs) are an essential element in setting the divertor heat load [274]. At the high fluctuation amplitudes interpretation of reflectometry measurements is complicated [275] and the lifetime of Langmuir probes is questionable.

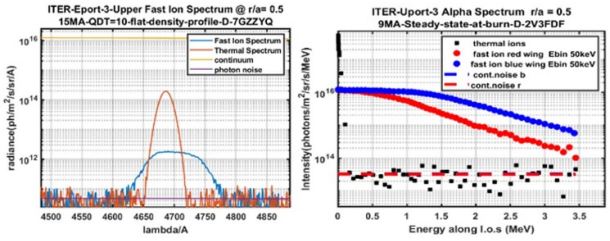

Figure 79. Confined alpha particle FICX spectrum for ITER core CXRS diagnostic in Uport-3 at $r/a = 0.5$, DNB, and the spectra plotted vs particle energy.

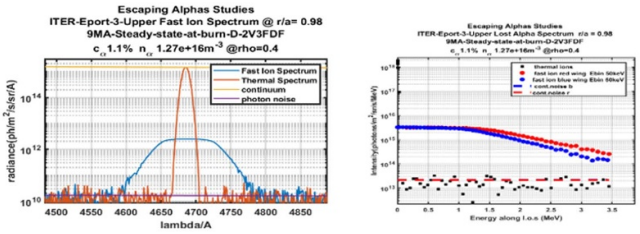

Figure 80. Escaping alpha particle study for ITER core CXRS diagnostic in Eport-3-Upper showing thermal and FI spectrum for outermost line of sight ($r/a = 0.98$), and the spectra plotted vs particle energy. Spectral noise level is determined by underlying continuum.

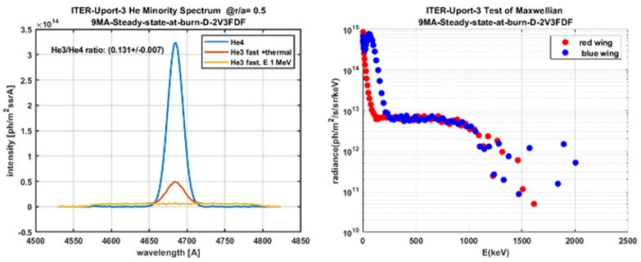

Figure 81. FICXS modeling of ICRH He3 minority heating assuming a minority concentration n(He3)/n (He4) of 10%. The minority birth energy is 1 MeV.

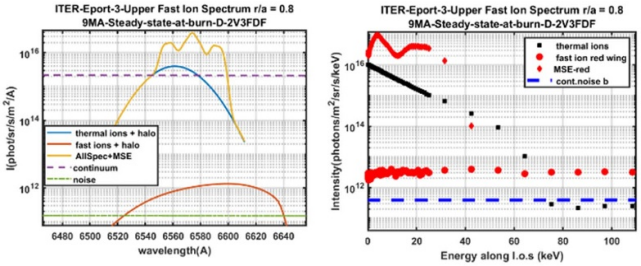

Figure 82. FICXS modeling of beam-ion slowing-down energy spectrum for ITER 9 MA-steady-state case including thermal, MSE and fast ions plus halo contributions. Only far end of red-wing fast ion spectrum visible just above continuum noise level.

Therefore, at the edge and SOL it is worthwhile considering fluctuation BES as an alternative to measure blobs [276] and MHD waves. Such a fast BES diagnostic could use the CXRS periscopes viewing the DNB. Two observation geometries were considered for fluctuation BES: the pedestal and

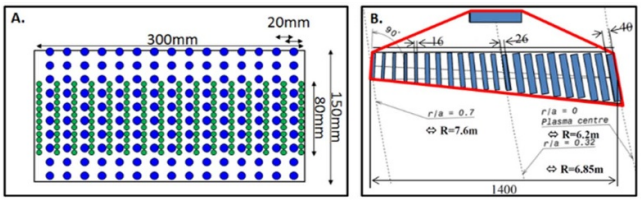

Figure 83. Modeled channel arrangement for feasibility study of fluctuation BES. (*A*) The studied arrangement for the pedestal system shows dedicated channels for BES (blue) between the CXRS channels (green). (*B*) The studied arrangement for the core BES system is proposed to piggy-back on the existing CXRS field of view (blue).

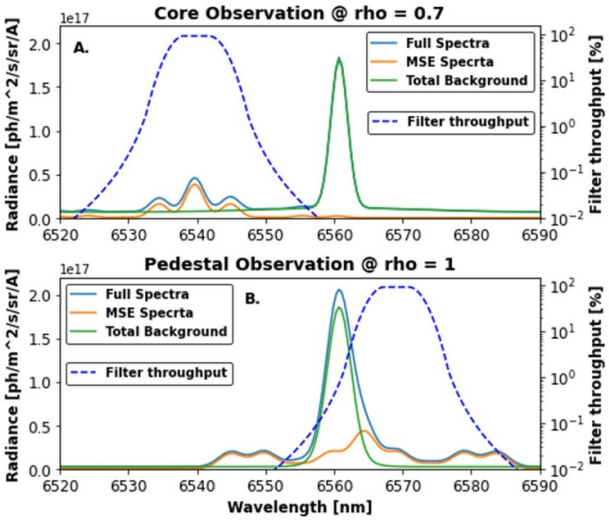

Figure 84. Observed and filtered spectra modeled by the SOS code: beam emission (MSE) spectrum (orange), total (continuous + edge) background (green) and their sum (blue). The right axis applies to the filter characteristic (dashed blue). (*A*) Outermost core field of view. (*B*) Outermost pedestal field of view.

the core observation. The fluctuation BES system could either piggy-back on existing optical fibers [277] or rely on extra fibers that can be installed to utilize the part of the beam image not used by the CXRS systems. The analysis presented here employed the first approach for the core system and the second approach for the pedestal system for ITER scenario 2 as shown in figure 83. It has to be noted, that in this configuration observation of the DNB is limited to $r/a < 1$, therefore SOL turbulence cannot be measured in this scenario. However, a slight modification of the plasma configuration might allow study of at least near-SOL turbulence.

For any fluctuation BES diagnostic three factors are important: separation of beam light from edge plasma radiation, SNR and spatial resolution resulting from the intersection of beam and observation.

The fundamental challenge with ITER BES observations lies in optimizing the narrow wavelength filter to maximize SNR and the SBR. The sheer size of ITER and harsh conditions result in observation geometries with small etendue and complicated optical systems with low optical transmission rates. ITER is also expected to feature high background plasma radiation foreshadowing challenges regarding the SBR. To study possibilities the SOS code [259] was used to model the expected light spectra for each detector channel. To achieve the desired filter spectral profile for each channel, a realistic filter characteristic resembling a three-cavity optical filter was shifted in wavelength. The flat-top region of the filter profile was kept at 90% throughput. Examples of the modeled spectra and the corresponding optimized filter characteristics are shown in figure 84.

By applying the optical filters on the simulated spectra (figure 84) one arrives to the filtered beam emission and corresponding background components, which in turn can be used to calculate the SBR of each channel (figure 85). The filter efficiency is calculated as the ratio of filtered beam emission to the unfiltered beam emission for each channel. The core CXRS features a perpendicular view of the DNB at $\rho = 0.15$, so in the central region the optimized filter can only utilize a side peak of the MSE spectrum to avoid the edge background radiation. This, combined with the large continuous background, results in an unfavorable SBR $\ll 1$. For the outer channels of the core system, the Doppler shift is sufficient (as seen in figure 84(*a*)), and thus the SBR rises to a tolerable value (figure 85). The pedestal observation geometry features a decreasing Doppler shift towards the LCFS, resulting in a significant drop of filter efficiency. However, even the worst-case filtering (as shown in figure 84(*b*)) yields a sufficiently high SBR due to the steadily decreasing background. SBR values in general are sub-optimal, and necessitate a careful methodology for background subtraction. The forthcoming analysis introduces two approaches to background correction. The 'optimistic' background scenario considers a background that is steady on the time scale of the studied fluctuations, and therefore it can be measured with a negligible statistical uncertainty. The 'conservative' approach assumes a fluctuating background that needs to be measured by a parallel fast detector system with a measurement uncertainty comparable to that of the fluctuating BES signal.

Considering the photon current values computed by applying the optimized filter throughputs on the simulated spectra, two detector types were considered for the ITER fluctuation measurements. An avalanche photodiode (APD) for the core observation geometry and multi pixel photon counter for the pedestal observation geometry, both at 500 kHz sampling frequency. To assess the expected noise, the SNR dependency on the photon current was used for the above stated detectors [278, 279]. An optimistic SNR estimate is calculated by assuming negligible background light fluctuation, while a conservative estimate assumes similar relative amplitude fluctuation for the background than for the beam light. Figure 85(*b*) shows the expected SNR values, where the realistically achievable values probably lie in between. The SNR range for the pedestal observation geometry is not very favorable, as the values range from 2 to 10 depending on the location and the above approaches to estimation. The SNR estimates for the core system outside of $\rho = 0.4$ are much better. Figure 85(*c*) shows the relative amplitude threshold for

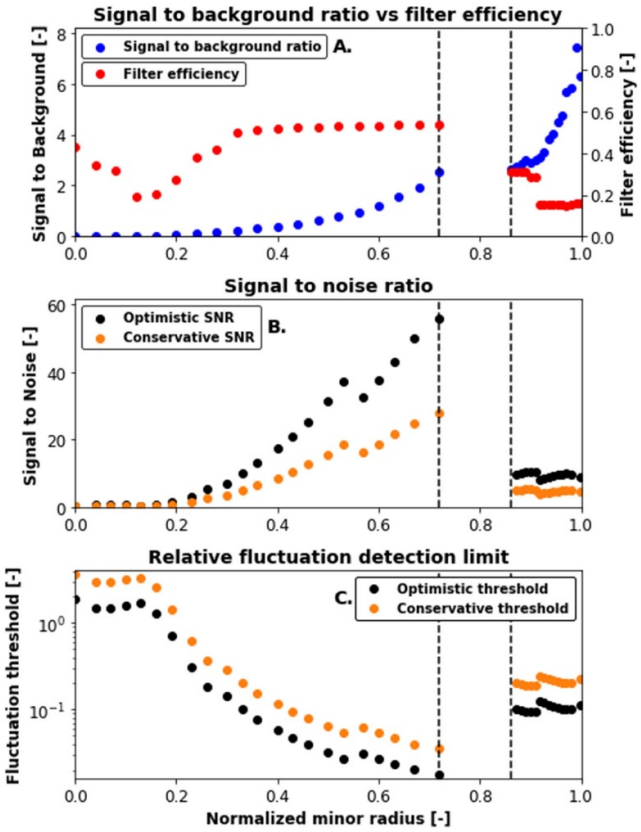

Figure 85. Expected performance parameters for both fluctuation BES systems plotted against the normalized minor radius. (*a*) Filter efficiency and SBR for each channel. (*b*) Range of expected SNR values. (*c*) Range of expected detection limits for individual fluctuation events in relative amplitude.

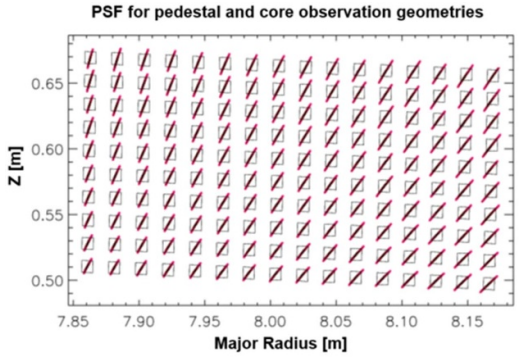

Figure 86. Spatial resolution of the pedestal fluctuation measurement for field-aligned perturbations. Poloidal projection of the proposed detector array and the extension of a field-aligned perturbation due to misalignment of LOS and magnetic field lines.

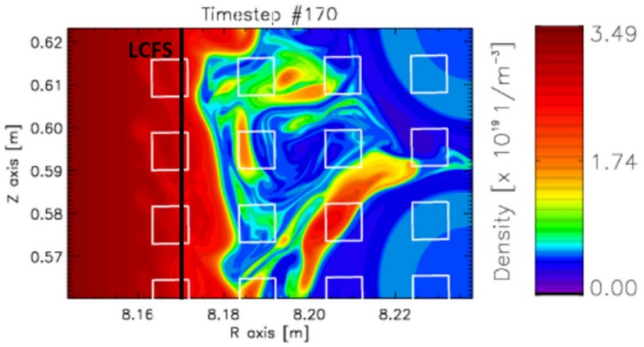

Figure 87. Poloidal snapshot of edge density turbulence simulated by HESEL, and the poloidal projections of possible fluctuation BES LOS of the pedestal CXRS viewing the scrape-off layer in inward-shifted scenario.

detection of individual transient events, as calculated from the corresponding SNR values. The core observation geometry is predicted to assess relative amplitudes as far as below 10%, while the pedestal observation scenario is predicted to be able to detect relative amplitudes of 10% in the best-case scenario or above. The actual detection limit greatly improves for stationary fluctuations, where statistical averaging or spectral methods can be applied.

Regarding the spatial resolution, the pedestal system should be capable of resolving the 2D structure of field-aligned perturbations, as the LOS are well aligned to the magnetic field lines across the beam [280]. The quantitative measure of the emission smearing resulting from the slight misalignment between magnetic field lines and LOS is characterized in figure 86. The smearing effect decreases from the LCFS towards the core, from values in the range of 15 mm, down to 5 mm. Furthermore, emission smearing due to the finite lifetime of excited states for the pedestal diagnostic was calculated to be 5 mm at the pedestal and 3 mm towards the core. Finally, accounting for the 10 mm radial width of the detector projections, the system's effective radial resolution is valued at 18 mm at the innermost edge, while 30 mm close to the LCFS. Similarly, an overall poloidal resolution range of 22 mm to 24 mm was estimated. Despite the considerable beam width, the proposed setup presents a reasonable spatial resolution, with the capacity to resolve plasma density fluctuations and filaments in a width range starting from 1–2 cm.

The close-to-vertical LOS of the core system view result in a poloidal resolution in the range of 100–150 mm, and a 35–50 mm of radial resolution in the outer region, where the signal quality was shown to be favorable. Therefore, a fluctuation BES system on the core CXRS periscope will not be able to detect turbulence, but it can be considered for the detection of MHD waves in the outer core region.

4.5.3. Synthetic BES diagnostic. In order to assess the measurement possibilities of a fluctuation BES system a synthetic diagnostics workflow was set up to provide synthetic signals [281] for SOL/edge turbulence using the HESEL code [282], and the synthetic fluctuation BES signal provided by RENATE [283]. Figure 87 shows a snapshot of the simulated turbulent 2D poloidal density field for Scenario 2 plasma, and the channel projections of the pedestal fluctuation BES system (as show in figure 83(*a*)) overlaid, assuming a slightly inwards shifted plasma. Emergent SOL filaments, as predicted by HESEL, will be smoothened as a result of the spatial smearing of the diagnostic system, but are still sufficiently large to be spatially resolved.

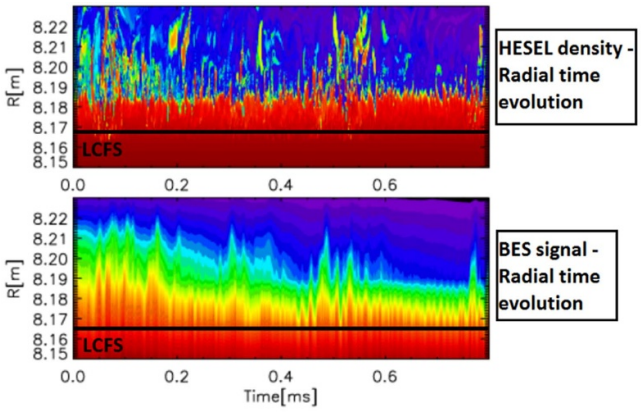

Figure 88. Turbulent density fluctuations in the SOL simulated by HESEL, and the corresponding response in BES signal amplitudes.

This conclusion is illustrated in figure 88, which shows the time evolution of the density along the central detector array of figure 87, and the time evolution of the corresponding BES signals without detector noise added. Tilted structures emerging from the LCFS are clear indicators of radial filament propagation, although the resolution might not suffice for accurate velocity measurements, it does suffice for the assessment of SOL filament statistical features as well as filament identification as long as they are sufficiently large to pass the detection threshold.

Measurement possibilities have been further analyzed by the introduction of realistic simulated measurement noise, by considering the deterministic signal as expected values [284]. First analysis shows that the low SNR values predicted for the pedestal fluctuation BES system significantly affect the signal statistics, therefore comparison of measurements with synthetic diagnostic signals is essential [285].

4.5.4. Diagnostic beam development. As described in section 1, for measuring active spectroscopy signals with good SNR and good spatial resolution, a 100 keV hydrogen DNB is considered for ITER [4]. The beam parameters desired to meet the ITER-CXRS diagnostics requirements [246, 252, 287] are listed in table 26. The injector consists of a 100 keV RF based negative ion source which produces energetic beams with controlled optics using a three-grid extractor and accelerator system, coupled to the source. The stringent requirement of beam divergence $\leqslant$7 mrad is met by using optimized aperture shapes, inter grid spacing, voltage tuning and appropriate control on the beamlet deflections due to various factors like the magnetic and filter fields, beamlet–beamlet interactions, etc [288]. Considering 60% neutralization efficiency of negative ions, transport losses over lengths of 21.7 m due to beam divergence, deflections and reionization losses, the desired extracted current from the RF source is 60 A @ 100 keV. However, for achieving a good SNR of CXRS signals, a neutral beam current of $\sim$20 A at 100 keV beam energy will be injected into ITER plasmas either with a modulation frequency of 5 Hz, 3 s ON/20 s OFF duty cycle (burst mode), or as a 100 ms pulse every 1.5 s continuous throughout the discharge (control mode). The passive signals recorded during beam off period will be used for an efficient background correction to retrieve the active signal which are otherwise convoluted with a strong passive signal.

Table 26. Parameters of the ITER DNB [286].

Parameter	Value
Beam energy	100 keV
Beam species	H
Extraction area	$\sim$0.2 m^2
Beam divergence	$<$7 mrad
Accelerated ion current	60 A
Accelerated current density	30 mA cm^{-2}
Beam power at $\sim$20.7 m	2 MW
Modulation	5 Hz during 3 s ON time
Duty cycle	3 s on, 20 s off

The extracted current passes through a 3 m neutralizer placed at 1 m from the source. The mixture of ion and neutrals is separated in the 1 m long residual ion dump (RID) placed at 0.75 m from the neutralizer. The neutral beam exiting from the RID is characterized with a calorimeter having two panels arranged in a V shape that can open and close under evacuated conditions. Considering the huge power and power densities of $\sim$10 MW m^{-2}, the panels of the calorimeter are made of a stack of CuCrZr elements working on the hypervapotron concept. Once characterized, the two arms of the calorimeter are opened to allow transport of the beam to the plasma.

There are large cryopumps (pumping speed: 10^6 l s^{-1}) installed, beginning from the neutralizer exit to the end of the injector, to pump out the Hydrogen gas. The reionization losses from the exit of the RID to the point at which the beam enters the ITER machine are estimated to be $\sim$20%. The ions born out of reionization of neutrals and deflected by the stray magnetic fields are collected on the frontend components and the duct which are lined with suitable liners. The design of the liner surface takes into account the heat loads and maximum power densities of the incident deflected ions on the surfaces due to focusing effects of the stray fields.

In order to establish the operation and performance of the DNB injector prior to its onsite commissioning at ITER, and to provide the beam operational database for supporting modeling and expected S/N ratios during CXRS measurements at ITER, an INdian Test facility (INTF) is conceptualized and is currently under commissioning at ITER-India laboratory, Bhat Gadhinagar. This is a voluntary task undertaken by INDA with a unique facility of transporting and characterizing ITER like beams over 21.5 m, similar to the beam transport path length at ITER. The operation of beam is optimized, and the performance is assessed by deploying several invasive and non-invasive diagnostics. An overview of different diagnostics, planned for INTF operation is shown schematically in figure 89 and a more detailed description can be found in [289–291].

The beam divergence and beam uniformity are measured by a Doppler shift spectroscopy (DSS) diagnostic. The negative ion density in the source and its uniformity near the large

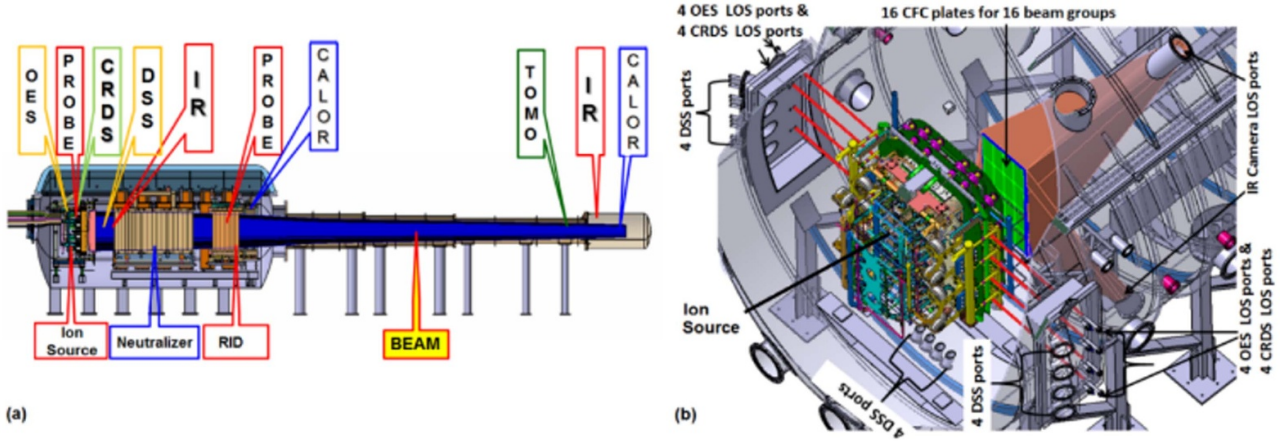

Figure 89. (*a*) Deployment of various diagnostics in INTF for characterizing the DNB. Figure 1(*b*) shows the details of the line of sights of Doppler shift spectroscopy diagnostics and the placement of the CFC based inertial calorimeter for the beam divergence and beam inhomogeneity measurements. Reproduced courtesy of IAEA. Figure from [291]. Copyright (2019) IAEA.

extraction plane will be monitored by cavity ring down spectroscopy. The beam power, power density and beam spatial divergence are measured using a water cooled V shaped calorimeter placed at ∼5.9 m and at 20.67 m from the Grounded Grid (GG), an inertial calorimeter (placed at ∼1 m from GG) made up of carbon fiber composite (CFC) with an IR camera will be used for imaging the beam footprint. Near to the beam duct and beam focusing location, arrays of visible cameras are placed to obtain a tomographic reconstruction of the beam emissivity [229, 230]. These beam characterization experiments will essentially aid the ITER-CXRS diagnostics to benchmark the actual DNB current that will be available to them for measurements when the DNB is operational.

4.5.5. Present status of ITER- DNB. The Indian efforts to operate and characterize beams for ITER follow a parallel path of beam and technology development. The road map for DNB development involves experiments on two additional test beds, ROBIN and TWIN.

The ROBIN test bed is established under a memorandum of understanding (MoU) with IPP Garching. It has a single RF driver source test bed where H- beams of 2 A with extracted current densities of 27 mA cm^{-2} have been established in a surface assisted Cesiated source [292, 293]. In the recent years ITER like H- current densities $\geqslant$30 mA cm^{-2} with e-/ion ratios $<$1 have been achieved. At present the ROBIN test bed has been upgraded to a neutral beam test bed to understand and operate neutral beams using ITER like electrostatic ion deflector (ERID) for separating the ionic component of the beam from the neutrals post neutralization.

The TWIN test bed is 1/4th of the DNB source in terms of its extraction area. It consists of a two-RF driver based indigenously developed ion source, using a coil configuration and connection to the RF generator similar to the one envisaged for the DNB source. TWIN is designed to operate in both air (where the RF drivers are exposed to air) and vacuum (where the entire ion source is inside a vacuum chamber, similar to ITER configuration) modes [294]. The aim is to learn power coupling to two drivers from a single RF generator, simulating thereby to a large extent the experiments with the full-sized source on the INTF and later at ITER. RF power to the tune of ∼70 kW have been coupled to produce plasma in the source. The source also has a 3-grid extractor and accelerator system with optics similar to the DNB 1 segment 3 grid extractor and accelerator system. The same has been manufactured and currently under assembly at the test bed.

The INTF is a replica of the ITER DNB beam line with a 21 m path length with an aim to generate database related to the availability of the neutral current at the location of the measurement using CXRS [287]. The facility consists of a VV, an 8 m long, 4.5 m diameter one with double O ring sealed openable top lid, and is coupled to a 12 m tapered duct consisting of cylindrical sections with reducing diameters. Ten modules of cryopumps each having a pumping speed of 10^5 l s^{-1} have been installed in the vessel. The beam source and the beam line components viz the neutralizer, ERID and the calorimeter shall be housed in the vessel to carry out the desired experiments of neutral beam production for ITER like parameters. The beam line components have been manufactured and installed in the VV. The source assembly and integration is underway at the factory with the delivery expected by the end of 2025. The 2nd calorimeter housed at the end of the beam line to determine the neutral beam characteristics after a traversal path length of 21 m has been procured and is currently under installation. Interfacing of the desired auxiliary systems like the hydraulic, gas and multichannel DAQ and control system along with the desired multi megawatt power supplies is underway. Table 27 provides a comparison of the important parameters related to the source and the beam characteristics.

4.6. Summary

Although active spectroscopy diagnostic on ITER will be possible only from the Pre-Fusion Power Operation Phase 2 (PFPO-2) good progress has been achieved in all active spectroscopy diagnostics. Physics, modeling, and technology background of all techniques have been clarified, but for more

Table 27. Parameters of the ITER DNB test devices.

Design Parameters	INTF	TWIN	ROBIN
Number of RF plasma drivers	8	2	1
Maximum RF power @1 MHz (kW)	800	180	100
Beam extraction area (cm^2)	∼1970	∼492	∼73
Number of beamlets (exposed to plasma)	1280	320	146
Plasma grid aperture diameter (cm)	1.4	1.4	0.8
Beam energy (keV)	100	50	45
Beam current (A)	60	15	2
Extracted electron-to-ion ratio	<1	<1	<1
Negative ion beam current density (mA cm^{-2})	>30	>30	>30

details measurements are still being done on existing tokamaks. Detailed design of the observation and detection systems is ongoing and is expected to be finished on time. A key element is the diagnostic beam, of which laboratory tests are progressing towards the final parameters.

In recent years it has been recognized that active spectra on ITER will contain more information than originally considered, therefore modeling has started for determining the possibility of extracting information on fast particles and turbulence. The results indicate that with modest extensions of the detection systems these measurements could be implemented.

5. Passive emission diagnostics for high performance metal tokamaks

M. G. O'Mullane[25], Ling Zhang[26], R. Barnsley[2], R. Tieulent[2], D. Mazon[1], D. Colette[1] and V. S. Neverov[27]

5.1. Importance of passive spectroscopy

Building theories and models to interpret the emission from plasmas has a long history and is still the only feasible approach for understanding the behavior of non-terrestrial sources. The quantum theory of the atom was uncovered to explain the spectra from both emission sources, stars, arcs, filaments, flames etc, and the absorption of gases [295]. Increasing sophistication in the instruments for measuring emission in different regions of the electromagnetic spectrum validated the theories and enabled more precise measurements of plasma parameters, which in turn led to ways of controlling plasmas based on a robust physical picture of the plasma. Magnetically confined plasmas for fusion rely on a controllable plasma with characteristics bounded in $n\tau$-T space, an extension of the Lawson criterion [296], where n is the plasma density, T the temperature and τ is the confinement time. For ignition this means $n\tau \geqslant 10^{20}\mathrm{m}^{-3}\mathrm{s}$ at $T > 10$ keV. Such operational requirements also set the size of the plasma, with the current largest machine JET having a plasma volume of ∼80 m^3 and ITER a factor of ten larger at ∼ 830 m^3. The size of the machine also determines the ease of access for diagnostic systems. Most current fusion devices are relatively accessible and their suite of diagnostics evolved in an ad hoc fashion. Newer machines incorporated diagnostic provision into the design of the machine, e.g. W7-X [297], and notably ITER has considered its diagnostics as an integral part of the design process [3]. The complexity introduced by the blanket and cryostat, the deleterious effects of the neutron flux from fusion DT products and the reliability requirements of licensing a nuclear facility introduce constraints on diagnostics not present in current devices. The accessibility constraints for DEMO may be even more restrictive [298] so it is important to maximize the capabilities and interpretation methodology of the diagnostic data from ITER.

A wide angle view of the JET plasma in the visible part of the spectrum, shown in figure 90, illustrates the scope and complications of using passive spectroscopy to diagnose fusion plasmas. All regions of the plasma, core, edge, SOL and divertor, emit radiation. The local plasma conditions in these regions vary widely and in the edge and divertor the gradients of the plasma temperature and density profiles are large. The degree of ionization and the energy of the local, background electrons is the main determinant of the type, and hence wavelength, of the emission. Generally visible light arises from the more loosely bound electrons of the neutral to a few times ionized ions, and therefore is more likely to occur in the lower temperature edge and divertor regions. VUV, SXR and x-rays are more characteristic of the confined plasma inside the last closed flux surface (LCFS). The central electron temperature of a high performance ITER plasma will be at ∼25 keV, sufficiently high to fully ionize argon, iron and xenon. The ionization potential of tungsten is 80.8 keV so will always retain bound electrons, which has negative implications if the operating scenario does not prevent impurity accumulation. For safe operation and maximum scientific return, measurements must be taken from all these regions of the plasma. Figure 90 also demonstrates that all, purely passive, instruments will give a measurement that is integrated along its LOS. To obtain profile information, multiple LOS or some form of scanning of a single LOS must be engineered in addition to an analysis workflow which can invert the measured signals, e.g. [299] for a visible system and [300] for an x-ray instrument. However single LOS instruments can be simpler to build and are more robust in use and their measurements do have value. In particular the primary role of some survey spectrometers is to detect what impurities are in the plasma, so just their presence or absence of a signal above the noise floor is

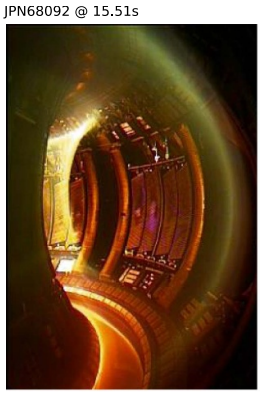

Figure 90. Interior of JET illuminated by its plasma emission, contaminated following a sodium influx. The yellow color shows that post-pulse analysis may not always be necessary. The complex interior surfaces and the sharp outline of the last closed flux surface can be seen.

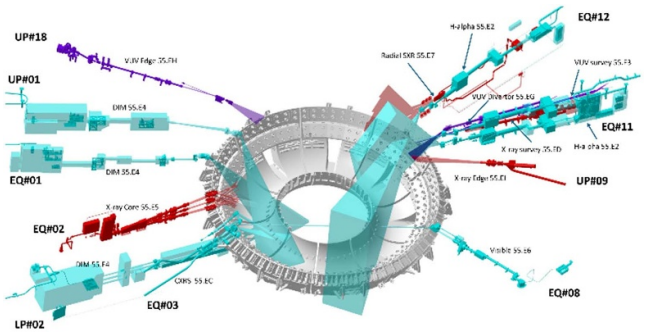

Figure 91. The port location, in upper (UP), lower (LP) or equatorial (EQ) ports, of the passive spectroscopy instruments of ITER with the extent of the cone of view for each instrument. See table 28 for measurement roles.

a sufficient indicator. The vessel walls will emit black-body radiation but this review is confined to emission originating from the plasma.

ITER will be a well diagnosed machine in keeping with its research remit and may well be the last burning plasma device with an extensive suite of general purpose spectroscopy systems. The choice of instruments is pragmatic and is based on the roles of MP and BC, AC and for physics understanding, in that order of importance. A set of measurement requirements determined the instrumentation as described in [4, 6]. Passive spectroscopy has a primary role in detecting and quantifying impurity content and an important secondary role, to provide redundancy and resilience, in many other measurements. Figure 91 shows the location and observation cones of ten systems based on visible, VUV or x-ray emission. Complete coverage of the plasma, in all wavelength regions, is impossible but a mixture of imaging and narrow LOS will sample emission from the core, edge and divertor plasma with time resolutions of the order of tens of milliseconds and spatial resolution in the centimeter range. The measurement expectations given in the early overview of the spectroscopic systems [301] are still relevant but, 20 years on, there are many detailed papers on the design and implementation of the various instruments. Table 28 lists the suite of passive spectroscopy diagnostics and some of the publications of note.

This is not an exhaustive review of passive emission diagnostics for a fusion machine; there are many general reviews and some specialized subsets dedicated to diagnostics in different wavelength regions e.g. [315–318], but rather reports on developments of interest to large tokamaks with metal plasma facing surfaces. The choice of ITER for a beryllium FW and tungsten tiles in the divertor [319], along with excluding carbon as an in-vessel material, prompted many investigations into the emission of tungsten at ITER conditions. The ILW at JET is the closest analogue [320] to the ITER concept but there have been numerous supplementary studies on different aspects of the behavior in a plasma, deficiencies in atomic data, investigation of transport and measurement/instrument challenges. The following sections review the current knowledge of tungsten spectral emission from neutral to highly-ionized systems, the investigation of radiation hard energy-resolved detectors and the emission model used to aid the design of many of the passive emission diagnostics in ITER. Finally the inverse problem of turning these measurements into useful engineering and operational quantities is outlined.

5.2. *The spectroscopy of tungsten*

ITER will be a metallic tokamak with a beryllium FW [321] and a tungsten divertor [322]. Beryllium getters oxygen and, as a low Z element, a significant quantity can be tolerated in the plasma. Tungsten can accept very high power loads and does not retain tritium [323] which is the principal reason for excluding carbon which would otherwise be an excellent PFC. Tungsten was used in the aperture limiters of early tokamaks and the first tungsten spectral feature reported was a 'quasicontinuum' (QC) x-ray feature at $\lambda \sim 5$ nm, from ORMAK [324]. This was attributed to 4 $f^{10}4\ f^{n} - 4d^{9}4f^{n+1}$,$4d^{10}5d^{n}$ transitions of Ag-like to Rh-like tungsten ions. Figure 92 shows that this is a characteristic signature of tungsten in all tokamak plasmas and that spectrometers with high spectral resolution have enabled contributions from individual ions to be identified [325].

The map of the strongest tungsten lines as a function of ionization stage in figure 93 shows that emission from tungsten is primarily in the VUV and x-ray spectral regions, which has the implication that any spectroscopic instruments for ITER must be vacuum coupled and designed to minimize the flux of neutrons onto any optical components and detectors.

The minimum electron temperature required to ionize the tungsten stages in the $\lambda \sim 5$ nm feature is ~ 1 keV and its structure and shape is sensitive to temperature. The long pulse lengths of WEST enabled a spatial scan corresponding to a peak temperature profile change of 2.07–3.35 keV [328] and the analysis confirms that at the higher temperatures the maximum charge state was W^{46+} but the lower temperature emission zone was dominated by W^{33+} and W^{34+} and lower. Radial profiles of W^{43+}–W^{45+} were measured with a space

Table 28. The suite of passive spectroscopy diagnostics to be installed on ITER. The internal naming convention (PBS) is given for convenience and the primary role is taken from the latest measurement requirements (accessed October 2022). Each instrument will also have supplementary and backup roles. Their location on the ITER tokamak is shown in figure 91.

System	PBS	Primary role	Recent references
H-α monitor	55.E2	C, O influx Be influx distribution ELM radiation L-H step change D +T chamber influx	[302, 303]
Divertor impurity monitor	55.E4	Position of ionization front Flux of D, T, Be, C and W T_{ion} profile	[[304], subchapters 6, 7]
VUV survey	55.E3	Be, C, O, Cu and W relative concentration Extrinsic Ne, Ar and Kr relative concentration	[95, 305]
VUV divertor	55.EG	Flux of Be, C and W	[96]
VUV edge	55.EH	Fractional impurity content for $Z < 10$ and $Z \geqslant 10$	[97]
Core x-ray	55.E5	T_{ion} profile Poloidal velocity Toroidal velocity Fractional impurity content for $Z > 10$	[306]
Visible spectroscopy	55.E6	Continuum measurement	[307, 308]
Reference system Survey x-ray	55.ED	Be, C, O, Cu and W influx and relative concentration Extrinsic Ne, Ar and Kr influx and relative concentration	[309–311]
Edge x-ray	55.EI	Poloidal velocity Edge T_{ion} profile	[312][a]
Radial x-ray camera	55.E7	$B_\theta/<B>$ MHD mode ELM temperature transient Runaway current Transient radiated power profile	[313, 314]

[a] Not the principal subject of paper.

resolved VUV instrument at EAST [329] and shows a wide profile for these ions (up to $\rho \sim 0.4$) and profiles which display a variation to core temperatures changes between 2.9 and 3.3 keV. This feature will be a key measurement for ITER but unlike ORMAK, ASDEX Upgrade, WEST, EAST and JET where the emission occurs in the confined plasma this will be an edge, or possibly pedestal, feature and thus may behave more like an influx measure.

The efficiency of tungsten radiation and its consequences for plasma viability were recognized even from simple average-ion calculations [330] so tungsten was not used in the next generation of large tokamaks such as TFTR, JET and JT-60. There were advances in atomic physics calculation capabilities of high-Z ions but experimental comparisons for tungsten came mainly from laser experiments, e.g. [331], or from occasional injection of heavy impurities into tokamaks [332]. A series of experiments at ASDEX Upgrade in the late 1990s [333] suggested that tungsten surfaces in a high density, low temperature divertor had advantageous sputtering and re-deposition characteristics and that a radiative mantle and ICRH heating could be used to mitigate any accumulation. These findings prompted renewed interest for tungsten in tokamaks leading to significant experimental programmes: the near 90% tungsten FW of ASDEX Upgrade [334], JET installed the ILW with a beryllium FW and tungsten divertor [58] and WEST repurposed Tore Supra to mimic ITER divertor heat flux [335] and EAST is now a full metal wall device with a molybdenum FW and tungsten upper and lower divertors [336]. Since the selection of tungsten as the primary divertor PFC in ITER almost every tokamak has a tungsten related programme.

Until this revival of interest detailed measurements and atomic structure calculations for other ionization stages of tungsten were patchy. Spectra of WI [337] and WII [338] from arc spectra were well known and there were more limited analyses of WIII-WVIII but then there was a gap until WXXVIII, the Ag-like system from the tokamak observations. The most current compilation of evaluated energy levels

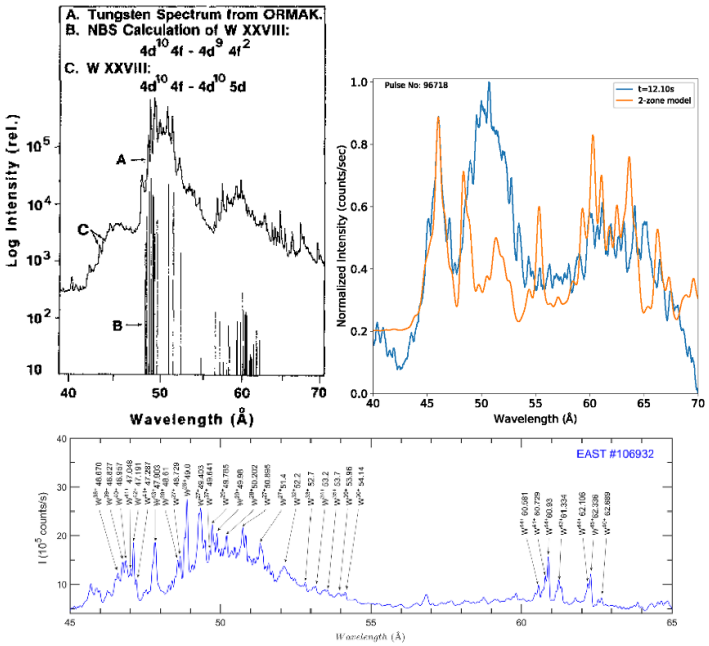

Figure 92. The $\lambda \sim 5$ nm tungsten feature from ORMAK (1980), JET (2020) and EAST (2021). The JET example shows a simplified 2 temperature zone fit to the feature—the spectrum was smoothed (Savitzky–Golay filter), with the background removed and normalized before fitting. The EAST spectrum identifies many of the contributing ionization stages. Reprinted figure with permission from [326], Copyright (1980) by the American Physical Society.

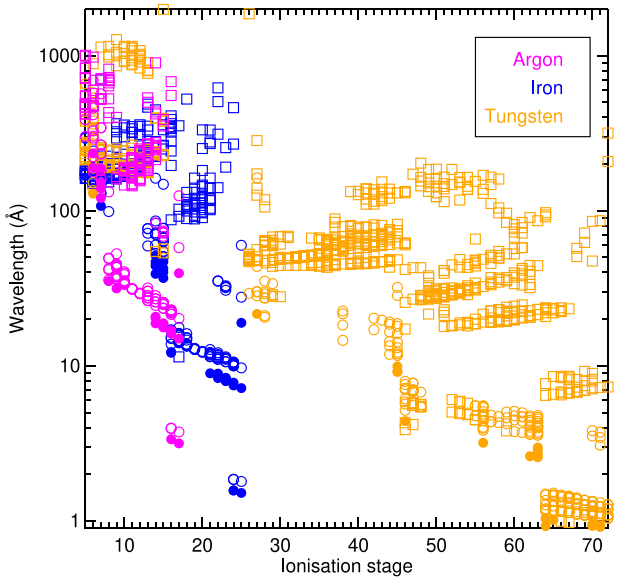

Figure 93. The wavelengths of contributing stages of Ar, Fe and W in the VUV and x-ray spectral ranges as a function of ionization stage. The $\Delta n = 0$, 1, 2 transitions are indicated by open squares, open circles and filled circles. The 20 strongest transition per stage were given by the photon emissivity coefficients taken from the calculations used in [327] but there is no ionization balance to rank their relative contribution due to the differing widths of each ion's emission shell.

and wavelengths is the NIST energy levels and lines database [339] and a comprehensive summary of tungsten data produced between 1980–2007 is described in [340].

The development of the electron beam ion trap (EBIT) revolutionized spectroscopy by enabling precise isolation of individual ionization stages. An early result from the Tokyo EBIT was a measurement of the neon-like W^{64+} spectrum at a beam trap energy of 20 keV [341]. As will be seen in the next section some of the seven lines from the $2s^2\ 2p^6\ {}^1S_0 - 2s^2\ 2p^5\ 3n^1$ transitions, spanning 0.1158–0.1492 nm, can be used to measure ion temperature and rotation velocity profiles [342]. Accurate wavelengths are essential when designing crystal based instruments since the wavelength bandpass of such instruments is dependent on the $2d$ lattice spacing and can therefore be quite narrow.

There have been many EBIT experiments filling-in the spectra of the unknown tungsten ions and table 29 shows the range of results and the different spectral regions required to make use of tungsten emission as a diagnostic. The EBIT plasma is very different from that in a tokamak being two orders of magnitude lower in density and with a very narrow range of electron energies, unlike the Maxwellian electron energy distributions of tokamaks. Even so a collisional-radiative model is required to interpret the observed intensities in EBIT spectra [343, 344]. Some metastables, see [345] for an example in Ti-like W^{52+}, can build up significant population and become extremely long lived. These are unlikely to occur in tokamak conditions because of the wider range of energies of the background electrons.

The EBIT observations have been used to disentangle the quasi-continuum features observed in tokamaks [358, 359] and employ grating and crystal spectrometers which are broadly similar to the designs for ITER. The EBIT observations in the visible spectrum are from forbidden M1

Table 29. Summary of EBIT results for tungsten ions. Multiple ions are reported in many papers and the wavelength range tabulated may be wider than measured but is given to indicate which diagnostic would be most suitable to observe in a tokamak.

Ion stage	Wavelength (Å)	Machine	Year	References
W^{5+} – W^{7+}	180–280	EBIT-I	2015	[346]
W^{5+} – W^{8+}	180–250	SH-HtscEBIT	2022	[347]
W7+ – W8+, W10+	4200–6400	SH-HtscEBIT	2015	[348]
W^{11+} – W^{15+}	160–270	SH-HtscEBIT	2015	[349]
W^{26+}	2600–5020	SH-PermEBIT	2014	[350]
W^{28+}	3300–4000	SH-HtscEBIT	2014	[351]
W^{21+} – W^{45+}	45–70	Berlin	2001	[352]
W^{24+} – W^{33+}	15–35	CoBIT	2013	[103]
W^{39+} – W^{47+}	40–200	NIST	2007	[353]
W^{40+} – W^{50+}	5–6	LLNL	2004	[354]
W^{45+}, W^{46+}	5.19–5.26	Shanghai	2018	[355]
W^{48+} – W^{61+}	27–41	LLNL	2013	[356]
W^{64+}	0.9–1.77	Tokoyo	1996	[341]
W^{65+} – W^{71+}	6.5–7.7	SuperEBIT	2009	[357]

transitions in the ground state term. Originally predicted in [360] that there may be a Ti-like line at 354.61 nm, thus allowing a simpler visible spectrometer to measure a highly charged tungsten ion, it has not yet been observed in a tokamak plasma. However the iso-electronic lines in krypton, molybdenum and xenon have been measured in LHD [361], although the temperatures required to ionize W^{52+} were not achievable. The research programme at LHD has observed other M1 lines from W^{26+} and W^{27+} (e.g. $4f^2\,{}^3F_4$ – $^3F_3$ at 333.7 nm) [362] with a 44-LOS visible spectrometer. The advantages of a visible spectrometer over vacuum coupled instruments are clear for DEMO and assessing the capabilities of using such transitions should be part of the ITER physics programme.

Measuring the influx of impurities into tokamak plasmas has usually relied on observing lines in the visible spectrum and relating this photon flux to a particle flux, typically via an ionizations per photon coefficient, S/XB where S is the ionization rate, X the excitation rate and B is the branching ratio [363]. Properly the S/XB coefficient is formed from the excitation part of the collisional-radiative matrix coefficients [364]. As an example, the erosion profile of a tungsten surface caused by ELMs in DIII-D is measured by converting the emission of the W^0 400.9 nm via a suitable S/XB coefficient [365]. This line, first identified by dedicated experiments at PSI-I [366] and confirmed in a tokamak setting in ASDEX Upgrade [367], has become the mainstay of tracking the influx of neutral tungsten into tokamak plasmas.

Characterizing this line has been one of the larger recent endeavors in passive spectroscopy, spanning fundamental atomic physics, numerous tokamak experiments and independent measurements of the S/XB coefficient. As seen in figure 94 the line is well isolated but this is not a 'simple' transition. The Grotrian diagram of figure 95 shows that the lower level is not the ground level and this complicates the calculation of an S/XB coefficient. There are other complexities which affect theoretical atomic calculations.

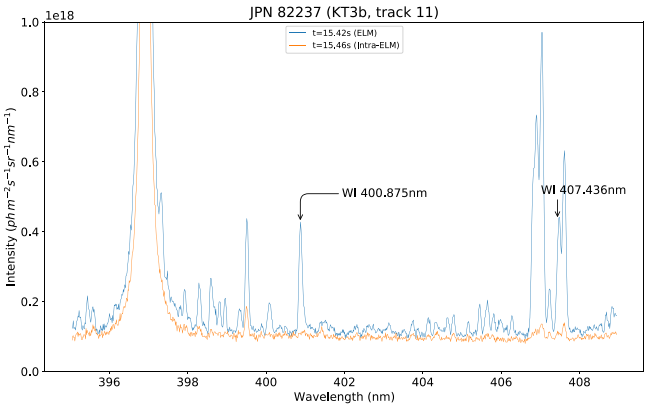

Figure 94. The WI line at 400.9 nm in a JET discharge during and between ELMs. The lines is well isolated but other tungsten lines are blended with lines from oxygen. Figure from A. Meigs.

Firstly, there is some disagreement in the identification of the upper level. The NIST database shows it as $5d^5(6S)6p\,^7P_4$ based on a *raie ultime* argument [368]. However analyzing arc spectra with different isotopes of tungsten did not show the large isotope shift expected from a pure $s - p$ transition [369] and concluded that the upper level is >85% $5d^46s6p\,^7P_4$. This agrees with later calculations [370, 371] and is also the designation in the ADAS dataset used in [365]. Secondly for W^0 ionization cross sections there are few experimental measurements [372] and unsatisfactory convergence in the theoretical cross sections [373] (there is better agreement for direct ionization but not from excited levels). Finally modeling, with ERO, of W^0 emission profiles in the PSI-2 linear device following sputtering by argon required following the evolution, and interplay, of the $5d^46s^2\,{}^5D$ and $5d^56s\,{}^7S$ metastables [374] which indicates that there is not a simple relationship between the emission and particle influx. Practically, this unfinished theoretical understanding of the atomic physics of neutral tungsten, has resulted in empirical

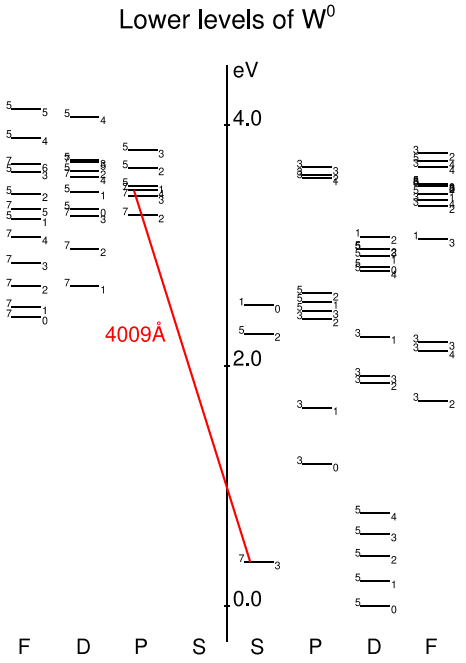

Figure 95. Grotrian diagram for neutral Wi showing the upper and lower levels of the 400.9 nm lines used for influx measurements.

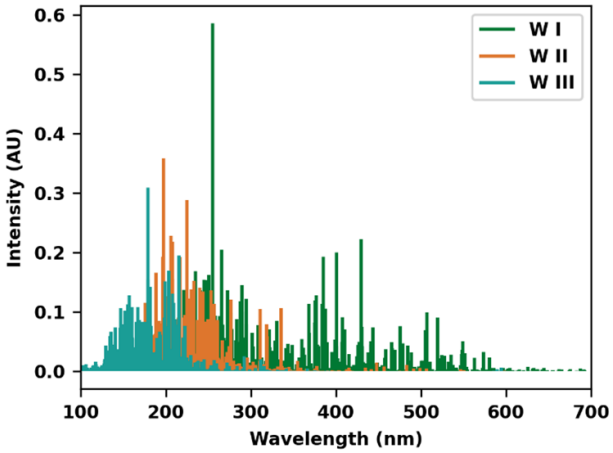

Figure 96. The spectral region of expected emission from W0–W2 +. The photon emissivities for prominent lines are calculated from ADAS adf04 data based on an atomic structure following the HFR +CP approach of [383]. This method has a wavelength accuracy of better than 5%. Figure from [381].

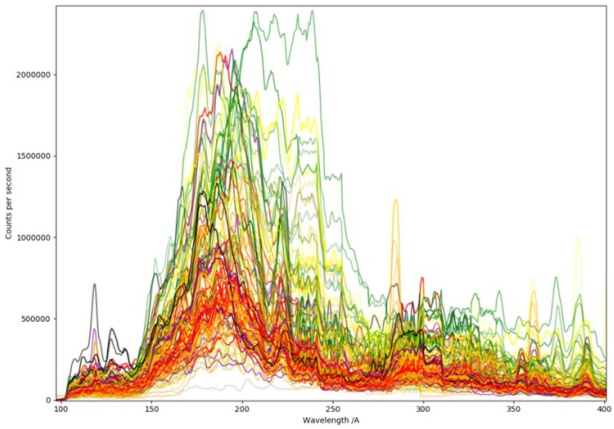

Figure 97. The wide variety of shapes of a tungsten spectral feature from the horizontal viewing SPRED VUV spectrometer at JET over a campaign. The background and contaminating nickel and chromium lines have been removed.

estimations of the S/XB coefficient to apply to the 400.9 nm line [375–377].

However, such a 'rule of thumb' approach is not ideal for first principles modeling of tungsten behavior. Emission lines of neutral tungsten originating from the ground term are in the near-UV region, ∼230–350 nm [378] but many of these lines connect different spin systems. This is also a difficult spectral region for diagnostics because the means for moving the optical components out of a direct LOS are not effective: UV fibers attenuate too quickly and the efficiency of reflectors is very poor at these wavelengths. Nevertheless direct observation of these lines at DIII-D and CTH [379] coupled with improved theoretical calculations [380] may be able to place the 400.9 nm line on a much more secure theoretical basis. A similar approach is underway for W^+ [381] with new atomic data of similar quality [382].

With increasing charge state the spectral emission tends to lower wavelengths. Figure 96 shows modeled emission of the first three ionization stages of tungsten from VUV to visible (100–700 nm). The atomic structure is calculated with the HFR +CP approach of [383] which gives a reasonable accuracy of better than 5%. There are usable lines in the visible for neutral tungsten, which is confirmed in many tokamak experiments. However W^+ is mostly in the near-UV and by W^{2+} the dominant spectral region is firmly in the VUV region with no usable visible lines. As shown in [384] it may be important to follow the ionization pathways of $W^0 \rightarrow W^+ \rightarrow W^{2+} \rightarrow W^{3+}$ to correctly determine the re-deposition of tungsten following sputtering. Measured emission from $W^{3+} \rightarrow W^{4+}$ may be needed for the higher densities of the ITER divertor.

Any model of the behavior of tungsten, from its influx to possible accumulation in the core, ideally requires measurements from all parts of the plasma. In practice this means that emission from nearly all stages of tungsten must be used. Additionally, knowledge of the composition of these spectral features is essential. Many of these observations will be isolated lines but the quasi-continua also contain significant information. There is a prominent tungsten spectral feature at 150–250 nm which is attributed to tungsten ionization stages below W^{26+} [358]. Its emission zone temperature is lower than the $\lambda \sim 5$ nm feature, so it reacts to edge conditions, as seen in the variation of shapes seen over a JET campaign in figure 97. The partially filled $4f$ subshells of these stages remains a difficult atomic structure problem so precise observations are still required and recent reports from HL-2A [385] and LHD [386] have identified some components of tungsten in this spectral region; lines from W^{5+} and W^{5+} have been identified. In very low temperature, T_e∼0.5 keV, plasmas at EAST, where tungsten accumulation is present, spectral lines from W^{5+}–W^{8+} become prominent.

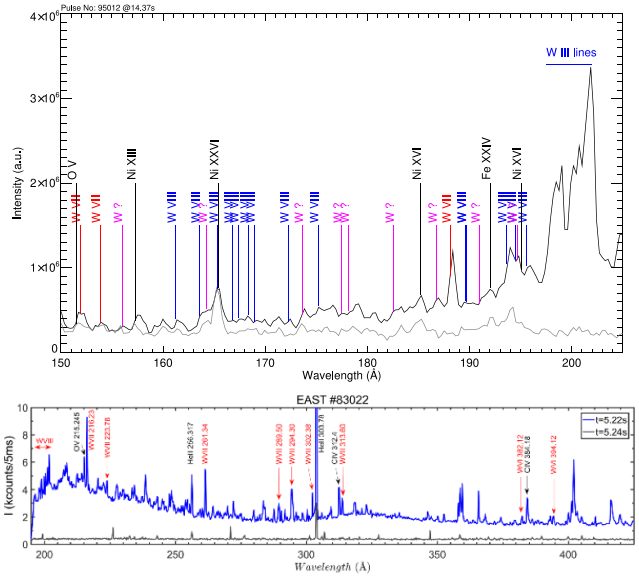

Figure 98. A part of the VUV spectrum along a line of sight looking through the outer leg of the JET divertor following a tungsten influx. The emission is mainly from WIV–WVII. Full identifications are in [389]. The lower figure shows similar tungsten stages in a low temperature (∼0.5 keV) EAST plasma from a line of sight through the core. Reproduced from [389]. © The Author(s). Published by IOP Publishing Ltd. CC BY 4.0.

Probable overlaps in the spectrum arising from stages in different spatial locations, which may be very close in the edge plasma due to large gradients in temperature, has prompted atomic structure calculations, laboratory experiments and detailed analysis of spectra from tokamaks. The line identifications from vacuum arc spectra of W^{7+} between 190 and 500 Å [387, 388] have recently been observed in a divertor spectrum [389] in typical JET operational conditions. 303 tungsten lines, from W^{3+}–W^{7+} have been identified, with a further 44 unattributed tungsten lines, in the divertor plasma of JET. Figure 98 shows a small portion of the 150–1325 Å range and detailed spectroscopy such as this is essential in building a set of observations which will be needed to fully understand the behavior of tungsten.

The design choices for the VUV spectrometers of ITER were made before the desirability of measuring emission from the first 5 stages of tungsten was apparent and are constrained by location and the wavelength response of optical elements. The Divertor Impurity Monitor (DIM) [304, 390] covers 200–1000 nm and the suite of main chamber VUV spectrometers have a number of spectral channels covering 2.4–160 nm for a single LOS of the main plasma [95], an imaging system over 17–32 nm in the upper edge plasma [97] and an imaging system over 14.4–32 nm viewing the divertor [96].

5.3. A common emission model for diagnostic design

Many of the passive spectroscopy diagnostics for ITER are refinements of existing technology and can be tested on existing machines, e.g. [96, 310]. However present day devices cannot achieve the same conditions as ITER so a flexible model of the expected emission is essential when developing diagnostics. Predicted signals can then be converted into practical units to show how successfully the system can achieve the measurement requirements. Apart from helium generated from fusion, doped pellet injection and gas puffing, all other impurities will originate from plasma surface interaction. Although sophisticated codes for modeling the edge plasma are used extensively in divertor design and scenario development [391] they are computationally expensive and do not have robust models for transient events. The models also rarely address the richer mix of impurities that will be present in ITER. Furthermore, the diagnostic systems are expected to measure a much wider range of possible conditions not considered in the models.

A common emission model has been used to support the design of x-ray [309, 342], VUV [96], bolometry [72] and SXR cameras [392] diagnostics. All these systems measure an emission integrated along a LOS. In general the intensity of an atomic line from an element is,

$$I(\lambda) = \int_{\mathrm{LOS}} N_{\mathrm{e}}(\xi)\left[N^{z+}(\xi)\,P\varepsilon C^{\mathrm{exc}}(\xi,\lambda) + N^{(z+1)}(\xi)\,P\varepsilon C^{\mathrm{rec}}(\xi,\lambda)\right]\mathrm{d}\xi$$

where $N_{\mathrm{e}}(\xi)$ is the electron density, $N^{z+}(\xi)$ the ionization stage density and PEC the photon emissivity coefficient which is an atomic quantity depending on the local electron temperature and density [364]. There are separate PECs for excitation and recombination and the emission profile is integrated along the LOS ξ of the instrument. Additionally there will be a background from the continuum emission contributed by this element and all other elements radiating in the LOS. The emission depends on the temperature and density profiles as well as the ionization balance at each point along the LOS. The ionization balance profile is determined by plasma transport but theoretical descriptions, although much improved, still give qualitative rather than quantitative predictions for these profiles [393]. Therefore for this diagnostic work, the impurity transport code used to predict spectroscopic line emission has three considered, but imposed, inputs: the time evolution of the influx, the final concentration in the confined plasma and the description of the transport coefficients. Using *typical* values, based on the experience of other machines and the more complete edge modeling, is sufficient for design needs because the diagnostics signals must not be marginal and adequate headroom to deal with unexpected behavior is also a design criterion.

The first use of the approach described here was for a design study of a high resolution x-ray spectrometer [394]. The temperature and density profiles were calculated with the ASTRA 1.5D transport code [395] where its self-consistent transport coefficients were adjusted to match the confinement time of what is now the ITPA global H-mode confinement database [396]. The profiles were available for one time-point in the flat-top of a high performance ($Q > 10$) DT discharge. The provenance of these background profiles, essential for diagnostic assessment, was unsatisfactory until the development of the integrated modeling & analysis suite (IMAS) [397] and the

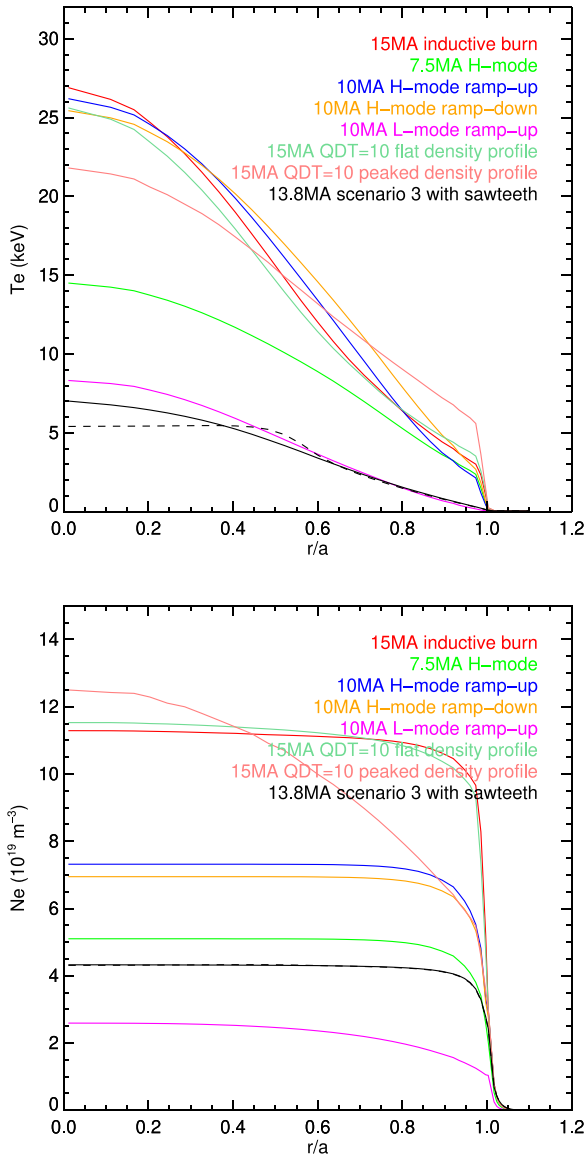

Figure 99. A range of modeled temperature and density profiles for ITER operational scenarios used as the steady-state background plasma for forward modeled impurity emission in support of diagnostic design.

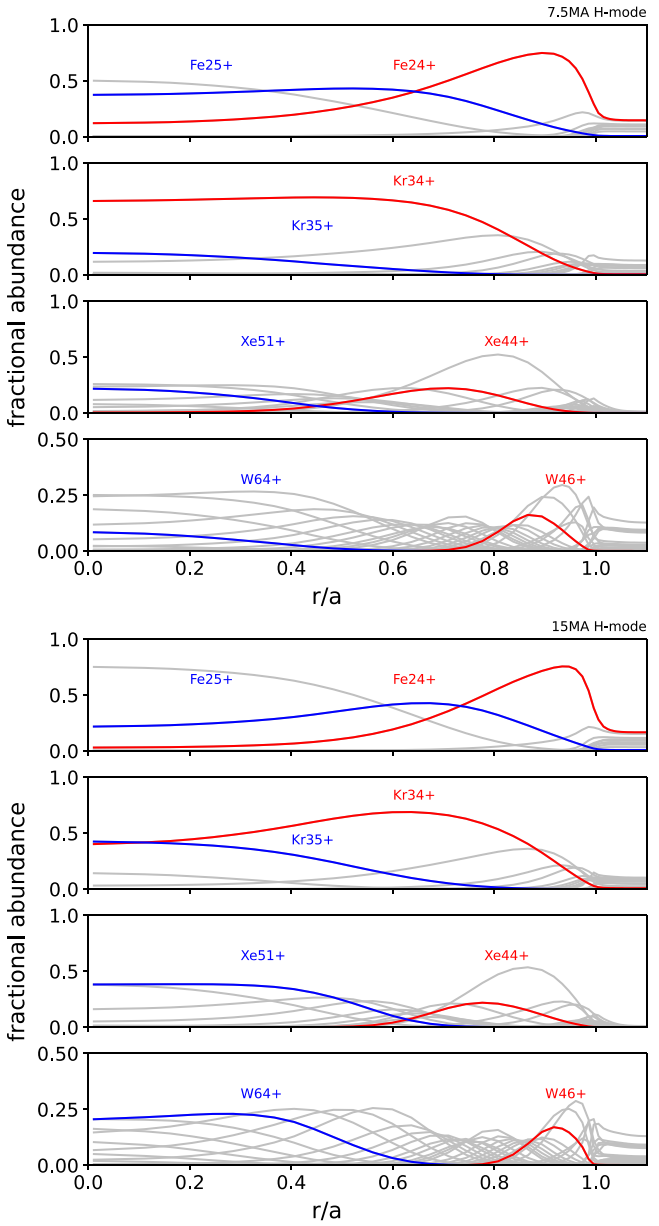

Figure 100. Profiles of the ionization stages for krypton, iron and tungsten for 7.5 MA (top) and 15 MA (bottom) H-mode ITER plasmas. The stages which give the strong, isolated lines are highlighted.

policy that IMAS is the preferred way to support the development of the ITER research plan and diagnostics [398]. Some of the profiles in this work are available via IMAS and figure 99 shows the range of scenarios considered.

The different plasma scenarios will affect the profiles of the ionization stages giving rise to the emission. Note that this effect is of limited importance to the light elements since they exist at low electron temperatures and should emit irrespective of the core conditions. Figure 100 shows the change for iron, krypton and tungsten profiles between the high performance 15 MA and the half-current 7.5 MA H-mode scenarios. Using the iron H-like Fe^{25+} transition as a diagnostic will work for either H-mode scenario. The increased core electron temperature brings the H-like krypton and Ne-like tungsten stages into greater prominence and hence their usefulness as a diagnostic. What is not shown in the figure is the relative abundance between the two scenarios. Figure 101 compares the emission profiles of the most prominent x-ray lines, i.e. those with one or two active electrons: the H- and He-like iron and krypton and Ni- and Ne-like tungsten detailed in table 29. The concentrations, in the confined plasmas inside the LCFS, are set to 'typical' values but the profiles will scale linearly with concentration. The behavior of these three elements in an L-mode scenario is markedly different in that the Ne-line W^{64+} stage is not ionized and the Ni-like W^{46+} becomes a core, rather than edge, emitter. The emission zone of the iron and krypton x-ray lines also move inwards but the He-like and H-like lines of these elements still have a reasonable spatial coverage. The tungsten lines show the greatest separation with plasma conditions, not

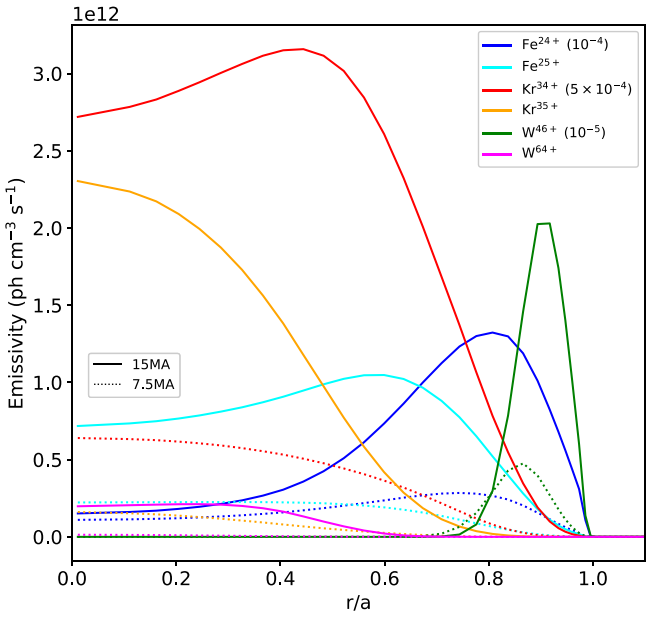

Figure 101. X-ray line emissivity profiles for iron, krypton and tungsten in full and half-current H-mode plasmas. The concentration is set to be the same for both scenarios.

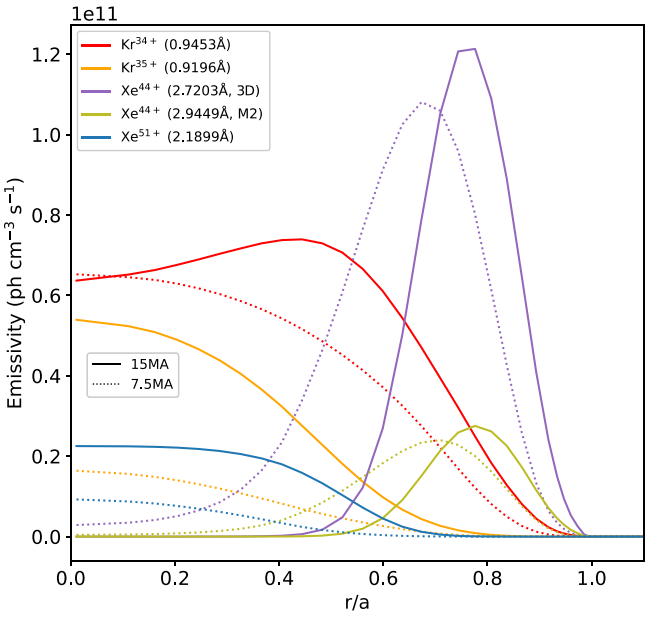

Figure 102. X-ray line emissivity profiles for krypton and xenon in full and half-current H-mode plasmas assuming that each element contributes 1 MW of radiated power in each scenario.

unexpectedly since only the 15 MA plasma attains conditions sufficient to strongly ionize the Ne-like shell. Krypton also shows that the H-like and He-like sample different regions of the core plasma so measuring both lines will be important to ensure full coverage [399–401].

Iron and tungsten are intrinsic impurities of ITER but operational priorities are likely to minimize their pollution of the confined plasma by adjusting gas fuelling which has been shown to reduce tungsten erosion and thus penetration [402]. The resulting concentrations may not be sufficient to be usable by diagnostics. Adding a known quantity of an extrinsic impurity is one method to mitigate emission from impurities falling below the detection threshold. The noble gases offer the most control on shaping the influx either by admixture with the fuel or via a dedicated injection system [403]. The choice of which gas to use is determined by measurement requirements, operating conditions and physics and engineering constraints of the diagnostic. As an example, the x-ray spectrometers have a role in measuring the ion temperature profile. This immediately excludes argon as a suitable impurity to diagnose a wide spatial coverage. Figure 102 compares the radial extent of the original choice of krypton with xenon lines and normalizes the relative intensities by fixing the additional radiation to 1 MW, assuming that this is a reasonable non-perturbing value and that the gas introduction systems are sufficiently responsive to maintain the required concentrations. These are 5×10^{-5} and 1.6×10^{-5} for Kr and Xe in the 7.5 MA scenario and lower at 1.2×10^{-5} and 3.8×10^{-6} in the high performance plasma, highlighting the greater efficiency as a radiator of the more ionized charge stages. There are other trade-offs: the factor of 3 lower emissivity of Xe^{51+} to Kr^{34+} in the core ($r/a < 0.4$) can be offset by the factor of 20 higher reflectivity of a germanium crystal at 0.3 nm than at 0.09 nm. The suggestion for considering xenon [404] has prompted measurements in exciting machines [405] and has informed the design of spectrometers for use in CFETR [406].

Impurities may have deleterious effects by diluting the fuel or, for high-Z elements, by reducing the temperature via radiation with the latter effect dominating with increasing nuclear charge. Such radiation is not always unwelcome. High performance discharges in ITER will rely on neon radiation to remove excess energy in the SOL and divertor [407] and xenon is under consideration for the same role in DEMO [408] where the dissipation needs are greater (40 MW vs 450 MW). Bolometers and SXR cameras are used to measuring and the same emission model used for spectroscopy can be used for energy-integrated radiation. The precision of modeling, and later interpreting, of the radiation measurements depends on the precision of the ionization balance and the power coefficients. For light elements the uncertainty on these atomic data is low [364] and there are efforts to rigorously quantify the uncertainty [409]. This is not the case for the high-Z elements. The choice of tungsten as a PFC for ITER also prompted new fundamental atomic cross section measurements. A storage ring measurement of the dielectronic recombination (DR) rate coefficient of W^{20+} showed that low energy resonances influence the rate at temperatures of its peak abundance in hot, fusion plasmas and that existing calculations of DR underestimated the rate by a factor of 4 [410]. A decade of new measurements [411], empirical adjustments to existing rates based on tokamak ion balance studies [358] and new calculations [412–414] have converged to improve the understanding of tungsten. Including sufficient pathways from stages with open $4d$ and $4f$ shells was required for DR calculations and the complex atomic structure has large effects on the radiated power also. Systematic studies of the atomic

configurations needed so as not to underestimate the cooling function of high-Z elements [415, 416] are being used, in conjunction with spectroscopy, to diagnose the metallic plasma content of JET [417]. Figure 103 shows the advance in the theoretical abundances and radiated power of tungsten from the time of the ORMAK spectra to today. There is a relatively small spread in the total (equilibrium) power for the core ions which reduces any atomic uncertainty in the confined plasma predictions. The greatest change among the lower charge ionization stages corresponds to temperatures up to ~3 keV which spans the important SOL and pedestal region for ITER. Verifying the radiation from these stages by independent experiment is more difficult but the identification of spectra from W^{6+}–W^{30+} in EBITs and fusion experiments will enable this [418].

The spatial profile of emission is largely determined by the local electron temperature and impurity transport. There is a lesser dependence on the local electron density through the effective atomic coefficients. For the emission model described here the evolution of an ionization stage, n_z, is given by the continuity equation

$$\frac{\partial n_z}{\partial t} = -\frac{1}{\psi}\frac{\partial}{\partial \psi}\left(\psi \Gamma_z\right) + n_e\left(n_{z-1}S_{z-1\rightarrow z} + n_{z+1}\alpha_{z+1\leftarrow z}\right)$$

where ψ is the flux surface, n_e the electron density, S the ionization rate and α the recombination rate. The particle flux is given by an empirical ansatz,

$$\Gamma_z = -D_z\frac{\partial n_z}{\partial \psi} + v_z n_z,$$

where D can be considered as a diffusion term and v describes a convection process. In the absence of a robust, predictive, model for impurity transport a sensitivity analysis is used to quantify the effect of transport on the predicted emission. Figure 104 shows the modeled emission of iron x-ray and VUV lines for a set of transport coefficients which fall into an envelope of values which should include the 'real' value. The D and v coefficients are paired to give a set of $n_D \times n_v$ combinations and the influx to the simulation is adjusted to give the same concentration, 10^{-4}, for each transport. This normalization results in a spread of total radiated power between 3.5–8.5 MW for the high performance scenario. Coronal equilibrium, corresponding to no transport, is a hard limiting case and falls within the envelope of possible emission. Since the spatial variation in the resultant emission is not of the same order of magnitude as the transport variation, the dependence of the modeled emission on transport can be taken to be not a primary driver and a generic set of coefficients may be safely used for the purposes of diagnostic design.

The typical transport used for previous emission modeling for diagnostic design, adopts a shaped diffusion profile, consistent with many experimental results, and an edge convection in the outer plasma (shown in red in figure 104). In the core where diffusion dominates ($0 < r/a < 0.7$) there is little difference from the coronal and constant diffusion models, although the radiation is 1%–5% smaller due to the lower diffusion inside r/a ~0.4. The biggest difference is as the edge

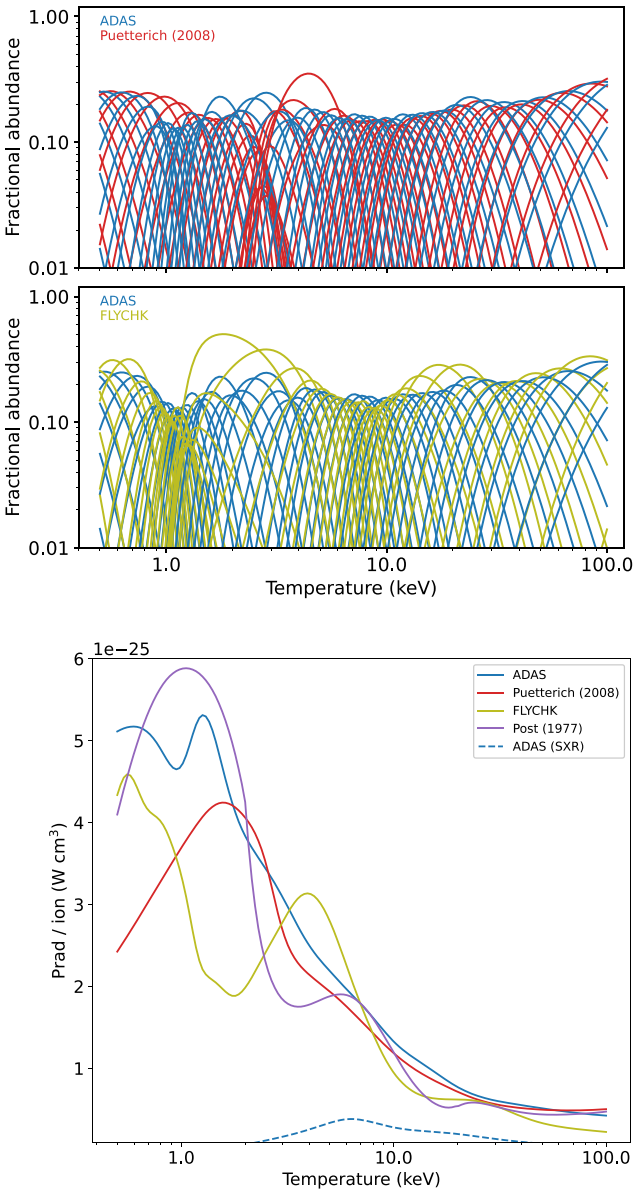

Figure 103. The fractional abundance and radiated power (cooling curve) of tungsten from the current ADAS recommendation, the empirical adjustment of ADPAK [358], FLYCHK [419] and the average ion method [329]. The dashed line shows the radiation fraction in the SXR energy band for a diagnostic with a 250 μm beryllium window and a Si-diode detector.

and is wholly due to the inclusion of the convection term. A number of papers analyzing JET transport [420–422] show an outward pinch, or positive convection, in the outer part of the plasma, peaking at $r/a \sim 0.8$. Including this effect gives a different distribution of ionization stages, although the effect on the total volume-average power is modest.

For SXR and bolometry the mixture of impurities is an additional choice since the current designs integrate over energy and therefore cannot discriminate between different impurities. The power coefficients are filtered over any transmission function, foil absorption and reflection in bolometers [423] or combined window and detector response in SXR cameras, similar to the JET system [424]. The emission model

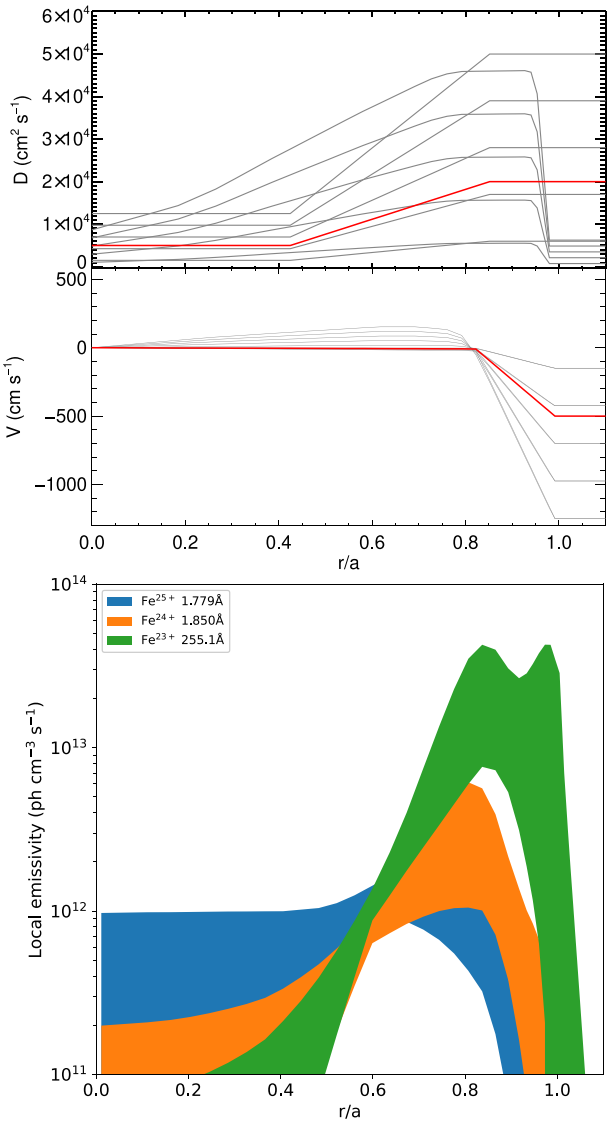

Figure 104. A transport sensitivity analysis for x-ray and VUV iron lines in a 15 MA high performance scenario. The coefficients in red are generic values used for most of the simulations. The transport was varied and the concentration normalized to 10^{-4}.

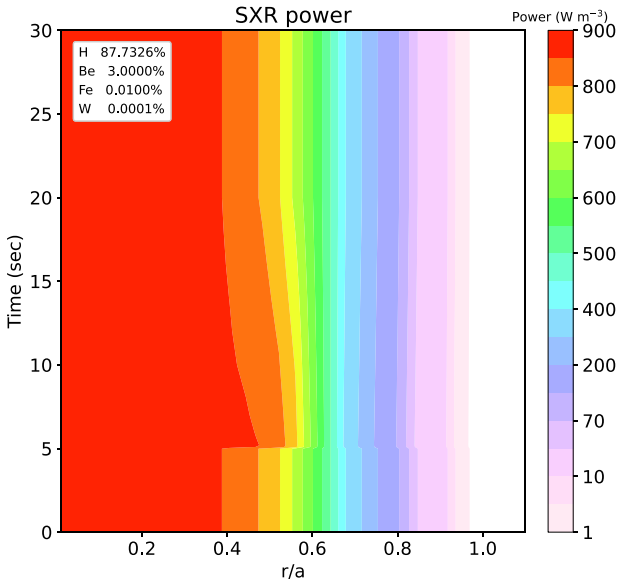

Figure 105. The SXR response of the emission from a plasma with 4% Be, 0.01% Fe and 0.0001% W in the steady state phase of a 13.8 MA hybrid ITER plasma. The SXR energy range is set by a 250 μm Be window and a Si-diode response [424].

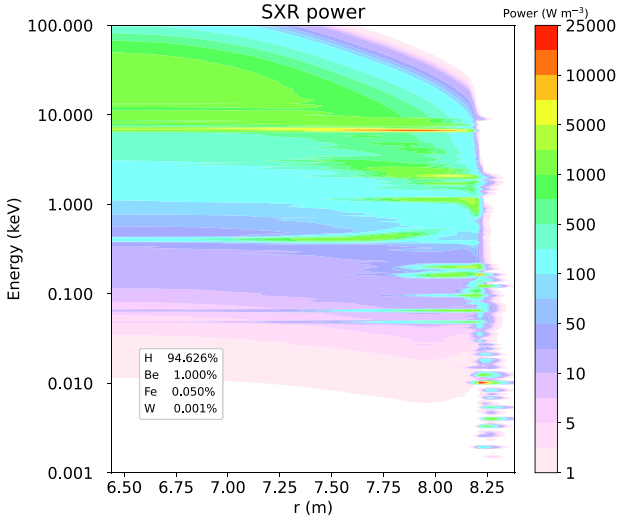

Figure 106. The radiation profile for a high power 15 MA ITER plasma with an expected impurity mix. The radiated power is split into 256 energy bins with the energy is distributed in bins of equal spacing in log-space.

can be extended in the time domain to simulate sawteeth and ELMs. Figure 105 shows the predicted response of a sawtooth crash on the SXR emission for a typical mix of ITER impurities.

5.4. Quasi-spectroscopy of energy-resolved SXRs

A map of the energy-resolved radiation profile, in figure 106, for a likely species mix in ITER shows the potential to extract enhanced diagnostic information if the SXR imaging system was extended in energy space, i.e. moving towards coarse spectroscopy but having a much wider energy overview than the narrow bandwidth of spectrometers. The shape of SXR emission in the core could be used to measure the temperature profile, simplifying multi-energy SXR analyses such as [425] by removing the need to disentangle SXR emission mediated by different foil thicknesses. Furthermore, depending on the resolution, dominant spectral lines many be measurable.

The proposed SXR camera for ITER [313] is a conventional design optimized for a fast temporal response when measuring MHD activity, disruption precursors and ELMs. The emission is integrated over a large energy range bounded by a beryllium window which filters emission below ~2 keV and a silicon diode detector which decreases in efficiency with increasing energy from near 100% at 4 keV to ~1% at ~30 keV [426]. Similar systems are in use in present day machines and operate successfully within their, potentially detector damaging, x-ray and gamma ray environments. ITER will have much larger

intensities and detectors will be exposed for much longer so enhanced radiation hardening may be required. There are significant advances in detector technology so an upgrade is envisaged before the DT phase of ITER operations.

The high x-ray luminosity of synchrotrons and particle colliders has led to the development of radiation hardened semiconductor detectors. The PILATUS3 detector from Dectris Ltd is an array of 195 $\times$ 487 photodiode pixels built on a 450 μm n-doped silicon substrate and is sensitive to x-ray photons between 1.6 and 30 keV. An imaging, multi-energy, SXR pinhole camera with this detector has been demonstrated at MST [427] where line emission and the SXR background, and even hard x-rays from runaway processes, has been clearly measured.

In astrophysics a spectral resolution of a few eV in the keV energy x-ray emission is required to address certain outstanding questions. Framing diagnostic needs, and the precision of other inputs such as atomic data, in such a fashion is typical [428]. Space borne instruments need to be radiation hard and microcalorimeters have been developed to provide the necessary resolution and robustness. The SXS high-resolution, high-throughput spectrometer on the ill-fated Hitomi Satellite had such a detector with an energy resolution of $\sim$7 eV at 6 keV and a range of 0.3–12 keV [327], although this is tuned to a narrower range of a few 100 eV for each observation. Microcalorimeter detectors have been proposed for the ITER core x-ray spectrometer [429] and were prototyped at MST [430]. However there is a concern that the neutron flux may cause a temperature rise in the microcalorimeter absorbers and thus affect the measurement.

In addition to high x-ray photon fluxes, tokamaks during DT operation will also generate a large flux of neutrons. The preliminary tritium experiment at JET showed that Si diode detectors would suffer neutron-induced noise to the signal and lasting damage [431]. Operating these diodes with a 3 V reverse bias reduced performance losses arising from radiation damage but a pinhole arrangement with concrete shielding [432] was required to enable successful measurements during the first JET DT experiments [433, 434]. This configuration was retained for the 2021 JET DT experiments. The DT neutron fluence onto the JET detector ($\sim 10^{13}$ncm^{-2} [432]) is a few orders of magnitude lower than the fluence expected for ITER ($\sim 10^{16}$ncm^{-2} [173]). Therefore, SXR detectors in ITER must also mitigate neutron damage.

A minimalist approach is to remove the detectors from a direct LOS to behind extensive shielding but this requires a method to guide x-rays of energies 0.1–15 keV (0.08–12 nm) along a light guide. The SXR wavelengths have a length scale similar to the lattice constants of crystals that can be considered as transmission guides but polycapillary lenses, which are thin hollow tubes of borosilicate glass, can be used to manipulate x-rays via multiple total external reflections at grazing incidence. However the transmission losses can exceed >99.9% [435]. The impurity mix in figure 106 results in a volume average power of 54 MW of which 35 MW is in the SXR 2–25 keV energy band. This results in a flux of 52kWm^{-2} through the LCFS so even though the transmission

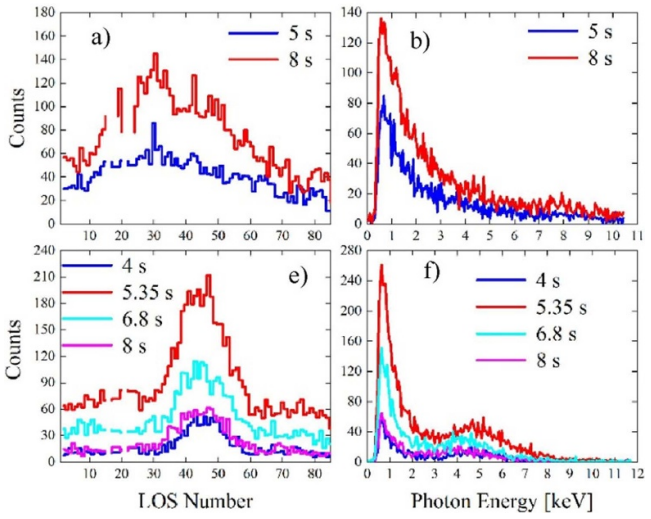

Figure 107. The measured counts per 50 ms from a pinhole imaging camera with GEM detectors on WEST for two shots. The channels start (#1) on the high field side and terminate on the low field side (#85). Reproduced from [440]. CC BY 4.0.

fraction of the polycapillary lens is small, the viewed flux is substantial. A study of the ITER SXR system with polycapillary x-ray transport concluded that their use in an ITER context is feasible [436]. However this loses the many advantages of a multi-energy measurement.

Detectors based on the interaction of tokamak originated x-rays and pressurized gas chambers such as the low voltage ionization chamber (LVIC) [437] and Gas Electron Multiplier (GEM) [438] have the potential to be extremely resistant to neutron damage. However unlike the semiconductor and microcalorimeter based detectors, these systems may need more post-processing to separate the photon energy into convenient bins.

GEM detectors operating in a photon counting mode can discriminate on the energy of the impinging photon [439]. An energy resolved measurement from an lower hybrid current drive heated WEST plasma [440] is shown in figure 107. This plasma is dominated by tungsten emission and good energy and spatial resolution has been demonstrated. The robustness of GEM detectors to neutron effects was examined in a post-mortem analysis of a test system at ASDEX Upgrade which showed that internal parts were activated by the neutron flux (DD so many orders of magnitude lower than ITER) and added noise to the signals [441]. All materials are affected to some degree but it may be possible to engineer a device for ITER to minimize this form of instrumental error.

The neutron resilience of LVIC detectors is based on their simplicity, being a simple tube with gas under pressure (up to 5 bar). Energy resolution may be achieved by adding multiple anodes [442]. Figure 108 shows the arrangement of 5 anodes placed along a 150 $\times$ 2 mm chamber. The positions at 1, 3, 10, 35 and 100 mm respond at increasingly higher energies. The response of the deeper chambers is dependent of the preceding ones *viz.*,

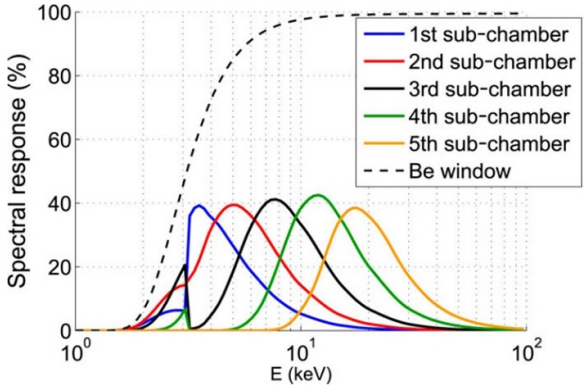

Figure 108. The spectral response of an argon filled LVIC with anodes placed at 1, 3, 10, 35, and 100 mm from the entrance which is a 250 μm beryllium layer. Reprinted from [442], with the permission of AIP Publishing.

$$\eta_i(h\nu) = T(h\nu)A_i(h\nu)\prod_{k=1}^{i-1}(1-A_k(h\nu)),$$

where T is the transmission of the beryllium filter and A_i the absorption of the ith chamber (defined in terms of the gas density and photoionization probability at the energy of the incoming x-ray photon $h\nu$ (section III-A of [442])). There are no measurements with multi-anode LVICs of SXR emission from tokamaks but the response of the detector to mono-energetic x-ray emission from a synchrotron has been characterized. The saturation voltage response of a prototype was measured at the Shanghai Synchrotron Radiation Facility [443]. There was good agreement with a model of the device for energies between 15 and 20 keV but the calculated responsivity was 60% overestimated at 10 keV. The results are promising but improvements are possible by reducing leakage current and choosing an optimal gas mixture. Further synchrotron experiments are planned before a prototype diagnostic is tested in a tokamak. This optimization, and future analysis, of LVIC measurements is best undertaken by constructing a synthetic diagnostic with controls over the LOS and the arrangement of the sub-chambers in each detector. This approach is relevant for all diagnostics and such work on passive spectroscopy is addressed in the next section.

5.5. Analysis and determining physics quantities

The measured signals must be transformed into usable quantities which for ITER are classified by their role in MP, plasma control or physics evaluation. A comprehensive set of *measurement requirements* details the desired measurement, resolution (spatial and temporal) and accuracy needed to achieve the measurement [4]. Different levels of sophistication in analysis are needed to achieve the various requirements from the passive spectroscopy diagnostics. For survey spectrometers just the appearance of a spectral line is sufficient to identify an impurity in the plasma. However even this most simple analysis depends on a good wavelength calibration and the tabulation of transitions, preferably previously observed in other

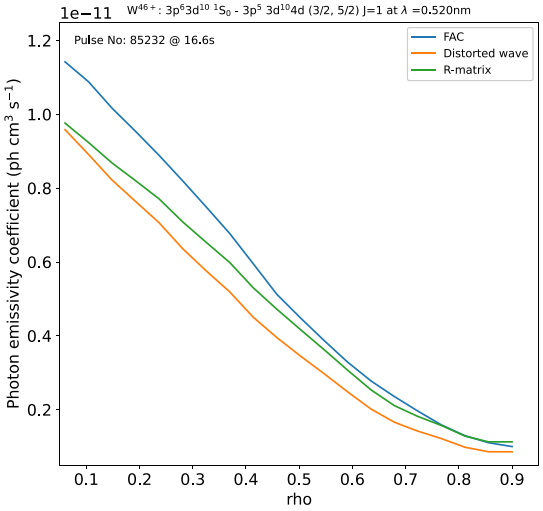

Figure 109. The photon emissivity coefficients, given as a function of the profile conditions for JET pulse #85 232 (central T_e~3.5 keV and N_e~4 × 10^{19}m^{-3}) for the Ni-like W^{46+} line used to determine a tungsten concentration [444].

tokamaks. Apart from tungsten, the plasma facing materials of ITER are well characterized, and the many spectroscopic investigations of tungsten outlined in section 2, have ensured that this analysis is well prepared for ITER plasmas.

Not all spectrometers in use on present day tokamaks are calibrated for intensity. However, a reliable intensity calibration is essential for quantitative measurements and periodic recalibration may be required to account for changes over time. Possible causes are due to mirrors or windows being coated by plasma detritus, degradation in detectors, optical fibers, cables and electronics from the x-ray and neutrons produced by the plasma (see other articles in this review).

Some of these issues are not present in vacuum-coupled systems, such as x-ray spectrometers, but the accuracy of the result is also determined by the precision of the atomic data used in the analysis. Inner shell x-ray transitions in Ni-like and Cu-like tungsten, have been used to estimate the tungsten concentration in JET (~10^{-5} in ELMy H-mode) [444]. That analysis used photon emissivities calculated with the relativistic distorted wave code FAC [445]. Figure 109 compares the PEC for the W^{46+}: $3p^6 3d^{10}\,{}^1S_0 - 3p^5 3d^{10}4d(3/2,5/2)J = 1$ line with Breit-Pauli distorted wave and a relativistic R-matrix with radiation damping calculation [401]. The plot follows the style of figure 4 of [444] showing the PECs across the JET plasma profile. The spread in values between the FAC and R-matrix models could be used as an error bar on this part of the analysis, which would suggest a contribution of ~20%. However the analysis in [444] is more refined in that it also uses a similar inner shell line from W^{45+} and Nelike W^{32+} lines. More than one ion brings in a dependence on the ionization balance, which introduces a further uncertainty as seen in the different models of fractional abundance in figure 103. It is likely that propagating the uncertainties of the atomic data can be as important, and may be even more dominant, than considering

the usual instrumental uncertainties. Historically computation effort in atomic data was directed to improving the scope of the atomic models but there is a growing activity to produce assessed uncertainties on *ab initio* atomic data, e.g. [446] for astrophysics. A number of technical meetings and workshops organized by IAEA have fostered this uncertainty quantification (UQ) effort in the fusion community [447].

Theoretical and computational improvements are still required for atomic data models. For example, it should be noted that there is no R-matrix data available for the equivalent inner shell transitions for W^{45+}. Another example is that differences of up to 40% in the S/XB coefficients for Ar^{+} transitions were found between simple R-matrix and R-matrix with pseudo states (RMPS) models [448]. The later model includes coupling to the continuum levels which are important for neutral and near-neutral ions. In this case using the theoretical spread of values would give a severe over-estimation of the atomic error.

Spectral features, such as the quasi-continuum of figure 92, are composed of many thousands of spectral lines from a number of ionization stages ($W^{27+}-W^{45+}$ for the 4–5 nm tungsten feature). The large number of transitions are due to the many possible energy levels when coupling partially open d and f shells. Combining the radiated power from lines, resolved by J total quantum number, of the lowest lying configurations with configuration-average rates for the rest is reasonable for total radiated power, or data for energy-resolved SXR emission [415]. However this approach may not be sufficient for a spectral prediction to be confronted with experiment. Furthermore, configuration interaction effects alter the shape of the QC features without affecting the total power radiated. An example from laser plasmas, a little higher in electron density than tokamak plasmas, shows that transitions between excited configurations also affect the shape of these QC features [449]. Including these, in the necessary J-resolved resolution, adds orders of magnitude more lines [450]. The shortcomings in the atomic spectral model can be seen in the, deliberately simple two-temperature zone model, with the ADAS fractional abundance data of figure 103 and distorted wave generated feature photon emissivities (f-PEC). The qualitative nature of a dominant low temperature part at ∼1.6 keV, with some emission from a higher ∼3.5 keV component, is compatible with the temperature profile and the cooling effect of a large tungsten influx. The identification of the contributing stages to the spectrum in [325] confirms that the missing piece of the modeled QC feature is due to emission from $W^{26+}-W^{29+}$. A more adaptive partitioning scheme in the atomic model will be needed to enable the modeled spectral feature to be fully used in a predictive capacity.

However, the QC feature can still be used in a pragmatic manner because of the nature of the emissivity coefficients. The photon emissivities of the many lines of similar wavelength from the different ionization stages vary little in temperature, a few percent between 1 and 15 keV, across the group so any changes in the measured spectrum can be attributed to changes in the relative abundances. Furthermore, the ratio of the power in the 5 nm QC band to the overall power also has a modest dependence on temperature. In a plasma with a flat density profile and little transport, the concentration of tungsten (c_W) is simply,

$$P_{\mathrm{tot}} = c_{\mathrm{W}} N_{\mathrm{e}}^2 L(T_{\mathrm{e}}, N_{\mathrm{e}}),$$

where P_{tot} is the power contributed by tungsten and L_z is the cooling curve (figure 103). The factor linking the intensity of the QC feature to the concentration of tungsten in a specific calibration measurement can then be extended to a wider range of conditions by adjusting the fractional abundance along the LOS of the observation. This method has been used at ASDEX Upgrade [358, 451] and JET and gives a robust measure of the tungsten concentration without the necessity of a high fidelity fit to the spectrum.

The energy binning of a wide coverage, multi-energy SXR (ME-SXR) detector may not be sufficient to resolve the 5 nm QC feature but the desirable characteristics of 2D imaging and fast response to MHD events remain. Tomographic techniques are used with current SXR diagnostics [69] and the consideration of the detector response is via filtered cooling rates. The fraction of radiated power filtered by the beryllium window and Si-diode detector is shown in the dashed (SXR) curve in figure 103. The SXR emission is moderately sensitive to the filter function, as seen in the mis-matched beryllium window widths of the vertical (250 μm) and horizontal (350 μm JET SXR system [424]. The difference in response can be accounted for in the tomography with a, computationally expensive, correction factor in the contribution matrix. Other effects such as the different energy signatures of each impurity can also be used to improve the SXR analysis [452]. However true ME-SXR requires that the detector response is properly included in the analysis. Incorporating the detector energy behavior into the tomographic analysis has been demonstrated at WEST. The GEM detector response over 1.5–10 keV was used to include a transport model which enabled the tungsten emission at different positions to be disentangled from the SXR signal (utilizing the variation similar to that in [453]). Figure 110 shows that a 5-position LVIC ionization chamber can reconstruct the energy dependent radiated power signature, including lines and the shape of the continuum background, in the 1–100 keV region for a high performance ITER plasma [442]. Figures of merit (FOM) for each pixel in the tomographic analysis are good in the core ($\rho < 0.8$) for strong line emission and for the background above 15 keV but are poor in the edge region. The 200 μm beryllium window cuts off much of the edge emission but the good core FOMs show the potential of ME-SXR for measuring general impurity content and as a way to measure the electron temperature profile at very high core temperatures where TS becomes difficult.

Extracting useful information from some measurements does require a sophisticated model of the emission. A measurement common to all tokamak plasmas is the visible Balmer-α line from hydrogen or its deuterium and tritium isotopes. Even before the current metallic wall choice for ITER, the difficulties caused by contamination of the signal due to reflections from the wall in DIII-D (CFC tiles) and Alcator C-Mod (molybdenum) was quantified as being small (<10%) for divertor views but could be significant (up to 50%) for the

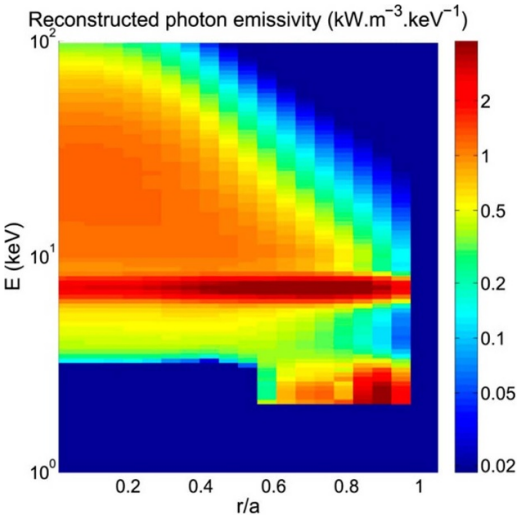

Figure 110. The reconstruction of the upper 20% (1–100 keV) radiation of the high performance ITER plasma of figure 106. The modeled LVIC detector chamber is filled with xenon at atmospheric pressure with anode sizes of 5, 30, 60, 100, and 150 μm behind a 200 μm thick beryllium window. Reprinted from [442], with the permission of AIP Publishing.

main chamber [454]. A model of the reflections of Balmer-α in an ITER scenario based on the measured BRDF of Inconel™ tiles from JET showed that diffuse reflection, in addition to specular, was significant [455]. A practical mitigation strategy is to terminate the LOS on a viewing dump but this is not always possible so a good synthetic model of the feature is necessary.

An additional complication for main chamber Balmer-α is the strongly non-Maxwellian VDF caused by recycling in the SOL. The effect of both recycling and stray light contamination is seen as an asymmetric line profile that requires a HES and a reflection propagation model to disentangle the contributions and provide a clean measurement. A model of the Balmer-α emission is constructed and used to solve the *inverse problem* [456]. Strong constraints from Zeeman splitting separate the low and high field emission regions and a semi-analytical description of the shape of the stray light from the divertor, assuming multiple specular reflections of a homogeneous divertor source [457], makes this a robust model for fitting. This approach has been successfully validated with JET observations and figure 111 shows the variation in shape of the line from a limiter view of JET [458]. The contributions of the SOL emission from the high field and low field are very different at different phases of the discharge and there is significant emission due to stray light reflections from the divertor.

An additional complication for main chamber Balmer-α is the strongly non-Maxwellian VDF caused by recycling in the SOL. The effect of both recycling and stray light contamination is seen as an asymmetric line profile that requires a HES and a reflection propagation model to disentangle the contributions and provide a clean measurement. A model of the Balmer-α emission is constructed and used to solve the *inverse problem* [456]. Strong constraints from Zeeman splitting separate the low and high field emission regions and a

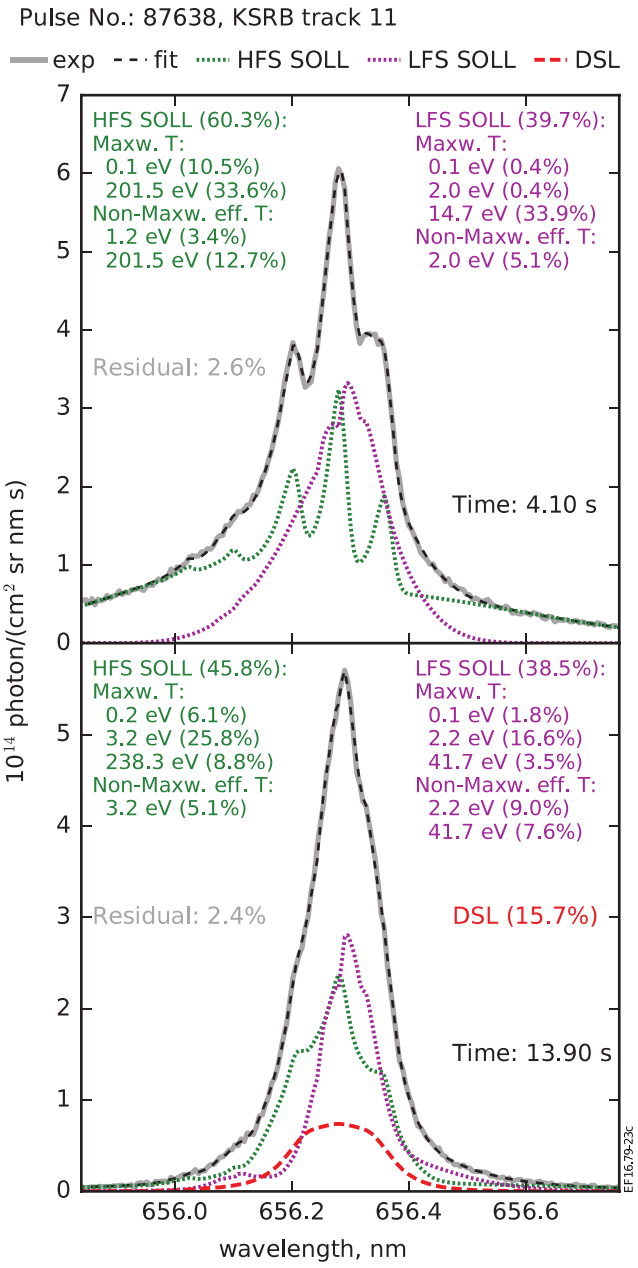

Figure 111. A fit to the Balmer-α spectrum from the inboard limiter in the octant 8 of JET (pulse 87 638 with KSRB spectrometer) during plasma ramp-up ($t = 4.1$) and at steady state with ICRH heating ($t = 13.9$ s). The fit parameters for the SOL light from the high field side (HFS) and low field side (LFS) are show, along with the contribution of stray light from the divertor (DSL). Reproduced from [458].

semi-analytical description of the shape of the stray light from the divertor, assuming multiple specular reflections of a homogeneous divertor source [457], makes this a robust model for fitting. This approach has been successfully validated with JET observations and figure 111 shows the variation in shape of the line from a limiter view of JET [458]. The contributions of the SOL emission from the high field and low field are very different at different phases of the discharge and there is significant emission due to stray light reflections from the divertor.

Reflections are typically modeled by optical ray-tracing to produce a transfer matrix relating the reflected light originating from different sources to each point in the plasma volume [459]. Tomographic techniques can then be used to incorporate this contribution in a diagnostic analysis. The accuracy depends on knowing the reflecting properties of the tokamak vessel's interior materials (BRDF) and the source and axisymmetry of the originating light—from the divertor, SOL or core. The reflectivity of in-vessel components will change during operations, via depositions and roughening (see subchapter 9 on mirrors) so ideal, or even measured pristine surface BRDFs may not be useful. However, ideal, rather than real, reflectivities are sufficient to determine favorable locations for diagnostics, as done with the Visible Spectroscopy Reference System (VSRS) diagnostic for ITER [307]. Calibrating the reflectivity response with a small volume plasma has been demonstrated on COMPASS [460] but this method may not be feasible to mimic the intense radiation from the divertor.

Combining a comprehensive emission model with a verisimilar reflection model produces a Balmer-α synthetic diagnostic [456]. The use of synthetic diagnostics, which is a methodology to generate numerically what the diagnostic system will see, can be used to test the success of the algorithms used to recover the desired MP. Many spectral emission models are being incorporated into the CHERAB [136] spectroscopy modeling framework, which uses ADAS as a primary source of atomic data. This implements an, optimized-for-tokamaks, ray tracing code Raysect [461] to model the reflections in a realistic geometry. Figure 112 taken from [462] shows how well a good synthetic diagnostic could be used to tune an analysis applied to assessing the best placement of the fields of view (FoV) for the DIM. The results are dependent on the environment and in particular on the unmeasured and uncharacterized BRDF. With a synthetic diagnostic the effect can be quantified by adjusting the roughness in the reflection model and a more refined error estimate, calculated for each FoV rather than a single overall percentage, may be determined [463].

A synthetic diagnostic for each spectroscopy system enables enhanced utilization. Two aspects are explored in detail in later chapters. Combining diagnostics provides a much fuller picture of the plasma performance, but its success relies on a good description of each input. A synthetic diagnostic may be parameterized, either by a reduced model or via machine learning, which enables complex analysis to be performed in real time.

5.6. Summary

Much of the worldwide effort in passive spectroscopy since the last ITPA review has revolved around preparing to make quantitative, high quality, measurements of the emission expected from ITER. The ITER environment with significant neutron, gamma and x-ray fluxes, and long duration discharges, will pose a challenge to deploying reliable and stable diagnostics. The spectroscopy of tungsten will be a defining aspect of the passive emission from ITER because it will radiate from all parts of the plasma and will be a mixture of quasi-continuum

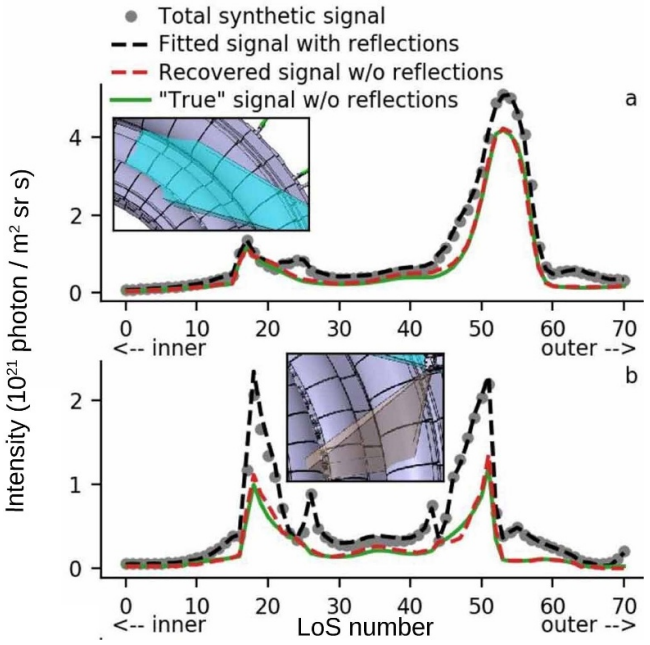

Figure 112. A The contribution of reflections to the D-α signal for an equatorial (*a*) and upper (*b*) port view of the divertor impurity monitor (DIM) diagnostic for ITER. Simulated signals and the recovery of the real signal by removing the contribution from reflection are shown. Reproduced from [462].

spectral features and individual lines. The 74 electrons of tungsten, and the need to consider in detail at least 70 of its stages—even ITER will not be hot enough to ionize the He- and H-like stages—has been a grand challenge to calculate atomic data which underpin the models and the analyses that flow from them [419].

Plasma experiments, dedicated spectroscopy programmes, new detector technologies, diagnostic system prototypes, fundamental atomic data calculations, atomic cross section measurements and the development of better algorithms and sophisticated analysis codes have been undertaken in recognizable fusion institutes but also in many universities and other laboratories so that useful measurements will be possible from the first ITER plasma.

6. Laser aided diagnostics

R. Scannell[28], H. Liu[26], E. Mukhin[29], E. Yatsuka[14], A. Gorbunov[27], L. Giudicotti[30], G. Kurskiev[29], J. Chen[10], M. A. Van Zeeland[4], D. Finkenthal[31], R. Imazawa[32], D. Brower[33], A. Sirinelli[2], T. Akiyama[4], T. Carlstrom[4], D.W. Johnson[21], M. Lesher[4], C. Watts[2] and M. Bassan[2]

6.1. Introduction

The required plasma measurements to make ITER a success, of which laser diagnostics are a crucial component, flow from the ITER overall PRs document [464]. The PRs document details what must be achieved by the ITER plant based on the underlying physics. From this document, the particular

requirements for individual diagnostic systems are derived and detailed in the ITER diagnostics requirements document [197]. The means of meeting the measurement requirements for ITER was initially addressed in [3] for the full diagnostic set and in particular for laser diagnostics in section 3.3 of this document. Further progress in diagnostics systems with specific examples was last set out in 2007 and published in [4].

This current paper details the status of the various laser diagnostics that will be used to meet the measurement requirements. Each section contains links to relevant background to properly introduce each diagnostic system.

As well as describing the various diagnostic systems themselves relevant techniques are also discussed. Polarimetric and dual laser TS techniques which are particularly useful for TS systems on ITER are introduced. Neither are routinely employed on existing tokamaks but they are being tested with a view to application on ITER. The polarimetric technique in particular has developed considerably since the last update to the ITER physics basis.

The Laser Induced Flourescence (LIF) diagnostic which will be integrated into the DTS diagnostic is a new advance also relative to the ITER physics basis published in 2007. The Toroidal Interferometer Polarimeter (TIP) system, which is planned to be used for real time density control at ITER, has recently been prototyped and deployed in a test capacity at DIII-D. While the PoPola (Poloidal Polarimeter diagnostic has been in the ITER diagnostic set for some time, it is proposed use for magnetic fluctuation measurements and plasma vertical control are a recent development. The final diagnostic discussed is the Dispersion interferometer which is another recent innovation. Due to its configuration, it is highly resistant to vibrations making it a very robust measurement tool and motivating its application for ITER.

6.2. Core TS

The ITER core plasma TS (CTPS) diagnostic was originally envisaged as a LIDAR design [465]. However, the design has been modified to follow a conventional TS layout, shown in figure 113, which operates at high scattering angle. A detailed design trade-off between the LIDAR and conventional design solutions was considered in making this decision. Some of the main factors motivating a conventional design were easier availability of detectors and laser, higher spatial resolution and longer beam dump lifetime.

The CPTS diagnostic must meet requirements on its performance which derive from the ITER PRs [464]. The CPTS diagnostic has a number of common elements with the edge TS diagnostic, since both systems are conventional systems based on Nd:YAG lasers operating at high scattering angle. Particularly important common elements include the beam dump [467, 468] and solutions for laser beam combination [469] as well as laser and collection optics alignment. Particularly important differences with the edge system are the more challenging optical labyrinth (neutron attenuation) trade-off for CPTS, larger first aperture and hence shutter requirement for the CPTS and requirement for the CPTS

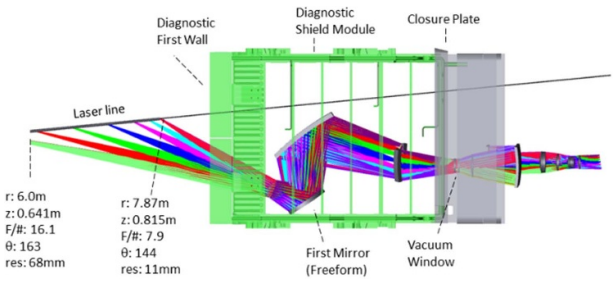

Figure 113. Optical design of CPTS diagnostic. Mirrors are number in order of light propagation from the plasma The first and second and sixth mirrors from the plasma are free form. The approximate parameters for the furthest in and out most measurement points are indicated. Reproduced from [466]. © 2017 ITER Organization. Published by IOP Publishing Ltd on behalf of Sissa Medialab. All rights reserved.

to measure to higher electron temperature and hence lower wavelength.

The main components of the proposed system are a 5 J, 100 Hz, 4 ns laser system, envisaged to consist of at least 2 lasers for redundancy, an optical system collecting at F/14.7 at $r/a \sim 0.02$ at ∼167degrees varying to F/7.6 at $r/a \sim 0.85$ at ∼155degrees. The CPTS system design has capability for measurement of 'p' as well as 's' polarized scattered light, originally proposed by [470] and detailed further in [471]. The proposed CPTS system also includes a 1319 nm 10 Hz 2 J laser operating in conjunction with the main 1064 nm laser. This multi-laser approach has been suggested for each of the ITER TS diagnostics motivated by requirements for calibration and to reach high electron temperature; a recent consideration has been made in [472].

In order to achieve good optical performance and neutron shielding, freeform optical elements have been included in the new optical design. These are challenging to implement, in particular in conjunction with the requirement for a mirror cleaning system for the first mirror but promise benefits in performance. Considering simulated ITER profiles, density and temperature gradients imply that higher spatial resolution is required in the mid-radius and outboard region than in the core. This higher resolution is naturally achieved for a fixed fiber bundle size due to the change in collection F/#.

The main challenges facing the diagnostic are in terms of survivability of PFCs in the harsh operating environment, the long duration of 4700 h of operations and the inaccessibility during this operating period. Some of these key engineering challenges are listed below:

- Survivability of the first mirror in a harsh and unknown plasma environment where deposition is expected [473].
- Demonstration of a mirror cleaning system compatible with the first mirror [474], particularly if free form.
- Engineering implementation of a mirror protection shutter at high reliability. This shutter must contain cooling channels.
- Active alignment of the scattering lasers to the beam dump to maintain sub-cm alignment during plasma pulses.
- Survivability of the laser beam dump.

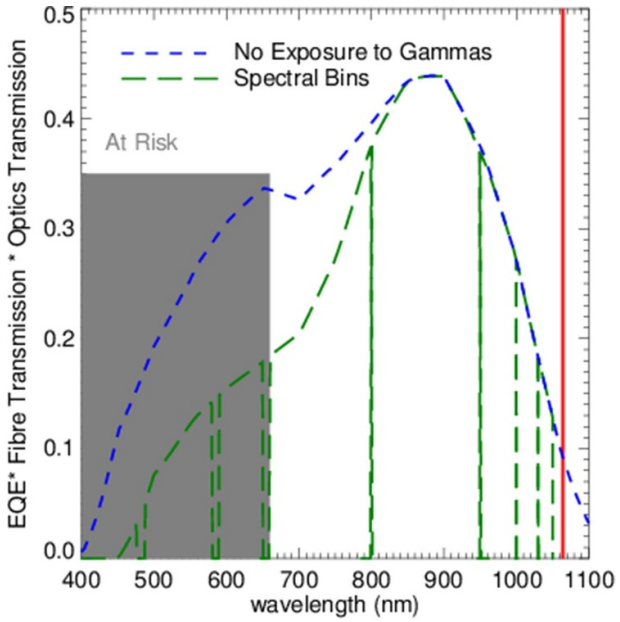

Figure 114. Optical transmission of the CPTS diagnostic including full information of spectral transmission of the various collection optic elements, the detector EQE and optical fiber transmission. The optical fiber transmission includes expected degradation for the 'intermediate' OH fiber after 10 kGy of radiation. The 'at risk' region, which may suffer further transmission losses is highlighted. Reproduced from [466]. © 2017 ITER Organization. Published by IOP Publishing Ltd on behalf of Sissa Medialab. All rights reserved.

As well as diagnosing electron temperature profiles more generally, one of the particular key goals of the CPTS diagnostic is to measure the peak core T_e value. This peak core T_e will be an important indicator of ITERs success. This implies that the diagnostic must measure to the lowest possible wavelength ~400 nm see figure 114. There are a number of factors that make measurement at this very low wavelength difficult, in particular first mirror reflectivity losses are expected to be high in this region, as will transmission losses for optical fibers and Cerium doped lens elements in the interspace. Also, there is significant line emission in the lower wavelength region. However, there are new diagnostic advances that should aid the CPTS in these crucial measurements and help distinguish from any spectral transmission uncertainty at the edge of the wavelength region. These advances are 'Polarimetric' TS, measuring the polarization of the scattered light and use of a 1318 nm Nd:YAG laser. The theoretical concepts behind these techniques have been further developed in the last few years. Polarimetric and two-wavelength TS are now being prototyped and tested on existing machines.

6.3. Edge TS (ETS)

ETS has an important specification to measure the region of $r/a > 0.85$ with a spatial resolution of 5 mm in order to measure the steep electron density and temperature gradient in H-mode discharges. The electron temperature range covered by ETS is 0.05–10 keV. This temperature range is measured from 590–1060 nm with six-channel polychromator spectrometers.

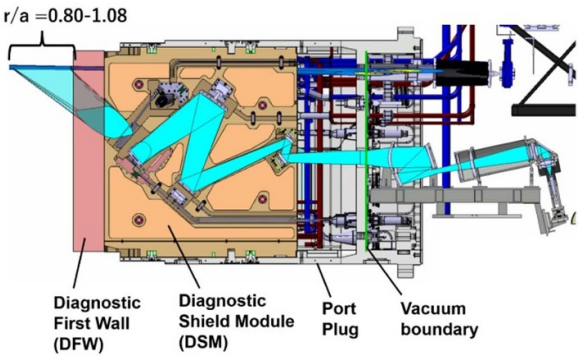

Figure 115. Configuration of the ETS collection optics. Inside the port plug, it consists of only mirrors, and outside the port plug, it consists of mirrors and lenses.

To detect enough photons, the F-number of the ETS collection optics varies from $F/15.2$ to 21.7. While using such a high collection optical system, it is a challenge to minimize chromatic aberration over the above-mentioned wavelength band and to be compatible with radiation shielding. The key engineering challenges are the same as the five listed in the CPTS section.

The optical path of the collection optics forms a labyrinth in the port plug to pass the collected light and to shield neutrons from the plasma. No lens is used in the port plug to avoid fracturing of glass due to vibrations during plasma disruptions. The collection optics are capable of collecting light from a normalized minor radius range between 0.80 and 1.08. The outermost LOS corresponds to the face of the DFW [475]. In order to suppress aberrations, the angle of incidence on the curved mirror was made as small as possible. Figure 115 shows the configuration of the ETS collection optics. Considering the radiation environment near the port plug, it is desirable that the field of view of the collection optics can be adjusted without human intervention. Light propagating in the opposite direction from the optical fiber hits the bracket near the upper port. By observing the vignetting of spots projected on the blanket, the relative relationship between DFW and the observation position can be maintained.

The laser beam dump is mechanically installed on the inner blanket. The space provided for the beam dump is 60 mm wide, 115 mm high and 77 mm deep, including a flange for mounting on the blanket. If the laser beam dump fails, the entire FW structure of a blanket module must be replaced by remote handling maintenance equipment. In order to reduce the risk of laser beam dump failure, the beam diameter should be as large as possible. For this purpose, the beam has to always be incident on the center of the laser beam dump. ETS achieves a temporal resolution of 100 Hz by alternately firing two 50 Hz laser beams. The use of two lasers enables us to perform the TS measurements at a temporal resolution of 50 Hz in case that one of the laser systems stops functioning. In order to maximize the light receiving surface of the laser beam dump, allow use of two laser beams, and suppress the streaming of neutrons along the beam optical path, it is necessary to align the two beams coaxially. Since the scattering angle is about 140 degrees and the measured electron temperature is up to 10 keV,

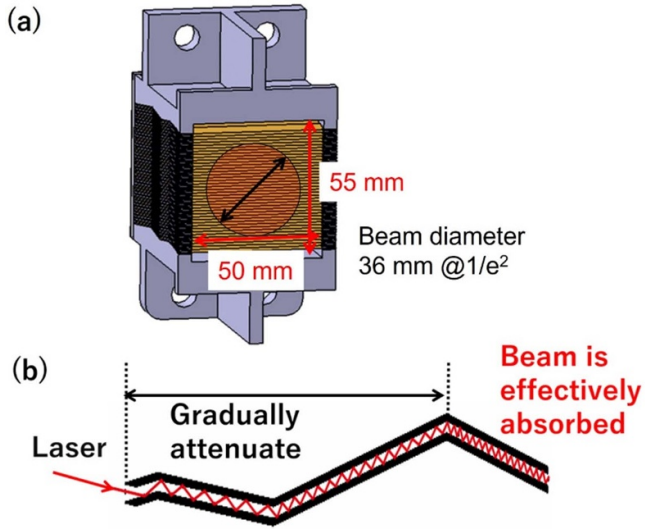

Figure 116. (*a*) Bird's eye view and (*b*) concept of the laser beam dump.

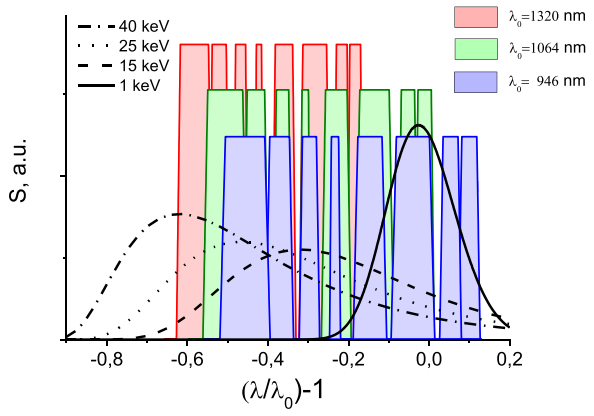

Figure 117. Effective increase in the number of spectral channels for the different YAG probing wavelengths with various T_e spectra overlaid. Reproduced from [472]. © 2015 IAEA, Vienna. All rights reserved.

the depolarization of scattered light is at most a few percent. In order to improve the ratio of Thomson scattered light to the background light of randomly polarized light, a polarizer is installed in the collection optics. The functional requirements for laser incidence and laser beam dump are summarized below. The two horizontally polarized beams must be coaxial and always incident at the center of the laser beam dump. The laser beam dump needs to survive for a long time under the severe heat load of ITER.

A rotating half-wave plate provides a lossless method for combining beams together with stable beam pointing. The polarization extinction ratio of the combined beams can exceed 1000 [476].

In order to inject the probing beam into the center of the laser beam dump, a method for detecting the beam position is required. The beam position at the laser beam dump is monitored by four alignment laser beams which propagate parallel to the probing Nd:YAG laser beam and imaging systems installed outside the port plug [469].

ITER is scheduled to operate for about 4700 h of plasma, and when the beam is incident at a repetition rate of 100 Hz, the number of pulses on the beam dump will be on the order of 10^9. The laser beam dump is made of molybdenum alloy and is designed to withstand high heat loads. To reduce the risk of laser induced damage, the internal structure of the laser beam dump has been proposed as shown in figure 116 [467]. It has a structure in which a large number of 0.5 mm molybdenum alloy sheets bent at several points are arranged in parallel with a clearance of 0.6 mm. In this structure, S-polarized beams are incident at a large angle of incidence (wide area). Therefore, the beam energy absorption density can be reduced to about 1/20 as compared with the case where the angle of incidence is 0. It has been experimentally shown that this structure is advantageous for the survival of the beam dump [468], and it has been confirmed that it can be manufactured [475].

In order for the laser beam to be injected into the plasma, it passes through a vacuum window. The vacuum window is also the confinement boundary for tritium and beryllium. Vacuum windows are expected to be exposed to a total gamma dose of several MGy. A 10 MGy gamma ray irradiation was performed on fused silica windows with an antireflection coating, and then a laser injection test was performed. It was confirmed that the laser-induced damage threshold did not deteriorate [477].

6.4. Multi-color TS

The main calibration laser candidates for the core TS are: second harmonic of Nd:YAG 532 nm and the alternative Nd:YAG lasing wavelengths 946 nm and 1320 nm. Using different probing wavelengths also leads to an effective increase in the number of spectral channels (see figure 117). This can enhance the diagnostics capabilities if the electron VDF deviates from a Maxwellian for example under a strong ECRH/ECCD [472]. For the temperature range 0.5–40 keV the calibration coefficient for each channel can be determined with an accuracy of about 10%. This is not enough since the calibration coefficients should be determined with an accuracy better than 1%–2%. Therefore, averaging over a hundred pulses is required, that poses a problem for usage of a three level Ruby laser with a suitable wavelength of 694 nm which has a low repetition rate. Due to the extremely wide T_e range there is no optimal choice of a supplementary laser, each choice has its own pros and cons. The use of both additional 1320 nm and 946 nm lasers seems to be preferable because this (a) allows successful operation when the spectral sensitivity changes quickly; (b) allows calibration of the system in the entire temperature range; (c) improves the accuracy in the case of non-Maxwellian electron VDF. Usage of a 1320 nm laser is sufficient for system calibration and accuracy improvement both for high T_e measurements and non-Maxwellian VDF. The Nd:YAG 532 nm laser is relevant for calibration only in special ITER regimes within the limited T_e

range. The benefits of additional lasers can be summarized as follows [472]:

- Nd:YAG 1320 nm—advantages: significantly increases accuracy for high temperature measurements $T_e > 10$ keV, spectral calibration is possible for $T_e > 1.5$ keV, increased accuracy in the case of non-Maxwellian electron VDF.
- Nd:YAG 1320 nm—disadvantages: the laser is not yet commercially available, poor T_e accuracy in double laser mode for $T_e < 1.5$ keV, different spectral channels will be calibrated at different temperatures.
- Nd:YAG 936 nm—advantages: calibration is possible over the full temperature range, could be used as the main laser if required.
- Nd:YAG 936 nm—disadvantages: poor T_e accuracy in double laser mode for $T_e > 10$ keV, not useful for non-Maxwellian electron VDF determination, different spectral channels require calibration at different temperatures.
- Nd:YAG 532 nm—advantages: availability, all channels can be calibrated at one temperature, but this range is very short.
- Nd:YAG 532 nm—disadvantages: good T_e accuracy in two laser mode only for 6 keV $< T_e <$ 15 keV, spectral calibration is possible only for 8 keV $< T_e <$ 20 keV, not useful for non-Maxwellian electron VDF determination.

Measurements of T_e as high as 40 keV in the plasma core of a large fusion device such as ITER encounter a number of issues. The most reliable techniques that can be used are TS and ECE diagnostics. In case of ECE a large relativistic and Doppler broadening will have a significant impact on the spatial resolution of the measurements. For example for regimes with core $T_e(0) = 30$ keV obtaining the required spatial resolution of a/30 will only be possible for the outer region of the plasma column, $r/a > 0.5$ [273, 478]. In case of TS diagnostics, the main issue is a significant blue shift for backscattering geometry, see figure 118, while the operational wavelength range is bounded on the blue side (400–500 nm) due to the collection optics transmission and the strong background radiation [472, 479]. The problem will be made worse due to the darkening of the collection optics and fibers under strong neutron and gamma irradiation. In the worst case scenario the lower wavelength limit could be increased to 700 nm thus limiting the TS system dynamic range to a few keV [466, 472]. At high T_e the σ_{Te}/T_e values expected from the 1064 nm laser are limited by the ability to determine the shape of the spectrum, in particular it becomes more difficult to distinguish between increasing temperature and density. Possible solutions to this problem include using an alternative geometry with lower scattering angle, depolarization measurements (see section 2 for details) or using an additional probing wavelength shifted deeper to the near IR range. Nd:YAG lasers have emission lines at 1319 nm and 1338 nm. Using large scale Nd:YAG crystals together with high-power laser diode pumping allows one to realize such lasers operating with pulse energy as high as 1–2 J and a repetition rate of 50–100 Hz. At present a TS system is currently being prepared for experiments at Wendelstein 7-X [480] using a 1319 nm laser. The main advantage of such an approach is the effective shift of spectral channels, see figure 119. This allows to significantly reduce the temperature and density error correlation for 20–40 keV for a 1319 nm laser in comparison with a 1064 nm laser thus increasing the measurement accuracy of n_e and T_e. Moreover, the other advantage of this technique is the inherent *in-situ* spectral calibration.

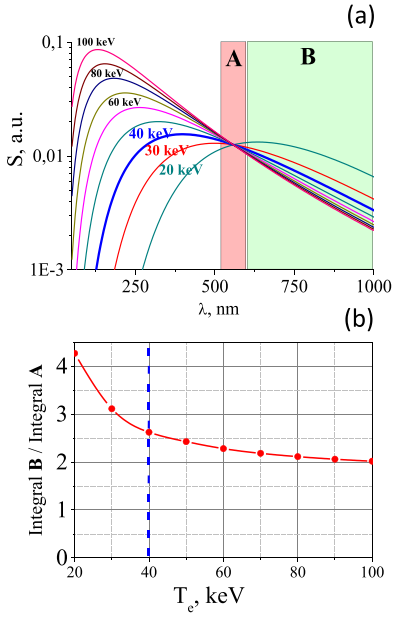

Figure 118. (*a*) Thomson scattering spectra for a scattering angle $\theta = 170°$ and $T_e = 20$–100 keV. The spectra are normalized by the integral in the wavelength range 'A'. (*b*) The ratio of integrals in wavelength ranges 'A' and 'B' versus T_e. Tor high T_e the uncertainty drastically increases due strong interdependence of T_e and n_e.

6.5. Polarimetric TS

Polarimetric TS is an advanced technique for the analysis of TS spectra that exploits the depolarization of the scattering radiation [470]. This is an effect barely noticeable in present-day fusion plasmas, but becomes important in plasmas with T_e of the order of tens of keV, as it is expected in the high T_e regimes of ITER [479]. Polarimetric TS has been suggested as a method to mitigate the loss of accuracy of the ITER CPTS system due to the fact that in the high T_e regimes of ITER the spread of the TS spectrum exceeds considerably the spectral region considered to be useful for the detection of the TS signal. This is the wavelength region 400 nm $< \lambda <$ 1060 nm and its limits are determined by the drop of the silicon APDs quantum efficiency on the long wavelength side and by the region of high background plasma light on the low wavelength side. The spectral region 400 nm $< \lambda <$ 650 nm while also used is considered 'at risk' of transmission loss due to darkening of windows and fiber optics from neutron irradiation. When the plasma T_e is high and the TS spectrum spreads outside the useful detection region, the reconstruction of the shape of the TS spectrum becomes difficult and the expected measurement errors increase. Polarimetric TS provides a method to mitigate this, contributing to keeping the T_e and n_e measurement errors low in the high T_e regime [471, 481]. Recently

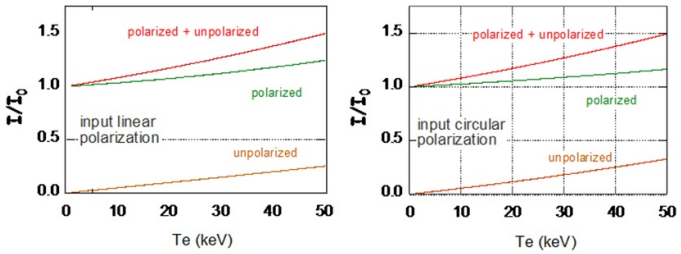

Figure 119. Intensity of the integrated scattering signal (into the full solid angle) as a function of T_e, for an input laser beam with linear and circular polarization. The intensity I is normalized to its value I_0 for a non-relativistic plasma (T_e approaching 0.) The completely polarized and the unpolarized components are also shown. At any T_e the total intensity I is identical for the two input polarizations and increases up to $I = 1.38\ I_0$ for $T_e = 40$ keV. The intensity of the unpolarized component is higher for a circularly polarized input beam, reaching $0.25\ I_0$ at $T_e = 40$ keV compared to $0.20\ I_0$ for a linearly polarized input beam. Reproduced from [481]. © 2017 IOP Publishing Ltd and Sissa Medialab. All rights reserved.

the depolarization of TS radiation has been experimentally observed in JET [482].

In order to describe the polarization properties of the scattering radiation it is convenient to use the Mueller calculus [483]. Theory shows [481] that the wavelength integrated radiation scattered by a high T_e, relativistic plasma is partially polarized and its Stokes vector can be written as $\boldsymbol{S} = \boldsymbol{C}_{PL}\boldsymbol{S}_{PL} + \boldsymbol{C}_{NP}\boldsymbol{S}_{NP}$ in which $\boldsymbol{S}_{PL} = (1, S_1, S_2, S_3)$ and $\boldsymbol{S}_{NP} = (1,0,0,0)$ are unit Stokes vectors representing the completely polarized and the unpolarized components of the radiation and C_{PL} and C_{NP} are their intensity coefficients. The quantity $P = C_{PL}/(C_{PL} + C_{NL})$ is the degree of polarization and $D = 1–P$ is conventionally called 'depolarization' [484]. Both are functions of the electron temperature only. The Stokes vector of the wavelength integrated scattering radiation is computed as $\boldsymbol{S}(T_e,\theta) = \boldsymbol{M}(T_e,\theta)\boldsymbol{S}_{IN}$ where $\boldsymbol{S}_{IN}$ is the Stokes vector of the incident laser beam and $\boldsymbol{M}(T_e,\theta)$ is the Mueller matrix of TS [485]. The scattering signal detected in a given spectral interval can be calculated from the spectral Stokes vector $\boldsymbol{S}_S(\lambda,T_e,\theta) = \boldsymbol{M}_S(\lambda,T_e,\theta)\boldsymbol{S}_{IN}$ in which $\boldsymbol{M}_S(\lambda,T_e,\theta)$ is the spectral Mueller matrix of TS that can be calculated either numerically [484] or by a semianalytic method [486, 487]. Note that these expressions are valid for any polarization state of the incident laser beam. Let us now consider these quantities for TS from an ITER plasma. Figure 119 shows the dependence from T_e of the intensities C_{PL} and C_{NP} and of the degree of polarization P of the scattering radiation from a position near the center of the scattering region in the ITER core plasma.

The unpolarized component increases steadily with T_e and at $T_e = 40$ keV accounts for up to 20% and to 25% of the intensity of an input beam with linear (as is typical) or circular polarization, respectively. For each input polarization the depolarization D has a very weak dependence on the wavelength but in any spectral interval it is only a function of T_e. Polarimetric TS allows the determination of T_e by measuring D. The technique can be implemented in any spectral interval and therefore does not suffer from limitations of the useful detected spectral range.

One way to exploit this depolarization effect in ITER is to include an additional polarimetric channel into a conventional filter polychromator as in figure 120 [481].

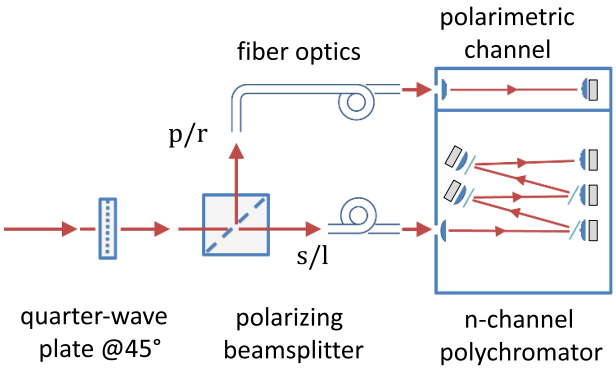

Figure 120. Layout of a TS detection scheme including n spectral and one polarimetric channel. If the input laser beam has linear polarization as usual, the quarter wave in input is not necessary and the scattering light is separated into the two linear 's' and 'p' polarizations. If the input laser beam has right circular polarization, then the quarter-wave plate at 45° must be added to separate the scattering light into left 'l' and right 'r' circular polarizations. Reproduced from [481]. © 2017 IOP Publishing Ltd and Sissa Medialab. All rights reserved.

The purpose of this polarimetric channel would be to detect the component of the scattering radiation with the polarization perpendicular to that of the incident laser beam, covering a spectral region as wide as possible within the useful detection range. This will provide an additional signal that, contrary to those of the conventional spectral channels, will be increasing with T_e, thus contributing to reducing the measurement error in the high T_e range. In figure 121 we show the expected effect of such a polarimetric channel on the accuracy of the measured T_e in ITER assuming that it has the same spectral extent of the full set of spectral channels [481].

These calculations show that the inclusion of the polarimetric channel becomes significant at about 20 keV and at $T_e = 40$ keV can decrease the T_e and n_e measurement errors by about 30% and 50% for an incident laser beam with linear and circular polarization, respectively. In these calculations the possibility of performing TS with a circularly polarized laser beam has been considered. In fact, in TS from a plasma, an incident beam with polarization different from linear perpendicular to the scattering plane has never been done.

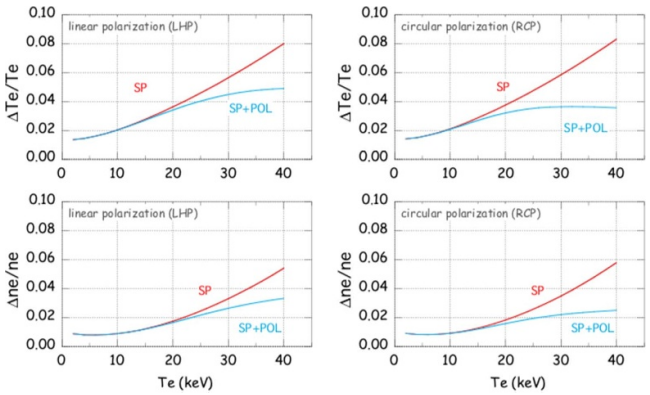

Figure 121. Relative error on T_e and n_e expected using the spectral channels only and with the addition of a polarimetric channel, for linear and circular input polarization in the ITER CPTS. We assumed $n_e = 5 \times 10^{19}$ m^{-3}, laser energy in the plasma volume $E = 3.2$ J, collection optics solid angle DW $= 3.14 \times 10^{-3}$ sr (F/9.8), scattering length $L = 48$ mm, scattering angle theta $= 159°$, APD excess noise factor $k = 2.5$ and no plasma light. The solid angle, scattering length and scattering angle are those of the measurement position in ITER at $R = 6.2$ m. Reproduced from [481].

The reason for this is that linear input polarization maximizes the scattering signal for any scattering angle. However in the almost backward scattering condition of ITER the difference between the scattering signal detected with linear and circular polarizations is hardly appreciable. In fact figure 121 shows that the accuracy of the spectral measurement is virtually the same at low T_e whereas the inclusion of a polarimetric channel is more effective at high T_e if the scattering is performed with a circularly polarized laser beam. In ITER however a polarizer, either linear or circular, depending on the polarization of the laser beam, must be inserted in the collection optics, to separate the two polarization components before the fiber optic bundles, as these will destroy the polarization of the scattering light [466, 488]. Such a polarizer must be sufficiently achromatic to operate on the entire detected spectral range and compliant with the requirement of neutron irradiation. A problem that may arise with an input circular polarization is due to the damage threshold of the laser beam dump, whose design was specific for a linearly polarized laser beam [489].

A second possibility to implement polarimetric TS in ITER is to use a double pulse technique, in which two laser pulses with different polarizations either linear horizontal/vertical or circular right/left are sent on the same path into the plasma with a small time delay. In this way only a single fiber bundle is necessary and also the polarimetric channel can be omitted because the unpolarized component will be measured by the same set of spectral channels on the second laser pulse. In this case however it is necessary to measure the power of the two pulses with good accuracy, and also introducing a beam dump of a different design. In conclusion, including a measurement of the unpolarized component of the TS signal may effectively improve the accuracy of the TS measurements at high T_e in the ITER CPTS system, counteracting the adverse effect of the limited detection spectral range.

Unfortunately the current constraints on the scattering geometry limit the advantages of polarimetric TS. An alternative access providing a more favorable scattering angle might become available for the ITER later experimental campaigns when the highest temperatures are expected.

Table 30. DTS measurement requirements.

	Coverage	Frequency	Accuracy
n_e	10^{19}–10^{22} m^{-3}	50 Hz	20%
T_e	1–200 eV 0.3–1 eV	50 Hz	20% 0.2 eV

6.6. DTS

The ITER DTS measures T_e and n_e in the outer divertor leg providing the link between upstream and target parameter measurements (e.g. from Langmuir probes). The diagnostic measurement requirements are presented in table 30. At the very low temperatures, corresponding to the region in which strong recombination and thus divertor plasma detachment will occur the requirement on measurement accuracy is reduced. This is reasonable in the sense that one of the most important roles of the DTS will be to provide experimental evidence that strong recombination is occurring in the target vicinity and to validate plasma boundary code simulations of the detachment behavior. Since the recombination rate increases more rapidly in the region with T_e below ∼0.5 eV in comparison with the interval ∼0.5–1.0 eV, it suffices for code validation that experiments provide a measurement, which can distinguish roughly between these regions [490].

The required temporal resolution is based on particle confinement times in the divertor plasma. In ITER, these timescales equate to ∼10 ms defining the minimum timescale upon which 'global' changes might be expected in the divertor plasma (not including, of course, very fast turbulent processes occurring on small spatial scales). The baseline time resolution of the DTS system of 20 ms (50 Hz) seems reasonable, especially given the possibility of achieving, if necessary, a factor of two higher resolution (10 ms) through simultaneous application of the spare laser system. The DTS optical layout uses crossed probing and viewing beams with front-end laser launcher located beneath the divertor cassettes. The laser chords (see figure 122) enter along the bottom of the divertor cassette and, then, travel upwards into the outer divertor SOL, passing through an ∼20 mm gap between adjacent divertor cassettes. Several interchangeable probing chords with common collection optics improve the diagnostic reliability.

Laser chords #1 are very close to the separatrix, coinciding with the main stream to the outer divertor leg, and are the most informative for detachment monitoring and control. Laser chords #2 and # 3 are less informative but are launched

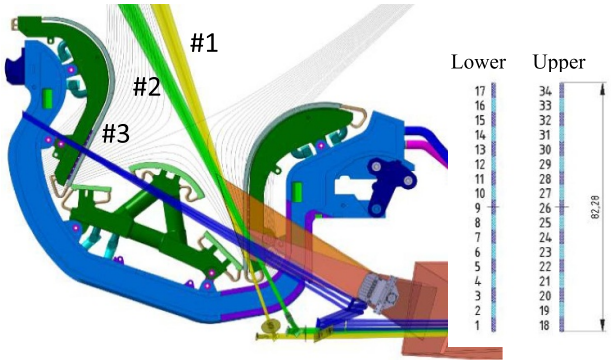

Figure 122. DTS probing chords and spatial channel arrangement on two fiber bundles. Numbering starts from the bottom of the divertor leg.

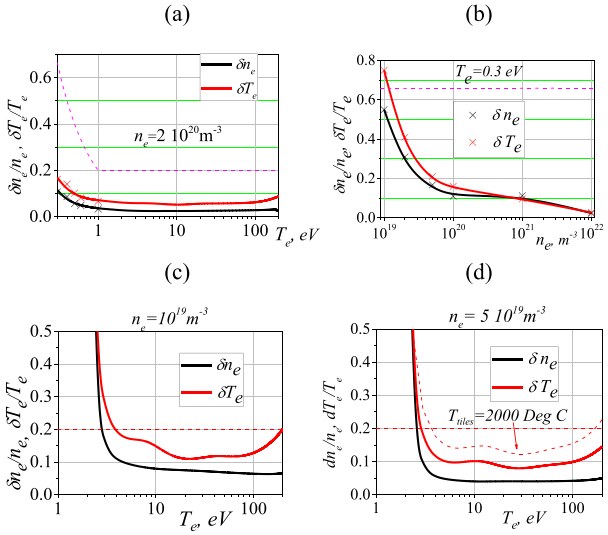

Figure 123. The expected $\delta T_e/T_e$ and $\delta n_e/n_e$ for run #1514 of the SOPLS 4.3 software package corresponding to a peak power flux density of 8 MW m^{-2}. The background radiation intensity scaled from matching $n_e{}^2$ dependence with five-fold overestimating. The dashed lines mark acceptable accuracy. (*a*) $\delta T_e/T_e$ at $n_e = 2 \times 10^{20}$ m^{-3}. Solid curves are analytical approximation, crosses—errors estimated in a numerical experiment; (*b*) $\delta n_e/n_e$ at $T_e = 0.3$ eV; (*c*) $\delta T_e/T_e$ at $n_e = 10^{19}$ m^{-3}—minimum density for the top of the divertor leg; (*d*) $\delta T_e/T_e$ at $n_e = 5 \times 10^{19}$ m^{-3}—the minimum density for the bottom of the divertor leg. The curve dashed line takes into account the blackbody radiation of the divertor tiles at a temperature of 2000 °C.

from mirrors located further from the outer divertor target but better protected from plasma interactions.

The standard processing of the TS spectrum assumes that the spectral width depends on T_e, while the total scattered signal intensity is linearly proportional to n_e. When studying a sufficiently dense and cold divertor plasma the Debye length approaches the differential scattering vector and the deviation of the TS spectral shape from Gaussian becomes very pronounced [491]. The intended processing of TS spectra is fitting the measured spectra with theoretical expectations, estimating the n_e and T_e measurement errors from simple analytical equations [472]. The DTS measurement capabilities were assessed by estimation of n_e and T_e relative errors for TS spectra with pronounced collective effects using the following algorithm:

(a) estimation of TS signals in spectral channels based on the known engineering parameters;
(b) multiple inverse problem solution (103 runs) recovering T_e and n_e from the TS signals simulated for given n_e and T_e with allowance for random deviations, where $k \sim 2.5$ APD excess noise, N_i and N_{bg} i—number of signal and background photoelectrons in ith spectral channel, $N_{amp} \sim 50$ contribution of the detector and amplifier noise reduced to the input of detector (minimal error of the scattered signal was assumed as 2.5%, taking into account probable systematic errors due to calibration);
(c) estimation of the T_e and n_e standard deviations from the obtained distributions of T_e and n_e.

The assessed relative errors of the measured T_e and n_e for the probing chord #1 are summarized in figure 123. Figures 123(*a*) and (*b*) show that the measurement errors of both T_e under $n_e = 2 \times 10^{20}$ m^{-3} and of n_e under $T_e = 0.3$ eV satisfy the requirements (plasma parameters near strike point). The same analysis for plasma parameters typical for upper part of the divertor leg is presented in figures 123(*c*) and (*d*).

The most important divertor plasma parameter is the degree of plasma detachment/attachment to divertor targets. Detachment requires ion–electron recombination in the plasma volume and this in turn requires the achievement of very low plasma temperatures (<1 eV) at which there is a transition from ionizing to recombining conditions. The ionization front location does not directly reflect the level of plasma detachment if there is at the same time a vertical displacement of the magnetic configuration, which can occur, for example, as a result of control errors or plasma instabilities. If these two effects can be sufficiently deconvoluted, it is possible to envisage the DTS as a potential sensor in a control loop designed to affect the degree of detachment. The profiles of T_e along the DTS probing chord #1 are shown in figure 124. Arbitrary vertical shifts of −50 mm, 0 and +50 mm have been applied to the profiles, simulating strike point movements. The figure 124(*b*) shows that the ratio of areas under curve taken for the upper and lower regions of the probing DTS chord gives a matrix of points representing the extent of movement and ionization front position. An operational diagram of this type could be envisaged as a way in which the peak heat flux could be controlled by DTS.

In the presence of inaccessible components (e.g. vacuum windows, mirrors inside the vacuum system), the spectral characteristics of the in-vessel optical components, which may change with time, have to be calibrated. For DTS, the procedure must include relative calibration for the temperature, to validate the relative spectral response curves and avoid incorrect measurement of the TS spectrum shape, and absolute calibration for the density, which requires absolute sensitivity. The relative calibration of slowly varying spectral

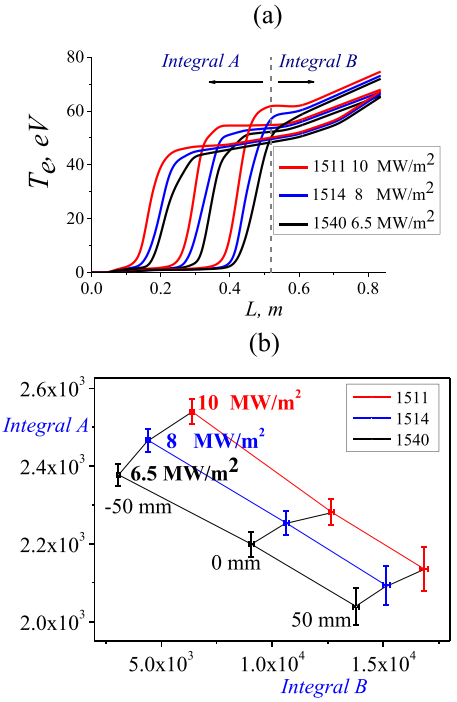

Figure 124. Illustration of deconvolution and decomposition of the influence on the plasma parameters in the outer divertor leg of two phenomena—different plasma detachment and different vertical displacement of the magnetic configuration. (*a*) T_e as a function of distance L along the probing chord, modeled for three runs of SOLPS #1511, #1514, #1540 with different degrees of detachment and, therefore, different peak stationary target power flux density on the target (10, 8, 6.5 MW m^{-2}) and for three vertical displacements of the magnetic configuration −50, 0 and +50 mm; (*b*) relationship between (*Integral A*) and (*Integral B*) of the T_e curves. Reproduced from [490]. © 2014 IAEA, Vienna. All rights reserved.

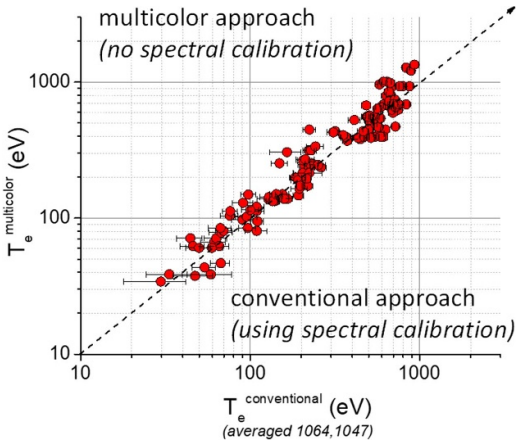

Figure 125. A comparison of the electron temperature measured at the Globus-M2 tokamak measured using multi-laser approach (spectral calibration of the system was not used, Nd:YAG 1064 nm and Nd:YLF 1047 nm lasers with 50 ns time delay) and conventional technique.

transmission is done comparing in different spectral channels the TS signals from two laser wavelengths [490]. The spectral channels used for measurements in the 5 eV–500 eV range can be calibrated using ratio of the TS signals from the 1064/1047 nm. If the T_e range is increased up to several keV's, e.g. during ELM activity in which toroidally asymmetric structures carrying plasma with temperature characteristic of the H-mode pedestal, the corresponding spectral channels can be can be calibrated using signal ratio of 1064/946 nm.

Recent experiments carried out using two diode pumped Nd:YAG and Nd:YLF lasers have demonstrated a possibility to measure T_e within the range $T_e = 0.02$–1 keV [492], see figure 125. The electro-optical shutters of the lasers were synchronized thus making it possible to detect TS signals with time delay of a few tens' nanoseconds. The characteristics of the probing and measuring system that was used allow multi-laser TS measurements in a steady-state regime, even for the case when the spectral characteristic of the collection optics was artificially distorted.

The absolute calibration of the diagnostic as a whole, including the entire optical path will use a light source with known intensity under the same geometry and alignment conditions. The main approach is to use Rayleigh and/or Raman scattering on a gas target. Both have advantages and disadvantages. The main limitation in calibrating by Rayleigh scattering for the DTS is stray light. The expected stray light delay is longer than the DTS laser pulse duration (3–4 ns) and potentially can be temporally separated. The TS/Rayleigh scattering cross-section ratio for N_2 is 2210 at 1064 nm, which determines the signal value from the gas target with a density of 2.2×10^{16} cm^{-3} (0.8 mbar) equivalent to the TS signal corresponding to $n_e = 10^{13}$ cm^{-3}. The practical advantage of the less intensive Raman compared with Rayleigh scattering is in its broad spectrum, which makes it suitable for both absolute and relative calibration of the spectral channels (see detail in Mukhin *ét al* [490]). Temporal shapes of LIF-derived HeI fluorescence can also be used as an extra method for absolute calibration of the collection system transmission. The fluorescence duration varies from 10 to 100 ns over the n_e range 10^{17}–10^{21} m^{-3}, its dependence on T_e from 0.3 to 200 eV is much weaker [491].

A well-known practical problem facing optical diagnostics on large fusion devices, especially in ITER divertor, is the eroded first-wall materials deposited on the front-end optics during normal operation, when shutters are unable to protect. This leads to decreasing diagnostic signals and can result in substantial errors in the interpretation of the data. There are several mitigating techniques for this. The plasma sputtered materials can reach the divertor diagnostic optics during pressure jumps of ∼1 ms pulse duration, when plasma blobs with core plasma parameters strike the divertor targets. The eroded material transport by diffusion is estimated using the MC code KITe (Kinetic Impurity Tracing) [493]. The impurity transport caused by convection flows will be minimized by a dust protecting box, situated between plasma and laser launcher following: (1) deviation of the hydrodynamic flow away from the optical axis and (2) absorption/pumping on the box walls [494–496]. The front-end laser optics will be thin quartz windows, which have to be self-cleaned by the laser ablation [497, 498]. The front-end collection optic will be cleaned by RF plasma [499–507]. The innovative diode-pumped Nd:YAG

Table 31. LIF measurement requirements.

	Range	Frequency	Accuracy
n_{He}	10^{17}–10^{21} m^{-3}	50 Hz	20%
T_i	0.3–200 eV	50 Hz	20%

laser 2 J/50 Hz/1064 nm is the main laser and the auxiliary 1 J/50 Hz/946 nm Nd:YAG and 2 J/50 Hz/3 ns Nd:YLF lasers were developed for probing and calibration by TS at the shifted wavelength. The short laser pulse duration helps to reduce both the accumulated plasma background and to separate in time the TS and stray light signals [508]. A digital filter polychromator with ultra-low noise pHEMT based preamplifiers $F_{3db} = 250$ MHz and onboard digitized signal processing system was developed for DTS measurements with probing laser pulses of 3–5 ns [473, 509–513].

6.7. LIF in the divertor

LIF is an active laser spectroscopy diagnostic of atoms/ions in plasma. The technique is based on laser excitation of atom/ion allowed transitions and subsequent measurement of fluorescent signals. LIF allows measuring of densities (n_a, n_i) using corresponding collision-radiative models (CRM) and provides information about electron temperature (T_e) and density (n_e). Other types of LIF measurements are related to pumping spectral line scanning with a narrowband tunable laser: temperature of the atoms/ions from Doppler broadening, projection of the particle velocities from Doppler shift, the magnetic field from Zeeman splitting etc.

The LIF diagnostic shall measure helium density (n_{He}) and ion temperature (T_i) in ITER divertor according to the requirements specified in table 31. The main role of LIF is to measure helium density distribution, characterizing the efficiency of the helium ash removal. In combination with a vacuum pumping system data and gas analyzer, LIF allows monitoring the helium ash level in the main plasma. Besides this, LIF is a backup diagnostic used for measurements of T_i. In combination with a DIM, which is the primary T_i diagnostics, LIF allows knowing the ion temperature distribution along the probing chords. The T_i distribution is essential for evaluating the pressure balance in the divertor plasma [514].

The diagnostic is combined with the DTS by using common laser-injection and signal collecting optics. The beams will be launched into the outer leg of the divertor close to the separatrix with laser mirrors arranged beneath the divertor cassettes (figure 122). Both the DTS and LIF signals will be collected through the gap between neighboring divertor cassettes providing more than 20 independent spatial points. Separation of LIF and DTS signals will be carried out in the diagnostic room with selective mirrors transmitting LIF and reflecting DTS spectral range. The similar measurement chords of LIF and DTS allow using n_e and T_e from DTS for evaluation of n_{He} with CRMs from LIF signals.

The LIF allows measuring both helium atoms (n_{HeI}) and hydrogen-like ions (n_{HeII}) densities. The measurements of n_{HeI}

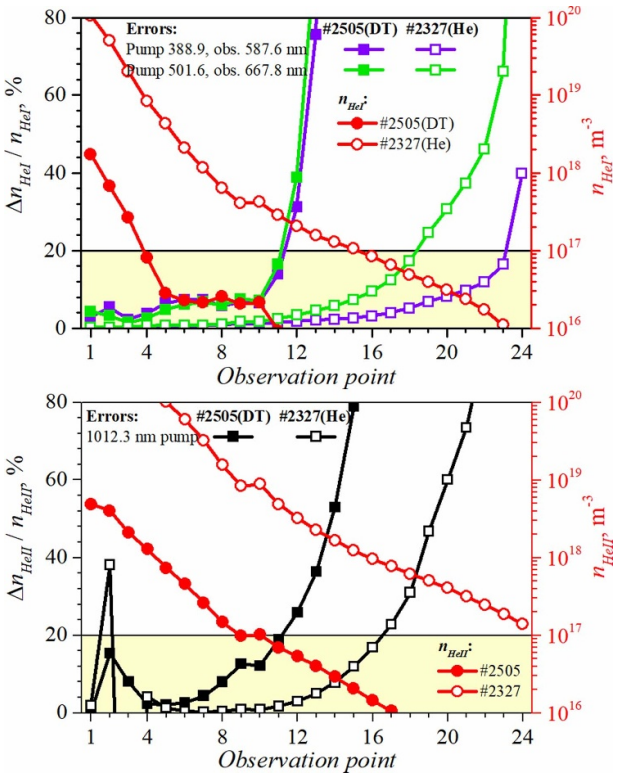

Figure 126. Relative errors of n_{HeI} (top) and n_{HeII} (bottom) measurements (left ordinates) and n_{HeI}, n_{HeII} densities respectively (right ordinates) for #2505 (DT) and #2327 (He) SOLPS runs. Reprinted from [516], Copyright (2019), with permission from Elsevier.

can be realized by two spectroscopic schemes: a triplet—laser pumping the 1s2s ^{3}S $\rightarrow$ 1s3p ^{3}P transition (388.9 nm) and viewing fluorescence in 1s3d ^{3}D $\rightarrow$ 1s2p ^{3}P (587.6 nm), and a singlet—pumping 1s2s ^{1}S $\rightarrow$ 1s3p ^{1}P (501.6 nm) and viewing 1s3d ^{1}D $\rightarrow$ 1s2p ^{1}P (667.8 nm) [514, 515].

He_{II} ion has a hydrogen-like structure of excited states limiting a set of spectroscopic schemes suitable for LIF. A new LIQ approach was developed for diagnostics of hydrogen and hydrogen-like ions [514]. LIQ for He_{II} is based on quenching the most intense line in the visible range 468.6 nm ($n = 4 \rightarrow 3$ transition) by laser pumping to the upper $n = 5$ state (transition $n = 4 \rightarrow 5$, line 1012.3 nm).

1 kHz pulsed OPO is suitable both for n_{HeI} (LIF) and n_{HeII} (LIQ) measurements. Figure 126 shows the expected measurement accuracy for DT and Helium scenarios of ITER. OPO gives n_{HeI} and n_{HeII} relative errors <20% in the lower and middle parts of the probing beam, where $n_{HeI} > 10^{17}$ m^{-3}.

Measurements of the ion temperature can be carried out on the main DT plasma impurity—helium ions. The measurement requires a tunable laser with a spectral width of about ten times narrower (at least) than the absorption line width. The SNR for T_i should be higher than for density measurements. A short-pulse laser (like OPO) does not provide the required SNR; thus, the time-modulated laser is proposed to achieve the accuracy by the signal accumulation over the long time. The transition $n = 4 \rightarrow 5$ (1012.3 nm) is chosen for the

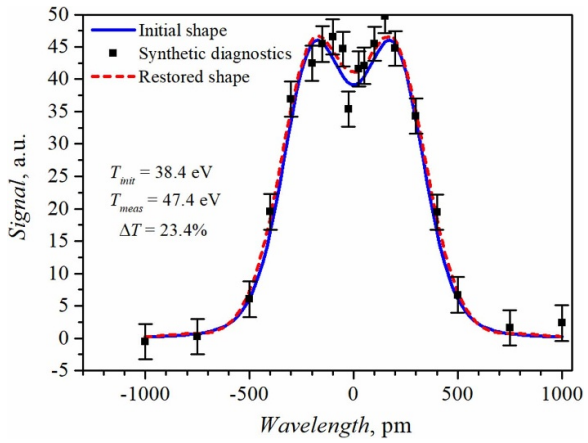

Figure 127. Simulation of the 1012.3 nm HeII spectral line shape for estimation of the T_i measurement accuracy. Reprinted from [516], Copyright (2019), with permission from Elsevier.

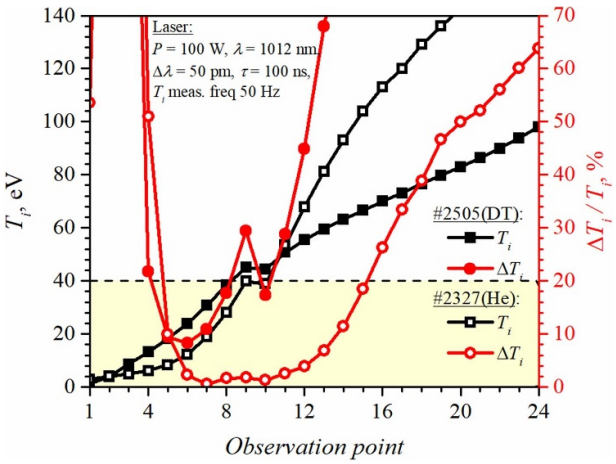

Figure 128. Relative accuracy (right ordinates) of T_i LIQ measurements and T_i distributions (left ordinates). Reprinted from [516], Copyright (2019), with permission from Elsevier.

468.6 nm He_{II} line quenching due to minimal required laser power [516].

CRM calculation of the expected quenching and background signals allows estimating the accuracy of the T_i using numerical simulations (figure 127) for Helium and DT ITER scenarios. The spectral line shapes were simulated considering calculated signals and noise sources. Doppler broadened emission spectra, once separated from Stark and Zeeman broadenings, provide a convenient means of making T_i measurements. The laser beam is linearly polarized to reduce the intensity of π- component and of corresponding influence of Zeeman splitting.

Results of the ΔT_i estimations are shown in figure 128. The T_i relative errors were calculated for the LIF/DTS ITER divertor geometry using the following equation: $\Delta T_i = (T_{init} - T_{meas})/T_{init}$, where T_{init} is the temperature taken from the SOLPS and T_{meas} is determined from the simulated spectral line shape. The simulation was carried out 10^4 times for every observation point. The n_e and T_e (from DTS) were used to consider Stark broadening. Zeeman splitting was estimated for the magnetic field $B = 5$ T and for the toroidal laser polarization.

The calculations show that the ability to measure T_i with relative errors <20% in the lower part of the probing chord is limited by the pronounced Stark effect. In the upper part of the divertor leg, the measurements are complicated by the low He_{II} ions density.

The LIQ technique can also be applied for hydrogen (deuterium, tritium) diagnostics in the ITER divertor [491] The laser pumping of one of the Paschen lines (e.g. $P_\alpha = 1875$ nm) quenches $H_\alpha = 656$ nm. Compared to the conventional LIF for hydrogen with laser pumping and viewing of the fluorescence in H_α, or laser photoionization (LII) of $H_\beta = 486$ nm by TS laser, LIQ combines benefits of both LIF and LII. The LIQ requires a low-power laser and allows spectral line scanning based measurements like LIF. The wavelength shift of detected radiation versus pumped transition reaches hundreds of nanometers and the laser stray light can be easily blocked as well as in LII.

The CRM assessments of the hydrogen density LIQ diagnostic in ITER divertor show possibility to measure $n_{HI} > 10^{17}$ m^{-3} with relative errors better than 20% by 1 kHz pulsed OPO. Using a time-modulated narrowband tunable laser allows scanning of the pumping $P_\alpha = 1875$ nm spectral line shape. Therefore, LIQ gives the possibility to measure local n_H/n_D, n_D/n_T ratios.

LIQ diagnostics of hydrogen atoms was already tested at Globus-M tokamak. The H_α signal was suppressed by laser radiation with $\lambda = 1005$ nm exciting transition $n = 3 \rightarrow 7$ (using OPO laser: $\Delta\lambda = 2000$ pm, $\tau = 10$ ns, $E = 2.2$ mJ). As well as OPO, the time-modulated fiber laser with $\lambda = 1875$ nm, $\Delta\lambda = 1200$ pm, $P_l = 5$ W and repetition rate of 1 MHz was specially designed and manufactured for the n_{HI} measurements in SOL and divertor plasma of Globus-M. The experiments show the possibility of measuring $n_{HI} > 10^{16}$ m^{-3} averaging quenching signals over 10 ms in SOL plasmas.

Another useful approach of LIF in ITER is the electron density measurements basing the analysis of HeI fluorescence pulse shapes [491]. The CRM developed for n_{HeI} describes the temporal behavior of the fluorescent signals depending on the laser pulse shape, exciting transition and local values of n_e and T_e. Particularly, LIF can be used to measure n_e in the range of 10^{17}–10^{21} m^{-3} under $T_e = 0.3$–200 eV by using pulsed OPO laser.

The CRM simulation shows that the fluorescence duration (FWHM) varies from 10 to 100 ns over the n_e range of 10^{17}–10^{21} m^{-3} while dependence on T_e in the range of 0.3–200 eV is much weaker. The lower limit of $n_e > 10^{17}$ m^{-3} is determined by reduced dependence on n_e since relaxation of the excited level and hence the fluorescence signal duration is determined mainly by spontaneous emission. Test measurement of n_e was carried out in Globus-M tokamak using TS collection optics. The LIF signal temporal shape satisfies $n_e = (2.00 \pm 0.65) \cdot 10^{19}$ m^{-3} that correlates well with the TS-data $n_e = (2.4 \pm 0.2) \cdot 10^{19}$ m^{-3}.

Comparison of n_e by LIF with n_e by DTS, which depends on the collection system transmission, can also be used as an

extra method for absolute *in-situ* calibration of the collection optics transmission in ITER.

6.8. Toroidal interferometer-polarimeter (TIP)

The primary system planned for real-time density control in ITER is the five channel combined TIP. TIP will also contribute to density profile reconstruction and play a secondary role as a diagnostic of core density fluctuations [4]. Initial design studies of the TIP were carried out in 1998 [517] and, in 2013, a more detailed design was published [518] following the successful CDR at ITER. The TIP presented at the CDR featured a traditional two-color vibration compensated interferometry measurement [519–523] with the 10.59 μm CO_2 and 5.42 μm CO laser lines combined with a 10.59 μm CO_2 polarimetry measurement of Faraday rotation using the R and L-wave technique [524–526]. Following prototyping activities, it is now envisioned that the CO laser will be replaced by a 4.6 μm QCL on ITER [527].

The two-color interferometry approach on TIP is an established technique that relies on using two separate colinear interferometers operating at different wavelengths to deconvolve dispersive plasma-induced phase shifts and motion induced phase shifts. In the cold-plasma approximation, the line-integrated density from TIP will be given by

$$\int n_e dL = \frac{\lambda_{CO2}}{r_e\left(\lambda_{CO2}^2 - \lambda_{QCL}^2\right)}\left[\phi_{CO2} - \frac{\lambda_{QCL}}{\lambda_{CO2}}\phi_{QCL}\right]$$

where $r_e = 2.82 \times 10^{15}$ m, λ_i and ϕ_i are the wavelengths and interferometric phase shifts respectively of each laser. Plasma-induced phase shifts of the 10.59 μm CO_2 laser beams in ITER are expected to be 10^3–10^4 degrees and motion-induced phase shifts will likely be 10^4 Deg. (1 mm) or larger [518]. In contrast, the polarimeter measures a phase shift given by

$$\phi_{pol} = 2C_p{\lambda_{CO2}}^2\int n_e\vec{B}\cdot\overrightarrow{dL}$$

with $C_P = 2.62 \times 10^{-13}$ rad T^{-1} and B is the local magnetic field, from which the Faraday rotation or field weighted line-integrated density can be obtained. Because polarimeter phase shifts are expected to be less than 180 Deg. [518] and the magnetic field is known, the inclusion of polarimetry allows the two-color system to recover unambiguously from fringe skips at all densities, up to and beyond the Greenwald limit as well as the potential to use the polarimeter itself for feedback density control.

The present TIP layout on ITER is shown in figure 129, where it can be seen that each of the five TIP chords will originate in the diagnostic hall from five independent optical tables. The plasma leg beam lines will be enclosed and transmit each chord to and from the ITER vessel through multiple containment zones. In equatorial port 9 (EP9) an optical labyrinth will transmit each chord through the FW where they will fan out and be sent to a set of corner cube retroreflectors that are placed in either of the other equatorial ports or neutral

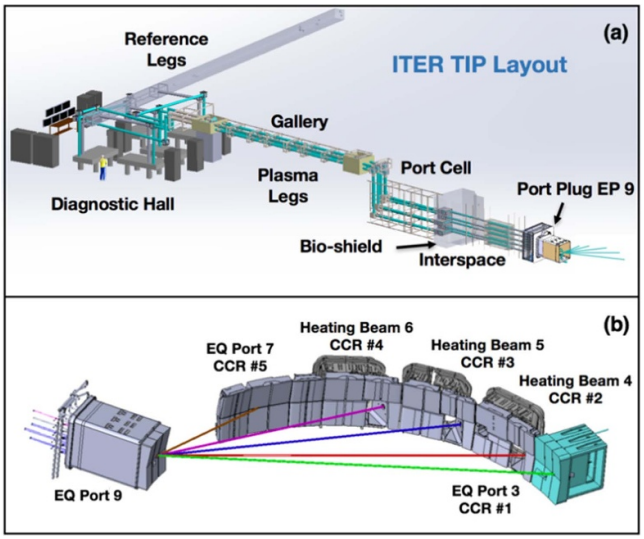

Figure 129. TIP Layout on ITER. (*a*) View showing TIP layout spanning various zones. (*b*) TIP chords in ITER vessel and retroreflector (CCR) locations.

beam ducts. The optical train in EP9 features five independent first mirrors and a common FW hole, to minimize penetration sizes and to reduce risks associated with deposition, erosion and neutron streaming.

While elements of TIP including separate CO2 laser-based two-color interferometry [520, 521] and R&L-wave polarimetery [528, 529] had been made previously, at the time of the CDR, no previous system had been demonstrated with the combination of characteristics required for TIP, i.e. combined two-color IR interferometry and polarimetry measurements, long ~100 m beam paths and steady-state ~1000 s, low-noise measurements. In 2015–2016, a fully functioning TIP lab prototype with the scale of that expected in ITER was constructed and tested [527]. Those tests included several phases, from bench testing to a full 120 m beam path with FPGA-based DAQ and a feedback alignment system that was subjected to motions typical of an ITER bake cycle. Over the course of the testing, the initial conceptual design was refined significantly as issues were identified and overcome. As mentioned, a major change was the shift from a CO to QCL used as the shorter wavelength vibration compensation laser (a 5.22 μm laser in lab tests but planned as a 4.6 μm laser for ITER). Following lab tests, the TIP prototype was moved and installed on DIII-D with encouraging initial results; DIII-D TIP prototype measurements compare well with expectations and the system design is capable of meeting ITER measurement requirements.

The DIII-D TIP prototype layout is shown in figure 130, where the ~100 m roundtrip beam path for the plasma and reference legs can be seen. A detailed description of the table and components are given in Van Zeeland *et al* [527] and [530]. A key element not shown is the optical table enclosure which reduces airflow, dust and regulates the temperature to help maintain alignment of the components. Like the ITER TIP, the DIII-D prototype features a tangential view

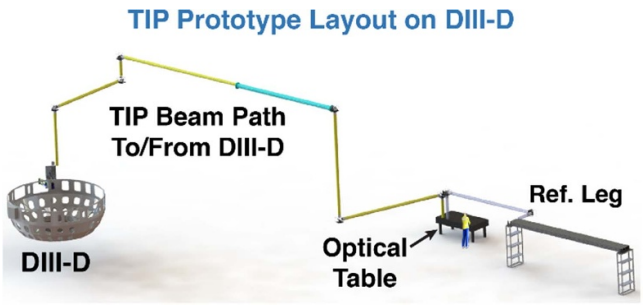

Figure 130. TIP prototype layout on DIII-D.

and feedback alignment system to keep the system aligned throughout motion associated with pulsed fields during a discharge as well as daily thermal cycles.

TIP prototype measurements of a DIII-D plasma are shown in figure 131, where the interferometer and polarimeter measurements are shown in figures 131(*a*) and (*b*) respectively along with the measured phase shifts. During DIII-D discharges, the measured phase resolution for the polarimeter and interferometer is 0.05 Deg. (100 Hz bandwidth) and 1.9 Deg. (1 kHz bandwidth), respectively [530], which are to be compared to the ITER target values of 0.1 and 10 Deg [518]. The corresponding line-integrated density resolution for the vibration-compensated interferometer is $nL = 1.5 \times 10^{18}$ m^{-2}, and the magnetic field-weighted line-integrated density from the polarimeter is $nBL = 1.5 \times 10^{19}$ Tm^{-2}. Both interferometer and polarimeter measurements compare well to expectations based on calculations using a synthetic TIP diagnostic which takes as inputs TS measured density profiles and EFIT magnetic equilibrium reconstructions [530]. As described in [531], the TIP prototype active feedback alignment system was essential to obtaining these low-noise data. In addition to line-integrated equilibrium density, 1 MS s^{-1} TIP prototype data clearly demonstrate the ability to resolve core density fluctuations such as Alfven eigenmodes in the 100 kHz range (see figure 7 of [531]).

While TIP prototype results are encouraging, several open issues and design questions remain. TIP faces many of the same issues discussed in the context of other laser-based diagnostics discussed in this summary including primarily first mirror degradation. At present, no shutter or mirror cleaning is envisioned, passive mitigation through the use of IR wavelengths, a single small aperture and a novel retroreflector design is the planned approach. An important issue that was identified in testing is atmospheric interaction and specifically, dispersion causing uncompensated interferometric phase shifts due to environmental variation. An example of this effect is given in figure 30 of [527], where a 0.5 C change over ~40 m of the air-filled beam line caused an uncompensated phase shift of about 25 Deg. or 250% of the TIP interferometer error budget. R&D work will be needed to identify a path forward to handle significant temperature variations but one option includes positive pressure in the beam lines with clean dry air and monitoring temperature variations then removing the uncompesated phase shifts through some experimental fit

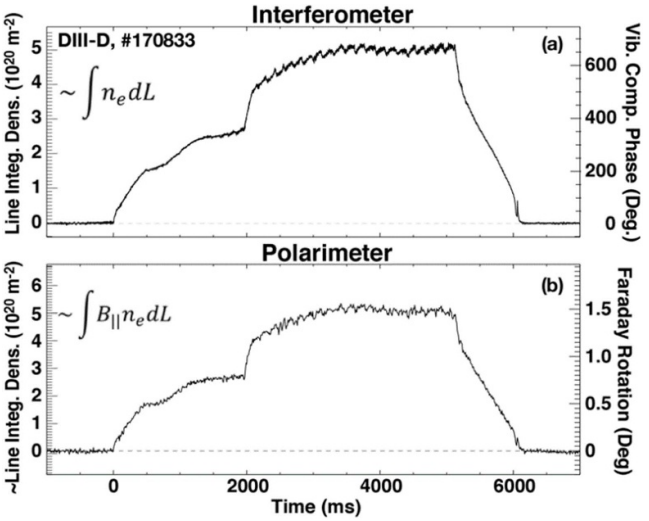

Figure 131. TIP prototype measurements of a DIII-D plasma. (*a*) Two-color interferometer. (*b*) Polarimeter.

to the effect. A similar approach has been employed on W7-X [532]. An alternative but difficult approach is the evacuation of the beam lines. Another open issue is the TIP primary vacuum window; leading candidates are BaF_2 and ZnSe. BaF_2 has been used on several devices including the DIII-D TIP prototype, has acceptable transmission and a low Verdet constant; however, it is sensitive to thermal shock and water exposure. While ZnSe is stronger than BaF_2, its higher index of refraction requires an AR coating (which use proprietary coatings with no guarantee of reproducibility) and Faraday rotation in the window must be corrected for to meet polarimeter measurement requirements. Presently, neither window material has been formally approved for use on ITER.

6.9. PoPola

PoPola injects thirteen far-IR (FIR) laser beams (wavelength: 119 μm) into the plasma as illustrated in figure 132. PoPola measures the polarization change of the FIR laser beams attributed to interaction between the plasma and the FIR laser beams. An equilibrium reconstruction code estimates the profile of plasma current, or equivalently safety factor q(r), by using the PoPola measurement data together with other diagnostics such as magnetics and CPTS. The q profile is used for physics, real-time suppression of neo-classical tearing modes (NTMs) and real-time reverse shear control. The design activity has been carried out, and progress has been made, for instance a retroreflector [533], a FIR laser, gamma and neutron irradiation tests of a piezo actuator, magneto-optic effect of quartz (window material), remote alignment method of laser beam position and passive stabilization of laser beam position (called as 'flexible light guide') [534–536]. This section focuses on two topics; equilibrium reconstruction taking into account both T_e effect and coupling between the Faraday effect and the CM effect, and a measurement technique.

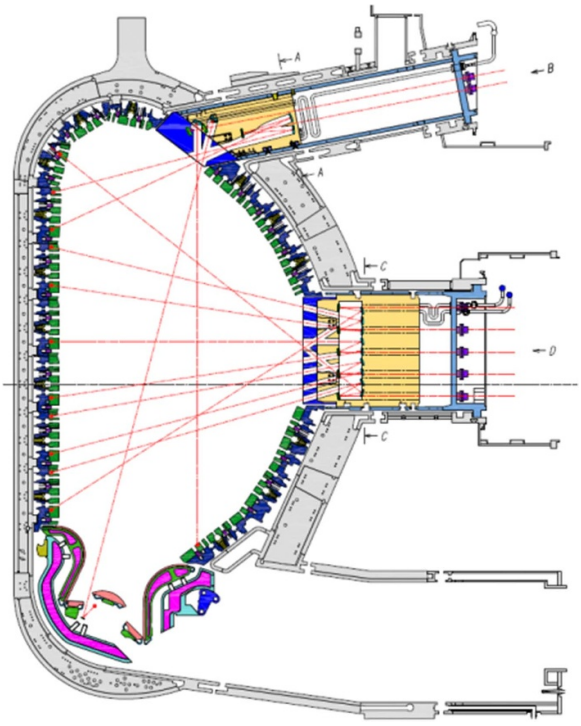

Figure 132. PoPola beam paths through *r,z* cross section of ITER.

The T_e effect and coupling between the Faraday effect and the CM effect are not mentioned in the previous papers, IPB [3] and Progress in IPB [4], but are of significant importance are for discussing the measurement accuracy of q profile identification. Polarimetry involves the measurement of a change in the polarization state, caused by the Faraday effect and the CM effect. The Faraday effect mainly changes an orientation angle, θ, of the polarization state and depends on the electron density of plasma, n_e, and magnetic field parallel to probing laser light, $B_{//}$. The CM effect mainly changes an ellipticity angle, ε, of the polarization state and depends on n_e and magnetic field perpendicular to probing laser light, $B_{\perp}$. When T_e is high, changes of θ and ε depend on not only B and n_e, but also T_e owing to breakdown of the cold plasma dispersion relation. For burning plasmas such as ITER plasma, the electron temperature is expected to be several tens of keV, and thus the T_e effects on the dispersion relation becomes important [537, 538]. In addition to the T_e effect, the coupling between the Faraday effect and the CM effect needs are also significant in the measurement condition of PoPola. Finally, the change of θ and ε are not expressed by using simple line-integral form, but a vector differential equation called a Stokes equation. So, it was an open question whether the q profile can be reconstructed with required accuracy (10% [197]) when the T_e effect and the coupling between the Faraday effect and CM effect are not negligible. The PoPola design team demonstrated for the first time that the q profile can be reconstructed even when the governing equation for the polarization change is given by the complex vector differential equation (i.e. Stokes equation) [539]. The PoPola design team found that the required accuracy of 10% cannot be met in the case of the steady state scenario of ITER plasma operation when the T_e effect is not taken into account. Thus, the Stokes equation taking into account the T_e effect needs to be solved for reconstructing the q profile. Moreover, it was found that the accuracy of q profile reconstruction using both θ and ε are higher than that using just θ. This is because the data of ε includes the information of the poloidal magnetic field because of the coupling and also includes the information of the toroiodal magnetic field caused by the plasma current. Although the measurement of ε was originally proposed for measuring line-averaged electron density, the measurement of ε is now implemented by PoPola for improving q-profile identification. The study regarding the q-profile identification leads to the specification of PoPola, which is that the measurement accuracy of θ and ε are 1° and 6°, respectively, and target to 0.1° and 0.6°, respectively.

The next topic is the measurement technique. This is one of future works that was listed in the Progress in IPB [4]. The PoPola design team examined the four techniques; the rotating waveplate method, the dual PEM method, the Dodel–Kunz method and JET polari-interferometer method. The rotating waveplate method was selected as the preferred option. The major reasons of the selection is the applicability to the wavelength of 119 μm, the capability of measuring the ellipticity angle (ε), the robustness to the deformation of in-vessel mirrors, mechanical vibration and the instability of laser frequency. This section explains only the selected method, and detailed information about the other methods is reported in [540]. The rotating waveplate method consists of a rotating quarter waveplate and a linear polarizer. Detector signal is modulated by the rotation of the quarterwave plate and Fourier analysis of the detector signal provides information identifying the polarization state. It is a well-known technique in the field of polarimetry, but there was no previous experience of measuring at the required time resolution of 10 ms in real time. The theory of the rotating waveplate method is simple and well-known, but practical application with high accuracy is not simple under non-ideal conditions such as concentric distribution of birefringence and non-flatness and wedged shape of the waveplate. The applicability of the rotating waveplate method to PoPola was demonstrated by using both He-Ne laser and quarter waveplate of multi-order retardation [541]. No drift of measurement data was found for 1000 s. The achieved time resolution was 3.3 ms, and the achieved precision of the orientation angle, ellipticity angle, and the Stokes parameter was 0.33°, 0.096°, and 1.2%, respectively. This error will be reduced by using the FIR laser because the error is attributed the run-out of the rotating waveplate, and the run-out normalized by wavelength of FIR laser is much smaller than that of He-Ne laser.

6.10. Expanded measurement capability potential for PoPola

Since publication of the Progress in IPB [4], two new measurement capabilities have been identified as possible for PoPola:

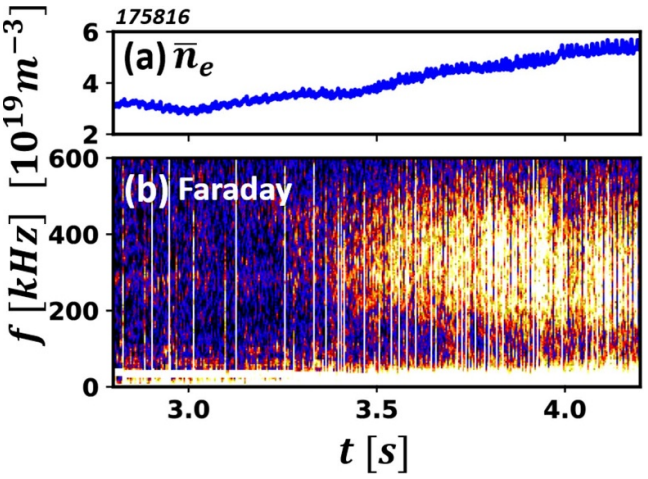

Figure 133. Faraday-effect polarimeter using R- and L-wave technique observed magnetic turbulence during a density ramp in a DIII-D H-mode discharge: (*a*) line-averaged electron density; (*b*) spectrogram of Faraday fluctuation measurement of magnetic turbulence.

(1) internal magnetic field fluctuations and (2) plasma vertical position.

6.10.1. Internal magnetic fluctuation measurement. Interest in internal measurements of magnetic fluctuation and non-axisymmetric 3D effects in ITER have significantly increased, due to needs of early detection of disrupting MHD instabilities [542] and predictions of unstable electromagnetic turbulence in ITER relevant plasmas [543]. Internal magnetic fluctuation measurements, a capability not available from any currently planned ITER diagnostic, may be the key to address these issues. Recent advances in polarimetry have shown that magnetic fluctuation measurements can be accomplished by using the R- and L-wave technique [526], which is also employed for the ITER TIP diagnostic described in section 8. The technique can detect the Faraday effect with low noise at sub-microsecond time scale, enabling measurements of Faraday effect fluctuations. The noise can be further reduced by using two detectors at each chord to suppress electronic noise via the application of correlation techniques [544]. The Faraday fluctuation measured via a horizontal radial chord near the plasma magnetic axis is dominated by magnetic fluctuations along the chord [545], providing a direct internal magnetic fluctuation measurement. In addition, electron density fluctuations along the same chord can be simultaneously measured by adding a local-oscillator [526]. By using the R- and L-wave technique for chords at or near the magnetic axis, broadband magnetic turbulence (100–500 kHz) is observed in ELMy H-mode DIII-D plasmas, shown in figure 133 which correlates with a density ramp and pedestal performance degradation [546]. Determined by the probe beam width (∼6 cm), the similar measurements on ITER would be sensitive to low-k ($k\rho_s < \sim 0.1$ for a 10 keV plasma in ITER) plasma instabilities, such as electron drift waves, MHD and fast ion driven instabilities.

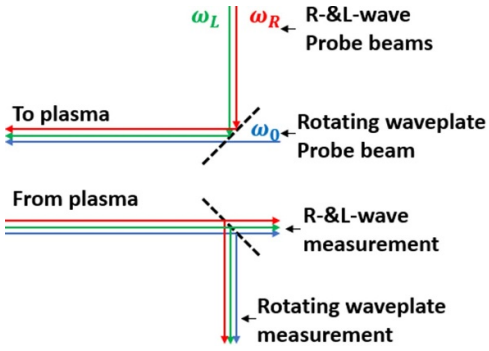

Figure 134. Layout for combination of R- and L-wave technique and rotating waveplate method in PoPola.

For PoPola, to achieve the magnetic fluctuation measurement capability, one would need to implement R- and L-wave technique for the chord(s) nearest the magnetic axis. This can be done without compromising PoPola's primary mission to determine the q-profile. There are two possible approaches. First approach is to combine the rotating waveplate method described in section 9 with the R- and L-wave technique, as illustrated in figure 134. The beam ω_0 with linear polarization is the probe beam for the rotating waveplate method and generated directly by laser. The probe beams of the R- and L-wave technique, beams ω_R and ω_L with counter-rotating circular polarizations, can be generated either by additional lasers with ∼10 MHz frequency difference from ω_0, or by splitting a portion of the ω_0 beam and shifting frequency using an acousto-optic modulator. The rotating waveplate and R- and L-wave methods are integrated by combining all the probe beams together before leaving the optical table, and splitting the return beams into two parts while preserving their polarizations. By appropriately separating the probe beam frequencies, the presence of beam ω_0 will not affect the R- and L-wave measurements. The presence of beams ω_R and ω_L do affect the rotating wave plate measurement, which is avoidable, e.g. by chopping beam ω_R and ω_L periodically: a clean rotating waveplate measurement is accomplished when beams ω_R and ω_L are blocked. The chopping frequency is optimized so that good rotating waveplate measurement at the millisecond scale and R- and L-wave measurement at the microsecond scale are realized. Another approach is to only use the R- and L-wave technique for the desired chord(s) near the magnetic axis. In this approach, the R- and L-wave measurement would also provide the q-profile constraint. A potential concern is that non-negligible contamination from CM effect in the R- and L-wave measurement [541, 547] may affect the accuracy of q-profile. However, this concern is largely alleviated by realizing that the absolute error due to the contamination is small (sub-degree level) for chords near the magnetic axis.

6.10.2. Plasma position measurement. Nine chords of the PoPola system view the plasma horizontally from a equatorial port and can therefore be exploited to provide a measurement of the plasma vertical position. The plasma vertical position

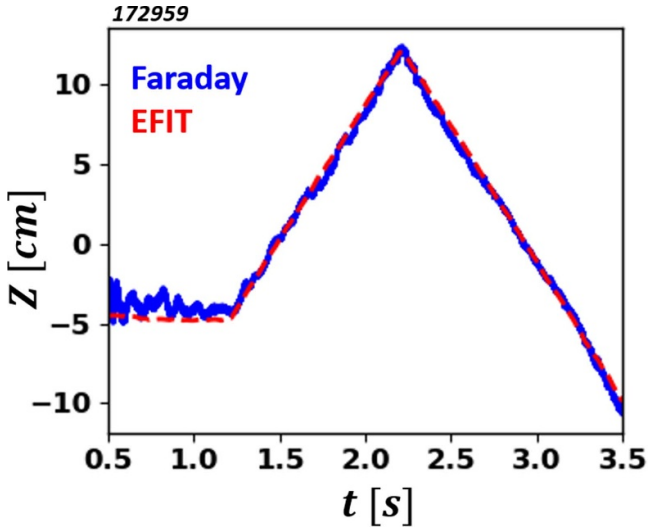

Figure 135. Vertical plasma position on DIII-D showing agreement between Faraday-effect (using 3 central chords) and EFIT results.

is determined by the magnetic axis where the radial magnetic field goes to zero and horizontal position is determined by the magnetic axis where the vertical magnetic field goes to zero. To directly measure the radial magnetic field, the double-pass, radially-viewing, PoPola system can be used.

The plasma vertical position, Z_F, can be related to the Faraday measurements, ψ_F, via $Z_F = -\psi_F(0)/\psi'_F(0)$, where $\psi'_F(0) \approx \Delta\psi_F/\Delta z$ [531]. The equation gives the center position of the innermost flux surface, Z_F, directly from the Faraday rotation measurement. The ψ'_F is calculated from the slope $\Delta\psi_F/\Delta z$ at $z = 0$. This is a simple linear relation between position and Faraday rotation measurements near the magnetic axis, $z \sim 0$, which provides essential information for a PCS [548]. This vertical position is independent of the time derivative, therefore, it is NOT subject to noise from long-time integration. Zero-crossing of Faraday effect measurement provides higher sensitivity to vertical position than other methods such as density or SXR emissivity profile measurements. It should be noted that vertical position is determined directly from the two line-integrated measurements and no inversion is needed. This approximation can enhance the capability of performing real-time control since the line-integrated Faraday-effect measurement can have excellent time resolution (especially when using the R- and L- wave approach) and requires no other equilibrium information.

This approach was recently demonstrated on both the EAST [531] and DIII-D tokamaks where horizontally viewing polarimetry chords are available. An example from DIII-D is shown in figure 135, where the Faraday measurement agrees well with the EFIT results (using external magnetics) through a programmed 25 cm vertical position scan. This approach can be used to independently and non-inductively measure the plasma position thereby providing a cross check for flux loop measurements. Since the Faraday measurements are internal to the plasma, they can also be exploited for plasma control related to vertical displacement events or disruptions.

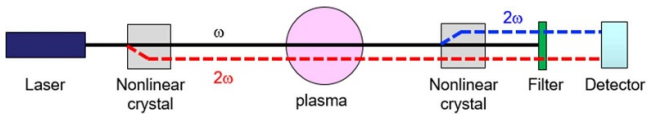

Figure 136. Basic concept of homodyne dispersion interferometer.

The plasma position, is the ratio of Faraday rotation to its gradient and is therefore insensitive to the CM effect itself as it largely cancels. This result simplifies use of polarimetry measurements for plasma position sensor in a PCS.

The value of a PoPola measurement of plasma position is threefold for ITER; (1) provides an independent, non-inductive measurement of position, (2) can be used to cross check and validate flux loops or serve as a backup in the event of flux loop failure in harsh ITER radiation environment, and (3) can provide an early warning of plasma vertical position changes related to instability or disruption.

6.11. DI for ITER

As described in the previous section, the two-color interferometer approach employed by the TIP can separate the phase shifts caused by a plasma and by mechanical vibrations. DI [549] is a relatively new interferometry configuration and is essentially a variation of the traditional two-color interferometer in that it also uses two different wavelengths. While a standard two-color interferometer measures the phase shift for each wavelength separately, and can solve for vibrations and plasma-induced phase shifts independently, the phase shift measured with DI contains essentially no vibration-induced phase shift, instead measuring the phase shift caused by dispersion of a medium. An additional advantage of DI is a simpler optical configuration. DI uses a single laser source and detector and has no requirement for a path-length matched reference chord.

The concept of DI is shown in figure 136. While a standard two-color interferometer is equipped with two laser sources with different wavelengths, DI utilizes a nonlinear crystal to generate the second harmonic component as the second color. The first nonlinear crystal generates the second harmonic component, after which a combination of co-linear fundamental and second harmonic components are launched through the plasma. After passing through the plasma, another nonlinear crystal is used to generate additional second harmonic power and the remaining fundamental component is blocked out. The dispersion interferometer measures the interference between the two second-harmonic beams only. In this approach, the vibration-induced phase shift is optically subtracted, because the two beams experience the same vibrations. In an ideal configuration, the measured phase shift results solely from dispersion through the plasma [549].

Starting with a homodyne configuration, several diagnostic techniques like phase modulation [550–553] and heterodyne detection [554], have been applied to the DI for improvements of time and density resolutions. As an example, the DI configuration on LHD is shown in figure 137. Since DI

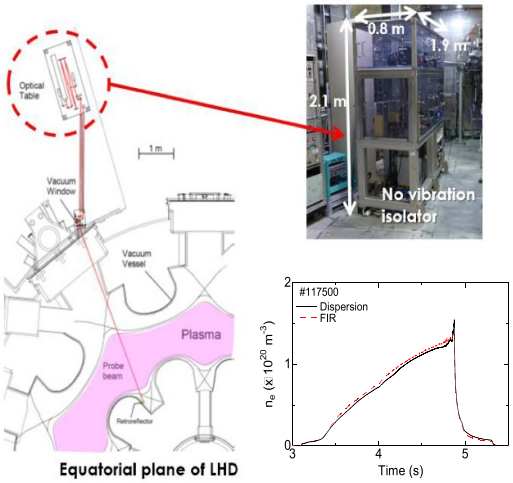

Figure 137. Dispersion interferometer on LHD.

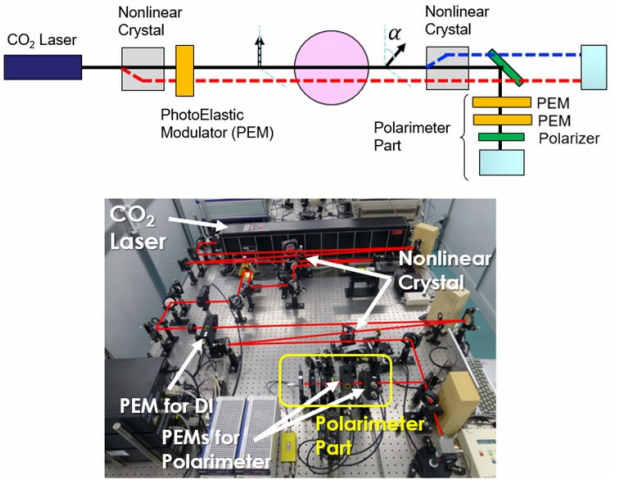

Figure 138. Concept of the combined dispersion interferometer and polarimeter as will be implemented on ITER's DIP.

is relatively insensitive to mechanical vibrations, the optical frame, where most optics were placed, had no vibration isolation and was directly installed to the diagnostic platform in the LHD hall. The laser source was a CO2 laser with a wavelength of 10.6 mm and output power of 7.5 W. The 5.3 mm component was generated using a AgGaSe2 crystal. The LHD DI utilized phase modulation with a PEM to improve the density (the phase) resolution. The probe beam injected into the LHD VV was reflected by a corner cube mirror installed inside the LHD vessel. The reflected probe beam returned to the optical frame, and was detected. The detailed evaluation method of the plasma phase shift and the electron density is described in [552]. The line density resolution, which was defined as the standard deviation of a 3 s long signal acquisition, was 2.5×10^{17} m^{-2} (0.6 deg.), with a response time of 0.1 ms. The measured electron density showed good agreement with the far IR laser interferometer. The response time was good enough to measure rapid density increases due to pellet injection [552].

The relatively simple configuration of a DI reduces its maintenance and the risk of components failure. The absence of a reference leg makes the system's footprint smaller enabling integration into limited spaces. Advantages of the DI like excellent line density resolution, ease of integration and reliability are reported from several devices, such as TEXTOR [550, 551], LHD [552], W7-X [553], and DIII-D [554]. They motivated the inclusion of DI in the ITER diagnostic set. Figure 137 shows a conceptual view of Density Interferometer Polarimeter (DIP) on ITER. DIP is a CO2 laser-based phase modulated DI combined with a polarimeter using PEMs. As with TIP, the polarimeter is incorporated in order to compensate for fringe skips, should they occur. The fundamental component, which is typically filtered out after the 2nd nonlinear crystal, is used for the polarimetry measurements. A PEM-based polarimeter has been previously demonstrated on JT-60U [555] and does not affect DI measurements, since it measures the polarization angle of the wavelength components which is not used finally in the standard DI. The combination of the DI and the PEM polarimeter was tested on a bench as shown in figure 138. In the prototype DIP, simultaneous measurements of the interferometer phase shift and the polarization angle were successfully demonstrated [556].

6.12. Conclusion

Since the ITER physics basis update in 2007, laser aided diagnostics have advanced considerably with many diagnostics going from outline concepts to detailed integrated design solutions ready for implementation.

With this advancement in design many particularly challenging diagnostic components have gone through testing and prototyping stages. For example, following prototyping and testing the TIP diagnostic now plans to use a QCL as its' secondary laser as opposed to a CO laser in addition to the main CO_2 laser. The ETS diagnostic has tested laser beam dump designs for longevity and a new laser beam combiner based on a rotating half-wave plate has been developed. Similarly, demonstration of a rotating waveplate for PoPola has been shown to measure Stokes parameters with no drift for over 1000 s.

The challenges of the diagnostic designs have lead to development of new hardware. New lasers have been specifically developed for the DTS diagnostic with diode pumped 2 J 50 Hz 1064 nm main laser and calibrating 1047 nm and 946 nm lasers with high pulse power and repetition rates. Additionally a digital polychromator design has been developed integrating digitizers within the traditional filter polychromator unit. There are still considerable challenges to be overcome, for example the CPTS diagnostic would greatly benefit from a free form front optic design. The ability to integrate such a large free form mirror into ITER and shutter and clean it has yet to be demonstrated.

New diagnostic techniques have also been developed since the last ITER physics basis update. Laser induced fluorescence has been proposed as a technique to measure Helium density and ion temperature. Similarly laser induced quenching, which pumps individual transition lines using an OPO laser, provides

the possibility to measure the n_H/n_D and n_D/n_T ratios. Existing diagnostics are expanding their remits taking on new measurements. The PoPola system is now expecting to measure plasma vertical position and magnetic fluctuations. DI is also proposed which using a simple optical configuration can provide phase shift measurements without any vibration induced phase shift.

The theoretical basis for measurements is also being advanced. Recent simulations have also shown that the PoPola must take into account the T_e effect in order to accurately diagnose the q-profile. While the proposal for polarimetric TS is not new, there has been very significant development in the theoretical basis behind this measurement capability. The development of polarimetric TS has been driven by that requirement being highlighted by ITER due to the need to accurately diagnostic high T_e.

Importantly laser aided diagnostic techniques proposed for ITER are being trialed on existing Tokamaks. On Globus-M a 1 MHz OPO laser was deployed in order to measure n_e using laser induced quenching. The TIP combined two-color interferometry and polarimetry measurements were first tested in the lab and then installed on DIII-D. The first observation of polarimetric TS measurements were recently obtained on JET. Vertical position measurements using PoPola were demonstrated on DIII-D. DI was demonstrated on a wide number of machines including LHD and TEXTOR. One of the key outputs of these tests on existing machines is it shows potential issues that need resolution, for example interferometric phase shifts were observed by TIP due to small temperature differences along the beam path. These lab demonstrations of advanced diagnostics and techniques on existing machines are crucial to de-risk the laser diagnostic implementation for ITER.

Appendix I—Abbreviations

Abbreviation	Meaning
AR	Anti-reflection
APD	Avalanche photo diode
CCR	Corner cube reflector
CM	Cotton–Mouton
CPTS	Core plasma Thomson scattering
CRM	Collisional radiative models
DAQ	Data AcQuisition
DFW	Diagnostic first wall
DI	Dispersion interferometry
DTS	Divertor Thomson scattering
ECCD	Electron cyclotron current drive
ECE	Electron cyclotron emission
ECRH	Electron cyclotron resonance heating
EFIT	Equilibrium FIT
EQE	Effective quantum efficiency
ETS	Edge Thomson scattering
FIR	Far infra-red
FPGA	Field programmable gate array
FWHM	Full width at half maximum
HeNe	Helium neon
LHD	Large helical device
LIDAR	Light imaging detection and ranging
LIF	Laser induced fluorescence
LIQ	Laser-induced quenching
Nd:YAG	Neodymium doped Yttrium aluminum garnet
Nd:YLF	Neodymium doped Yttrium lithium fluoride
OPO	Optical parametric oscillator
PEM	Photo-elastic modulator
PoPola	Poloidal polarimeter
QCL	Quantum cascade laser
RCP	Right circular polarization
SNR	Signal to noise ratio
SOL	Scrape off layer
TIP	Tangential interferometer polarimeter
TS	Thomson scattering
VDF	Velocity distribution function

7. Microwave diagnostics

M. Austin[34,4], S. B. Korsholm[35], Y. Liu[2,26], S. Danani[18], C. Muscatello[2], W. L. Rowan[34], V. Vershkov[24], G. Wang[33], J. L. Xie[36], M. Zerbini[10] and Y. L. Zhu[37]

7.1. Introduction

Plasma diagnostics based on microwave radiation (inclusive of millimeter-wave and higher frequencies) have a long history going back over 70 years. Early diagnostic work is summarized by Heald and Wharton [557], with later summaries by Hartfuss [558] and Donné [4]. Looking forward, many aspects of microwave diagnostics will be favorable for next step fusion plasma devices. Both active (e.g. reflectometry, polarimetry) and passive (e.g. ECE) diagnostics are usually able to operate with launchers and receivers that are safely distanced from the edge of the reactor grade plasmas. And the radiation is generally able to be transmitted by low loss methods (mostly waveguide) that are not subject to radiation damage and degradation. Additionally, the associated sources and detectors of these systems are readily available at reasonable cost, and due to the transmission lines, can be stationed well away from the fusion device. Overall this bodes well for robust and reliable measurements from microwave diagnostics.

As described in the sections below, there have been advances in microwave systems which all lead to more accurate and reliable measurements of key plasma parameters. Refinements in theory, techniques, and hardware bring the diagnostics to full readiness for burning plasma conditions. Although most of the sections apply to ITER, the advances described will be relevant for fusion devices beyond that project, like a demonstration or pilot plant machine. Additional breakthroughs and new techniques will almost certainly be required for microwave diagnostics to meet the needs of the energy producing follow-ons to ITER.

Robustness will be an important quality for microwave systems as they will be subjected to the harshest conditions seen to date. If they can meet the proscribed reliability, the systems will be key to primary control systems that the machine will rely on to protect itself. However, certain challenges remain. In most cases (excluding the sources for CTS) the power levels for both active and passive diagnostics lie in the watts to nanowatts ranges. This is in the face of multiple megawatts

Table 32. ITER measurement parameters that microwave diagnostics contribute to.

	Primary	Backup	Supplementary
Electron cyclotron emission	Core T_e NTM $\delta T/T_e$	ELM temperature transient	β_P P_{rad} E_{max} runaway I Runaway Edge T_e TAE $\delta n/n_e$ & $\delta T/T_e$
Low field side (LFS) reflectometer	ELM density transient Edge n_e TAE $\delta n/n_e$ & $\delta T/T_e$	Core ne	Profiles of electron density V_{pol}
High field side (HFS) reflectometer	ELM density transient Core n_e TAE $\delta n/n_e$ & $\delta T/T_e$		Line-averaged electron density
Collective Thomson Scattering (CTS)	Alpha density profile Alpha energy spectrum p, D, T, ^{3}He Energy Spectrum		n_T/n_D in plasma core Core T_i Edge T_i n_H/n_D Core

of microwaves expected to be employed in reactor devices for ECH (certainly ITER). The challenges for the instruments are twofold: (1) to not be blinded by the high power direct and scattered power, and (2) to not be damaged by the same. The latter is expected not to be too serious a challenge since the ECH will be in known, narrow frequency values so appropriate stop band, high- or low-pass filtering can be employed to prevent interference of the measurement or destruction of the instrument. In fact all diagnostic systems for ITER have some protection of this sort for the stray gyrotron power.

But there is another potential source of interference for microwave diagnostics that will have to be dealt with, and that is intense, essentially random bursts of strong microwave emission from the plasma itself. A type of this phenomenon, bursts at ECE frequencies, was first reported from one of the early tokamaks to operate at high auxiliary heating power, TFTR [559]. Subsequently bursting at ECE frequencies has been reported from many other tokamak plasmas, as seen in [560, 561] and the articles referenced within those. Although there has not been a comprehensive study so far, from these reports one sees that a common situation in most cases is low collisionality. That is, bursting emission from plasmas in the range of ECE occurs for plasmas heated to high electron temperature and relatively low density. This is what leads to the deduction that in ITER and other future fusion devices, bursting emission will be a common and frequent occurrence.

The upshot is that this emission will be an ever present annoyance, and sometimes threat, for both active and passive millimeter wave diagnostics in these future devices. With the frequency of emission bursts so random and uncertain, it will be difficult to devise avoidance and protection schemes. And with the expected high electron beta in the plasmas, it is conceivable that the intensity of these bursts will be enough to inflict damage; there is anecdotal evidence from both DIII-D and AUG tokomaks that bursts have damaged microwave diagnostic instruments. A reasonable plan to deal with the bursts might be to have the capability, at least at the instrument end, to insert suitable filters once the nature of that devices bursts are understood and become predictable.

So moving forward, the microwave diagnosticians can expect some challenges in dealing with power coming from the reactor-grade plasma itself. The technology is available to deal with the issues, in terms of frequency-domain and time-domain filtering; it is a solvable problem. Therefore no doubt the advanced hardware and techniques described in the following sections will be able to make their full contributions to the fusion effort.

7.2. MPs for ITER

Microwave diagnostics contribute to a variety of ITER plasma MPs. Those MPs provide the plasma information such as Core/Edge $T_e/n_e/T_i$, ELM Temperature/Density Transient, MHD induced T_e/n_e fluctuations, dynamics of alpha particles and other energetic particles, etc. A complete list is summarized in table 32.

The table 33 lists the requirements of the MPs for those where microwave diagnostics have a primary role. All of those MPs are either for advanced plasma control (AC) or for physics studies (PHY). Among those MPs, some of them can only be measured by a single system. For example, ECE is the only system that contributes to NTM $\delta T/T_e$, and CTS is the only system contributing to both alpha energy spectrum and the p, D, T, and ^{3}He energy spectrum. Therefore, the requirements of those MPs shall be completely met by the sole system. For other MPs that several systems contribute to, the requirements of those MPs shall be met by the combination of those systems. In consequence, the requirements of the MPs that microwave diagnostics have a primary role are driving the system design.

Table 33. Measurement requirements of the measurement parameters for which microwave diagnostics have a primary role.

Parameter	Condition	Range	Time Res.	Spatial Res.	Accuracy	Role
ELM transient	$r/a > 0.85$	5×10^{18}–3×10^{20} m^{-3}	10 ms	5 mm	5%	PHY
Core T_e	$r/a < 0.85$	0.5–40 keV	10 ms	$a/30$	10%	AC
Core n_e	$r/a < 0.85$	3×10^{19}–3×10^{20} m^{-3}	10 ms	$a/30$	5%	AC
Edge n_e	$r/a > 0.85$	5×10^{18}–3×10^{20} m^{-3}	10 ms	5 mm	5%	AC
NTM $\delta T/T_e$	$T_e > 1$ keV	1×10^{-2}–5×10^{-2}	0.1–10 kHz	Island wid $\geqslant$ 20 mm	1%	AC
TAE $\delta n/n_e$ & $\delta T/T_e$	—	5×10^{-6}–5×10^{-4}	30 kHz—0.5 MHz	$n = 2$–50	30% (rel)	PHY
Alpha density profile	—	1×10^{17}–2×10^{18} m^{-3}	100 ms	$a/10$	20%	PHY
Alpha energy spectrum	—	0.1–3.5 MeV	100 ms	$a/10$	20%	PHY
p, D, T, ^{3}He Energy Spectrum	—	0.1–1 MeV	100 ms	$a/10$	20%	PHY

7.3. ECE diagnostic for ITER

7.3.1. Introduction. In ITER, ECE in the range from 100 GHz to 1 THz will be used for measurement of electron temperature (T_e) profiles with high spatial and temporal resolution, for detection of high frequency instabilities (MHD, neoclassical tearing modes (NTM), Alfven eigenmodes, turbulence) and for measurement of the energy loss due to ECE. Both profile and NTM information are required by the Plant Control System in real time. A complicating factor is that recent results in DT plasmas [562, 563] have reinforced an earlier result [49] in which ECE did not agree with Thomson scattering, an alternate diagnostic for electron temperature profiles. The ECE diagnostic has the facility to detect the non-thermal electron distributions, which may cause this. Development of the diagnostic is a collaboration among the USDA, the INDA, and the IO.

The ECE diagnostic will measure electron temperature profiles for full-field and half-field ITER scenarios. Plasma access for ECE with X-mode polarization is illustrated for one full-field ITER scenario in figure 139. The figure represents an H-mode scenario with an axial toroidal field 5.3 T and with peak T_e of 22.5 keV and peak electron density of 1.3×10^{20} m^{-3} (IMAS scenario 130 506, run 403, time 230 s, DT fuel, $I_P = 15$ MA). Figure 139 illustrates that the second harmonic X-mode EC emission can be used for measurements in the pedestal and confinement regions. The core of the plasma is accessible to ECE measurements using 1st harmonic O-mode.

The ECE diagnostic comprises three parts, front end, polarization splitter units (PSU) and transmission lines, and detectors. Each will be described in the next sections.

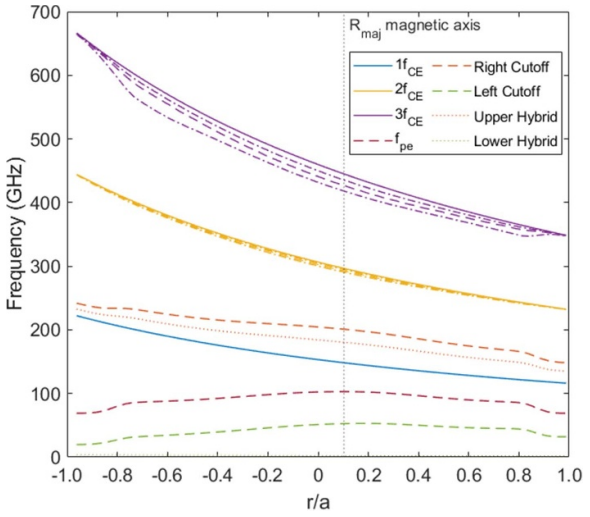

Figure 139. Calculated X-Mode ECE access and limits. Solid lines indicate cold plasma ECE approximation. Yellow and purple dashed lines show location of the relativistic shift of emission peaks for second and third harmonics, respectively. Dot–dash lines indicate relativistic broadening of emission for second (yellow) and third (purple) harmonics.

7.3.2. The front end. The front end (figure 140) collects the ECE from the plasma along two high-resolution views of the plasma, one view radial and the other oblique. One challenge is to collect sufficient emission with high spatial resolution to allow high temporal resolution. Since the captured plasma emission contains information both in its intensity and its polarization, a second challenge for the front-end design is to preserve both. The front-end system is in the middle DSM of equatorial port 9 (DSM EQ9, figure 140). The large distance from the diagnostic flange to the plasma center (>3 m) and the large plasma diameter (>6 m) require collection with minimum divergence angles. Quasi-optical (QO) [564] collection optics offer one means for achieving all of these requirements [565]. Compactness is another requirement. The design of the QO collection optics for ITER is similar to the compact Ellis-Austin periscope, which was developed for DIII-D [566] and achieves the required high spatial resolution with modest frequency dependence using just one ellipsoidal focusing mirror.

In figure 140, an ellipsoidal mirror for each view (M1 for the radial view) collects emission from the plasma. A flat mirror (M2) redirects the emission through the vacuum window (W) to the system aperture (A) which sets the spatial resolution in the plasma. The calibration source (HS) can be switched into the system for intensity calibration using a flat mirror. More on this later. The sizes of the optics are chosen to be a factor of three larger than the Gaussian beam width derived from the QO analysis. That assures transmission of more than 98% of the emission and much simplifies the secondary ECE requirement to measure the total ECE from the plasma.

The size of the collection volume of the ECE beam is tracked from the high field side (HFS) of the plasma through

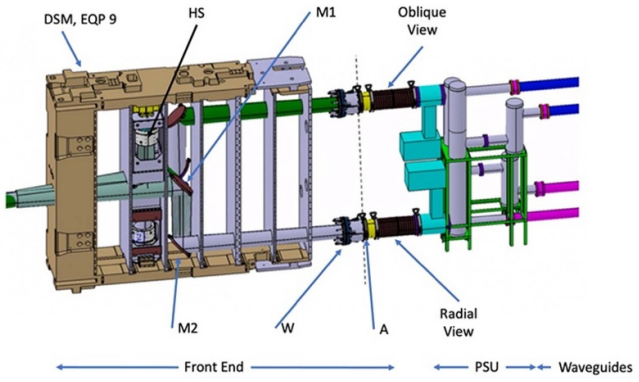

Figure 140. Front end components and the PSU. Component labels are for the radial view and are defined in the text.

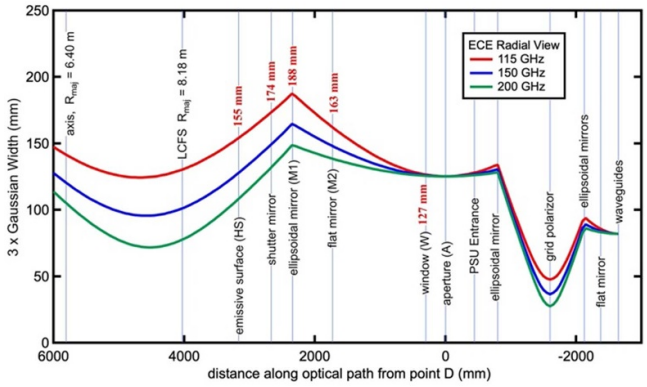

Figure 141. The size of the Gaussian beam from the waveguides to the scenario axis of ITER along the optical path. The size is taken to be 3*(Gaussian width). The reference location is the system aperture.

the entire QO system to the entrance to the waveguides in figure 141. The locations of the QO components are shown and their sizes are fixed by this QO calculation. The design results in component sizes that are consistent with the restricted space in the equatorial port yet large enough to reasonably meet the ITER measurement requirements. The size of the observed volume varies across the plasma (distance >4000 mm in figure 141), and as expected there is a frequency dependence. Still, the spatial resolution requirements for ITER are met. Since the initial design, the front-end optics have been modified repeatedly and successfully to follow the progress of port integration and that has demonstrated its robustness and flexibility.

Discrepancies between electron temperature derived from analysis of ECE and Thomson Scattering occur in some instances and appear to be due to departures from Maxwellian distributions [562, 563, 49, 564–569]. The ECE collected from an oblique view is sensitive to non-Maxwellian distributions [569] and has been used to evaluate the discrepancy. The resolution of this discrepancy was shown [49] to require analysis of higher harmonic ECE. This will require a wide bandwidth detection system such as the Fourier transform spectrometer (FTS). An oblique view is included in this diagnostic design (figure 140) which is quite similar to the radial view described above. In addition, an FTS of the Martin–Pulpett interferometer type is included in the ITER ECE instrument array. The oblique view can provide a redundant measure of $T_e(R)$. The need for an oblique view then follows from the primary role to measure electron temperature with high reliability.

Mirrors are used to collect ECE. Since they are in-vacuum, indirectly exposed to plasma, and inaccessible for extended periods, degradation is a significant issue that requires *in-situ* mitigation. A calibration source is integrated into the design of both radial and oblique views. Each can be directly substituted for the plasma emission by the switching of a single mirror in each case and this provides a reference calibration for the ECE. The hot calibration source for the radial view is shown in figure 140 (HS). The primary component of the hot source is a SiC surface that is contoured [570] to produce a large diameter, uniform source of blackbody emission. When heated to its target temperature of 700 °C, its blackbody emission is easily distinguishable from the ambient emission of the other front-end components. The design is complex, as it must produce a uniform emission across a large surface for the many hours required for calibration. Design and successful prototyping are described in detail elsewhere [571–573].

7.3.3. PSU and transmission line. The front-end optics are designed to preserve the polarization to a high degree, but the emission is conducted to the detection instruments, which are located more than 40 m from the tokamak, via purged waveguides. Waveguides will not preserve the polarization, so the polarizations for each view are separated in the PSU (figure 140), a QO unit. The polarized emission for each view is conducted to the detectors via a separate waveguide.

The transmission line is smooth-walled circular aluminum tube, which meets loss requirements of <15 dB (70–400 GHz) and <22 dB (400–1000 GHz). The waveguide will be purged with dry air to limit absorption features in the ECE spectrum.

7.3.4. Detection. After all this, the ECE emission spectrum arrives at the instruments where it is spectrally analyzed, digitized, and the data sent to the archive. There will be two standard radiometers [574, 575]. One covers the range from 220 GHz to 340 GHz. While it pushes the limits for contemporary designs, a similar unit was deployed at C-Mod [576]. The limitations of that design were addressed in a prototype [577, 578]. At full field, it will cover the confinement region and pedestal in X-mode. A second, conventional radiometer will operate in the range of 122–230 GHz. At full field, it will be used for core measurements in O-mode. There will be two FTS spectrometers to cover the range of 70–1000 GHz with 3.75 GHz resolution. These will facilitate detection of non-thermal distributions and measurement of energy loss.

7.3.5. Prospects. The design of all components are nearing completion. Prototyping of components is in progress. Port integration is actively in progress.

7.4. A low-loss microwave transmission line for ITER ECE

The ITER ECE diagnostic will be used to determine the plasma electron temperature by measuring the intensity of ECE in the frequency range 70 GHz–1 THz. One of the challenging requirements for the ITER ECE diagnostic TL is achieving low attenuation for the long distance (∼43 m) between the front end and the instrument room over the broad frequency range. This is particularly challenging because of the low power (∼few nW) thermal radiation emitted from the *in-situ* calibration sources located in the front end, which plays a vital role in determining the accuracy of measurements performed.

To meet the ITER ECE transmission line measurement requirement, an 8 m long prototype TL was developed at ITER-India. This TL is made up of oversized smooth walled straight waveguide sections (each of length 2 m and ID of 72 mm), miter bends and waveguide joints. The experimental set-up for attenuation measurement of this prototype line consists of a millimeter wave black body source, a FTS and the TL with required supports for proper alignment and coupling. The FTS is based on a Martin–Puplett interferometer (MPI) configuration [579] and covers the spectral range from 70–1000 GHz. The MPI operates under vacuum, has high throughput, excellent time resolution of 10 ms, and a scan displacement of 15 mm that provides a spectral resolution better than 10 GHz [580]. There are two input ports available on the FTS. One or both of them can be connected to the oversized waveguide (up to 99 mm). A 3 mm thick polypropylene window is provided for both of the FTS input ports to separate the FTS from all of the external interfaces and maintain a vacuum seal. A manually actuated shutter is provided on each of the input ports to enable blocking of the radiation from the input ports that are not in use. Eccosorb® is attached to these shutters which acts as a reference radiation source at room temperature. The input ports on the FTS are standard ISO 100F-type vacuum flanges. For the prototype TL measurements, port 1 of the FTS was kept at LN_2 temperature and port 2 was kept at high temperature ∼500 °C, in order to increase the SNR. The recorded interferograms (30 000) were coherently added to average out the random noise. The attenuation was estimated by taking the ratio of the spectrum (derived by performing FFT of interferograms) measured for ∼8 m TL length to the reference spectrum. The average and standard deviation of attenuation are derived for several data sets of attenuation measurement and are shown in figure 142. It is found that the error in TL attenuation is ∼60% for frequencies below 250 GHz and <5% for frequencies above 250 GHz.

Considering the uncertainty associated due to various factors such as microwave source power, TL alignment, detector sensitivity and atmospheric effects (i.e. line and continuum absorption) a safety factor of two has been taken for deriving the ITER ECE transmission line loss for 43 m length as shown in figure 143. Since the TL is not under vacuum, water vapor absorption lines are observed in the spectrum at 380, 448, 552, 752, 916 and 988 GHz. It has been observed that, the overall transmission is improved in case of rough vacuum measurement as both the water line absorption and

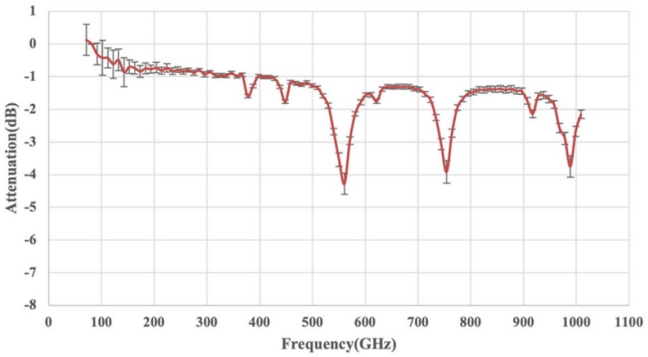

Figure 142. Measured transmission attenuation for ∼8 m length smooth waveguide TL.

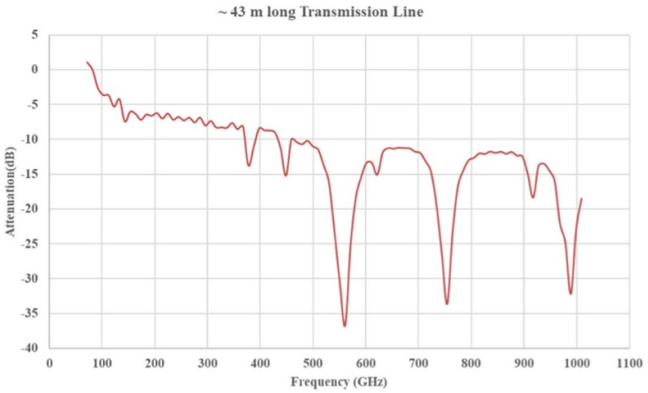

Figure 143. Estimated loss for ITER ECE TL for smooth-walled waveguide (∼43 m length and 6 Miter Bends), based on measured attenuation of prototype system.

the continuum absorption are lower in an evacuated TL [581]. It is also inferred from comparison between air and vacuum measurements that there is some level of continuum absorption of the radiation in this frequency range by atmospheric gases. The broadband transmission attenuation is decreased by ∼2 dB (average value) above 500 GHz.

From the above measurement results, it is determined that a smooth walled TL gives a maximum loss of 13 dB in the 500–800 GHz range, and even better performance in the 100–350 GHz which is the range for primary measurement of the ECE Diagnostic. This meets the ITER ECE transmission line attenuation requirements of <15 dB attenuation in frequency range 70–400 GHz and <22 dB attenuation in 400–1000 GHz.

The results have been assessed to understand the cause of large error in TL attenuation for frequencies below 250 GHz. This can be attributed to the low sensitivity of the FTS detector, 1/f noise and low source power. FTS is a wide band system with coverage up to 1800 GHz (upper limit) but with weaker sensitivity in the lower frequency range. A reduced error could be achieved with longer integration times, e.g. ∼8 h. However, if the detector element is replaced by one with enhanced low frequency sensitivity, then this problem can be resolved. It is therefore concluded that in case of high signal level from the plasma and having an FTS with optimized detector, will resolve the concern of large error in attenuation

in the low frequency range of the spectrum even in case of low signal (as in the case of the calibration source). In order to further improve the prototype TL attenuation results, another hot source, having good temperature uniformity and temperature stability, is also being considered, which will improve the S/N ratio. Also, there is scope of improvement in the FTS data analysis techniques which are also being looked into. Further experiments are being planned in near future with improved data analysis and hot-cold techniques.

7.5. Correlation ECE measurement of electron temperature turbulence

Multi-field turbulent fluctuations, e.g. turbulence in temperature, density, magnetic field, radial electric field, etc have been considered possible mechanisms to explain the observed anomalous radial transport and therefore define the particle and energy confinement in magnetic confinement fusion devices. The correlation ECE (CECE) radiometer has been developed as an effective electron temperature turbulence diagnostic for core to edge pedestal measurement in the last two to three decades on tokamaks and stellarators (referring to a 2007 review paper by Watts [582] and the references therein, and [583–591] for CECE systems on existing machines). The CECE measurement of electron temperature turbulence has contributed to various physics studies, e.g. in earlier days, core heat transport in TEXT-U [592], sawtooth physics in TEXT-U [593], core transport in W7-AS stellarator [594], hot ion instabilities in Tore Supra [595], and others (see review article [582]). Recently, CECE has been utilized to study core transport in I-mode [596], negative triangularity shape plasma operations [597, 598], edge pedestal transport in RMP ELM-controlled H-mode [599] and quiescent H-mode [600], NTM physics [601], and validation of gyrokinetic simulations [602], etc.

The ECE signals are comprised of blackbody thermal radiation with inherent fluctuations [603] generally larger than or at the same level of electron temperature turbulence. The CECE diagnostic utilizes two closely spaced (generally radially spaced) ECE channels which contain uncorrelated thermal noise as well as correlated electron temperature turbulence; small turbulent electron temperature fluctuations are extracted by performing correlation analysis between the two ECE channels [582]. In ITER, ECE has a range of roles in the delivery of the core electron temperature profile and detection of NTMs, the measurement of the H-mode pedestal, and plasma energy, radiated power, runaway electrons, edge electron temperature profile and high frequency instabilities [604]. The CECE technique for electron temperature turbulence measurement can be applicable in ITER and contribute to transport and MHD physics studies in various operational modes and scenarios in ITER.

Recently, a new, improved analysis of correlation ECE data to accurately determine turbulent electron temperature spectra and magnitudes has been proposed [605], which has been verified both numerically through the simulation of synthetic ECE radiometer data, as well as through analysis of experimental data from the CECE system on DIII-D. The new formulation places coherency-based analysis on a firm foundation and corrects some currently published methodologies. This new method accurately accounts for bias error in the coherence function and correctly calculates noise levels for a fixed data record length. It provides excellent accuracy in determining temperature fluctuation level (e.g. $<10\%$ error) even for a small realization number in the ensemble average. The method also has a smaller uncertainty (i.e. error bar) in the power spectrum when compared to the more standard cross-power method when evaluated at low coherency. Direct calculation of system noise level using correlation between randomized IF signals is recommended.

The new form of the normalized electron temperature fluctuation power spectrum $P_{\tilde{T}}(f)$ is derived [605] as:

$$P_{\tilde{T}}(f) = \frac{1}{B_{IF}} \frac{\gamma_c(f)}{1-\gamma_c(f)}, \tag{7.1}$$

Where B_{IF} is the intermediate frequency (IF) bandwidth and $\gamma_c(f) = \sqrt{\gamma^2(f) - \gamma_b^2(f)}$, where $\gamma^2(f)$ is the coherence spectrum between the two ECE signals, $\gamma_b^2(f) = \left(1-\gamma^2(f)\right)^2/M$ is the bias error in calculating $\gamma^2(f)$, M is the realization number for calculating $\gamma^2(f)$. This new formulation has several advantages. The first being that an average or DC measurement of the ECE signals are not required for the evaluation of $P_{\tilde{T}}(f)$ since the calculation of the coherency spectrum $\gamma(f)$ is not sensitive to DC components. Secondly, the standard cross-power spectrum for evaluating $P_{\tilde{T}}(f)$ tends to have a bias at low realizations and/or low coherency cases. In addition, the statistical error is smaller than the cross-power spectrum with the same ensemble average calculations at low $\gamma(f)$ [605].

In CECE literature the minimum measurable electron temperature fluctuation level $\left(\tilde{T}_{\rm RMS}/\bar{T}\right)_{\rm min}$ is often predicted from the following radiometer noise formula [582]:

$$\left(\frac{\tilde{T}_{\rm RMS}}{\bar{T}}\right)_{\rm min} = \sqrt{\frac{1}{N^{1/2}}\frac{2B_{\rm vid}}{B_{\rm IF}}}, \tag{7.2}$$

where $N = 2B_{\rm vid}{\rm d}t$ is the number of data points, $B_{\rm vid}$ is the video bandwidth, and dt is the data record length. In fact, formula (7.2) can be found [605] to be the square root of the standard error of measured $\left(\tilde{T}_{\rm RMS}/\bar{T}\right)^2$ using correlation analysis. The simulations and DIII-D data show that the actual system noise level is underestimated by equation (7.2) (by tens of percent). A direct calculation of the minimum measurable electron temperature fluctuation level $\left(\tilde{T}_{\rm RMS}/\bar{T}\right)_{\rm min}$ using randomized IF signals and equation (7.1) is recommended.

For ITER there would be significant challenges to getting useful data from a high resolution CECE instrument but some form of it could likely be implemented, i.e. a system focusing on the low-field-side edge. This could be part of the ECE or reflectometer systems; for the LFS pedestal region the plasma would be in the near field of both system's optics and hence have the best antenna spatial resolution. Additionally the pedestal T_e values are expected to be such that relativistic broadening would be small, again allowing for sufficiently small ECE volumes for CECE to have decent resolution. These

measurements could contribute to understanding how turbulent and mode fluctuations affect the pedestal, its height and the region's transport properties.

7.6. CTS for ITER

The primary role of the ITER fast ion CTS diagnostic is to provide information on the VDF of the confined fast ions—in particular the fusion born alpha particles. The CTS diagnostic was included in the ITER Baseline in 2007 as an enabled diagnostic. This means that primarily the in-vessel parts of the diagnostic will be developed and installed for first plasma. The in-vessel front-end part of the diagnostic has passed its FDR in October 2021 [606].

The fast ion CTS diagnostic is a relatively young diagnostic first being proposed for JET in the 1990s [607, 608]. Below we will briefly outline the development maturing the fast ion CTS diagnostic to becoming an ITER diagnostic. Following this the present design and status of the ITER CTS diagnostic is presented.

In brief, the basic principle of fast ion CTS is that a powerful source beam—typically a gyrotron microwave beam in the frequency range near the fundamental or second harmonic at a power of several 100's kW—is injected via quasi-optical mirrors. The probe beam interacts with microscopic fluctuations—primarily electron density fluctuations—and scattered radiation is emitted [609]. A quasi-optical receiver transmission line picks up a portion of the scattered signal that contains information about the dynamics in the volume constituted by the overlap of the probe beam and the receiver beam. By choosing the scattering geometry and the probe frequency appropriately, one can ensure that the spectral information in the received signal primarily stems from collective motion of the electrons in turn originating from the dynamics of the ions. Hence, a properly designed fast ion CTS diagnostic can provide information on the VDF of the confined fast ions both spatially and temporally resolved. For more details, see [609, 610].

7.6.1. Developments of the CTS diagnostic. The fast ion CTS diagnostic was proposed, implemented, and tested on JET with moderate success [607, 608]. The primary challenge for the JET CTS diagnostic system was the choice of frequency in the 'window' between the fundamental and second harmonic EC resonance. With the high temperatures of JET, the background (ECE) noise hampered the SNR.

Following the JET CTS experience, an important step towards the maturation of the diagnostic was made in the implementation at TEXTOR [611] and later ASDEX Upgrade [612]. In parallel to this development feasibility studies for a CTS diagnostic for ITER were performed at Risø National Laboratory [613–624]. These early works laid the foundation for the inclusion of CTS in the ITER Baseline, and the system proposed in the feasibility study is conceptually alike the current ITER CTS design—being described in the next section.

While the ITER CTS diagnostic has been chosen to focus on fast ion physics, the versatility of the CTS diagnostic has been demonstrated at TEXTOR and ASDEX Upgrade [610, 625]. For specific scattering geometries, CTS can provide information on the fuel ion ratio in the core of a burning plasma, and geometries and equipment can be optimized to provide bulk ion information such as temperature and rotation velocity [616–618].

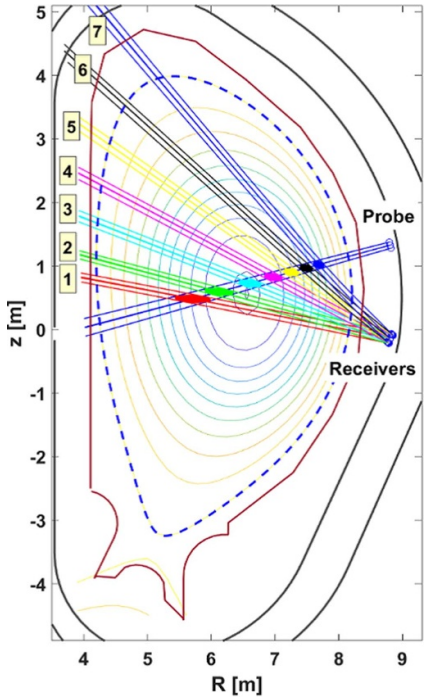

Figure 144. Geometry of the ITER CTS diagnostic. Probe beam in blue. Shown for the ITER steady-state scenario, $I_p = 10$ MA, $B_t = 5.3$ T.

Furthermore, it was demonstrated on ASDEX Upgrade that bulk ion features in the CTS signal are so powerful that measurements of e.g. bulk ion temperature, T_i, and bulk ion rotation, v_{rot}, can be made even while EC resonances are in the plasma [619]. This means that bulk ion CTS can be made in piggy-back by simply detecting the scattered signal due to the heating gyrotrons. This opens up new possibilities for more flexible CTS diagnostic systems on machines with ECRH.

While the CTS diagnostic is still a relatively young diagnostic, it is being implemented on several machines for ion measurements e.g. on LHD [620, 621] and W7-X [622].

7.6.2. Status of development of the ITER CTS diagnostic. The ITER CTS diagnostic will operate using a dedicated gyrotron operating at 60 GHz delivering at minimum 1 MW with 50% modulation duty cycle for ECE background subtraction [606]. The scattered signal is picked up by an array of seven receiver beams intersecting the probe beam in seven confined scattering volumes across the plasma diameter (see figure 144). The spatial resolution of the diagnostic varies across the diameter with a radial extent of the volume of 20 cm near the edge and of 50–80 cm in the core of ITER. The temporal resolution is 100 ms fulfilling the ITER measurement

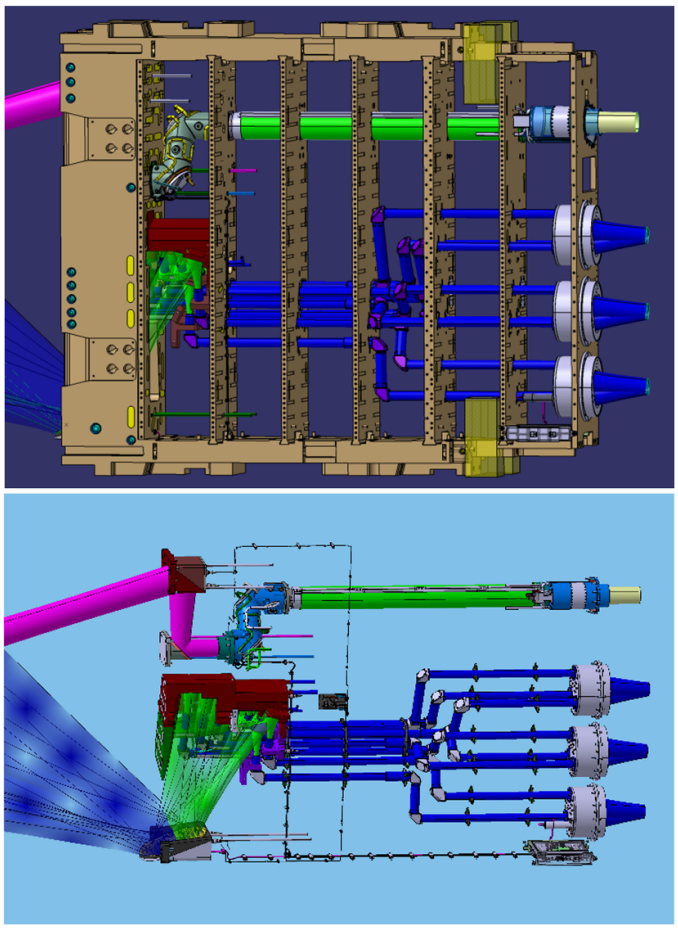

Figure 145. Drawings of the ITER CTS diagnostic in EPP12 drawer #3. The (pink) beam to the upper left is the gyrotron probe beam that intersects with the seven (blue) receiver beams in defined locations across the plasma diameter.

requirements for the parameters that CTS has as primary function:

- alpha density profile
- alpha energy spectrum
- p, D, T, ^{3}He energy spectrum.

The probing frequency of 60 GHz has been chosen in order to reduce the ECE background noise, which is very low in ITER at frequencies below 65 GHz [623]. This also means that the diagnostic must be operated in X-mode. However, this leads to another challenge, that the probing beam passes the fundamental EC resonance inside the portplug—an issue we return to shortly. At the same time, the frequency range is very close to an X-mode cut-off, leading to significant refraction of both the probe and receiver beams. Nevertheless, extensive modeling and analysis of the diagnostic performance has been performed and the proposed ITER CTS diagnostic will be able to measure the fusion born alphas within the desired accuracy [624, 626–630].

The in-vessel part of the diagnostic is located in an exclusive drawer (#3) of EPP #12. All in-vessel components have been developed and designed under contracts with Fusion for Energy (see figure 145). The in-vessel part of the fast ion CTS diagnostic for ITER passed the PDR in March 2020 and the FDR in October 2021.

Besides the more generic challenges of ITER diagnostic systems, such as radiation and neutronic damage, the CTS diagnostic has some specific challenges. The primary challenge is the fundamental EC resonance for 60 GHz being located in the middle of the EPP #12. The risk is that an EC-assisted breakdown of residual neutral gas could happen, since the neutral pressure is known to increase during plasma discharges—as seen in JET. This would lead to plasma formation in the CTS in-vessel transmission line, which in turn would lead to absorption of fractions of the 1 MW gyrotron beam inside the port plug transmission line components. The risk mitigating design feature is the use of a longitudinally split electrically-biased waveguide (SBWG). The functionality of such a SBWG has been demonstrated in prior implementations on e.g. DITE [631, 632]. The principal idea is that any free electrons inside the SBWG are swept to the positively biased half so fast that they cannot start an ionization cascade, which would otherwise lead to plasma breakdown inside the waveguide. The design and extensive modeling results are described in [631, 632].

The present paper cannot describe all aspects of the design and analysis, hence the reader is referred to the following literature describing the development towards a complete design of the ITER CTS diagnostic [610, 631–639].

7.7. LFS reflectometer for ITER

The Low-field side reflectometer (LFSR) for ITER will supply simultaneously three important plasma measurements: (1) electron density profile, (2) electron density fluctuations, and (3) poloidal plasma rotation. In addition, an indicator of edge transients (e.g. L-H transition, ELMs) will be derived from the time evolution of the electron density profile. The ITER PCS will use real-time measurements of the density profile and poloidal rotation from LFSR for advanced feedback control. In addition to feedback control input to ITER, LFSR data will be useful for plasma stability and turbulence studies. It is capable of detecting low-to-intermediate wavenumber fluctuations, enabling an extensive range of physics studies. The PPR that was originally foreseen in the 2007 ITER Baseline [4] has been abandoned on ITER because integration became prohibitively too difficult and the so-called captive components would not be delivered on time

The broad measurement capability of LFSR is enabled by an array of six monostatic antennas which inject from an equatorial port on the outboard side of the ITER vessel. Low-loss transmission lines, consisting of corrugated, overmoded waveguide and miter bends, transmit the 30–165 GHz, O- and X-mode signals to and from the ITER plasma. Integrated transmission-line components serve a range of purposes, such as protection from high-power stray RF radiation, accommodation of transmission-line displacement, and simultaneous measurement of reference and plasma phases throughout the discharge. Broadband transmission signals are realized by full-band microwave transceivers combined with quasi-optical multiplexing. Both frequency-modulated continuous wave (FMCW) operation for profile and fluctuation measurements and fixed-frequency continuous wave operation for poloidal rotation (Doppler) measurements are incorporated. Considering the fast-paced evolution of microwave and analog-to-digital conversion technologies, collection of FMCW data with bandwidths well above 1 GHz is planned for LFSR. With this capability, LFSR will perform full-band, ultrafast sweeps (<1 μs) with unprecedented time resolution. Density and plasma rotation profiles will be processed in real-time with <10 ms time resolution by FPGA modules. Detailed descriptions of the end-to-end design of LFSR can be found in previously published works [640, 641].

The design of LFSR has been optimized to probe the edge region ($r/a > 0.85$) for a broad range of ITER conditions. However, penetration into the core is possible under certain scenarios. Figure 146(*a*) shows full-field ITER baseline profiles for electron density (n_e), electron temperature (T_e), and magnetic field (B). O-mode and X-mode cutoffs and EC resonances at the midplane are plotted in figure 146(*b*); relativistic modification to the electron mass is included. Contour plots of cutoff frequency versus B, T_e, and n_e are shown in figures 146(*c*) and (*d*) for upper X-mode and O-mode polarizations. The T_e profile is mapped to the B profile at the midplane according to the profiles shown in figure 146(*a*). They are plotted along the vertical axes of figures 146(*c*) and (*d*). The horizontal dashed line indicates the magnetic field near the edge ($R = 8.40$ m). The vertical dashed line indicates the Greenwald density with plasma current of 15 MA and minor radius at the midplane of 2 m. With upper X-mode, the outboard n_e profile can be probed from the far SOL to the top of the pedestal, where n_e can be as high as 1×10^{20} m^{-3}. For lower n_e at the top of the pedestal, access into the core is possible, limited by the upper-bound probe frequency (165 GHz contour in figure 146(*c*)). The n_e profile in ITER is expected to be flat in the core, so O-mode measurements provide limited coverage. However, the measurement is still useful and provides a partially redundant and B-independent dataset to compare and verify with the upper X-mode measurements.

Various performance metrics of LFSR have been studied at a dedicated test facility consisting of a full-scale transmission line, representative of the current design. Two of the most important metrics to reflectometry are antenna efficiency and power budget. Previous works have investigated these performance metrics in detail [641, 642], and the results are summarized here. The front-end of LFSR includes the antenna assembly, ECH protection mirror, phase calibration mirror, and dual-disc vacuum window. The microwave signal traverses each of these components twice (one on transmit and second on receive). Mode conversion caused by these components can ultimately lead to degraded signal-to-noise. Representative antenna patterns measured for 55, 120, and 160 GHz are shown in figure 147. The profiles are peaked near the axis and exhibit a side-lobe power level which is generally less than -20 dB of the main lobe. The effect of the front-end components on the waveguide mode content is quantified with a phase retrieval algorithm using antenna pattern measurements collected at several distances from the antenna. The HE_{11} mode is the ideal propagating mode and couples to a free-space Gaussian beam with 98% efficiency [643]. The results of the mode analysis give the percentage of the total beam power contained in the HE_{11} mode and higher-order modes as a function of frequency. The HE_{11} mode content for 55, 120, and 160 GHz is 94.4%, 88.1%, and 87.5% respectively, i.e. it is highest at low frequency. In other words, loss of about 1 dB due to mode conversion can be expected at the highest frequencies. Inspection of the radiated profiles and the results of the mode analysis indicate the front-end components of LFSR impose only a small and acceptable fraction of mode conversion.

The metric used to assess the upper bound on the spatial resolution of LFSR density profile measurements is the range precision. The range precision depends explicitly on the SNR and the RF bandwidth [644], providing a means to assess the effect of output power, loss, and noise on the performance. Selecting a reasonable bandwidth of $\delta f = 0.25$ GHz, a SNR of 26 dB or larger is required to obtain a spatial resolution of 5 mm or better. Four main factors determine the ultimate SNR of the system: (1) power output of the transceivers, (2) loss due

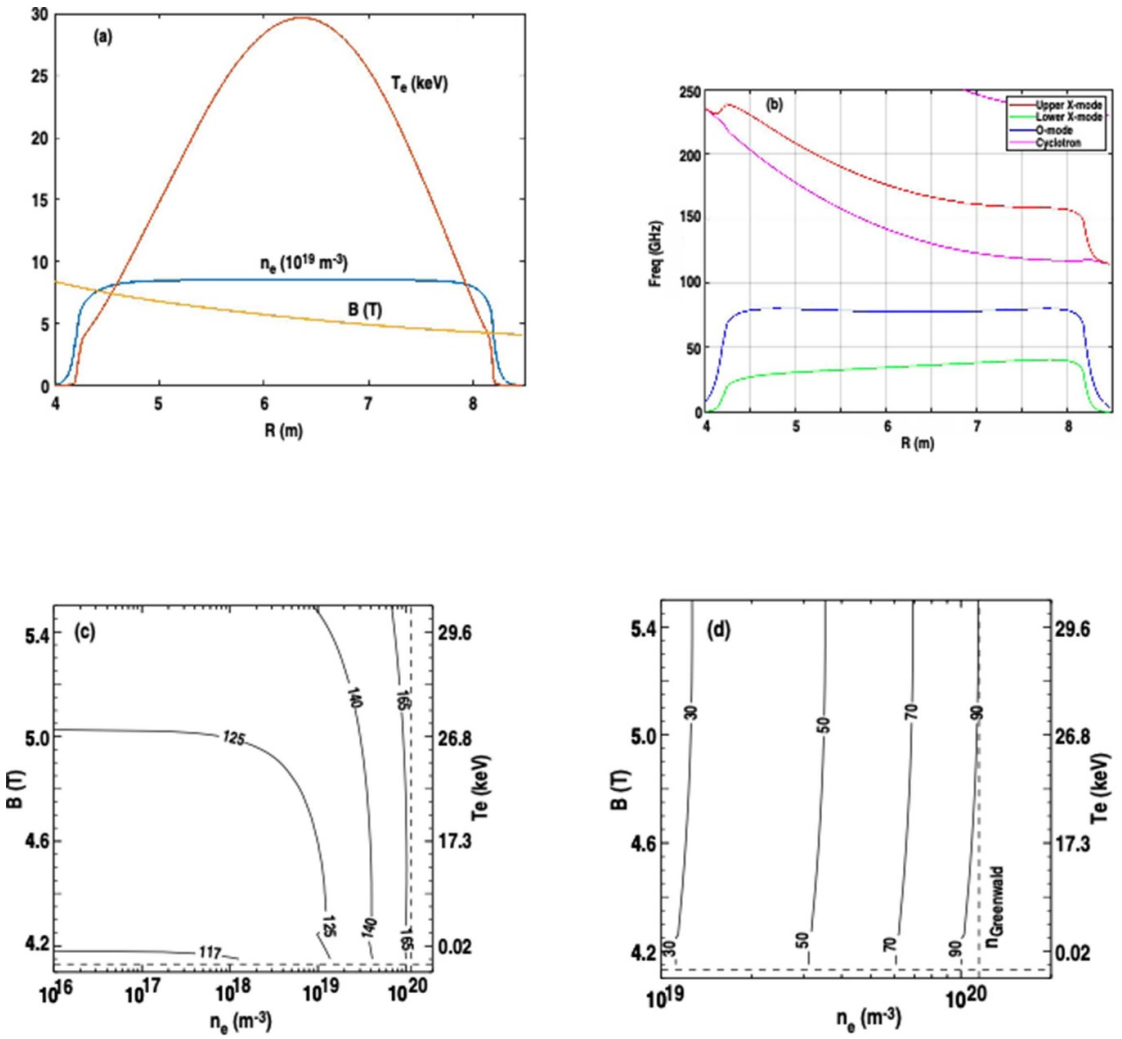

Figure 146. (*a*) Full-field ITER baseline profiles of n_e, T_e, and B. (*b*) Corresponding cut-off and cyclotron frequency profiles with relativistic correction. Contour plots of constant frequency (in GHz) versus n_e, B, and T_e for (*c*) upper X-mode and (*d*) O-mode polarizations. The horizontal dashed line indicates the field at the plasma edge (R = 8.40 m). The Greenwald density is plotted as the vertical dashed line.

to TL components, (3) plasma-induced losses, and (4) plasma-induced noise. Factor 1 is measured directly at the LFSR test facility. Factor 2 is also measured directly and compared to theoretical estimates of the loss. Factor 3 is estimated with full-wave reflectometer simulations for a range of density fluctuation parameters. Factor 4 is calculated assuming ECE is the main source of noise. A plot of the SNR is shown in figure 148, which does not include loss from turbulence and assumes the plasma midplane is vertically aligned to the antenna.

The horizontal dashed line indicates the minimum SNR of 26 dB to achieve 5 mm spatial resolution. Except for a narrow region around 60 GHz, SNR $>$ 26 dB over the full frequency range of LFSR. The drop at 60 GHz is due to a 60 dB notch filter to protect the LFSR microwave electronics from scattered signal from the CTS diagnostic. In general, turbulence increases loss, and the magnitude of additional loss depends strongly on the spectral and spatial characteristics of the turbulence. Over the range of fluctuation parameters run in the full-wave simulations, turbulence-induced losses up to 10 dB resulted. Even with this additional loss, LFSR still achieves acceptable SNR except near the edges of the discrete microwave bands (30, 50, 75, 92, 110, 137, 165 GHz) that comprise the full range.

The ITER LFSR will provide important measurements of electron density profile, density fluctuations, and plasma rotation. The design largely represents a traditional reflectometer in terms of basic functionality, but its combination of low-loss waveguide components, broadband-enabling technologies, and ultrafast, real-time process capabilities will permit measurements with high robustness and accuracy. Data from a full-scale test facility and modeling results suggest that high signal-to-noise is achievable with the current design, enabling sub-centimeter spatial resolution of the edge density profile.

7.8. HFS reflectometry (HFSR) for ITER

HFSR is based on the analysis of the amplitude and phase of the reflected mm-waves probing plasma from the inner

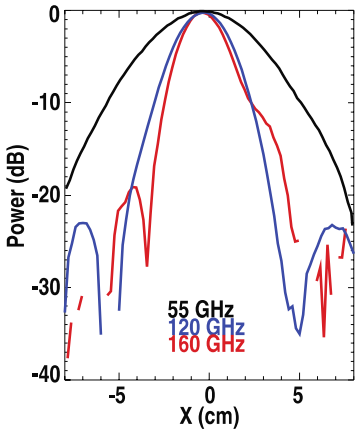

Figure 147. Radiated beam profiles for 55 GHz, 120 GHz, and 160 GHz.

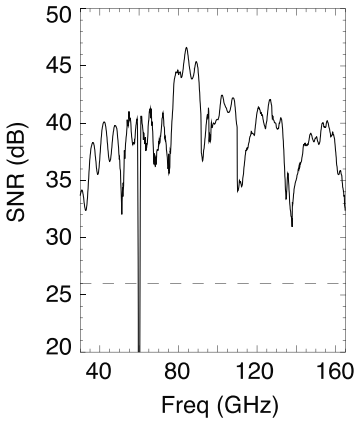

Figure 148. Signal-to-noise ratio considering transmission-line loss, plasma-antenna coupling loss, and ECE noise. The horizontal dashed line indicates the minimum SNR of 26 dB required for 5 mm spatial resolution.

circumference of the plasma torus. As the cutoff position of the reflection surface depends on the probing frequency, it is possible to investigate the radial density profile and its fluctuations by a frequency scan. The probing of the plasma can be made with the ordinary (O) and two extraordinary (X-) waves. The cut-off positions of these waves are shown in figure 149. The cut-off position of the O-wave depends only on the density. So it cannot access to the plasma core in the case of a flat density profile, expected in ITER [645], and can be used mainly at the edge. The cut-off position of the High- and Low-Frequency extraordinary waves (XU and XL) depends both on density and magnetic field, which gives the possibility to access the plasma core. But as seen from figure 149, in the case of HFS launch only the XL mode can access the plasma core. The great advantage of this wave is the utilization of lower frequencies and a small influence of the relativistic high temperature effect. Taking into account the operation density range of ITER discharges, frequency bands for O-mode of 18–140 GHz and for XL-mode of 12–90 GHz were chosen. The required wide frequency range, exceeding one decade, caused significant technical challenges in transmission of mm-waves along

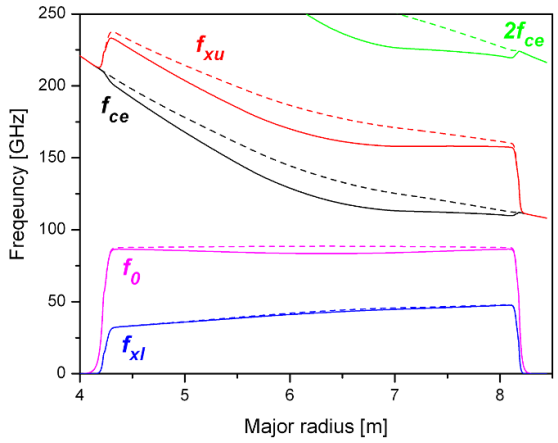

Figure 149. Radial dependencies of different frequencies in ITER for scenario 2. Dashed lines correspond to the cold plasma case ($T_e = 0$), solid ones to the real plasma temperature. f_{xl}—lower cut-off for X-mode; f_O—O–mode cut-off; f_{ce}—electron cyclotron frequency; f_{xu}—upper cut-off for X-mode; $2f_{ce}$—second harmonic of the electron cyclotron frequency.

the curved trajectory from external source to the ITER HFS and locating efficient antennas in the slit between the blanket modules. The first problem was solved by the use of rectangular waveguides (inner cross-section 20 × 12 mm) and special forms of the bends (hyperbolic secant) [646]. In order to decrease the induced eddy currents during plasma disruptions and to withstand the thermal stresses under neutron heating the Inconel Alloy 718 was chosen as the waveguide material inside the VV. The inner surface of the waveguides is coated with a thin Cu layer. The second problem was solved by the use of special antennas with horn for launch and mirror antenna for the receiver.

Recently the HFSR system was enhanced with the addition of a refractometry channel. The concept of refractometry was proposed in [647]. It analyses the phase of the wave which is launched from the low field side (LFS) and received at the HFS. Refractomery uses extraordinary wave in the transparency window between the cyclotron frequency and the lower extraordinary cut off.

The HFSR reflectometry layout in section #8th is shown in figure 150. One can see the HFSR horn-mirror antenna (1) which is connected through a 90 degree bend and the transmission line along the vacuum chamber with the upper port. The vacuum part of the transmission system is terminated by the double vacuum window, located at the vacuum port extension tube. The refractometry antenna is located only in equatorial port #8 in front of the HFSR antenna, as shown in figure 150. The HFSR is comprised of four systems. Two are located in the upper port of section #8 and the other two systems are located in sections 9 and 17. The top view of HFSR locations is shown in figure 151.

Each atmospheric transmission line begins from the first vacuum window and ends in the Diagnostic Area, where the mm-wave equipment and instrument and control systems are located.

The two systems in sector 4 are used for density profile measurements in O and XL mode. The systems in sectors 9

Figure 150. HFSR in-vessel layout in upper and equatorial ports of section #8. 1—HFS reflectometer antenna system; 2—Transmitting refractometry antenna.

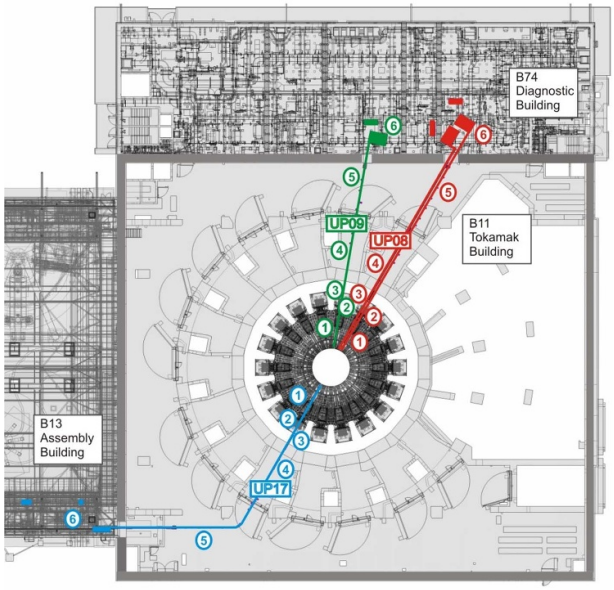

Figure 151. A top view indicating the general locations of the HFSR diagnostic. (1—Vacuum Vessel, 2—Upper port, 3—Interspace, 4—Port Cell, 5—Gallery, 6—Diagnostic Area in Buildings 74/13).

and 17 are used for the measurement of density fluctuations in XL and O modes, respectively.

As HFSR uses a very wide frequency range, quasioptical couplers are used to combine/decombine the signals in five frequency bands in single waveguides [648].

The diagnostic back-end utilizes voltage controlled oscillators (VCOs) as the main mm-wave source in the frequency band 8–20 GHz. The VCO is controlled by a highly-integrated control unit that also contains a 125 MHz digital-to-analogue converter to form the required tuning voltage shape, 20 V DC amplifier, several sine generators as IF sources and IQ detectors. A frequency-calibration system that is based on RF coax-cable delay line is used to pre-pulse measurements of VCO tuning characteristic and tuning voltage shaping. RF coax-cable delay lines reduce the difference of signal path in RF and LO legs. This approach has been successfully tested in the T-10 tokamak [649]. 1 GS s^{-1} ADCs will be used in the corresponding acquisition system and 10 MS s^{-1} ADCs in subsytems for fluctuation and live-averaged density measurements.

The planned mm-wave source frequencies lead to an electron density profile measurement range $3 \cdot 10^{19}$ m^{-3}–$2.65 \cdot 10^{20}$ m^{-3} and the line density measurement range $8 \cdot 10^{18}$ m^{-2}–$8 \cdot 10^{20}$ $m^{-2.}$ The density profile will be measured using a FMCW technique [650]. The diagnostic is planned to provide the cutoff layer position with an absolute error of about 1 cm and a relative error of about 5%. The relative density error at the measurement point will be about 10%. It is planned to have about 20 density points per frequency band that roughly corresponds to 30 density points in the plasma core in the baseline ITER scenario. A 5 μs frequency sweep with 10 kHz repetition rate is planned now as the main measurement scenario. This allows to have spectrogram averaging to reduce the influence of turbulence keeping the time resolution about 1 ms. It should be noted that the repetition rate is determined by the existing I&C hardware solution whereas the rest of back-end equipment allows to operate with 100 kHz repetition rate.

Since HFSR cannot provide the line-averaged density via standard reflectometer measurements, this parameter will be estimated by a see-through channel in Sector 4. Due to uncertainties in the determination of the line-averaged density, the diagnostic will provide the integrated electron density along the viewline in the range 8.0×10^{18}–8.0×10^{20} m^{-2}, that roughly corresponds to 2.0×10^{18}–2.0×10^{20} m^{-3} averaged density. The measurement accuracy is determined by hardware limitations that lead to an absolute error of $8.0 \cdot 10^{18}$ m^{-2} and reconstruction error of about 2%. It should be emphasized that in real-time operation one can expect an increase of the error to 10% because of strict latency limitations.

Small-scale turbulence measurements can provide information on broad-band turbulence and quasi-monochromatic modes (TAE, RSAE, MHD etc) in the frequency band 30 kHz–2 MHz. Since the HFSR utilizes XL mode probing, the reflected signal is sensitive to fluctuations of both electron density and magnetic field at the cutoff layer.

7.9. System-on-Chip (SoC) technology for millimeter-wave diagnostics

There are serious issues raised by the harsh environment of ITER which is the first magnetic confinement fusion device to be able to produce net fusion power and will generate radiation levels, i.e. neutrons and gamma rays, that are orders of magnitude higher than present-day experimental machines as well as stray microwave and millimeter wave radiation and microwave bursting. There is thus a strong need to protect diagnostics electronics. This is partially accomplished by the use of chicanes, filters, limiters, and siting in the diagnostic hall beyond a shield wall. However, this does not suffice and

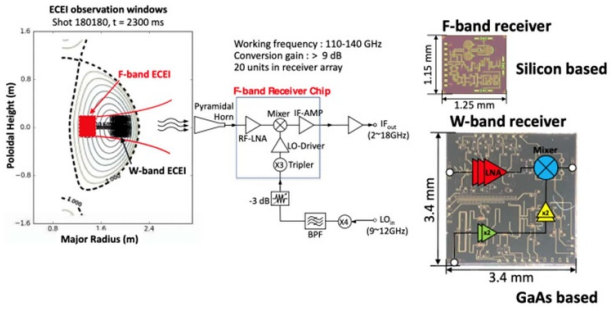

Figure 152. W-band and F-band receiver chip development for deep plasma temperature measurement on DIII-D. The pre-LNA, balanced mixer, IF-amplifier, and internal LO multiplier are merged on a single chip.

therefore motivates the development of electronics with higher performance and capability, as well as robustness to survive the hostile burning plasma environment.

Monolithic, 'system-on-chip' (SoC) millimeter wave integrated circuit technology, provides dramatic advances for millimeter-wave diagnostics in fusion reactors, including over 30 dB signal gain and 85% electronics noise suppression [651, 652]. The transmitter and receiver chips have been developed with extremely high-level integration size (square millimeter level for each piece). The prototype approaches have been fabricated and employed as individual modules on DIII-D diagnostics, including V-band (55–75 GHz), E-band (72–80 GHz), W-band (75–110 GHz), and F-band (110–140 GHz). W-band and F-band receiver chips for plasma temperature measurement have been developed and successfully applied on DIII-D. The pre-LNA, balanced mixer, IF-amplifier, and internal LO frequency multiplier/driver are merged onto a single chip (see figure 152), which can be packaged as a general module for radiometer, reflectometer, interferometer, polarimeter, and scattering system applications. The W-band image-rejection SoC receivers have been successfully designed and fabricated using both Taiwan Semiconductor Manufacturing Company (TSMC) 90- and 40 nm CMOS as well as WIN Semiconductors 0.1 μm GaAs processes.

For SoC technology, the chip material should have the capability to tolerate the strong radiation, which dictates the use of the gallium nitride (GaN) wide bandgap semiconductor material (3.39 eV versus 1.43 and 1.11 for GaAs and Si, respectively). GaN has been selected due to its high power, high breakdown voltages, and low noise beyond 200 GHz capabilities [653] here with the HRL T3 40 nm process providing f_T/f_{max} of 200 GHz/400 GHz and the T4A 20 nm process providing f_T/f_{max} of 329 GHz/558 GHz [654].

A key focus is on the characterization of the millimeter wave performance under radiation and neutron active environments of both individual GaN devices and SoCs. The SoC approach of microwave transmitter and receiver modules have wide application potential in the fusion plasma diagnostics field. For example, the full frequency bandwidth in W/F bands or higher provides wide radial observation windows for ECE Radiometer and Density Reflectometer diagnostics for fundamental parameter measurements in burning plasma.

7.10. Polarimeter-interferometer system based on terahertz solid state source (SSS)

With the rapid progress of Terahertz technology in recent years, terahertz SSSs with modest power output have been applied in interferometer system on several machines [655–658] to replace the traditional FIR lasers. Compared with FIR lasers, the solid-state sources have many advantages, such as compactness, stable frequency, turn-key operation and easy maintenance. The major shortage, which is the modest power output (around mw), can be amended by the significant improvement of detection sensitivity of planar diode mixers.

The multichannel heterodyne interferometer on KTX utilizes two beams based on the principle of the Michelson interferometer. One beam serves as reference signal with fixed frequency about 650 GHz, and the other serves as probing signal with tunable frequency (630–660 GHz). The SSS with maximum output power approximately 2 mW is composed of an amplifier and multiplier chain with a local oscillator (fixed at 13.45 GHz for the reference beam and a finely tunable synthesizer range from 12.9 to 13.95 GHz for probing beam). The planar diode mixers are optimized for high sensitivity $\sim$750 V W^{-1} and then followed by pre-amplifiers with gain factor 500. To fully use the beam power, the whole system was set on a light weight and compact platform ($\sim$3 m $\times$ 3 m) and installed just beside the VV ring [659]. The optical design has been optimized for uniform distribution of beam light and beam width minimization. The interferometer system with five-chord signals has recently been successfully installed on the machine [660]. The beam width across the plasma is about 20 mm and the minimum phase noise can reach 0.004π with 1 MHz bandwidth, which corresponds to about 0.1% density fluctuation amplitude. The density profile has been reconstructed by fitting the line-integrated data into an equilibrium program. The future work is to develop a polarimeter-interferometer for simultaneous measurements of Faraday rotation angle and electron density by upgrading the existing multi-channel interferometer system based on solid-state sources.

7.11. The potential of THz-TDS diagnostics for next step fusion experiments

7.11.1. THz time domain spectroscopy (TDS). The Terahertz (THz) band of the electromagnetic spectrum is nowadays defined as the frequency range [0.1–10]THz (1 THz = 10^{12} Hz), between microwaves and mid-IR electromagnetic radiation, where electronic and optical technologies overlap. The last decade has seen an enormous development of spectroscopy techniques in this area, with the full development of the so-called TDS. The starting point of this approach lies in the fact that femtosecond laser pulses (usually $\sim$800 nm wavelength) can be used to generate extremely broadband (100 GHz–30 THz) single-cycle THz pulses with less than

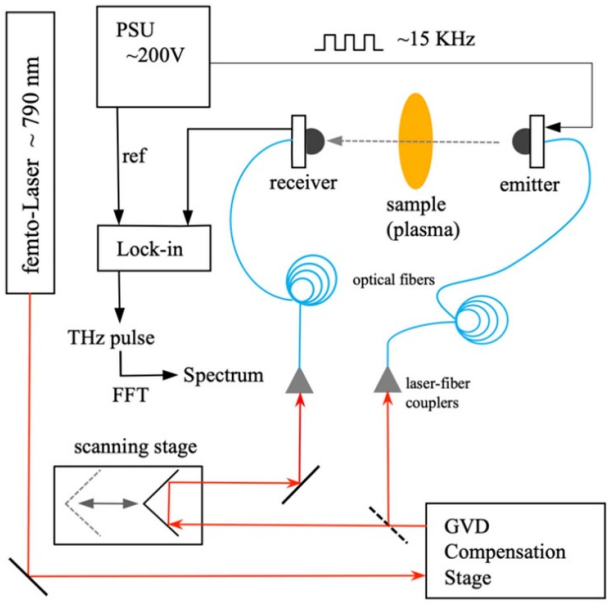

Figure 153. Schematic of a fiber optics THz-TDS setup for plasma diagnostics applications. In addition to the hyper-hemispherical lenses shown here, Gaussian collimation optics will be required to match emitter and receiver across the long beam path in tokamaks.

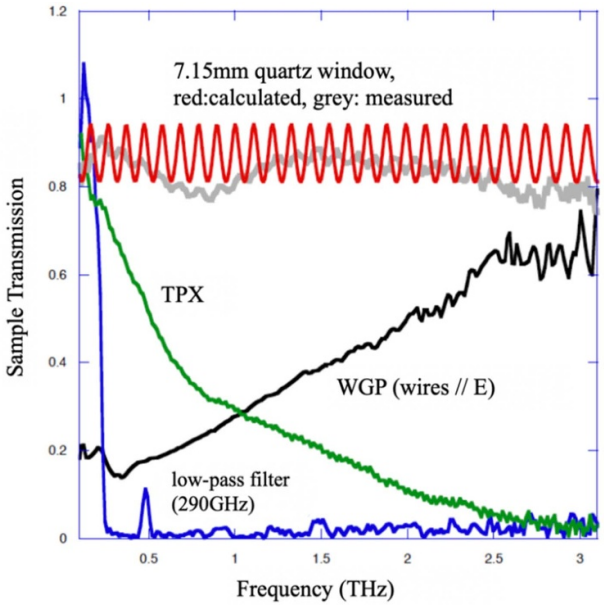

Figure 154. Spectral transmission of tokamak diagnostics components measured over the relevant FIR frequency range by the THz-TDS spectrometer in figure 153.

1 ps duration, through the well known process of photoconductive generation of Terahertz radiation (spark-gap emitter) [661]. Such transients contain a truncated cycle of the electric field and therefore, according to the Fourier Theorem, have a frequency spectrum extending over a broad range. With the appropriate choice of emitter, the THz, the mid-IR and even the FIR radiation regimes can be covered in their entirety.

In a typical THz-TDS spectrometer (figure 153) the receiver detector, gated by a fraction of the laser beam generating the pulse, is used to measure the THz pulses amplitude. By varying the path difference between emitter and receiver the full extension of the pulse waveform is covered, so that the complete knowledge of amplitude and phase of the transmitted (or reflected) THz pulse, i.e. its spectrum, is obtained via Fourier transform. This is the TDS technique. The spark-gap emitter THz power is fairly low (microWatt), but the combination of detector gating and a suitable modulation of the emitter bias to drive a lock-in amplifier, increases the SNR to diagnostic-grade values, even for the short measurement time required for plasma phenomena. With the use of photoconductive polarization-resolving detectors the two polarizations of the probing wave can be resolved simultaneously [661, 662]. Another great advantage of those techniques comes from the nature of THz-TDS components, based on solid state devices operating at room temperature, hence cheaper, more stable and compact than those used in conventional FIR and microwave applications. Finally, the pump and gate laser beams can be channeled to the emitter and receiving heads using optical fibers, gaining extreme flexibility in the routing, hence easing up the tokamak access issues. Since optical fibers are dispersive components, a group velocity delay compensation stage will be required. Finally, the use of the wide range of frequencies associated with the probing THz pulse, permits the determination of several sample parameters simultaneously.

All these aspects have raised interest in THz-TDS plasma measurements for density and Faraday rotation in the region of microwave and FIR since the early days [663]. The applicability of THz-TDS to the diagnostic environment has already been tested in laboratory by sampling the spectral response of FIR diagnostic components over a broad frequency range (figure 154) and with preliminary table-top plasma measurements [664].

7.11.2. Tokamak diagnostics applications. One of the most promising diagnostic applications of THz-TDS is interferometry [558], a technique based on the measurement of plasma refractive index through the detection of the phase difference between a microwave beam traversing the plasma column vertically (i.e. parallel to the tokamak axis) and a reference beam travelling the same distance in air. A THz-TDS spectrometer with emitter and receiver located at the opposite ends of a vertical chord, will provide the same information of the interferometric arrangement. In addition by using several spectral components of the THz beam the plasma refractive index (hence the density) can be measured directly and the calibration accuracy of the diagnostics is increased.

Polarimetry measures Faraday rotation of the plane of polarization of a FIR beam which leads to the calculation of the local magnetic field strength [558]. By selecting the relevant frequency of the wide THz-TDS spectrum the same measurement can be performed with a high degree of simplification, also providing a straightforward implementation of the combined measurement of interferometry and polarimetry, without the extra components normally required by the heterodyne-style detection [557].

A more challenging diagnostic application of THz-TDS comes with reflectometry [557, 665], in which the phase variation of a selected frequency component reflected on the critical density (or cutoff) plasma layer where the refractive index vanishes, can be used to diagnose the plasma density profile or the density fluctuations. Traditionally a source at fixed frequency, or swept across the required frequency range is used [666]. The THz-TDS reflectometer will be instead an evolution of the Ultrashort Pulse Radar technique [667], with the broadband spectrum required for the diagnostic obtained through a Terahertz switch. By resolving the phase-shift of selected components the radial density profile can be obtained via Abel inversion.

The THZ diagnostic development is presently progressing along the lines of transition from table-top THz-TDS spectroscopy to plasma diagnostics on a tokamak, which will require a complete change of the layout and work scales. Paths will be in the order of meters, and the 'sample' is a large plasma column. The measurement time will necessarily be short, in order to follow the timescale of plasma phenomena (milliseconds). The coupling of emitter and receiver across the tokamak geometry distances will have to be optimized with tailored Gaussian beam optics telescopes. All considered, it can be safely stated that THz-TDS has great potential for evolution of diagnostics capabilities, beyond the routine plasma density and temperature measurements, towards the measurement of magnetic field, charge density and conductivity, with unprecedented resolution and reliability [668].

8. Influence of radiation effects on the refinement of the ITER design

I. Ďuran[38], A. Gusarov[39] and K. Vukolov[27]

8.1. Introduction: requirements for diagnostic systems for ITER

The requirements for diagnostic systems for ITER are specified in the SRD-55 [197] and in the PRs [669]. For each parameter the measurement range and the diagnostic systems performing the measurements are defined. An important difference between ITER and already existing machines is a significant increase of nuclear radiation loads combined with a long-term stable operation. In particular, the in-vessel diagnostics will be subject to high energy neutron and gamma radiation fluxes and may not survive long enough to be considered as robust in the nuclear phases, when it will be most needed to guarantee a safe operation. It is necessary to evaluate the radiation hardness of each diagnostic and if necessary to consider mitigating measures to achieve their reliable operation. This evaluation must be confirmed by radiation testing in representative conditions.

8.2. ITER radiation environment

During nuclear operation, the ITER plasma will generate intense fluxes of fast neutrons and MeV-range γ—rays [670]. The principal source of radiation is the D–T reaction, which generates neutrons with a mean 14.1 MeV energy. Subsequent neutron-matter interaction results in a broad neutron energy spectrum, and it also gives rise to secondary gamma radiation, with both prompt and delayed components. Therefore, the radiation environment at a sensor location is very complex and varies from one location to another.

Numerous diagnostic systems must perform correctly during the ITER life-time to guarantee a successful machine operation. Thanks to carefully selecting locations and to dedicated shielding, the nuclear loads on the sensors are significantly lower as compared to those to the ITER first wall materials. However, the sensors are considerably more vulnerable because they need to maintain over the long time not only the mechanical integrity but also specific properties such as optical transmission, electrical insulation, thermal conductivity, etc. This further highlights the potential problems of material transmutation and helium accumulation which might have significant impact on sensors performance and reliability.

It is necessary to analyze the impact of the nuclear environment on both each individual component and the system as a whole. This analysis requires an integrated approach to the design, when radiation effects and various environmental parameters such as elevated temperatures, vacuum, vibrations, must be considered simultaneously. Moreover, the systems must be compatible with multiple additional requirements, like remote handling operations, personnel safety and nuclear facility licensing requirements.

In the present publication we illustrate the complexity of the analysis using several diagnostics operating on different physical principles.

Simulating the ITER radiation environment presents a significant problem. In practice, there is no possibility to exactly reproduce ITER conditions in radiation tests. NGs can generate neutrons with corresponding energies, but the fluxes are very low and can hardly be considered as representative. To achieve the desirable total neutron fluence, the exposure has to be performed in a fission reactor, where the energy of neutrons is significantly lower than 14 MeV.

Exposure of materials to high energy radiation results in the generation of microscopic defects and changes of macroscopic properties. In the case of fast neutrons formation of lattice defects via kinetic energy transfer is usually considered as the most important effect. This effect is usually expressed by the 'displacement per atom' parameter (dpa). It is better to analyze such physical processes by means of numerical analysis, because it is practically impossible to make it experimentally for ITER conditions.

The dpa is defined as a ratio between atomic displacements (lattice defects) occurring within a given volume and a number of atoms within the same volume. To produce a permanent displacement, the energy transferred to an atom should be bigger than its binding energy. Otherwise, the transferred energy will dissipate without any stable defect created. If the energy transferred to an atom is significantly higher than the binding energy, the displaced atom will move through the lattice and can create more defects. According to the modified Kinchin–Pease model, the total number of defects is defined as [671]:

$$N = 0 \qquad \text{for } T < E_\mathrm{d}$$
$$N = 1 \qquad \text{for } E_\mathrm{d} < T < 2.5\,E_\mathrm{d},$$
$$N = \frac{T}{2.5E_\mathrm{d}} \qquad \text{for } T > 2.5E_\mathrm{d},$$

where T is the kinetic energy of the incoming neutron and E_d is the energy required to remove an atom from a lattice position. The integral dpa rate $d(t)$ is calculated as:

$$d(t) = \int \mathrm{d}E\sigma_\mathrm{d}(E)\,\varphi(E,t),$$

where E is energy, $\sigma_d(E)$ is the dpa cross-section and $\varphi(E, t)$ is the neutron flux energy spectrum and the total dpa is obtained by integration over time t.

Thanks to its apparent simplicity the dpa is often taken as a convenient figure of merit to quantitatively characterize neutron radiation damage. For example, 0.1 dpa means that one atom out of ten was displaced from its lattice position, which provides a simple visualization for the actual radiation effect. Alternatively, the ionizing radiation dose in Grays (1 Gray equals 1 Joul absorbed within 1 kg of material) is used as a measure of radiation damage. However, there is less obvious link between the value of ionizing radiation dose and the actual microscopic changes within irradiated material as it is a more abstract quantity.

Nevertheless, care should be taken when using a dpa value to characterize radiation damage. The amount of dpa cannot be measured and it is not directly proportional to changes in material properties. The threshold displacement energy E_d plays a crucial role in the dpa concept. For some materials, there are big variations in the threshold displacement energies predicted by different models. In case of crystalline materials, each crystal direction has its own E_d due to crystal anisotropy. It is possible to calculate an average over different directions. However, in case of directional radiation (accelerators) of a monocrystalline material the sample orientation will play an important role.

To prepare an irradiation test of an ITER component, there are several important conditions which should be respected. Firstly, it is important to achieve the neutron fluence and gamma dose at levels corresponding to those expected during operation of the component on ITER. The aim is to approximate as close as possible the kinetics of gamma-neutron processes occurring in ITER during the test. Moreover, several times higher neutron fluence can be required when samples are irradiated in a nuclear reactor to compensate the quantitative difference in the fission neutron energy compared to the thermonuclear neutrons. Secondly, if the effect of the neutron irradiation is not decisive in the process under study, then only gamma irradiation, usually at a Co-60 source, can be used for the tests. In some cases tests should be performed at a DT neutron source with the maximum achievable neutron fluence to determine the influence of thermonuclear neutrons on the physical process under study.

Activation, transmutation and He production are radiation effects, which are extremely difficult to reproduce in a way representative for ITER. The cross sections of nuclear reactions are extremely sensitive to the neutron spectrum. The ratio fast/thermal neutron flux in a material testing fission reactor depends on the location, but in most of cases it is lower than in ITER. As a result, it is virtually impossible to achieve the representative values of the displacement damage, transmutation fraction, and amount of He in a single thermal fission reactor irradiation. Usually, obtaining the desired value of the dpa, in a fission reactor experiment means that the transmutation effect is significantly higher than it will take place in ITER. Therefore, separate tests should be considered to study displacement damage, transmutation, and He production. The neutron energy distribution for the tests should be properly scaled to be representative to the spectrum at the location of the test sample in the ITER.

The numerical simulation of these effects can be considered for ITER conditions as a sufficiently accurate way to analyze radiation damage, activation and transmutation while taking into account the energy spectrum of neutrons and gammas. The Monte–Carlo N-particle (MCNP) transport code is officially adopted for calculations in ITER [198]. Neutron calculations are performed using the official reactor model 'C-Model R181031 REV. 190110 issued 10/01/2019' [672]. This is a three-dimensional CAD model of a toroidal 40° ITER sector with its main structures. The neutron source is given for the basic ITER scenario with a maximum thermonuclear D-T reaction power of 500 MW at plasma current of 15 MA [673].

For the neutronic analysis, the diagnostic components must be added to the C-Model with the geometry of their placement and corresponding materials contained. The MCNP code calculates the neutron spectra at each interaction of a neutron with the material. The statistical error of the calculated neutron flux is about a few percent, but the actual accuracy of the calculated neutron spectra depends on the correctness of the model geometry and the material composition.

The activation, transmutation and degree of radiation damage of diagnostic components can be estimated on the basis of data on neutron fluxes, taking into account neutron spectra, as well as using libraries of micro-constants of nuclear reaction cross sections.

Nevertheless, radiation testing of diagnostic elements is absolutely necessary to justify their suitability, and therefore available facilities, even though they cannot provide a fully representative environment, have to be used. This means that compromises are required to choose an installation, which allows for the best evaluation of the most important performance parameters. Often, measurements of properties of irradiated materials are difficult due to their high radioactivity. Safety requirements exist for such type of measurements that make them very complicated and sometimes even impossible.

8.3. Optical diagnostics

Optical diagnostics are widely used in modern thermonuclear devices. They can measure *in situ* the main characteristics of the plasma, such as temperature, density of electrons and ions, concentration of impurities, local electric and magnetic fields, etc. Optical diagnostics are essential for tokamak

physics studies, but available designs cannot be directly transferred to ITER without improvement of the radiation hardness, especially since ITER sets high requirements for the measurement accuracy. The ITER optical elements will change properties under gamma-neutron radiation emitted by the hot plasma. Transparent glass elements (windows, lenses, prisms, filters and optical fibers) that are needed to collect radiation from the plasma and to guide it to detectors will quickly lose transmittivity (effect of radiation induced absorption—RIA), especially in the UV spectral range. Besides that, some glasses radiate light due to radio-luminescence and/or Cherenkov effects under gamma-neutron irradiation. Detectors (PMTS, video cameras, etc) placed close to the plasma also can be damaged by the irradiation.

The vacuum window assembly is an example of a component containing optical material subject to strong radiation. The plasma and the first wall diagnostic system in ITER will use more than 100 diagnostic windows required for optical, microwave, and x-ray diagnostic systems. In addition to transmitting the diagnostic signal, they must also maintain the safety barrier between the radioactive plasma and the external atmosphere.

Window assemblies are located on the VV port plugs and the port interspace seal plates. They are difficult to replace and are inaccessible during machine operation and during movement of main in-vessel components for the duration of a shutdown. The assemblies must be available continuously during the full operating life of ITER. Therefore a high reliability of the window assemblies is required.

Two types of silica glass KU-1 and KS-4V with hydroxyl content OH $<$ 1000 ppm and OH $<$ 0.1 ppm, respectively, were investigated under ITER relevant conditions during round-robin irradiation tests [674]. A water-pool nuclear reactor, a Co-60 gamma source, and a NG were used for this. It was shown that both types of silica glass have good radiation hardness in the visible spectral range and can be used as window materials for ITER optical diagnostics.

An initial window assembly design considers using brazing to attach the transparent element to the housing, figure 155. Irradiation of such assemblies was performed in the BR1 reactor of SCK•CEN in Mol at 150 °C during 5.5 months up to a total fast ($E > 0.1$ MeV) fluence of $\sim 2 \times 10^{16}$ n cm^{-2} [675]. Post-irradiation thermo-mechanical and He-leak tests were performed in a hot cell. The examination was concluded with a destructive push-out test. Different damage patterns were observed for different window assemblies. A general conclusion was that after thermal cycling and reactor irradiation the windows remain sufficiently strong to sustain mechanical loads relevant for the ITER operation.

The current window assembly design considers the use of two fused silica 2 cm thick plane plates [676]. The first plate is tilted by 5 degrees around the horizontal axis, the second surface is tilted by 5 degrees around the vertical axis in order to reduce multiple reflection effect arising between the innermost window surfaces. MCNP calculations yield that neutron fluxes at the window can reach 10^8 n (cm^{-2} s^{-1}) in spite of effective neutron shielding located in the port-plug. Radiation testing of such assemblies is planned for the period 2022–24.

Figure 155. Brazed prototype window assemblies, UKAEA design.

Fiber optic bundles are intended to transfer plasma light from the ITER Port areas to detectors in the diagnostic room [677]. They will be exposed to gamma-neutron radiation along significant fraction of their length (near 10 m) and it is better to locate them as far as possible from the plasma to decrease the effect of RIA. In present, suitable types of radiation-resistant silica fibers have been identified and their production technologies have been developed. The silica optical fiber doped with H_2 and coated by a thin carbon film has a high radiation resistance and their transmittance can be recovered during pauses between ITER plasma pulses by exposing them to gamma irradiation [252, 678]. Therefore, such fibers are candidates for the manufacture of fiber bundles.

8.4. Magnetic diagnostics

Successful operation of ITER will rely on the use of a large set of magnetic diagnostics [4]. From data obtained with those systems, fundamental parameters such as plasma position, shape, and current will be derived to allow for real-time plasma control by a set of poloidal coils as well as for MP.

8.4.1. Cables and connectors. The ITER magnetic diagnostic systems usually require detection of low currents or voltages. Therefore, mitigation of radiation and thermal effects induced within the sensor's cable path, such as radiation induced conductivity (RIC), radiation induced electromotive force (RIEMF), temperature induced electromotive force (TIEMF), radiation induced thermo electric sensitivity (RITES), and radiation induced electric degradation (RIED) presents a very significant challenge. These effects were addressed in numerous publications. It is concluded that the internally twisted mineral insulated cables often offer the best intrinsic balance for most of these effects and for rejection of most long wavelength external effects, leaving only the defect-driven TIEMF as the main source of spurious voltage. However, the problem that still requires significant attention is the cable termination and the connection to the delicate wiring of a particular sensors.

In addition, dedicated experiment was performed in order to asses potential dimensional changes of glass to metal sealing (GTMS) inserts within ITER electrical feedthroughs (figure 156) due to neutron radiation. Dimensional changes of

Figure 156. Example of ITER electrical feedthroughs with borosilicate GTMS inserts.

these inserts could potentially compromise vacuum tightness of the feedthroughs.

Four samples of borosilicate GTMS inserts with outer diameter ∼7.1 mm were irradiated in LVR-15 experimental fission reactor in CVŘ Řež, Czech Republic. The samples were irradiated inside cadmium shielded container in order to increase fast to thermal neutron ratio to better approximate actual neutron spectrum the feedthroughs will be exposed to on ITER. The total accumulated neutron fluence during this irradiation as measured by embedded activation foils reached 6×10^{17} cm^{-2} (E <0.1 MeV) and 5×10^{17} cm^{-2} ($E > 0.1$ MeV). The outer diameter of the samples was measured before irradiation using optical measurement system Vertex 251 located in the LVR-15 hot chambers with measurement accuracy ∼1 μm. The same measurement of outer diameter was done on irradiated samples. Measured differences between pre-irradiated and post-irradiated samples were comparable with measurement accuracy of the Vertex 251 system, i.e. ∼1 μm. It was concluded that radiation induced dimensional changes of these borosilicate glass GTMS inserts pose no risk with respect to the potential loss of vacuum accident on ITER.

8.4.2. Inductive sensors. Until now, magnetic measurements in tokamaks are successfully performed using inductive sensors, where the signal (voltage) is proportional to the derivative of the magnetic flux through the sensor. To find the plasma current or magnetic field an integration step is necessary. Currently used analogue integrators have known intrinsic problems. Two most important are the integrator drift, which introduces an absolute error increasing with the integration time, and saturation of the integrator input stage in the case of fast flux variation, for example during plasma disruptions.

In ITER during the long stationary phase, the signals to be integrated are essentially zero, and for relevant changes of the plasma equilibrium the resulting magnetic signals are small. This makes the magnetic diagnostics sensitive to any spurious voltages that may arise from RIEMF and TIEMF [6].

The inner vessel sensors, which include different types of coils and loops, are the main magnetic set. They are distributed just behind the blanket modules or mounted on the instrumented divertor cassettes. Because of their in-vessel location, they are subject to significant radiation loads, in particular in the divertor region.

The measurement accuracy of magnetic sensors defines margins to the machine engineering limits and the operational flexibility. The coils are the most critical element, because their effective area must be rather small, which limits acceptable parasitic voltages to values below 0.5 μV for long-pulse operation. On the other hand, the size is still big to allow for temperature gradients, which may influence the sensor accuracy.

An option for magnetic sensors selected for ITER is the use of LTCC coils. The LTCC sensor consist of thin ceramic layers, on which metallic tracks are printed and then the unit is sintered. Such sensors were proposed as the most promising solution to meet the requirements imposed by the ITER operating conditions [679].

To check that LTCC sensors will perform satisfactorily under the ITER radiation environment two types of prototype ITER LTCC coils were irradiated up to 72 MGy using a Co60 source at ∼50 °C [680]. LTCC-Ag/10 had 10 ceramic layers with silver tracks, and LTCC-Au/30 had 30 ceramic layers with printed gold conductors. The continuity and the insulation resistance were measured *in situ*. The leak currents for the coils during irradiation were 70 nA and 35 nA at 50 V, for Ag and Au coils respectively, which corresponds to an insulation resistance in the GOhm range. One LTCC-Ag/10 coil was broken during the rig assembly, likely due to a non-uniform compression of the coil. Also, the fragility of the connectors was identified as a problem, which is actually relevant for various diagnostics at ITER.

A neutron irradiation of LTCC sensors has also been performed at the LVR-15 nuclear reactor [15]. Four samples, including LTCC-Ag/10 from the above gamma-irradiation experiment, were exposed. The accumulated fast ($E > 0.1$ MeV) neutron fluence was ∼10^{20} cm^{-2}, exceeding the expected ITER lifetime fluence for these sensors. Due to the high activation, only visual inspection of the sensors was possible after the irradiation. The sensor pre-exposed to gamma radiation which was also subject to highest thermal gradient during neutron irradiation was cracked and three others maintained their physical integrity. The failure was attributed to the thermal stresses which occurred due to radiation heating and exceeded LTCC ceramic material limits. Effect of possible gamma-radiation induced ageing was concluded to be negligible. Without electrical measurements being possible due to high activation of the samples, the question about changes of performance characteristics of the exposed sensors remains open.

The risk of the in-vessel sensors failures due to damage induced by radiation effects will be mitigated by installation of additional sensors on the outer surface of the VV, where the neutron flux is an order of magnitude lower [6]. The shielding by the vessel, however, drastically reduces the frequency response of these sensors down to a ∼Hz level [681], which means they can only be used for slow plasma position drift correction. An additional design constraint for these sensors is

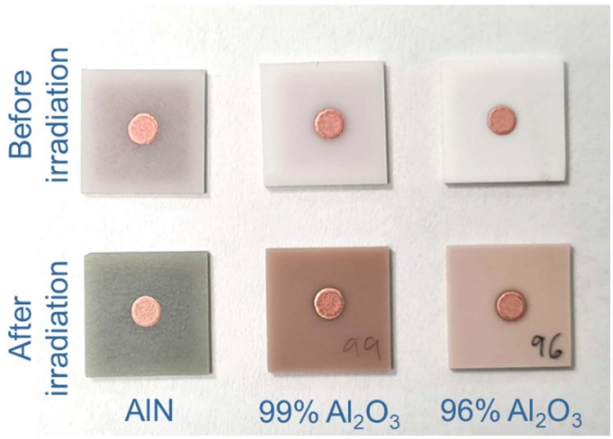

Figure 157. Samples of ceramics metallized by copper using thick printing technology before and after irradiation on LVR-15 fission reactor.

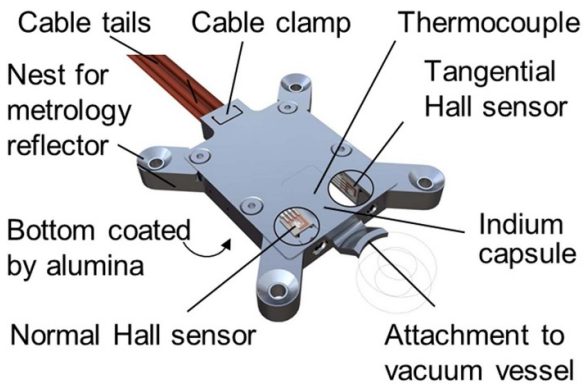

Figure 158. Design layout of the ITER OVSS sensors.

a space less than 10 mm in the radial direction, which is the width of the gap between the VV and the thermal shield.

Recently, a few innovative concepts of inductive sensors are appearing and are being developed and qualified primarily with respect to their deployment on future fusion reactors beyond ITER.

One of such new approaches is application of thick printing (TP) technology to manufacture robust and radiation hard inductive sensors [682, 683]. Here, the spiral-like pattern of metallic ink is screen printed onto already sintered ceramic substrate creating effectively a coil-like structure. The substrate with screen printed ink is then fired to create and stabilize final metallic tracks. Various materials can be used both for ceramic substrates, while the most common one is Al_2O_3, and also for metallic ink, where the most common are those based on copper. Stacking of several layers of such metallized ceramic patterns is foreseen creating similar structure as it is in the case of LTCC sensors. The main advantage of TP technology is separation of ceramic sintering procedure from the metallic ink firing procedure. This reduces the risks and removes technological peculiarities associated with LTCC sensors manufacturing [18] where dimensional changes of metallized ceramic tapes during firing can lead to sensor defects. On the other hand, TP technology leads rather to a laminar sensor structure compared to a compact ceramic block typical for LTCC sensors.

Initial study of radiation hardness of TP copper metallization of two types of Al_2O_3 (96% and 99% purity) and also AlN substrates was done at LVR-15 fission reactor, figure 157. Several samples were irradiated by total neutron fluence of 4×10^{18} cm^{-2} and adhesion of the copper layer on irradiated samples was tested. The copper layer adhesion was not significantly affected by the neutron irradiation and in all cases the post irradiation adhesion was better than 35 N mm^{-2}.

Another new approach to design and manufacturing of local magnetic field inductive sensors is employment of photolithography (PL) technology [684]. Here, the ultrathin $\sim$10 μm conductive golden tracks can be shaped using standard PL technology on SiO_2 wafers. The main advantage of this approach is achievement of large total effective area of the resulting coil while keeping its self-inductance small which allows to use the same sensor both for equilibrium magnetic field reconstruction and also for detection of high frequency MHD events. Key aspects of this technology are being developed like stacking and reliable electrical connection of such multilayer coils, using substrate and metallization materials more relevant to harsh fusion environment etc. Initial neutron irradiation tests of the first prototypes are also foreseen in the near future.

8.4.3. Hall effect sensors. Hall sensors are included in the ITER design to mitigate the risk of voltage drift in the inductive sensors due to RIEMF and TIEMF. Three ITER VV sectors (8, 5, and 2—in order of installation) will be equipped with full poloidal arrays of outer vessel steady state (OVSS) magnetic field sensors based on bismuth and antimony. Sensors will be mounted within a narrow gap between the outer VV skin and the thermal shield. Each probe will contain two Hall sensors, oriented perpendicularly to each other, to measure poloidal magnetic field and N type thermocouple to properly compensate for temperature dependence of sensors sensitivity.

No maintenance is possible for these sensors due to lack of access after ITER VV assembly. As a result, they will have to survive for the full ITER lifetime, which calls for the extensive qualification and testing including radiation hardness assessment.

Design and material choice for the ITER OVSS see figure 158 was driven by three main criteria:

1. Radiation hardness up to maximum expected ITER life time neutron fluence $\sim 2 \times 10^{18}$ cm^{-2}.
2. Compatibility with long term exposure to ITER VV baking temperature of 220 °C in vacuum.
3. Achieving as high sensitivity as possible to improve SNR and achieve required absolute accuracy with measurement error not exceeding 4 mT.

The first generation of the OVSS sensors [36] employed $\sim$1 μm layer of bismuth prepared by magneto sputtering as sensitive material. AlN ceramic substrates metallized by copper using commercial direct bond copper (DBC) technology

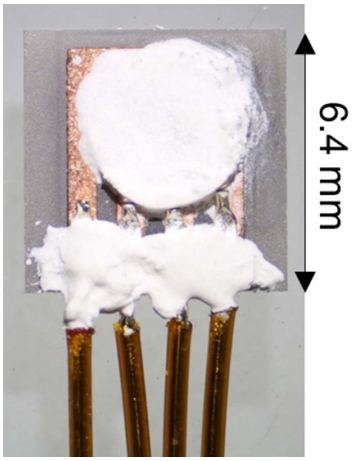

Figure 159. Bismuth Hall sensor before installation into the ITER OVSS probe.

were used while proper layout of sensor electrodes was shaped by etching. Sensitive layer was encapsulated by ∼4 μm thick layer of Al_2O_3, prepared by reactive magneto sputtering, with a few millimeters of Al_2O_3 ceramic paste on top. Copper wires were resistively welded to the sensor electrodes and the bond areas were further mechanically reinforced by Al_2O_3 ceramic paste. Detail view of the resulting sensor is shown in figure 159.

The sensors were subject to extensive testing, characterization and qualification [685–688] including neutron irradiation testing [689]. Here, the sample sensor inside Cd shield was exposed to the total neutron fluence of 2.5×10^{18} cm^{-2} with the fast (0.1–20 MeV) neutron fluence of 6×10^{17} cm^{-2}. This neutron irradiation dose exceeds by a factor of 2 the expected maximum life time neutron fluence of the sensors on ITER. Sensor sensitivity before and after irradiation was measured in the temperature range from room to 220 °C. The sensitivity changes at 100 °C (operational temperature on ITER) was 1.3% which is compatible with overall required stability of the sensors.

Moreover, impact of transmutation on periodic *in-situ* recalibration of N type thermocouples embedded inside OVSS sensors was assessed using nuclear inventory code FISPACT [690]. Thermocouples within OVSS units will be periodically recalibrated using integrated e-beam welded capsule containing high-purity indium with well established melting point. Transient flat top on the thermocouple signal evolution along the periodic heat up of OVSS during ITER VV baking occurring at indium melting temperature will be employed as one point periodic recalibration. FISPACT simulations confirmed that changes of indium material composition due to transmutation over the ITER life time will not compromise accuracy of the thermocouple recalibration beyond acceptable margins.

Later after manufacturing process of the OVSS probes, the follow up calibration revealed the issue with gradual increase of bismuth Hall sensors resistances for a fraction of assembled OVSS probes along long storage time (∼year) which separated probes assembling from their calibration. It was concluded that the most probable cause of the observed phenomena were imperfections in Al_2O_3 encapsulation layers for some of the OVSS sensors and consequent gradual oxidation of bismuth layers which was manifested by gradual resistance increase. Long term exposure of the order of years at ambient atmosphere cannot be avoided for OVSS sensors due to long time interval between installation on ITER VV segments and the first pump down of ITER cryostat. These findings highlight the fact that although assessment of radiation induced effects is indeed very important for reliable operation of fusion reactor diagnostic components, other aspects like chemical stability, diffusion processes or aging over very long time scales can be equally important particularly for the components not allowing any maintenance along their operation on ITER.

Consequently, the R&D was focused on antimony which is another perspective material for ITER OVSS sensors [691, 692]. Antimony is much less prone to oxidation compared to bismuth, it offers wider temperature margin with melting temperature 630.6 °C versus 271.4 °C for bismuth and independence of sensitivity on magnetic field which simplifies calibration and data evaluation. The drawback of antimony is about 20 times lower Hall coefficient resulting in lower sensitivity of the sensors though, this can be partly compensated by sensitivity gain due to lower thickness of the sensitive layer and higher gain of the first stage amplifier. New generation of OVSS sensors based on Antimony was prototyped and tested in order to refurbish those OVSS sensors with manifested long-term drift of resistance. Recent technological advancements were implemented in sensors design namely change of DBC metalized AlN substrates and following etching process by thick printed copper metalized Al_2O_3 substrates where the required shape of sensor electrodes is screen printed without the need of follow up etching process. Resistive welding of sensor output wires was changed to ultrasonic bonding and contacting electrodes were moved further away from the sensitive layer in order to eliminate the risk of sensor damage during wire bonding.

Neutron irradiation test of the antimony-based Hall sensors at LVR-15 fission reactor where the sample was exposed to a total neutron fluence of 9.3×10^{17} cm^{-2} with fast ($E > 0.1$ MeV) neutron fluence of 5.7×10^{17} cm^{-2} demonstrated comparable radiation hardness of antimony sensors compared to previously tested bismuth ones [693].

Following the successful qualification of the new antimony Hall sensors, ITER VV sectors number 5 and 2 will be instrumented by the new antimony-based Hall sensors while the originally installed bismuth-based sensors are kept at sector 8.

In parallel, there is an ongoing R&D activity toward development and qualification of new Hall effect-based sensors for future DEMO fusion reactor where sensors will be exposed to about two orders of magnitude higher neutron fluences and potentially also to higher temperatures. Assessment of transmutation under DEMO relevant neutron loads was done for a set of candidate sensitive materials including bismuth, antimony, chromium, gold, carbon (in form of graphene) and others [692]. Initial neutron irradiation test of a chromium Hall sensor was conducted on LVR-15 fission reactor up to the total neutron fluence of 4×10^{18} cm^{-2}. Change of the sensor sensitivity of the order of a fraction of percent was measured

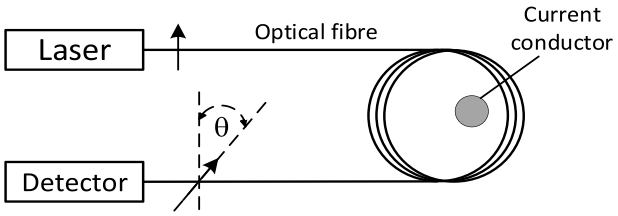

Figure 160. FOCS basic scheme. The arrows indicate the linear light polarizations at the light source output and the detector input rotated by angle θ as a result of the Faraday effect.

at 100 °C which shows good potential of these sensors for DEMO from radiation stability point of view. On the other hand, drawback of chromium is about two orders of magnitude lower sensitivity compared to antimony [694]. Sensors based on golden nanolayers are also being developed [695]. They were successfully tested in a fission reactor up to neutron fluence of 10^{20} cm^{-2} [695], but gold has in terms of transmutation rather low radiation resistance [692] which might compromise stability of the sensors at still higher fluences. Moreover, the tested sensors had a weaker signal than the chromium sensors reported in [694]. The first tests of graphene Hall sensors contemplating their application on fusion reactors were presented in [696]. These sensors would offer extremely high sensitivity and potentially very good radiation hardness but unfortunately, their technology is currently limited to operational temperatures only up to 150 °C [697].

8.4.4. Fiber optic current sensors (FOCS). FOCS is another steady-state magnetic diagnostic. The FOCS must satisfy the standard requirements defined for the ex-vessel plasma current diagnostics on the plasma current measurements [698], p 96: 'for plasma currents below 1 MA the accuracy must be better than 10 kA, and for 1–20 MA plasma currents, the accuracy must be better than 1%. The time resolution for FOCS is 10 ms. The ranges are ambipolar'.

FOCS operation relies on the Faraday effect experienced by light travelling in optical fibers exposed to a magnetic field; a rotation of the plane of polarization is induced by the magnetic field component aligned to the fiber's propagation axis. If a fiber with no intrinsic birefringence makes a loop around a current, the polarization rotation angle θ of a linearly polarized light is directly proportional to the enclosed current I [699]:

$$\theta = NVI,$$

where V is the Verdet constant, and N is the number of fiber turns around the current. For silica fibers $V \sim 0.7$ rad MA^{-1} at 1550 nm [700]. The wavelength dependence of the Verdet constant can be approximated as $\sim\lambda^{-2}$. The basic scheme of typical FOCS experimental arrangement is shown in figure 160.

In practice, the situation is complicated by the presence of intrinsic and induced birefringence [699]. The Verdet constant dependence on temperature [701] and on wavelength [700] creates an additional calibration issue.

FOCS is included into ITER research plan as an upgrade beyond the 2016 baseline. However, FOCS requires installation of components on the VV, which means that the FOCS design must be completed before the closure of the cryostat.

The ITER FOCS system includes three major components: the sensing fiber, the transport fiber, and the DAQ installed in the cubicle area, see figure 161. The sensor can operate in transmission regime or in reflection regime with the Faraday mirror. The DAQ components are selected based on the availability of preferably commercial components and the compatibility with the ITER requirements. The sensing fiber placed on the VV must sustain the combination of vacuum, nuclear radiation, and high temperature. The ITER FOCS system design allows to replace the fiber. However, preforming this operation during the nuclear operation of ITER would be technically challenging due to safety requirements. Using a fiber, which maintains its performance under radiation is by far the preferable option.

The part in the cryostat area will be irradiated at low temperatures. This sensing fiber will be replaceable.

Taking account of radiation effects has a significant impact on the FOCS design. Radiation flux estimations in table 34 relevant for the VV external surface are reproduced from [702].

For the energies relevant for the FOCS location, ionization is the most important mechanism of radiation damage. The equivalent dose rate is ∼0.5 Gy s^{-1}, corresponding to a total dose of 8.5 MGy for 4700 h of operation. It is also proposed in [702] that a 20% margin should be added in the design. Therefore, 10 MGy is a conservative upper limit for the FOCS life-time dose.

A known radiation effect is an increase of attenuation due to RIA. The RIA in the FOCS sensing fiber decreases the useful signal, making measurements inaccurate or even impossible. For the polarimetry detection scheme a 40 dB dynamic range of the analyzer at a +3 dBm detected signal is a reasonable estimation. A standard light source power is up to 13 dBm, which increases the dynamic range by 10 dB. The FOCS performance can be improved by operating it in reflection with a Faraday mirror [703]. In this case the optical length exposed to intense radiation is the double length on the VV, ∼56 m. Therefore, the acceptable RIA is up to 0.9 dB m^{-1}.

This estimation puts an immediate constraint on the system design. In any available optical fiber, the RIA levels in the visible and shorter wavelength at ∼MGy are significantly higher than 1 dB m^{-1}. Therefore, the system must operate at wavelengths in the IR range. As a result of the Verdet constant wavelength dependence, a change of the operation wavelength from 633 nm to 1.55 μm means a sensitivity decrease by a factor 6.

Typical absorption values for Ge-doped fibers at the 1.55 μm are below 0.3 dB m^{-1} at a 1 MGy dose of 20 keV x-rays [704], and should remain below 0.6 dB m^{-1}, when extrapolated to 10 MGy. The results presented in [704] are obtained for continuous high dose rate irradiation, while ITER operation is extended over 20 years with multiple interruptions. The ambient temperature of the FOCS fibers during ITER operation will be ∼100 °C, which will promote RIA annealing [705], additionally accelerated during baking periods, when

Table 34. Irradiation conditions for the FOCS.

	<0.1 MeV, n	14 MeV, n	Total n	γ
Flux $cm^{-2}s^{-1}$	1.7×10^8–3.3×10^{10}	4.3×10^6–2.6×10^9	3.8×10^8–7.7×10^{10}	2×10^8–4.2×10^{10}
Fluence cm^{-2} for 3000 s pulse	Up to 10^{14}	Up to 7.8×10^{12}	Up to 2.3×10^{13}	Up to 1.3×10^{14}
Fluence life (4700 h)	Up to 5.6×10^{17}	Up to 4.4×10^{16}	Up to 1.3×10^{18}	Up to 7.1×10^{17}

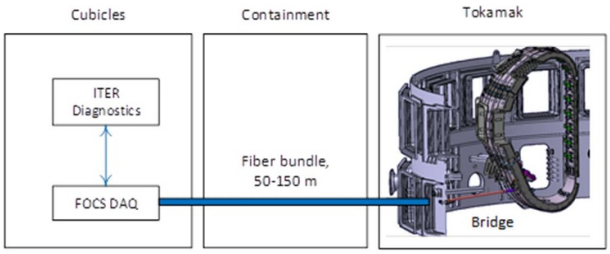

Figure 161. ITER FOCS data acquisition diagram.

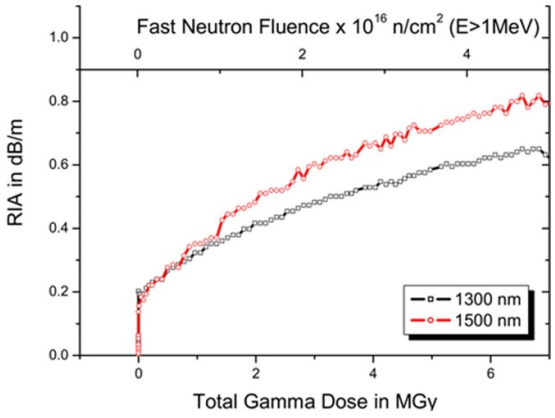

Figure 162. RIA evolution in a pure silica core single mode fiber irradiated in the BR2 fission reactor.

the temperature will rise to 200 °C with a 20 °C margin [706]. Therefore, the actual RIA levels at 10 MGy should remain acceptable.

An additional improvement can be obtained by using radiation-hard pure silica core fibers instead of standard Ge-doped fibers. For example, RIA levels of 16 and 27 dB km^{-1} after Co60 at 5 Gy s^{-1} dose rate for doses of 1 and 3 MGy, respectively, were reported in [707] for high-temperature acrylate-coated fibers. It is also important to notice that a ∼Gy s^{-1} dose rate relevant for ITER is a value that is common for such tests.

A ∼6 m length of the fiber in the cryostat penetration (FOCS bridge) can be exposed at temperatures below 0 °C and possibly down to 80 K. The radiation loads on the fiber in this area are smaller than on the VV surface thanks to the cryostat shielding effect and the geometrical factor. Still, a temperature decrease down to 80 K results in a very strong fiber radiation sensitivity increase: a dose of only several hundreds of Gy may result in an inacceptable RIA increase above 10 dB m^{-1} [708, 709]. 80 K temperatures are expected only in accidental conditions. During normal operation the temperature of the fiber in the bridge area should be higher. However, an accurate estimation of the temperature during operation is required.

The presence of neutrons should not change the estimation of the RIA. Usually, in case of fission reactor irradiations, the RIA contributions of neutrons and gammas for a same dose of radiations have similar scales [710–713]. Figure 162 shows the RIA measured in a pure silica core single mode optical fiber exposed at a temperature of 100 °C in the BR2 fission reactor [714] to a total gamma dose of 7 MGy and a fast ($E > 1$ MeV) neutron flux of 5×10^{16} cm^{-2}. The RIA level remains below 0.9 dB m^{-1}. The dose rate and the flux were up to 6 MGy h^{-1} and 10^{13} $cm^{-2}s^{-1}$, respectively. The ITER radiation environment is less severe.

Still, the impact of 14 MeV neutrons characteristic for the ITER nuclear phase cannot be addressed in a fission reactor. FOCS systems installed at JET should provide an answer to this question [703]. In terms of the dose-rate the radiation exposure during D–T operation will be completely relevant for ITER.

Ionizing radiation also changes the refractive index, and can consequently modify the fiber Verdet constant. This question is not addressed in literature. Off-line tests performed at SCK CEN demonstrated that both for gamma doses up to 5 MGy and fission reactor (BR1) irradiation up to a total neutron fluence of 10^{15} cm^{-2} changes were within the measurement accuracy, which was probably close to ±10% [711]. The low accuracy does not allow to draw conclusions relevant for ITER. Regular re-calibration of the FOCS during ITER operation using other plasma current measurement systems can be a simple yet reliable mitigation measure.

The exposure to high temperature and intense radiation may compromise the mechanical reliability of the sensing fiber. The temperature of the VV surface will be ∼100 °C during normal operation and 200 °C–220 °C during baking periods. The use of polyimide coated fibers seems relevant in this situation because the standard acrylate fiber coating is rated up to 85 °C. Polyimide is also considered as radiation resistant material. Unfortunately, the use of polyimide results in a significant degradation of the fiber polarization characteristics. On the other hand, the experience shows that the temperature limit of acrylate coated fibers can be increased if the fiber is exposed to elevated temperature in an inert atmosphere. For example, the sensing fiber of the FOCS installed at JET was exposed to ∼200 °C during operation and 320 °C during baking periods [703, 715]. The system is operational for more than five years. The coating probably deteriorated, but that did not prevent the system from performing current measurements. The actual state of the coating is unknown as the systems

continue operation. Unfortunately, this example is not completely representative for ITER because of the low radiation levels at JET.

8.5. Bolometers

In ITER, bolometers will be used to obtain information on the total radiated power and its spatial distribution from the main plasma and in the divertor region. Bolometer arrays will be installed in selected locations on the VV, and on the divertor [716]. Operation of a bolometer is based on the absorption of radiation. The absorbed power is determined by measuring the corresponding temperature increase, which is derived from changes of the electrical resistance of a meander shaped metal conductor on the back side of the absorber. The bolometers are directly open to plasma and have to withstand high neutron fluxes as well as ambient temperatures exceeding 200 °C, which presents a serious challenge with respect to maintaining their characteristics.

The ITER bolometers are an example how taking into account radiation effects may influence the design. Initially, it was supposed to use JET type high-temperature bolometers, which employ a thin mica substrate as the support for a gold meander shaped electrical resistor. However, a reactor experiment performed at the Japan Materials Testing Reactor (JMTR) in Oarai, Japan, indicated that such bolometers may not sustain the 0.02 dpa [Al] dose of neutron radiation expected for ITER due to both the mica instability and the transmutation of gold into mercury [717]. To answer those problems several modifications in the bolometer construction have been proposed. First, mica was replaced with aluminum nitride or alumina ceramics, which were expected to be stable under radiation and which have the added advantage of considerably increasing the upper temperature limit for continuous use above the 500 °C recommended for mica. To mitigate the transmutation Au was replaced with Pt. The new development was done at IPP in Garching [718].

A prototype of the radiation hard bolometer with the bolometer bridge formed by a thin Pt-meander sputtered on a Si_3N_4 foil was exposed in a reflector channel of the BR2 fission reactor up to a total dose of ∼0.02 dpa. The bolometer remained operational during the 19 d of irradiation at a temperature of ∼400 °C [719]. The four bolometer bridge resistances were continuously measured during irradiation. The measured values closely followed small temperature and neutron flux variations related to the reactor operation. Two meander resistances showed a small drift under irradiation, while two other meanders experienced first an increase in their resistance and then after almost two weeks of irradiation the resistances returned to values close to the initial ones.

Although, the post-irradiation examination indicated possible problem with the Pt meander adhesion on the substrate, see figure 163, it was concluded that the design could be considered as a solution for an ITER-compatible device.

Following significant work, an improved version of the bolometer with Si_3N_4 substrate and a Pt resistors was proposed [720]. This prototype bolometer successfully passed reactor irradiation test up to a 0.3 dpa dose with an acceptable increase of the resistance [721]. A new reactor irradiation test is being planned where the bolometer meander resistivity and the time constant will be measured under irradiation at temperatures in the range 225 °C–275 °C.

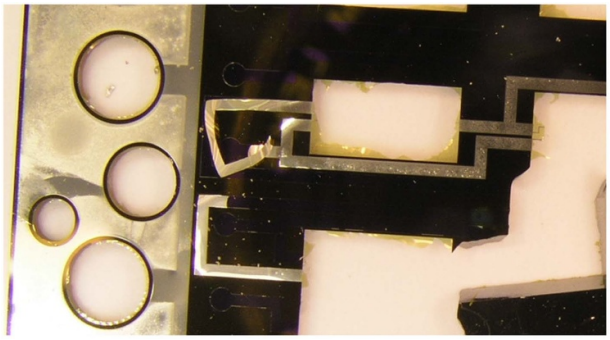

Figure 163. Delamination of Pt tracks from the Si_3N_4 substrate observed during dismantling of the irradiated bolometer in a hot cell.

The power deposited onto the absorber is expected to be in a range 0.5 μW–2 mW. The maximum noise level of the voltage measurements of 50 μV is acceptable, which is based on the requirement for the dynamic range of the diagnostic and the noise budget for signal cables of 0.3–3 μV m^{-1} and it corresponds to a noise level of 2.5 μW [716]. For bolometers, the intrinsic noise level is ∼20 μV. A comparison with the relevant power levels shows both a need for optimizing this diagnostic and reducing the noise levels in the connecting cables.

The question to what extent the results obtained at JMTR are relevant for ITER was considered. The neutron capture cross-section for gold is maximal for thermalized neutrons (<2.5 eV). A significant flux of thermal neutrons in the JMTR test explains the high transmutation yield. In ITER, the bolometers will be open to the main plasma, with a harder neutron energy spectrum and the thermal neutron flux will be significantly lower than that at the JMTR. As a consequence, the transmutation rate will also be significantly lower. It was concluded that after 5 years of 'hot' ITER operation the transmutation level should not exceed 2%, which has acceptable impact on the reliability of the bolometers.

8.6. Needs for future research and standardization of the testing approach

8.6.1. R&D for refining the ITER design for suppressing radiation effects (neutron calculations, irradiation test of samples and prototypes, neutron shielding development). To allow for long-term operation of plasma diagnostics at ITER, combination of radiation resistant components and systems while providing efficient radiation shielding against gamma and neutron fluxes from the hot plasma is necessary. This means that it is necessary to evaluate the gamma and neutron fields, identify radiation-resistant materials and elements, and determine the levels of their permissible exposure in ITER. Three areas of the researches have been identified, in this regard, almost from the very beginning of the ITER diagnostics development.

The first area is the calculation of neutron fluxes and gamma dose rates in which diagnostic elements will be located. For this purpose, methods for calculating of the gamma and neutron fields in ITER were developed. ITER diagnostics should be worked out in detail to obtain reliable results of the calculations, including the materials and geometry of the individual elements. In parallel with the design development of the diagnostic systems, three-dimensional models of the ITER installation were created. Neutron calculations were performed using a Monte Carlo method. Specialized numerical methods (MCNP code) and libraries for cross sections of the nuclear reactions in construction materials were used. The results of these calculations give the gamma and neutron fields with a high accuracy, at least inside the vacuum part of the ITER installation, provided that the geometry and materials are specified precisely. In turn, this makes it possible to set conditions for particular radiation tests. In addition, the data obtained must (or can) prove that the diagnostic design meets the ITER nuclear safety requirements.

The second research area is the experimental investigation of materials and critical diagnostic elements under irradiation. To perform experiments at conditions that are close to ITER attention should be given to radiation dosimetry. Early experiments were performed at high radiation levels, based on the assumption of a high load under ITER conditions. For example, for optical glasses it was shown [722, 723] that only pure silica for the visible range can withstand long-term intense gamma and neutron irradiation, but even such glasses quickly lose transmission in the UV range. This made it clear that the optics needs to be protected from radiation, to minimize the fluxes of the neutrons and secondary gamma radiation where the optical elements need to be placed. But even with the use of the neutron shielding in port plugs, radiation levels remain high. Subsequent irradiation tests [674] have shown that it is practically impossible to use silica glass for collecting and transmitting UV radiation to detectors in ITER.

The third area is the neutron shielding development and modifications in ITER port plugs. Neutron calculations have shown that when boron carbide blocks are placed in the port plugs together with an iron-water neutron shield and periscope channels are used to collect light from the plasma, the radiation loads become less critical beyond the vacuum boundary. As a result, the critical diagnostic elements shall be located as much as possible far from plasma, e.g. in the Port Interspace & Cell. It should be noted that drastic measures to strengthen neutron shielding requires changes in the design of diagnostics.

8.6.2. Refinement of the ITER design. DSMs design was changed in 2016 due to the insufficient effectiveness of the previous neutron shielding relatively to nuclear facility licensing requirements. So-called 'LEGO design' of the DSM was developed for maximum reduction of weight of the steel parts and filling of all voids with a light but effective neutron absorber, in which boron carbide blocks were used to weaken neutron fluxes. The neutron flux was decreased significantly, which led to reduced radiation loads on optics and detectors in the Port Cell area. Such refinement of the DSM design was forced and led to an increase of the project cost. As a rule, diagnostic characteristics (measurement accuracy, spatial and temporal resolution) have suffered as a result. On the other hand, without these changes, diagnostics would simply not be able to function for both physical reasons (degradation of optical characteristics, too high background from gamma and neutron fluxes to the detectors) and formal reasons (violation of the nuclear safety requirements).

8.6.3. Other examples of the design changes. Some other refinements were made in the design of the plasma diagnostics due to radiation problems. Here are the main ones: using of the mirror telescopes for plasma light transmission in Port Interspace and Port Cell, the periscope legs lengthening in the DSM neutron shielding, shifting of the entrance pupil of optical diagnostics deeper into the port plug further away from the plasma, reducing of the solid angle of the plasma light collection, using of the fiber optics to transmit light to remote diagnostic rooms, etc.

8.7. Summary

Overview of the impact of recent radiation effect studies on design and qualification of various ITER diagnostic systems is presented. Compatibility with ITER radiation fields is highlighted as one of the main design drivers for diagnostics. Experimental testing of diagnostic functional components in radiation fields with parameters as close as possible to the target ones is still seen as the main approach to their qualification. This shall be accompanied with numerical simulation of radiation effects whenever technically feasible. Significant progress in development and qualification of various ITER diagnostic systems from radiation-hardness point of view is reported.

Sufficient radiation hardness of the vacuum window assemblies based on silica glass was successfully demonstrated during irradiation tests using nuclear reactor, a Co-60 gamma source, and a NG. In particular, such assemblies were irradiated in the BR1 reactor of SCK•CEN in Mol at 150 °C during 5.5 months up to a total fast ($E > 0.1$ MeV) neutron fluence of $\sim 2 \times 10^{16}$ cm^{-2} with positive outcome of post-irradiation thermo-mechanical and He-leak tests.

Borosilicate glass inserts of the ITER vacuum electrical feedthroughs were irradiated at LVR-15 reactor of CVŘ Řež up to the total fast ($E > 0.1$ MeV) neutron fluence of 5×10^{17} cm^{-2}. It was concluded that radiation induced dimensional changes of these borosilicate glass inserts pose no risk with respect to the potential loss of vacuum accident on ITER.

Radiation hardness of ITER in-vessel LTCC magnetic sensors was investigated using Co-60 gamma source up to 72 MGy and also at LVR-15 fission reactor up to neutron fluence $\sim 10^{20}$ cm^{-2} with positive outcome.

New technologies potentially applicable for magnetic sensors future designs were highlighted. In particular, samples of ceramic substrates metallized by copper using TP technology were irradiation by total neutron fluence of 4×10^{18} cm^{-2} at LVR-15 reactor while the samples showed satisfactory

adhesion of copper layer to ceramic substrates better than 35 N mm^{-2}.

Steady state magnetic field sensors based on Hall effect which use both bismuth and antimony sensitive layers were also successfully qualified at LVR-15 reactor with respect to their expected total neutron exposure on ITER.

Compatibility of FOCS fibers, to be used for plasma current measurement on ITER, with gamma radiation, neutron fluxes and elevated temperature was investigated. Silica core single mode optical fiber was exposed at a temperature of 100 °C in the BR2 fission reactor to a total gamma dose of 7 MGy and a fast ($E > 1$ MeV) neutron flux of 5×10^{16} cm^{-2}. The RIA level remains acceptable below 0.9 dB m^{-1}. Operation of FOCS in inert atmosphere was suggested as solution to achieve compatibility of fibers with elevated temperatures even up to 320 °C as demonstrated during operation of FOCS prototype on JET.

ITER bolometers are presented as an example of a diagnostic where taking into account radiation effects had significant impact on its design. Bolometer with Si_3N_4 substrate and a Pt resistors successfully passed reactor irradiation test up to a 0.3 dpa dose with an acceptable increase of the resistance.

Finally, three main directions of R&D to be continuously pursued are identified, namely, 3D modeling of radiation fields using real fusion reactor geometry and materials, experimental qualification of diagnostic functional components in radiation environment as close as possible to the target one and optimization of neutron shielding and overall engineering design of implementation of various diagnostic components on ITER in order to minimize their radiation exposure.

9. Diagnostic mirrors for ITER: status and perspectives

A. Litnovsky[40], L. Moser[2,41], N. Babinov[29], A. Dmitriev[41,29], B. Kim[5], L. Marot[41], A. Razdobarin[29], A. Rogov[42], D. Samsonov[29], C. Seon[43], K. Soni[41], M. W. Walsh[2], R. Yan[26] and E. Yatsuka[43]

9.1. Diagnostic mirrors in ITER

9.1.1. Role and mission of mirrors. The ITER international experimental fusion reactor being built in Cadarache, South France by the EU, Russian Federation, Japan, South Korea, the United States, China and India will be equipped with highly sophisticated and versatile diagnostic systems. Diagnostic overviews are provided in [4, 724] and an update can be found in [725]. Among others, there will be twenty-three optical diagnostics monitoring crucial physics and engineering parameters of the reactor, such as the temperature of divertor plates, electron and ion densities and temperatures [724, 726]. Due to harsh neutron environment, optical systems will be based on reflective optics using mirrors to guide plasma radiation towards spectrometers and detectors. The plasma-facing mirror (FM) will be affected at most from the plasma particles and intensive radiation. The lifetime of a first mirror will affect the entire performance of the corresponding mirror-based diagnostic and hence, have a direct impact on ITER operation. Maintaining the lifetime of diagnostic mirrors is a significant physics and engineering challenge. There will be about 80 first mirrors employed in optical and laser-based diagnostics operating in a wide wavelength range spreading from 2 nm, for the VUV spectrometer in the divertor [96] up to 118 micrometers as foreseen for the polarimeter system [727, 728]. An example of the first mirror for ITER H_α diagnostic system is shown in figures 164(*b*) and (*c*). According to the design regulations, the lifetime of the mirrors has to be guaranteed for the entire service life of the reactor. Maintenance and servicing of diagnostic mirrors are to be avoided whenever possible. These critical requirements have triggered a significant international research and development (R&D) program on diagnostic mirrors.

9.1.2. Phasing of diagnostics. In the course of the planning of ITER diagnostics, there was a clear understanding that the simultaneous delivery of the entire diagnostic set to ITER is not feasible due to logistics, engineering and budget constraints. Therefore, it was decided to make a prioritized list of diagnostics based on their impact on machine commissioning, operation and physics program. This list is also known as diagnostic phasing. The first diagnostics in the list had to be procured earlier. In total, there are three categories of diagnostics in the list:

Category 0

- Diagnostics required for machine start and commissioning.

Category 1

- Diagnostics required for machine operation.

and

Category 1a

- Diagnostics required for fulfillment of the physics program in ITER.

The detailed list of diagnostics according to each category (phase) can be found e.g. in [729]. As can be seen from the list, among optical-based diagnostics, there are several which are required for the basic machine operation. For instance, divertor thermography is an inevitable instrument for detection of dangerous operation conditions in the divertor target area.

9.2. Risks and issues

The initial stage of the coordinated research and development program on diagnostic mirrors involved dedicated and accompanied experiments with special mirror assemblies to address the specific environmental conditions in ITER diagnostics. These studies were complemented by the analyses of mirrors in existing diagnostics in present-day tokamaks. The respective overviews of results are available in [730–741].

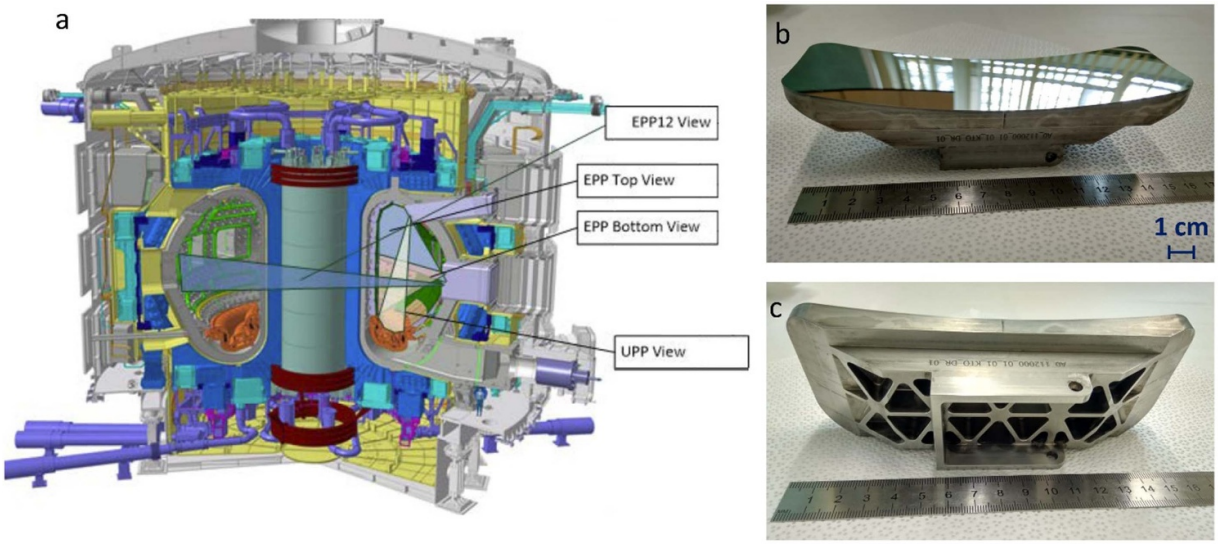

Figure 164. ITER Hα as an example of mirror-based diagnostic and its first mirror: (*a*) diagnostic locations in ITER equatorial port plugs (EPP) and upper port plugs (UPP), (*b*) the reflecting surface of the first mirror and (*c*) rear view of the mirror. The single crystal molybdenum reflecting surface has dimensions of 164 × 60 × 42 mm and a radius of 364 mm.

These studies were aimed at identifying the major risk factors for diagnostic mirrors. The major risk factors expected for diagnostic mirrors in ITER are summarized below.

9.2.1. Erosion. Erosion of the mirror surfaces was treated as a major risk for diagnostic mirrors from the beginning of research and development (R&D). Under the term 'erosion' usually two different processes are meant: chemical erosion in the reactive environment and physical sputtering.

Chemical erosion played the major role in defining the mirror performance at an early stage of the ITER project. The deposition of volatile hydrocarbon radicals on the mirrors originating from the carbon-based old divertor was treated as a critical risk factor for e.g. divertor mirrors [740, 742–745]. In the current ITER design, the plasma-facing materials will be beryllium at the first wall and tungsten in the divertor. Carbon was excluded mostly due to safety considerations related to chemical erosion of first walls and subsequent transport of tritiated carbon radicals. Therefore, the chemical erosion issue does not represent a major concern anymore.

Sputtering of the mirror surface currently represents the major risk for the mirror performance. Physical sputtering is expected in ITER due to energetic neutrals originating from the CX reactions in the core DT plasmas. The CX-fluxes to the first wall of ITER were assessed by modeling by several research groups. Modeling results predict quite intensive fluxes reaching 10^{19} atoms m^{-2} as reported in [724]. Recent modeling assessment based on SOLPS 4.2 code provided a detailed overview of CX fluxes for different operation scenarios of ITER. The flux of CX neutrals with energies of about 200 eV will cause sputtering of the mirror surface. Sputtering may provoke a drastic increase of mirror roughness and unfortunately, the abrupt and rapid degradation of mirror reflectivity. The natural CX fluxes in modern tokamaks are rather small making the experimental reproduction of the sputtering environment expected in ITER challenging. An effective way of addressing the mirror performance under sputtering conditions formed by fusion plasmas, was to perform the sputtering exposures in tokamak SOL plasmas and substituting the CX fluxes with plasma ion fluxes of nearly the same energy featuring much higher flux density. These studies [746] allowed making estimates of the mirror lifetime under erosion conditions in ITER.

However, CX neutrals originating from the regular plasma operation of ITER is not the only sputtering source. An experiment made in the Tore Supra tokamak brought a remarkable result [747, 748]. Here, a copper mirror was severely sputtered, almost losing its reflectivity in the visible range. The accompanying research has demonstrated non-ambiguously, that the sputtering of mirror surfaces has been caused by wall conditioning discharge. The wall conditioning based on a radio-frequency stimulated glow discharge can produce high-energy ions which can penetrate several tens of centimeter deep into the diagnostic ducts while sputtering the mirrors. One respective estimate has been made e.g. in Litnovsky *et al* [749]. Photographs of mirrors suffered from sputtering are provided in figure 165(*a*).

Studies of the effects caused by sputtering made a decisive impact on the choice of mirror material described later in this paper.

9.2.2. Deposition. Deposition is another crucial factor degrading the mirror performance in ITER. Plasma impurities sputtered or molten from the plasma-facing components may be transported by plasma particles toward mirrors and become deposited on mirror surface. The formed deposition layer has its own reflectivity drastically affecting the reflectivity of the mirror. A mirror with a deposit formed in the course

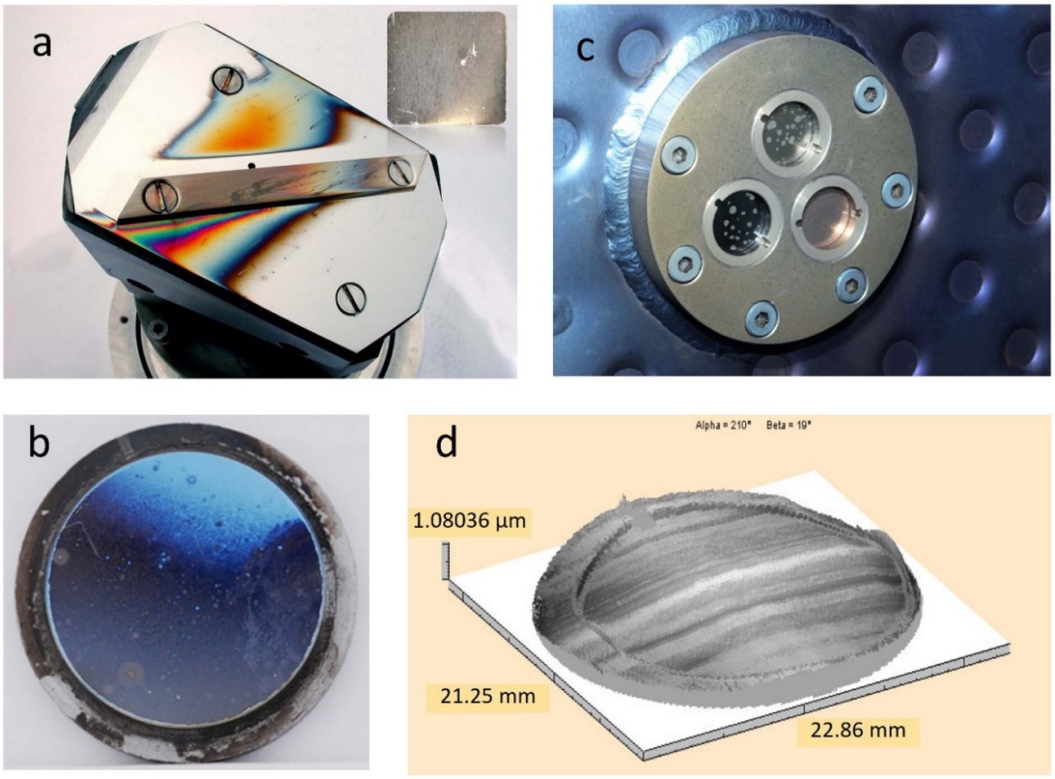

Figure 165. Diagnostic mirrors affected by (*a*) sputtering, as seen on the shiny part of a mirror exposed in TEXTOR [743] and rough surface of a mirror exposed in the JET divertor (inlay, Reprinted from [739], Copyright (2019), with permission from Elsevier), (*b*) deposition, as seen on the mirror exposed in the divertor of the ASDEX Upgrade. Reproduced from [750].© 2013 IAEA, Vienna. All rights reserved, (*c*) water leak/steam event affected mirrors in the Tore-Supra first wall. Reprinted from [747], Copyright (2006), with permission from Elsevier and (*d*) wall conditioning leading to severe sputtering of a mirror located in Tore Supra first wall. Reproduced with permission from [751].

of exposure can be seen in figure 165(*b*). General information on erosion and deposition is reported in the dedicated chapter devoted to the first wall diagnostic in this issue.

Intensive research program has been made within the ITPA on several major tokamaks worldwide to study the effect of deposition [730, 734, 739, 740, 742, 747, 750, 752, 753]. The key adverse feature of deposition of impurities are identified to be the following:

1. The deposition pattern is usually highly inhomogeneous i.e. no systematic correction of reflectivity is possible for the affected mirror.
2. Even a very thin deposited layer of 10 nm is enough to have a dominating effect on the reflectivity in the visible range.
3. Deposits are mostly rough, inevitably leading to the reflectivity degradation.
4. Deposition is a process in part involving volatile radicals and/or atoms. Therefore, deposition can be expected even at far distance from plasma.
5. In the presence of energetic plasma particle, e.g. from neutral beam, deposition can be accompanied with the implantation of impurities into the mirror substrate and/or formation of mixed layers with substrate material.

These adverse properties of deposition underline the severity of the problem. As in the case of sputtering, the regular plasma operation is not the only source of deposition in ITER. Wall conditioning sometimes plays a decisive role in mirror surface contamination, as can be inferred from the following sub-sections.

9.2.3. Steam ingress. In ITER, diagnostic mirrors are also vulnerable to a 'Vacuum Vessel Ingress of Coolant Event' (VVICE, where VVICE category IV also called Loss-of-Coolant Accident) in ITER [754–756], also known as a steam ingress. The in-vessel components of ITER are cooled with water. A large number of tubes connected by welding are located inside the vacuum chamber. Vibration of in-vessel components, high thermal and electromagnetic loads on the structural elements lead to an increased probability of depressurization of the water-cooling system and water ingress into the VV. A steam event is anticipated in case of an accidental rupture of the cooling loops inside the VV or due to damage caused to the cooling pipes by runaway electrons generated during plasma disruptions. As a result, several negative factors can simultaneously affect the in-vessel mirrors: increased temperature of 250 °C during baking, and up to 400 °C in case of accidents during regular plasma discharges, and a contact with steam at an increased pressure. As a result of the interaction of steam with a reflecting mirror material, a volumetric degradation of the mirror surface can occur along with the formation of hydroxide layers on it. These processes will lead to degradation of optical properties of affected mirrors. A

photograph of the mirror assembly exposed in Tore-Supra tokamak and suffered from steam and water ingress is provided in figure 165(*c*).

During a steam ingress event, the FMs will be exposed to steam at pressures of up to 1.5 bar [755, 757] at temperature up to 250 °C—the maximum temperature during the ITER baking process [756, 757]. The steam may also mobilize dust, which could eventually be deposited on the mirror surfaces further degrading the optical properties of FMs [758].

9.2.4. Wall conditioning. Wall conditioning necessary for plasma and particle control in ITER, represents an additional risk for the lifetime of diagnostic mirrors. The effect of wall conditioning has been assessed in a number of dedicated experiments. These studies show that the wall conditioning effect on diagnostic mirrors can be manifold. An experimental campaign undertaken at Tore Supra tokamak [747, 751] demonstrated a severe sputtering effect caused by the glow discharge wall conditioning to mirrors located at the first wall, figure 165(*d*). This effect may be relevant to the mirrors in ITER that are closest to burning plasma.

At the same time, the results of a reference experiment performed in the KSTAR tokamak [759] demonstrate explicitly that wall conditioning and baking can also lead to deposition of impurities on mirrors. In this experiment the deposition mitigation assembly (DeMi) was installed into the midplane location of the machine. The DeMi is a system of tubes imitating the diagnostic ducts with sensors at their ends, acting as mirrors in real duct systems. A detailed description of the DeMi system can be found in [759].

To measure the *in-situ* deposition or erosion effect on the mirror surface with the baffle duct, QCM's were installed in KSTAR. The first QCM-1 located 1.5 m away from the plasma measured the deposition quantity *in situ* through the short-baffled duct. QCM-2 is positioned near QCM-1 inside an enclosure case. The QCM-2 provided a reference signal for the compensation of the error in QCM-1 signal due to temperature or noise effects. The net amount of deposited mass was derived by subtracting QCM-2 signal from the QCM-1 signal. The result of the deposition measurement during the 2015 KSTAR campaign is depicted in figure 166. The experimental data explicitly shows that the wall recovery operation with the GDC and baking resulted in heaviest deposition on the QCM surface, while the plasma operation and the sole GDC have resulted in ten-fold less deposition rate. Impurity deposition conditions caused by wall conditioning may be expected for mirrors in ITER located in diagnostic ducts far away from plasma.

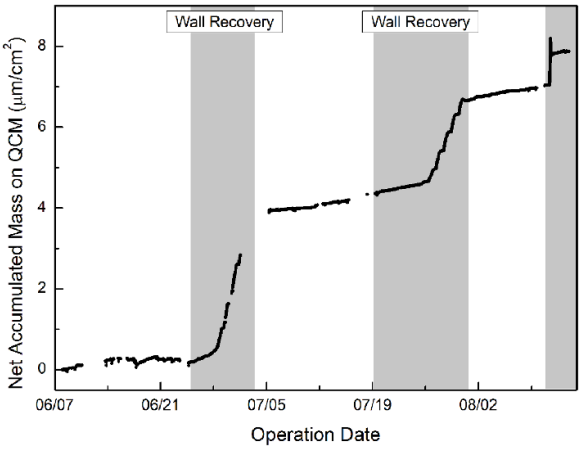

Figure 166. The net accumulated mass (deposition) data from the QCM measurement in the 2015 KSTAR campaign. The major deposition on QCMs occurred during wall recovery period including baking and the GDC. A maximum value of 170 pm h^{-1} was found during the GDC+ baking condition assuming graphite for deposition material. Reprinted from [759], Copyright (2018), with permission from Elsevier.

9.3. Risks evaluation and mitigation

Adverse factors affecting diagnostic mirrors were discussed and analyzed in numerous expert meetings, conferences and dedicated seminars involving the ITER Team and representatives of domestic agencies. In the course of these meetings, all aforementioned aspects were thoroughly and critically assessed leading to a number of crucial decisions. Important decisions, influencing the entire diagnostic mirror philosophy are shortly outlined below.

In the course of evolution of the ITER diagnostic systems, the position of the first mirrors was changed with time. For more than fifteen years, the FMs were close to the first wall position [760]. After a careful assessment of major risks for the first mirrors imposed by the deposition of impurities and sputtering of the reflecting mirror surfaces, it was finally decided to use any possibility of moving the FMUs of all diagnostics whenever possible, far away from the plasma. In this decision, the persisting uncertainty in predicting transient events which are supposed to have an instant and devastating impact on mirrors, was considered as a high risk. However, transient heat loads which are unfortunately, not fully predictable till now, could momentarily damage the mirror terminally.

Diagnostic mirrors positioned close to the plasma, will be exposed to a high heat load from the neutron flux which induces deformation even for a water-cooled FM [761]. Moreover, being close to the first wall and having a large area open to the plasma lead to physical sputtering of the surface due to CX neutrals [725]. These considerations have triggered the re-positioning of the FM, whenever possible, further away from the first wall [504]. In addition to moving away from the plasma to the farthest distance possible, additional engineering measures, such as using diagnostic pupils with a possibly small aperture for viewing the plasma were prescribed for diagnostic engineers.

The a wide scope of options has been assessed to alleviate the diagnostic mirror challenge. A possibility of a general change of the probing wavelengths from the UV and VIS range toward the less vulnerable IR range [762] was assessed along with a possibility of substituting the optical diagnostics with ones not using any optics in ITER [763]. In general, however, this assessment did not lead to a significant change of

the projected diagnostic suite and its principal parameters as planned for ITER.

It was decided to develop a solution for the first mirror problem using a coordinated R&D effort with several well-defined focus areas. Attaining progress or a solution in the dedicated area contributes to a solution of the entire diagnostic mirror problem. These areas were initially defined in the Work Plan of the First Mirror R&D [764] and then further evolved [732, 764]. Based on initial critical assessment of mirror risks provided in e.g. [765], five crucial areas of first mirror R&D were identified as follows:

1. mirror material choice
2. predictive modeling of mirror performance
3. mirror surface recovery (MSR)—a crucial set of measures for a prolongation of mirror lifetime comprising the passive mitigation of mirror contamination, the use of engineering tools for mirror protection and active mirror cleaning. The MSR will be described later in this paper in more detail.
4. Tests under harsh environmental conditions involving studies under neutron, gamma and steam conditions

and

5. engineering solutions for ITER mirrors.

In the past decades experimental and theoretical predictive modeling efforts were aligned along these main topics. Significant progress was attained in all these directions. At the same time, as the project evolved, several crucial decisions remained actual for the present diagnostic mirror R&D, while others had to be discarded due to a major change in design and because of other boundary conditions.

Here, the authors feel it necessary to briefly list decisions which were despite success in their elaboration, discarded from the further consideration due to reasons mentioned above.

1. Engineering solutions using retractable diagnostic tubes with mirrors. Tubes were discarded from the design of optical diagnostics as being too complex.
2. Mirror cleaning using lasers was discarded as a prime generic cleaning technique due to the complexity of realization in ITER geometry.
3. Feeding deuterium in front of the mirror to stimulate chemical erosion of carbon impurities. Discarded due to reason mentioned above.

In addition to the mentioned 'grand' decisions, such as moving mirrors further away from plasma, there are crucial specific achievements and decisions that remained fully in power and actual in ITER design. Among those decisions are:

- The use of single crystal and possibly nano-crystalline materials instead of any polycrystalline mirrors including those made through powder metallurgical route
- The use of *in-situ* mirror cleaning system
- The use of shutters and flaps
- The use of so-called 'gas shutters' a gas, usually helium or argon feeding across the plasma particle flow in order to intercept the contamination flow toward the mirror.

Interestingly, the mirror heating initially proposed for stimulating the chemical erosion of carbon impurities was preserved. The use of mirror heating, active and passive was found useful and effective for reduction of deposition of plasma impurities on the mirror surface.

These decisions are described in detail in the following section. Certainly, this list is not full and several prospective mirror solutions are under consideration. Authors, however, believe that providing both lists is a necessary aide for physicists and engineers working on mirror solutions, possibly saving an extra effort on discarded directions and allowing a more efficient R&D on the priority topics.

9.4. Solutions

9.4.1. Mirror material. The choice of mirror material is one of the key topics of the ITER Research plan, see e.g. Task A.8 [56]. In the course of an intensive R&D [732, 734, 746, 766–769], the prime candidate mirror materials were identified. Currently, molybdenum (Mo) and rhodium (Rh) are two main candidate materials for the FM. Molybdenum, due to its low sputtering yield, is more advantageous under sputtering conditions [504, 734, 746, 751, 753–772]. Rhodium, on the other hand, provides a better reflectivity (between 70% and 80%) in the visible range [773] as well as near-IR and IR ranges (around 85% at 1 μm). Rh also has low chemical reactivity, suppressing oxide and carbide formation [774]. In the case of polycrystalline mirrors composed of many grains with random orientation of faces, the sputtering yield can vary strongly over the material surface depending on the crystallographic plane of each individual grain and its orientation with respect to the incoming particle flux. It is also important to keep the surface relief pattern i.e. the roughness of a polycrystalline mirror small compared to the wavelength of the reflected light in order to minimize the effect of diffuse reflection on the measurements. Generally, this indicates that the mirrors must have small grain sizes and preferably similar crystal orientations to be homogeneously sputtered. These requirements can be fulfilled, for instance, by using a single crystal [302, 734, 775] or by coating the surface with nanometer-sized crystallites [766].

The advantages of single crystals under sputtering conditions were extensively studied under laboratory conditions in e.g. subchapter 5 and [734, 776], a direct comparative test in a tokamak was performed in TEXTOR [746]. The series of dedicated sputtering tests revealed the outstanding ability of both single crystal molybdenum and rhodium to preserve their optical reflectivity despite the severe sputtering [768, 769]. At the same time, the availability of large single crystals and high price of rhodium presently make the mirror solution based on nano-crystallite coating particularly attractive for several diagnostics [766, 777, 778].

For several diagnostics, there are diagnostic-specific mirror materials addressing the performance requirements of

these diagnostics. An example is the ITER VUV spectrometer operating at an extremely short wavelength range of several nanometers [96]. Here, several materials such as silicon carbide and Ni–P plated stainless steel substrate mirrors along with gold (Au) coated stainless steel mirrors were tested. The steam ingress event as well as thermal cycling played a crucial role in the selection of mirror material for this diagnostic. Based on results of thermal cycling from room temperature up to 240 °C for 100 cycles, silicon carbide was selected as a prime mirror material for the VUV spectrometer.

9.4.2. Predictive modeling. Modeling was initially anticipated to provide a crucially important estimate of the main mirror risk factors, such as sputtering and deposition rates. These rates had to be used during the e.g. engineering and design of cleaning systems. Several approaches to modeling the effects on mirrors were pursued so far [779–782]. Among the most prominent is the so-called conservative approach followed in the modeling studies of Kotov *et al* [780–783], also known as 'Kotov model'. The main characteristic feature of the model is in providing conservative estimates for expected effects—the extreme results on erosion and deposition rates were taken and multiplied by conservative factors, reaching 10.

In this model, the B2-EIRENE [784] codes were used to calculate the plasma parameters: electron and ion temperature, ion and neutral density at the vicinity of diagnostic ports. Later, the model was extended towards the inside of diagnostic ducts and was using the unified interface with engineering CAD programs [783]. In the latest stages of development, the Kotov model was extended to 3D geometry and incorporated among others, 2.5D plasma parameters. According to modeling, the calculated worst case gross deposition rate of beryllium in the middle of the port plug faces reaches almost 0.1 nm s^{-1}. At the same time, the Be erosion to deposition ratio at those locations is always larger than 5, indicating a high probability of net erosion conditions there [780].

Another approach was followed by Rode *et al* [785] later. Here, like in the Kotov model, the 3D distributions of particle fluxes at the surface of the mirrors were used. Contrary to Kotov's model, the precise balance between erosion and deposition was the focus of the modeling. The results of the modeling using the new model are pending and will be the subject of a dedicated publication.

At the same time, there are dedicated modeling efforts ongoing for addressing the issues of the specific ITER diagnostics. As an example, the modeling using the domestic-made code KITe [493] is underway at the Ioffe Institute (Russia) along with a use of the German particle-in-cell (PIC) Monte Carlo (MC) code package Fraunhofer IST [786] (Germany). The results of these diagnostic-specific efforts are reported later in this overview.

9.4.3. Shutters and ducts. Shutters and ducts are vital elements in the passive protection of diagnostic mirrors from the adverse factors degrading their performance. The shutters minimize the undesirable fluxes of plasma particles towards the mirrors by reducing the exposure time, leaving the diagnostic ducts open only for the time necessary for measurements.

Diagnostic ducts may provide a sink of particle fluxes by depositing these particles on the duct walls and hence, minimizing the amount of particles reaching the mirror. Some modeling codes have predicted a positive effect of duct shaping in order to reduce particle fluxes towards the mirrors. In order to address it experimentally, a dedicated task within the International Energy Agency (IEA)—ITPA Joint eXperiment (JEX) program was initiated. In the framework of this task performed in large and medium-scale tokamaks, duct systems of different shapes and lengths, such as Mirror Station [749] were exposed in several tokamaks, including TEXTOR, ASDEX Upgrade, DIII-D and JET [739], whereas the Deposition Mitigation (DeMi) system following a similar intrinsic design was exposed in KSTAR [759]. The results are summarized in e.g. [739, 742, 759]. A positive effect of the duct length on suppression of deposition was experimentally confirmed, whereas the predicted advantages due to duct geometry, revealed only a slight practical positive effect. At the same time, during the recent experiment in KSTAR [759] the mitigation efficiency was tested using three different baffled duct geometries: short, long and short with extended volume via fins. Mirror degradation was evaluated *ex-situ* by measuring the reflectivity of the mirror samples using D_α line at 654.9 nm wavelength. The baffled duct with the expanded volume before the mirror sample did show the most effective mitigation effect. Therefore, the investigations of the effect of fins needs to be continued.

9.4.4. Mirror cleaning. The FMs, being the initial elements in the optical path in the diagnostic systems, will be vulnerable to several effects influencing their optical properties. In addition to deposition of the first wall materials (Be and W) [738, 739], they are also vulnerable to surface oxidation following long-term maintenance (LTM) [504, 787] as well as oxidation and structural damage from steam ingress events [757]. As the only technique for an active recovery, mirror cleaning is envisaged [500, 504, 732]. Following the requirement of the minimum service to be applied to diagnostic mirrors in ITER mentioned earlier, the *in situ* cleaning by plasma is currently seen as the only option [788]. In the course of the cleaning, particles from the cleaning plasma sputter the contaminants from the mirror surface along with a part of the mirror material, possibly affected by e.g. contaminants diffused into the mirror bulk.

Such a cleaning technique, despite its relative complexity, allows avoiding the time and resource-consuming pull out of the entire diagnostic port plug needed for mirror service and replacement—as required by the ITER maintenance procedure [787].

There are two main techniques currently under consideration for achieving the desirable ions with energies specific to plasma cleaning: radiofrequency (RF)-based along with pulsed direct current (DC) plasma cleaning techniques. In both

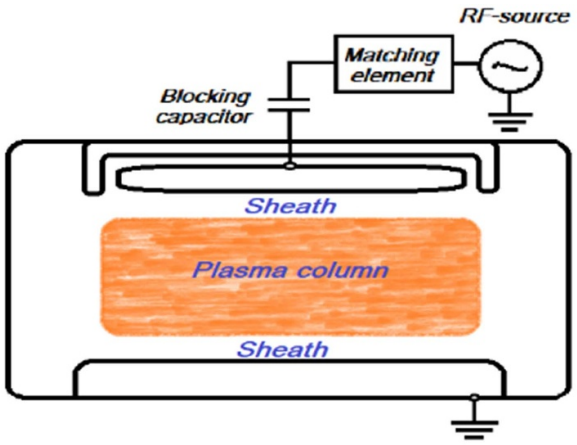

Figure 167. Scheme of a capacitively coupled radiofrequency cell.

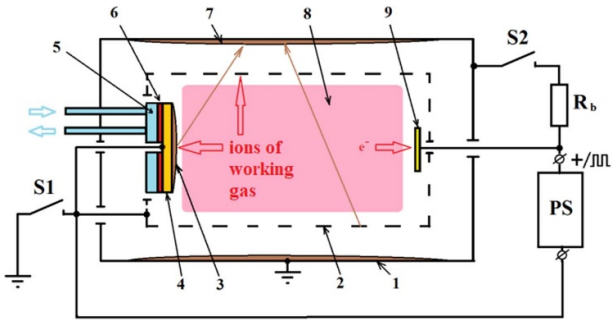

Figure 168. Scheme of a mirror cleaning system based on a DC/p-DC discharge: 1—VV walls; 2—mesh hollow cathode; 3—contamination; 4—mirror; 5—water cooled grounded mirror body; 6—insulating thermal interface (for insulated mirror cleaning mode only); 7—surface for the deposition of impurities sputtered during the cleaning process; 8—discharge area; 9—anode; PS—DC/p-DC power supply; S1 opened—mirror insulated mode, S1 closed—mirror grounded mode (insulator 6 not required).

these techniques, the mirror acts as an electrode and the RF or DC plasma is ignited around the mirror. There are several particular advantages as well as technological challenges for both techniques, which will be described in detail later.

The capacitively coupled RF (CCRF) discharge comprises applying an RF-voltage with the frequencies varying in the rage 10–100 MHz to the mirror serving itself as a plasma source [500–502, 789, 790]. CCRF-discharge has been widely used due to its ability to treat both dielectric and metallic electrodes. The CCRF-discharge is generated between two electrodes, one of which is grounded and the other one is RF-powered, see figure 167. Electrons oscillate in the electrode gap at the applied frequency while ions are mostly immobile in the bulk RF-plasma column. Electrons located near the electrode are captured by the electrode surface. Areas of positive spatial charge, the so-called near-electrode sheath, are formed in front of each electrode. Depending on the RF voltage phase each sheath is filled with plasma or represented as a gap. Ions are accelerated in the gap and impinge on the electrode surface providing physical sputtering of the surface of the electrode.

The ability of a cleaning system to remove the contaminants from the mirrors on a regular cyclic basis is of crucial importance for the validation of mirror cleaning in ITER. Cyclic contamination—cleaning cycles were performed on single crystal molybdenum (SC Mo), rhodium (SC Rh) and Rh-coated mirror with coating thickness exceeding 10 μm. For SC Mo, the specular reflectivity was not changed after 100 cycles. However, after the subsequent air storage and the following new cleaning cycles, it was observed that pits and ripples formation induced a rapid decrease of the reflectivity [791].

In a symmetric discharge when the surface areas of both electrodes are equal the average sheath thickness and voltage drop are equal for each of electrodes. However, most CCRF-reactors are asymmetric due to the grounded vacuum chamber walls. Their surface plays the role of a grounded electrode. In this case the smaller (driven) electrode is automatically biased negatively with respect to the larger (grounded) electrode to ensure zero direct current. Consequently, the voltage drop near the powered electrode becomes equal to sum of the so-called DC-bias and plasma potential. Usually DC-bias is in the range of hundred volts. The voltage drop at the grounded electrode in this case is almost equal to the plasma potential and takes values of 20–40 V for low-pressure CCRF-discharges.

The realization of the RF-based mirror cleaning system should enable compatibility with mirror cooling system. Currently cooling of the mirror can be realized using different approaches. The first one is by passive radiation cooling of the mirrors which is used in Hα and VS diagnostics [792]. Most of the mirrors are however, actively water-cooled due to fine tolerance requirements, see [793]. In this scenario the mirror is connected to the grounded cooling lines directly by welding or indirectly by a ceramic spacer between mirror and cooled carrier [250]. Ceramic solution can provide good electrical insulation, but it can lead to additional heating due to RF-losses in the spacer. Direct connection of the mirror to cooling system pipes requires grounding of the mirror to be done using $\lambda/4$ coaxial lines—the so called notch filter, described later integrated with the water pipes [500, 790].

The pulsed-direct current (p-DC) systems represent an alternative class of local plasma generators suggested for mirror cleaning. In the case of a DC/p-DC cleaning system, a contaminated mirror will be treated in a low-pressure DC or p-DC gas discharge localized near the mirror surface [794, 795]. The application of a gas discharge with oscillating electrons (hollow cathode) additionally increases the cleaning efficiency. The scheme of a mirror cleaning system based on a DC/p-DC discharge is shown in figure 168.

The use of the medium-frequency pulse mode of the gas discharge in the frequency range from 10 to 200 kHz, as well as the RF mode, ensures the sputtering of thin dielectric impurities with a thickness of up to 100 nm [796]. During the negative pulse, DC sputtering mode is implemented. Therefore, the use of matching devices in the power supply line is not required, which greatly simplifies the first mirror assembly. The duration of the interval between pulses should ensure full compensation of the accumulated charge. Thus, the choice of DC cleaning mode depends on the size, thickness, and permittivity

of the contamination. The optimum choice of the operating frequency and pulse duty cycle can ensure high sputtering efficiency. When removing conductive contaminants, the maximum efficiency is provided by the DC sputtering mode. This technology provides cleaning of both grounded and insulated mirrors. The generalized electrical scheme of the discharge cell connections of a mirror cleaning system based on a DC/p-DC discharge is also shown in figures 168.

Mirror and a mesh represent there a cathode and its surface is sputtered by ions emitted from the discharge. The energy of sputtering ions depends on the discharge voltage and the working gas pressure and is usually several hundred eV. It exceeds the threshold sputtering energy for any type of contaminants expected in ITER.

The main cleaning mode is a DC mode without magnetic field, $B_t = 0$, which is used to remove conductive contaminants. It can also be used effectively to remove impurities formed during steam ingress [797]. The applicability of this method of removing contaminants in a strong magnetic field has also been confirmed experimentally. At the same time, the cleaning efficiency significantly depends on the orientation of the mirror relative to the magnetic field and the design of the discharge cell. The maximum contaminant removal rate was obtained with the orientation orthogonal to the direction of toroidal magnetic field [798]. The disadvantages of DC/dc cleaning systems include the inability to remove thick (more than 100 nm) dielectric contaminants and a need in increased pressure needed to start a discharge.

9.4.5. Mirror activation and neutron-related effects. A significant factor affecting the mirrors installed inside the ITER VV is heating caused by intense fluxes of neutron and gamma radiation [499, 799]. In [793], the thermal calculation of the first mirror is given under conditions of radiation heating. The specific power incident on the mirror surface was limited up to 16 kW m^{-2}, which corresponds to the total ITER thermonuclear power of 500 MW. The study of the effect of the cooling method on the maximum temperature of the mirror and on its deformation caused by temperature gradients demonstrated the advantage of using a water-cooling system [793, 799, 800].

Exposure to intense ionizing radiation also negatively affects the optical parameters of metal mirrors. To simulate neutron radiation characteristic of a tokamak, irradiation of targets with their own ions is often used in experimental studies. It was shown [801] that irradiation of polycrystalline molybdenum mirrors with $^{98}Mo^{+}$ and $^{4}He^{+}$ ions with an energy of 350 keV and fluences corresponding to radiation exposure of 1 dpa (displacement per atom) leads to an insignificant (2%–3%) decrease in the reflection coefficient. In this case, irradiation of mirrors with helium ions with a fluence above 3×10^{17} cm^{-2}, corresponding to the effect of 30 dpa, leads to a significant drop of the reflectivity [802]. Considering the estimate, that the impact on the first wall of the ITER is about to 1–2 dpa, it can be assumed that ionizing radiation and fluxes of CX atoms will have an insignificant effect on the characteristics of mirrors, in comparison to other effects.

Dielectric first mirrors for some laser diagnostics possess altering layers of high-*n* and low-*n* materials deposited on a glass substrate. Such mirrors are proven to withstand neutron radiation worse than metallic mirrors. In [803] it was shown that high neutron doses (1 dpa for HfO2/SiO2 and 4 dpa for Al2O3/SiO2) resulted in a drastic drop of optical reflectance due to failure of the multilayer coating. Lower neutron fluxes (up to 0.1 dpa), which are expected in ITER at dielectric mirror location [804], lead to modification of the multilayer coating as well, but do not result in degradation of optical performance.

9.4.6. Engineering of mirror systems. Engineering and qualification of the diagnostic-specific mirror systems is the final step toward the implementation of mirror solutions into respective ITER diagnostics. This is also a challenging step comprising not only the mirror itself, but the whole complex mirror infrastructure. There are several aspects which are being compulsory addressed by the diagnostic designers and engineers:

1. detailed design of the first mirror system with all necessary *in vacuo* and *ex vacuo* interfaces to the ITER infrastructure;
2. scaling-up the diagnostic mirrors to the sizes required;
3. design and construction of the *in-situ* mirror cleaning system for the specific diagnostic;
4. mirror cooling system;
5. *in-situ* mirror characterization—calibration system with a 'cleaning stop' indicator;
6. shutters, flaps and diagnostic ducts;
7. performance testing of the mirror system including mechanical tests.

In the course of addressing the engineering aspect, a common way was identified to be building the so-called FMU [302, 504, 777, 805]. Usually, the FMU contains all the vital elements of the mirror infrastructure of the particular diagnostics. The FMU is sometimes equipped with mock-ups of diagnostic mirrors. The FMUs provide an efficient platform for multiple qualification tests in the relevant environment. In the course of this chapter, the majority of engineering challenges is described and addressed in detail. The example of FMU of an ITER diagnostic is provided as well.

9.4.7. Generic mirror solution for maximum performance and durability. As can be seen from the previous sections of the paper, the proposed risk mitigation strategies are dependent, synergistically complementing each other toward attaining the maximum mirror performance and endurance of the service life. The combination of risk mitigation strategies represents the so-called 'generic mirror solution'. This solution is a desirable (and maximum) set of measures prescribed as far as it is feasible, for every mirror—based diagnostic.

The generic mirror solution prescribes using prime mirror candidate materials, such as single crystals and nano-crystal coated mirrors. The choice of mirror position should be made involving modeling calculations. This can be done by adapting

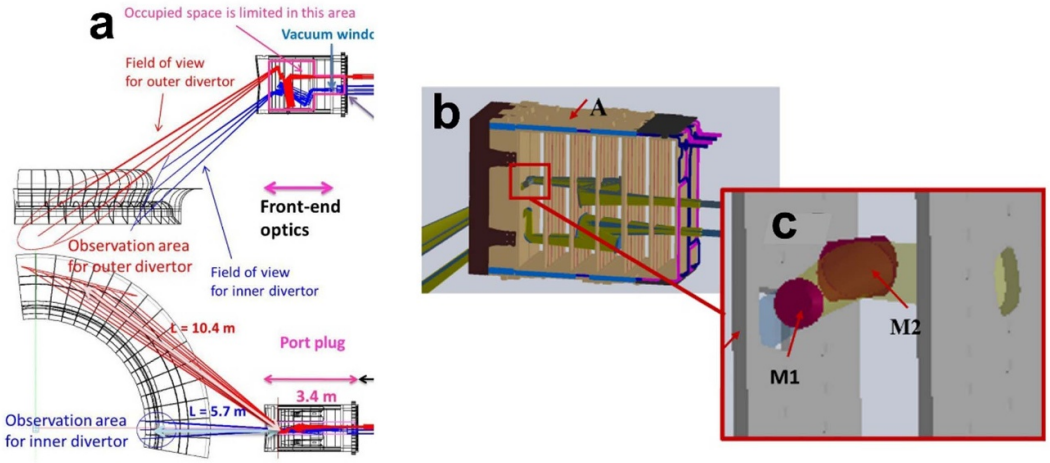

Figure 169. ITER infrared thermography diagnostic [806]: (*a*) an overall view of the optical design for divertor IR thermography, (*b*) the side view and the (*c*) first mirrors system installed in the DSM, where M1 and M2 are the first and the second mirror respectively.

the existing modeling tools as it has been made for core CX (cCXRS) diagnostic system [783]. Alternatively, dedicated modeling tools can be developed and applied to a specific diagnostic as described later.

The set of MSR tools comprising both passive: shutters, flaps and diagnostic ducts should be supported by the application of *in-situ* mirror cleaning system. Preferentially, such a cleaning system should use the RF-stimulated or pulsed-DC discharge for local cleaning plasma source.

Certainly, an intensive prototyping, building the working mockup of the FMU should be done beforehand. This unit should be tested in the environment that is as close as possible to that in ITER, prior to the final FMU design of ITER diagnostic.

As an example of implementation of the generic mirror solution to ITER IR thermography system is described in the next section.

9.5. *Practical application on example of ITER IR thermography diagnostic*

The ITER divertor IR thermography system (55.G6) is intended for measurements of the temperature distribution of the divertor plates using passive observation of thermal radiation [806]. The system is located in an equatorial port while LOS is directed towards the divertor plates, see figure 169 for details.

The aforementioned solutions were applied in the ITER IR thermography system. Here in general, we will follow the structure of the previous section to go through this example of a particular application in a simplest way.

The FMU of the diagnostic consists of two plane mirrors M1 and M2, forming a dog-leg structure inside the equatorial port neuron shielding, see figures 169(*a*) and (*b*). Both mirrors should be water-cooled as they are located close to the main ITER plasma causing a high level of volumetric radiation heating while the diagnostic operating in the IR range is sensitive to the parasitic thermal radiation of the mirrors. At the same time, the mirrors do not require an adjustment during ITER operation thus greatly simplifying the design and integration as no movable parts, as actuators etc are needed.

9.5.1. Mirror material. Plane and relatively small 50 cm^2 to 100 cm^2 mirrors make it natural to use single-crystal materials for the reflective surfaces as the most reliable solution for optical surface survivability during cleaning. Currently single-crystal molybdenum has been chosen as the main candidate as it has high reflectivity in the IR range, good thermal and mechanical properties while the manufacturing technology for this kind of mirror is relatively well developed.

9.5.2. Predictive modeling. As mentioned in section 3, numerical simulations were performed in order to evaluate the required performance of the candidate mirror cleaning system and to generate estimates necessary for the FMU optimization. The approach was applied to address RF-discharge cleaning in the IR thermography FMU. The following processes are included in the simulation workflow: the discharge itself, surface erosion of all plasma-wetted surfaces (including FMU walls), particles transport in ambient gas and corresponding re-deposition.

The CCRF discharge was simulated by means of the PIC-MC Fraunhofer-IST code [786], while materials transport, sputtering and re-deposition was simulated using the KITe MC software [493]. Ion fluxes and ion energy distribution functions (IEDFs) from the Fraunhofer-IST code have served as input data for the KITe.

Simulations have shown the presence of the deposition dominated areas near the edges of the mirrors. This deposition is associated with shaded areas formed by the mirror and surrounding structures. Based on simulation results it was possible to define necessary geometry modification to ensure that the entire mirror surface is in an erosion-dominated area. Figure 170 shows the net erosion profile simulated at 2 Pa background pressure He with 20 W of input RF power. The deposition dominated areas can be clearly seen near the edges

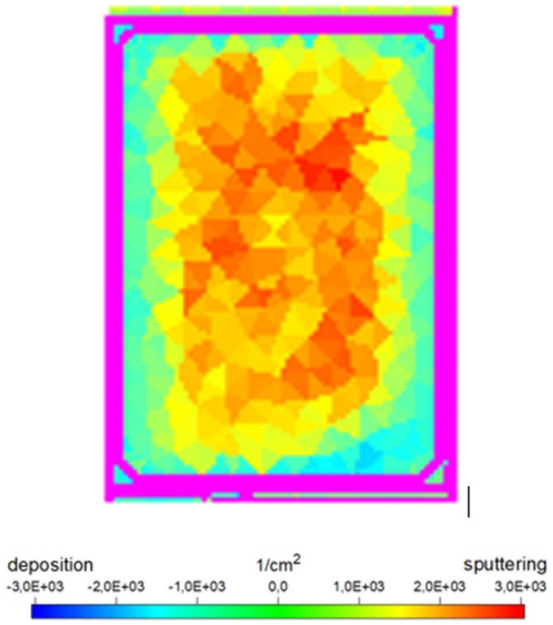

Figure 170. Simulated patterns of beryllium deposition (blue colors) and erosion (red and orange colors) on the 2nd mirror of 55.G6 FMU during the cleaning at 20 W of RF power in helium.

with a large zone in the right bottom corner which is shaded by the surrounding FMU walls.

9.5.3. MSR for diagnostic mirrors in ITER IR thermography system.

9.5.3.1. Passive mitigation techniques. As the 55.G6 IR Thermography system should observe a large area on the divertor plates, figure 169(*a*), it requires a relatively large aperture in the DFW. To prevent deposition on the mirrors during ITER wall conditioning (very large contaminant fluxes are expected in these regimes), a diagnostic shutter is absolutely necessary for this system. It is to be designed yet, the required space is reserved in the current FMU design.

A stainless-steel diagnostic duct is equipped with a socket in the DFW providing a direct path from the plasma to the M1.

9.5.3.2. Active recovery technique: in situ *cleaning system.* In the ITER Thermography Diagnostic 55.G6 FMU utilizes two mirrors: first (M1) and the second (M2) mirrors serving as water-cooled RF-electrodes. The CCRF discharge will operate to alternately clean M1 or M2 [501, 502, 790]. As the two mirrors are located close to each other, both of them require an RF cleaning system as cleaning of one mirror will affect the other. The two mirrors are to be cleaned in a series. They have independent power circuits and while RF power is supplied to one mirror, the second one is grounded.

The 55.G6 IR thermography FMU consists of two mirror assemblies (MAS), electrical distribution circuit, water distribution circuit and the support structure (housing), providing structural/optical stability and Remote Handling compatibility. The general view of the MAS developed following the principles above is shown in figure 171(*a*). Each mirror

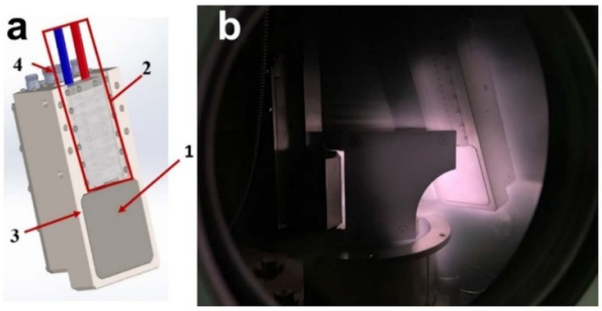

Figure 171. First mirror assembly: (*a*) general view of the FMU housing containing mirror itself (1), water cooling pipes combined with RF notch filter (2), combined with electric shields (3), RF and electrical connectors (4), (*b*) FMU inside the test chamber with RF discharge operation.

Table 35. Set of mechanical and environmental tests of the FMU mock-up.

Test No.	Test title and description
1	Demonstration of the plasma generation in the FMU mock-up
2	Delivering at least 100 W of RF power to the mirrors for at least 1 h
3	Baking in vacuum better than 10^{-3} Pa
4	DC high-voltage ($\leqslant$1 kV) breakdown test

assembly is equipped with an RF plasma cleaning system and consists of the mirror itself, water cooling pipes combined with an RF notch filter, a housing combined with electric shields and RF electrical connectors. The RF components utilize planar RF design concept and are implemented as printed circuits on a ceramic substrate. Two mirror assemblies are installed in a housing which than is to be connected to the DSM. The photo of plasma cleaning operation in the FMU is presented in figure 171(*b*).

The requirement for water cooling makes it almost unavoidable to use the RF cleaning with DC coupling where a quarter-lambda filter is used to detach the mirrors from the ground at the RF cleaning frequency. In the FMU water pipes are combined with such a filter enclosed into rectangular housing filled with AlN ceramics to prevent the parasitic breakdown. After the grounding point, there is no need in further shielding the water pipes.

9.5.4. Engineering solutions.

Preliminary mechanical and environmental tests of the designed FMU mock-up were conducted to ensure the FMU integrity. Tests are listed in table 35 below, in the order they were conducted. The order was selected considering potential risks of the FMU damage during tests, allowing to perform successive tests even in case such damage would occur.

Tests No. 1 and 2 were combined since they require the same experimental conditions. Only one of the mirrors was fed by RF power at a time whereas the second one was grounded. The RF discharge plasma was generated and successfully sustained for 1 h in Ar at 2 Pa. The power delivered to the RF

vacuum feedthrough was 150 W at 81.36 MHz, a fraction of about 100 W was expected to be delivered to the RF discharge.

9.6. Open questions and issues

9.6.1. Physics issues. The remaining issues and open questions of design and procurement of reliable and efficient diagnostic mirrors can be divided into two main classes: physics issues and engineering issues. Physics issues are mostly not related to mirrors directly, but originate from external factors which may nevertheless affect the mirror performance. Environmental effects of plasma operation, and the impact of ITER commissioning on mirrors are good examples of such external factors.

9.6.1.1. Early (unstable) ITER: list of actions. Presently, the commissioning of ITER and its first plasma (FP) are treated as significant risks for diagnostic mirrors. The following stages of an early ITER can be identified already:

- commissioning risks
- risks caused by the wall conditioning actions, and
- risks during the FP and initial plasma operation.

Under commissioning risks the mechanical damage during e.g. installation of the components can be understood. During the integrated commissioning of ITER, the plasma-facing modules for instance, will not be installed for the FP. Their subsequent installation can mechanically damage the mirror assembly. Also, unpredictable damage such as failure of the water-cooling supply system, may dramatically affect the mirror performance.

Wall conditioning will precede the FP [807]. As was shown in previous sections, the impact of wall conditioning on non- or badly protected mirrors can be highly detrimental.

Finally, risks caused by initial plasma operation should not be underestimated. ITER is planned to attain the FP with a very basic set of magnetic diagnostics and without many components installed. The first plasma operation will not be NBI-powered, but will feature ECH heating [807]. During the initial plasma operation, the risk of e.g. plasma disruption and loss of control is the highest. An extensive work ongoing on plasma-control system of ITER [808] including modeling of possible plasma scenarios involving unpredictable and sudden events. Nevertheless, the sudden risks due to faulty plasma controls, initial errors of operators etc cannot be excluded.

The general strategy to address the aforementioned challenges during the early ITER operation should include:

- Favor the later installation of mirror-based systems.
- When possible, avoid commissioning with mirrors open to plasma. Pragmatically, if possible, only mirror-based systems directly involved to commissioning should be involved.
- The mirror-based diagnostic should not be operated, unless it is absolutely needed for the FP and subsequent initial plasma operation.

9.6.1.2. Modeling level. Several modeling approaches were pursued in order to estimate mirror risks and provide guidelines for engineers [779–783]. Generally, however there is neither a unified modeling code nor modeling results which are widely accepted by the diagnostic community. Mostly, this is due to the remaining large uncertainties in modeling results and vulnerability of predictive codes to a change of boundary conditions. It is believed that modeling of mirror performance needs to be intensified in order to be pragmatically useful for the diagnostic mirror R&D.

At the same time, the diagnostic-specific modeling efforts are proven to be rather successful. Modeling of the cleaning system of the ITER IR Thermography diagnostic pursued at Ioffe institute by using the KITe [493] and Fraunhofer IST [786] codes, has delivered important results. These results are implemented into the design of the mirror-cleaning system already.

9.6.1.3. Thermal cycling. During the operation, mirrors in ITER diagnostics will be subjected to intensive thermal cycling. This will originate from e.g. inter-discharge phases and during wall conditioning and VV baking operation. Technical shutdowns due to installation of new equipment will cause a change of temperature conditions. Therefore, the study of operation of diagnostic mirrors under varying and cyclic temperature conditions are important. An example of a thermal cycle test on diagnostic mirrors is provided below.

A temperature cycle test was performed on mirrors having rhodium films formed on SS316 substrates. The mirror samples have outer diameters of 25 mm and substrate thickness of 5 mm with rhodium film thickness of 5 and 10 μm respectively. To form rhodium films with good adhesion, chromium inter-layers between the rhodium and SS316 are applied. The surface roughness after rhodium film formation was 10–13 nm depending on the location. A temperature of the cooling channel at the start of plasma operation of ITER is 70 °C. Baking temperature of the divertor cassette is 350 °C and those in port plugs and lower port racks are 240 °C. Temperature cycle from 70 °C to 350 °C was repeatedly applied 500 times. The period of one cycle was approximately 2500 s. A SS316 substrate (dummy mirror) having the same dimensions as the mirror sample was also installed. Figure 172 shows the surface temperature of the dummy mirror measured with a thermocouple up to the 9th cycle.

As shown in figure 173, the thermal cycle did not degrade spectral reflectivity. It looks as if the reflectivity is slightly improved. However, the tested samples had lower reflectivity in the UV region than the one reported in [809]: reflectivity of rhodium coating at 200 nm was 25% in experiments, while the reference value for rhodium revealed 55%.

In a similar manner the thermal cycling was made for several mirror materials of the ITER VUV divertor spectroscopy diagnostic [96]. The procedure of thermal cycling test followed the ITER baking scenario, and the change of the mirror surface condition was measured between each cycle. The

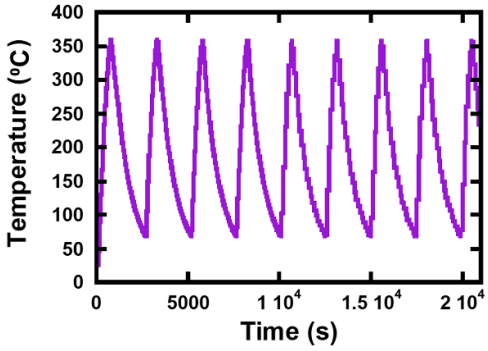

Figure 172. Time history of mirror surface temperature.

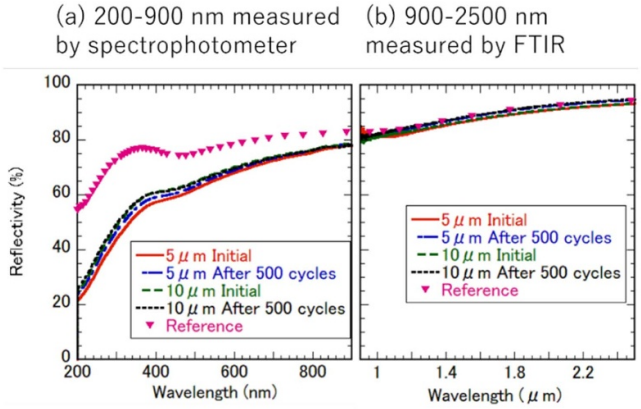

Figure 173. Reflectivity of Rh film mirrors after 500 temperature cycles in the wavelength range of (*a*) 200–900 nm measured by spectrophotometer and (*b*) 900–2500 nm measured by Fourier transform infrared spectroscopy.

appropriate candidate materials of the first mirror for the VUV wavelength range are chosen to be gold (Au)-coated stainless steel substrate mirrors, bare coated Ni-P plated stainless steel substrate mirrors, or silicon carbide (SiC) mirrors considering their mechanical strength and optical performance in VUV wavelength range. From the thermal cycling test, however, the Au coated stainless steel mirror was found to be damaged since its Au coating peeled off in case with a Cr inter-layer. For the case of Au coated Ni–P plating mirror without Cr inter-layer, peeling-off of the coating did not occur, however the mirror roughness of the Au coating surface was increased up to ∼10 nm (rms) due to the aggregation of Au in the baking temperature of approximately 240 °C. For this reason, Au-coated mirror was found not to be appropriate for the VUV wavelength range. In the following tests, bare Ni–P plated stainless steel mirror without Au coating and SiC mirror were tested, and both showed good results meeting requirement for the thermal cycling test. The roughness change over 100 cycles was measured to be ±0.2 nm on Ni–P plating surface of the mirror sample. The other thermal cycle test with SiC mirror showed a mirror surface roughness change of ±0.1 nm after 100 thermal cycles.

9.6.1.4. Steam event. Steam ingress, mentioned earlier in our chapter, significantly deteriorates the optical properties of diagnostic mirrors [810]. In most cases, the ability to recover the specular reflectivity after the steam event leads to the down selection of the mirror material. For instance, the mirrors for the ITER VUV Divertor Spectroscopy System qualified after the thermal cycling tests described in the previous section, were subjected to the steam ingress event testing. The conditions of a steam ingress event VVICE IV [754, 756] were reproduced during the testing. After steam ingress test, bare Ni-P plating on the stainless-steel substrate was found to be oxidized and it peeled off as inferred from analyses of scanning electron microscope (SEM) images. On the other hand, the roughness and topology data on the silicon carbide mirror surface evidenced no change or damage after the steam ingress test. As an outcome of the series of qualification tests, the material of the first mirror for the ITER VUV spectrometers was chosen to be silicon carbide.

For some first mirror materials, it was possible to recover reflectivity almost entirely using the RF-plasma cleaning. The nano-crystalline Rh samples had developed'voids' along the thickness of the mirror coating after a steam ingress, which increased their diffuse reflectivity. However, it was also possible to remove these voids by the RF plasma cleaning [811].

There are still several open questions in the topic including the impact of a steam event when the mirrors are already polluted by first wall deposits, steam induced risk on the FM substrate interface for coatings and the impact of irradiation. For the mirror material itself, nano-crystalline rhodium is considerably better in resisting the surface oxidation than single crystal molybdenum [245, 764, 810, 811], giving it a larger estimated lifetime in ITER. Mo mirrors in particular have been shown to degrade in all considered scenarios of exposure to water and steam, however they can be made less sensitive to water/steam by reducing the operating temperature of the mirrors [798]. A recent study [812] outlined the detailed consequences of a steam event that occurred in ASDEX Upgrade during the baking procedure. The water condensate was found all around the torus as well as alt-like remnants from reaction of steam with first wall deposits as well as rust around the welding seams. In order to minimize the risk of a steam event during baking, it was suggested increasing the pH of hot water to 8.5 to avoid erosion of copper-containing components as well as increasing pressure for routine leak testing before infill of water from 10 bar to 20 bar. Furthermore, a control logic was defined to stop the baking of the vessel in the event of a leak (i.e. when a pressure increase of 10^{-1} mbar is detected) and prompt conditioning/drying of vessel to avoid further erosion in remote areas. Similar steps can also be adopted for the baking procedure for ITER to mitigate steam event effects.

It should be noted that steam ingress conditions will affect all in-vessel mirrors, and not only the first mirror equipped with a cleaning system. Therefore, it is necessary to select the materials carefully for the both the first and secondary mirrors. To date, several studies of candidate materials for the role of in-vessel mirrors have been carried out [813]. The best

steam resistance was shown by mirrors made of Rh and Cr (figure 168), as well as mirrors with a protective dielectric coating including multilayer dielectric mirrors and $Al + SiO_2$, $Al + Al_2O_3$, $SiC + Al + SiO_2$, $SS + Ag + SiN_x/SiO_x$ mirrors. Here, a precise evaluation of the given steam ingress scenarios and their consequences for diagnostic mirrors is needed.

9.6.1.5. Re-deposition during cleaning. As mentioned in section 4.4, a high plasma potential associated with DC-grounding of FMs poses a significant challenge towards plasma cleaning of the mirrors accompanied with a massive re-deposition of sputtered material on the FMs [814]. The redeposition of the wall material ends up competing with the erosion of the FMs, making the plasma cleaning process inefficient. Hence, mitigation strategies are necessary to minimize the wall redeposition and promote FM cleaning.

Four different techniques were pursued to reduce the sputtering and re-deposition of wall material on the FMs as follows:

1. Mechanically profiled walls. It was observed that using a'saw-tooth' shaped wall introduced a significant asymmetry (over 40%) in the ejected distribution profile—effectively moving the sputtered material away from the mirror. However, this technique does not reduce the wall sputtering itself and a resultant re-deposition on the FMs while reduced, is still not negligible.
2. Metallic GGs: in this technique, GGs with transparency of 70% were placed a few centimeters above the walls to act as 'interim' walls for the plasma. This technique has a great potential for application in ITER, however its benefits may not be as pronounced in the presence of B field [815].
3. Floating walls: in this technique, the walls of the FMU were isolated from the ground and remained at the floating potential in the plasma discharge. The ion energy at the floating walls was constant at 30 eV, while the ion energy at the grounded FMs could be increased by several times keeping the FMs are in a net erosion regime. This technique is potentially of crucial importance for ITER, as specific wall regions in the FMU initially prone to sputtering can be isolated to minimize re-deposition [816].
4. Wall material of FMU: the choice of materials with high sputtering threshold can minimize re-deposition. However, the threshold is greatly influenced by the presence of native oxides on the surface and needs to be taken into consideration for selection of ITER relevant wall materials [816].

Single or multiple solutions could be implemented in FMUs, depending on their size, orientation to B-field, etc. It must be noted that those solutions are not universal, and their application needs to be assessed for each particular diagnostic. Generally, wall geometry, competing with redeposition of contaminants can be treated as an extension of the passive mitigation techniques, such as shutters and diagnostic ducts described earlier in section 4.3.

9.6.1.6. Adverse effects caused by high deuterium and helium fluxes. Within their lifetime, the first mirrors are naturally subject to deuterium, tritium and helium fluxes originating from the fusion plasma. In addition, cleaning plasma will inevitably affect the surface of mirrors. The most process gases used for cleaning plasmas are those which allow removal of light elements such as beryllium while preserving rhodium or molybdenum mirrors [817–819]. Yet, the atoms and molecules of those gases, such as deuterium (D_2) or helium (He) likely will pass along the boundaries of sub-grains and grains accumulating at the grain boundaries, vacancies, dislocations or ion-induced defects, see e.g. [820, 821]. Accumulated D_2 or He can then form bubbles and blisters [791, 801, 821–824] at the inter-grain boundary due to interstitial diffusion through the grain body [825], as well inter-grain boundary diffusion [826]. Material structure, plasma species, surface temperature, ion flux and fluence can influence the blister formation. Blister nucleation was found on polycrystalline Mo, which was polished with diamond paste, after exposure to D_2 plasma with an incident ion energy of 30–80 eV at the fluence exceeding 10^{23} m^{-2} [827]. Besides, the large size blisters were found to form on the surface of the first mirror made of TZM substrate with 100 μm Ni layer after exposure in a (H_2 + 10%Ar) plasma with a fluence of 6×10^{25} m^{-2} [828]. Helium blisters can be formed only at temperatures higher than about 0.2 times the melting point, about 600 °C with incident energy higher than several hundred eV. As the FMU should operate in the temperature range of 100 °C–300 °C for actively cooled single crystal mirrors in ITER, the risk of blister formation is relatively small. At the same time, understanding and prevention of blister formation on e.g. nanocrystalline mirror material is important.

The formation of blisters during mirror cleaning leads to irreversible destruction of the mirror surface. This effect is observed when mirrors are exposed to He or D atoms or ions in the course of the mirror cleaning. Formation of nanoscale bubbles was observed during bombardment of single crystal molybdenum mirrors with He ions [795]. Blistering and bubble formation changes the spectral reflectivity of the mirror. At the same time, it was found that the mirror polishing procedure has a large effect on blistering [829].

Recently, the formation of pits was observed during sequential exposure of single crystal polished Mo mirrors to helium and argon ions. At the same time, the use of single crystal material with a particular orientation can mitigate formation of blisters [821, 830]. Adverse factors due to mirror preparation and *in situ* cleaning processes must be taken into account when choosing working gases and the cleaning mode with using cleaning systems in optical diagnostics [797].

9.6.1.7. Mirror in magnetic field. The magnetic field of ITER can reach 5.3 T on the magnetic axis of the machine [831]. Currently, cleaning of diagnostic mirrors in the presence of B field is envisaged to minimize the dedicated service time.

The uniformity of first mirror cleaning by plasma sputtering using 81.36 MHz RF discharges was studied in a 0.05 T field [501]. An enhanced sputtering rate within the center of the

electrode was reported and it was noted that the longitudinal field improved sputtering uniformity along the edges. Results of the study gave evidence that the net sputtering profile in magnetic fields is determined not only by the ion flux distribution but also by the re-deposition process. Mirror cleaning experiments performed in a magnetic field up to 0.5 T with Penning discharges in helium gas were reported in [795]. The efficient removal of aluminum (Al) contamination coatings from molybdenum mirrors was observed. In these studies, aluminum was used as beryllium proxy. The maximum thickness of removed Al was up to 200 nm. Mirror cleaning was accompanied with recovery of the optical properties. Cleaning of Mo mirrors from Al_2O_3 films with 13.56 MHz RF argon (Ar) discharges in a magnetic field of 0.35 T was reported in [832]. In particular, the cleaning performance was enhanced when the field lines were nearly parallel (within a few degrees) to the mirror surface. In another study, sputtering cleaning experiments with RF plasma in 3.5 T field were performed. The formation of filaments and strong inhomogeneities due to erosion profile drifts on the FM surface were detected, whereas the maximum and minimum erosion rate ratio on the FM sample was as high as 14 [833]. CCRF plasma cleaning experiments on the ETS mock-up in a 1.7 T magnetic field were conducted in the EAST tokamak [834]. The presence of the magnetic field reportedly decreased the self-bias on the FMs up to 10 times, and the cleaning rate was increased by 40 times compared to those in identical experiments without a magnetic field. A complete recovery of the total reflectivity of the FMs was reported, whereas the diffuse reflectivity and surface roughness at the center of the mirror assembly were enhanced. Experimental results describing the impact of an axial 0.5 T field on CCRF discharges in the DC-coupled scheme were presented in [504]. Here, a similar decrease in the DC current with magnetic field was observed as reported above. Furthermore, the effect of the field was more pronounced for the low-pressure discharge at lower excitation frequencies and at fields >0.3 T, where ions and electrons are both magnetized [835, 836]. For RF-cleaning plasma this would mean that for both ions and electrons the Larmor radii are much smaller than the characteristic length scales of a plasma and the cyclotron frequency is much smaller than the collision frequency leading to momentum transfer. Ion energies obtained were identical both in the presence as well as in absence of the notch filter. In a recent study, an RF plasma cleaning with notch filter in a 3 T magnetic field using the mock-up of a FMU was investigated [837]. The areas of sputtering and net deposition on the FM surfaces were dependent on the angle between the FM surface and the magnetic field. Remarkably, the net deposition could be eliminated completely at certain angles. This also has implications for the design of FMs in ITER. Since the plasma extends in the direction of B field, the FMs need to be oriented in such a way that the sputtering of wall surface from the extended plasma column is far from the mirrors in the FMU to minimize the probability of redeposition.

Regarding the efficiency of a particular discharge type used for the mirror cleaning: CCRF or pulsed DC, the current results look promising for both discharge schemes. The CCRF-discharge is known to successfully operate in the presence of an external magnetic field. The presence of longitudinal magnetic field is known to symmetrize the CCRF-discharge due to particle magnetization already at a weak magnetic value of $\sim$0.3 T. The spatial inhomogeneity of the sputtering in this case was found to be decreased even in moderate B-field providing magnetization of the electrons only. The concept of CCRF-cleaning of inclined mirror in high magnetic field of 1.7 T was successfully tested in the EAST tokamak for angles to magnetic field of 5° and 20° [834]. The experimental results give evidence of the remaining DC-bias due to building up the discharge symmetry. The 5° case revealed a high asymmetry of sputtering. A study of the CCRF-discharge application in magnetic field is underway.

As for the pulsed DC-based cleaning system, experiments have demonstrated its feasibility and efficiency in a magnetic field $B_t \leqslant 3$ T. The highest cleaning rate was obtained for the orthogonal orientation of the magnetic field to the mirror surface ($R \approx 0.2$ nm min^{-1} at a power of $P_d = 100$ W). With the same discharge power and a parallel orientation of the magnetic field to the mirror surface, the cleaning rate significantly decreases ($R \approx 0.01$ nm min^{-1}). The use of a fully closed discharge cell, however, can significantly increase the sputtering rate and uniformity of cleaning.

9.6.2. Engineering issues. In contrast to physics issues, engineering issues are most likely caused by internal factors, parts of construction, design or an assembly directly related to the mirror itself. The mirror material, its availability, machinability, and scale-up forecast are good examples of such internal factors. Below are engineering issues which were identified as having a high importance.

9.6.2.1. End of cleaning indicator. Operational feedback should be implemented in a mirror cleaning system, which stops the plasma discharge as soon as the deposits have been removed to prevent sputtering of mirror surface.

The most obvious parameter indicating the complete recovery of the mirror surface is mirror reflectivity. The *in-situ* measurement of the absolute reflectance requires, however, a calibrated light source and a light collection and transmission scheme, stable throughout the ITER operation. The optical scheme is preferably to be the same as the diagnostic one, since any additional optical components located close to the first mirror will be subjected to deposition as well. The use of plasma discharge emission as the light source seems to be troublesome because of uncontrolled variation of discharge parameters resulting, among others from the increase of power loss in feeding lines with their heating. The idea to compare the optical emission of fast hydrogen atoms with that reflected from the FM has been suggested in [250, 838]. The ability to measure absolute values of mirror reflectivity was demonstrated. The validation of this technique is necessary for RF cleaning discharge operating at higher pressures in FMU geometry. Alternatively, a retroreflector can be used, being hidden during ITER operation. This can be done e.g. by mounting the reflecting surface on the back side of the shutter allowing the

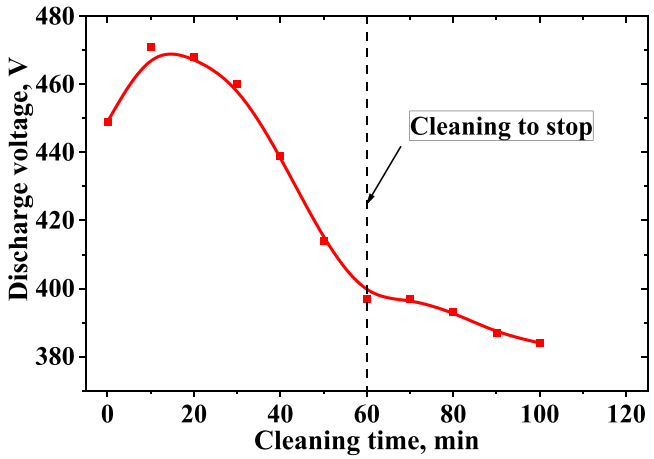

Figure 174. Discharge voltage evolution during cleaning in DC mode: $P_{Ar} = 2$ Pa, $I_d = 200$ mA, current stabilization mode.

usage of the same diagnostic optical path for light input and collection [839, 840].

Another technique suggested to monitor the plasma-cleaning process is optical emission spectroscopy of sputtered species in the discharge column. Potentially, the intensity of spectral lines of both deposited and mirror material can be taken as an end-of-cleaning indicator. Experiments with an CCRF discharge at 13.6 and 60 MHz, Ar and self-bias of 140–280 V revealed the presence of Mo and Rh and absence of Be lines in plasma emission spectra [841]. The technique also should be tested in schemes with notch filter and/or in B-field with a much smaller (or even zero) value of self-bias and, consequently, smaller sputtering yields.

For the RF-based cleaning system, monitoring of plasma and voltage/current parameters is widely used to control the process in a number of RF sputtering/deposition techniques [842]. In particular, the evolution of higher harmonics of the applied frequency in the current and voltage characteristics of the discharges was shown to be a sensitive tool to monitor changes in plasma conditions and composition. These studies were performed both in inductively coupled plasmas and during reactive magnetron sputtering [843, 844]. However, it is not clear whether the effect will be observable for metal pairs Be/Rh or Be/Mo and in a symmetric discharge in the presence of the B-field.

In a DC-based mirror cleaning system, it is possible to control the presence of impurities on the cathode elements of the discharge cell. A change in the composition of the sputtered surface leads to a change in its ion-electron emission coefficient. Therefore, at a fixed discharge current, the end of cleaning can be determined by the discharge voltage reaching a new stable level, corresponding to that measured on a clean mirror. An example of the discharge voltage evolution during the cleaning process is shown in figure 174.

With the sound progress made in end-of-cleaning indicator research and development, presently, there is no clearly favorable generic solution suitable for all diagnostic systems. The final decision should be based on the geometry of the FMU, space available, cleaning regime, power feeding scheme and should be qualified for each particular diagnostic.

9.6.2.2. Notch filter. The necessity of the notch filter was discussed earlier in the chapter. However, an application of such a filter increases the plasma potential significantly allowing for an enhanced sputtering of FMs. At the same time, this could also trigger an increased sputtering of walls surrounding the FM and its re-deposition on the FMs during the cleaning process, for which additional coping strategies might be necessary [816].

In the case of a capacitively coupled discharge, application of the notch filter results in vanishing of the DC-bias and increase of the plasma potential [790]. The discharge non-symmetry reveals itself in this case as direct current flowing through the circuit. Due to absence of DC self-bias the energy of ions bombarding both powered and grounded electrodes become equal. This leads to comparable sputtering rates of the RF powered and grounded surfaces [790, 814]. Hence, the redeposition of the material sputtered from the grounded constructions is non-negligible for the case of notch filter as it is for the case of the insulated RF-powered electrode. Therefore, the redeposition phenomena also need to be taken into consideration in the design of the RF cleaning systems for ITER.

9.6.2.3. Power delivery issue. For the DC-coupled RF discharge scheme, considered as one of the primary-candidate for mirror cleaning in ITER, the RF power density of 1–4 W cm^{-2} at a frequency of 10…100 MHz is required to achieve effective cleaning [502, 790]. Depending on the size and shape of electrodes, the total RF power delivered to the discharge should be in the range of 0.5–2.5 kW. One of the feeder candidates for solving this problem in ITER is mineral insulated (MI) cable. However, due to overheating caused by high insertion losses, applicability of a single MI cable for feeding RF power for all cases may be limited. The most important parameter for this MI cable type is the dependence of its attenuation on frequency and temperature [845]. As a result of these studies, the following options for attaining the required power were proposed:

- RF Power Modulation by HF pulses (∼10 kHz);
- using a heat sink at the beginning section of the MI cable;
- RF Power combiner/splitter devices.

The modulation of RF power results in an increase of power in the pulse linearly with the reverse value of the duty factor while keeping the mean power value constant [846]. A low-frequency RF power modulation is an effective tool, which allows to decrease the supplied RF power required for mirror cleaning from hard-to-sputter deposits in ITER. An acceptable sputtering rate ∼1 nm min^{-1} of both Be and BeO can be achieved in the case of pulsed RF power feeding in B-field at power density of approximately 0.6 W cm^{-2}. Without B-field the much higher power is needed to remove BeO in DC-coupled scheme.

9.6.2.4. Scale-up of mirrors. The dimensional requirements for mirrors in ITER are dictated by the corresponding design solutions. In general, however, there are several mirrors with dimensions reaching several tens of centimeter that are required. As an example, the mirror unit of the ITER core CX recombination spectroscopy has a projected length of 30 cm [778], whereas the dimensions of the second mirror in the VUV DIM can reach 100 cm [96].

Significant R&D was performed for several ITER diagnostics in order to find a suitable solution for the required size of the mirror. Here, two approaches were investigated: making a large single crystal or nanocrystalline mirror out of many pieces or attaining a one-piece mirror solution [847]. Although the single-piece mirror solution was favored in [847], the largest size molybdenum single crystals commercially available to date, does not exceed 200 mm. A possible way to overcome such a limitation is assembling a large reflective surface from a set of smaller single crystal molybdenum plates. These plates can be bonded to a full-size base plate made of polycrystalline molybdenum by brazing, electron beam- or diffusion welding [847]. This was demonstrated for mirror dimensions of 100 $\times$ 80 mm. In this design, the reflecting part was produced from several parts of single-crystal molybdenum with the same orientation in the crystallographic planes. The mirror part was joined by diffusion welding with the base of a mirror made of non-magnetic material with a heat conductivity coefficient and a linear thermal expansion coefficient similar to those of molybdenum. As structural materials for molybdenum tiled mirrors, a diffusion bonding to the titanium—aluminum—vanadium (Ti-6Al-4V) and vanadium-chromium-titanium (V-4Cr-Ti) alloys acting as substrate plates [848] was proposed.

Recently a Rh coating with a thickness exceeding 10 μm was deposited by magnetron sputtering technique. As a structural element for rhodium, the tungsten–copper (W–Cu) alloy was chosen [778] in order to attain the required mirror dimension. Presently, industrial-type ITER water-cooled first mirror mock-ups with up to 109 mm in diameter with Rh and Mo reflecting coatings have been manufactured. The mirror scale-up efforts are ongoing.

9.7. Summary and outlook

In this chapter we provided a concise overview of the main results of the structured and coordinated international R&D in the field of diagnostic mirrors for ITER during the past decade. An important element of the overview is that the major decisions on mirrors taken by the international groups of mirror experts with an active interaction with ITER Team and domestic agencies are described to the knowledge of authors, for the first time. These decisions can be found in the section 'Risk evaluation and mitigation'.

Another important aspect of this overview, which is different from the research published earlier [730–732], is a list of successful, but in the course of evolution of ITER project, presently irrelevant studies. The authors believe that providing such a list will help to streamline the current mirror R&D. The list of past milestone results of the R&D which are valid for ITER diagnostic mirrors is presented as well in the section 'Risk evaluation and mitigation'. The use of single crystal and possibly nanocrystalline mirrors, the use of shutters, the necessity of MSR are viewed as necessary measures for ensuring the longest mirror service life possible.

A high priority research on mirror surface recovery is presented in the dedicated section on MSR. Here, the importance of the *in-situ* mirror cleaning is clearly presented along with the currently favorite mirror cleaning solutions including the RF and pulsed DC discharges. Generally, a set of measures, technologies and scenarios allow issuing the optimistic forecast for the mirror lifetime for majority of ITER diagnostics. An application of the envisaged solutions was demonstrated on the FMU of the ITER IR Thermography system, used as an example.

At the same time, there are several still unresolved questions needing immediate attention. Among those, the impact of a steam event and addressing its consequences needs more thorough investigations. Especially, an applicability of an *in-situ* cleaning system to recover a mirror from of a steam event must be evaluated. If necessary, the cleaning system must be made capable of recovery after a steam ingress. The use of steam-resistant mirror materials, such as silicon carbide used e.g. in the space VUV systems [849], must be assessed. Such an assessment is especially important for mirrors in ITER which are distant from burning plasma. Several urgent engineering solutions, among others, the use of a notch filter, the robust and reliable cleaning-stop indicator need to be finalized. The capability of modeling for making robust and reliable predictions still reveals significant doubts. Here, the opportunity of conservative estimates necessary for outstanding engineering must be evaluated at the cost of discarding the predictive feature.

The resolution of the mentioned outstanding open questions will surely employ the most coordinated R&D efforts in the field of ITER diagnostic mirrors in the nearest future.

As for a longer-term perspective, thorough thinking must be given to address the late stage of ITER exploitation. The research and engineering program in the late ITER phases will need to be focused on preparation for the exploitation of a fusion power plant, such as the DEMOnstration power plant. We can assume that during commissioning and at early stages of operation, a power plant will possess a diagnostic suite similar to that of ITER. Later, the plant-relevant aspects, resembling those in ITER significantly, will be inevitably introduced. A quasi-stationary operation, the orders of magnitude higher neutron fluences on the in-vessel components are among factors which will define the future use of diagnostic mirrors in DEMO. A possible and logically understandable approach will be in limiting the use of diagnostic mirrors in DEMO to necessary diagnostics only, providing reserve mirror channels and backup mirror units. An example of critical thinking on the first mirror application is given in e.g. [298]. Addressing the coming long-term challenges relevant to a fusion power plant will certainly employ the first mirror research and development efforts in a longer-term perspective.

10. Synthetic diagnostics for real time plasma control studies and diagnostic design

M. R. de. Baar[44,45], D. Mazon[1], L. Zabeo[2], M. de Bock[2], M. Schneider[2], Th. Blanken[44,45], Th. Bosman[44], T. Ravensbergen[2], B. van de Boorn[44] and C. Orrico[45]

10.1. Introduction

The purpose of ITER is the study of plasmas with significant alpha particle heating. In addition to an extensive science and technology programme, ITER has two ultimate deliverables: (1) the development of an inductive plasma scenario (in which the plasma current is driven with a set of primary transformer coils) with a power multiplication factor (the ratio between the fusion power and coupled input power required to sustain the conditions) of $Q = 10$ and (2) a non-inductive scenario (in which the current is driven without transformer action) with $Q = 5$.

The topic of plasma control is a branch of the field of system and control research with a few peculiarities. First, a fusion plant is operated close to operational and machine limits. A second complication is the use of actuators that are shared between various control tasks, while these in turn are strongly coupled. The optimization of the fusion reactivity is associated with the control of a number of distributed parameters. The sensor and actuator park is distributed poloidaly and toroidally as well as radially. The interpretation of the sensor data and the actuator input is plasma state dependent. To deal with these complexities, the design of a PCS relies on model-based approaches.

ITPA diagnostics and ITER-IO have started and activity on the development of synthetic diagnostics for IDA and validation (IDAV) and application Real Time (RT) control systems. The purpose of this activity is to develop, adapt and validate **synthetic diagnostic models** with associated **test cases** for their use in the ITER Integrated Modeling and Analysis Suite (IMAS) to make them available prior each phase of the ITER Research Plan. An IDA workflow will be implemented at ITER, starting with a rudimentary **IDA workflow** based on just a few diagnostics (those already available). In addition, a subset of synthetic models will be defined to be used for **control applications**, namely for the development of the ITER PCS simulation platform (PCSSP).

Examples of the use of synthetic diagnostics in diagnostic design validation are given throughout this special issue, with special emphasis on integrated data-analysis in the next subchapter 11. This subchapter presents one example of diagnostic design and design validation for the VSRS, but mainly focusses on the use synthetic diagnostics in real-time forward modeling for real-time control.

A significant part of this activity consists of **validating the models** onto existing fusion devices. As a starting point, AUG and WEST have committed to provide the data for model validation but the list of contributing devices is expected to grow.

A workflow to run and combine Synthetic Diagnostics together has been developed. It is written in python following the same spirit as the python H&CD workflow. The Minerva platform to apply Bayesian techniques for deducing the best answer from combining models together has been installed on ITER cluster. Specific synthetic diagnostics have been under development in this context: magnetics, VSRS, H-alpha, etc. A prototype workflow for IDA combining ECE, Thomson Scattering and interferometry is being developed. In this context, specific methods are defined for physics models to be exploitable in the context of an IDA iteration loop. To provide the required input for each synthetic diagnostic, a machine description database has been developed and populated, which contains the geometry of the various diagnostics. It completes the already existing scenario database that provides the plasma conditions (equilibrium, kinetic profiles) for the models to be executed. The plan is to continue the development describe above and to get new contributors/new models to cover all the synthetic diagnostics for each phase of the ITER Research Plan.

In this contribution, it is discussed how of synthetic diagnostics are used for diagnostic design and design validation and for the formulation of model-based plasma control for ITER.

This paper is organized as follows. First we classify the plasma control topics and discuss their interactions, and the evolution of modern systems and control methods is summarized. Notably, it is explained how models of the input-output dynamics can be used in real time for optimal data analysis. Then we give a number of examples of synthetic diagnostics models and their application in ITER diagnostic design and model-based control design: Iterative learning control (ILC) for discharge optimization, model predictive control (MPC) for current density and temperature, observation and sensor fusion of the density profile and MPC for the density distribution, synthetic diagnostics for the magnetics with application to neo-classical tearing modes (NTMs) suppression and a model of the VSRS diagnostic with the view to design an optical dump and to simulate spectra.

10.2. Systems and control perspective on nuclear fusion

10.2.1. Classes of control tasks. Traditionally, most of the plasma control of reactors is done in feed-forward. In feed-forward control the waveforms for the actuators are pre-programmed by the tokamak operator. In spite of modeling support, the feedforward waveforms are often not optimized against multiple requirements and constraints. Moreover, the feed-forward waveforms are intrinsically not able to deal with varying limits, varying plant conditions, disturbances or actuator failure.

A case where feed-forward control maybe essential is the start-up optimization, consisting of the breakdown, the burn through and current ramp phase. Start-up must be carried out with a high success rate, and low loads on the central solenoid and heating systems. A key issue is that during the start-up phase the current and density are low, and associated quantities such as plasma position are difficult to diagnose as the signals are small. Moreover, given the realistic path lengths of the gas-feeds, long time lags are introduced. Consequently, stable position, current and density feed-back control is hard to

achieve in this phase. This introduces the first control category: determination of optimal start-up feed-forward waveforms.

Once the plasma is established in feed-forward, the magnetic configuration control needs to take control of the plasma shape, boundaries to the wall, location of the X-point and strikes and total current while rejecting the vertical instability. This is the second control category. The poloidal field coils are the actuators while the central solenoid is used to drive the Ohmic current in the plasma. Mathematically, the dynamics associated with these control tasks can be formulated as ordinary differential equations [846]. Magnetic configuration control has one unstable mode, associated with the vertical position and velocity of the plasma centroid. Key challenges for the magnetic configuration control in ITER and DEMO are the sensors and the coupling with confinement physics. The traditional magnetic pick-up coils used in fusion research are prone to thermal gradients and neutron fluxes. These will give rise to drifts. The coupling to the confinement physics, such as during LH back transitions, could give rise to variations in beta and li that are too fast to be rejected by the magnetic control system.

The SOL (with open field lines that intersect the machine walls) interfaces the plasma with the reactor wall. It is used to shield the core plasma from undesirable impurity influxes and to abate the fluxes of heat and particles to the PFCs and to guide the heat fluxes to regions in the tokamak designed to deal with these fluxes. Tungsten components with active cooling can tolerate up to 10 MWm^{-2}. However, in ITER, if no measures were taken the steady state and dynamic heat fluxes would well exceed this. These fluxes would damage the reactor wall components.

Detached plasmas are likely to drive the fluxes down to acceptable limits. Plasma detachment can be induced by a high neutral gas density in the divertor, a high electron density, low temperatures and the introduction of low-Z radiative impurities (such as Nitrogen and Neon) in the plasma periphery and possibly radiating high Z impurities (Argon, Krypton) within the last closed flux-surface. Under these conditions, loss processes are introduced leading to a pressure gradient along the field lines. Radiative instabilities may emerge from the non-monotonic relation between temperature and radiative power losses per unit volume. In some temperature ranges, radiative power losses decrease with temperature leading to instabilities. It follows that to actively control the edge radiative power it is required to ensure sufficient dissipation of energy and momentum. This introduces the third category: Exhaust control. This entails the controlled introduction of low Z radiating impurities in the plasma periphery, and the control of their distribution.

The exhaust control is strongly coupled with the core plasma. First, the required radiative power is subject to the total heating power, including the fusion power. Second, the inward transport of low and high Z impurities depends on gradients lengths in the ion temperature and the ion density distributions. This introduces constraints on the distributions of T_i and n_i that can be formulated to ensure neo-classical shielding of high Z-impurity and falls into the group for profile control and the need for active control density profile control.

The core plasma is organized in concentric surfaces with constant toroidal and poloidal flux, magnetic winding number q and magnetic shear s, pressure p and electron and ion temperature $T_\mathrm{e,i}$. Strictly speaking, the particle density is not a flux-surface quantity, but in most ITER relevant cases with low toroidal rotation and low effective ion charge Z_eff, this quantity can be treated in good approximation as a flux-surface quantity. The consequence is that for the closed flux-surfaces, the abovementioned quantities are functions of the flux surface label ρ only. The transport of these quantities is perpendicular to the flux-surfaces, and subject to 1D diffusion, or diffusion-convection equations. It is very important to note the various couplings between the transport channels, such as the couplings between pressure and bootstrap current, temperature and resistivity, magnetic winding number distribution and transport, temperature and density gradient-length and heat diffusivity and neo-classical impurity fluxes. The heating and fueling systems deposit power and particles at various radial locations. Non-linear coupled transport equations with a single spatial coordinate (ρ) describe the relations between the deposition locations, the fluxes and the distributions and the gradients therein. The fourth category of control challenges is often referred to as profile control. The challenge here is to simultaneously maintain optimal distributions for the above-mentioned quantities using the limited set-of actuators.

The profile optimization strongly couples to operational limits associated with maximum density, maximum pressure and current density gradients. Magnetohydrodynamic (MHD) instabilities limit the achievable pressure and current density gradients. NTMs can form at flux surfaces where q takes on a simple rational value, such as $q = 3/2$, 2/1 and 3/1 in the pressure gradient zone. The sawtooth instability (ST) develops at the surface with $q = 1/1$ and reorganizes the complete plasma core. The fifth control category is MHD control and suppression. This entails NTM suppression, ST amplitude control, or in general, control of resistive MHD modes often using ECRH as an actuator. Control-oriented models for the sawtooth evolution are often based on current diffusion, Porcelli conditions for the crash and a profile reset. Models for the NTM evolution are often based on the generalized Rutherford equation.

The sixth class of control challenges emerges where the control system interfaces with the plant safety system and must induce a safe shut down. There are three typical examples. Reactive, in which the controller tries to reject an event but cannot and triggers a shut-down, pro-active, in which a MPC anticipates problems and ramps-down the plasma, or blind/lame, in which the controller has to ramp-down the plasma with less than the nominal actuator and sensor availability.

These are special cases of event driven control. In the general case, a supervisory controller needs to be designed that can switch controller functionality and allocate actuators to various control tasks in a plasma state dependent and objective and tractable manner. The design of such a supervisory control represents the seventh ITER controller challenge.

In addition to controller functionality, there is the aspect of sensor and actuator design. The overall schematics is shown in figure 175.

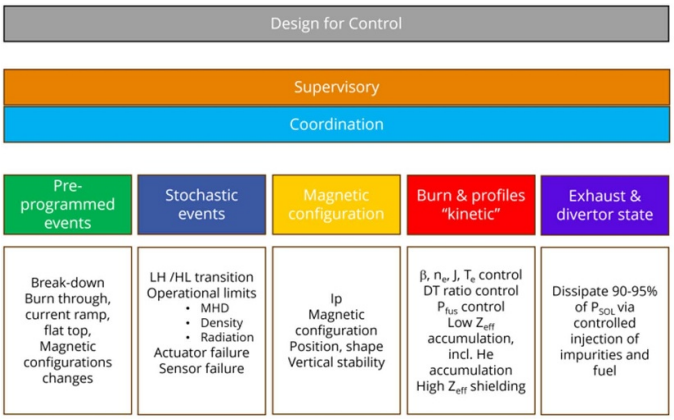

Figure 175. Plasma control functions. Three continuous domains (magnetics, kinetics and exhaust) as well as two domains of events (preprogramme and stochastic) need to be controlled. This calls for controllers in the domains, coordination between the domains, and supervisory control. This requires a systematic, model based design approach.

It will be now discussed how these challenges connect to advances in the development of the field of system and control.

10.2.2. Overview development control technology. Classical control engineering was developed between 1940 and 1960. The applications were controlled by single input single output controllers (SISO). A reference was set, outputs were measured and compared to the reference. The residual was then used in a control law to calculate the control input. A typical method to do this is by making the control law a function that simultaneously has a Proportional, an Integral and a Derivative term (PID).

Between 1960 and 1980 the state-space formalism was introduced. This formalism introduces the state. The state contains all information of the evolution of the unperturbed and unactuated system. In general, the variation of the state x' is a function of the state itself, the actuation u and the external disturbances d, $x' = f(x,u,d)$. The output y is a static projection of the state and the input, $y = h(x,u)$. Linearization yields the state space equations $x' = Ax + Bu$ and $y = Cx$, in which A, B and C are the system, the actuator and sensor matrices, respectively. The state-space formalism is highly relevant for the analysis and optimization of SISO systems and essential for large-scale systems with MIMOs.

As shown above, the measurements only provide a static projection of the state. However, the state-space formalism allowed for an iterative process for the estimation of the state, known as Kalman observation. In Kalman observation, a model of the input-output dynamics is interfaced with synthetic diagnostics. The model is subjected to the same inputs as the plant and outputs of the plant and the synthetic diagnostics can be compared. The residual is used to update the state. As Kalman observation is a statistical procedure, it deals with uncertainties in the measurements and can assess how much confidence has to be put on the measurements. Advanced implementations can deal with multiple sensors that measure various aspects of the state at various locations.

Also the field of robust control emerged in the seventies and eighties. This is a branch of linear control theory that explicitly takes bound uncertainties into account. In H∞ methods, control problems are expressed as a mathematical optimization problem, and the controller is the result of this optimization. H∞ techniques are used to synthesize controllers to achieve stabilization with guaranteed performance and are readily applicable to multivariate systems with cross-coupling between channels. Robust control requires *a priori* information about the bounds on these uncertain or time-varying parameters; if the changes are within given bounds the control law needs not be modified. This is in contrast with adaptive control, which is concerned with changing the control laws to adapt to a controlled system with varying (or initially uncertain) parameters. The foundation of adaptive control is parameter estimation. A common method of estimation is gradient descent, providing an updated control law, which is then used to modify estimates while the system operates.

The field of system identification (SI) arose between 1980 and 1990. In SI, statistical methods are applied to build mathematical models of dynamical systems from measured data. SI also aims at the optimal design of experiments for efficiently generating informative data for fitting such models as well as model reduction. A common approach is to start from measurements of the behavior of the system and the inputs to the system, the disturbances and noise, and try to determine a mathematical relation between them.

Very relevant for nuclear fusion is the identification of partial differential equations, notably transport equations. This is a field that is being developed now. Also very relevant for our discussion is that the quality of parameter observers depends on many factors such as the SNR of the measurements, sensor availability, sensor locations, quality of the models available, time scales of the processes, and if the operational regime features non-linearities, transitions between regimes. As we discussed above, many of the parameters in DEMO that need to be observed are distributed quantities (time-spatial), e.g. density, temperature, current density. This implies that both the temporal evolution and the spatial distribution are important.

This also affects the sensor placement and choices in time-spatial ratios.

Another problem which is highly relevant is the case in which different sensors are used to observe a quantity not measurable by either of the individual diagnostics. This requires a dynamic model describing how the measurements indirectly describe this parameter. Identification methods need to be applied to build such an accurate dynamic model, and the dynamic model needs to be implemented in a real-time environment.

From 1990–2000, MPC, was developed. MPC optimizes a finite time-horizon, but only implementing the current timeslot and then optimizing again. The merit of this approach is that a process can be controlled while satisfying a set of limits and constraints and anticipating future events. MPCs rely on dynamic (typically linear) models of the process. These can be from white or grey box modeling or from empirical models obtained by system identification.

From 2000–2010 hybrid (event-driven) system theory was developed. Hybrid systems combine discrete logics with continuous controllers. For our purposes, the relevance is that this enables a systematic analysis of the class of control problems in which control tasks need to be modified. This can be due to a limit in the plasma (e.g. an instability emerged in the plasma) or varying constraints (e.g. because less actuators become available during the experiment).

In the same period, the field of distributed control emerged. Normally, control is developed for systems that can dynamically be modeled with ordinary differential equations, only taking the time evolution of the control parameters into account. Distributed control deals with the control of systems in which both time and location need to be taken into account. These are described by partial differential equations such as the transport equations for flux or temperature.

In the last decade, the use of artificial intelligence and machine learning have been applied in controllers, often in situations where there are ample modeling results available. Recent developments suggest that reinforcement learning allows for direct inference of complex controllers from modeled data.

Control theory is not only involved with feedback control. ILC is an active field of research with the view to find optimal feed-forward control for systems that work in a repetitive mode. In each of these tasks the system is required to perform the same action over and over again with high precision. Repetition allows the system to improve tracking accuracy from repetition to repetition, in effect learning the required input needed to track the reference exactly. The learning process uses information from previous repetitions to improve the control signal ultimately enabling a suitable control action can be found iteratively. The internal model principle yields conditions under which perfect tracking can be achieved but the design of the control algorithm still leaves many decisions to be made to suit the application.

10.3. Model based plasma control and synthetic diagnostics for ITER

10.3.1. Magnetic configuration control. The control of the plasma boundary, the plasma current and the radial and vertical position of the plasma centroid, as well as the suppression of the vertical instability all fall in the frame work of magnetic configuration control. This was the first domain in tokamak physics that was cast in a proper control theoretical framework [850]. Although the theoretical framework is mature, the field is still under development as a consequence of the requirements that a fusion reactor poses to the controller. These are associated with the development of new sensors for the plasma boundary (such as Hall probes (see e.g. [851], reflectometers [852] or visible imaging [853]) and [854] or with more stringent safety margins that require more precise controllers that can deal with limits and constraints (see e.g. [855] or [856]. The field is also driven by new divertor configurations such as the super-X with flaring strike points, or new, reactor relevant, plasma dynamics that needs to be rejected (see e.g. [857] or [858] by modifying the plasma volume and shaping to off-set undulations in the plasma burn. State of the art in reinforcement learning in plasma control is the development of controllers for the magnetic configuration [859].

10.3.2. Profile control and confinement optimization. Predicting and controlling turbulent energy transport is a grand challenge in nuclear fusion science. Control of the spatial distribution profile of the toroidal plasma current density distribution helps realizing improved confinement and MHD stability. A high fraction of non-inductively driven plasma current, could enable steady-state reactor operation with high fusion gain. The dynamic evolution of the current profile is nonlinearly coupled with several plasma parameters, motivating the design of model-based control algorithms that can exploit knowledge of the system to achieve desired performance.

Models for the input output dynamics using different actuators were developed, see e.g. [860]. RAPTOR is a fast dynamic model for the non-linear evolution of the coupled distributions of the current density, the electron density and the electron temperature. RAPTOR can be run in interpretative mode, as an extended Kalman filter [861–864].

Boyer [865] uses a first-principles-driven, control-oriented model of the current profile evolution in low confinement mode (L-mode) discharges in DIII-D to design a feedback control law for regulating the profile around a desired trajectory. The model combines the magnetic diffusion equations with empirical correlations for the electron temperature, resistivity, and non-inductive current drive. To improve tracking performance of the system, a nonlinear input transformation is combined with a linear-quadratic-integral optimal controller designed to minimize a weighted combination of the tracking error and controller effort.

Maljaars [866–869] exploited the fact the tokamaks are typically operated in scenarios and showed that, using RAPTOR to estimate the non-linear state, a MPC can be synthesized to achieve the optimal distribution of the current density in ITER plasmas [866]. The MPC was set-up to use the four Upper Port ECH systems, the neutral beam injector and the primary poloidal field coil as actuators to avoid the current density profile peaking in ITER hybrid scenarios.

The density profile is notoriously difficult to control. Initial real-time density control schemes were based on PID schemes with interferometers as sensors and gas introduction valves as actuators. This scheme is associated with a number of complications: The interferometers may suffer from fringe jumps, which may be difficult to compensate in real-time. New generations interferometers use multiple wavelength to become robust against fringe jumps. In some case, mm-wave heating systems distort the sensor signal e.g. [870]. The interaction with the wall varies per discharge or even during the discharge. This is particularly relevant in long pulses, with or without on-line wall conditioning using lithium power [871]. Heating schemes can affect the particle transport and the pumping of the divertor cryo-pumps is plasma configuration dependent. PID density controllers may respond to confinement back-transitions by increasing the fueling rates, which may further deteriorate the confinement. These effects may render the PID tuning ineffective or even unstable. Gas introduction valves have only a limited particle deposition depth. Other actuators such as NBI and pellets have a deeper deposition but the deposition location is plasma state dependent.

To deal with these complexities, RAPTOR was extended to include the distribution of the electron density. It is assumed that for cases with low torque input and low plasma rotation, the electron density distribution is with sufficient accuracy a flux surface quantity and that also the transport equation for the electron density is dependent on the radial location ρ only. RAPDENS is a 1D + 0D multi-inventory model of the particle transport in a tokamak. The particles inside the vessel are attributed to one of three inventories: the plasma, the wall, or the vacuum.

The model contains a 0D representation of the particles contained in the wall and the vacuum surrounding the plasma, a 1D representation of the flux surface averaged electron density in the plasma. The evolution of the density distribution is represented by the 1D particle conservation law. The particle transport $\Gamma(\rho, t)$ is modeled by a drift-diffusion equation with empirical transport coefficients. The particle sources and sinks $S(\rho, t)$ include particles injected via NBI and pellet injection, particles entering the plasma due to ionization of neutrals at the edge of the plasma and the loss of particles due to recombination of ions at the edge of the plasma.

Blanken validated this model for the density evolution (a.k.a. RAPDENS) off-line and showed that the model managed to reconstruct the evolution of the central density as well as the distributions of the density right in both TCV and ASDEX Upgrade [872, 873]. Closed loop density control experiments were successfully carried out in ASDEX Upgrade and TCV with RAPDENS in observer mode [874].

Highly relevant for fusion reactors is the control of the distributions of the deuterium and tritium densities n_D and n_T. At present, experimentation at JET [875] and gyrokinetic modeling [876] suggest that the transport from the LCFS to the core is quite equal for D and T and in fact it suffices to guarantee $n_D(\rho = 1) = n_T(\rho = 1)$ to achieve $n_D(\rho = 0) = n_T(\rho = 0)$. If, however, a significant isotope effect would emerge in DEMO, the distributions of D and T must be controlled to ensure $n_D(\rho = 0) = n_T(\rho = 0)$.

10.3.3. MHD control and suppression. The control of NTMs requires an intense micro-wave beam to be focused and deposited at the location where the magnetic island crosses the EC wave deposition resonance. The island's radial location as well as the mm-wave ray propagation and resonant absorption condition are plasma state dependent and difficult to estimate. Moreover, the island rotates, and can be attributed a frequency and a phase. The power has to be deposited when a poloidal deficiency in current density (the O-point) crosses the resonance condition. The frequency and phase of the rotating island must be determined in real-time and used to modulate the ECCD system.

DIII-D [877] and ASDEX Upgrade teams [878] have set-up an NTM control scheme that use multiple sensors. As an example, the DIII-D implementation uses ECE and Mirnov coils, magnetics, and MSE as sensors. Multiple real-time estimators for the mode rational surface location and real-time raytracing are required to identify the optimal launcher angle to aim the ECH beam to the mode rational surface. This scheme is the ITER reference [879].

An alternative scheme uses deep (120 dB) and narrow (1 GHz) notch filter around the gyrotron frequency. This allows for measuring the plasma temperature with ECE in close vicinity of the ECCD deposition, along the same optical path as the heating beam. This concept eliminates the equilibrium and the ray-tracing from the problem.

The challenge for in-line ECE is to design a notch filter with 120 dB suppression of the ECCD frequency (140 GHz on TEXTOR and ASDEX Upgrade) with a quality of better than 1 GHz. This then isolates the ECE channels from the ECCD and allows for measuring the temperature fluctuations associated with the island [880]. An ITER relevant notch was designed and constructed based on the mm-wave cavity FADIS. A mover coil was used for cavity tuning, in particular to couple the ECE to the radiometer and the residual ECCD to a dump [881]. A prototype, designed for 500 kW ECCD power was mounted on ASDEX Upgrade [882]. A similar set-up was achieved on DIII-D [883]. The EU DEMO concept for NTM suppression (also known as quasi in-line ECE) is derived from this concept [884, 885].

Hennen used in-line ECE for closed loop MHD track-and-kill experiments in TEXTOR. A linear control technical analysis was set-up by casting the Rutherford equation for the island evolution into a state-space formalism [886]. Also, the control performance analysis of the ITER NTM suppression system was done by casting the generalized Rutherford

equation in state-space formalism for typical ITER high performance discharge conditions with the view to sustain islands that have sizes below the critical island width [887].

Van de Brand demonstrated on ASDEX Upgrade that the fluctuations associated with small magnetic islands could be observed after correlation of the in-line ECE system with the interferometer and that interferometer was associated with the correct alignment of the radial location of the tearing mode could be identified [888].

Various methods were tried to determine the phase and frequency of the rotating modes in real time: Hilbert transforms on FPGA, a phased locked loop [887] and various variants of Kalman filters [889].

Another intriguing aspect of magnetic islands is that the rotating magnetic perturbations induce mirror currents in the conducting walls of the tokamak. The slower the islands rotate, the easier the mirror currents are induced. The mirror currents, however, lead to a deceleration of the plasma rotation, which promotes further growth of the islands. This mechanism, known as mode-locking is responsible for violent events, known as disruptions. La Haye coupled the equations for the island-wall interaction with the generalized Rutherford equation to study the combined dynamics. Van de Brand used this modeling to derive the requirements of the ITER NTM stabilization system [890].

Witvoet developed a control-oriented model for the sawtooth. This is based on the evolution of the current density profile, leading to varying magnetic shear at the $q = 1$ radius. If the magnetic shear exceeds a threshold, the profiles are reset to their starting condition. This model has been used to successfully tune SISO [891, 892], MISO [893] and adaptive [894] controllers and to test their performance.

Paley *et al* [895], Van Berkel *et al* [896] and van den Brand *et al* [897] developed advanced real time sawteeth period estimators.

A particular aspect of Witvoet's control-oriented sawtooth model is that it predicted strong non-linear response to modulated ECCD input, a phenomenon called locking [891]. The relevance of locking is that it allows for a very strong response of the plasma state to feed-forward waveforms. Witvoet and Lauret obtained corroborating experimental evidence for locking in the TCV tokamak [898]. Lauret described the sawtooth locking phenomenon with a simple model for the evolution of the magnetic shear. Lerche applied the concept of sawtooth locking on JET discharges using ICRH [899].

Lennholm did control and physics experiments in which the energetic ion population was varied by Ion Cyclotron Heating. Lennholm derived a control-oriented model for sawteeth with the destabilizing magnetic and stabilizing fast particle effects [900]. Alexandre Gomes (IST Lisbon) set-up a heuristic model for the fast particle generation and losses and interfaced this with Lennholm's sawtooth model. Gomes derived an adaptive controller for two actuators (ICRH and ECCD). The ICRH is used to pump destabilizing ion orbits at the inboard of the $q = 1$ surface while the ECCD acts on the magnetic shear.

10.3.4. Edge dissipation control, radiation and plasma exhaust control. ASDEX upgrade team tuned a PID controller to keep the radiation induced with nitrogen seeding in high performance H-modes in close proximity to the X-point while remaining detached. The sensing was done with real-time x-ray tomography [901].

MANTIS is a ten camera multi-imaging spectroscopy system that allows for the observation of a single field of view with multiple real-time cameras, while each camera has a different filter for line-radiation. The first MANTIS system was mounted on the TCV divertor. The TCV divertor area can be imaged in real-time, in different wavelengths [902].

Ravensbergen adapted the optical boundary recognition procedure from Hommen [854, 903, 904] to find fronts in the divertor region [905]. Assuming the CIII emission front as a proxy for detachment, Ravensbergen and van Berkel applied a system approach to identify the input output dynamics and derived a controller to position the radiation front in the TCV divertor in both L-mode and H-mode. Controllers were derived and successfully applied [906].

Recently, the control of the x-point radiator was improved by applying system identification [901]. Multi-input-multi output system identification was done to achieve simultaneous core density control as well as radiation front control in TCV [907].

10.3.5. Break-down optimization. Ravensbergen developed ILC for the gas introduction system in ITER [908] and shows that optimal feed-forward waveforms can be obtained for the breakdown and burn-through phase.

As a conclusion, we see a development towards state-controllers rather than output controllers. This is motivated by the need to deal with limits and constraints, as well as managing the complexity of the plasma by coordinated control and supervisory control.

All these methods rely on the availability of the complex plasma state, rather than a physics parameter. This motivates the development of state-observers, which are forward models (FMs) of the plasma dynamics interfaced with synthetic diagnostics.

10.4. Synthetic diagnostics and applications

10.4.1. VSRS. The VSRS is a passive optical diagnostic. Its primary purpose is to provide measurement data of the Bremsstrahlung continuum radiation in the visible light range. From this data, the line-averaged effective ion charge (Z_{eff}) can be determined, which in turn can provide information on the impurity content of the plasma. Also, Z_{eff} is used to provide an early warning on HNB shine-through. In case of neutral beam shine-through a part of the beam power passes through the plasma and is deposited on the wall of the tokamak which may damage the wall.

Decreasing Z_{eff} or n_{e} in the plasma core increases the beam shine-through fraction. The back-up role of the VSRS

is therefore to provide a value for the line-averaged electron density, in case the designated diagnostic for electron density, the system for toroidal interferometry and polarimetry fails. The continuum emission measured by the VSRS scales with electron density squared $n_e{}^2$, square root of the electron temperature $T^{-1/2}$ and the effective ion charge Z_{eff}. In case of measurement failure of the former, the latter two are set at their current value and the VSRS is used to measure ne. This role is strictly meant to shut down the plasma in an orderly manner and not as a means to keep the experiment running.

The VSRS diagnostic collects line integrated data on a single line-of-sight that passes through the plasma from Equatorial Port #8 to Equatorial Port #3 at a height just above the midplane of the tokamak, corresponding to a height of about $Z = 0.60$ m measured from the mid-plane. Coincidentally, the VSRS line-of-sight also crosses the DNB in the core of the plasma. Therefore, also active exchange occurring in the beam at the cross section is measured. Both of these emission measurements are supplementary roles of the VSRS diagnostic. The first mirror, that forms the start of the line-of-sight, is positioned Equatorial Port #8 and at the other end in Equatorial Port #3, a viewing dump is located. The purpose of this viewing dump is to decrease the reflections from the divertor region of the tokamak that are measured by the VSRS. The functioning of the viewing dump plays an important role in achieving the main purpose of the VSRS. Both the first mirror and viewing dump are positioned relatively far behind the port plug in order to decrease reflections and damage from incoming particle fluxes. The viewing dump is visible from inside of the vessel through a hole in the port-plug and is encased in a cavity of which the final design is not yet determined.

A synthetic diagnostic for the VSRS has been developed in python. This model produces representative output of the diagnostic, in the form of emission spectra in the visible light range, using raytracing simulations. The raytracer module Raysect is used as a framework upon which the synthetic diagnostic is built, as it is used for the definition of geometry, light sources and detectors within the model. In order to use a plasma as light source and to allow for the implementation of other physics properties, Raysect is used in conjunction with the CHERAB spectroscopy modeling framework. Atomic 0data is provided by the ADAS database.

The synthetic diagnostic is developed such that VSRS spectra can be modeled see figure 176 based on plasma simulations stored in IMAS scenarios and used to investigate the functionality of the viewing dump of the VSRS diagnostic, for which use of the retroreflector of 55. FA, the DIP, is projected. It is main purpose is to decrease reflections of radiation on the inner vessel wall of ITER from the divertor region of the plasma. These reflections cloud the measurement results and should be suppressed.

The functionality of the viewing dump is determined in two representative cases see figure 177: a case with reflections, but without viewing dump and a case with reflections and with viewing dump. The information on the reflection sources is of major importance to the VSRS. The diagnostic should be able to measure small changes in the continuum radiation in the

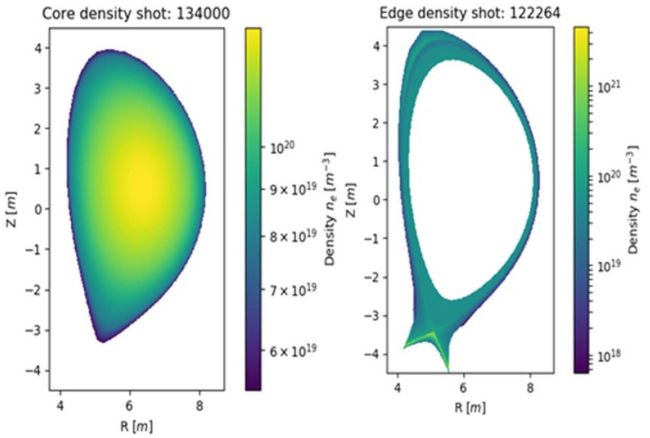

Figure 176. Plasma model for core (left) ad edge (right) radiation.

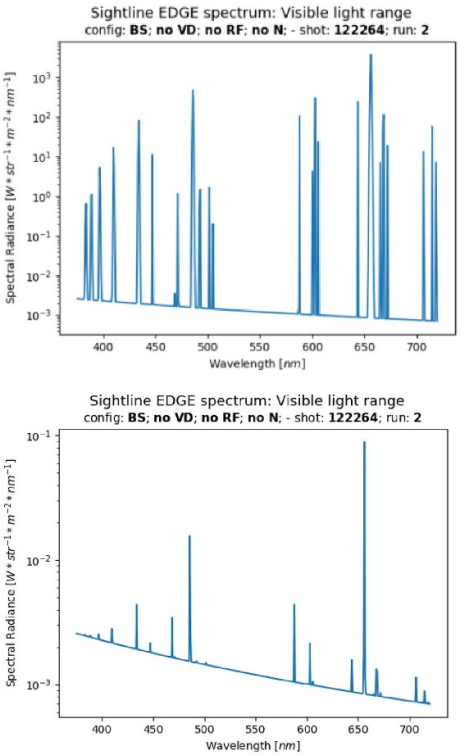

Figure 177. Modeled Bremsstrahlung spectrum for visible spectroscopy reference system with reflections without a viewing-dump (top figure) and with a viewing dump (bottom figure).

core of the plasma. Reflections from the edge of the plasma can cloud this measurement and would make it almost impossible to know whether measured bremsstrahlung changes are caused by the core or the divertor. Separate simulations of these two areas of the plasma provide a positive result in this regard; only 0.39% of 2.34% reflections stem from the edge and divertor region while the majority comes from the core. This edge/-divertor value is lower than the desired 1% overall accuracy for the VSRS Bremsstrahlung measurement and can therefore effectively be disregarded.

The impact of changing the reflectively of the retroreflector surface is investigated see figure 178. It is discovered that

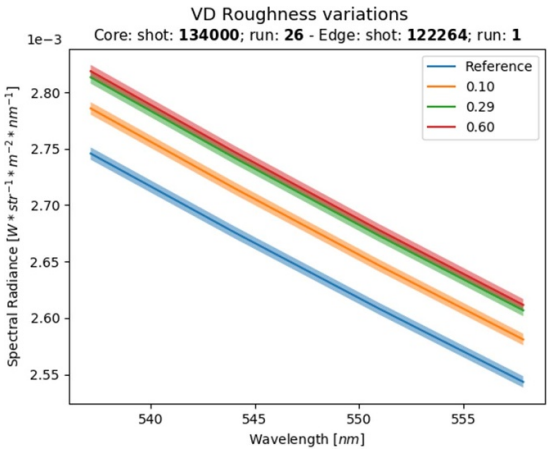

Figure 178. Effect of roughness on the viewing dump efficiency.

a more mirror-like surface decreases the reflections, while a more'rough' surface has negligible impact. Due to the small improvement, the standard DIP retroreflector does not require adaptation for the VSRS system.

The geometry of the enclosure in which the viewing dump is positioned is not set. The two most extreme case shapes are analyzed, a large box around the viewing dump and a cylinder that closely wraps viewing dump. The reflections are slightly decreased when using the cylinder shape, but it is questioned whether this slight impact warrants the increase in manufacturing complexity of this shape. The VSRS Synthetic diagnostic is currently too slow for real-time control and the model structure is not suited for a Kalman filtering approach.

10.4.2. RT analysis of magnetic signals for NTM suppression. The poloidal magnetic field is measured by a system of high frequency multiple magnetic pick-up coils. These coils are used to measure the time resolved MHD perturbed poloidal component of the magnetic fields The individual pick-up coils are mounted on cooled mounts and distributed both poloidally and toroidally, as indicated in figures 179(*a*) and (*b*).

A model is set up of the dynamic magnetic fields due to rotating NTMs. The island width growth dynamics for w is modeled by the Modified Rutherford Equation (MRE), $\frac{\tau_r^*}{r_s}\frac{\mathrm{d}w}{\mathrm{d}t} = -r_s\Delta_0^{'} + r_s\Delta_{BS}^{'} - r_s\Delta_{CD}^{'}$, in which w is the island width, rs is the mode-rational surface, $\Delta_0^{'}, \Delta_{BS}^{'}$ *and* $\Delta_{CD}^{'}$ are the contributions to the mode growth due to the nominal tearing mode stability, the Bootstrap current and the stabilizing non-inductive current drive from the Upper Port ECCD systems.

The MRE is coupled to the Lahaye equation for the island rotation frequency dynamics ω which is dependent on both w and ω, $\frac{\mathrm{d}\omega}{\mathrm{d}t} = \frac{\omega_0}{\tau_{E0}} - \frac{\omega}{\tau_E} - \frac{1}{mC_w\tau_{A0}^2\omega\tau_w}\left(\frac{w}{a}\right)^3$. Although this is very much a simplified representation, it provides a good basis for the synthetic HF pick-up coil diagnostic and a good test case for the unscented Kalman filter frequency tracker and the extremum seeking control (ESC) algorithm. In particular, it does not contain the effects of other MHD activity, such as the sawtooth instability or edge localized modes. As methods have been discussed in the literature to filter spike-like disturbances from continuously varying signals, this omission was not expected to be a problem. Moreover, the MRE is well-studied and could therefore conveniently be extended with the efficiency maps for modulation and misalignment necessary for the ESC scheme. The parameters used in the NTM model can be validated and tuned to match the simulated NTM development, once ITER is operated experimentally.

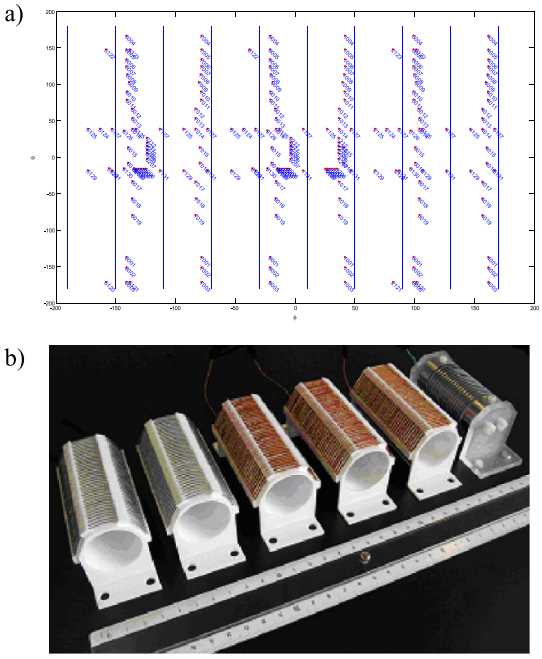

Figure 179. (*a*) Poloidal and toroidal distribution of HF pick-up coils (*b*). For the analysis presented here, all coils have been modeled at a single toroidal location.

Synthetic HF pick-up coil signals are generated by modeling the magnetic perturbation in the plasma as a result from the NTM dynamics using the following equation:

$$\frac{\mathrm{dB}}{\mathrm{dt}}\left(\mathrm{r_{m,n}}, \omega_{\mathrm{m,n}}, \theta, \phi\right) = -\omega_{\mathrm{m,n}}\tilde{b}_\theta\left(\frac{\mathrm{r_{m,n}}}{\mathrm{r_c}}\right)^{\mathrm{m+1}} \sin\left(m\theta - \frac{\mathrm{mr_{m,n}}}{\mathrm{R_0}} \times \left(\beta_\theta + \frac{\mathrm{l_i}}{2} + 1\right)\sin(\theta) + \mathrm{n}\phi + \omega_{\mathrm{m,n}}\mathrm{t}\right)$$

These signals are used to test the unscented Kalman filter for frequency tracking (UKFFT). The UKFFT is an instantaneous, computationally inexpensive algorithm for signal property estimation. It is shown that the UKFFT algorithm is robust and able to track both synthetic and actual coil data. The output of the UKFFT are the frequency, the amplitude and the phase of the mode. Phase differences that have not been incorporated in the synthetic diagnostic could exist due to eddy currents in the metal structures surrounding the diagnostic. These should be experimentally determined and incorporated in the diagnostic afterwards. This would have acted as added noise to the UKFFT algorithm, which was synthetically applied in simulations.

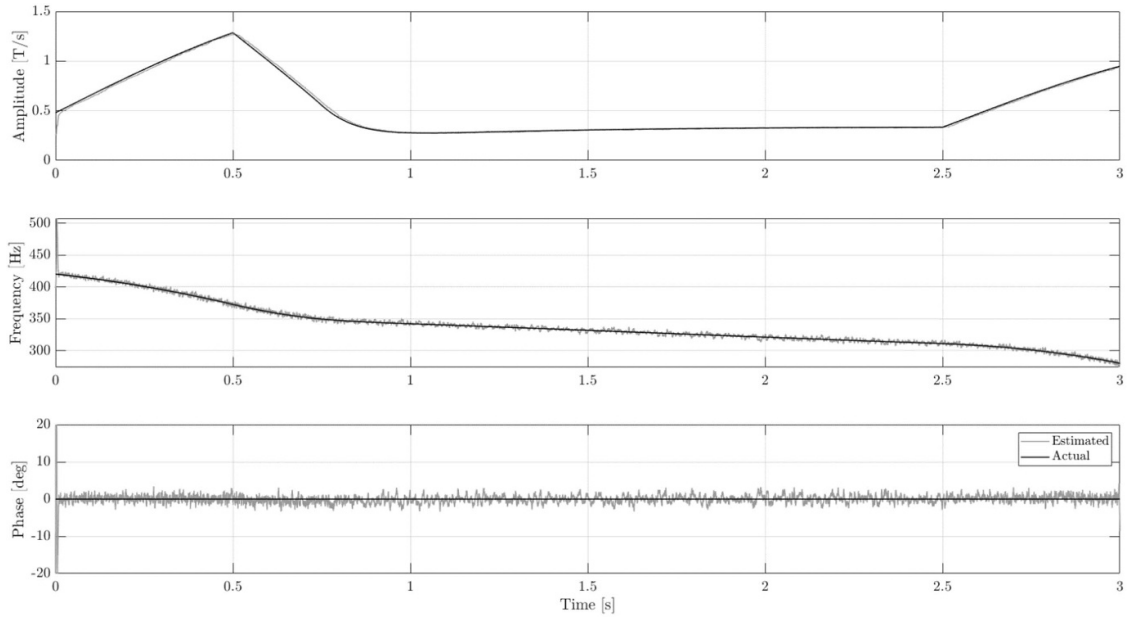

Figure 180. Synthetic signals from NTM model with 10% white noise and 0.2 ms input delay, estimated with UKFFT. 10 ms to converge. Max. error e_f <3% and e_θ <1%, Expected noise level for HF pick-up coil in ITER as given in [698].

The UKFFT algorithm has proven to have robust signal estimation capabilities with fast convergence (<10 ms) for both the synthetic and actual coil data, figure 180. When the algorithm is applied to the synthetic data, it shows strong performance with disturbances well over the ITER requirements (tracking achieved for signals with SNR of 10.45 dB and 12 mm measurement delay). The performance of the algorithm is for these reasons deemed satisfactory and could be useful for the tracking of harmonic signals found in other diagnostics as it is a computationally inexpensive method for signal property estimation.

The estimates from the UKFFT are utilized for the application of NTM suppression with ECCD. The ESC scheme is self-optimizing and does not rely on a model to achieve performance. The scheme is used to autonomously steer the ECCD to drive current at the optimal location in the plasma, which lies at the center of the magnetic island. Besides the misalignment, the ECCD modulation is successfully optimized as well.

The extremum-seeking control scheme applied here follows the approach applied in [906] and the references therein. An harmonic perturbation y_p is mixed with the input of the controller. This leads to a variation of the cost function, which can be used to estimate the gradient in the cost-function, and the size and direction of the control action, see figure 181.

In the noise-less case, see figure 182, this scheme proved able to optimize both the modulation frequency and phase as well as the radial misalignment of the ECCD deposition. The scheme does not converge to the optimal modulation when subjected to ITER noise levels. The reason for this is that the scheme cannot distinguish the effect of the modulation from the added noise. Also, as the extremum-seeking control scheme only converges to a local minimum, convergence might fail in cases of too significant initial misalignment.

10.4.3. Detachment diagnostics. Reliable diagnostics that measure the detached state of the ITER divertor plasma will be necessary to adequately control heat flux to the ITER divertor targets during steady state operation. The feasibility of the ITER shunt diagnostic as a lightweight, robust, and real time detachment sensor has ne. The ITER shunt diagnostic is a set of shunt lead pairs affixed to the body of the ITER divertor cassette that measures the voltage drop along the CB.

This measurement is combined with impedance modeling of the divertor cassette assembly to calculate the current flowing through the divertor, which is equal to the current flowing through the plasma SOL. The relationship between the SOL current and the detached state of the divertor plasma is established using several SOLPS-ITER boundary simulation cases for control-relevant ITER plasma scenarios. Across all simulation data studied, there is a clear and significant decrease in thermoelectric current through the SOL coinciding with the onset of partial detachment at the outer divertor target. Preliminary electromagnetic modeling of a simplified divertor cassette assembly was set-up to develop a control-oriented resistance-inductance circuit model, from which SOL currents can be calculated given shunt pair voltage measurements. The reliability of this model-based approach is then verified. The sensitivity and frequency-response of the resulting system to evaluate the availability of the diagnostic system is determined. Due to modeling limitations, we conclude that physical impedance measurements of the ITER divertor cassette are necessary to calculate accurate SOL current values from divertor shunt measurements. Given these measurements, combined with further development of time dependent SOL plasma simulations and inclusion of future SOLPS-ITER data, the ITER shunt diagnostic will adequately reconstruct the detached state of the divertor plasma for steady-state control purposes [29].

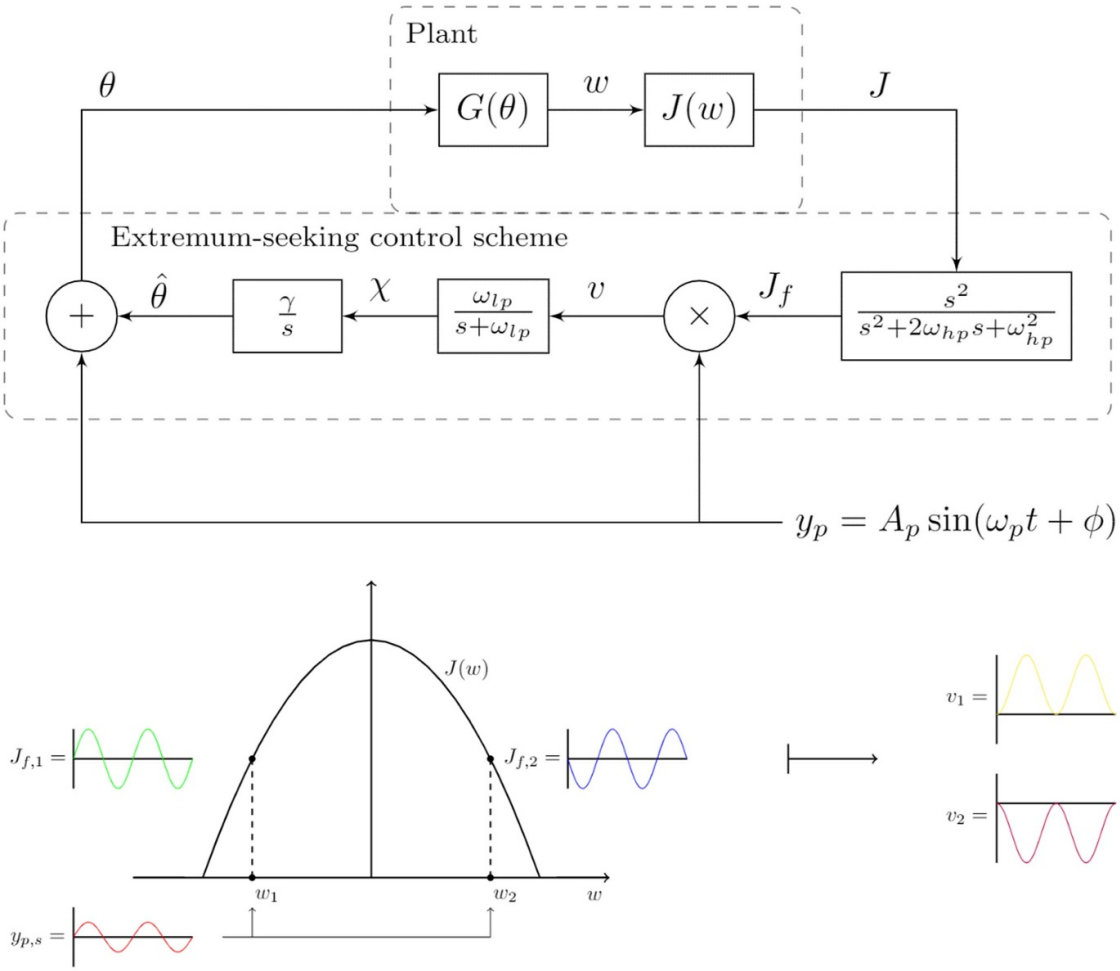

Figure 181. The added perturbation y_p induces a perturbation of the cost function (w), from which the unbiased signal is extracted by applying a second-order high-pass filter. The filtered cost function output J_f is multiplied by the perturbation signal for these signals. The gradient is obtained using a moving average.

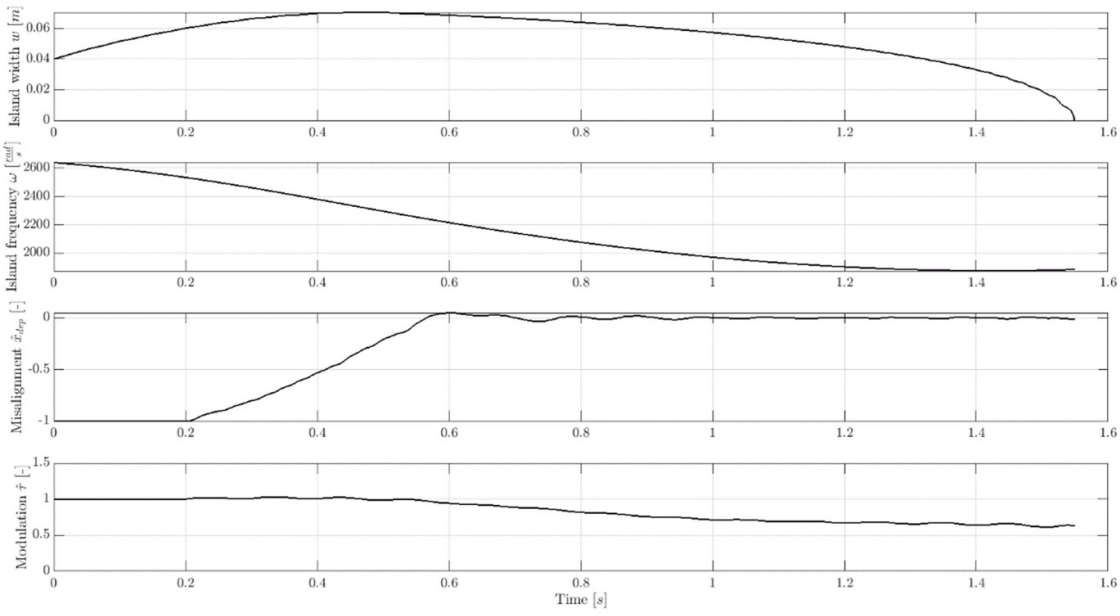

Figure 182. Noiseless case. The UKFFT extracts successfully the phase, amplitude and frequency of the NTM. The power deposition and modulation of the ECCD system are varied to estimate the gradient of the cost function and suppress the NTM.

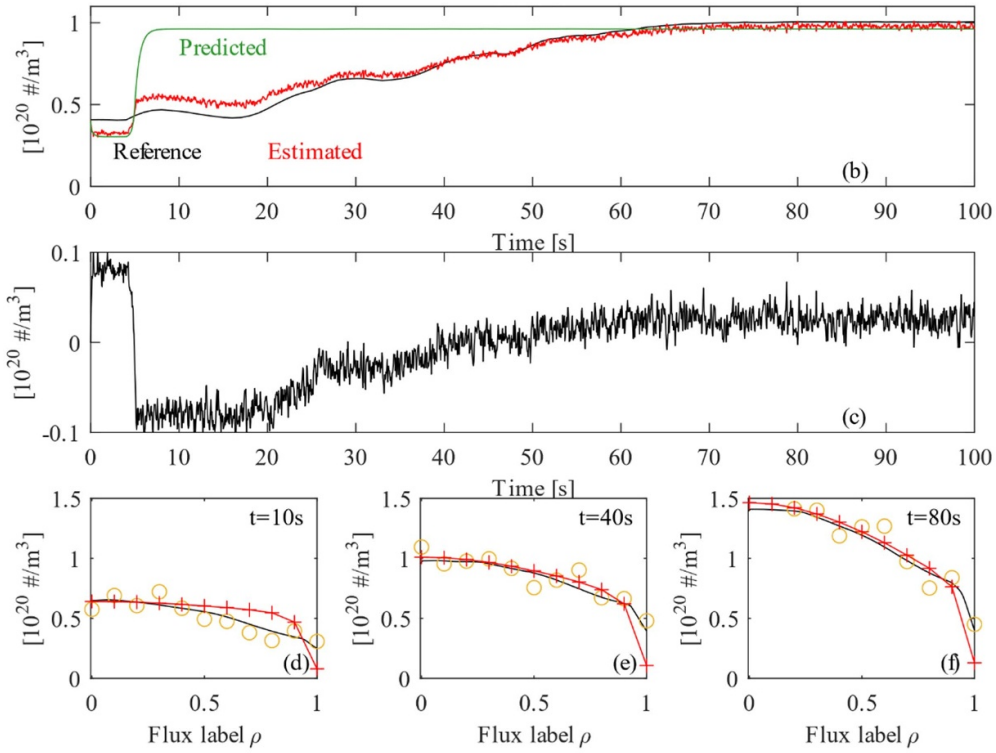

Figure 183. Dynamic state observer using multiple diagnostics on ITER, including real-time Thomson scattering. The top box presents the time evolution of the core density. The predicted density is wrong in terms of absolute value and does not correlate with the reference (green), while the state estimation follows the reference very well. The middle box shows the discrepancy between the reference and the estimated value. After an initial discrepancy of ∼15%, the discrepancy decreases to ∼3%. The bottom box shows the estimate of the density distribution at three instances. The inclusion of Thomson scattering profile yields very good estimates, including the pedestal.

10.4.4. Density distribution control. Initial ITPA diagnostic focused on the control of the line-integrated density with interpretation of the interferometry. Recently, the control of the density distribution has been extended in two ways. First, a multi sensor Kalman state estimator was developed which also includes real time TS. Simulations show that high quality density profile estimation can be achieved with this Estimator, see figure 183.

Second, an ITER relevant robust MPC is developed as a strategy to regulate the density profile while avoiding limits associated with the total density (Greenwald limit) or gradients in the density distribution (e.g. neoclassical impurity transport). Simulations show the controller is capable of regulating the distribution as desired, including the observation of the limits [909].

10.5. Summary and conclusions

For the systematic development of the various controllers taking the various couplings into account, a model-based controller design is required. An activity has been started within the ITPA diagnostics group to provide the synthetic diagnostic needed for the design of diagnostics, the optimal interpretation of the physics experiments and for real time control.

After giving a rudimentary introduction in systems and control theory and an overview how control engineering has been applied to nuclear fusion plasma research and operation, it is shown how sensor models or synthetic diagnostics are used in model based controller synthesis.

A plasma and synthetic diagnostic have been set-up for the VSRS have been set-up, and used for the design optimization of the viewing dump.

A synthetic diagnostic of a section of high frequency pick-up coils for MHD characterization. The signals of these coils can be interpreted using an UKFFT to estimate the frequency, amplitude and phase of a rotating NTM. The UKFFT can be interfaced to an extremum seeking controller to optimize the radial deposition, the modulation frequency and phase. In the noiseless case, this approach works for the deposition, phase and frequency. In case of realistic noise, the gradients in the cost function for the phase are shown to be too shallow for convergence.

An robust MPC has been developed for control of the density distribution with gas feed and pellet injection as actuators, taking limits and constraints into account. This scheme relies on a Kalman filter for the real-time estimation of the density profile. The addition of the TS data in the Kalman filter gives fast and very good convergence.

A synthetic diagnostic has been set up for the divertor shunts and tested numerically.

As we have seen from e.g. the observer for the density, the requirements of the presented models for control and

observation are not very stringent in accuracy. It is critical that the model formulation is such that it can be cast into the Kalman observation framework. Then the real-time constraining of the model by multiple measurements will ensure convergence. In this context, a key requirement is that the models are tractable, and can be evaluated on timescales that are faster than the dynamics that needs to be controlled. For physics interpretation or diagnostic design, the fidelity-requirements of the models are more stringent.

10.6. Outlook

The development of synthetic diagnostics for real time control will be further pursued. Focus will be put on the diagnostics needed for 1st plasma. Special attention will be put on the real time estimation of the pellet fueling efficiency, the optimal control of the density distribution and the impurity transport. Finally, we will focus on data integration aspects. Multiple diagnostics with similar outputs need to be integrated. The associated control capabilities and robustness against failure, degradation, and limitations due to long pulses need to be assessed. The real-time WG has just started an effort to set-up an Multi-Domain Matrix of the elements of the control system, including the plasma. This approach will be pursued to model the structure of the control system including aspects of real-time sensor or actuator failure and the real-time diagnosis thereof.

11. Integrated data analysis and validation

R. Fischer[46], A. Bock[46], S. S. Denk[47], A. Medvedeva[48], M. Salewski[449], M. Schneider[2] and D. Stieglitz[46]

11.1. Introduction

In present and future fusion devices huge amounts of measurements coming from many diagnostic systems have to be analyzed. The information obtained from these measurements are and will be used for machine control and safety as well as for physics studies. The goal of the IDA method is to integrate measured data and their analyses to optimize information available for plasma operation and physics studies. The measured data from diagnostics providing redundant or complementary information are combined, together with available physics knowledge and modeling information within a probabilistic framework.

The IDAV specialist WG within the ITPA diagnostics TG was founded in the year 2020. It was motivated by the usefulness of IDA applications at present day machines [910–922]. The goal of the IDAV specialist WG is to provide and apply an IDA framework for present and next generation fusion devices such as ITER and DEMO for self-consistent data analysis and validation procedures.

A comparison of the concept of IDA with a traditional approach for data analysis, based on the analysis of individual diagnostics data and a subsequent combination of the results, can be found in [923].

IDA in the framework of Bayesian probability theory (BPT) provides a concept to analyze a coherent combination of measured data from heterogeneous diagnostics and to combine them with physics knowledge and modeling information [924]. Since every piece of information from measurements and modeling are subject to uncertainties, quantification and processing of uncertain information is central to this probabilistic approach. Complex error propagation is obtained automatically combining data in a concise probabilistic one-step analysis. The extended set of measurements and modeling information allows for an improved treatment of ill-posed inversion problems of, e.g. profile reconstruction, tomography or equilibrium reconstruction. Different techniques for measuring the same subset of physical parameters provide complementary and redundant data for, e.g. improving the reliability of physical parameters, increasing the spatial and temporal resolution of profiles, resolving data inconsistencies, and for reducing the ambiguity of parameters to be estimated without employing non-physical constraints.

IDA was developed and first applied to reconstruct electron density n_e and temperature T_e profiles from a probabilistic analysis of Thomson scattering (TS) data [925] in combination with interferometry and SXR measurements at the W7-AS stellarator [910]. A corresponding application at the ASDEX Upgrade tokamak includes additionally to the TS and interferometry data also data from ECE and the lithium beam (LIB) diagnostic for which an improved FM was developed [914, 926]. This LIB FM was additionally used in a probabilistic analysis of the JET LIB diagnostic [913]. At W7-AS, Bayesian graphical models were introduced for integrating diagnostic data analyses [927]. IDA was then applied at ASDEX Upgrade to reconstruct the effective ion charge Z_{eff} profiles from various CXRS measurements [915]. A non-Maxwellian electron energy distribution function in the positive column of a neon dc-discharge was reconstructed from the visible emission spectrum using IDA [911]. At JET the Bayesian combined analysis of LIDAR, edge LIDAR and interferometry diagnostics provided n_e and T_e profiles [912]. At the TJ-II stellarator the ne profile was reconstructed in an IDA approach using data from interferometry, reflectometry, TS, and the helium beam [916]. At the Madison symmetric torus (MST) reversed field pinch (RFP) the T_e profiles were estimated in the probabilistic framework from a combination of the double-foil SXR system and the TS diagnostic [917]. Additionally, at the MST RFP Z_{eff} profiles were determined by the integration of SXR tomography and CXRS impurity density measurements [918]. The ion temperature T_i and rotation profiles v_{rot} were reconstructed at ASDEX Upgrade in a probabilistic integrated approach from various CXRS measurements using Gaussian process regression [920]. Recent Bayesian analyses combining various diagnostics can be found at W7-X [921, 923], at ASDEX Upgrade and JET [919], and the MST RFP [928].

The present paper aims at showing the basic ingredients of IDA in the Bayesian framework, reviewing the work previously done, and some examples highlighting typical realizations. More details of the implementation of IDA can be found in publications which are cited as appropriate. The references

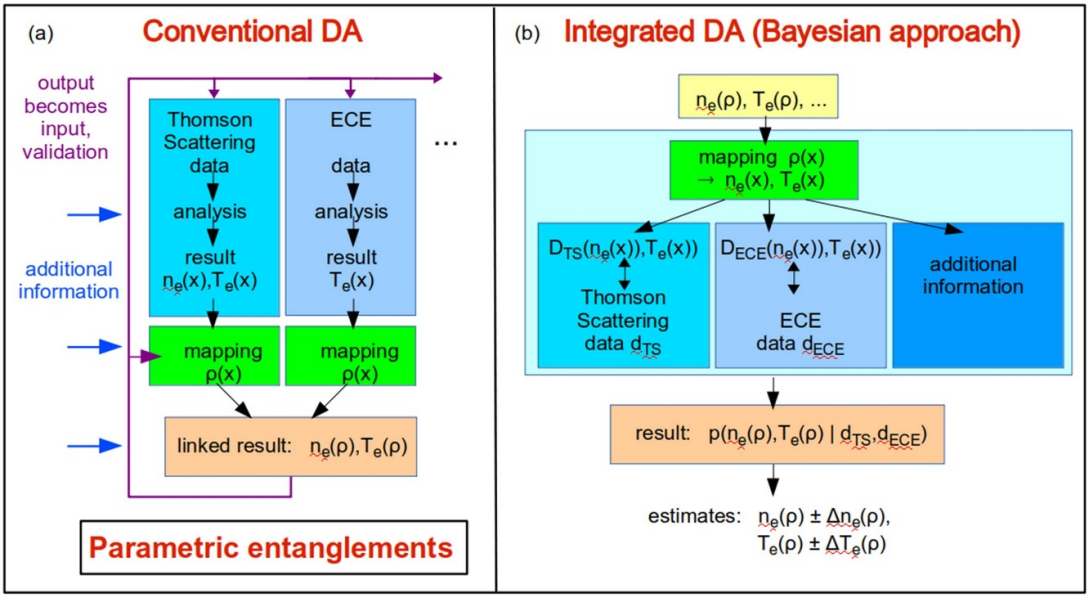

Figure 184. Simplified flow-charts for typical data analysis steps inferring electron temperature T_e and density n_e profiles for magnetic confinement fusion experiments from the Thomson scattering and electron cyclotron emission (ECE) diagnostics in (*a*) a conventional approach and (*b*) within the IDA concept.

in this paper cannot be exhaustive as they should only provide an entrance point for the interested reader.

Section 11.2 compares IDA with a conventional data analysis approach for multiple-diagnostic data analysis and summarizes the main ingredients of IDA: BPT (section 11.2.1), FMs (11.2.2), uncertainty quantification (11.2.3), likelihoods (11.2.4), prior information (11.2.5), parameterization (11.2.6), methods for parameter and uncertainty estimation (11.2.7), validation (11.2.8) and numerical implementation (11.2.9). Section 11.3 addresses the ITER IMAS for physics modeling and data analysis as a standardized way to access and process data. Section 11.4 shows examples applying IDA to obtain synergistic effects (11.4.1), profile reconstruction (11.4.2), equilibrium reconstruction (11.4.3) and velocity-space tomography (11.4.4). Section 11.5 summarizes.

11.2. IDA

The IDA approach in the framework of BPT is conceptually different from an often used sequential (*conventional*) data analysis approach. Frequently, due to the large amount of diagnostics available at fusion devices, in conventional data analysis the individual diagnostics are analyzed by the responsible diagnosticians familiar with the hardware, physics and analysis details (figure 184(*a*)). To obtain a unique (*linked*) result the various results of the heterogeneous diagnostics are mapped on a common, typically magnetic, coordinate system and fitted with a joint parameter set. Often the analysis of the single diagnostics are augmented with additional information to regularize ill-posed inversion problems and obtain, e.g. smooth and well-defined results. The linked result might then be used as input for the equilibrium (mapping) estimation, the analysis of other diagnostics or for result validation and consistency checks.

Various challenges of this conventional approach arise from the parametric entanglements involved. In this iterative procedure it might be difficult to obtain a (self-)consistent result, in particular if many diagnostics are involved as is the case for present and future fusion devices. An automation of this analysis chain is challenging if a huge amount of data has to be analyzed. The propagation of information between diagnostics might be incomplete if single estimates from one diagnostic are used as input for other diagnostics, neglecting complex parameter interdependencies. Error propagation is frequently neglected, resulting in an underestimation of the estimation uncertainties. Data and result validation and overall consistency checks between coupled diagnostics might be a non-trivial task because a quantitative and unified description and processing of statistical and systematic uncertainties is missing. Furthermore, often backward inversion techniques are used which might be prone to noise fitting or numerical instabilities necessary to be regularized by additional constraints or data binning. The estimated parameters (linked result) and their uncertainties often miss a description of the non-linear dependencies.

These difficulties are resolved by the IDA approach using a probabilistic combination of different diagnostics (figure 184(*b*)). The scheme starts with a complete set of physical parameters (section 11.2.6), as a function of a common coordinate system, which is sufficient to describe all diagnostics data. Only forward modeling is used which allows one to evaluate the diagnostics data given the parameters of interest (11.2.2). Forward modeling is known to be numerically stable. The measured data of a diagnostic is compared to the forward modeled data with a likelihood probability distribution function (pdf) (11.2.4) describing the distribution of the data uncertainties (11.2.3). Additional physical information and its uncertainty can readily be integrated with a

probabilistic description and is used only once in the analysis of the combined set of diagnostics (11.2.5). Systematic effects are described with *nuisance* parameters. Their uncertainties are quantified with probability distributions. The nuisance parameters are integrated out (*marginalized*) such that the uncertainty in these parameters propagate to the uncertainty of the parameters of interest. Uncertain nuisance parameters can arise from calibration *constants*, atomic data, or quantification of systematic effects which are candidates for diagnostic inconsistencies. Quantification of inconsistency effects might help to resolve the reason for diverging diagnostics results. Finally, the result of the Bayesian approach is a multi-dimensional probability distribution which quantifies how reliable a certain set of parameter values is in the light of all measured data and the additional information provided (11.2.1). This *posterior* probability distribution includes all parameter interdependencies. Low-dimensional properties of this posterior pdf allows for estimating the parameters (maximum or mean), their dependencies (covariance) and their uncertainties (variance) (11.2.7).

11.2.1. BPT. The interpretative and numerical framework of IDA is given by BPT. BPT provides a unique interpretation of probability as a measure of uncertainty and rules to combine and process (uncertain) information. Uncertainty in the Bayesian framework is lack of knowledge. An introduction to Bayesian inference and further references can be found in [929]. Measured data as well as most information used to describe the measured data or constrain the parameter space of interest suffer from uncertainties. Therefore, a unique framework to handle any kind of uncertainty is mandatory if different sources of information have to be analyzed jointly. An overview of various types of uncertainties encompassed by BPT is given in section 11.2.3.

Additional to the unique quantification of information and its uncertainty, BPT provides rules to combine and process information. Bayes' theorem in its most reduced form relates the posterior pdf $p(f|d)$ for the parameters of interest f given the data d with the likelihood pdf $p(d|f)$, the prior pdf $p(f)$ and the evidence $p(d)$:

$$p(f|d) = \frac{p(d|f) \times p(f)}{p(d)} \tag{11.1}$$

$p(A|B)$ means probability that A is true given (assuming) B is true. The power of Bayes' formula is that it provides what we actually want to know from what the FM by themselves can produce. The likelihood pdf with the FM of the measured data provide the probability of the measurement data, given the parameters of interest, $p(d|f)$. But we actually want to know the probability (reliability) of the parameters of interest, given the diagnostic data, $p(f|d)$.

The Bayesian scheme can be expanded by taking the product of all likelihood pdfs describing all diagnostic measurements and prior pdfs describing any kind of additional physical information used. Therefore, the likelihood $p(d|f)$ in the IDA framework consists of the product of the likelihoods of the various diagnostic data to be analyzed jointly, $p(d|f) = \prod_k (p_k d_k|f)$, where the data of diagnostic k, d_k, are described with the likelihood $p_k(d_k|f)$. The functional form of a likelihood pdf depends on the uncertainty distribution of the measured data and might differ for the various diagnostics (see section 11.2.3.1). As a likelihood pdf describes the probability of measuring a certain data value assuming one knows the underlying physics, the likelihood links the measured data with a FM of the measurement process $D_k(f)$ (2.2), which typically also varies for the heterogeneous diagnostics. The likelihood for each diagnostic, $p_k(d_k|f)$, is typically a product of likelihoods of the measured data points if the data uncertainties are uncorrelated or a multi-dimensional likelihood if the uncertainties are correlated.

The prior pdf, $p(f)$, describes what we know about the parameter of interest independent of the measurements. Typical information to be encoded in the prior are non-negativity constraints for, e.g. temperature and density, monotonicity constraints, smoothness constraints, constraints from physics modeling such as for profile gradients. More examples for useful prior information can be found in the velocity-space tomography section 11.4.4.3.

11.2.2. FMs. A FM evaluates synthetic data to be compared with the measured data within the likelihood pdf. Various fidelity levels of FMs for a diagnostic might be available for various purposes. High-fidelity FMs are typically used for post-plasma analysis where the most reliable results are aimed at. For post-plasma analyses numerical resources and time restrictions are less crucial. Low-fidelity FMs are typically used for time critical applications as real-time analyses or if numerical resources are limited. An example for a low-fidelity FM is given by ECE analyses where optically thick thermal plasmas are assumed. For optically thick plasmas black-body radiation can be assumed which results in a radiation temperature which equals the electron temperature, $T_{\mathrm{rad}} = T_{\mathrm{e}}$. This ECE FM belongs to one of the simplest FMs where the parameter of interest, here T_{e}, is proportional to the measured intensity. A high-fidelity ECE FM is given by solving the radiation transport equation [930, 931]. An implementation of the radiation transport FM can be found in the ECRad code [931]. The ECRad FM is capable of analyzing optically thin plasmas with broadened EC emission regions due to high temperatures, as expected for ITER, or due to low-density scenarios. Additionally, it is capable to describe oblique ECE measurements, harmonic overlap, different polarizations and emission from non-thermal electron energy distribution functions [932]. For the analysis of ECE data with this sophisticated model electron density n_{e} profiles are necessary. Therefore, a combination of the ECE diagnostic with density diagnostics, e.g. Thomson scattering or interferometry, within an IDA framework is mandatory.

Another example for a multiple-fidelity FM is given by CXRS. Frequently, ion quantities as ion temperature T_{i} and rotation velocity are pre-evaluated and available from databases. These data allow for low-fidelity FMs as the parameter of interest, a profile of the ion parameter, can easily be evaluated at the measurement positions. Ideally, the database

provides also information about the uncertainties of the measured values. A high-fidelity FM for CXRS data describes directly the measured spectra [933]. Although numerically more expensive, this high-fidelity FM would allow to incorporate nuisance parameters describing, e.g. uncertainties in calibration quantities or in the atomic data [911].

The preparation of a FM and its combination with other diagnostics FMs in a probabilistic framework is typically less challenging than developing and combining inversion techniques which additionally might suffer from noise fitting or numerical instabilities as for, e.g. Abel inversion techniques. An example of a multiple-purpose FM for velocity-space tomography (*weight function*) can be found in section 11.4.4.

11.2.3. Uncertainty quantification. Uncertainties in the Bayesian framework are interpreted as lack of knowledge covering any type of uncertainty. Statistical uncertainties are distinguished from systematic uncertainties which, in contrast to statistical uncertainties, cannot be reduced by increasing the data sample. As the results of data analysis depend critically on the uncertainties associated with the data, the quantification of uncertainties of measured data (likelihood) and of additional information (prior) is a major part of a parameter estimation problem. Uncertainties determine the absolute amount of information available and determine the weight of measurements of various diagnostics and prior information relative to each other. Especially for the detection and resolution of inconsistent measurements, uncertainties play a major role as consistency is obtained if all data and prior information are *reasonably* well described within their uncertainties. Details about the interpretation and definition of uncertainties can be found in *Evaluation of measurement data—Guide to the expression of uncertainty in measurement (GUM)* [934].

11.2.3.1. Uncertainties in measured data. Statistical measurement noise is always quantified with the likelihood pdf (section 11.2.4). A systematic measurement uncertainty is typically described with a prior pdf (2.3.2). For example, a calibration uncertainty can be quantified with a prior pdf on a calibration nuisance parameter. In special cases this systematic uncertainty can be propagated to the likelihood pdf (see (11.2.4) and [925]).

The distribution of measurement noise is frequently described with a standard deviation. Higher moments are often neglected. This defines the use of a multivariate Gaussian distribution suitable for normally distributed measurement errors. Depending on the measurement scheme other distributions such as the Poisson distribution for counting measurements might be suitable. The measurement uncertainty of the lithium beam diagnostic at ASDEX Upgrade was estimated by assuming a Poisson distribution for the photon counts with unknown offset and amplification factor of the measured signal [926]. In case of unknown measurement uncertainties, contributions to the measurement with unknown source or contributions not described in the FM, or in case of data failure, robust estimation techniques are mandatory as described in (11.2.4).

11.2.3.2. Uncertainties in physics models. FMs describing measured data or physical models providing prior knowledge to constrain the parameter space frequently are not exactly known and are, therefore, subject to uncertainties. Typical uncertainties arise from uncertainties in calibration 'constants' from calibration measurements, from degrading effect of, e.g. optical components or glass fibers, or from atomic data which themselves are determined by measurements or uncertain modeling. An example for this is given in section 11.4.4.4 for uncertainties in the FM (weight matrix) for the velocity-space tomography.

Such systematic uncertainties are tackled in the Bayesian framework by *nuisance* parameters which describe the variability of the model due to the unknown systematic effect. The uncertainty of the nuisance parameters are quantified with prior distributions and marginalized (integrated out). This way the uncertainty of the nuisance parameter propagates into the uncertainty of the parameter of interest. A systematic (*bias*) uncertainty might arise due to uncertainties in the prior information as, e.g. the functional form and weight of the regularization term (see section 11.4.4.4).

11.2.3.3. Uncertainties in estimated quantities. Uncertainties in estimated quantities should describe the reliability with which parameters can be inferred from measured data and modeling information. These uncertainties arise due to statistical and systematic measurement uncertainties, uncertainties in the FM and uncertainties in the prior information used. Various methods for uncertainty estimation exist which are summarized in section (11.2.7).

11.2.4. Likelihoods. The likelihood pdf quantifies the probability of measuring a certain data set given the FM which links the parameters of interest and the measured quantity. Since the probability of measuring certain data is closely related to the measurement uncertainties, the likelihood quantifies the uncertainty distribution of the data. The most often used likelihood is given by the Gaussian pdf with the familiar χ^2 -misfit between the data d and the forward modeled data $D(f)$

$$p(d|f) \propto \exp\left\{-\chi^2/2\right\}$$
$$\chi^2 = \sum_i \chi_i^2 = \sum_i \left(d_i - D_i\right)^2/\sigma_i^2 \qquad (11.2)$$

given here in its most simplified version. The use of the Gaussian likelihood is justified for normally distributed measurement errors $\in$ with variance $\langle \in^2 \rangle = \sigma^2$ and mean error $\langle \in \rangle = 0$. Frequently only the measurement uncertainty describing the statistical distribution of the measurement error is considered. The Bayesian interpretation of measurement uncertainties additionally comprises systematic uncertainties from, e.g. calibration or modeling uncertainties which can be considered in the likelihood pdf in special cases. An example of the use of the Gaussian likelihood with an extended interpretation of the uncertainty can be found in the analysis of Thomson scattering data measured at the stellarator

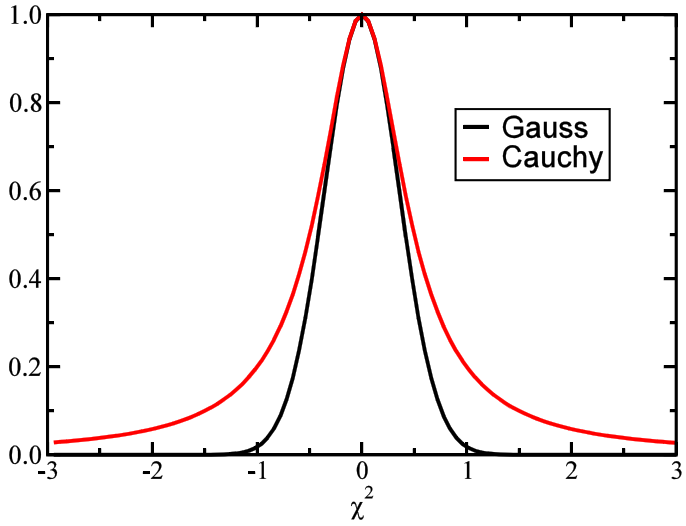

Figure 185. Comparison of a Gaussian with a Cauchy distribution appropriate for outlier robust estimation.

Wendelstein 7-AS, see subchapter 8. The statistical uncertainties of the TS data are augmented with the uncertainties of the background-estimation data, the uncertainty of the calibration measurement, uncertainties of physical model parameters and uncertainties of measured nuisance parameters. A sensitivity analysis of the uncertainties and model parameters allows for finding the crucial uncertainties which have most impact on the diagnostic performance [925].

If measurements suffer from outliers, e.g. due to misspecified uncertainties, measurement failure or physical contributions not included in the FM, an outlier robust likelihood is recommended. The Student's t-distribution treats outliers leniently due to its heavy tails [935]

$$p(d|f) \propto \prod_i / \{a + \chi_i^2\, 2\}^{-(a+1/2)}. \qquad (11.3)$$

The Cauchy pdf is obtained for $a = 1/2$ and the Gaussian pdf in the limit of $a \to \infty$. The heavy tails give outlying data less weight in the fitting process than the Gaussian pdf (figure 185). The Student's t-distribution can also be used if the standard deviation of the uncertainty is not known [935]. The parameter a of the Student's t-distribution allows one to select the weights of the wing, and therefore the weight outlying data have in the fitting process.

This outlier robust likelihood is used routinely at ASDEX Upgrade for estimating electron temperature and density profiles in the IDA framework [914]. Examples for outlying data are given in the following examples: Fringe jumps in interferometry measurements, remaining after a fringe-jump correction procedure, typically occur for rapid density changes due to, e.g. pellet injection or signal cross-over due to ICRH. ECE data might be deteriorated, e.g. from cut-off, non-thermal electron distributions or harmonic overlay when not described properly by the standard black-body radiation assumption or the more sophisticated radiation transport modeling [930–932, 936]. Thomson scattering data might be affected by non-Gaussian calibration uncertainties, low SNR especially at the low-density edge of the plasma, or by transient events such as filaments which are resolved in the TS diagnostic, which typically has a temporal resolution of about 20 ns, and which are not resolved with other diagnostics. Lithium beam data might be deteriorated by beam drifts typically not covered by the calibration procedure performed after a plasma discharge, local filaments not measured simultaneously at the positions of the interferometry or TS channels, or background subtraction uncertainties due to frequent events (ELMs) during the beam-off phases [926]. The emission profile of the thermal helium beam data is typically located at the plasma edge with low SNR at the far scrape-off-layer with low density and temperature values and within the separatrix where the neutral helium beam diminishes due to ionization [937]. This low SNR in the intensities easily produces outlying data in the line-ratio data when the denominator comes close to zero destroying any Gaussian assumption about the error distribution.

11.2.5. Prior information. The Bayesian approach allows to combine measured data from multiple diagnostics with additional information from physical considerations. In the Bayesian terminology the data independent information and its uncertainty/reliability is quantified with the prior pdfs.

Ubiquitous in profile or tomographic reconstruction is the assumptions of some degree of smoothness, non-negativity or monotonicity. Smoothness constraints are typically applied using Tikhonov regularization. Most often Tikhonov regularization is used to penalize the amplitude (zeroth-order), gradient (first-order) or curvature (second-order) of distributions. An example for Tikhonov regularization can be found in section 11.4.4 with velocity-space tomography.

Non-negativity constraints are less frequently applied due to its degrading performance in the optimization steps. Nevertheless, optimization routines for estimating best fitting parameters providing boundary constraints are available although at the expense of increased computation time. An example for the use of a non-negativity constraint can be found

in the tomographic reconstruction example in section 11.4.4. An alternative for boundary constraints for parameters is to quantify a positive parameter with an exponential, e.g. $T(x) = \exp(f(x))$ where $f(x)$ could be an unbounded spline representation.

The exponential of a spline is used at ASDEX Upgrade for the estimation of the temperature and density profiles within the IDA framework and the estimation of the effective ion charge $Z_{\mathrm{eff}} = 1 + \exp(f(x))$ which lower bound is 1 [915]. An unbounded estimation of Z_{eff} can easily go below 1 due to uncertainties in the data but also due to a deteriorating calibration of the data in case of, e.g. degrading optical components. The exponential representation of Z_{eff} avoids values below one which is justified if the data are described reasonably well within their uncertainties. As an estimation of $Z_{\mathrm{eff}} = 1$ is physically meaningful, it is frequently an indication of a problematic data set. At ASDEX Upgrade Z_{eff} is estimated from the line-integrated bremsstrahlung background of CX recombination spectra (CXRS) [915]. A degradation of an optical component (coatings on lenses or mirrors, degradation of glass fibers) of the CXRS system is most sensitively detected with an estimated Z_{eff} value at the lower limit for a clean, high-density discharge closely after boronization where Z_{eff} is expected to be between 1.0 and 1.2. If, additionally to an estimated $Z_{eff} = 1$, the residuals between the measured and forward modeled bremsstrahlung data is systematically negative, this is a clear indication of a degradation of an optical component. This Z_{eff} criterion is more sensitive to a deterioration of the calibration than monitoring impurity concentrations determined by CXRS. Future fusion devices working in a harsh environment might use the $Z_{eff} = 1$ criterion together with the data residuals for an early detection and quantification of a degradation of optical components and to specify the need for a recalibration or a cleaning procedure.

Monotonicity constraints or penalty for non-monotonicity can easily be applied similarly to Tikhonov regularization

$$p(f) \propto \exp\left\{ -\sum_i \left(df(x_i)/dx\right)^2 / \left(2\sigma_m^2\right) \right\} \tag{11.4}$$

where the sum goes over positions x_i where $\mathrm{d}f(x_i)/\mathrm{d}x$ has the wrong sign. σ_m quantifies the amount of tolerance from the monotonicity penalty. As σ_m decreases, the penalty becomes a constraint. A strongly monotonic function can be obtained equivalently to the non-negativity constraint by using for the function derivative an exponential of, e.g. a spline. A subsequent integration with appropriate boundary conditions then yields a monotonic function without applying a non-monotonicity penalizing prior.

Another valuable prior information might arise from physical modeling. Examples are discussed in section 11.4.4 with the example of velocity-space tomography where, e.g. the velocity space is restricted or penalized due to simulations or the slowing-down physics is included as a regularizing prior.

11.2.6. Parameterization. The assignment of the parameter space affects the results of data interpretation. As shown in section 11.2.5 the choice of parameters allows one to include physics knowledge as positivity, boundary or monotonicity constraints via parameter space reduction. Additionally, the choice of the parameter set determines the flexibility of the results. For example, the number and position of spline knots in profile reconstruction determines the spatial resolution. A reduction of the number of spline knots as well as an increase of the spline knot distance reduces the spatial resolution of data fitting. Similarly to the smoothness priors, a sparse parameter setting is suitable to reduce noise fitting as well as to mitigate fitting of problematic data if an outlier robust likelihood pdf is applied.

Comparable to the flexibility in the number of the parameters, Gaussian process regression (GPR) allows to reduce profile flexibility by introducing spatial correlation. Gaussian process regression is applied, e.g. in fits to electron density and temperature profile data and the estimation of impurity transport coefficients from Alcator C-Mod [938], in the reconstruction of various plasma parameters as in the estimation of ion temperature and rotation profiles at ASDEX Upgrade [920], for estimating Z_{eff} profiles from line integrated bremsstrahlung spectra at Wendelstein 7-X [921], and tomography for SXR spectroscopy at WEST [939]. GPR is beneficial for linear problems, e.g. for interpolation and smoothing of noisy data. For these cases GPR is computationally fast because analytical formulas for the best estimate and for the estimation uncertainty are available. Additionally, with a Monte Carlo sampling approach any derived profile, e.g. logarithmic profile gradient and its uncertainties [920], can efficiently be calculated using the covariance matrix.

To estimate how much flexibility in the parameter setting is needed, e.g. how much spline knots to be chosen for the profiles, criteria are necessary for complexity estimation. The preferred criterion is to allow as much flexibility as necessary to describe the significant information in the data and reduce flexibility otherwise to avoid noise fitting (Occam's Razor). Various Bayesian and non-Bayesian techniques are available to (automatically) select the necessary flexibility [929, 938, 940].

11.2.7. Methods for parameter and uncertainty estimation. The result of a Bayesian analysis is a *posterior* pdf for the parameters of interest given all the data and additional information. The posterior pdf quantifies how reliable a set of parameters is in the light of the information used. It contains all the parameter interdependencies.

Parameter estimates can be obtained with various methods distinguishing different properties of the posterior pdf. The most popular estimate is given by the maximum-a-posterior (MAP) solution where the posteriori pdf is maximized with respect to the parameters. For numerical reasons it is preferred to maximize the logarithm of the pdf. For Gaussian likelihood and prior pdfs, this is equivalent to minimizing the sum of

all χ^2 -terms. The uncertainty of the estimate can be derived from the covariance matrix of the parameters at the MAP solution. This is equivalent to approximating the typically non-Gaussian posterior pdf with a Gaussian pdf at the MAP estimate (*Laplace approximation*) [929]. The parameter covariance includes the parameter dependencies but fails for strongly asymmetric pdfs as they occur, e.g. when non-negativity constraints are applied.

For an alternative estimate the mean of the posterior pdf can be used which is different from the MAP estimate for asymmetric pdfs. Asymmetric pdfs typically occur for non-linear FMs. Since usually the mean of a multidimensional pdf with non-linear parameter dependencies are not available analytically, Monte-Carlo (MC) sampling methods are used to explore the full pdf [929]. Among various sampling methods, Markov chain Monte Carlo (MCMC) sampling is frequently used because it is efficient and rather easy to implement. It allows to sample the full parameter space, to find multimodal pdfs with multiple estimate candidates, to visualize marginal distributions for finding an unresolved subspace or parameter correlations not resolved by the data. In case of an uni-modal posterior pdf, the mean of the parameter samples provide an estimate, which can be compared to the MAP solution, and the covariance of the samples provides information about the estimation uncertainty. Furthermore, any derived quantity from a parameter sample can also be averaged and its uncertainty estimated. As an example see [920] where the electron density and temperature profiles were estimated from MCMC sampling of the posterior pdf of an IDA approach of multiple diagnostics at ASDEX Upgrade. The uncertainties of the profiles as well as estimates for the profile gradient and the logarithmic gradients and their uncertainties were obtained applying MCMC sampling.

In any case when a new data inference problem is tackled, it is recommended to explore a posterior pdf with MCMC methods at least once to learn about the subtleties of the data analysis problem at hand.

11.2.8. Validation. The validation of the results from a Bayesian analysis is closely related to the methods for parameter estimation and the estimation of the parameter uncertainties (section 11.2.3.3). Exploring the parameter space of the posterior pdf via MCMC sampling and comparing the mean and the MAP solutions and their uncertainties is recommended as a first validation step. Multi-modal pdfs with similar weights around the posterior maxima cannot easily be summarized by single estimates and uncertainties. Furthermore, they can result in misleading estimates in parameter ranges not supported by any of the diagnostics data [935]. Such a multi-modal posterior pdf can be obtained, e.g. for inconsistent diagnostics data when the individual analyses of the diagnostics result in distant estimates with non-overlapping uncertainties, for outliers within a set of data, or for a misspecified uncertainty level for the data [935]. As outliers of known or unknown source and misspecified uncertainties can be tackled with an outlier robust likelihood (section 2.4), inconsistent diagnostics need to be studied in more detail. After a thorough inspection of sources for the inconsistency, candidate sources can be quantified with additional *nuisance* parameters, its uncertainties with a corresponding prior pdf, and marginalized (integrated out) from the posterior pdf. This way the uncertainty of the nuisance parameter propagates to the parameters of interest. If the posterior pdf becomes a unimodal distribution with parameter estimates and uncertainties capable of describing all diagnostics, a reasonable candidate for the inconsistency is found. This way various candidates for the inconsistency can be tested and compared for their success in explaining all data simultaneously. Please note, that with this method reasonable candidates can be identified, but the method does not guarantee to find the correct source of the inconsistency. Nevertheless, this probabilistic method puts any inconsistency study on quantitative grounds.

Similar methods as for inconsistent diagnostics are applied for diagnostics deterioration, e.g. degradation of optical components (see also section 11.2.5). An IDA method combining data from multiple diagnostics including calibration data provides a self-consistent approach to constrain uncertain and varying calibration *nuisance* parameters. This approach becomes important in any harsh environment of future fusion devices as DEMO.

An extension of the validation methods described so far is given by the combination of measured data with modeling information. Physical modeling allows to avoid non-physical prior information, to reduce the parameter space on physical grounds, and to validate the measured data. Transport analyses, e.g. given by ASTRA modeling, might help to identify diagnostics lack of strength, e.g. unresolved parameter dependencies, as well as, e.g. limiting profile gradients not restricted by diagnostics data within their uncertainty. Validation typically performs best if all relevant information, measured data and modeling information, are jointly analyzed. The most important criterion is given by reasonable data residuals. Successful validation needs data residuals within the uncertainties and data residuals scattering according to the likelihood pdf used. Again, successful probabilistic validation does not imply a physically correct description of the data and correct physical modeling, but it provides a quantitative framework for the validation process.

11.2.9. Numerical implementation. Nowadays ample experience exists from applying IDA at various fusion devices (W7-AS, ASDEX Upgrade, JET, W7-X, TJ-II, and MST RFP), for various diagnostic combinations and for various parameter sets. Based on this experience and due to the conceptional clearly defined Bayesian approach an open-source IDA toolbox written in python and designed to be modular and flexible to be used at present and next generation fusion devices is presently under development. The code is intended to be highly modular in the set of diagnostics considered, in the type of likelihoods to address different uncertainty conditions, in the multi-fidelity FMs (synthetic diagnostics) to allow for fast analysis with reduced physics for real-time applications

up to post-plasma data analysis with highly-sophisticated diagnostics models, modular in the parameterization (splines, Gaussian process regression, …), in the priors encompassing non-physical conditions (e.g. smoothness) or physical information from modeling codes, and modular in the evaluation and representation of results using MAP solutions or using MCMC sampling to explore the full probabilistic parameter space. A first implementation showing the combination of a synthetic set of interferometry, Thomson scattering and ECE diagnostics for the estimation of electron density and temperature profiles is described in section 11.4.2.

The IDA workflow is controlled by code parameters for, e.g. the selection of the set of diagnostics to be analyzed, the likelihood and FM to be used for each diagnostic, the equilibrium to be used, the time frame and temporal resolution with which the physical quantities are to be estimated, the parameterization of the physical quantities (profiles) to be estimated, the prior constraints to be applied (smoothness, physical models), or the parameter and uncertainty estimation methods (MAP, MCMC). A frequently used format for code parameters is given by the XML format. The present IDA implementation relies on the YAML format which is easier to be read and edited by humans.

11.3. IMAS

A multiple purpose data analysis framework should be adaptable to handle any data input and output method. Nevertheless, a standardized communication scheme between codes and databases is beneficial for an efficient workflow.

The ITER IMAS is the implementation of a physics modeling and data analysis suite for plasma operation and research. It provides standardized access to experimental and simulated data [397]. The data are organized in interface data structures (IDS) which are designed for high modularity and flexibility to be suitable for any fusion device. The IDS provide within a data dictionary a definition of data structures in a tree configuration and the names of the data to be used with the most popular programming languages. New IDS are continuously developed and existing ones are extended according to the needs of code developers and users.

IMAS is designed to provide workflows for plasma modeling, data analysis and data structures. The IDS encompass, e.g. the full description of the tokamak subsystems (diagnostic, heating system, etc) or the physical concepts describing the plasma (equilibrium, set of core plasma profiles, wave propagation, etc) [397]. IMAS is used within the IDA framework, at present, by reading the machine description data for the diagnostics properties (geometry), the diagnostics data, diagnostics FMs, and the equilibrium. The linkage with IMAS will be extended as further diagnostics and FMs will be provided.

For a diagnostic FM provided by IMAS to be used, the parameter representation internal to the IDA framework has to be mapped to the corresponding IDS needed as input to the IMAS FM. For example the spline representation of profiles within the IDA framework has to be mapped to the core-profile IDS defining the interface to the IMAS routines.

Eventually, the results of the data analysis, e.g. the estimated profiles and their uncertainties, and the forward modeled data and the residuals have to be written into the corresponding IMAS database for further usage. The residuals, which describe the misfit of the measured data or modeling prior information with the forward modeled data, is of central importance for a (later) validation of the estimation results.

FMs provided by IMAS ideally have to be provided in a numerically-efficient modular way since the estimation of physical parameters requires a fitting (MAP solution) or a sampling (MCMC approach) procedure where the FM is evaluated multiple times. Separate sub-functions for initialization and evaluation of synthetic signals, such that only the evaluation method is iterated in the IDA loop, have to be distinguished. Three instances of the FM are to be separated: First, the initialization of time independent (static) quantities such as reading the geometry of the interferometer LOSs from the IMAS machine database which has to be done only once for the complete evaluation of a plasma pulse. Second, the initialization of time dependent (dynamic) quantities such as the magnetic equilibrium and the magnetic coordinates along the interferometer LOSs, which has to be done once for each time point. Third, the evaluation of the FM (synthetic diagnostic signal) from the parameters to be estimated. The third and innermost part of the IDA iteration loop defines the most critical part for numerical efficiency.

11.4. Examples

11.4.1. Synergistic effect. The result of a Bayesian analysis is a probability distribution of the parameters of interest. In case of a multidimensional probability distribution, the pdf contains the dependencies between the parameters. These dependencies allow one to obtain a synergistic effect where the result of a diagnostic set is more informative than the sum of the results of individual measurements. This is depicted in figure 186 where Thomson scattering data are analyzed together with SXR data [910].

The left panel shows the two-dimensional likelihood pdf as a function of density and temperature using only the TS data. The hyperbolic structure is typical for this TS diagnostics which was most sensitive to the electron pressure. The middle panel shows the pdf of a SXR analysis where only temperature information was obtained, to be seen in the structure-less shape with respect to the density. Assuming we are interested in the density only, the two-dimensional posterior pdfs have to be marginalized over the temperature. The result of this marginalization is shown in the right panel for the Thomson data only (dashed curve), SXR data only (dotted flat curve) and the joint analysis taken from the product of the two pdfs (solid line). Although the SXR data do not provide any information about the density, the joint analysis shows a 30% reduction of the estimation uncertainty (width of the marginal distribution) of the density. This example shows on the one hand the mechanism how a probabilistic synergistic effect is obtained, and, on the other hand, that exploiting the dependencies between the parameters are valuable for the combined analysis of heterogeneous diagnostics.

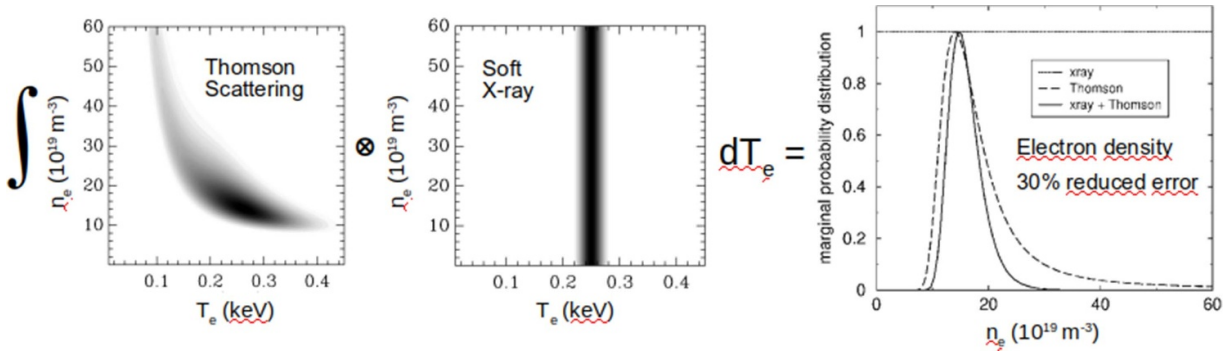

Figure 186. Synergistic effect by exploiting full probability distribution.

11.4.2. Profile reconstruction. Various applications for profile reconstruction using IDA at the W7-AS stellarator [910], at the ASDEX Upgrade tokamak [914, 915, 920, 926], at the JET tokamak [912], at the TJ-II stellarator [916], at the MST RFP [917, 918], and at W7-X stellarator [921, 922] can be found.

Due to the conceptional clearly arranged Bayesian approach a general-purpose IDA toolbox, written in python, for present and next generation fusion devices was developed and will continuously be complemented as new diagnostics or parameterizations are requested. The ingredients are summarized in section 11.2. A first application of this IDA toolbox implemented at ITER combines synthetic diagnostic data from artificial ECE and TS diagnostics. These two diagnostics were augmented with a synthetic data set from the TIP [518]. The IDA software package allows for selecting (via the YAML parameter file) for the diagnostics individually among Gaussian and Student's t-likelihoods and for the profile parameterization between a spline representation optionally with non-negativity constraints or an exponential of a spline representation which is by definition positive. The profiles can be estimated in two ways, by finding the MAP solution of the posterior pdf or by evaluating the mean profiles from MCMC samples from the posterior pdf. Both estimation techniques allow to evaluate profile uncertainties.

The IDA software package reads from the ITER:IMAS database: From the ITER machine description database the interferometry geometry of 5 LOS (figure 187) and from the ITER scenario database an ITER equilibrium were taken. For the TIP a synthetic data set was generated by line-integrating a core density profile corresponding to profiles from the ITER scenario database. Random noise with a standard deviation of 5% was added to the TIP data. The ECE data and TS data were generated similarly at arbitrary positions within the plasma due to, at present, lack of realistic coordinates of the two diagnostics in the machine database. For the ECE FM the basic assumption of a thermal and optically-thick plasma (blackbody radiation) is assumed where the radiation temperature equals the electron temperature ($T_{\mathrm{rad}} = T_{\mathrm{e}}$) at the cold resonance position. This frequently used, trivial ECE FM will be complemented with the radiation transport forward modeling using the ECRad code [930, 931]. For simulating TS data, T_{e} and n_{e} pair values are taken at various positions in the plasma

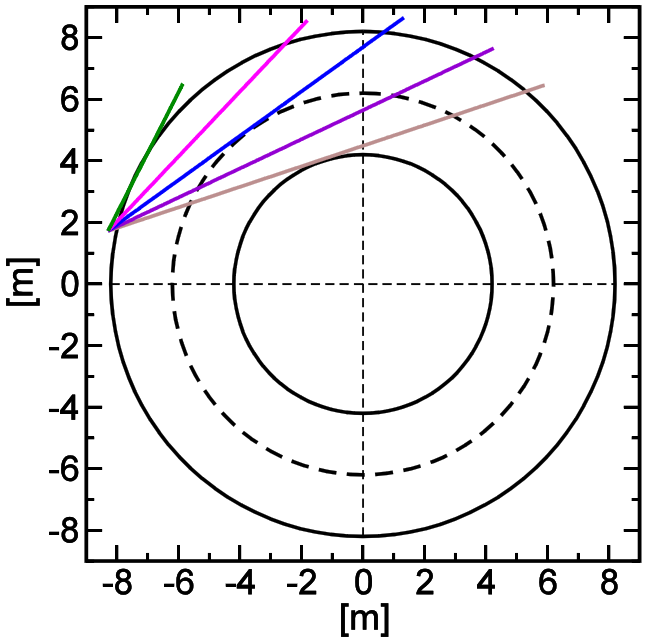

Figure 187. Toroidal plane of ITER (major radius 6.2 m, minor radius 2 m) and the 5 TIP LOSs.

from the temperature and density profiles. Random noise of 10% for both ECE and TS data were added.

The profiles taken for generating the data sets for the three diagnostics are shown in figure 188 as black solid lines (original). The noisy data are shown as crosses (TS blue, ECE green, TIP orange) where the length of the vertical line corresponds to the uncertainty chosen. As the TIP data are line integrated, the data are normalized to the lengths of the LOSs as shown in figure 189. The 5 TIP data are plotted at arbitrary plasma position sorted according to the smallest (largest) length of the LOS to the largest (smallest) ρ_{pol}, correspondingly.

The profiles were parameterized with the exponential of a spline which ensures non-negativity. For the ECE and TS data the Student's t and for the TIP data the Gaussian likelihood were arbitrarily chosen. If sporadic fringe jumps in the TIP data are expected and routine (unsupervised) analysis

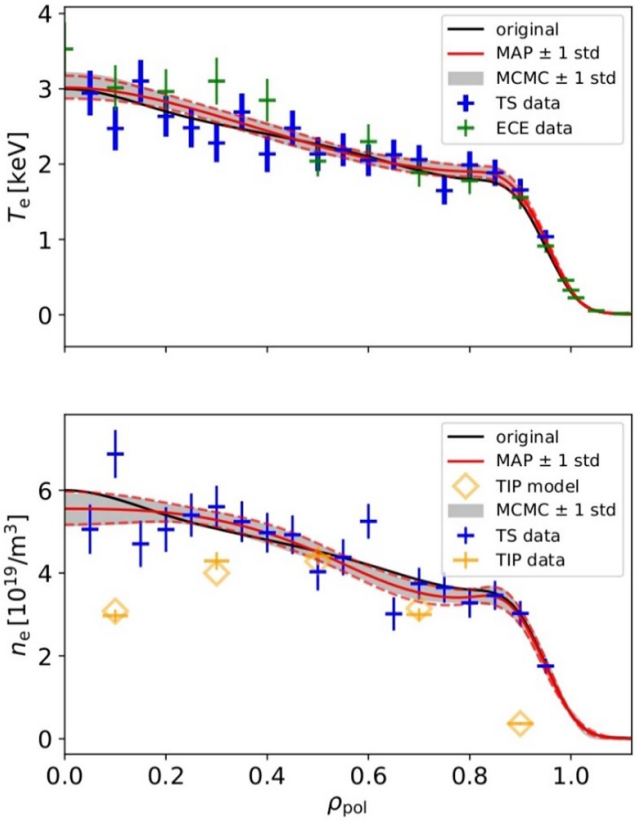

Figure 188. Simulated (black solid line) and reconstructed (red solid line) temperature and density profiles estimated from the noisy data from the ECE (green), TS (blue) and TIP (orange) diagnostics. The open diamonds depict the forward modeled TIP data using the fitted density profile. The dashed area covers the uncertainty band from a MCMC sampling method.

is foreseen, the Student's t-likelihood is beneficial in down-weighting the corrupted data, as routinely used within the IDA approach at ASDEX Upgrade. No smoothing prior is applied.

The profiles estimated from the set of noisy data using the MAP solution are shown as red solid lines (MAP) with uncertainties employing the Gaussian approximation as red dashed lines. The profiles from the mean of the MCMC samples hardly deviates from the MAP profiles (not shown). The uncertainty band estimated from the upper and lower standard deviations of the MCMC samples relative to the mean values are shown as shaded area (MCMC). Please note that the use of upper and lower standard deviations typically result in asymmetric uncertainty bands if the posterior pdf is not symmetric with respect to its mean value. As expected, the MAP and MCMC estimates for this test example agree within the evaluated uncertainties with the original profiles.

11.4.3. Equilibrium reconstruction. A reliable magnetic equilibrium reconstruction is essential for stability and transport studies as well as for the development of advanced plasma operation or steady-state tokamak operation with high bootstrap current fraction and non-inductive current drive [941, 942]. Additionally, a reliable equilibrium is of major importance for the mapping of the diagnostics on a common coordinate system in the IDA framework. Various equilibrium reconstruction codes and methods are available at the various fusion devices (see e.g. [943–948]). Frequently, for early availability and robustness equilibrium reconstruction is based on a reduced data set as, e.g. magnetic probe measurements only. But this usually results in reduced reliability especially of the core parameters (current and q -profiles and flux surfaces). Therefore, for best performance the equilibrium reconstruction is part of the IDA workflow where a lot of relevant information for an improved equilibrium can be provided.

Often abundant measurement and modeling information is available for an improved reconstruction of the magnetic equilibrium. This is exemplified with the ASDEX Upgrade equilibrium reconstruction using the IDE code package [948, 949]. This framework is based on coupling of a Grad–Shafranov solver with current diffusion modeling. The neo-classic current diffusion model (CDM) describes the temporal evolution of the equilibrium between two successive equilibrium reconstructions employing the Grad-Shafranov solver [950]. The CDM predicts the flux-surface averaged current density profile which provides data including their uncertainties additionally to all the other measurements to constrain the next equilibrium reconstruction. The free-boundary equilibrium solver employs data from magnetic measurements (field probes and flux measurements), diamagnetic measurements [951], pressure profiles from electron [914] and ion temperature and density measurements [920] and fast-ion pressure modeling (RABBIT [952] for NBI or TRANSP [953] for NBI and ICRH), effective ion charge Z_{eff} [915], internal current measurements from MSE and IMSE [954] and polarimetry [955], tile (halo) currents for SOL currents, loop voltage measurements, q -constraints from mode analyses, topological isoflux constraints from multiple measurements of T_e or T_i on the same flux surface [945, 956], and plasma rotation measurements for considering centrifugal effects in an extended Grad-Shafranov equation [945, 957]. For the neo-classical current diffusion the electron and ion temperature and density and the Zeff profiles are needed for the bootstrap current and the conductivity. Additionally, the EC and neutral beam driven currents are provided by the TORBEAM and RABBIT codes. Sawtooth reconnection events are described by two different sawtooth models for the sawtooth induced current re-distribution [949]. All these inputs provide redundant and complementary data for an improved and validated magnetic equilibrium.

The close interdependencies between the IDA profile estimation and the equilibrium reconstruction mutually influence also their reliabilities [920, 946]. As a fully integrated IDA approach covering profile estimation and equilibrium reconstruction simultaneously is still to be provided, a pragmatic approach is given by an alternating iteration of profile estimation and equilibrium reconstruction which was observed to converge within a few iterations. The uncertainties of the input data for the equilibrium reconstruction are taken into account in the fitting part of the Picard iteration, and, therefore, propagate to the uncertainties of the equilibrium quantities. The equilibrium uncertainties for the profile estimation can be considered by a MC approach sampling the base-function

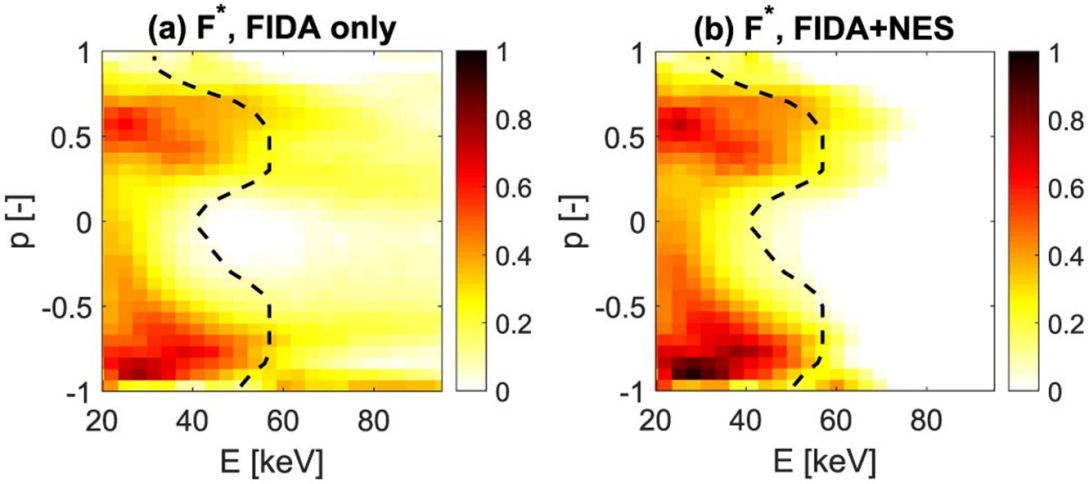

Figure 189. Measurement of a fast-ion velocity distribution function [a.u.] in the center of a plasma heated by co-current and counter-current neutral beam injection at EAST. The tomographic inversion is based on *(a)* FIDA spectra using two detectors, and *(b)* additionally a NES spectrum. The expected ion densities to the right of the dashed line are low as expected from a calculation with TRANSP/NUBEAM. Reproduced from [958].

equilibrium coefficients from their covariance matrix and evaluate a random sample of equilibria to be used for the study of equilibrium-induced profile uncertainties.

11.4.4. IDA by velocity-space tomography. An application of IDA, which has emerged in recent years, is the measurement of fast ion VDFs by velocity-space tomography [959–961]. As for any tomography application, IDA of all available measurements is essential. Position-space plasma tomography systems are usually designed with nominally identical or at least similar detectors. Velocity-space tomography uses any available detector monitoring the same spatial measurement volume, regardless of the type of diagnostic [960].

An example appears in figure 189 showing the VDF at EAST for a plasma heated by co- and counter-current NBI [941]. E is the energy and p is the pitch. The measurements are analyzed using (a) only two fast-ion D $_\alpha$ (FIDA) spectroscopy detectors and (b) the two FIDA detectors and in addition neutron emission spectroscopy (NES).

The dashed line represents the upper boundary of a VDF computed with TRANSP/NUBEAM. Few ions are expected to the right of the dashed line because only NBI heating was used and no acceleration of ions is expected. If, on the one hand, only the two FIDA detectors are used to compute the tomographic image, large ion densities at energies significantly larger than the NBI injection energies are erroneously found. We additionally recognize these as artifacts since similar artifacts appear in tomographic inversions of synthetic measurements, where the true solution is known, for this diagnostic setup. If, on the other hand, in addition NES measurements are used, they force the distribution function to very small values at large energies. This works well since NES measurements are highly sensitive at large energies [962, 963]. This example shows that the IDA of FIDA and NES here suppresses the artifacts at large energies. A second example in addition to figure 189 is velocity-space tomography based on γ -ray spectroscopy (GRS) measurements and NES measurements at JET [964]. The NES measurements are made by TOF, liquid scintillator and single-crystal diamond detectors [965], so that in total four different detector types were used in the tomographic inversion.

Until now velocity-space tomography has been applied at ASDEX Upgrade [961, 966–971], JET [964], MAST [972], DIII-D [941], EAST [973, 974] and TCV [975]. Various combinations of data from FIDA, NES, GRS as well as CTS with two to five simultaneous detectors have been used at these tokamaks. VDFs in plasmas heated by NBI as well as electromagnetic wave heating in ion cyclotron range of frequencies (ICRF) have been measured.

At ITER, velocity-space tomography of the α -particle distribution function based on GRS and CTS has been shown to be feasible for energies from about 1.7 MeV upwards [629]. However, since all currently foreseen diagnostics observe in a perpendicular direction with respect to the magnetic field, the sign of the pitch p of the α -particles cannot be determined. But the absolute value $|p|$ can be determined, so that the VDF $f(E, |p|)$ can be measured. If an oblique γ -ray detector is installed, the sign of the pitch can be found, too [629].

Velocity-space tomography is also applied to measure anisotropic deuterium temperatures $T_\parallel$ and $T_\perp$ as well as the deuterium density and drift velocity [976]. In this application, the full (fast and thermal) VDF is determined based on simultaneous measurements with several D_α -spectroscopy detectors, and then the lowest moments of the full VDF are computed [976].

Reviews of velocity-space tomography are available in [962, 977]. In the following we will focus on methods of velocity-space tomography and discuss the FM, the inverse problem, prior information, uncertainties as well as related 1D to 5D tomography problems.

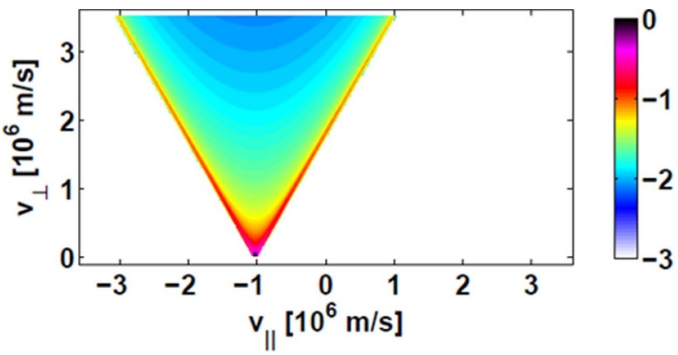

Figure 190. Exemplary weight function showing the velocity-space sensitivity of a CTS measurement at a particular Doppler shift. Reproduced from [961]. © 2014 IAEA, Vienna. All rights reserved.

11.4.4.1. The FM: synthetic diagnostics. To do tomography in velocity space, we need to quantify the sensitivity of the diagnostics in velocity space. This is analogous to modeling the lines-of-sight in traditional position-space tomography. Weight functions quantifying this velocity-space sensitivity have been developed for all major fast-ion diagnostics: FIDA [978, 979], NPAs [978], CTS [627], NES [980, 981], GRS [982, 983] and FILDs [984]. Recently, weight functions for 3 MeV proton diagnostics [985] and ion cyclotron emission spectroscopy weight functions [986] have been numerically computed, too. A weight function w relates a 2D fast-ion distribution function f to a measurement s through the integral equation [627, 978–983]

$$s(m_1,m_2) = \int_0^\infty \int_{-\infty}^\infty w(m_1\, m_2, v_p, v_\perp) \times f\left(v_\parallel, v_\perp\right) \mathrm{d}v_\parallel \mathrm{d}v_\perp \tag{11.5}$$

$s(m_1,m_2)$ is the measured signal in the spectral bin $[m_1,m_2]$. FIDA measures spectra in wavelength [987], GRS in γ -ray energies [988], TOF NES in flight times [963], and CTS in wave frequency [989]. $\left(v_\parallel, v_\perp\right)$ are the velocities parallel and perpendicular to the magnetic field, respectively. (E,p) coordinates are also often used but in $\left(v_\parallel, v_\perp\right)$ the geometrical shape of weight functions is often clearest. The weight function hence shows the quantity [signal/fast ion] where the units of the signal are particular to the instrument. An example of a weight function appears in figure 190. The colored regions are observable for the given measurement bin whereas the white regions are not observable.

Substitution of a δ -function modeling N_f ions at coordinates $(v_{\parallel 0}, v_{\perp 0})$ into equation (11.5) and integration shows that the amplitude of a weight function at velocity-space position $\left(v_{\parallel 0}, v_{\perp 0}\right)$ is readily computed from

$$w\left(m_1,m_2,v_{\parallel 0},v_{\perp 0}\right) = \frac{s(m_1,m_2)}{N_f} \tag{11.6}$$

using a standard synthetic diagnostic code for the diagnostic. The computation of the signal by weight functions neglects spatial effects, which is usually fairly accurate for the plasma center where plasma profiles are flat and spatial effects are hence negligible.

Knowing the weight functions for all available measurement bins in a measured spectrum, we can write the FM of the diagnostic as the matrix equation

$$S = WF \tag{11.7}$$

which summarizes a discretization of equation (11.6) [959]. S is a vector holding the measurement data of all available diagnostics, F holds the VDF rearranged as column vector, and each line of the matrix W holds a weight function rearranged as a row vector. Given a simulation F and knowing the weight matrix W, we can rapidly compute the corresponding synthetic signals S for all diagnostics.

11.4.4.2. Likelihood. To determine F, given W and S, equation (11.7) has mathematically the same form as any traditional position-space tomography problem. However, velocity-space tomography often requires combinations of entirely different diagnostics or detector types. For practical reasons, to combine measurements with vastly different amplitudes by orders of magnitude, each individual measurement in S and its corresponding weight function is normalized by its uncertainty [960]. This is equivalent to the unnormalized data if likelihoods with the χ^2 -misfit between the data and the forward modeled data weighted with the measurement uncertainty are used as, e.g. for the Gaussian and Student's t-likelihood (equations (11.2) and (11.3)). In the present inverse problem of velocity-space tomography the Gaussian likelihood is employed.

11.4.4.3. Prior information. The amount of measured fast-ion diagnostic data is always small in fusion plasmas due to the limited access to the plasma and the often comparatively low SNR for tomography applications. Furthermore, there are never more than just a few detectors, such that we must always determine the 2D image from just a few projections (medical tomography uses hundreds of projection directions). Due to this limited amount of data and projection directions, the use of prior information for this ill-posed inference problem is often essential to reduce noise fitting and obtain meaningful images

[966], in particular in velocity-space regions observed by only one or two detectors [629, 919, 941, 972].

As in many tomography problems, the problem to find F from W and S is ill-posed and must be regularized with additional (prior) information. The most successful regularization method in velocity-space tomography has been the Tikhonov regularization in which we solve a least-square problem of the form [966]

$$\underset{F}{\text{minimize}} \left\| \begin{pmatrix} W \\ \lambda L \end{pmatrix} F - \begin{pmatrix} S \\ 0 \end{pmatrix} \right\|_2 . \tag{11.8}$$

The upper row of this matrix equation seeks to fit the data whereas the lower row penalizes undesired features of the solution. L is the regularization matrix. Velocity-space tomography usually uses zeroth order Tikhonov regularization, where L is the identity matrix, or first-order Tikhonov regularization, where L is a matrix effecting a gradient. This penalizes large absolute values or large gradients, reflecting our prior information that we believe the VDF to be smooth due to collisions. Equation (11.8) is equivalent to maximizing a posterior pdf given by the product of a Gaussian likelihood with a Gaussian prior pdf with the Tikhonov term in the exponent [919].

λ is the regularization strength that balances data fitting versus the regularization requirement. λ is a free parameter of the problem that must be determined as part of the solution. Various methods to choose λ automatically have been tested, e.g. the L-curve or the generalized cross validation method [966]. However, no method is clearly always advantageous, and they usually produce similar λ's within a factor 10. It is advisable to inspect a range of λ's to make sure that no phenomena are missed.

This is the standard regularization technique in many plasma tomography applications. If no constraints are introduced, the solution is given by the so-called normal equation

$$F_\lambda = \left(W^T W + \lambda^2 L^T L\right)^{0.75[1.0]-1} W^T S. \tag{11.9}$$

We write the index λ in F_λ to emphasize that the solution depends on the regularization strength. However, F_λ computed with the normal equation usually becomes negative in some velocity-space regions, which is unphysical. This can be remedied by further prior information about non-negativity constraints. We are certain that the fast-ion VDF is not negative. This prior can be encoded by solving a least-square problem with non-negativity constraint [966]:

$$\underset{F}{\text{minimize}} \left\| \begin{pmatrix} W \\ \lambda L \end{pmatrix} F - \begin{pmatrix} S \\ 0 \end{pmatrix} \right\|_2 \quad \textit{subjectto} \quad F \geqslant 0. \tag{11.10}$$

One can simply use a non-negative least-squares algorithm [990]. Alternatively, one may penalize negative values and hence force them to become small [967]. The non-negativity constraint also acts as a useful smoothing regularizer since it tends to dampen high-frequency spatial oscillations in the solution. Since the prior information of non-negativity is absolutely certain, we regard the non-negative Tikhonov problem as our standard method.

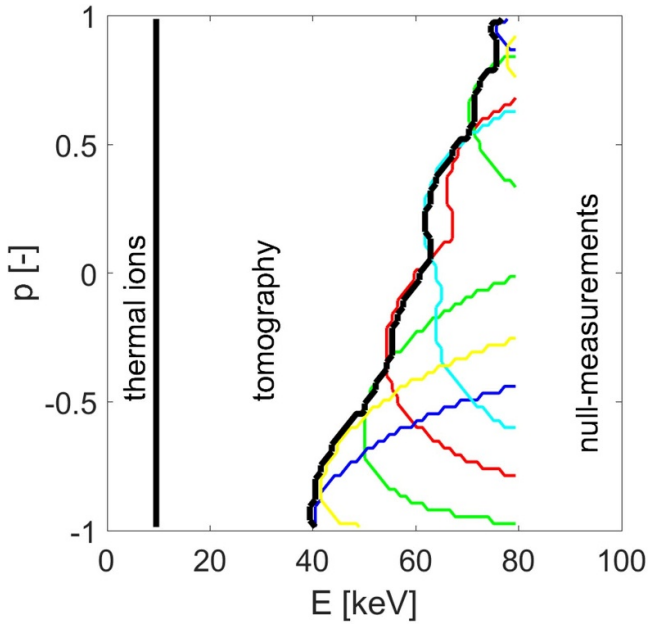

Figure 191. The colored lines are boundaries of weight functions connected to null-measurements. The black line is their envelope, presenting a boundary to the velocity space region empty of fast ions. Reproduced from [966]. © 2016 EURATOM. All rights reserved.

Several other constraints have been implemented in addition to non-negativity: isotropy, monotonicity, or restrictions on the target velocity space to be reconstructed. For example, a minimization problem with non-negativity, restricted velocity space, and monotonicity constraint in energy can be written as

$$\underset{F}{\text{minimize}} \left\| \begin{pmatrix} W \\ \lambda L \end{pmatrix} F - \begin{pmatrix} S \\ 0 \end{pmatrix} \right\|_2$$

$$\textit{subjectto} \begin{cases} F \geqslant 0, \\ F(E_0, p_0) = 0, \\ L_{1,E} F(E_m, p_m) \leqslant 0. \end{cases} \tag{11.11}$$

$F(E_0, p_0) = 0$ is the velocity-space region with negligible fast-ion densities according to null-measurements, as identified by weight functions [966]. A null-measurement in the measured signal S is the measured absence of evidence for fast ions. An example of an experimentally determined null-measurement velocity space region at ASDEX Upgrade is illustrated in figure 191. It is advantageous to use null-measurements as they restrict the velocity space by reducing the number of unknowns [966]. Null-measurements are perhaps more intuitively understood in position-space tomography problems: A ray that misses the object altogether will measure the absence of any material, and thus this part of position-space does not need to be reconstructed.

A monotonicity constraint in one of the coordinate directions, in equation (11.11) the energy, can be advantageous if

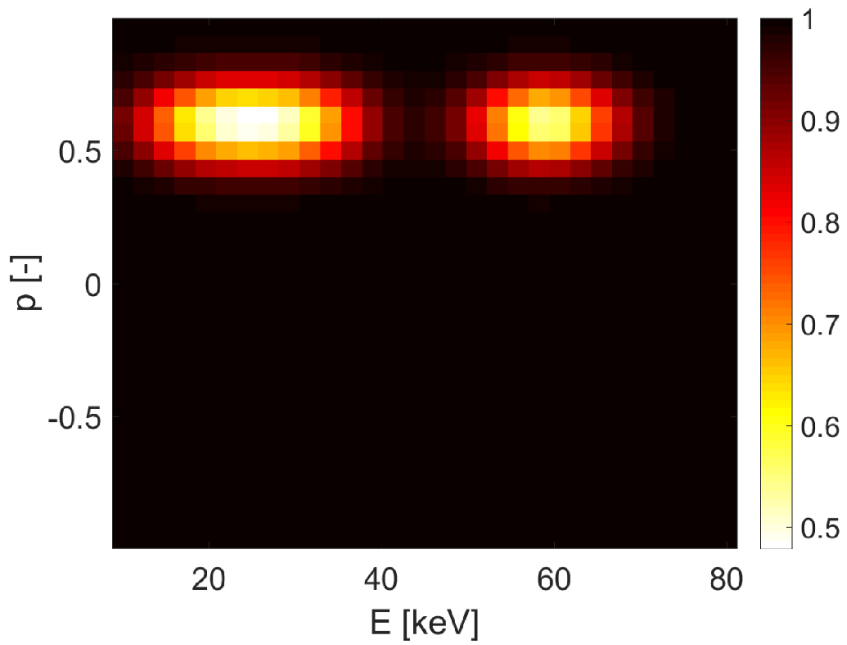

Figure 192. $\kappa_1(E,p)$ encodes the NBI injection energies and pitch. Reproduced from [966]. © 2016 EURATOM. All rights reserved.

one is confident that the distribution function is monotonous [941]. This is likely a good assumption for α -particles or usually ICRF fast-ion tails. However, any local minimum in the distribution function may be physical, which would be missed when this mathematical constraint is enforced.

Prior information may also be encoded by modifying the penalty function to become dependent on the velocity-space coordinates. For example, to promote nearly isotropic solutions, we can penalize gradients in pitch direction much more strongly than in energy direction [919, 991]. This idea is similar to anisotropic regularization along flux surfaces in position-space plasma tomography. We may further enforce isotropy as constraint by assuming the solution to be constant in pitch direction [977].

Another way to modify the penalty function is to introduce a function $\kappa_1(E,p)$ acting with a first-order Tikhonov regularizer or another function $\kappa_0(E,p)$ acting with a zeroth-order Tikhonov regularizer [941, 966, 972, 973]. The minimization problem with a mix of zeroth- and first-order Tikhonov terms is written as

$$\underset{F}{\text{minimize}} \left\| \begin{pmatrix} W \\ \lambda_1 \kappa_1(E,p) L_1 \\ \lambda_0 \kappa_0(E,p) L_0 \end{pmatrix} F - \begin{pmatrix} S \\ 0 \\ 0 \end{pmatrix} \right\|_2 \tag{11.12}$$

$\kappa_1(E,p)$ used with the first-order Tikhonov penalty term $\lambda_1 L_1$ can encode the velocity-space positions of the particle sources of an NBI. The velocity-space positions of the particle sources at the full-, half- and one-third NBI injection energies at a particular pitch are well-known. If $\kappa_1(E,p)$ is chosen to have minima at these well-known peak locations, as illustrated in figure 192, gradients are penalized less in the vicinity of the particle sources than elsewhere [966]. This can allow the formation of peaks in the image but does not force it. Observe that when the gradients are penalized less, a local minimum is equally well formed as a local maximum. Data will usually dictate the formation of a maximum.

Instead of a formulation of null-measurements as a mathematical constraint, we can introduce a zeroth order Tikhonov penalty in the null-measurement velocity space as $\lambda_0 \kappa_0(E,p) L_0$ [972]. This method can be used if we are in doubt if the velocity-space is empty, e.g. if the null-measurements are too uncertain to set the related velocity space to zero. An example of a function κ_0 for a velocity-space tomography problem at the MAST tokamak appears in figure 193.

The increasing penalty with energy reflects our increasing doubt to find ions at increasing energies [972]. If the boundary between the null-measurement velocity space and the target velocity space cannot be found from measurements, we can use a numerical simulation, for example using TRANSP/NUBEAM, to restrict the velocity-space region considered for the inversion [972]. This assumes that there is no acceleration mechanism for fast ions to accelerate them beyond the boundary from the neoclassical simulation.

A recent idea is to expand the VDF into a series of slowing-down distribution functions f_{SD} [973]. The tomography problem is then to determine the coefficients a_i associated with the ith base function. In matrix form this expansion can be written as

$$F = F_{\mathrm{SD}} A \tag{11.13}$$

where the vector A holds the expansion coefficients, and the matrix F_{SD} holds the slowing-down distribution functions rearranged as columns. The forward problem becomes

$$S = W F_{\mathrm{SD}} A. \tag{11.14}$$

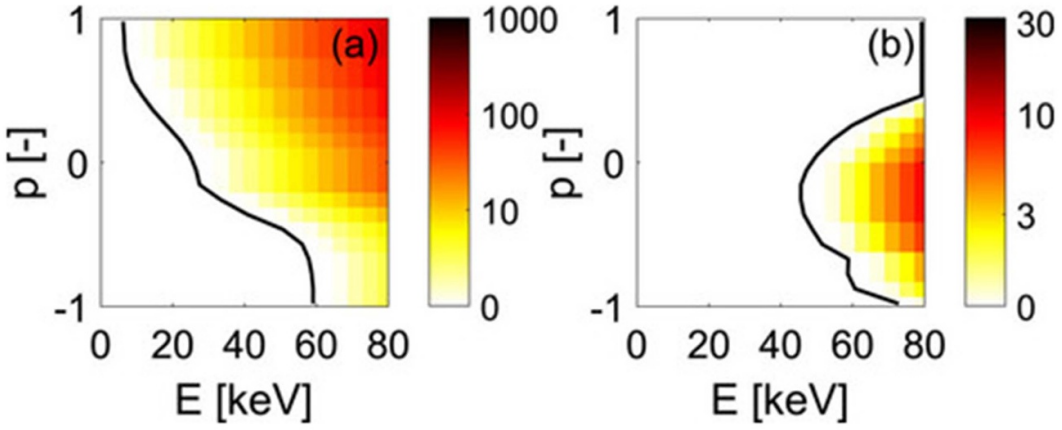

Figure 193. Prior information of unlikely velocity space for velocity-space tomography at MAST according to (*a*) TRANSP/NUBEAM and (*b*) null-measurements. The monotonously growing $\kappa_0(E,p)$ towards higher energies expresses our increasing doubt to find ions. Reprinted from [972], with the permission of AIP Publishing.

Given A and knowing W and F_{SD}, we can calculate the signal S. Calculating A, given S, is an ill-posed problem, as the tomography problem with the expansion. We can then solve a zeroth-order Tikhonov problem in the expansion coefficients A of the form

$$\underset{A}{\text{minimize}} \left\| \begin{pmatrix} WF_{\mathrm{SD}} \\ \lambda I \end{pmatrix} A - \begin{pmatrix} S \\ 0 \end{pmatrix} \right\|_2 . \tag{11.15}$$

If F_{SD} is invertible, we can substitute $A = F_{\mathrm{SD}}^{-1} F$, and equation (11.15) can be equivalently written as

$$\underset{F}{\text{minimize}} \left\| \begin{pmatrix} W \\ \lambda F_{\mathrm{SD}}^{-1} \end{pmatrix} F - \begin{pmatrix} S \\ 0 \end{pmatrix} \right\|_2 \tag{11.16}$$

which shows that the expansion in basis functions can be formulated as a standard Tikhonov problem with ${F_{SD}}^{-1}$ as the regularization matrix L. This allows us to interpret this expansion in slowing-down basis functions as slowing-down regularization. This type of regularization reflects our prior belief that the usual slowing-down physics will in part determine the shape of the distribution function. However, if data dictates otherwise, deviations will appear due to the upper row of equation (11.16).

Lastly, if there is not enough data to do a full tomographic inversion, we can use a numerical simulation F_{sim} as prior information and penalize any deviation from the simulation [966]. The penalty term becomes $\|L(F - Fsim)\|_2$, and we write the problem as

$$\underset{F}{\text{minimize}} \left\| \begin{pmatrix} W \\ \lambda L \end{pmatrix} F - \begin{pmatrix} S \\ \lambda L F_{sim} \end{pmatrix} \right\|_2 . \tag{11.17}$$

Other prior information can still be added in the same way as described. However, observe that this Tikhonov problem pursues a less ambitious goal than a full tomographic inversion due to the use of the simulation. Our goal here is only to identify regions in velocity space where the measurements suggest deviations from $Fsim$ which we can find by successively decreasing λ.

We summarize the different types of prior information that has be used in velocity-space tomography:

- smoothness (zeroth- or first-order Tikhonov)
- non-negativity constraint or penalty for negative values
- restricted velocity space by null-measurements or according to a simulation (constraint)
- unlikely velocity space by null-measurements or according to a simulations (penalty)
- monotonicity constraint
- isotropy constraint or penalty for deviation from isotropy
- beam injection peak locations
- slowing-down physics as regularizer
- numerical simulation as prior.

11.4.4.4. Uncertainties. Sources for uncertainties in the estimated velocity-space distribution can be divided into four categories: (1) uncertainties due to (statistical) measurement noise [960], (2) bias uncertainties in the measurements (systematic uncertainties), (3) uncertainties in the weight matrix W (FM) due to uncertainties in nuisance parameters [970] and (4) bias uncertainties due to the regularization [970] (prior information).

Analytic formulas for estimating uncertainties due to measurement noise and uncertainties in the nuisance parameters can be given for the unconstrained Tikhonov problem [629, 969]. For the constrained Tikhonov problem, these uncertainties can be found by sampling. The fast-ion measurements and the nuisance parameters are sampled from their probability distributions. For each sample we obtain an inversion. Hence we generate a population of N inversions, $F_{\lambda,i}$. Its mean is the best estimate of the velocity-distribution function, and its standard deviation is the uncertainty due to uncertainties in the signal

and the nuisance parameters:

$$\langle F_\lambda \rangle = \frac{1}{N} \sum_i F_{\lambda,i}, \tag{11.18}$$

$$\delta F_\lambda = \sqrt{\frac{1}{N-1} \sum_i \left(F_{\lambda,i} - \langle F_\lambda \rangle\right)^2}. \tag{11.19}$$

Each pixel in the inversion hence has its own uncertainty [969, 970]. The two contributions can also be individually calculated if required.

The computation of bias uncertainties due to regularization and due to systematic errors in the measurements are open problems. Bias uncertainties make it impossible to reconstruct the true distribution function even with perfect, noise-free measurements. To quantify this bias, we would need to know the true solution, which we never do [919].

Systematic bias uncertainties in the measurement data are also notoriously difficult to detect. But such systematic measurement errors can lead to systematic artifacts which can sometimes reveal that some error is present. For example, errors in the calibration of the measurements lead to systematic artifacts that can give clues to what might be wrong.

11.4.4.5. Discussion. To make optimal use of the diagnostic set at ITER or other tokamaks and stellarators, we must develop 1D to 5D inversion tools and be able to use prior information to deal with the sparsity of data on these devices. The methods presented here will allow measurements of α-particle VDFs for energies from 1.7 MeV upwards based on IDA of GRS and CTS [629]. Hence energy spectra in ITER, as requested by the ITER measurement requirements [4], can also be determined. Below α-particle energies of 1.7 MeV, CTS will be the only diagnostic for α-particles. If only one detector is available, 1D inversion techniques need to be used to determine energy spectra, for example by assuming isotropy or near-isotropy as prior [977, 991].

It is now also becoming possible to measure 3D phase-space distribution functions by orbit tomography [992, 993]. This approach is analogous to velocity-space tomography, but in 3D phase-space of constants of motion which covers the entire ion population in the tokamak. Each grid point in 3D phase space corresponds to an orbit in the tokamak. The FM computes the signal generated by fast ions on each orbit. In the tomography problem, the 3D phase-space distribution function of all fast ions in the plasma is inferred from the measurements of all detectors. The computed orbits constitute the prior information for orbit tomography. This approach has worked well at ASDEX Upgrade [994] and is being implemented at JET [993]. It requires many measurements to cover the 3D target phase space, but with appropriate additional prior information it will hopefully be useful at ITER.

Lastly, the presented method to expand the distribution function in 2D base functions is actually not restricted to 2D. The base functions can be 3D, 4D or 5D functions. For non-axisymmetric plasmas, the entire phase-space distribution function is described by 3D in position space and only 2D in velocity space due to the fast gyromotion. 5D tomography would allow IDA of all measurements on stellarators or non-axisymmetric tokamaks.

11.5. Summary

IDA in the framework of BPT provides a method for improved results by a coherent combination of heterogeneous diagnostic measurements with physical prior and modeling information to restrict the parameter space of otherwise ill-posed inversion techniques. The concept of IDA is outlined and contrasted with conventional data analysis. The ingredients of this probabilistic approach is given by forward modeling, suitable likelihood pdfs with comprehensive uncertainty quantification of measurements, probabilistic quantification of prior information, and probabilistic quantification of nuisance parameters and their marginalization. The probabilistic approach enables us to obtain synergistic effects by exploiting the parameter correlation structure and diagnostics interdependencies.

A general purpose IDA toolbox was developed for present and next generation fusion devices and applied to a combination of ITER profile diagnostics. Profile estimation and equilibrium reconstruction is closely correlated and is recommended to be combined in an IDA approach. An example of IDA by velocity-space tomography highlights the benefit of combining various heterogeneous diagnostics with physical prior information including their uncertainties.

Acknowledgment

All the ITPA TG on Diagnostics would like to express his gratitude to the strong and efficient support provided by the Guest Editors in particular by Professor Tony Donné for his very accurate comments and corrections who help us to improve the quality or our paper and to Dr David Campbell for his permanent support in preparing this paper, interacting with us with great efficiency and answering our numerous questions. We thank also very much Dr Axel Jardin for his active help in improving the layout of the document.

Subchapter 1: There are hundreds of contributors to the progress of ITER diagnostic measurement, including the authors of the subchapters that are listed here, but also their predecessors in the ITPA and ITER expert groups. The authors wish to acknowledge them all and those who helped with the editing of this chapter by providing internal and external critical review and Radija Bouhamou and Masanari Hosokawa for the maintenance of the measurement requirement and ITPA databases, respectively. For the magnetics section, the work reviewed is the work of the authors of [8–43, 395]. The views expressed in this paper do not necessarily reflect the views of the ITER Organization.

Subchapter 2: The work leading to this publication has been funded partially by Fusion for Energy under the Contract F4E-FPA-327. This publication reflects the views only of the author

and Fusion for Energy cannot be held responsible for any use which may be made of the information contained therein.

Subchapter 3: The work leading to this publication was initiated by the ITPA Diagnostic Group. This publication reflects the views of the authors only, and the ITER Organization is not responsible for any use that may be made of the information contained therein.

Subchapter 4: G. I. Pokol and O. Asztalos acknowledge the support of the National Research, Development and Innovation Office (NKFIH) Grant FK132134." The views and opinions expressed herein do not necessarily reflect those of the ITER Organization. J. Ko acknowledges the support from the Korean Ministry of Science and ICT under KFE R&D Program (Grant No. KFE-EN2301-14). Part of this work has been carried out within the framework of the EUROfusion Consortium, funded by the European Union via the Euratom Research and Training Programme (Grant Agreement No. 101052200—EUROfusion). Views and opinions expressed are however those of the author(s) only and do not necessarily reflect those of the European Union or the European Commission. Neither the European Union nor the European Commission can be held responsible for them. Parts of this work (the core-CXRS section) were supported by Fusion for Energy under the Framework Partnership Agreement F4E-FPA-408 (DG). The views and opinions expressed reflect the authors' views. Fusion for Energy is not liable for any use that may be made of the information contained herein.

Subchapter 5: The authors would like to thank the ITPA TG Diagnostic for his permanent support and fruitfull discussion.

Subchapter 6: This work has been carried out within the framework of the EUROfusion Consortium, funded by the European Union via the Euratom Research and Training Programme (Grant Agreement No 101052200—EUROfusion) and from the EPSRC [Grant Numbers EP/W006839/1Views and opinions expressed are however those of the author(s) only and do not necessarily reflect those of the European Union or the European Commission. Neither the European Union nor the European Commission can be held responsible for them.

This report supported in part Divertor Thomson scattering by Rosatom (contract—№ Н.4а.241.19.19.1009) and by Ioffe Institute (Russian Federation state funding assignments 0034-2019-0001 and 0040-2019-0023) was prepared as an account of work for the ITER Organization.

Work supported by the U.S. DOE under Contracts DE-FC02-04ER54698 and No. DE-AC02-09CH11466 with Princeton University. All U.S. activities are managed by the U.S. ITER Project Office, hosted by Oak Ridge National Laboratory with partner labs Princeton Plasma Physics Laboratory and Savannah River National Laboratory. The project is being accomplished through a collaboration of DOE Laboratories, universities and industry. This work is supported by funds from Grant-in-Aid for Young Scientists (B) (Grant No. 20760584) and by NIFS ULHH027. The views and opinions expressed herein do not necessarily reflect those of the ITER Organization.

The views and opinions expressed herein do not necessarily reflect those of the ITER Organization.

Subchapter 7: *Acknowledgements for ECE section:* Work of WLR and JPZ supported by the U.S. DOE under Contract No. DE-AC02-09CH11466 with Princeton University. All U.S. activities are managed by the U.S. ITER Project Office, hosted by Oak Ridge National Laboratory with partner labs Princeton Plasma Physics Laboratory and Savannah River National Laboratory. The project is being accomplished through a collaboration of DOE Laboratories, universities and industry. The views and opinions expressed herein do not necessarily reflect those of the ITER Organization. Acknowledgements for CTS section: The work leading to this publication has been funded partially by Fusion for Energy under the Framework Partnership Agreement F4E-FPA-393. This publication reflects the views only of the author, and Fusion for Energy cannot be held responsible for any use which may be made of the information contained therein.

Subchapter 8: Authors would like to thank Tonny Done and George Vayakis for carefull proof reading of the paper and for numerous suggestions which led to improvement of the resulting paper from the view point of scientific content as well as clarity of its presentation. Authors are also gratefull to Didier Mazon for his continuous support and for providing necessary organizational momentum along the paper preparation. The paper presents an overview of a rather extensive set of experimental results and research effort which was possible thanks to a dedication and enthusiasm of a scientific community engaged in the investigation of radiation effects in ITER diagnostic components. We would like to thank research and operation teams of SCK•CEN, Mol, Belgium and CVŘ, Řež, Czech Republic where the most of the irradiation tests presented within this paper were conducted.

Subchapter 9: The authors are grateful to all colleagues who helped in compiling this paper. Specifically, we thank Dr Andrey Alekseev, Dr Ilya Orlovsky for graphic material on Hα diagnostic and Dr Yury Kapustin for his help in endorsing Figure 11. We are grateful to Dr Felix Klein and Dr Marcin Rasinski for performing analyses on diagnostic mirrors and Dr Arkady Kreter for reference plasma experiments, Dr Philippe Mertens for his enthusiastic advice on content. The author team acknowledges constant help and support from ITER Organization and from the ITPA. The experimental work was in part supported by the ITER Organization via purchase order 4100006576. Investigations were also partly supported by the Ministry of Science and ICT of Korea, through the ITER project contract RS-2022-00154842. The views and opinions expressed herein do not necessarily reflect those of the ITER Organization. In part, this work has been carried out within the framework of the EUROfusion Consortium,

funded by the European Union via the Euratom Research and Training Programme (Grant Agreement No 101052200 (EUROfusion). Views and opinions expressed are, however, those of the author(s) only and do not necessarily reflect those of the European Union or the European Commission. Neither the European Union nor the European Commission can be held responsible for them. This work was supported by the Swiss State Secretariat for Education, Research, and Innovation (SERI) under contract number 22.00424. Several studies reported in the contribution were supported by RSF grant No 22-12-00360 of the Russian Federation.

Subchapter 10: Former TU/e students Jochem Manders (presently at VDL ETG) and Mustahsan Majeed (presently at ASML) are kindly acknowledged for their work.

Subchapter 11: The authors thank S. Pinches from the ITER organization, K. Fujii from the Kyoto University and D. Mazon from CEA Cadarache for promoting and supporting this new WG.

This work has been carried out within the framework of the EUROfusion Consortium, funded by the European Union via the Euratom Research and Training Programme (Grant Agreement No 101052200—EUROfusion). Views and opinions expressed are however those of the author(s) only and do not necessarily reflect those of the European Union or the European Commission. Neither the European Union nor the European Commission can be held responsible for them.

ORCID iDs

D. Mazon 0000-0001-5560-2277
G. Yun 0000-0002-1880-5865
M.H. Aumeunier 0009-0009-6207-5079
A. Bultel 0000-0003-4792-9995
C. Klepper 0000-0001-9107-8337
D. Rasmussen 0000-0003-1949-3549
S. Oh 0000-0003-1233-676X
M. Scholz 0000-0002-7330-1782
B. Esposito 0000-0002-0005-5680
B. Coriton 0000-0002-0067-967X

References

[1] Stott P.E., Gorini G. and Sindoni E. (eds) 1995 *Diagnostics for Experimental Fusion Reactors* (Plenum Press)
[2] Stott P.E., Gorini G., Prandoni P. and Sindoni E. (eds) 1998 *Diagnostics for Experimental Fusion Reactors 2* (Plenum Press)
[3] ITER Physics Expert Group on Diagnostics and ITER Physics Basis Editors 1999 *Nucl. Fusion* **39** 2541
[4] Donné A.J.H. *et al* 2007 *Nucl. Fusion* **47** S337
[5] ITER Organization 2018 ITER research plan within the staged approach (Level III—final version) *Report ITR*-24-005 (available at: www.iter.org/technical-reports)
[6] Vayakis G., Hodgson E.R., Voitsenya V. and Walker C.I. 2008 *Fusion Sci. Technol.* **53** 699
[7] Vayakis G. *et al* 2012 *Rev. Sci. Instrum.* **83** 10D712
[8] Chavan R. *et al* 2009 *Fusion Eng. Des.* **84** 295–9
[9] Testa D. *et al* 2010 *IEEE Trans. Plasma Sci.* **38** 284–94
[10] Neto A.C. *et al* 2015 *Fusion Eng. Des.* **96–97** 887–90
[11] Werner A. 2006 *Rev. Sci. Instrum.* **77** 10E307
[12] Batista A.J.N. *et al* 2017 *Fusion Eng. Des.* **123** 1025–8
[13] Vayakis G. *et al* 2011 *J. Nucl. Mater.* **417** 780–6
[14] Chitarin G., Grando L., Peruzzo S. and Taccon C. 2007 *Fusion Eng. Des.* **82** 1341–7
[15] Peruzzo S. *et al* 2016 *IEEE Trans. Plasma Sci.* **44** 1704–10
[16] Ma Y., Vayakis G., Carmona J.-M., Pascual Q., Walton R. and Walsh M. 2019 *Fusion Eng. Des.* **146** 887–93
[17] Marin A., Bertolini C., Lucca F., Ma Y., Pagani I., Vayakis G., Viganò F. and Walsh M. 2019 *Fusion Eng. Des.* **146** 2644–8
[18] Adaikkan M., Ma Y., Walach U., Bochard M., Bechtold F., Vayakis G., Walsh M., Lino M.P.C. and Counsell G. 2022 *Fusion Eng. Des.* **184** 113316
[19] Moreau P. *et al* 2015 *Fusion Eng. Des.* **96–97** 878–81
[20] Quercia A., Albanese R., Fresa R., Minucci S., Arshad S. and Vayakis G. 2017 *Nucl. Fusion* **57** 126049
[21] Moreau P. *et al* 2013 *Fusion Eng. Des.* **88** 1165–9
[22] Ma Y. *et al* 2023 *Fusion Eng. Des.* **196** 113984
[23] Wuilpart M., Vanus B., Andrasan A., Gusarov A., Moreau P. and Mégret P. 2016 *Proc. SPIE* **9916** 99160L
[24] Chengshuo S., Danisi A., Vayakis G., Ding Y. and Walsh M. *Fusion Eng. Des.* submitted
[25] Gusarov A., Leysen W., Wuilpart M. and Mégret P. 2018 *Fusion Eng. Des.* **136** 477–80
[26] Gusarov A., Leysen W., Kim S.M., Dandu P., Wuilpart M., Danisis A., Barbero Soto J.L. and Vayakis G. 2023 *Fusion Eng. Des.* **192** 113626
[27] Huang Y. *et al* 2020 *Nucl. Fusion* **60** 076023
[28] Huang Y., Mele A., Luo Z., Mattei M., Pironti A., Xiao B. and Yuan Q. 2022 *Nucl. Fusion* **62** 086010
[29] Orrico C.A., Ravensbergen T., Pitts R.A., Bonnin X., Kaveeva E., Park J.S., Rozhansky V., Senichenkov I., Watts C. and de Baar M. 2023 *Nucl. Fusion* **63** 086002
[30] Clough M., Casal N., Suarez Diaz A., Vayakis G. and Walsh M. 2014 Engineering challenges and solutions for the ITER magnetic diagnostics flux loops *Proc. European Nuclear Conf.—ENC 2014* (*Marseille, France 11–14 May 2014*) p 1238 (available at: https://old.euronuclear.org/events/enc/enc2014/index.htm)
[31] Arpaia P., Buzio M., Di Capua V., Grassini S., Parvis M. and Pentella M. 2021 *Sensors* **22** 182
[32] Ambrosino R., De Tommasi G., Mattei M. and Pironti A. 2015 Model based optimization and estimation of the field map during the breakdown phase in the ITER tokamak *2015 IEEE Conf. on Control Applications (CCA) (Sydney, 21–23 September 2015)* (https://doi.org/10.1109/CCA.2015.7320789)
[33] Moreau P., Le-Luyer A., Hertout P., Saint-Laurent F., Zwingmann W., Moret J.M. and Martin Y. 2009 *Fusion Eng. Des.* **84** 1344–50
[34] Bolshakova I., Duran I., Holyaka R., Hristoforou E. and Marusenkov A. 2007 *Sens. Lett.* **5** 283–8
[35] Ďuran I., Bolshakova I., Viererbl L., Sentkerestiová J., Holyaka R., Lahodová Z. and Bém P. 2010 *Rev. Sci. Instrum.* **81** 10E122
[36] Kocan M. *et al* 2017 *Fusion Eng. Des.* **123** 936–9
[37] Entler S., Duran I., Kocan M., Vayakis G., Sladek P., Grover O., Sebek J. and Vyborny K. 2021 *Fusion Eng. Des.* **168** 112398
[38] Fresa R. *et al* 2015 *Fusion Eng. Des.* **100** 133–41
[39] Ma Y. *et al* 2016 *Fusion Eng. Des.* **112** 594–612
[40] Alessi E., Cavinato M. and Chitarin G. 2008 *Rev. Sci. Instrum.* **79** 10F332
[41] Peruzzo S., Bettini P., Marconato N., Soppelsa A., Albanese R., Caputano M., Mattei M., Rubinacci G. and Villone F. 2011 Integrated procedure for halo current

reconstruction in ITER *2011 IEEE/NPSS 24th Symp. on Fusion Engineering (Chicago, 26–30 June 2011)* (https://doi.org/10.1109/SOFE.2011.6052248)
[42] Peruzzo S., Albanese R., Bettini P., Caputano M., Marconato N., Mattei M., Rubinacci G., Soppelsa A. and Villone F. 2013 *IEEE Trans. Plasma Sci.* **41** 257–62
[43] Donné A.J.H. and Costley A. Fusion energy 2008, key R&D activities for ITER diagnostics, *(Proc. 22nd Int. Conf. Geneva, 2008)* (Vienna: IAEA) CD-ROM file [IT/P6-20] (available at: https://nucleus.iaea.org/sites/fusionportal/Pages/fec-landing.aspx)
[44] Counsell G., de Vere A.P.C., St. J. Braithwaite N., Hillier S. and Bjorkman P. 2006 *Rev. Sci. Instrum.* **77** 093501
[45] Kawano Y., Brower D.L. and Vayakis G. 2016, Overview of ITPA R&D activities for improvement of ITER diagnostic performance *Proc. 26th IAEA Int. Conf. on Fusion Energy* (*Kyoto*, *2016*) (available at: https://nucleus.iaea.org/sites/fusionportal/Pages/fec-landing.aspx) p FIP–P4–11
[46] Brower D.L., Mazon D. and Vayakis G. Overview of ITPA diagnostic topical group activities in support of ITER *Preprint: 2018 IAEA Fusion Energy Conf.* (*Gandhinagar, 22–27 October 2018*) p FIP–P1–15 (available at: https://nucleus.iaea.org/sites/fusionportal/Pages/fec-landing.aspx)
[47] Boivin R.L. *et al* Fusion energy 2010, R&D ITPA activities in support of optimizing ITER diagnostic performance *Proc. 23rd Int. Conf. (Daejeon, Republic of Korea, 10–16 October 2010) CD-ROM file [ITR/P1-02]* (IAEA) (available at: https://nucleus.iaea.org/sites/fusionportal/Pages/fec-landing.aspx)
[48] Kawano Y., Zoletnik S., Park H.K. and Vayakis G. 2014 Overview of ITPA R&D activities for optimization of ITER diagnostic performance *FIP-P4-5, Paper Presented at 25th IAEA Int. Conf. on Fusion Energy (St Petersburg, Russian Federation, 13–18 October 2014)* (available at: https://nucleus.iaea.org/sites/fusionportal/Pages/fec-landing.aspx)
[49] De La Luna E., Krivenski V., Giruzzi G., Gowers C., Prentice R., Travere J.M. and Zerbini M. 2003 *Rev. Sci. Instrum.* **74** 1414–20
[50] White A.E. *et al* 2012 *Nucl. Fusion* **52** 063021
[51] Hawke J., Scannell R., Maslov M. and Migozzi J.B. 2013 *Rev. Sci. Instrum.* **84** 103507
[52] Fontana M. *et al* 2023 *EPJ Web Conf.* **277** 03006
[53] Pinches S.D. *et al* 2021 Fusion energy 2020, integrated modelling & analysis suite: developments to address ITER needs *Proc. 28th Int. Conf., CD-ROM file [TH/P2-22] (Daejeon) (Virtual Conference, 10–15 May 2021)* (available at: https://nucleus.iaea.org/sites/fusionportal/Pages/fec-landing.aspx)
[54] Choi C.-H., Tesini A., Subramanian R., Rolfe A., Mills S., Scott R., Froud T., Haist B. and McCarron E. 2015 *Fusion Eng. Des.* **98–99** 1448–52
[55] Garcia-Munoz M. *et al* 2016 *Rev. Sci. Instrum.* **87** 11D829
[56] Loarte A. 2020 Required R&D in existing fusion facilities to support the ITER research plan *Report ITR-20-008* (available at: www.iter.org/technical-reports)
[57] Reichle R. *et al* 2021 *SRD-55 (Diagnostics) from DOORS v. 5.5 Revision F* (Private communication)
[58] Litaudon X. *et al* 2017 *Nucl. Fusion* **57** 102001
[59] Linke J., Du J., Loewenhoff T., Pintsuk G., Spilker B., Steudel I. and Wirtz M. 2019 *Matter Radiat. Extremes* **4** 056201
[60] Humphreys D. *et al* 2015 *Phys. Plasmas* **22** 021806
[61] Gonzalez de Vicente S.M. *et al* 2022 *Nucl. Fusion* **62** 085001
[62] Bountin D.A. and Shiplyuk M.A. 2019 *J. Phys.: Conf. Ser.* **1359** 012089
[63] Reichle R. *et al* 2015 *J. Nucl. Mater.* **463** 180
[64] Kajita S. *et al* 2013 *Plasma Phys. Control. Fusion* **55** 085020
[65] Shimada M. *et al* 2013 *J. Nucl. Mater.* **438** S996
[66] Langley S.P. 1880 *The Bolometer* (American Metrological Society)
[67] Karr H.J., Knapp E.A. and Osher J.E. 1961 *Phys. Fluids* **4** 424
[68] Mast K.F., Vallet J.C., Andelfinger C., Betzler P., Kraus H. and Schramm G. 1991 *Rev. Sci. Instrum.* **62** 744
[69] Ingesson L.C., Alper B., Peterson B.J. and Vallet J.-C. 2008 *Fusion Sci. Technol.* **53** 528
[70] Leonard A.W., Meyer W.H., Geer B., Behne D.M. and Hill D.N. 1995 *Rev. Sci. Instrum.* **66** 1201
[71] Meister H., Kannamüller M., Koll J., Pathak A., Penzel F., Trautmann T., Detemple P., Schmitt S. and Langer H. 2012 *Rev. Sci. Instrum.* **83** 10D724
[72] Meister H. *et al* 2019 *J. Instrum.* **14** C10004
[73] Peterson B.J. 2000 *Rev. Sci. Instrum.* **71** 3696
[74] Peterson B.J., Kostrioukov A.Y., Ashikawa N., Osakabe M. and Sudo S. 2003 *Rev. Sci. Instrum.* **74** 2040–3
[75] Reinke M.L., Terry J.L., van Eden G.G., Peterson B.J., Mukai K., Gray T.K. and Stratton B.C. 2018 *Rev. Sci. Instrum.* **89** 103507
[76] Giannone L., Mast K.F. and Schubert M. 2002 *Rev. Sci. Instrum.* **73** 3205
[77] Mukai K., Peterson B.J., Pandya S.N. and Sano R. 2014 *Rev. Sci. Instrum.* **85** 11E435
[78] Mukai K., Abe R., Peterson B.J. and Takayama S. 2018 *Rev. Sci. Instrum.* **89** 10E114
[79] Pandya S.N., Peterson B.J., Mukai K., Sano R., Enokuchi A. and Takeyama N. 2014 *Rev. Sci. Instrum.* **85** 073107
[80] Peterson B.J., Parchamy H., Ashikawa N., Kawashima H., Konoshima S., Kostryukov A.Y., Miroshnikov I.V., Seo D.C. and Omori T. 2008 *Rev. Sci. Instrum.* **79** 10E301
[81] Peterson B.J., Oh S., Seo D., Jang J., Park J.S., Mukai K. and Choe W. 2018 *Rev. Sci. Instrum.* **89** 10E115
[82] Federici F., Reinke M.L., Lipschultz B., Thornton A.J., Harrison J.R., Lovell J.J. and Bernert M. (MAST Upgrade Team) 2023 *Rev. Sci. Instrum.* **94** 033502
[83] Pandya S.N., Peterson B.J., Sano R., Mukai K., Drapiko E.A., Alekseyev A.G., Akiyama T., Itomi M. and Watanabe T. 2014 *Rev. Sci. Instrum.* **85** 054902
[84] Drapiko E.A., Peterson B.J., Alekseyev A. and Seo D.C. 2010 *Rev. Sci. Instrum.* **81** 10E116
[85] Parchamy H., Peterson B.J., Konoshima S., Hayashi H., Seo D.C. and Ashikawa N. (the JT-60U Team) 2006 *Rev. Sci. Instrum.* **77** 10E515
[86] Araghy H.P., Peterson B.J., Hayashi H., Konoshima S., Ashikawa N. and Seo D.C. (the JT-60U TEAM) 2007 *Plasma Fusion Res.* **2** S1116
[87] Peterson B.J., Osakabe M., Shoji M. and Ashikawa N. 2001 *Rev. Sci. Instrum.* **72** 923–6
[88] Pandya S.N. *et al* 2016 *Nucl. Fusion* **56** 046002
[89] Sano R., Peterson B.J., Teranishi M., Iwama N., Kobayashi M., Mukai K. and Pandya S.N. 2016 *Rev. Sci. Instrum.* **87** 053502
[90] Peterson B.J., Konoshima S., Parchamy H., Kaneko M., Omori T., Seo D.C., Ashikawa N. and Sukegawa A. (the JT-60U Team) 2007 *J. Nucl. Mater.* **363–365** 412–5
[91] Liu Y., Tamura N., Peterson B.J., Iwama N. and Konoshima S. 2007 *Plasma Fusion Res.* **2** S1124
[92] Jang J., Choe W., Peterson B.J., Seo D.C., Mukai K., Sano R., Oh S., Hong S.H., Hong J. and Lee H.Y. 2018 *Curr. Appl. Phys.* **18** 461
[93] Peterson B.J., Reichle R., Pandya S., O'Mullane M.G. and Mukai K. 2021 *Rev. Sci. Instrum.* **92** 043534
[94] Peterson B.J., Nishitani T., Reichle R., Munechika K., O'Mullane M.G. and Mukai K. 2022 *J. Instrum.* **17** P06034
[95] Seon C.R. *et al* 2017 *Rev. Sci. Instrum.* **88** 083511

[96] Seon C.R. *et al* 2017 *Eur. Phys. J. D* **71** 313
[97] Seon C.R., Jeon J.S., Cheon M.S., Pak S., Lee H.G., Bernascolle P. and Barnsleym R. 2016 *Fusion Eng. Des.* **109–111** 656–60
[98] Biel W. and Bertschinger G. (the TEXTOR Team) 2004 *Rev. Sci. Instrum.* **75** 2471
[99] Lauro-Taroni L. *et al* 1994 *21st EPS Conf. on controlled fusion, plasma physics* (Montpellier) p 102 (available at: https://cds.cern.ch/record/276664?ln=zh_CN)
[100] Bonnin X., Dekeyser W., Pitts R., Coster D., Voskoboynikov S. and Wiesen S. 2016 *Plasma Fusion Res.* **11** 1403102
[101] Barnsley R., Coffey I.H., Lucock R. and Stamp M.F. 2003 *Rev. Sci. Instrum.* **74** 1969
[102] Ebisawa K., Ando T., Costley A.E., Janeschitz G., Martin E. and Sugie T. 1999 *Rev. Sci. Instrum.* **70** 328
[103] Morita S. *et al* 2013 *AIP Conf. Proc.* **1545** 143
[104] Morita S., Dong C.F., Kato D., Liu Y., Zhang L., Cui Z.Y., Goto M., Kawamoto Y., Murakami I. and Oishi T. 2019 *J. Phys.: Conf. Ser.* **1289** 012005
[105] Miziolek A.W., Palleschi V. and Schechter I. 2006 *Laser-Induced Breakdown Spectroscopy (LIBS) Fundamentals and Applications* (Cambridge University Press)
[106] Li C., Feng C.-L., Oderji H.Y., Luo G.-N. and Ding H.-B. 2016 *Front. Phys.* **11** 114214
[107] Maurya G.S., Marín-Roldán A., Veis P., Pathak A.K. and Sen P. 2020 *J. Nucl. Mater.* **541** 152417
[108] Hahn D.W. and Omenetto N. 2012 *Appl. Spectrosc.* **66** 347–419
[109] Windom B.C. and Hahn D.W. 2009 *J. Anal. At. Spectrom.* **24** 1665–75
[110] Elhassan A., Cristoforetti G., Legnaioli S., Palleschi V., Salvetti A., Tognoni E., Ingo G. and Harith M.A. 2007 LIBS calibration curves and determination of limits of detection (LOD) in single and double pulse configuration for quantitative LIBS analysis of bronzes *Proc. Int. Conf. on Conservation Strategies for Saving Indoor Metallic Collections* (*Cairo, Egypt, 25 February–1 March 2007*) pp 72–76 (available at: https://www.academia.edu/download/35321908/ARGYROPOULOS_FINAL.pdf#page=72)
[111] Hermann J., Axente E., Pelascini F. and Craciun V. 2009 *Anal. Chem.* **91** 2544–50
[112] Semerok A. and Grisolia C. 2013 *Nucl. Instrum. Methods Phys. Res. A* **720** 31
[113] Mercadier L., Semerok A., Kizub P.A., Leontyev A.V., Hermann J., Grisolia C. and Thro P.-Y. 2011 *J. Nucl. Mater.* **414** 485
[114] Gasior P., Bieda M., Kubkowska M., Neu R. and Wolowski J. 2011 *Fusion Eng. Des.* **86** 1239–42
[115] Zhao D. *et al* (W7-X team) 2022 *Phys. Scr.* **97** 024005
[116] Veis P., Marín-Roldán A., Dwivedi V., Karhunen J., Paris P., Jõgi I., Porosnicu C., Lungu C.P., Nemanic V. and Hakola A. 2020 *Phys. Scr.* **2020** 014073
[117] Oelmann J., Würst E., Sergienko G. and Brezinsek S. 2021 *Phys. Scr.* **96** 124064
[118] Weiss Z. 2021 *Hydrogen* **2** 225–45
[119] Semerok A., L'Hermite D., Weulersse J.-M., Lacour J.-L., Cheymol G., Kempenaars M., Bekris N. and Grisolia C. 2016 *Spectrochim. Acta B* **123** 121–8
[120] Shaw G., Bannister M., Biewer T.M., Martin M.Z., Meyer F. and Wirth B.D. 2018 *Appl. Surf. Sci.* **427** 695–703
[121] Favre A., Morel V., Bultel A., Godard G., Idlahcen S. and Grisolia C. 2021 *Spectrochim. Acta B* **175** 106011
[122] Favre *et al* 2023 *J. Nucl. Mater.* submitted
[123] Gasior P., Gromelski W., Kastek M. and Kwasnik A. 2023 *Spectrochim. Acta B* **199** 106576
[124] Liu P. *et al* 2018 *Plasma Phys. Control. Fusion* **60** 085019
[125] Hu Z. *et al* 2017 *Plasma Sci. Technol.* **19** 025502
[126] Almaviva S. *et al* 2020 *Fusion Eng. Des.* **157** 111685
[127] Sankhé M.L. *et al Fusion Eng. Des.* submitted
[128] Klepper C.C. *et al* 2022 *IEEE Trans. Plasma Sci.* **50** 4970–9
[129] Klepper C.C. *et al* 2020 *Nucl. Fusion* **60** 016021
[130] ITER Research Plan within the Staged Approach (Level III—Provisional Version) 2018 (available at: www.iter.org/sites/default/files/media/2024-04/iter_research_plan_within_the_staged_approach_leviii_provversion.pdf)
[131] Aumeunier M.-H., Travere J.-M., Loarer T. and Benoit F. 2011 *IEEE Trans. Plasma Sci.* **39** 3014–5
[132] Aumeunier M.-H., Firdaouss M., Travère J.-M., Loarer T., Gauthier E., Martin V., Chabaud D. and Humbert E. 2012 *Rev. Sci. Instrum.* **83** 10D522
[133] Aumeunier M.-H. *et al* 2021 *Nucl. Mater. Energy* **26** 100879
[134] Aumeunier M.-H., Travere J.-M., Reichle R., Loarer T., Gauthier E., Chabaud D. and Humbert E. 2012 *IEEE Trans. Plasma Sci.* **40** 753–60
[135] Carr M., Meakins A., Bernert M., David P., Giroud C., Harrison J., Henderson S., Lipschultz B. and Reimold F. 2018 *Rev. Sci. Instrum.* **89** 083506
[136] Carr M. *et al* 2019 *Rev. Sci. Instrum.* **90** 043504
[137] Oh S.T. *et al* Ray trace study for visible/IR system in KSTAR *ITPA DIAG TG Meeting* (*Canberra, Australia, 8–11 April 2019*) (available at: https://itpa2019.anu.edu.au/)
[138] Ben Yaala M., Aumeunier M.-H., Steiner R., Schönenberger M., Martin C., Le Bohec M., Talatizi C., Marot L. and Meyer E. 2021 *Rev. Sci. Instrum.* **92** 093501
[139] Gaspar J. *et al* 2019 *Fusion Eng. Des.* **146** 757–60
[140] Gaspar J. *et al* 2020 *Nucl. Mater. Energy* **25** 100851
[141] Talatizi C., Aumeunier M.-H., Rigollet F., Le Bohec M., Gérardin J., Gaspar J., Le Niliot C. and Herrmann A. 2020 *Fusion Eng. Des.* **159** 111867
[142] Talatizi C. *et al* 2021 *Fusion Eng. Des.* **171** 112570
[143] Aumeunier M.-H., Le Bohec M., Brunet R., Juven A., Adel M., Artusi X., Miorelli R., Reboud C. and Rigollet F. 2022 *Nucl. Mater. Energy* **33** 101231
[144] Marcus F.B. *et al* 1998 *Diagnostics for Experimental Thermonuclear Fusion Reactor 2* (Plenum) p 419
[145] Krasilnikov A.V., Walker C.I., Kashchuk Y.A. and Prosvirin D.V. 2004 *Instrum. Exp. Technol.* **47** 5
[146] Nishitani T. *et al* 1998 *Diagnostics for Experimental Thermonuclear Fusion Reactor 2* (Plenum) p 491
[147] Asai K., Iguchi T., Watanabe K., Kawarabayashi J., Nishitani T. and Walker C.I. 2005 *Rev. Sci. Instrum.* **75** 3537
[148] Kaschuck Y.A., Gladush G.G., Krasilnikov A.V., Rodionov N.B., Frunze V.V. and Walker C.I. 2003 *Fusion Sci. Technol.* **43** 1
[149] Scholz M. *et al* 2019 *Nucl. Fusion* **59** 065001
[150] Kallne J., Ballabio L., Frenje J., Conroy S., Ericsson G., Tardocchi M., Traneus E. and Gorini G. 2000 *Phys. Rev. Lett.* **85** 1246
[151] Kiptily V.G. *et al* 2002 *Nucl. Fusion* **42** 999
[152] Sjostrand H. *et al* 2009 *Fusion Sci. Technol.* **57** 162
[153] Chugunov I., Shevelev A.E., Gin D.B., Naidenov V.O., Kiptily V., Edlington T. and Syme B. 2008 *Instrum. Exp. Technol.* **51** 166
[154] Tardocchi M. *et al* 2011 *Phys. Rev. Lett.* **107** 205002
[155] The MCNP Code, Los Alamos National Laboratory (available at: https://mcnp.lanl.gov)
[156] Nocente M. *et al* 2017 *Nucl. Fusion* **57** 076016
[157] Garcia-Munoz M., Fahrbach H.-U. and Zohm H. 2009 *Rev. Sci. Instrum.* **80** 053503
[158] Zweben S.J., Boivin R.L., Diesso M., Hayes S., Hendel H.W., Park H. and Strachan J.D. 1990 *Nucl. Fusion* **30** 1551
[159] Darrow D.S., Herrmann H.W., Johnson D.W., Marsala R.J., Palladino R.W., Zweben S.J. and Tuszewski M. 1995 *Rev. Sci. Instrum.* **66** 476

[160] Isobe M. *et al* 1999 *Rev. Sci. Instrum.* **70** 827
[161] Darrow D.S., Isobe M., Kondo T. and Sasao M. 1999 *Rev. Sci. Instrum.* **70** 838
[162] Darrow D.S., Werner A. and Weller A. 2001 *Rev. Sci. Instrum.* **72** 2936
[163] Werner A., Weller A. and Darrow D.S. 2001 *Rev. Sci. Instrum.* **72** 780
[164] Nishiura M., Isobe M., Saida T., Sasao M. and Darrow D.S. 2004 *Rev. Sci. Instrum.* **75** 3646
[165] Baeumel S. *et al* 2004 *Rev. Sci. Instrum.* **75** 3563
[166] Darrow D.S. 2008 *Rev. Sci. Instrum.* **79** 023502
[167] Rivero-Rodriguez J.F. *et al* 2018 *Rev. Sci. Instrum.* **89** 10I112
[168] Gonzalez-Martin J. *et al* 2021 *Rev. Sci. Instrum.* **92** 053538
[169] ITER_D_VK4MN8 v3.3, 5.5.P01.EU.15 Annex B for 55.B1 RNC (Private Communication)
[170] Dongiovanni D., Esposito B., Marocco D. and Marzullo D. 2018 *Fusion Eng. Des.* **137** 378
[171] Centioli C. *et al* 2018 *IEEE Trans. Nucl. Sci.* **65** 2046
[172] Baccaro S. *et al* 2018 *IEEE Trans. Nucl. Sci.* **65** 2046
[173] Pompili F. *et al* 2019 *Nucl. Instrum. Methods Phys. Res.* **A936** 62
[174] Passeri M., Pompili F., Esposito B., Pillon M., Angelone M., Marocco D., Pagano G., Podda S. and Riva M. 2021 *Nucl. Instrum. Methods Phys. Res. A* **1010** 165574
[175] Ducasse Q., Esposito B., Zimbal A., Riva M., Marocco D. and Podda S. 2021 *Nucl. Instrum. Methods Phys. Res. A* **998** 165168
[176] Passeri M., Carnevale D., Esposito B., Marocco D., Podda S., Pompili F. and Riva M. 2020 *Nucl. Instrum. Methods Phys. Res. A* **974** 164195
[177] Moro F., Esposito B., Marocco D., Podda S., Pompili F., Riva M., Flammini D., Colangeli A. and Kantor R. 2019 *Fusion Eng. Des.* **146** 236
[178] Cecconello M., Miklaszewski R., Marocco D., Conroy S., Moro F., Esposito B., Podda S., Bienkowska B. and Szydlowski A. 2019 *Fusion Eng. Des.* **146B** 2049
[179] Esposito B. *et al* 2022 *J. Fusion Energy* **41** 22
[180] Marocco D., Esposito B. and Moro F. 2011 *Nucl. Fusion* **51** 053011
[181] Marocco D., Esposito B. and Moro F. 2012 *J. Instrum.* **7** C03033
[182] Odstrcil M., Mlynar J., Odstrcil T., Alper B. and Murari A. 2012 *Nucl. Instrum. Methods Phys. Res. A* **686** 156
[183] Mikszuta-Michalika K., Imrisek M., Esposito B., Marocco D., Mlynar J. and Ficker O. 2020 *Fusion Eng. Des.* **160** 111840
[184] Costa-Pereira R. *et al* 2017 *Fusion Eng. Des.* **123** 901
[185] Cruz N. *et al* 2019 *IEEE Trans. Nucl. Sci.* **66** 1310
[186] Fernandes A. *et al* 2019 *IEEE Trans. Nucl. Sci.* **66** 1318
[187] Santos B. *et al* 2019 *IEEE Trans. Nucl. Sci.* **66** 1324
[188] Riva M., Marocco D., Belli F., Esposito B., Pollastrone F., Bielecki J., Giacomelli L., Milocco A. and Popovichev S. 2017 *Fusion Eng. Des.* **123** 873
[189] Vayakis G. *et al* 2012 Evolution of the ITER diagnostic set specifications *Proc. 24th Int. Conf. on Fusion Energy (San Diego USA, 8–13 October 2012)* pp ITR/P5–37 (available at: https://nucleus.iaea.org/sites/fusionportal/Pages/fec-landing.aspx)
[190] Rodionov R., Nemtcev G., Barnsley R., Bertalot L. and Khafizov R. 2021 *Fusion Eng. Des.* **166** 112341
[191] Rodionov R., Kumpilov D., Nemtcev G., Bertalot L. and Vysokih J. 2021 *Fusion Eng. Des.* **173** 112874
[192] Zhuravlev M., Nemtcev G., Nagornyi N., Meshchaninov S., Rodionov R., Mironov A., Zvonareva A., Mironova E. and Portone S. 2021 *EPJ Web Conf.* **253** 03002
[193] Martin V. *et al* 2015 *PoS* **091** 1–7
[194] Yang J., Qingwei Y., Gongshan X., Wei Z., Xianying S. and Xu L. 2008 *Plasma Sci. Technol.* **10** 141
[195] Kashchuk Y.A., Krasil'nikov A.V., Prosvirin D.V., Tsutskikh A.Y., Frunze V.V. and Walker C.I. 2006 *Instrum. Exp. Technol.* **49** 179
[196] Ishikawa M. *et al* 2016 *Fusion Eng. Des.* **109–111** 1399
[197] Reichle R. *et al* 2021 *SRD-55 (Diagnostics) from DOORS, ITER_D_28B39L v5.5* (ITER Private Communication)
[198] Monte Carlo Team 2003 *MCNP—A General Monte Carlo N-Particle Transport Code, Version 5, in:* LA-UR-03-1987 (Los Alamos National Laboratory)
[199] Ishikawa M., Kondoh T., Nishitani T. and Kusama Y. 2008 *Rev. Sci. Instrum.* **79** 10E507
[200] Krasilnikov A. *et al* 2005 *Nucl. Fusion* **45** 1503–9
[201] Cheon M.S., Seon C.R., Pak S., Lee H.G. and Bertalot L. 2012 *Rev. Sci. Instrum.* **83** 10D303
[202] Barnes C.W., Loughlin M.J. and Nishitani T. 1997 *Rev. Sci. Instrum.* **68** 577
[203] Encheva A., Bertalot L., Macklin B., Vayakis G. and Walker C. 2009 *Fusion Eng. Des.* **84** 736–42
[204] Lee Y., Dang J., Jo J., Chun K., Hwang Y., Cheon M., Lee H. and Bertalot L. 2014 *Fusion Eng. Des.* **89** 1894–8
[205] Andersson Sundén E. *et al* 2009 *Nucl. Instrum. Methods Phys. Res. A* **610** 682
[206] Hellesen C., Eriksson J., Binda F., Conroy S., Ericsson G., Hjalmarsson A., Skiba M. and Weiszflog M. 2015 *Nucl. Fusion* **55** 023005
[207] Hawkes N.P., Bond D.S., Croft S., Jarvis O.N. and Sherwood A.C. 2002 *Nucl. Instrum. Methods Phys. Res. A* **476** 506–10
[208] Hawkes N.P., van Belle P., Bond D.S., Croft S. and Jarvis O.N. 1999 *Rev. Sci. Instrum.* **70** 1134
[209] Marcinkevicius B. *et al* Accepted for publication in Fus. Eng. Des. 2022, preprint available at SSRN 4081801 (available at: https://papers.ssrn.com/sol3/papers.cfm?abstract_id=4081801)
[210] Gatu Johnson M. *et al* 2008 *Nucl. Instrum. Methods Phys. Res. A* **591** 417430
[211] Agostinelli S. *et al* 2003 *Nucl. Instrum. Methods Phys. Res. A* **506** 250303
[212] Werner J. *et al* MCNP USER'S MANUAL code version 6.2 LA-UR-17-29981
[213] Skiba M., Ericsson G., Hjalmarsson A., Hellesen C., Conroy S., Andersson-Sundén E., Eriksson J. and Contributors J. 2016 *Nucl. Instrum. Methods Phys. Res. A* **833** 94–104
[214] Skiba M., Ericsson G., Hjalmarsson A., Hellesen C., Conroy S., Andersson-Sundén E., Eriksson J. and Contributors J. 2016 *Nucl. Instrum. Methods Phys. Res. A* **838** 82–88
[215] Hellesen C., Andersson-Sundén E., Conroy S., Dzysiuk N., Ericsson G., Hjalmarsson A., Eriksson J. and Marcinkevicius B. 2017 *Nucl. Fusion* **57** 066021
[216] Eriksson B. *M.Sc Thesis* Uppsala University urn:nbn:se:uu:diva-359981
[217] Eriksson B. *et al* 2022 *Plasma Phys. Control. Fusion* **64** 055008
[218] Hillis D.L., Klepper C.C., Von Hellermann M., Ehrenberg J., Finken K.H. and Mank G. 1997 *Fusion Eng. Des.* **34–35** 347–51
[219] Hillis D.L., Morgan P.D., Ehrenberg J.K., Groth M., Stamp M.F., von Hellermann M. and Kumar V. 1999 *Rev. Sci. Instrum.* **70** 359
[220] Skiba M. *PhD Thesis* Uppsala University urn:nbn:se:uu:diva-304383
[221] Marcinkevicius B. (private Communication)
[222] Henriksson H. *PhD Thesis* Uppsala University urn:nbn:se:uu:diva-3492
[223] Eriksson B., Conroy S., Ericsson G., Eriksson J., Giacomelli L., Hjalmarsson A. and Weiszflog M. 2021 *Rev. Sci. Instrum.* **92** 033538

[224] Bertalot L. *et al* 2008 *Proc. 35th Plasma Physics Conf., 2008 (Hersonissos, Crete, 9–13 June 2008)* (available at: https://iopscience.iop.org/article/10.1088/0741-3335/50/12/120301)
[225] Thomas D.M., McKee G.R., Burrell K.H., Levinton F., Foley E.L. and Fisher R.K. 2007 *Fusion Sci. Technol.* **53** 487
[226] Levinton F.M., Fonck R.J., Gammel G.M., Kaita R., Kugel H.W., Powell E.T. and Roberts D.W. 1989 *Phys. Rev. Lett.* **63** 2060
[227] Foley E., Levinton F., Yuh H. and Zakharov L. 2008 *Rev. Sci. Instrum.* **79** 10F521
[228] Mandl W., Wolf R.C., von Hellermann M.G. and Summers H.P. 1993 *Plasma Phys. Control. Fusion* **35** 1373
[229] Reimer R., Dinklage A., Wolf R., Dunne M., Geiger B., Hobirk J., Reich M. and Mc Carthy P.J. 2017 *Nucl. Fusion* **57** 046005
[230] Burrell K.H., Lao L.L. and Grierson B.A. 2008 *Rev. Sci. Instrum.* **79** 10F521
[231] Pablant N.A. *et al* 2010 *Rev. Sci. Instrum.* **81** 10D729
[232] Geelen P. 2012 Simulation of the motional Stark effect on C-MOD using MSESIM and PERF *Internship Report—CST 2012.097* (MIT) (available at: https://library.psfc.mit.edu/catalog/reports/2010/12rr/12rr013/12rr013_full.pdf)
[233] Ko J., Den Hartog D.J., Caspary K.J., Den Hartog E.A., Pablant N.A. and Summers H.P. 2010 *Rev. Sci. Instrum.* **81** 10D702
[234] Ko J. and Klabacha J. 2012 *Rev. Sci. Instrum.* **83** 10D513
[235] Ko J., Chung J., Lange A.G.G. and de Bock M.F.M. 2013 *J. Instrum.* **8** C10022
[236] Ko J., Chung J. and Jaspers R.J.E. 2015 *J. Instrum.* **10** P10009
[237] Foley E., Levinton F., Yuh H. and Zakharov L. 2008 *Nucl. Fusion* **48** 085004
[238] 2016 *General Atomics Report GA–C28350 "Modifications to EFIT Code—ITER MSE" by Project Staff*
[239] Feder R., Posner S., Qin Y., Zheng J., Chow S.-C. and Garman K.S.,2018 *ITER Memo Hold Point 1 Decision on MSE-LS vs. MSE-LP for the ITER MSE Diagnostic, ITER_D_VMF4FH v1.0* (ITER Private Communication) (https://doi.org/10.1111/hel.12540)
[240] Ko J., Chung J. and Messmer M.C.C. 2016 *Fusion Eng. Des.* **109–111** 742
[241] Lee K., Ko J., Jo J.H. and Chung J. 2017 *Fusion Eng. Des.* **121** 301–7
[242] Tugarinov S., Krasilnikov A., Dokouka V., Khayrutdinov R., Beigman I., Tolstikhina I., Vainshtein L., von Hellermann M. and Malaquias A. 2003 *Rev. Sci. Instrum.* **74** 2075
[243] von Hellermann M. *et al* 2004 *Rev. Sci. Instrum.* **75** 3458
[244] Malaquias A. *et al* 2004 *Rev. Sci. Instrum.* **75** 3393
[245] von Hellermann M. *et al* 2006 *Rev. Sci. Instrum.* **77** 10F516
[246] von Hellermann M.G. *et al* 2008 *AIP Conf. Proc.* **988** 165
[247] von Hellermann M.G. *et al* 2010 *Nucl. Instrum. Methods Phys. Res. A* **623** 720
[248] Krimmer A. *et al* 2019 *Fusion Eng. Des.* **146** 228
[249] Mertens P. 2019 *J. Fusion Energy* **38** 264
[250] Mertens P. *et al* 2019 *Fusion Eng. Des.* **146** 2514
[251] Friese S. *et al* 2021 *Fusion Eng. Des.* **168** 112391
[252] Vukolov K.Y., Andreenko E.N., Orlovskiy I.I. and Shikalov V.F. 2019 *Fusion Eng. Des.* **146** 796–9
[253] Serov S.V., De Bock M., von Hellermann M.G. and Tugarinov S.N. 2021 *Rev. Sci. Instrum.* **92** 053517
[254] Menmuir S., Giroud C., Biewer T.M., Coffey I.H., Delabie E., Hawkes N.C. and Sertoli M. 2014 *Rev. Sci. Instrum.* **85** 11E412
[255] Thorman A., Litherland-Smith E., Menmuir S., Hawkes N., O'Mullane M., Delabie E., Lomanowski B., Fontdecaba J.M. and Scully S. 2021 *Phys. Scr.* **96** 125631
[256] Lomanowski B. *et al* 2019 *61st Annual Meeting of the APS Division of Plasma Physics (Fort Lauderdale, Florida, October 21–25, 2019)* vol 64 (available at: https://meetings.aps.org/Meeting/DPP19/Content/3779)
[257] Tunklev M., Breger P., Günther K., Hellermann M.V., König R., O'Mullane M. and Zastrow K.-D. 1999 *Plasma Phys. Control. Fusion* **41** 985
[258] Viezzer E., Pütterich T., Dux R. and Kallenbach A. (ASDEX Upgrade Team) 2011 *Plasma Phys. Control. Fusion* **53** 035002
[259] von Hellermann M.G. *et al* 2019 *Atoms* **30** 1–27
[260] Atomic Data and Analysis Structure (available at:www.adas.ac.uk)
[261] von Hellermann M.G. *et al* 2005 *Phys. Scr.* **19** 19–29
[262] Jaspers R.J.E., von Hellermann M.G., Delabie E., Biel W., Marchuk O. and Yao L. 2008 *Rev. Sci. Instrum.* **79** 10F526
[263] Huang J. *et al* 2016 *Rev. Sci. Instrum.* **87** 11E542
[264] Serov S.V., Tugarinov S.N. and von Hellermann M. 2019 *3rd European Conf. on Plasma Diagnostics ECPD* (*Técnico Lisboa) (Lisbon, Portugal, 6–9 May 2019)* p P1.17 (available at: https://www.ipfn.tecnico.ulisboa.pt/ECPD2019/welcome.html)
[265] Tugarinov S.N. *et al* 2016 *Inst. Exp. Tech.* **59** 104
[266] Jaspers R. *et al* 2012 *Rev. Sci. Instrum.* **83** 10D515
[267] Kappatou A., McDermott R.M., Pütterich T., Dux R., Geiger B., Jaspers R.J.E., Donné A.J.H., Viezzer E. and Cavedon M. 2018 *Plasma Phys. Control. Fusion* **60** 055006
[268] Kappatou A., Delabie E., Jaspers R.J.E. and von Hellermann M.G. 2012 *Nucl. Fusion* **52** 043007
[269] Ford O.P. *et al* 2020 *Rev. Sci. Instrum.* **91** 023507
[270] Shabashov A.Y., Serov S.V., Tugarinov S.N. and Yartsev V.P. 2019 *Instrum. Exp. Technol.* **62** 675
[271] von Hellermann M.G., Core W.G.F., Horton H.D., Koenig R.W.T., Frieling J., Mandl W. and Summers H.P. 1993 *Plasma Phys. Control. Fusion* **35** 799
[272] Princeton University Team TRANSP Code (available at: https://transp.pppl.gov)
[273] Vayakis G. *et al* 2006 *Nucl. Fusion* **46** S836–845
[274] Horacek J. *et al* 2020 *Nucl. Fusion* **60** 066016
[275] Vicente J. *et al* 2019 *J. Instrum.* **14** C10043
[276] Lampert M., Zoletnik S., Bak J.G. and Nam Y.U. 2018 *Phys. Plasmas* **25** 042507
[277] Pokol G.I. *et al* 2013 *Fusion Eng. Des.* **88** 1386
[278] Dunai D., Zoletnik S., Sárközi J. and Field A.R. 2010 *Rev. Sci. Instrum.* **81** 103503
[279] Fusion Isntruments Kft. APDCAM SNR Considerations 2016
[280] Asztalos O. *et al* 2017 *Proc. EPS Conf. on Plasma Physics (Belfast, Northern Ireland (UK), 26–30 June 2017)* p P4.109 (available at: https://info.fusion.ciemat.es/OCS/EPS2017PAP/pdf/P4.109.pdf)
[281] Nielsen A.H. *et al* 2019 *Nucl. Fusion* **59** 086059
[282] Nielsen A.H. *et al* 2016 *Plasma Phys. Control. Fusion* **59** 025012
[283] Guszejnov D. *et al* 2012 *Rev. Sci. Instrum.* **83** 113501
[284] Asztalos O. 2022 Modell-aided design and interpretation of beam emission spectroscopy measurements on fusion devices *PhD Thesis* Budapest University of Technology and Economics (https://doi.org/10.1016/j.jacc.2021.12.036)
[285] Asztalos O. *et al* 2021 *Proc. EPS Conf. on Plasma Physics (Virtual Conferenc, 21–25 June 2021)* P3.1072 (available at: https://info.fusion.ciemat.es/OCS/EPS2021PAP/pdf/P3.1072.pdf)

[286] Chakraborty A., Rotti C., Bandyopadhyay M., Singh M.J., Gangadharan Nair R., Shah S., Baruah U.K., Hemsworth R.S. and Schunke B. 2010 *IEEE Trans. Plasma Sci.* **38** 248
[287] Singh M.J. *et al* 2019 *Nucl. Fusion* **59** 096034
[288] Singh M.J. and De Esch H.P.L. 2010 *Rev. Sci. Instrum.* **81** 013305
[289] Singh M.J. *et al* 2011 *Fusion Eng. Des.* **86** 732
[290] Bandyopadhyay M., Sudhir D. and Chakraborty A. 2016 *Rev. Sci. Instrum.* **87** 02B906
[291] Bandyopadhyay M. *et al* 2019 *Nucl. Fusion* **59** 085001
[292] Pandya K. *et al* 2017 *Fusion Eng. Des.* **114** 187
[293] Pandya K. *et al* 2025 *Rev. Sci. Instrum.* **96** 043309
[294] Pandey R. *et al* 2017 *J. Phys.: Conf. Ser.* **823** 012029
[295] Herzberg G. 1944 *Atomic Spectra and Atomic Structure* (Dover publications)
[296] Lawson J.D. 1957 *Proc. Phys. Soc. B* **70** 6–10
[297] Hartfuss H.J. *et al* 1997 *Rev. Sci. Instrum.* **68** 1244–9
[298] Biel W. *et al* 2019 *Fusion Eng. Des.* **146** 465–72
[299] Lafrance D., Boileau A., Stansfield B.L. and Zuzak W. 1990 *Rev. Sci. Instrum.* **61** 3793–6
[300] Reinke M.L. *et al* 2012 *Rev. Sci. Instrum.* **83** 113504
[301] Sugie T., Costley A., Malaquias A. and Walker C. 2003 *J. Plasma Fusion Res. Ser.* **79** 1051–61
[302] Orlovskiy I., Alekseev A., Andreenko E., Vukolov K., Denisov V., Klyatskin A., Lukin A., Melnikov A. and Muslimov E. 2015 *Fusion Eng. Des.* **96–97** 899–902
[303] Gorshkov A.V., Alekseev A.G., Andreenko E.N., Asadulin G.M., Ageorges N., Kampf D. and Naumenko N.N. 2019 *Fusion Eng. Des.* **146** 329–35
[304] Sugie T., Ogawa H., Nishitani T., Kasai S., Katsunuma J., Maruo M., Ebisawa K., Ando T. and Kita Y. 1999 *Rev. Sci. Instrum.* **70** 351–4
[305] Seon C.R., Choi S.H., Cheon M.S., Pak S., Lee H.G., Biel W. and Barnsley R. 2010 *Rev. Sci. Instrum.* **81** 10E508
[306] Cheng Z. *et al* 2022 *Rev. Sci. Instrum.* **93** 073502
[307] Kajita S., Bock M.D., Desjardins M. and Barnsley R. 2019 *Plasma Fusion Res.* **14** 1405042
[308] Ushakov A., Verlaan A., Stephan U., Steinke O., de Bock M., Maniscalco M.P. and Verhoeff P. 2020 *Fusion Eng. Des.* **154** 111546
[309] Varshney S.K., Barnsley R., O'Mullane M.G. and Jakhar S. 2012 *Rev. Sci. Instrum.* **83** 10E126
[310] Varshney S. *et al* 2017 *J. Phys.: Conf. Ser.* **823** 012055
[311] Subhash P.V. *et al* 2017 *Fusion Sci. Technol.* **71** 215–24
[312] Singh M.J. *et al* 2021 Fusion technology development in India to ensure ITER deliverables *Preprint 2020 IAEA Fusion Energy Conf. (Virtual Conference, 10–15 May 2021)* p OV/P–3 (available at: https://nucleus.iaea.org/sites/fusionportal/Pages/fec-landing.aspx)
[313] Hu L. *et al* 2017 *Nucl. Instrum. Methods Phys. Res. A* **870** 50–54
[314] Chen K. *et al* 2021 *Fusion Eng. Des.* **165** 112234
[315] Orlinskij D. and Magyar G. 1988 *Nucl. Fusion* **28** 611–97
[316] Källne E., Källne J., Marmor E.S. and Rice J.E. 1985 *Phys. Scr.* **31** 551–64
[317] Peacock N.J. 1996 *Astrophys. Space Sci.* **237** 341–99
[318] Stratton B.C., Bitter M., Hill K.W., Hillis D.L. and Hogan J.T. 2008 *Fusion Sci. Technol.* **53** 431–86
[319] Thomser C. *et al* (JET-EFDA Contributors) 2012 *Fusion Sci. Technol.* **62** 1–8
[320] Matthews G.F. *et al* (EFDA-JET contributors) 2011 *Phys. Scr.* **2011** 014001
[321] Hirai T. *et al* 2016 *Phys. Scr.* **T167** 014072
[322] Pitts R.A. *et al* 2013 *J. Nucl. Mater.* **438** S48–S56
[323] Causey R., Wilson K., Venhaus T. and Wampler W.R. 1999 *J. Nucl. Mater.* **266–269** 467–71
[324] Isler R.C., Neidigh R.V. and Cowan R.D. 1977 *Phys. Lett. A* **63** 295–7
[325] Xu Z. *et al* 2021 *Nucl. Instrum. Methods Phys. Res. A* **1010** 165545
[326] Sugar Et J. and Kaufman V. 2096 *Phys. Rev. A* **21** 609–13
[327] Takahashi T. *et al* 2018 *J. Astron. Telesc. Instrum. Syst.* **4** 1
[328] Guirlet R., Song I., Moureau G., Batal T., Schwob J., Seon C., Desgranges C., Vartanian S., Shin H. and Choe W. 2019 *J. Inst.* **14** C10036
[329] Zhang L. *et al* 2019 *Nucl. Instrum. Methods Phys. Res. A* **916** 169–78
[330] Post D.E., Jensen R.V., Tarter C.B., Grasberger W.H. and Lokke W.A. 1977 *At. Data Nucl. Data Tables* **20** 397–439
[331] Seely J.F., Behring W.E. and Brown C.M. 1989 *J. Opt. Soc. Am. B* **6** 3–6
[332] Seely J.F., Feldman U., Wouters A.W., Schwob J.L. and Suckewer S. 1989 *Phys. Rev. A* **40** 5020–5
[333] Naujoks D. *et al* 1996 *Nucl. Fusion* **36** 671–87
[334] Neu R. *et al* 2013 *J. Nucl. Mater.* **438** S34–S41
[335] Diez M. *et al* (the WEST Team) 2021 *Nucl. Fusion* **61** 106011
[336] Xu G.S. *et al* (the EAST Team) 2021 *Nucl. Fusion* **61** 126070
[337] Laun D.D. and Corliss C. 1968 *J. Res. Natl Bur. Stand. A* **72A** 609
[338] Laun D.D. and Corliss C. 1964 *J. Res. Natl Bur. Stand. A* **68A** 207
[339] Kramida A., Ralchenko Y. and Reader J. (NIST ASD Team) 2021 NIST atomic spectra database (version 5.9) (National Institute of Standards and Technology (available at: https://physics.nist.gov/asd)
[340] Kramida A.E. and Shirai T. 2009 *At. Data Nucl. Data Tables* **95** 305–474
[341] Currell F.J. *et al* 1996 *J. Phys. Soc. Japan* **65** 3186–92
[342] Hill K.W. *et al* 2010 *Rev. Sci. Instrum.* **81** 10E322
[343] Ralchenko Y. 2013 *Plasma Fusion Res.* **8** 2503024
[344] Ding X., Zhang F., Yang Y., Zhang L., Koike F., Murakami I., Kato D., Sakaue H.A., Nakamura N. and Dong C. 2020 *Phys. Rev. A* **101**
[345] Tu B. *et al* 2017 *Phys. Rev. A* **96** 032705
[346] Clementson J., Lennartsson T. and Beiersdorfer P. 2015 *Atoms* **3** 407–21
[347] Yan C.L. 2022 *Phys. Rev. A* **105** 1–7
[348] Lu Q., Yan C.L., Meng J., Xu G.Q., Yang Y., Chen C.Y., Xiao J., Li J.G., Wang J.G. and Zou Y. 2021 *Phys. Rev. A* **103**
[349] Li W., Shi Z., Yang Y., Xiao J., Brage T., Hutton R. and Zou Y. 2015 *Phys. Rev. A* **91** 062501
[350] Fei Z., Li W., Grumer J., Shi Z., Zhao R., Brage T., Huldt S., Yao K., Hutton R. and Zou Y. 2014 *Phys. Rev. A* **90** 052517
[351] Qiu M.L. *et al* 2014 *J. Phys. B: At. Mol. Opt. Phys.* **47** 175002
[352] Radtke R., Biedermann C., Schwob J.L., Mandelbaum P. and Doron R. 2001 *Phys. Rev. A* **64** 012720
[353] Ralchenko Y., Reader J., Pomeroy J.M., Tan J.N. and Gillaspy J.D. 2007 *J. Phys. B* **40** 3861–75
[354] Neill P., Harris C., Safronova A.S., Hamasha S., Hansen S., Safronova U.I. and Beiersdorfer P. 2004 *Can. J. Phys.* **82** 931–42
[355] Rzadkiewicz J. *et al* (JET Contributors) 2018 *Phys. Rev. A* **97** 052501
[356] Lennartsson T., Clementson J. and Beiersdorfer P. 2013 *Phys. Rev. A* **87** 062505
[357] Podpaly Y., Clementson J., Beiersdorfer P., Williamson J., Brown G.V. and Gu M.F. 2009 *Phys. Rev. A* **80** 052504
[358] Pütterich T., Neu R., Dux R., Whiteford A.D. and O'Mullane M.G. (the ASDEX Upgrade Team) 2008 *Plasma Phys. Control. Fusion* **50** 085016

[359] Nakano T., Asakura N., Kubo H., Yanagibayashi J. and Ueda Y. 2009 *Nucl. Fusion* **49** 115024
[360] Feldman U., Indelicato P. and Sugar J. 1991 *J. Opt. Soc. Am. B* **8** 3
[361] Katai R., Morita S. and Goto M. 2007 *Plasma Fusion Res.* **2** 006
[362] Kato D., Sakaue H.A., Murakami I., Goto M., Oishi T., Tamura N., Funaba H. and Morita S. 2021 *Nucl. Fusion* **61** 116008
[363] Behringer K., Summers H.P., Denne B., Forrest M. and Stamp M. 1989 *Plasma Phys. Control. Fusion* **31** 2059–99
[364] Summers H.P., Dickson W.J., O'Mullane M.G., Badnell N.R., Whiteford A.D., Brooks D.H., Lang J., Loch S.D. and Griffin D.C. 2006 *Plasma Phys. Control. Fusion* **48** 263–93
[365] Xu G.L., Guterl J., Abrams T., Wang H.Q., Zhang P.F., Elder J.D., Unterberg E.A., Thomas D.M., Guo H.Y. and Ye M.Y. 2019 *Nucl. Mater. Energy* **18** 141–6
[366] Steinbrink J., Wenzel U., Bohmeyer W. and Fussmann G. (the PSI-Team) 1997 Sputtered tungsten atoms investigated in a linear plasma generator *Proc. 24th EPS Conf. on Controlled Fusion and Plasma Physics* vol 21A (*Berchtesgaden, Germany*, *9–13 June 1997*) p P4.1809 (available at: https://library.ipp.mpg.de/EPS_24_Vol4_1997.pdf)
[367] Thoma A., Asmussen K., Dux R., Krieger K., Herrmann A., Napiontek B., Neu R., Steinbrink J., Weinlich M. and Wenzel U. (the ASDEX Upgrade Team) 1997 *Plasma Phys. Control. Fusion* **39** 1487–99
[368] Moore C.E. 1952 Atomic energy levels *Tech. Rep. Natl. Bur. Stand. (U.S.) Circular No. 467* (U.S. GPO, Washington DC, 1958)
[369] Aufmuth P., Steudel A., Tegtmeier W. and Wobker E. 1988 *J. Phys. B* **21** 2253–60
[370] Wyart J. 2010 *J. Phys. B* **43** 074018
[371] Quinet P., Vinogradoff V., Palmeri P. and É B. 2010 *J. Phys. B* **43** 144003
[372] Schlummer T. *et al* 2017 *Phys. Scr.* **T170** 014075
[373] Purohit G., Kato D., Murakami I., Gupta S. and Sinha P. 2021 *Eur. Phys. J. D* **75** 1–7
[374] Eksaeva A., Marenkov E., Borodin D., Kreter A., Reinhart M., Kirschner A., Romazanov J., Terra A., Brezinsek S. and Nordlund K. 2017 *Nucl. Mater. Energy* **12** 253–60
[375] Nishijima D., Doerner R.P., Baldwin M.J., Pospieszczyk A. and Kreter A. 2009 *Phys. Plasmas* **16** 122503
[376] Pospieszczyk A., Borodin D., Brezinsek S., Huber A., Kirschner A., Mertens P., Sergienko G., Schweer B., Beigman I.L. and Vainshtein L. 2010 *J. Phys. B* **43** 144017
[377] Brezinsek S., Laengner M., Coenen J.W., O'Mullane M.G., Pospieszczyk A., Sergienko G. and Samm U. 2017 *Phys. Scr.* **2017** 014052
[378] Kling R. and Kock M. 1999 *J. Quant. Spectrosc. Radiat. Transfer* **62** 129–40
[379] Johnson C.A. *et al* 2019 *Plasma Phys. Control. Fusion* **61** 095006
[380] Smyth R.T., Ballance C.P., Ramsbottom C.A., Johnson C.A., Ennis D.A. and Loch S.D. 2018 *Phys. Rev. A* **97** 052705
[381] Loch S., Ennis D., Johnson C., White A., Dunleavy N. and Ballance C. 2021 An update on atomic data for the low charge states of W for use in simulation codes and erosion/redeposition diagnostics APS *Division of Plasma Physics Meeting Abstracts (APS Meeting Abstracts) (Pittsburgh, PA, 8–12 November, 2021)* vol 2021 p UP11.116 (available at: https://meetings.aps.org/Meeting/DPP21/Content/4081)
[382] Dunleavy N.L., Ballance C.P., Ramsbottom C.A., Johnson C.A., Loch S.D. and Ennis D.A. 2022 *J. Phys. B* **55** 175002
[383] Quinet P., Palmeri P., É B., McCurdy M.M., Rieger G., Pinnington E.H., Wickliffe M.E. and Lawler J.E. 1999 *Mon. Not. R. Astron. Soc.* **307** 934–40
[384] Guterl J., Bykov I., Ding R. and Snyder P. 2021 *Nucl. Mater. Energy* **27** 100948
[385] Dong C.F. *et al* 2018 *Nucl. Fusion* **59** 016020
[386] Oishi T., Morita S., Kato D., Murakami I., Sakaue H.A., Kawamoto Y., Kawate T. and Goto M. 2021 *Atoms* **9** 69
[387] Ryabtsev A.N., Kononov E.Y., Kildiyarova R.R., Tchang-Brillet W.U.L. and Wyart J.F. 2013 *Phys. Scr.* **87** 045303
[388] Ryabtsev A., Kononov E., Kildiyarova R., Tchang-Brillet W.U.L., Wyart J.F., Champion N. and Blaess C. 2015 *Atoms* **3** 273–98
[389] Lawson K., Pawelec E., Coffey I.H., Groth M., Litherland-Smith E., Meigs A. and Scully S. 2022 *Phys. Scr.* **97** 055605
[390] Maruyama T., Oikawa T., Kitazawa S.I., Ioki K., Mera S., Nomura I., Ogawa H., Tanaka S. and Hatae T. 2019 *Plasma Fusion Res.* **14** 3405080
[391] Pitts R. *et al* 2019 *Nucl. Mater. Energy* **20** 100696
[392] Colette D., Mazon D., Barnsley R., Sirinelli A., Jardin A., O'Mullane M. and Walsh M. 2020 *Rev. Sci. Instrum.* **91** 073504
[393] Angioni C. 2021 *Plasma Phys. Control. Fusion* **63** 073001
[394] Barnsley R., O'Mullane M., Ingesson L.C. and Malaquias A. 2004 *Rev. Sci. Instrum.* **75** 3743–6
[395] Polevoi A.R., Medvedev S.Y., Mukhovatov V.S., Kukushkin A.S., Murakami Y., Shimada M. and Ivanov A.A. 2002 *J. Plasma Fusion Res.* **5** 82–87
[396] Verdoolaege G. *et al* (the ASDEX Upgrade Team, the EUROfusion MST1 Team and JET Contributors) 2021 *Nucl. Fusion* **61** 076006
[397] Imbeaux F. *et al* 2015 *Nucl. Fusion* **55** 123006
[398] Pinches S.D. *et al* Progress in the iter integrated modelling programme and the use and validation of imas within the iter members *Preprint: 2016 IAEA Fusion Energy Conf.* (*Kyoto, 17–22 October 2016*) p TH/P2–14 (available at: https://nucleus.iaea.org/sites/fusionportal/Pages/fec-landing.aspx)
[399] Whiteford A.D., Badnell N.R., Ballance C.P., O'Mullane M.G., Summers H.P. and Thomas A.L. 2001 *J. Phys. B* **34** 3179–91
[400] Ballance C.P., Badnell N.R. and Berrington K.A. 2002 *J. Phys. B* **35** 1095–102
[401] Ballance C.P. and Griffin D.C. 2006 *J. Phys. B* **39** 3617–28
[402] Neu R.L. *et al* (ASDEX Upgrade Team and JET EFDA Contributors) 2014 *IEEE Trans. Plasma Sci.* **42** 552–62
[403] Kubo H., Sasaki A., Moribayashi K., Higashijima S., Takenaga H., Shimizu K., Nakano T., Whiteford A. and Sugie T. 2007 *J. Nucl. Mater.* **363–365** 1441–5
[404] Hu R.J. *et al* 2018 *Rev. Sci. Instrum.* **89** 10F110
[405] Rice J.E., Fournier K.B., Kemp G.E., Bitter M., Cao N., Delgado-Aparicio L., Hill K., Hubbard A.E., Hughes J.W. and Reinke M.L. 2020 *J. Phys. B* **53** 055701
[406] Lu D. *et al* 2021 *Rev. Sci. Instrum.* **92** 043544
[407] Wiesen S., Köchl F., Belo P., Kotov V., Loarte A., Parail V., Corrigan G., Garzotti L. and Harting D. 2017 *Nucl. Fusion* **57** 076020
[408] Lang P.T., Ploeckl B., Bernert M., Bock A., Dux R., Kallenbach A., Rohde V., Siccinio M., Suttrop W. and Zito A. 2021 *Fusion Sci. Technol.* **77** 42–50
[409] Ballance C.P., Loch S.D., Foster A.R., Smith R.K., Witthoeft M.C. and Kallman T.R. 2013 *Fusion Sci. Technol.* **63** 358–62
[410] Schippers S. *et al* 2011 *Phys. Rev. A* **83** 012711
[411] Krantz C., Badnell N.R., Müller A., Schippers S. and Wolf A. 2017 *J. Phys. B* **50** 052001
[412] Badnell N.R. *et al* 2016 *Phys. Rev. A* **93** 052703

[413] Kwon D.H. *et al* 2018 *At. Data Nucl. Data Tables* **119** 250–62
[414] Preval S.P., Badnell N.R. and O'Mullane M.G. 2019 *J. Phys. B* **52** 025201
[415] Henderson S.S., Bluteau M., Foster A., Giunta A., O'Mullane M.G., Pütterich T. and Summers H.P. 2017 *Plasma Phys. Control. Fusion* **59** 055010
[416] Pütterich T., Fable E., Dux R., O'Mullane M., Neu R. and Siccinio M. 2019 *Nucl. Fusion* **59** 056013
[417] Sertoli M., Carvalho P.J., Giroud C. and Menmuir S. (contributors J) 2019 *J. Plasma Phys.* **85** 905850504
[418] Murakami I., Kato D., Oishi T., Goto M., Kawamoto Y., Suzuki C., Sakaue H.A. and Morita S. 2021 *Nucl. Mater. Energy* **26** 100923
[419] Chung H., Chen M.H., Morgan W.L., Ralchenko Y. and Lee R.W. 2005 *High Energy Density Phys.* **1** 3–12
[420] Valisa M. *et al* (JET-EFDA contributors) 2011 *Nucl. Fusion* **51** 033002
[421] Giroud C. *et al* (the JET EFDA Contributors) 2007 *Nucl. Fusion* **47** 313–30
[422] Puiatti M.E., Valisa M., Angioni C., Garzotti L., Mantica P., Mattioli M., Carraro L., Coffey I. and Sozzi C. (JET-EFDA Contributors) 2006 *Phys. Plasmas* **13** 042501
[423] Meister H., Willmeroth M., Zhang D., Gottwald A., Krumrey M. and Scholze F. 2013 *Rev. Sci. Instrum.* **84** 123501
[424] Mlynar J., Tomes M., Imrisek M., Alper B., O'Mullane M., Odstrcil T. and Puetterich T. 2015 *Fusion Eng. Des.* **96–97** 869–72
[425] Delgado-Aparicio L., Tritz K., Kramer T., Stutman D., Finkenthal M., Hill K. and Bitter M. 2010 *Rev. Sci. Instrum.* **81** 10E303
[426] Cho T. *et al* 1999 *Rev. Sci. Instrum.* **70** 577–80
[427] Delgado-Aparicio L.F. *et al* 2021 *Rev. Sci. Instrum.* **92** 073502
[428] Smith R. *et al* 2020 *J. Phys. B: At. Mol. Opt. Phys.* **53** 092001
[429] Beiersdorfer P. *et al* 2010 *J. Phys. B: At. Mol. Opt. Phys.* **43** 144008
[430] Eckart M.E. *et al* 2021 *Rev. Sci. Instrum.* **92** 063520
[431] Gill R.D., Alper B. and Edwards A.W. 1992 Effects of neutrons on the JET soft x-ray detectors *Proc. 19th EPS Conf. on Controlled Fusion and Plasma Physics* vol 16C (*Innsbruck, 29 June–3 July 1992*) pp II–1051 (available at: http://libero.ipp.mpg.de/libero/PDF/EPS_19_Vol2_1992.pdf)
[432] Alper B., Dillon S., Edwards A.W., Gill R.D., Robins R. and Wilson D.J. 1997 *Rev. Sci. Instrum.* **68** 778–81
[433] Gill R.D., Alper B. and Edwards A.W. 1997 First results in D-T from the radiation hardened soft x-ray cameras *Tech. Rep. JET-R(97)11 JET Joint Undertaking* (available at: https://scipub.euro-fusion.org/archives/jet-archive/first-results-in-d-t-from-the-radiation-hardened-soft-x-ray-cameras)
[434] Maas A.C. *et al* 1999 *Fusion Eng. Des.* **47** 247–65
[435] Mazon D., Abadie Q., Dorchies F., Lecherbourg L., Mollard A., Malard P. and Dabagov S. 2015 *Nucl. Instrum. Methods Phys. Res. B* **355** 301–6
[436] Mazon D., Liegeard C., Jardin A., Barnsley R., Walsh M., O'Mullane M., Sirinelli A. and Dorchies F. 2016 *Rev. Sci. Instrum.* **87** 11E302
[437] Gott Y.V. and Stepanenko M.M. 2009 *Instrum. Exp. Tech.* **52** 260–4
[438] Mazon D. *et al* 2015 *Fusion Eng. Des.* **96–97** 856–60
[439] Czarski T., Chernyshova M., Malinowski K., Pozniak K.T., Kasprowicz G., Kolasinski P., Krawczyk R., Wojenski A. and Zabolotny W. 2016 *Rev. Sci. Instrum.* **87** 11E336
[440] Chernyshova M. *et al* 2020 *Nucl. Mater. Energy* **25** 100850
[441] Jednorog S., Bienkowska B., Chernyshova M., Łaszynska E., Prokopowicz R. and Ziołkowski A. 2015 *Proc. SPIE* **9662** 96622Y
[442] Colette D., Mazon D., Barnsley R., O'Mullane M., Jardin A. and Sirinelli A. 2021 *Rev. Sci. Instrum.* **92** 083511
[443] Li C., Zhang J., Chen K., Hu L., Zhao J., Cao H. and Zhang Z. 2021 *Nucl. Instrum. Methods Phys. Res. A* **1003** 165324
[444] Nakano T. *et al* (JET Contributors) 2015 *J. Phys. B* **48** 144023
[445] Gu M.F. 2008 *Can. J. Phys.* **86** 675–89
[446] Heuer K., Foster A.R. and Smith R. 2021 *Astrophys. J.* **908** 3
[447] Uncertainty Quantification (available at: https://amdis.iaea.org/meetings/uncertainty-quantification/)
[448] Griffin D.C., Ballance C.P., Loch S.D. and Pindzola M.S. 2007 *J. Phys. B* **48** 4537–50
[449] Torretti F. *et al* 2020 *Nat. Commun.* **11** 2334
[450] Pütterich T., Jonauskas V., Neu R. and Dux R. (ASDEX Upgrade Team) 2013 The extreme ultraviolet emissions of w23+ (4f5) *8th Int. Conf. on Atomic and Molecular Data and Their Applications (Gaithersburg, Maryland, USA, 30 September–4 October, 2012)* pp 132–42 (available at: https://physics.nist.gov/Icamdata/index.php)
[451] Pütterich T., Neu R., Dux R., Kallenbach A., Fuchs C., O'Mullane M., Whiteford A. and Summers H.P. (the ASDEX Upgrade Team) 2004 Atomic data for tungsten in fusion devices *Proc. 31st EPS Conf.* vol 28G (*London, UK, 28 June–2 July*) p P4.136 (available at: http://ocs.ciemat.es/EPS2004/pdf/P4_136.pdf)
[452] Vezinet D., Mazon D., Guirlet R., Decker J. and Peysson Y. 2014 *Nucl. Fusion* **54** 083011
[453] Jardin A., Bielecki J., Mazon D., Dankowski J., Król K., Peysson Y. and Scholz M. 2020 *J. Fusion Energy* **39** 240–50
[454] Hollmann E.M., Pigarov A.Y. and Doerner R.P. 2003 *Rev. Sci. Instrum.* **74** 3984–90
[455] Zastrow K.D., Keatings S.R., Marot L., O'Mullane M.G. and de Temmerman G. (JET-EFDA Contributors) 2008 *Rev. Sci. Instrum.* **79** 10F527
[456] Kukushkin A.B., Neverov V.S., Alekseev A.G., Lisgo S.W. and Kukushkin A.S. 2016 *Fusion Sci. Technol.* **69** 628–42
[457] Kukushkin A.B. *et al* 2012 Theoretical issues of high resolution h-α spectroscopy measurements in ITER *Proc. 24th Int. Conf. on Fusion Energy* (*San Diego, 2012*) (available at: www-naweb.iaea.org/napc/physics/FEC/FEC2012/papers/514_ITRP544.pdf) p ITR/P5–44
[458] Neverov V.S., Kukushkin A.B., Stamp M.F., Alekseev A.G., Brezinsek S. and von Hellermann M. (JET Contributors) 2017 *Nucl. Fusion* **57** 016031
[459] Kajita S., Veshchev E., Barnsley R. and Walsh M. 2016 *Contrib. Plasma Phys.* **56** 837–45
[460] Odstrčil M., Mlynář J., Weinzettl V., Háček P., Odstrčil T., Verdoolaege G., Berta M., Szabolics T. and Bencze A. 2014 *Rev. Sci. Instrum.* **85** 013509
[461] Carr M. *et al* 2017 Towards integrated data analysis of divertor diagnostics with ray-tracing. *44th EPS Conf. on Plasma Physics* (*Belfast, Northern Ireland (UK), 26–30 June 2017*) (available at: https://info.fusion.ciemat.es/OCS/EPS2017PAP/pdf/O5.130.pdf)
[462] Neverov V.S. *et al* 2020 *Plasma Phys. Control. Fusion* **62** 115014
[463] Natsume H. *et al* 2021 *Plasma Fusion Res.* **16** 2405019
[464] Chiocchio S. and Grosset K. 2020 *ITER Project Requirements Document* (Private Communication)
[465] Walsh M., Beurskens M., Carolan P.G., Gilbert M., Loughlin M., Morris A.W., Riccardo V., Xue Y., Huxford R.B. and Walker C.I. 2006 *Rev. Sci. Instrum.* **77** 10E525
[466] Scannell R. *et al* 2017 *J. Instrum.* **12** C11010

[467] Yatsuka E., Hatae T., Vayakis G., Bassan M. and Itami K. 2013 *Rev. Sci. Instrum.* **84** 103503
[468] Yatsuka E., Hatae T., Bassan M., Vayakis G., Walsh M. and Itami K. 2015 *Fusion Eng. Des.* **100** 461–7
[469] Yatsuka E., Hatae T., Suitoh S., Ohara M., Hagita K., Inoue K., Bassan M., Walsh M. and Itami K. 2016 *J. Instrum.* **11** C01006
[470] Orsitto F. and Tartoni N. 1999 *Rev. Sci. Instrum.* **70** 798
[471] Giudicotti L., Bassan M., Orsitto F.P., Pasqualotto R., Kempenaars M. and Flanagan J. 2016 *J. Instrum.* **11** C01071
[472] Kurskiev G.S. *et al* 2015 *Nucl. Fusion* **55** 053024
[473] Mukhin E. *et al* 2012 *J. Instrum.* **7** C02063
[474] Litnovsky A., Laengner M., Matveeva M., Schulz C., Marot L., Voitsenya V.S., Philipps V., Biel W. and Samm U. 2010 *Fusion Eng. Des.* **86** 1780–3
[475] Yatsuka E., Bassan M., Hatae T., Yamamoto T., Shimada T., Torimoto K. and Itami K. 2018 *Fusion Eng. Des.* **136** 1068–72
[476] Yatsuka E., Yamamoto T., Hatae T., Torimoto K. and Itami K. 2017 *Rev. Sci. Instrum.* **88** 076107
[477] Yatsuka E., Torimoto K., Ishikawa M. and Hatae T. 2020 *Fusion Eng. Des.* **160** 111846
[478] Bartlett D 1996 Physics issues of ECE and ECA for ITER diagnostics for experimental thermonuclear fusion reactors *Diagnostics For Experimental Thermonuclear Fusion Reactors* ed R.R. Parker (Springer) p 183
[479] Bassan M., Andrew P., Kurskiev G., Mukhin E., Hatae T., Vayakis G., Yatsuka E. and Walsh M. 2016 *J. Instrum.* **11** C01052
[480] Pasch E., Beurskens M.N.A., Bozhenkov S.A., Fuchert G. and Wolf R.C. 2018 *Rev. Sci. Instrum.* **89** 10C115
[481] Giudicotti L. 2017 *J. Instrum.* **12** C11002
[482] Giudicotti L., Kempenaars M., McCormack O., Flanagan J. and Pasqualotto R. 2018 *Nucl. Fusion* **58** 044003
[483] Goldstein D. 2003 *Polarised Light* (Marcel Dekker Inc)
[484] Segre S.E. and Zanza V. 2000 *Phys. Plasmas* **7** 2677
[485] Parke E., Mirnov V.V. and Hartog D.J.D. 2014 *J. Instrum.* **9** C02030
[486] Mirnov V., Den Hartog D.J. and Parke E. 2016 *Phys. Plasmas* **23** 052108
[487] Mirnov V. and Hartog D.J.D. 2017 *Plasma Phys. Control. Fusion* **59** 063001
[488] Huxford R. and Bassan M. 2018 ITER Document Management (IDM) system, document # PWQ6QW
[489] Vayakis G. and Scannell R. 2017 *Beam Dump for the ITER Core Plasma TS, ITER_D_PVDCCS v2.0* (ITER Private Communication)
[490] Mukhin E. *et al* 2014 *Nucl. Fusion* **54** 043007
[491] Mukhin E. *et al* 2019 *Nucl. Fusion* **59** 086052
[492] Kurskiev G. 2022 *Tech. Phys. Lett.* **47** 41–5
[493] Varshavchik L. *et al* 2021 *Plasma Phys. Control. Fusion* **63** 025005
[494] Bukreev I., Mukhin E.E., Bulovich S.V., Razdobarin A.G., Semenov V.V., Tolstyakov S.Y., Kochergin M.M., Kurskiev G.S., Masyukevich S.V. and Chernakov P.V. 2014 *Instrum. Exp. Tech.* **57** 156–65
[495] Bukreev I. *et al* 2019 *J. Phys.: Conf. Ser.* **1400** 077040
[496] De Bock M. 2016 *J. Instrum.* **11** 08010–P08010
[497] Razdobarin A.G. *et al* Deposition mitigation and in-vessel optics recovery in ITER *Preprint: 2016 IAEA Fusion Energy Conf.* (*Kyoto 17–22 October 2016*) p MPT/P5–40 (available at: https://nucleus.iaea.org/sites/fusionportal/Pages/fec-landing.aspx)
[498] Mukhin E. *et al* 2009 *Nucl. Fusion* **49** 085032
[499] Mukhin E. *et al* 2011 *Nucl. Fusion* **52** 013017
[500] Leipold F. *et al* 2016 *Rev. Sci. Instrum.* **87** 11D439
[501] Razdobarin A. *et al* 2015 *Nucl. Fusion* **55** 093022
[502] Dmitriev A. *et al* 2017 *Phys. Scr.* **T170** 014072
[503] Gorodetsky A. 2021 *Tech. Phys.* **66** 288–97
[504] Shigin P. *et al* 2021 *Fusion Eng. Des.* **164** 112162
[505] Arkhipov I. *et al* 2011 *J. Nucl. Mater.* **415** S1210–3
[506] Razdobarin A. *et al* 2011 *Fusion Eng. Des.* **86** 1341–4
[507] Gorodetsky A. *et al* 2020 *J. Surf. Invest. X-ray Synchrotron Neutron Tech.* **14** 1003–15
[508] Kornev A. *et al* 2019 *Fusion Eng. Des.* **146** 1019–22
[509] Makarov A., Kornev A.F., Katsev Y.V. and Stupnikov V.K. 2021 *Appl. Opt.* **60** 547–50
[510] Kurskiev G. *et al* 2020 *Nucl. Instrum. Methods Phys. Res.* **963** 163734
[511] Zhiltsov N.S., Kurskiev G.S., Mukhin E.E., Solovey V.A., Tolstyakov S.Y., Aleksandrov S.E., Bazhenov A.N. and Chernakov A.P. 2020 *Nucl. Instrum. Methods Phys. Res.* **976** 164289
[512] Chernakov A. *et al* 2020 *Fusion Eng. Des.* **156** 11158
[513] Mukhin E. *et al* 2017 *Fusion Eng. Des.* **123** 686–9
[514] Gorbunov A., Mukhin E.E., Berik E.B., Vukolov K.Y., Lisitsa V.S., Kukushkin A.S., Levashova M.G., Barnsley R., Vayakis G. and Walsh M.J. 2017 *Fusion Eng. Des.* **123** 695–8
[515] Munoz Burgos J., Griener M., Loreau J., Gorbunov A., Lunt T., Schmitz O. and Wolfrum E. 2019 *Phys. Plasmas* **26** 063301
[516] Gorbunov A. *et al* 2019 *Fusion Eng. Des.* **146** 2703–6
[517] Carlstrom T. 1998 *Diagnostics for Experimental Thermonuclear Fusion Reactors 2* ed P. Scott (Plenum Press)
[518] Van Zeeland M.A. *et al* 2013 *Rev. Sci. Instrum.* **84** 043501
[519] Irby J., Marmar E.S., Sevillano E. and Wolfe S.M. 1988 *Rev. Sci. Instrum.* **59** 1568
[520] Carlstrom T.N., Ahlgren D.R. and Crosbie J. 1988 *Rev. Sci. Instrum.* **59** 1063
[521] Kawano Y., Nagashima A., Hatae T. and Gunji S. 1996 *Rev. Sci. Instrum.* **67** 1520
[522] Innocente P., Martini S., Canton A. and Tasinato L. 1997 *Rev. Sci. Instrum.* **68** 694
[523] Gil C., Barbuti A., Elbèze D., Pastor P., Philip J. and Toulouse L. 2008 *Rev. Sci. Instrum.* **79** 10E710
[524] Dodel G. and Kunz W. 1978 *Infrared Phys.* **18** 773–6
[525] Rommers J.H. and Howard J. 1996 *Plasma Phys. Control. Fusion* **38** 1805–16
[526] Brower D., Jiang Y., Ding W.X., Terry S.D., Lanier N.E., Anderson J.K., Forest C.B. and Holly D. 2001 *Rev. Sci. Instrum.* **72** 1077
[527] Van Zeeland M.A. *et al* 2017 *Plasma Phys. Control. Fusion* **59** 125005
[528] Akiyama T., Tsuji-Iio S., Shimada R., Nakayama K., Okajima S., Takahashi M., Terai K., Tanaka K., Tokuzawa T. and Kawahata K. 2003 *Rev. Sci. Instrum.* **74** 2695
[529] Van Zeeland M.A., Boivin R.L., Carlstrom T.N. and Deterly T.M. 2008 *Rev. Sci. Instrum.* **79** 10E719
[530] Van Zeeland M.A. *et al* 2018 *Rev. Sci. Instrum.* **10** 10B102
[531] Ding W.X. *et al* 2018 *Rev. Sci. Instrum.* **89** 10B103
[532] Brunner K.J., Knauer J., Meineke J., Stern M., Hirsch M., Kursinski B. and Wolf R.C. 2019 *J. Instrum.* **14** P11016
[533] Imazawa R., Ono T., Watts C., Ishikawa M., Shimada T., Itami K. and Hatae T. 2020 *Fusion Eng. Des.* **155** 111570
[534] Imazawa R., NAKAYAMA K. and AKIYAMA T. 2018 *Plasma Fusion Res.* **13** 1405112
[535] Imazawa R. *et al* Development of the far-infrared laser polarimetry for current profile measurement on ITER *Preprint: 2018 IAEA Fusion Energy Conf.* (*Gandhinagar 22–27 October 2018*) p FIP/P1–14 (available at: https://nucleus.iaea.org/sites/fusionportal/Pages/fec-landing.aspx)
[536] Imazawa R., Ono T., Hatae T. and Itami K. 2018 *Rev. Sci. Instrum.* **89** 103104

[537] Mirnov V.V., Ding W.X., Brower D.L., Van Zeeland M.A. and Carlstrom T.N. 2007 *Phys. Plasmas* **14** S337–S84
[538] Ford O.P., Svensson J., Boboc A. and McDonald D.C. 2009 *Plasma Phys. Control. Fusion* **51** 065004
[539] Imazawa R., Kawano Y. and Kusama Y. 2011 *Nucl. Fusion* **51** 113022
[540] Imazawa R. 2014 *Proc. 41 st Plasma Physics Conf. on Plasma Physics (EPS2014) (Berlin, Germany, 23–27 June 2014)* (IOP) (available at: http://ocs.ciemat.es/EPS2014PAP/pdf/P5.008.pdf)
[541] Imazawa R., Kawano Y., Ono T. and Itami K. 2016 *Rev. Sci. Instrum.* **87** 013503
[542] Eidietis N.W. 2021 *Fusion Sci. Technol.* **77** 738–44
[543] Terry P.W. *et al* 2015 *Nucl. Fusion* **55** 104001
[544] Chen J., Brower D., Ding W., Yoneda R. and Finkenthal D. 2021 *Rev. Sci. Instrum.* **92** 043502
[545] Ding W.X., Brower D.L., Terry S.D., Craig D., Prager S.C., Sarff J.S. and Wright J.C. 2003 *Phys. Rev. Lett.* **90** 035002
[546] Chen J. *et al* 2021 *Phys. Plasmas* **28** 022506
[547] Chen J., Ding W.X. and Brower D.L. 2018 *Plasma Phys. Control. Fusion* **60** 085001
[548] Soltwisch H. 1983 *Nucl. Fusion* **23** 1681
[549] Drachev V.P., Krasnikov Y.I. and Bagryansky P.A. 1993 *Rev. Sci. Instrum.* **64** 1010
[550] Bagryansky P.A., Khilchenko A.D., Kvashnin A.N., Lizunov A.A., Voskoboynikov R.V., Solomakhin A.L. and Koslowski H.R. 2006 *Rev. Sci. Instrum.* **77** 053501
[551] Dreier H., Bagryansky P., Baumgarten N., Biel W., Lambertz H.T., Lehnen M., Lizunov A. and Solomakhin A. 2011 *Rev. Sci. Instrum.* **82** 063509
[552] Akiyama T., Yasuhara R., Kawahata K., Okajima S. and Nakayama K. 2014 *Rev. Sci. Instrum.* **85** 11D301
[553] Brunner K.J., Akiyama T., Hirsch M., Knauer J., Kornejew P., Kursinski B., Laqua H., Meineke J., Trimiño Mora H. and Wolf R.C. 2018 *J. Instrum.* **13** P09002
[554] Akiyama T. *et al* 2018 *Rev. Sci. Instrum.* **89** 10B105
[555] Kawano Y., Chiba S.-I. and Inoue A. 2001 *Rev. Sci. Instrum.* **72** 1068
[556] Akiyama T., Sirinelli A., Watts C., Shigin P., Vayakis G. and Walsh M. 2016 *Rev. Sci. Instrum.* **87** 11E133
[557] Heald M.A. and Wharton C.B. 1965 *Plasma Diagnostics with Microwaves* (John Wiley and Sons, Inc.)
[558] Hartfuss H.J. and Geist T. 2013 *Fusion Plasma Diagnostics with mm-Waves* (John Wiley and Sons, Inc.)
[559] Taylor G., Bush C.E., Fredrickson E.D., Park H.K. and Ramsey A.T. 1992 *Nucl. Fusion* **32** 1867
[560] Fuchs C. and Austin M.E. 2001 *Phys. Plasmas* **8** 1594
[561] Liu Y., Zhou T., Hu Y., Liu C., Zhou R., Zhang T., Zhao H., Zhu Z., Liu X. and Ling B. 2019 *Nucl. Fusion* **59** 106024
[562] Orsitto F.P. *et al* (JET Contributors) 2022 *High Temperature Diagnostics Conf.* (*Rochester*, *15–19 May 2022*) (available at: https://htpd.lle.rochester.edu/)
[563] Giruzzi G. *et al* (JET Contributors) 2002 *Proc. 21st Joint Workshop on ECE and ECRH* (*Aix, FR*, *June 2022*)
[564] Goldsmith P.F. 1998 *Quasioptical Systems, Gaussian Beam Quasioptical Propagation and Applications* (IEEE Press/Chapman & Hall Publishers)
[565] Harfuss H.J. 1996 *Instrumentation of ECE for ITER in Diagnostics for Experimental Thermonuclear Fusion Reactors* ed P.E. Stott (Plenum Press)
[566] Ellis R.F. and Austin M.E. 2006 *Proc. 14th Joint Workshop on ECE and ECRH* (*Santorini Island, Greece*, *May 2006*)
[567] Taylor G. *et al Proc. 8th Joint Workshop on ECE and ECRH* ed H. Hartfuss (*Gut Ising, Germany 19–21 October 1992*) p 277 (available at: https://inis.iaea.org/records/z1h0k-tpt16)
[568] Taylor G. *et al Proc. 9th Joint Workshop on ECE and ECRH* ed J. Lohr (*Borrego Springs, USA, 22–26 January 1995*) (World Scientific) p 485
[569] Taylor G. and Harvey R.W. 2008 Assessment of an oblique ECE diagnostic for ITER *Report PPPL-4332* (Princeton Plasma Physics Laboratory) (available at: https://bp-pub.pppl.gov/pub_report/2008/PPPL-4332.pdf)
[570] Sapritsky V. and Prokhorov A. 2020 *Blackbody Radiometry Volume 1: Fundamentals* (Springer) pp 281–302
[571] Ouroua A., Beno J.H., Bryant A., Weeks D., Phillips P. and Rowan W.L. 2017 *Fusion Sci. Technol.* **72** 331–6
[572] Rowan W.L. *et al* 2015 *Symp. on Fusion Engineering (Austin, Texas, USA, 31 May–4 June 2015)* (available at: https://ppcsofe2015.unm.edu/)
[573] Ouroua A., Beno J., Bryant A., Khodak A., Phillips P., Rowan W., Taylor G. and Weeks D. 2018 *IEEE Trans. Plasma Sci.* **46** 1239
[574] Hartfuss H.J., Geist T. and Hirsch M. 1997 *Plasma Phys. Control. Fusion* **39** 1693–769
[575] Hartfuss H.-J. 2013 *Heterodyne Detection in Fusion Plasma Diagnostics with mm-Waves* (Wiley-VCH Verlag GmbH & Co)
[576] Chatterjee R., Phillips P.E., Heard J., Watts C., Gandy R. and Hubbard A. 2001 *Fusion Eng. Des.* **53** 113–21
[577] Bryerton E.W., Koller D., Hesler J.L. and Crowe T. 2014 *39th Int. Conf. on Infrared, Millimeter, and THz Waves, W4_C-27.3* (*Tucson, Arizona*, *12–19 September 2014*) (https://doi.org/10.1109/IRMMW-THz31325.2014)
[578] Austin M.E., Brookman M.W., Rowan W.L., Danani S., Bryerton E.W. and Dougherty P. 2016 *Rev. Sci. Instrum.* **87** 11E111
[579] Martin D.H. and Puplett E. 1969 *Infrared Phys.* **10** 105
[580] Pandya H.B. *et al* Preliminary results of prototype Martin–Puplett interferometer and transmission line developed for ITER ECE diagnostic *Preprint: 2018 IAEA Fusion Energy Conf.* (*Gandhinagar, 22–27 October 2018*) p FIP/P1–52P1 (available at: https://nucleus.iaea.org/sites/fusionportal/Pages/fec-landing.aspx)
[581] Kumar R. *et al* 2019 *EPJ Web Conf.* **203** 04009
[582] Watts C. 2007 *Fusion Sci. Technol.* **52** 176
[583] White A.E. *et al* 2008 *Rev. Sci. Instrum.* **79** 103505
[584] Sung C., White A.E., Irby J.H., Leccacorvi R., Vieira R., Oi C.Y., Peebles W.A. and Nguyen X. 2012 *Rev. Sci. Instrum.* **83** 10E311
[585] Howard N.T., Sung C. and White A.E. 2014 *Rev. Sci. Instrum.* **85** 11D811
[586] Yang Z.J., Xiao Y., Ma X.D., Pan X.M. and Xiao J.S. 2015 *Rev. Sci. Instrum.* **86** 043501
[587] Freethy S.J., Conway G.D., Classen I., Creely A.J., Happel T., Koehn A., Vanovac B. and White A.E. 2016 *Rev. Sci. Instrum.* **87** 11E102
[588] Sung C., Peebles W.A., Wannberg C., Rhodes T.L., Nguyen X., Lantsov R. and Bardoczi L. 2016 *Rev. Sci. Instrum.* **87** 11E123
[589] Fontana M., Porte L. and Cabrera P.M. 2017 *Rev. Sci. Instrum.* **88** 083506
[590] Creely A.J., Freethy S.J., Burke W.M., Conway G.D., Leccacorvi R., Parkin W.C., Terry D.R. and White A.E. 2018 *Rev. Sci. Instrum.* **89** 053503
[591] Fang K.R. *et al* 2019 *Rev. Sci. Instrum.* **90** 063503
[592] Cima G., Bravenec R.V., Wootton A.J., Rempel T.D., Gandy F.L.F., Watts C. and Kwon M. 1995 *Phys. Plasmas* **2** 720
[593] Watts C. and Gandy R.F. 1995 *Phys. Rev. Lett.* **75** 1759
[594] Sattler S. and Hartfuss H.J. (W7-AS Team) 1994 *Phys. Rev. Lett.* **72** 653
[595] Udintsev V.S. *et al* 2006 *Plasma Phys. Control. Fusion* **48** 33
[596] White A.E. *et al* 2014 *Nucl. Fusion* **54** 083019

[597] Porte L., Coda S., Goodman T.P., Pochelon A., Udintsev V.S. and Vuille V. 2012 *EPJ Web Conf.* **32** 03007
[598] Austin M.E. *et al* 2019 *Phys. Rev. Lett.* **122** 115001
[599] Sung C. *et al* 2017 *Phys. Plasmas* **24** 112305
[600] Sung C., Rhodes T.L., Staebler G.M., Yan Z., McKee G.R., Smith S.P., Osborne T.H. and Peebles W.A. 2018 *Phys. Plasmas* **25** 055904
[601] Bardóczi L., Sung C., Bañón Navarro A., Rhodes T.L., Carter T.A. and Jenko F. 2020 *Plasma Phys. Control. Fusion* **62** 025020
[602] Freethy S.J., Görler T., Creely A.J., Conway G.D., Denk S.S., Happel T., Koenen C., Hennequin P. and White A.E. (ASDEX Upgrade Team) 2018 *Phys. Plasmas* **25** 055903
[603] Bekefi G. 1966 *Radiation Processes in Plasmas* (Wiley)
[604] Udintsev V.S. *et al* 2019 *EPJ Web Conf.* **203** 03003
[605] Wang G., Rhodes T.L. and Peebles W.A. 2021 *Rev Sci Instrum* **92** 043523
[606] Korsholm S.B. *et al* 2022 *Rev Sci Instrum* **93** 103539
[607] Hoekzema J.A. *et al* 1997 *Rev Sci Instrum* **68** 275
[608] Bindslev H., Hoekzema J.A., Egedal J., Fessey J.A., Hughes T.P. and Machuzak J.S. 1999 *Phys. Rev. Lett.* **83** 3206
[609] Bindslev H. 1996 *J. Atmos. Terr. Phys.* **58** 983–9
[610] Korsholm S.B., Bindslev H., Furtula V., Leipold F., Meo F., Michelsen P.K., Moseev D., Nielsen S.K., Salewski M. and Stejner M. 2010 *Nucl. Instrum. Methods Phys. Res.* **623** 677–80
[611] Bindslev H. *et al* 2006 *Phys. Rev. Lett.* **97** 205005
[612] Meo F. *et al* 2008 *Rev Sci Instrum* **79** 10E501
[613] Bindslev H., Meo F., Tsakadze E.L., Korsholm S.B. and Woskov P. 2004 *Rev Sci Instrum* **75** 3598
[614] Meo F., Bindslev H., Korsholm S.B., Tsakadze E.L., Walker C.I., Woskov P. and Vayakis G. 2004 *Rev Sci Instrum* **75** 3585
[615] Leipold F., Furtula V., Salewski M., Bindslev H., Korsholm S.B., Meo F., Michelsen P.K., Moseev D., Nielsen S.K. and Stejner M. 2009 *Rev. Sci. Instrum.* **80** 093501
[616] Korsholm S.B. *et al* 2011 *Phys. Rev. Lett.* **106** 165004
[617] Stejner M., Nielsen S.K., Bindslev H., Korsholm S.B. and Salewski M. 2011 *Plasma Phys. Control. Fusion* **53** 065020
[618] Stejner M. *et al* 2012 *Rev. Sci. Instrum.* **83** 10E307
[619] Stejner M. *et al* 2017 *Plasma Phys. Control. Fusion* **59** 075009
[620] Kubo S. *et al* 2010 *Rev. Sci. Instrum.* **81** 10D535
[621] Nishiura M. *et al* 2014 *Nucl. Fusion* **54** 023006
[622] Moseev D. *et al* 2019 *Rev. Sci. Instrum.* **90** 013503
[623] Rasmussen J. *et al* 2019 *Plasma Phys. Control. Fusion* **61** 095002
[624] Salewski M. *et al* 2009 *Plasma Phys. Control. Fusion* **51** 035006
[625] Nielsen S.K. *et al* 2017 *Phys. Scr.* **92** 024001
[626] Salewski M., Eriksson L.-G., Bindslev H., Korsholm S.B., Leipold F., Meo F., Michelsen P.K. and Nielsen S.K. 2009 *Nucl. Fusion* **49** 025006
[627] Salewski M. *et al* 2011 *Nucl. Fusion* **51** 083014
[628] Stejner M., Korsholm S.B., Nielsen S.K., Salewski M., Bindslev H., Furtula V., Leipold F., Michelsen P.K., Meo F. and Moseev D. 2012 *Nucl. Fusion* **52** 023011
[629] Salewski M. *et al* 2018 *Nucl. Fusion* **58** 096019
[630] Rasmussen J., Stejner M., Jensen T., Klinkby E.B., Korsholm S.B., Larsen A.W., Leipold F., Nielsen S.K. and Salewski M. 2019 *Nucl. Fusion* **59** 096051
[631] Larsen A.W. *et al* 2019 *J. Instrum.* **14** C11009
[632] Trieschmann J., Larsen A.W., Mussenbrock T. and Korsholm S.B. 2021 *Phys. Plasmas* **28** 082505
[633] Korsholm S.B., Leipold F., Madsen R.B., Gutierrez H., Jensen T., Jessen M., Larsen A.W., Rasmussen J. and Salewski M. 2021 *Rev. Sci. Instrum.* **92** 033509
[634] Vidal C. *et al* 2019 *Fusion Eng. Des.* **140** 123–32
[635] Infante V. *et al* 2017 *Fusion Eng. Des.* **123** 663–8
[636] Rechena D., Infante V., Henriques E., Korsholm S.B., Larsen A.W., Gonçalves B., Vale A. and Luís R. 2021 *Fusion Eng. Des.* **168** 112454
[637] Rechena D., Infante V., Henriques E., Korsholm S.B., Larsen A.W., Gonçalves B., Vale A. and Luís R. 2021 *Fusion Eng. Des.* **171** 112593
[638] Lopes A. *et al* 2018 *Fusion Eng. Des.* **134** 22–28
[639] Lopes A. *et al* 2020 *Fusion Eng. Des.* **161** 111994
[640] Muscatello C.M. *et al* 2019 Design overview of the low-field side reflectometer for ITER *Proc. 14th Int. Reflectometry Workshop* (*Lausanne, Switzerland, 22–24 May 2019*) (available at: www.aug.ipp.mpg.de/IRW/IRW14/papers/113-IRW14-Muscatello-paper.pdf) p 113
[641] Muscatello C.M. *et al* 2020 *Nucl. Fusion* **60** 066005
[642] Muscatello C.M. *et al* 2021 *Rev. Sci. Instrum.* **92** 033524
[643] Clarricoats P.J.B. and Olver A. 1984 *Corrugated Horns for Microwave Antennas* (The Institution of Engineering and Technology)
[644] Lanzisera S. and Pister K. 2008 Burst mode two-way ranging with {Cramér-Rao} bound noise performance *IEEE Globecom 2008* Ad Hoc, *Sens. Mesh Netw. Symp. (New Orleans, LA, USA, 30 November–04 December 2008)* pp 1–5 (available at: https://globecom2008.ieee-globecom.org/symposium/adhoc.html)
[645] Casper T., Gribov Y., Kavin A., Lukash V., Khayrutdinov R. and Fujieda H. (C. Kessel for the ITER Organization and ITER Domestic Agencies) 2014 *Nucl. Fusion* **54** 013005
[646] Doane J.L. 1984 *IEEE Trans. Microw. Theory Tech.* **32** 1362–71
[647] Petrov A.A. and Petrov V.G. 2003 *Rev Sci Instrum* **74** 1465–9
[648] Belousov V.I., Vershkov V.A., Denisov G.G., Khozin M.A. and Shelukhin D.A. 2017 *Tech. Phys. Lett.* **43** 1037–40
[649] Shelukhin D.A., Vershkov V.A., Subbotin G.F., Sarychev D.V., Petrov A.A., Petrov V.G., Sokolov M.M. and Igonkina G.B. 2018 *Rev Sci Instrum* **89** 094708
[650] Simonet F. 1985 *Rev. Sci. Instrum.* **56** 664
[651] Zhu Y. *et al* 2021 *Rev. Sci. Instrum.* **92** 053522
[652] Zhu Y. *et al* 2020 Wide bandwidth millimeter-wave system-on-chip development and applications *2020 45th Int. Conf. on Infrared, Millimeter, and Terahertz Waves (IRMMW-THz)* (IEEE) *(Buffalo, New York, USA, 8–13 November 2020)* (available at: https://ieeexplore.ieee.org/xpl/conhome/9370343/proceeding)
[653] Margomenos A. *et al IEEE Trans. Microw. Theory Tech.* **68** 2957–83
[654] Advancing high-frequency and high-power electron device technology *Conf. Report: IEDM 2016* (San Francisco, California, USA, 3–7 December 2016) (available at: https://www.proceedings.com/content/033/033317webtoc.pdf)
[655] Xie J., Wang H., Ding W., Li H., Lan T., Liu A., Liu W. and Yu C. 2014 *Rev. Sci. Instrum.* **85** 11D828
[656] Zhongbing S.H.I., Zhong W. and Jiang M. 2018 *Plasma Sci. Technol.* **20** 094007
[657] Li J. *et al* 2020 *J. Instrum.* **15** C02048
[658] Liu D.K., Ding W.X., Mao W.Z., Zhang Q.F., Fan F.B., Sang L.L., Lu Q.M. and Xie J.L. 2021 *Rev. Sci. Instrum.* **92** 053516
[659] Mao W., Yuan P., Zheng J., Ding W., Li H., Lan T., Liu A., Liu W. and Xie J. 2016 *Rev. Sci. Instrum.* **87** 11E122
[660] Mao W. *et al* 2021 *Rev. Sci. Instrum.* **92** 053514
[661] Auston D.H., Cheung K.P. and Smith P.R. 1984 *Appl. Phys. Lett.* **45** 284–6

[662] Castro-Camus E., Lloyd-Hughes J., Johnston M.B., Fraser M.D., Tan H.H. and Jagadish C. 2005 *Appl. Phys. Lett.* **86** 1–3
[663] Jamison S.P., Shen J., Jones D.R., Issac R.C., Ersfeld B., Clark D. and Jaroszynski D.A. 2003 *J. Appl. Phys.* **93** 4334–6
[664] Teka G.G., Zerbini M., Bombarda F. and Damry D. 2018 THz- TDS transmission measurements of spectroscopic lamps plasma *2018, 43rd Int. Conf. on Infrared, Millimeter, and Terahertz Waves (IRMMW-THz)* (*Nagoya (Japan) 9–14 September 2018*) pp 1–2
[665] Mazzucato E. 1998 *Rev. Sci. Instrum.* **69** 2201–17
[666] Zerbini M., Amadeo P. and Buratti P. 1997 *Rev. Sci. Instrum.* **68** 428–30
[667] Heijnen S.H. 1995 Pulsed-radar reflectometry *PhD thesis* FOM-instituut voor Plasmafysica
[668] Zerbini M., Bombarda F., Doria A., Galatola-Teka G. and Giovenale E. 2016 From FIR and mm waves to THz plasma diagnostics applications *41st Int. Conf. on Infrared, MM, and THz waves (IRMMW-THz)* (*Copenhagen (Denmark) 25–30 September 2016*) (https://doi.org/10.1109/IRMMW-THz.2016.7758535)
[669] Chiocchio S. 2014 *Project Requirements (PR)* (ITER private communication)
[670] Iida H., Khripunov V., Petrizzi L. and Federici G. 2004 *Nuclear Analysis Report (NAR)* (ITER Private Communication)
[671] Norgett M.J., Robinson M.T. and Torrens I.M. 1975 *Nucl. Eng. Des.* **33** 50–54
[672] C-model_R181031 model document ITER_D_ XETSWC
[673] Juárez R., Catalan J.P., Ogando F., Lopez-Revelles A.J., Sauvan P., Jakhar S., Polunovskiy E., Loughlin M. and Sanz J. 2018 *Nucl. Fusion* **58** 126012
[674] Vukolov K.Y. 2009 *Fusion Eng. Des.* **84** 1961–3
[675] Gusarov A. 2013 *Fusion Eng. Des.* **88** 1192–5
[676] Udintsev V.S. *et al* 2019 *IEEE Trans. Plasma Sci.* **47** 864–8
[677] Vukolov K.Y. 2017 *Fusion Eng. Des.* **123** 919–22
[678] Gusarov A., Vukolov K.Y., Orlovskiy I.I. and Andreenko E.N. 2020 *Fusion Eng. Des.* **151** 111356
[679] Peruzzo S., Arshad S., Brombin M., Chitarin G., Gonzalez W., Grando L., Portales M., Rizzolo A., Vayakis G. and Vermeeren L. 2013 *Fusion Eng. Des.* **88** 1302–5
[680] Vermeeren L. and Leysen W. 2013 *Fusion Eng. Des.* **88** 1161–4
[681] Golluccio G. 2022 System design description (DDD) 55.A0 magnetic diagnostic *ITER_D_3UYQGX* (ITER Private Communication) (https://doi.org/10.3390/s22176341)
[682] Reboun J., Hromadka K., Hermansky V. and Johan J. 2017 *Microelectron. Eng.* **167** 58–62
[683] Hlina J., Reboun J. and Hamacek K. 2020 *Scr. Mater.* **176** 23–27
[684] Testa D., Cemes M., Douhane A. and Tanguy F. 2023 *J. Instrum.* **18** C06002
[685] Duran I., Entler S., Kohout M., Kočan M. and Vayakis G. 2016 *Rev. Sci. Instrum.* **87** 11D446
[686] Entler S., Duran I., Kocan M. and Vayakis G. 2017 *J. Instrum.* **12** C07007
[687] Entler S., Sebek J., Duran I., Vyborny K., Grover O., Kocan M. and Vayakis G. 2018 *Rev. Sci. Instrum.* **89** 10J112
[688] Entler S., Kocan M., Duran I., Vayakis G., Lucca F., Vigano F. and Cantu R. 2018 *IEEE Trans. Plasma Sci.* **46** 1276–80
[689] Duran I., Entler S., Kocan M., Kohout M., Viererbl L., Mušálek R., Chráska T. and Vayakis G. 2017 *Fusion Eng. Des.* **123** 690–4
[690] Duran I. *et al* 2019 *Fusion Eng. Des.* **146** 2397–400
[691] Entler S. *et al* 2020 *Fusion Eng. Des.* **153** 111454
[692] Kovarik K., Entler S., Duran I. and Eade T. 2020 *Fusion Eng. Des.* **155** 111670
[693] Entler S., Duran I., Simonovsky M., Reboun J., Turjanica P., Soban Z., Sladek P. and Viererbl L. 2023 *Fusion Eng. Des.* **189** 113476
[694] Entler S., Soban Z., Duran I., Kovarik K., Vyborny K., Sebek J., Tazlaru S., Strelecek J. and Sladek P. 2021 *Sensors* **21** 721
[695] Bolshakova I. *et al* 2017 *Nucl. Fusion* **57** 116042
[696] Bolshakova I. *et al* 2020 Nanofilm materials for devices of magnetic field measurement in radiation environment *IEEE 15th Int. Conf. on Advanced Trends in Radioelectronics, Telecommunications and Computer Engineering (TCSET)* (*Ukraine, 25–29 February 2020*) (available at: https://ieeexplore.ieee.org/document/9088653)
[697] 2022 Graphene hall sensors brochure 05/2022 (Paragraf Ltd)
[698] Snipes J.A. *et al* 2012 *Fusion Eng. Des.* **87** 1900–6
[699] Rogers A. 1988 *Int. J. Optoelectron.* **3** 391–407
[700] Rose A.H., Etzel S.M. and Wang C.M. 1997 *J Lightwave Technol.* **15** 803–7
[701] Williams P.A., Rose A.H., Day G.W., Milner T.E. and Deeter M.N. 1991 *Appl. Opt.* **30** 1176–8
[702] Vacas C. *et al* 2016 Load specifications for OVSS 55.A-55.A6 *ITER_D_R6KD82* (ITER Private Communication)
[703] Gusarov A., Leysen W., Beaumont P., Wuilpart M., Dandu P., Boboc A., Croft D., Bekris N. and Batistoni P. 2021 *Fusion Eng. Des.* **165** 112228
[704] Girard S. *et al* 2019 *Rev. Phys.* **4** 100032
[705] Brichard B., van Ierschot S. and Hendrickx C. 2007 On the use of photobleaching and thermal annealing to recover the optical transmission in irradiated pure silica fibres *9th European Conf. on Radiation and Its Effects on Components and Systems, RADECS 2007* (*Deauville, France, 10–14 September 2007*) (https://doi.org/10.1109/RADECS.2007.5205428)
[706] Clough M. 2014 Load specifications for outer vessel magnetic sensors (PBS: 55.A3-A9) *ITER_D_3PBH57* (ITER Private Communication)
[707] Mélin G., Guitton P., Montron R., Gotter T., Robin T., Overton B., Morana A., Rizzolo S. and Girard S. 2019 *IEEE Trans. Nucl. Sci.* **66** 1657–62
[708] Ott M. 2000 *TID Radiation Induced Attenuation Testing at 1300 Nm Using ISS Requirements on Three Optical Fibers Manufactured by Lucent SFT* (NASA Goddard Space Flight Center)
[709] Kuhnhenn J., Hoeffgen S.K., Köhn O., Schumann O., Weinand U. and Wolf R. 2014 Irradiation tests of optical fibres below 20 K *Int. Conf. on Space Optics* (SPIE) *(Tenerife, Canary Islands, Spain, 6–10 October 2014)* (available at: https://spie.org/Publications/Proceedings/Volume/10563)
[710] Cheymol G., Long H., Villard J.F. and Brichard B. 2008 *IEEE Trans. Nucl. Sci.* **55** 2252–8
[711] Brichard B. 2009 Final report on the irradiation testing of a fibre-optic sensor suitable for plasma-current measurement *SCK-CEN 30* (Private Communication)
[712] Brichard B. 2010 Works on ITER prototypes at SCK•CEN under support of the Belgian Federal Government *Annual Progress Report 2010, SCK-CEN 56* (Private Communication)
[713] Morana A. *et al* 2015 *Opt. Mater. Express* **5** 898–911
[714] Brichard B. 2006 Final report on initial assessment of optical fibres as current sensors: gamma radiation effects Mol *SCK•CEN 20* (Private Communication)
[715] Leysen W., Gusarov A., Wuilpart M., Beaumont P., Boboc A., Croft D., Bekris N. and Batistoni P. (JET Contributors) 2020 *Fusion Eng. Des.* **160** 111754

[716] Meister H., Penzel F., Szabo-Balint Z., Reichle R. and Ingesson L.C. 2019 *Fusion Eng. Des.* **146** 1015–8
[717] Reichle R. 2001 Radiation hardness test of mica bolometers for ITER in JMTR *28th EPS Conf. on Contr. Fusion and Plasma Phys. (Funchal) (Madeira, Portugal, 18–22 June 2001)* (available at: https://info.fusion.ciemat.es/OCS/EPS2001/html/index.html)
[718] Meister H. *et al* 2008 *Rev. Sci. Instrum.* **79** 511–5
[719] Gusarov A., Huysmans S., Giannone L. and Meister H. 2011 *Fusion Eng. Des.* **86** 1200–3
[720] Meister H. *et al* 2017 *Fusion Eng. Des.* **120** 21–26
[721] Meister H., Schmitt S., Szenthe I., Szakál A., Albrecht H. and Gillemot F. 2020 *Fusion Eng. Des.* **161** 111995
[722] Hodgson E.R. 1998 Radiation Problems and Testing of ITER Diagnostic Components *Diagnostics for Experimental Thermonuclear Fusion Reactors 2* ed P. Stott, G. Gorini, P. Prandoni and E. Sindoni (Springer US) pp 261–8
[723] Orlinski D.V. and Vukolov K.Y. 1999 *Plasma Devices Oper.* **7** 195–204
[724] Costley A.E., Campbell D.J., Kasai S., Young K.E. and Zaveriaev V. 2001 *Fusion Eng. Des.* **55** 331–46
[725] Walsh M. *et al* 2011 ITER diagnostic challenges *2011 IEEE/NPSS 24th Symp. on Fusion Engineering* (*Chicago, IL, USA, 26–30 June 2011*) pp 1–8 (available at: https://ieeexplore.ieee.org/xpl/conhome/6036254/proceeding)
[726] Costley A.E., Sugie T., Vayakis G. and Walker C.I. 2005 *Fusion Eng. Des.* **74** 109–19
[727] Donné A.J.H., Edlington T., Joffrin E., Koslowski H.R., Nieswand C., Segre S.E., Stott P.E. and Walker C. 1999 *Rev. Sci. Instrum.* **70** 726–9
[728] Donné A.J.H. *et al* 2004 *Rev. Sci. Instrum.* **75** 4694–701
[729] Costley A.E. 2001 Requirements and issues in diagnostics for next step burning plasma experiments *Proc. Int. Conf. on Advanced Diagnostic for Magnetic and Inertial Fusion* (*Varenna, Italy, 3–7 September 2001*) p 10 (available at: https://link.springer.com/book/10.1007/978-1-4419-8696-2)
[730] Litnovsky A., Voitsenya V.S.S., Costley A. and Donné A.J.H.J.H. 2007 *Nucl. Fusion* **47** 833
[731] Litnovsky A. *et al* 2009 *Nucl. Fusion* **49** 075014
[732] Litnovsky A. *et al* 2019 *Nucl. Fusion* **59** 066029
[733] Litnovsky A. *et al* 2007 *J Nucl Mater* **363–365** 1395-1402
[734] Voitsenya V. *et al* 2001 *Rev. Sci. Instrum.* **72** 475–82
[735] Voitsenya V.S.S. and Litnovsky A. 2009 *Plasma Devices Oper.* **17** 309–18
[736] Rubel M.J., De Temmerman G., Coad J.P., Vince J., Drake J.R., Le Guern F., Murari A., Pitts R.A., Walker C. and Contributors J.-E. 2006 *Rev. Sci. Instrum.* **77** 1–6
[737] Rubel M., Temmerman G.D., Sundelin P., Coad J.P., Widdowson A., Hole D., Guern F.L., Stamp M. and Vince J. 2009 *J. Nucl. Mater.* **390–391** 1066–9
[738] Ivanova D., Rubel M., Widdowson A., Petersson P., Likonen J., Marot L., Alves E., Garcia-Carrasco A. and Pintsuk G. 2014 *Phys. Scr.* **2014** 014011
[739] Moon S., Petersson P., Rubel M., Fortuna-Zalesna E., Widdowson A., Jachmich S., Litnovsky A. and Alves E. 2019 *Nucl. Mater. Energy* **19** 59–66
[740] Rudakov D.L. *et al* 2006 *Rev. Sci. Instrum.* **77** 10F126
[741] De Temmerman G., Pitts R.A., Voitsenya V.S., Marot L., Veres G., Maurer M. and Oelhafen P. 2007 *J Nucl Mater* **363–365** 259–63
[742] Litnovsky A. *et al* 2008 *Fusion Eng. Des.* **83** 79–89
[743] Wienhold P. *et al* 2005 *J. Nucl. Mater.* **337–339** 1116–20
[744] Matveeva M., Litnovsky A., Marchuk O., Schulz C., Möller S., Wienhold P., Philipps V., Stoschus H. and Samm U. 2011 *Phys. Scr.* **2011** 014072
[745] Litnovsky A. *et al* 2011 *J. Nucl. Mater.* **417** 830–3
[746] Litnovsky A. *et al* 2007 *Fusion Eng. Des.* **82** 123–32
[747] Lipa M. *et al* 2006 *Fusion Eng. Des.* **81** 221–5
[748] Voitsenya V.S., Bardamid A.F., Belyaeva A.I., Bondarenko V.N., De Temmerman G., Konovalov V.G., Lipa M., Litnovsky A., Ryzhkov I.V. and Schunke B. 2008 *Plasma Devices Oper.* **16** 1–10
[749] Litnovsky A. *et al* 2015 *Nucl. Fusion* **55** 093015
[750] Litnovsky A. *et al* 2013 *Nucl. Fusion* **53** 073033
[751] Lipa M., Schunke B. and Gil C. 2005 First mirror study in Tore-Supra *EFDA Report on Task TW2-TPDS-DIADEV-D02*
[752] Litnovsky A. *et al* 2007 *J. Nucl. Mater.* **363–365** 1395–402
[753] Gil C., Elbeze D., Beraud A., Echard B., Patterlini J.C., Philip J., Toulouse L., Lipa M. and Litnovsky A. 2007 *Fusion Eng. Des.* **82** 1238–44
[754] Takase K., Akimoto H. and Topilski L.N. 2001 *Fusion Eng. Des.* **54** 593–603
[755] Mazed D., Lo Frano R., Aquaro D., Del Serra D., Sekachev I. and Olcese M. 2018 *Nucl. Eng. Des.* **335** 241–54
[756] Almazan R.M. *et al* 2017 *Technical Report on F4E Task F4E-FPA-407—SG07 FPA for Diagnostic Development and Design Equatorial Visible/InfraRed Wide Angle Viewing System D04—Steam and Humidity Test Report (F4E Barcelona)* (Private Communication)
[757] Lo Frano R., Mazed D., Aquaro D., Del Serra D. and Orlandi F. 2017 *Fusion Eng. Des.* **122** 42–46
[758] Rosanvallon S. *et al* 2009 *J. Nucl. Mater.* **390–391** 57–60
[759] Kim B., Seon C., Oh S.-G.-G., Kim Y.K., An Y., Bang E., Hong S.-H.-H., Pak S., Cheon M. and Lee H.G. 2018 *Fusion Eng Des* **129** 269–76
[760] Sugie T., Costley A.E. and Litnovsky A. 2007 *Update of First Mirror Table Proc. 12th Meeting of the ITPA Topical Group on Diagnostics* (*Princeton, USA*) p 1 (available at: https://nstx.pppl.gov/DragNDrop/Scientific_Conferences/ITPA/2007/ITPA_DIAG_2007_MTG/)
[761] Joanny M. *et al* 2012 *Rev. Sci. Instrum.* **83** 10E506
[762] Soukhanovskii V.A., McLean A.G. and Allen S.L. 2014 *Rev. Sci. Instrum.* **85** 11E418
[763] Lister J.B., Portone A. and Gribov Y. 2006 *IEEE Control Syst. Mag.* **26** 79–91
[764] Litnovsky A. (Diagnostics I T G on and Team I) 2009 *Work Plan of the First Mirror R&D* (Private Communication)
[765] Johnson D., Thomas D. and Vayakis G. 2010 Impact of first mirror risk on ITER measurement capability—A start *16th Meeting of the ITPA Topical Group on Diagnostics (Pohang, Korea, 12–15 October 2009)* ((ITER Organization), Private Communication) (available at: https://www.iter.org/sites/default/files/media/2024-03/2010_diag_report.pdf)
[766] Marot L., De Temmerman G., Oelhafen P., Covarel G. and Litnovsky A. 2007 *Rev. Sci. Instrum.* **78** 103507
[767] Eren B., Marot L., Litnovsky A., Matveeva M., Steiner R., Emberger V., Wisse M., Mathys D., Covarel G. and Meyer E. 2011 *Fusion Eng. Des.* **86** 2593–6
[768] Peng J., Litnovsky A., Kreter A., Krasikov Y.Y., Rasinski M., Breuer U. and Chen J.L.L. 2018 *Fusion Eng. Des.* **128** 107–12
[769] Litnovsky A., Peng J., Kreter A., Krasikov Y.Y., Rasinski M., Nordlund K., Granberg F., Jussila J., Breuer U. and Linsmeier C.C. 2019 *Fusion Eng Des* **146** 1450–3
[770] Litnovsky A., Krasikov Y., Rasinski M., Kreter A., Linsmeier C., Mertens P., Unterberg B., Breuer U. and Wegener T. 2017 *Fusion Eng. Des.* **123** 674–7
[771] Eckstein W., Roth J., Garcia-Rosales C. and Ottenberger W. 1993 Sputtering data *Report of IPP Garching IPP 9/82*
[772] Yamamura Y. and Tawara H. 1996 *At. Data Nucl. Data Tables* **62** 149–253
[773] Palik E.D. 1998 *Handbook of Optical Constants of Solids* (Academic Press)

[774] Marot L., Arnoux G., Huber A., Huber V., Mertens P., Sergienko G. and Meyer E. (Contributors J E T) 2015 *J. Coat. Sci. Technol.* **2** 72
[775] Denisov V.N., Klyatskin A.S., Butrim V.N., Beresnev A.G., Vagin V.P., Alekseev A.G., Orlovskiy I.I. and Smekalin V.P. 2017 *Weld. Int.* **31** 571
[776] Yayakis G., Hodgson E.R., Voitsenya V. and Walker C.I. 2008 *Fusion Sci. Technol.* **53** 699–750
[777] Ushakov A. *et al* 2018 *Fusion Eng Des* **131** 54–60
[778] Krasikov Y. *et al* 2021 *Fusion Eng. Des.* **169** 112408
[779] Brooks J.N. and Allain J.P. 2008 *Nucl. Fusion* **48** 45003
[780] Kotov V., Litnovsky A., Kukushkin A.S.S., Reiter D. and Kirschner A. 2009 *J. Nucl. Mater.* **390–391** 528–31
[781] Kotov V., Reiter D., Kukushkin A.S. and Pacher H.D. 2011 *Fusion Eng. Des.* **86** 1583–6
[782] Kotov V. 2016 *Nucl. Fusion* **56** 106027
[783] Kotov V., Reiter D., Litnovsky A., Krimmer A., Kirschner A. and Krasikov Y. 2011 *Phys. Scr.* **2011** 014071
[784] Reiter D., Baelmans M. and Börner P. 2005 *Fusion Sci. Technol.* **47** 172–86
[785] Rode S. *et al* Multi-staged ERO2.0 simulation of material erosion and deposition in recessed mirror assemblies in JET and ITER *Preprint: 2023 IAEA Fusion Energy Conf. (London)* [p TH-M] (available at: https://nucleus.iaea.org/sites/fusionportal/Pages/fec-landing.aspx)
[786] Schwanke C., Pflug A., Siemers M. and Szyszka B. 2012 *Parallel Particle-in-Cell Monte-Carlo Algorithm for Simulation of Gas Discharges under PVM and MPI Applied Parallel and Scientific Computing* ed K. Jónasson (Springer Berlin Heidelberg) pp 213–9
[787] Friconneau J.-P., Beaudoin V., Dammann A., Dremel C., Martins J.P. and Pitcher C.S. 2017 *Fusion Eng. Des.* **124** 673–6
[788] Litnovsky A., Laengner M., Matveeva M., Schulz C., Marot L., Voitsenya V.S., Philipps V., Biel W. and Samm U. 2011 *Fusion Eng. Des.* **86** 1780
[789] Moser L., Marot L., Eren B., Steiner R., Mathys D., Leipold F., Reichle R. and Meyer E. 2015 *Nucl. Fusion* **55** 063020
[790] Dmitriev A.M. *et al* 2019 *Fusion Eng. Des.* **146** 1390–3
[791] Sanchez F. *et al* 2023 *J. Nucl. Mater.* **581** 154382
[792] Orlovskiy I., Alekseev A., Andreenko E., Asadulin G. and Gorshkov A. 2017 *Fusion Eng. Des.* **123** 1011–4
[793] Salewski M., Meo F., Bindslev H., Furtula V., Korsholm S.B., Lauritzen B., Leipold F., Michelsen P.K., Nielsen S.K. and Nonbøl E. 2008 *Rev. Sci. Instrum.* **79** 10E729
[794] Rogov A.V., Kapustin Y.V. and Alekseev A.G. 2015 *Inst. Exp. Tech.* **58** 161–6
[795] Rogov A.V., Kapustin Y.V. and Martynenko Y.V. 2021 *Tech. Phys.* **66** 1268–74
[796] Kapustin Y.V., Rogov A.V., Vukolov K.Y. and Gorbunov A.V. 2016 The integration of DC/PDC cleaning system electrodes into H-alpha diagnostic first mirror unit *30th Meeting of the ITPA Topical Group on Diagnostics (Novosibirsk, Russia, 21–24 June 2016)* (ITER Organization, Private Communication) p 1 (available at: https://indico.inp.nsk.su/event/6/)
[797] Rogov A.V., Kapustin Y.V., Gureev V.M. and Domantovskii A.G. 2021 *J. Surf. Invest. X-ray Synchrotron Neutron Tech.* **15** 563–9
[798] Kapustin Y.V. and Rogov A.V. 2020 *Phys. At. Nucl.* **83** 1093–100
[799] Joanny M., Travere J.M., Salasca S., Marot L., Meyer E., Thellier C., Cammarata C., Gallay G. and Ferme J.J. 2012 *IEEE Trans. Plasma Sci.* **40** 692
[800] Travere J.M. *et al* 2011 The ITER VIS/IR wide angle viewing system: challenges and on-going R&D *ANIMMA 2011—Proc.: 2nd Int. Conf. on Advancements in Nuclear Instrumentation, Measurement Methods and their Applications (Ghent, Belgium, 6–9 Jun 2011)* vol 43 pp 1–9 (available at: https://ieeexplore.ieee.org/xpl/conhome/6170427/proceeding)
[801] Krawczynska A.T., Ciupiński Ł. and Petersson P. 2020 *Phys. Scr.* **2020** 014019
[802] Garcia-Carrasco A., Petersson P., Hallén A., Grzonka J., Gilbert M.R., Fortuna-Zalesna E. and Rubel M. 2016 *Nucl. Instrum. Methods Phys. Res. B* **382** 91–95
[803] Kumar N.A.P.K., Leonard K.J., Jellison G.E. and Snead L.L. 2015 *Fusion Sci. Technol.* **67** 771–83
[804] Snead L.L., Leonard K.J., Jellison G.E., Sawan M. and Lehecka T. 2009 *Fusion Sci. Technol.* **56** 1069–77
[805] Samsonov D. *et al* 2020 First mirror unit and large-scale collecting mirror conceptual designs for ITER optical diagnostics *Proc. 31st Symp. on Fusion Technology (SOFT 2020) II 1 (Virtual Conference, 20–25 September 202)* (available at: https://soft2020.eu/)
[806] Takeuchi M., Sugie T., Ogawa H., Ishikawa M., SHIMADA T. and Kusama Y. 2013 *Plasma Fusion Res.* **8** 2402147
[807] Bigot B. 2022 *Nucl. Fusion* **62** 042001
[808] Cinque M. *et al* 2020 *IEEE Trans. Plasma Sci.* **48** 1768–78
[809] Rumble J. 2017 *The CRC Handbook on Chemistry and Physics* (CRC Press)
[810] Pereira A. *et al* 2020 *IEEE Trans. Plasma Sci.* **48** 1619–24
[811] Soni K., Moser L., Steiner R., Mathys D., Le Guern F., Piqueras J., Marot L. and Meyer E. 2019 *Nucl. Mater. Energy* **21** 100702
[812] Herrmann A., Rohde V., Schall G., Balden M., Bösser D., Hegele K., Hunger K., Stober J., Vierle T. and Vorbrugg S. 2021 *Fusion Eng. Des.* **167** 112385
[813] Samsonov D. *et al* 2019 First mirror unit and large-scale collecting mirror conceptual designs for ITER optical diagnostics design of FMU mock-up for ITER RF power distribution in the FMU mirror assembly design of FMU ceramic RF components large-scale collecting mirror design of II 2823 (https://doi.org/10.3389/fped.2019.00155)
[814] Soni K., Moser L., Donkó Z., Hartmann P., Korolov I., Antunes R., Juhasz Z., Steiner R., Marot L. and Meyer E. 2021 *Plasma Phys. Control. Fusion* **63** 045005
[815] Soni K., Antunes R., Steiner R., Moser L., Marot L. and Meyer E. 2022 *Plasma Sources Sci. Technol.* **31** 075009
[816] Soni K., Steiner R., Antunes R., Moser L., Shigin P., Reichle R., Marot L. and Meyer E. 2021 *Nucl. Fusion* **61** 126017
[817] Litnovsky A., Duran I., Coenen J.W., Gasparyan Y., Gilbert M.R., Hollmann E., Linsmeier C., Nogami S., Skinner C.H. and Zinkle S. 2021 *Fusion—Reactor Materials Encyclopedia of Nuclear Energy* vol 3, ed E. Greenspan (Elsevier Inc.) pp 594–619
[818] Soni K., Moser L., Porosnicu C., Antunes R., Arredondo R., Dinca P., Steiner R., Marot L. and Meyer E. 2022 *J. Nucl. Mater.* **564** 153671
[819] Dmitriev A.M. *et al* 2022 *Nucl. Mater. Energy* **30** 101111
[820] Ryabtsev S., Gasparyan Y., Zibrov M., Shubina A. and Pisarev A. 2016 *Nucl. Instrum. Methods Phys. Res. B* **382** 101–4
[821] Shu W.M., Kawasuso A., Miwa Y., Wakai E., Luo G.-N.-N. and Yamanishi T. 2007 *Phys. Scr.* **T128** 96–99
[822] Buzi L., Temmerman G.D., Unterberg B., Reinhart M., Litnovsky A., Philipps V., Oost G.V. and Möller S. 2014 *J. Nucl. Mater.* **455** 316–9
[823] Shu W.M., Wakai E. and Yamanishi T. 2007 *Nucl. Fusion* **47** 201–9
[824] Manhard A., Balden M. and von Toussaint U. 2017 *Nucl. Fusion* **57** 126012
[825] Tanabe T., Yamanishi Y. and Imoto S. 1992 *J. Nucl. Mater.* **191–194** 439–43

[826] von Toussaint U., Gori S., Manhard A., Höschen T. and Höschen C. 2011 *Phys. Scr.* **2011** 14036
[827] Rogov A.V. and Vukolov K.Y. 2006 *Tech. Phys.* **51** 499–503
[828] Marot L., De Temmerman G., Van Den Berg M.A., Renault P.O., Covarel G., Joanny M., Travère J.M., Steiner R., Mathys D. and Meyer E. 2016 *Nucl. Fusion* **56** 066015
[829] Gorodetsky A.E., Zalavutdinov R.K., Bukhovets V.L., Markin A.V., Zakharov A.P., Rybkina T.V., Zolotarevsky V.I., Mukhin E.E., Razdobarin A.G. and Dmitriev A.M. 2016 *J. Surf. Invest.* **10** 1214–25
[830] Sharpe J.P., Kolasinski R.D., Shimada M., Calderoni P. and Causey R.A. 2009 *J. Nucl. Mater.* **390–391** 709–12
[831] Knaster J. *et al* 2011 *Fusion Eng. Des.* **86** 1053–6
[832] Moser L., Steiner R., Leipold F., Reichle R., Marot L. and Meyer E. 2015 *J. Nucl. Mater.* **463** 940–3
[833] Moser L. *et al* 2017 *Phys. Scr.* **T170** 014047
[834] Yan R. *et al* 2018 *Nucl. Fusion* **58** 026008
[835] Dmitriev A.M., Razdobarin A.G., Snigirev L.A., Elets D.I., Bukreev I.M., Mukhin E.E., Tolstyakov S.Y., Kupriyanov I.B. and Moser L. 2024 *Fusion Eng. Des.* **209** 114724
[836] Hiret P. *et al* 2023 *Plasma Sources Sci. Technol.* **32** 095021
[837] Soni K., Iyyakkunnel S., Steiner R., Antunes R., Moser L., Bieri O., Marot L. and Meyer E. 2022 *Nucl. Fusion* **62** 126009
[838] Marchuk O. *et al* 2020 *Atoms* **7** 1–16
[839] Huber A. *et al* 2012 *Rev. Sci. Instrum.* **83** 10D511
[840] Huber A. *et al* 2013 *Fusion Eng. Des.* **88** 1361–5
[841] Marot L. *et al* 2021 *Fusion Eng. Des.* **163** 112140
[842] Patel V., Singh B. and Thomas J.H. 1992 *Appl. Phys. Lett.* **61** 1912–4
[843] Sobolewski M.A. and Lahr D.L. 2012 *J. Vac. Sci. Technol. A* **30** 051303
[844] Vašina P. and Dvořák P. 2009 *Europhys. Lett.* **85** 15002
[845] Razdobarin A., Dmitriev A. and Samsonov D. RF discharge mirror cleaning basis, report on Deliverable 3 "Analysis of power handling characteristics of MI cables and hollow feeders", contract :IO/17/CT/4300001626, ITER Document ID: ITER_D_VYKMFC v0.0
[846] Samara V., Bowden M.D. and Braithwaite N.S.J. 2010 *J. Phys. D: Appl. Phys.* **43** 124017
[847] Krasikov Y., Panin A., Biel W., Krimmer A., Litnovsky A., Mertens P., Neubauer O. and Schrader M. 2015 *Fusion Eng. Des.* **96–97** 812–6
[848] Krasikov Y., Panin A., Litnovsky A., Mertens P. and Schrader M. 2017 *Fusion Eng. Des.* **124** 548–52
[849] Schühle U., Uhlig H., Curdt W., Feigl T., Theissen A. and Tariaca L. 2006 Thin silicon carbide coating of the primary mirror of VUV imaging instruments of solar orbiter *Proc. Second Solar Orbiter Workshop 2006* (*Athens, Greece*, *16–20 October 2006*) (ESA Publications Division) 2007 (ESA SP 641) Paper P83 (available at: http://conferences.phys.uoa.gr/solo2006/)
[850] Ariola M. and Pironti M. 2016 *Magnetic Control of Tokamak Plasmas* (*Advances in Industrial Control*) 2nd edn (Springer) (https://doi.org/10.1007/978-3-319-29890-0)
[851] Kovarik K., Ďuran I., Boshakova I., Holyaka R. and Erashok V. 2006 *Czech. J. Phys.* **56** B104–B10
[852] Ricardo E., Silva F.D., Heuraux S. and Silva A. 2019 *JINST* **14** C08010
[853] Zhang H., Xiao B., Luo Z., Hang Q., Yang J. and Weldon D. 2018 *IEEE Trans. Plasma Sci.* **46** 2162–9
[854] Hommen G., Baar M.D., Duval B.P., Andrebe Y., Le H.B., Klop M.A., Doelman N.J., Witvoet G. and Steinbuch M. 2014 *Nucl. Fusion* **54** 073018
[855] Mattei M., Labate C.V. and Famularo D. 2013 *Automatica* **49** 169–77
[856] Schuster E., Walker M.L., Humphreys D.A. and Krstić M. 2005 *Automatica* **41** 1173–9
[857] Ambrosino R., Ariola M., Bachmann C., Castaldo A., Maviglia F., Mattei M. and Tartaglione G. 2021 *Fusion Eng. Des.* **171** 112640
[858] Ariola M., Pironti A., Ambrosino R., Mattei M., Biel W. and Franke T. 2019 *Fusion Eng. Des.* **146** 728–31
[859] Delgrave J. *et al* 2022 *Nature* **602** 414–9
[860] Moreau D. 2008 *Nucl. Fusion* **48** 106001
[861] Felici F., Sauter O., Coda S., Duval B.P., Goodman T.P., Moret J.-M. and Paley J.I. 2011 *Nucl. Fusion* **51** 083052
[862] Felici F. *et al* 2012 *Plasma Phys. Control. Fusion* **54** 025002
[863] Felici F. *et al* 2013 *Fusion Eng. Des.* **89** 165–76
[864] Felici F. 2015 Enhancing current density profile control in tokamak experiments using iterative learning control *54th IEEE Conf. on Decision and Control.* (*Osaka, Japan 15–18 December 2015*) (available at: http://cdc2015.ieeecss.org/)
[865] Boyer M., Barton J., Schuster E., Luce T.C., Ferron J.R., Walker M.L., Humphreys D.A., Penaflor B.G. and Johnson R.D. 2013 *Plasma Phys. Control. Fusion* **55** 105007
[866] Maljaars E., Felici F., de Baar M.R., van Dongen J., Hogeweij G.M.D., Geelen P.J.M. and Steinbuch M. 2015 *Nucl. Fusion* **55** 023001
[867] Maljaars E. *et al* 2015 Simultaneous control of plasma profiles and neoclassical tearing modes with actuator management in tokamaks *Proc. 42nd EPS Conf. on Plasma Physics* (*Lisbon*, *June 2015*) p P1.184 (available at: https://info.fusion.ciemat.es/OCS/EPS2015PAP/pdf/P1.184.pdf)
[868] Maljaars E. *et al* 2017 *Nucl. Fusion* **57** 126063
[869] Maljaars E. and Felici F. 2017 *Fusion Eng. Des.* **122** 94–112
[870] Bosman T., Kudláček O., Fable E., van Berkel M., Felici F., Bock A., Luda T. and de Baar M.R. 2021 *Fusion Eng. Des.* **170** 112510
[871] Yu Y.W. *et al* 2019 *Nucl. Fusion* **59** 126036
[872] Blanken T., Felici F., Rapson C.J., de Baar M.R. and Heemels W.P.M.H. 2018 *Fusion Eng. Des.* **126** 87–103
[873] Blanken T., Felici F., Galperti C., Vu N.M.T., Kong M., Sauter O. and de Baar M.R. 2018 *Nucl. Fusion* **59** 026017
[874] Blanken T. *et al* 2019 *Fusion Eng. Des.* **147** 111211
[875] Valovic M. *et al* 2019 *Nucl. Fusion* **59** 106047
[876] Bourdelle C., Camenen Y., Citrin J., Marin M., Casson F.J., Koechl F. and Maslov M. 2018 *Nucl. Fusion* **58** 076028
[877] Koleman E., Welander A.S., La Haye R.J., Eidietis N.W., Humphreys D.A., Lohr J., Noraky V., Penaflor B.G., Prater R. and Turco F. 2014 *Nucl. Fusion* **54** 073020
[878] Maraschek M. *et al* 2005 *Nucl. Fusion* **45** 1369
[879] Henderson M. 2009 An overview of the ITER electron cyclotron H&CD system *34th Int. Conf. on Infrared, Millimeter, and Terahertz Waves* (IEEE) *(Busan, Korea, 21–25 September 2009)* pp 21–25 (available at: https://ieeexplore.ieee.org/xpl/conhome/5306513/proceeding)
[880] Oosterbeek J. *et al* 2008 *Rev. Sci. Instrum.* **79** 093503
[881] Doelman N. 2012 *EPJ Web of Conf.* **32** 04005
[882] Bongers W. *et al* 2009 *Fusion Sci. Technol.* **55** 188–203
[883] Volpe F. 2018 Oblique-ECE radial and phase detector of rotating magnetic Islands applied toAlignment and phase-locked modulation of ECCD for NTM stabilization (available at: https://arxiv.org/pdf/1302.7054.pdf)
[884] Biel W., de Baar M., Dinklage A., Felici F., König R., Meister H., Treutterer W. and Wenninger R. 2015 *Fusion Eng. Des.* **96** 8–15
[885] Biel W. *et al* 2022 *Fusion Eng. Des.* **179** 113122
[886] Hennen B., Westerhof E., Oosterbeek J.W., Nuij P.W.J.M., De Lazzari D., Spakman G.W., de Baar M. and Steinbuch M. 2009 *Fusion Eng. Des.* **84** 928–34

[887] Hennen B., Westerhof E., Nuij P.W.J.M., Oosterbeek J.W., de Baar M.R., Bongers W.A., Bürger A., Thoen D.J. and Steinbuch M. 2010 *Plasma Phys. Control. Fusion* **52** 104006

[888] Brand H.V. *et al* 2018 *Nucl. Fusion* **59** 016013

[889] Borgers D., Lauret M. and de Baar M.R. 2013 *Fusion Eng. Des.* **88** 2922–32

[890] Brand H.V., de Baar M.R., Lopes Cardozo N.J. and Westerhof E. 2012 *Nucl. Fusion* **53** 013005

[891] Witvoet G., Lauret M., de Baar M.R., Westerhof E. and Steinbuch M. 2011 *Nucl. Fusion* **51** 103043

[892] Witvoet G. 2011 *Nucl. Fusion* **51** 073024

[893] Witvoet G., Steinbuch M., de Baar M.R., Doelman N.J. and Westerhof E. 2012 *Nucl. Fusion* **52** 074005

[894] Bolder J., Witvoet G., de Baar M.R., van de Wouw N., Haring M.A.M., Westerhof E., Doelman N.J. and Steinbuch M. 2012 *Nucl. Fusion* **52** 074006

[895] Paley J., Felici F., Coda S. and Goodman T.P. 2009 *Plasma Phys. Control. Fusion* **51** 124041

[896] Berkel M.V., Witvoet G., de Baar M.R., Nuij P.W.J.M., ter Morsche H.G. and Steinbuch M. 2011 *Fusion Eng. Des.* **86** 2908–19

[897] Brand H.V., de Baar M.R., van Berkel M., Blanken T.C., Felici F., Westerhof E. and Willensdorfer M. 2016 *Plasma Phys. Control. Fusion* **58** 075002

[898] Lauret M., Felici F., Witvoet G., Goodman T.P., Vandersteen G., Sauter O. and de Baar M.R. 2012 *Nucl. Fusion* **52** 062002

[899] Lerche E., Lennholm M., Carvalho I.S., Dumortier P., Durodie F., Van Eester D., Graves J., Jacquet P. and Murari A. 2017 *Nucl. Fusion* **57** 036027

[900] Lennholm M. 2014 Real time control of the Sawtooth instability in fusions plasmas with large fast ion populations. Eindhoven *PhD Thesis 2 (Research NOT TU/e/Graduation TU/e), Mechanical Engineering* Technische Universiteit Eindhoven (https://doi.org/10.6100/IR783107)

[901] Bernert M. 2019 X-point radiation and detachment control at ASDEX Upgrade *IAEA Topical Meeting on Divertor Concepts* (*Vienna, 4–7 November 2019*) (available at: https://conferences.iaea.org/event/192/overview)

[902] Perek A. *et al* 2019 *Rev. Sci. Instrum.* **90** 123514

[903] Hommen G., de Baar M., Nuij P., McArdle G., Akers R. and Steinbuch M. 2010 *Rev. Sci. Instrum.* **81** 113504

[904] Hommen G., de Baar M., Citrin J., de Blank H.J., Voorhoeve R.J., de Bock M.F.M. and Steinbuch M. 2013 *Plasma Phys. Control. Fusion* **55** 025007

[905] Ravensbergen T. *et al* 2020 *Nucl. Fusion* **60** 066017

[906] Ravensbergen T. *et al* 2021 *Nat. Commun.* **12** 1105

[907] Koenders J.T.W., Wensing M., Ravensbergen T., Février O., Perek A. and van Berkel M. (TCV Team, EUROfusion MST1 Team) 2022 *Nucl. Fusion* **62** 066025

[908] Ravensbergen T., de Vries P.C., Felici F., Blanken T.C., Nouailletas R. and Zabeo L. 2017 *Nucl. Fusion* **58** 016048

[909] Bosman T., van Berkel M. and de Baar M.R. 2021-2 *J. Phys. Commun.* **5** 115015

[910] Fischer R., Dinklage A. and Pasch E. 2003 *Plasma Phys. Control. Fusion* **45** 1095–111

[911] Dodt D., Dinklage A., Fischer R., Bartschat K., Zatsarinny O. and Loffhagen D. 2008 *J. Phys. D: Appl. Phys.* **41** 205207

[912] Ford O., Svensson J., Beurskens M., Boboc A., Flanagan J., Kempenaars M., McDonald D.C. and Meakins A. (JET EFDA Contributors) 2009 Bayesian combined analysis of JET LIDAR, edge LIDAR and interferometry diagnostics *EPS 2009/Europhysics Conf. Abstracts (Sofia, Bulgaria, 29 June–3 July 2009)* vol 33E, ed M. Mateev and E. Benova (European Physical Society) p P–2.150 (available at: http://eps2009.uni-sofia.bg/)

[913] Dodt D., Fischer R., Korotkov A. and Eich T. (JET-EFDA Contributors) Electron density profiles from the probabilistic analysis of the lithium beam at JET *2009 EPS 2009/Europhysics Conf. Abstracts (Sofia, Bulgaria, 29 June–3 July 2009)* vol 33E pp P–2.148 (available at: http://eps2009.uni-sofia.bg/)

[914] Fischer R., Fuchs C.J., Kurzan B., Suttrop W. and Wolfrum E. (ASDEX Upgrade Team) 2010 *Fusion Sci. Technol.* **58** 675–84

[915] Rathgeber S.K., Fischer R., Fietz S., Hobirk J., Kallenbach A., Meister H., Pütterich T., Ryter F., Tardini G. and Wolfrum E. (the ASDEX Upgrade Team) 2010 *Plasma Phys. Control. Fusion* **52** 095008

[916] van Milligen B.P., Estrada T., Ascasíbar E., Tafalla D., López-Bruna D., Fraguas A.L., Jiménez J.A., García-Cortés I., Dinklage A. and Fischer R. 2011 *Rev. Sci. Instrum.* **82** 073503

[917] Reusch L.M., Galante M.E., Franz P., Johnson J.R., McGarry M.B., Stephens H.D. and Den Hartog D.J. (JET-EFDA Contributors) 2014 *Rev. Sci. Instrum.* **85** 11D844

[918] Galante M.E., Reusch L.M., Hartog D.J.D., Franz P., Johnson J.R., McGarry M.B., Nornberg M.D. and Stephens H.D. 2015 *Nucl. Fusion* **55** 123016

[919] Salewski M. *et al* 2018 *Fusion Sci. Technol.* **74** 23–36

[920] Fischer R., Giannone L., Illerhaus J., McCarthy P.J. and McDermott R.M. (ASDEX Upgrade Team) 2020 *Fusion Sci. Technol.* **76** 879–93

[921] Kwak S. *et al* (Wendelstein 7-X Team) 2021 *Rev. Sci. Instrum.* **92** 043505

[922] Kwak S., Svensson J., Bozhenkov S., Trimino Mora H., Höfel U., Pavone A., Krychowiak M., Langenberg A. and Ghim Y.C. (W7-X Team) 2021 Bayesian modelling of multiple plasma diagnostics at Wendelstein 7-X (arXiv:2103.07582)

[923] Fischer R. and Dinklage A. 2007 The concept of integrated data analysis of complementary experiments *Bayesian Inference and Maximum Entropy Methods in Science and Engineering, volume Conf. Proc. 954 (Saratoga Springs, NY, United States, 8–13 July 2007)* ed K.H. Knuth (AIP) pp 195–202 (available at: http://www.maxent2007.org/)

[924] Fischer R. and Dinklage A. 2004 *Rev. Sci. Instrum.* **75** 4237–9

[925] Fischer R., Wendland C., Dinklage A., Gori S. and Dose V. (the W7-AS Team) 2002 *Plasma Phys. Control. Fusion* **44** 1501–19

[926] Fischer R., Wolfrum E. and Schweinzer J. (the ASDEX Upgrade Team) 2008 *Plasma Phys. Control. Fusion* **50** 1–26

[927] Svensson J., Dinklage A., Geiger J., Werner A. and Fischer R. 2004 *Rev. Sci. Instrum.* **75** 4219–21

[928] Reusch L.M., Nornberg M.D., Goetz J.A. and Den Hartog D.J. 2018 *Rev. Sci. Instrum.* **89** 10K103

[929] Toussaint U.V. 2011 *Rev. Mod. Phys.* **83** 943

[930] Denk S.S. *et al* (the ASDEX Upgrade Team) 2018 *Plasma Phys. Control. Fusion* **60** 105010

[931] Denk S.S., Fischer R., Poli E., Maj O., Nielsen S.K., Rasmussen J., Stejner M. and Willensdorfer M. (the ASDEX Upgrade Team) 2020 *Commun. Comput. Phys.* **253** 107175

[932] Denk S.S. *et al* (the ASDEX Upgrade Team) 2021 *Plasma Phys. Control. Fusion* **63** 015003

[933] McDermott R.M. *et al* (ASDEX Upgrade Team) 2017 *Rev. Sci. Instrum.* **88** 073508

[934] Working Group 1 of the Joint Committee for Guides in Metrology (JCGM/WG 1) 2008 Evaluation of measurement data—Guide to the expression of uncertainty in measurement, volume JCGM 100:2008 BIPM, IEC,

IFCC, ILAC, ISO, IUPAC, IUPAP and OIML (available at: https://www.bipm.org/documents/20126/2071204/JCGM_100_2008_E.pdf)
[935] Dose V. and von der Linden W. 1999 Outlier tolerant parameter estimation *Maximum Entropy and Bayesian Methods* ed W. von der Linden, V. Dose, R. Fischer and R. Preuss (Kluwer Academic Publishers)
[936] Rathgeber S.K., Fischer R., Fietz S., Hobirk J., Kallenbach A., Meister H., Pütterich T., Ryter F., Tardini G. and Wolfrum E. (the ASDEX Upgrade Team) 2013 *Plasma Phys. Control. Fusion* **55** 025004
[937] Wendler D., Dux R., Fischer R., Griener M., Wolfrum E., Birkenmeier G. and Stroth U. (the ASDEX Upgrade Team) 2022 *Plasma Phys. Control. Fusion* **64** 045004
[938] Chilenski M.A., Greenwald M., Marzouk Y., Howard N.T., White A.E., Rice J.E. and Walk J.R. 2015 *Nucl. Fusion* **55** 023012
[939] Wang T., Mazon D., Svensson J., Li D., Jardin A. and Verdoolaege G. 2018 *Rev. Sci. Instrum.* **89** 063505
[940] Fischer R., Hanson K.M., Dose V. and von der Linden W. 2000 *Phys. Rev. E* **61** 1152
[941] Bock A. *et al* (the ASDEX Upgrade Team) 2017 *Nucl. Fusion* **57** 126041
[942] Bock A. *et al* (the ASDEX Upgrade Team) 2018 *Phys. Plasmas* **25** 056115
[943] McCarthy P.J., Schneider W. and Martin P. 1999 The CLISTE interpretive equilibrium code *Technical Report IPP5/85* (Max-Planck-Institut für Plasmaphysik)
[944] McCarthy P.J. 2012 *Plasma Phys. Control. Fusion* **54** 015010
[945] Lao L.L., St. John H.E., Peng Q., Ferron J.R., Strait E.J., Taylor T.S., Meyer W.H., Zhang C. and You K.I. 2005 *Fusion Sci. Technol.* **48** 968–77
[946] Brix M., Hawkes N., Boboc A., Drozdov V. and Sharapov S. 2008 *Rev. Sci. Instrum.* **79** 10F325, 11
[947] Blum J., Boulbe C. and Faugeras B. 2012 *J. Comput. Phys.* **231** 960–80
[948] Fischer R. *et al* (ASDEX Upgrade Team) 2016 *Fusion Sci. Technol.* **69** 526–36
[949] Fischer R., Bock A., Burckhart A., Ford O.P., Giannone L., Igochine V., Weiland M. and Willensdorfer M. (ASDEX Upgrade Team) 2019 *Nucl. Fusion* **59** 056010
[950] Rampp M., Preuss R. and Fischer R. (the ASDEX Upgrade Team) 2016 *Fusion Sci. Technol.* **70** 1–13
[951] Giannone L. *et al* (the ASDEX Upgrade Team) 2021 *Nucl. Fusion* **61** 066021
[952] Weiland M., Bilato R., Dux R., Geiger B., Lebschy A., Felici F., Fischer R., Rittich D. and Van Zeeland M. (the ASDEX Upgrade team, and the Eurofusion MST1 team) 2018 *Nucl. Fusion* **58** 082032
[953] Budny R.V. *et al* 1992 *Nucl. Fusion* **32** 429
[954] Burckhart A., Ford O., Reich M. and Wolf R. (the ASDEX Upgrade Team) 2015 Design of the new imaging motional Stark effect diagnostic at ASDEX Upgrade *EPS 2015/Europhysics Conf. Abstracts (Lisbon, Portugal, 22–26 June 2015)* vol 39E, ed R. Bingham, W. Suttrop, S. Atzeni, R. Foest, K. McClements, B. Goncalves, C. Silva and R. Coelho (European Physical Society) p P1.143 (available at: https://info.fusion.ciemat.es/OCS/EPS2015PAP/pdf/P1.143.pdf)
[955] Mlynek A., Fischer R., Ford O., Lang P. and Plöckl B. (ASDEX Upgrade Team) 2016 First results from the new sub-millimeter polarimeter on the ASDEX Upgrade tokamak *21st Topical Conf. on High Temperature Plasma Diagnostics (HTPD 2016) (Madison, Wisconsin, US, 5–9 June 2016)* (available at: https://hdl.handle.net/11858/00-001M-0000-002B-0593-B)
[956] Fischer R. *et al* (ASDEX Upgrade Team) 2013 Magnetic equilibrium reconstruction using geometric information from temperature measurements at ASDEX Upgrade *40th EPS Conf. on Plasma Physics (Espoo, Finlan, 1–5 July 2013)* ed V. Naulin *et al* vol 37D (European Physical Society) p P2.139 (available at: https://info.fusion.ciemat.es/OCS/EPS2013PAP/pdf/P2.139.pdf)
[957] Fischer R., Giannone L., Lackner K., McDermott R.M., Viezzer E. and Zehrfeld H.P. (ASDEX Upgrade Team) 2015 Effect of measured toroidal flows on tokamak equilibria *42th EPS Conf. on Plasma Physics (Lisbon, Portugal, 22–26 June 2015)* (European Physical Society) p P1.117 (available at: https://info.fusion.ciemat.es/OCS/EPS2015PAP/pdf/P1.117.pdf)
[958] Madsen B., Salewski M., Heidbrink W.W., Stagner L., Podestà M., Lin D., Garcia A.V., Hansen P.C. and Huang J. 2020 *Nucl. Fusion* **60** 066024
[959] Salewski M. *et al* 2012 *Nucl. Fusion* **52** 103008
[960] Salewski M. *et al* 2013 *Nucl. Fusion* **53** 063019
[961] Salewski M. *et al* 2014 *Nucl. Fusion* **54** 023005
[962] Moseev D., Salewski M., Garcia-Munoz M., Geiger B. and Nocente M. 2018 *Rev. Mod. Plasma Phys.* **2** 7
[963] Eriksson J. *et al* 2019 *Plasma Phys. Control. Fusion* **61** 014027
[964] Salewski M. *et al* 2017 *Nucl. Fusion* **57** 056001
[965] Eriksson J. *et al* 2015 *Nucl. Fusion* **55** 123026
[966] Salewski M. *et al* 2016 *Nucl. Fusion* **56** 106024
[967] Weiland M., Geiger B., Jacobsen A.S., Reich M., Salewski M. and Odstrčil T. 2016 *Plasma Phys. Control. Fusion* **58** 025012
[968] Weiland M., Bilato R., Geiger B., Schneider P.A., Tardini G., Garcia-Muñoz M., Ryter F., Salewski M. and Zohm H. 2017 *Nucl. Fusion* **57** 116058
[969] Jacobsen A.S., Salewski M., Geiger B., Korsholm S.B., Leipold F., Nielsen S.K., Rasmussen J., Stejner M. and Weiland M. 2016 *Plasma Phys. Control. Fusion* **58** 042002
[970] Jacobsen A.S. *et al* 2016 *Plasma Phys. Control. Fusion* **58** 045016
[971] Rasmussen J. *et al* 2016 *Nucl. Fusion* **56** 112014
[972] Madsen B., Salewski M., Huang J., Jacobsen A.S., Jones O. and McClements K.G. 2018 *Rev. Sci. Instrum.* **89** :10D125
[973] Madsen B. *et al* 2020 *Plasma Phys. Control. Fusion* **62** 115019
[974] Su J. *et al* 2021 *Plasma Sci. Technol.* **23** 095103
[975] Geiger B., Karpushov A.N., Duval B.P., Marini C., Sauter O., Andrebe Y., Testa D., Marascheck M., Salewski M. and Schneider P.A. 2017 *Plasma Phys. Control. Fusion* **59** 115002
[976] Salewski M. *et al* 2018 *Nucl. Fusion* **58** 036017
[977] Salewski M. Fast-ion diagnostic in fusion plasmas by velocity-space tomography *Dr Techn. Thesis* Technical University of Denmark
[978] Heidbrink W.W., Luo Y., Burrell K.H., Harvey R.W., Pinsker R.I. and Ruskov E. 2007 *Plasma Phys. Control. Fusion* **49** 1457–75
[979] Salewski M. *et al* 2014 *Plasma Phys. Control. Fusion* **56** 105005
[980] Jacobsen A.S., Salewski M., Eriksson J., Ericsson G., Korsholm S.B., Leipold F., Nielsen S.K., Rasmussen J. and Stejner M. 2015 *Nucl. Fusion* **55** 053013
[981] Jacobsen A.S., Binda F., Cazzaniga C., Eriksson J., Hjalmarsson A., Nocente M., Salewski M. and Tardini G. 2017 *Rev. Sci. Instrum.* **88** 073506
[982] Salewski M. *et al* 2015 *Nucl. Fusion* **55** 093029
[983] Salewski M. *et al* 2016 *Nucl. Fusion* **56** 046009
[984] Galdon-Quiroga J. *et al* 2018 *Plasma Phys. Control. Fusion* **60** 105005
[985] Heidbrink W.W., Garcia A., Boeglin W. and Salewski M. 2021 *Plasma Phys. Control. Fusion* **63** 055008

[986] Schmidt B.S. *et al* 2021 *Rev. Sci. Instrum.* **92** 053528
[987] Heidbrink W.W. 2010 *Rev. Sci. Instrum.* **81** 10D727
[988] Nocente M. *et al* 2020 *Plasma Phys. Control. Fusion* **62** 014015
[989] Salewski M. *et al* 2010 *Nucl. Fusion* **50** 035012
[990] Lawson C.L. and Hanson R.J. 1974 *Solving Least Squares Problems* (Prentic-Hall)
[991] Salewski M. *et al* 2019 *J. Instrum.* **14** C05019
[992] Stagner L. and Heidbrink W.W. 2017 *Phys. Plasmas* **24** 092505
[993] Järleblad H., Stagner L., Salewski M., Eriksson J., Benjamin S., Madsen B., Nocente M., Rasmussen J. and Schmidt B.S. 2021 *Rev. Sci. Instrum.* **92** 043526
[994] Stagner L., Heidbrink W.W., Salewski M., Jacobsen A.S., Geiger B. and Diii-d T. (ASDEX Upgrade Teams) 2022 *Nucl. Fusion* **62** 026033